DEPORTMENT OF RADIONUCLIDES IN COPPER CONCENTRATE FROM OLYMPIC DAM

MARK EDWARD ROLLOG

This thesis is submitted for the degree of Doctor of Philosophy

in the

School of Chemical Engineering and Advanced Materials

Faculty of Engineering, Computer and Mathematical Sciences

at

The University of Adelaide

THE UNIVERSITY of ADELAIDE

August 2019

TABLE OF CONTENTS

ABSTRACT

The Olympic copper-gold province of South Australia is home to the world's largest uranium resource, representing at least 23% of the known global uranium budget. The primary commodity produced is copper, with secondary Au, Ag, and U (as U_3O_8) also recoverable in economic quantities. Processing the complex, fine-grained ore from Olympic Dam involves multiple, customisable stages of physical and chemical separation of target elements from non-target elements. During some stages of processing, deleterious components of the ore may behave adversely, affecting recovery efficiency or purity of product. Of particular interest to process engineers are daughter radionuclides (RNs) created from decay of ^{232}Th, ^{235}U, and especially ^{238}U. Specific activities of ^{226}Ra, ^{210}Pb, and ^{210}Po are such that even concentrations of parts-per-trillion may be above acceptable levels for marketable copper concentrate.

Most conventional analytical platforms emphasise either sensitivity (solution inductively coupled plasma mass spectrometry, thermal ionisation mass spectrometry) or high-resolution imaging (transmission electron microscopy, atom probe tomography). Ultra-trace-level RN concentrations combined with the extremely fine-grained nano-included mineral textures of Olympic Dam ore present an unusual challenge for researchers, in that few analytical techniques excel in both sensitivity and resolution. A comparison of available methods yielded excellent results from the CAMECA nanoscale secondary ion mass spectrometry (nanoSIMS) platform, capable of detecting (for the first time) extremely low RN signals in minerals with sub-micron resolution; consequently, nanoSIMS was chosen as the primary analytical method for this project.

Subsequent to extensive method development and testing, over 3200 isotopic spatial distribution maps were collected on mineral samples from raw ore material, flotation concentrate, and acid-leached concentrate provided by BHP Olympic Dam. A qualitative RN

budget has been created, prioritising minerals which contain significant RNs but also including unexpected minor host minerals and surficial adherence.

Four manuscripts have resulted from these analyses, detailing RN host capabilities of various minerals including uraninite, brannerite, coffinite, thorianite, euxenite, apatite, fluorite, xenotime, monazite, baryte, anglesite, and Sr- and Ca-rich alunite-series phases. Mechanisms for surface-sequestration of RNs in high surface area minerals such as covellite and molybdenite have been identified, as well as electrokinetic effects responsible for substantial uptake of RNs on the surface of sulphide minerals.

Additionally, diffusion experiments were performed on synthetic minerals to determine mobility of Sr, Ba, Pb, and Ra under varying conditions common to mineral processing. Two manuscripts have resulted from these investigations, emphasizing that baryte and anglesite are well-suited to remove substantial amounts of Ra and Pb from processing streams, especially during acid-leaching, through coupled dissolution-reprecipitation mechanisms. Laser ablation inductively coupled plasma mass spectrometry and nanoSIMS both provided excellent visual evidence for Ra uptake, well in agreement with published results from other research teams.

As a whole, the data set produced during this project has greatly increased our understanding of the deportment of radionuclides at Olympic Dam – and in uranium-bearing ore systems in general. Provided these data, process engineers are now better-suited to design and implement efficient RN removal procedures, thereby resulting in cleaner ore concentrates available to the global marketplace.

DECLARATION

I certify that this work contains no material which has been accepted for the award of any other degree or diploma in my name in any university or other tertiary institution and, to the best of my knowledge and belief, contains no material previously published or written by another person, except where due reference has been made in the text. In addition, I certify that no part of this work will, in the future, be used in a submission in my name for any other degree or diploma in any university or other tertiary institution without the prior approval of the University of Adelaide and where applicable, any partner institution responsible for the joint award of this degree.

I acknowledge that copyright of published works contained within this thesis resides with the copyright holder(s) of those works.

I also give permission for the digital version of my thesis to be made available on the web, via the University's digital research repository, the Library Search and also through web search engines, unless permission has been granted by the University to restrict access for a period of time.

I acknowledge the support I have received for my research through the provision of an Australian Government Research Training Program Scholarship.

Signed _____ Date 24.08.19

ACKNOWLEDGEMENTS

I would like to extend my warmest thanks and gratitude to my supervisors, Prof. Nigel Cook and Dr. Kathy Ehrig. Nigel, your constant attention yet unwavering patience was exactly the feedback I needed to be productive but not overstressed. Kathy, your attention to detail and honest evaluations were a most welcome addition and served as the optimal example of an industry-academia partnership. It was a pleasure and a privilege working with both of you, and I hope to do so again in the future.

My successes would have been impossible if not for the unsung heroes behind the instruments – the technical staff. Being a member myself, I know only too well the potential for being overworked, underpaid, overqualified, and underappreciated. The decades of cumulative expertise provided by Mr. Ken Neubauer, Dr. Sarah Gilbert, Dr. Benjamin Wade, and Dr. Animesh Basak from Adelaide Microscopy and Dr. Paul Guagliardo from the Centre for Microscopy, Characterisation, and Analysis made this project progress as smoothly as one could hope. Additionally, invaluable input and technical expertise was provided by Dr. Cristi Ciobanu, Dr. Tony Hooker, Prof. Matt Kilburn, Mr. Angus Netting, Dr. Tony Milnes, Dr. Jason Gascooke, Dr. Steven Reddy, Dr. David Saxey, Dr. Denis Fougerouse, Dr. William Rickard, Dr. Alec Walsh, and Dr. Jon Tyler.

It is also vital to remember that I was not working alone, but as part of a team. The dozens of members of the ARC Research Hub (too numerous to name) were all instrumental in my success, as was the staff of IMER. I'd like to single out Prof. Stephen Grano and Dr. Ruth Shaw for their organisational leadership, as well as Louise Beazley for keeping the wheels turning. The teams from IMER, IPAS, UQ, Flinders, Monash, and BHP Olympic Dam have cooperated to accomplish a difficult task, and have provided the scientific community with valuable insight on multiple research fronts. I am proud to have been a member.

And finally, I'd like to thank all the other students experiencing the same trials and tribulations as myself, in both Nigel's group and Cristi's: Alkis, Danielle, Jing, Liam, Luke, Matt, Marija, Max, Nick, Sasha, Wenyuan, William, and Urs. Even the most difficult of times aren't so bad when you have good company.

PREFACE

This thesis is based on six manuscripts which have been published, accepted for publication, or submitted for publication in international peer-reviewed journals. The journals to which these manuscripts were submitted include *Geochemistry: Exploration, Environment, Analysis* (Chapter 3, published); *Minerals* (Chapter 4, published); *Geochemical Transactions* (Chapter 5, in review); *Hydrometallurgy* (Chapter 6, in review); *Minerals Engineering* (Chapter 7, in review); and *Applied Geochemistry* (Chapter 8, in review). Chapters 3, 4, 6, and 7 are similar in nature and are all based primarily on nanoscale secondary ion mass spectrometry (nanoSIMS) spatial distribution isotope maps of samples provided by BHP Olympic Dam. Chapters 5 and 8 are based around laser ablation inductively coupled plasma mass spectrometry (LA-ICP-MS) analyses of synthetic mineral analogues.

The two papers and four manuscripts which form the foundation of this thesis are:

1. Rollog, M., Cook, N.J., Guagliardo, P., Ehrig, K., Kilburn, M., 2019. *In situ* spatial distribution mapping of radionuclides in minerals by nanoSIMS. Geochemistry: Exploration, Environment, Analysis 19(3), 245-254. doi:10.1144/geochem2018-038

2. Rollog, M., Cook, N.J., Guagliardo, P., Ehrig, K.J., Ciobanu, C., Kilburn, M., 2019. Detection of trace elements/isotopes in Olympic Dam copper concentrates by nanoSIMS. Minerals 9(6), 336. doi:10.3390/min9060336

3. Rollog, M., Cook, N.J., Guagliardo, P., Ehrig, K.J., Gilbert, S.E., Kilburn, M., 2019. Intermobility of barium, strontium, and lead in chloride and sulphate leach solution. Geochemical Transactions 20(4), 1-23. doi:10.1186/s12932-019-0064-0

4. Rollog, M., Cook, N.J., Guagliardo, P., Ehrig, K.J., Kilburn, M., 2019. Radionuclide-bearing minerals in Olympic Dam copper concentrates. Hydrometallurgy 190, 105153 doi:10.1016/j.hydromet.2019.105153

5. Rollog, M., Cook, N.J., Guagliardo, P., Ehrig, K.J., Kilburn, M., 2019. Radionuclide distributions in Olympic Dam copper concentrates: the importance of minor hosts, incorporation mechanisms, and mineral surfaces. Minerals Engineering (in review, submitted 19 June 2019).

6. Rollog, M., Cook, N.J., Ehrig, K.J., Gilbert, S.E., 2019. Rapid, competitive radium uptake in strontium, barium, and lead sulphates during sulphuric acid leaching. Applied Geochemistry (revision submitted 26 November 2019).

An introduction and brief literature review of existing research is presented in Chapter 1. Chapters 2 and 9 describe the methodology and instrumentation used in gathering data for this study. A summary of the results as well as suggestions for future avenues of research are provided in Chapter 10.

Supplementary information for Chapter 2 and additional material comprised of peer-reviewed conference abstracts and co-authored papers – all generated during the Ph.D. candidature – are included in Chapter 11, as follows:

A. Appendix A for Chapter 2

B. Rollog, M., Cook, N.J., Schmandt, D.S., Clarke, M., Ottaway, D.J., Spooner, N.A., Kalnins, C.A.G., Ehrig, K., Ciobanu, C.L., Triffett, B., Grano, S., 2016. Identification and characterisation of extremely low-concentration non-target components in copper ores and concentrates (abstract, oral presentation). Australian Earth Science Conference (AESC), Adelaide, Australia, 26-30 June 2016. p. 386.

C. Rollog, M., Cook, N.J., Schmandt, D.S., Clarke, M., Ottaway, D.J., Spooner, N.A., Kalnins, C.A.G., Ehrig, K., Ciobanu, C.L., Triffett, B., Grano, S., 2016. Identifying and characterising non-target elements in South Australian iron oxide-copper-gold (IOCG) deposits (poster). Australian Earth Science Conference (AESC), Adelaide, Australia, 26-30 June 2016.

D. Rollog, M., Cook, N.J., Schmandt, D.S., Clarke, M., Ottaway, D.J., Spooner, N.A., Kalnins, C.A.G., Ehrig, K., Ciobanu, C.L., Triffett, B., Grano, S., 2016. A pathway to improving methods for remediation of uranium and daughter products from South Australian iron oxide-copper-gold (IOCG) deposits (abstract, oral presentation). Australasian Radiation Protection Society (ARPS) conference, Adelaide, Australia, 11-14 September 2016.

E. Rollog, M., Cook, N.J., Schmandt, D.S., Ehrig, K., Triffett, B., 2016. Hosts for non-target uranium and associated radionuclides in South Australian copper ores and concentrates (abstract, oral presentation). Chemeca Conference, Adelaide, Australia, 25-28 September 2016.

F. Rollog, M., Cook, N.J., Guagliardo, P., Kilburn, M.R., Ehrig, K., Ciobanu, C.L., 2017. NanoSIMS mapping of ^{210}Rn and ^{226}Ra in South Australian copper concentrates (abstract, oral presentation). Goldschmidt Conference, Paris, France, 13-18 August 2017. https://goldschmidtabstracts.info/2017/3392.pdf.

G. Rollog, M., Cook, N.J., Guagliardo, P., Kilburn, M.R., Ehrig, K., Ciobanu, C.L., 2018. Nanoscale spatial distribution maps of trace elements/isotopes in South Australian copper concentrates (abstract, oral presentation). Goldschmidt Conference, Boston, MA, 12-17 August 2018. https://goldschmidtabstracts.info/2018/2177.pdf.

H. Rollog, M., Cook, N.J., Guagliardo, P., Ciobanu, C.L., Ehrig, K., Kilburn, M.R., 2018. Mobility of radionuclides in the Olympic Dam Cu-U-Au-Ag deposit, South Australia (extended abstract). Proceedings, 15th Quadrennial International Association on the Genesis of Ore Deposits (IAGOD) symposium, Salta, Argentina, 28-31 August 2018. pp. 183-184.

I. Rollog, M., Cook, N.J., Guagliardo, P., Ciobanu, C.L., Ehrig, K., Kilburn, M.R., 2019. *In situ* mapping of radionuclides in Olympic Dam copper concentrates by nanoSIMS (abstract, oral presentation). AusIMM Uranium 2019 conference, Adelaide, Australia, 4-5 June 2019.

J. Cook, N.J., Ehrig, K.J., Rollog, M., Ciobanu, C.L., Lane, D.J., Schmandt, D.S., Owen, N.D., Hamilton, T., Grano, S., 2018. ^{210}Pb and ^{210}Po in geological and related anthropogenic materials: implications for their mineralogical distribution in base metal ores. Minerals 8(5), 211, 1-28, doi:10.3390/min8050211

K. Schmandt, D.S., Cook, N.J., Ehrig, K., Gilbert, S., Wade, B.P., Rollog, M., Ciobanu, C.L., Kamenetsky, V.S., 2019. Uptake of trace elements by baryte during copper ore processing: A case study from Olympic Dam, South Australia. Minerals Engineering 135, 83–94. doi:10.1016//j.mineng.2019.02.034

L. Owen, N.D., Cook, N.J., Rollog, M., Ehrig, K.J., Schmandt, D.S., Ram, R., Brugger, J., Ciobanu, C.L., Wade, B., Guagliardo, P., 2019. REE-, Sr- Ca-aluminum-phosphate-sulfate minerals of the alunite supergroup and their role as hosts for radionuclides. American Mineralogist, (accepted for publication July 16, 2019).

M. Owen, N.D., Cook, N.J., Ram, R., Etschmann, B., Ehrig, K., Schmandt, D.S., Rollog, M., Guagliardo, P., Brugger, J., 2019. A sponge for radionuclides: A study on the dynamic

uptake of lead by synthetic aluminium-phosphate-sulphates. The Journal of Hazardous Materials. (submitted 28 August 2019).

Chapter 12 concludes this dissertation by providing a comprehensive bibliography of all works referenced within the manuscripts, chapters, and additional material submitted herein.

Chapter 1

Introduction

Chapter 1: Introduction

Humankind has spent centuries, and in some cases millennia, perfecting methods for extraction of valuable metals and non-metals from the Earth. As time progressed and exceedingly rich metal deposits were discovered, exploited, and then exhausted, technology advanced to allow miners to economically exploit deeper, more complex, lower concentration ores.

Traditionally, end-products headed for the world market have been allowed reasonable levels of impurities so long as performance of those products was not affected. Although increased demand and higher quality standards have resulted in the reduction of allowable impurities in products such as copper concentrate, a range of contaminant elements (e.g., Ni, Zn, As, Pb, Sb, F) may still be allowed, even if financial penalties may be imposed (Lane et al., 2016).

Global copper refineries currently produce around 23 Mt (valued at ~USD 150 billion) annually (www.statista.com). Though not ubiquitous, uranium is not uncommon in copper deposits and may even be present in concentrations at which it may itself be economic to extract. Although uranium (and thorium, if present) are relatively simple to separate from copper concentrate via the application of relatively straightforward hydrometallurgical procedures, the daughter products from radioactive decay may present a more significant challenge. These radionuclides thus represent a special category of "non-target elements" and need to be carefully monitored due to the extremely low concentration limits permissible in concentrates for sale on world markets.

Processing techniques have remained largely unchanged over the years, even if efficiencies have been vastly improved in some areas. Froth flotation, solvent extraction, and electrowinning/electrorefining processing techniques have all been in common industrial use for roughly a century or less. Even with technological advancements in processing methods of

all kinds, and the improved optimisation of processing circuits allowed by advances in real-time sensing and digital plant modelling, there still exist major challenges to producing high quality raw materials for world markets with ever decreasing concentrations of deleterious elements. This is particularly valid for the reduction/elimination of daughter products from radioactive decay, where successful innovation in extractive metallurgy is dependent on a comprehensive understanding of the deportment of these unwanted components. Despite some verifiable facts underpinned by theory and a range of logical assumptions about the likely distribution of U-238 decay chain radionuclides in Cu-U ores and processing circuits, there was, at the start of this Ph.D. project, no comprehensive mineral-by-mineral documentation of radionuclide distributions in any active mining-processing operation. The work reported here is intended to fill this research gap.

1.1 Background

1.1.1 Radioactive decay

Not recognised as hazardous materials until around 100 years ago (Martland et al.,1925), the natural radioactive daughters of ^{238}U, ^{235}U, and ^{232}Th decay represent hidden, but omnipresent components of any ore containing U or Th. In the Olympic Dam system, daughters from the ^{232}Th and ^{235}U decay chains have concentrations such that they are of little concern in mining-processing operations. Activities of these daughters are too low to accumulate during the timeframes of mine-to-concentrate-to-smelter processing (days to months). The ^{238}U decay chain, however, does have a few members which have the right combination of half-life and concentration to accumulate in various materials within the processing circuit. Figure 1.1 shows the ^{238}U decay chain, highlighting radioisotopes towards the end of the decay chain which are a particular focus of this thesis because of their half-lives, concentrations and

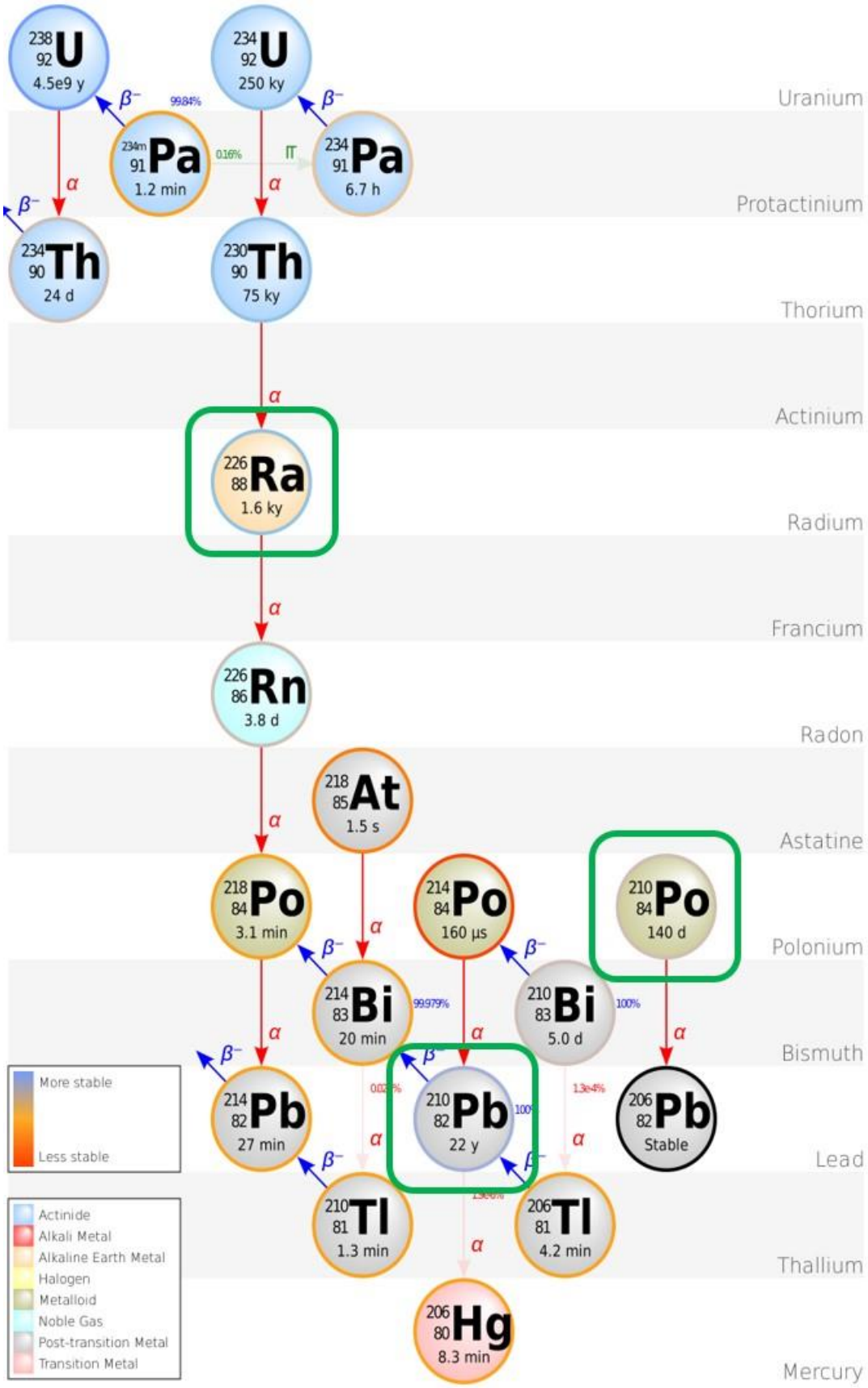

Figure 1.1. Schematic illustration of the ^{238}U decay chain with half-lives. The isotopes of interest are circled in green. Modified by Mark Rollog based on the "Decay Chain of Uranium-238" svg image by Wikipedia contributor ThaLibster.

geochemical behaviour. In addition to these, ^{226}Ra also is also an isotope of interest due to its chemical similarity to Pb, at least with respect to sulphate chemistry.

1.1.2 Olympic Dam

The natural samples analysed during this project were provided by BHP Olympic Dam, owner and operator of the Olympic Dam mine, processing plant, smelter and refinery operation located approximately 525 kilometres NNW of Adelaide, South Australia. As such, brief descriptions of the deposit, its geology, mineralogy, and processing operations are included to provide context for the project and to better understand the nature of research undertaken.

Discovered in 1975 under 350 m of sedimentary cover and first described a few years later (Roberts and Hudson, 1983), the Olympic Dam Cu-U-Au-Ag deposit boasts a (June 2016) reserve of 10 727 Mt at 0.72% Cu, 250 ppm U_3O_8, 0.3 g/t Au and 1.0 g/t Ag (BHP, 2018). Early description of the deposit formed the basis for a new class of magmatic-hydrothermal ore deposits, so-called iron oxide copper gold (or IOCG) deposits (Hitzman et al., 1992) that have since been recognised on all continents. IOCG deposits are conspicuous by the dominance of iron oxides (hematite and/or magnetite) over all other minerals. Although many IOCG systems are relatively enriched in uranium (e.g., Barton, 2014), Olympic Dam is unique in that uranium is present at concentrations at which it can be economically exploited. It is currently the world's largest known uranium deposit, third largest gold deposit, and fifth largest copper deposit (Ehrig et al., 2012). Mining operations commenced in 1988 producing copper cathode, gold and silver bullion, and uranium oxide concentrate (UOC).

The deposit lies within the Olympic Dam Breccia Complex (Reeve et al., 1990), which is in turn hosted entirely within, and largely derived from, the albitised Roxby Downs Granite (RDG). Olympic Dam is the largest of many IOCG systems on the eastern margin of the Gawler Craton (the Olympic Cu-Au Province; Skirrow et al., 2007; Reid, 2019). These deposits, which

display many similarities in terms of mineralogy despite divergent host rocks are considered to be precipitated from hydrothermal fluids associated with the Hiltaba Suite, of which the RDG is affiliated, and the co-genetic extrusive Gawler Range Volcanics (Fanning et al., 1988; Flint, 1993; Creaser and Cooper, 1993; Johnson and Cross, 1995). Together, these magmatic rocks are the product of the 1600-1585 Ma Gawler Silicic Large Igneous Province (LIP; Allen et al., 2008) contemporaneous with break-up of the Columbia palaeosupercontinent. Although a ~1590 Ma age for Olympic Dam has been established for some time (Johnson and Cross, 1995), the timing of RDG emplacement and Olympic Dam formation has recently been better constrained from a combination of U-Pb dating of RDG-hosted magmatic zircon (Cherry et al., 2018) and hydrothermal hematite (Courtney-Davies et al., 2019) at ~1593 Ma.

Extensive research at Olympic Dam and adjacent prospects over the past decade have recognised the impact of several subsequent geological events, including the 1565-1540 Ma Kararan orogeny (Flint, 1993), a less well-defined event possibly associated with the long-lived Musgravian orogeny in Central Australia at 1220-1120 Ma (Cherry et al., 2017), intrusion of the 830-800 Ma Gairdner LIP dike swarm basalts and dolerites (Huang et al., 2015), and the 514-490 Ma Delamerian orogeny (Foden et al., 2006). Debate has centred on whether these events contributed additional metals or merely provided the heat and fluids necessary to drive observed cycles of replacement, remobilisation and recrystallisation that have been recognised in a wide range of minerals from Olympic Dam and elsewhere in the Olympic Cu-Au Province.

The Olympic Dam deposit is enriched in at least 40 elements relative to crustal values (Ehrig et al., 2012). As a result, the mineralogy of the deposit is extraordinarily complex (Ehrig et al., 2012, 2017) and has received much attention in recent years as part of efforts to better constrain ore genesis, and for mine planning and processing optimisation (i.e. geometallurgy). Much of the resource consists of a hematite breccia (Roberts and Hudson, 1983; Ehrig et al., 2012, 2017 and references therein). Ores are dominantly made up of hematite (up to 80% of the ore;

Verdugo-Ihl et al., 2017), copper minerals (bornite, chalcopyrite and chalcocite; Ehrig et al., 2012; Ciobanu et al., 2017a), and a wide range of gangue minerals, dominated by iron oxides but also including quartz, feldspars (Kontonikas-Charos et al., 2017), siderite and other carbonates (Apukhtina, 2016), chlorite, pyrite, baryte (Schmandt et al., 2019b), fluorite (Schmandt, 2019) and apatite (Krneta et al., 2016, 2017). Uranium minerals are represented by uraninite, coffinite and brannerite in approximately equal abundance (Macmillan et al., 2016, 2017), although minor yet measurable U is also noted in hematite (Ciobanu et al., 2013; Verdugo-Ihl et al., 2017) and many other gangue minerals. The deposit contains significant concentrations of rare earth elements, dominated by bastnäsite (Ciobanu et al., 2017b; Schmandt et al., 2017), with lesser florencite and xenotime (Schmandt et al., 2019a), synchysite, and complex phosphate-sulphates of the alunite supergroup (Owen et al., 2019). Mineral textures and relationships between species are equally complex, with widespread evidence for heterogeneity down to the nanoscale (e.g., Ciobanu et al., 2019; Verdugo-Ihl et al., 2019b).

The deposit is roughly zoned with regard to copper mineralisation and progresses from pyrite → chalcopyrite → bornite → chalcocite from the margin to the centre (Reeve et al., 1990; Ehrig et al., 2012). Zoning patterns are considered to be primary features and have not been destroyed during later overprinting (Ehrig et al., 2012, 2017; Dmitrijeva et al., 2019; Verdugo-Ihl et al., 2019a). At least two stages of uraninite deposition have been identified. Early high-temperature, high-Pb uraninites are 10-50 µm euhedral cubic crystals, while later, low-Pb generations exhibit zonation, cob-web structures, and are suggestive of low temperature (<250 ˚C) hydrothermal formation (Macmillan et al., 2016). High precision $^{238}U/^{235}U$ analysis (Kirchenbaur et al., 2016) is indicative of uranium originating from the host granitoid, felsic volcanic or similar igneous shallow crustal source, but also indicates the possible addition of uranium between 1590 Ma and 500 Ma.

1.2 Ore processing and radionuclide distributions

Processing circuits at Olympic Dam are described in BHP Billiton (2009). Ores are crushed and ground to a P_{80} of -32 μm prior to froth flotation. Uranium is recovered via mildly aggressive oxidative, sulphuric acid leaching of Cu-sulphide depleted flotation tailings (8-12 hours at pH = 1-1.5). Uranium is then extracted from the leach liquors via solvent extraction, ammonium diuranate precipitation, and calcination to produce UOC. Uranium is also recovered from sulphuric acid leaching of flotation concentrates, a step primarily designed to remove fluorite prior to smelting (Ragozzini and Sparrow, 1987).

As in any processing operation, care must be taken to minimise concentrations of non-target elements in concentrates. Olympic Dam ores do not contain high levels of the more common non-target (penalty) elements such as As, Sb, Bi or Pb (e.g., Lane et al., 2016). There needs, however, to be careful monitoring of the concentrations of radionuclides (RNs) produced from the decay of Uranium-238, notably ^{226}Ra, ^{210}Pb, and ^{210}Po. These short-lived, high specific activity RNs may become relatively enriched in flotation concentrates compared to ore, and at sufficiently high concentrations may impact downstream processing. Notably, the more volatile ^{210}Po readily vaporises as diatomic Po_2 and accumulates as dust in the smelter gas cleaning circuit.

Radionuclide activities in representative flotation feed (ore), unleached copper concentrate and leached copper concentrate samples are given in Table 1.1. There is a marked increase in all RN activities from ore to flotation concentrate while retaining secular equilibrium, indicating that RNs are preferentially associated with Cu-sulphides. Most importantly, leached concentrate is not in secular equilibrium, being particularly enriched in ^{210}Po relative to the unleached analogue – although this is due in part to the recycling of $CuSO_4$-enriched smelter dust (also enriched in ^{210}Po) back into the processing stream. The measured lack of equilibrium suggests that ^{226}Ra, ^{210}Po and ^{210}Pb are not removed along with U, in turn implying that they

are either not co-hosted with U, or that these RNs are leached and then are either solubilised or are adsorbed onto other minerals.

Table 1.1. Uranium concentration (ital.) and radionuclide activities at Olympic Dam (Bq/g), after BHP Billiton (2011).

	Flotation feed	Unleached copper concentrates	Leached copper concentrates	1 Bq/g equivalent
U (ppm)	*600*	*2100*	*145*	
^{238}U	7.4	26	1.8	79 ppm
^{230}Th	7.5	30	2.5	1.3 ppb
^{226}Ra	7.2	24	27.5	28 ppt
^{210}Pb	6.6	30	26	400 ppq
^{210}Po	7.6	30	58	6.7 ppq

Understanding the physical and chemical nature of these RNs in ore and processing products is thus an essential requirement for any attempts to remove them. Generating products with <1 Bq/g per radionuclide (International Atomic Energy Agency, 2004) provides BHP the option of sending concentrate directly to market or submitting for further in-house processing, smelting and refining. With this in mind, the Australian Research Council (ARC) Research Hub for Australian Copper-Uranium was established to provide new data and interpretations that would document the mineralogical deportment of radionuclides and guide development of methodologies to reduce the activities of each radionuclide to <1 Bq/g. Doing so is in the direct interest of sustainable exploitation of IOCG deposits in South Australia but with broad application elsewhere in Australia and overseas.

The ARC Research Hub for Australian Copper-Uranium, to which this thesis and contained publications are a contribution, is the first major interdisciplinary research project to address the key issue of these specific non-target elements in copper ores. Analysis of ^{226}Ra and individual ^{210}RNs have, to this point, been largely limited to bulk analysis (Hondros, 2014). The decision was made to investigate this issue further, in far greater detail and at appropriate scales of observation, with the expectation that analysing the mineralogical and chemical make-

up of the ore down to the atomic level would shed light on the counterintuitive and counterproductive behaviour of ^{210}Pb and ^{210}Po.

Figure 1.2 shows a simplified flowsheet for minerals processing, terminating in the final economic products of copper cathode, gold and silver bullion, and UOC. Since RNs behave differently throughout the process stream, samples provided for investigation included ore feed, flotation feed, flotation tailings, flotation concentrate, concentrate leach discharge, and tailings leach discharge. Analyses focussed on flotation concentrate and concentrate leach discharge, but all sample types were at least surveyed and characterised using optical microscopy and scanning electron microscopy.

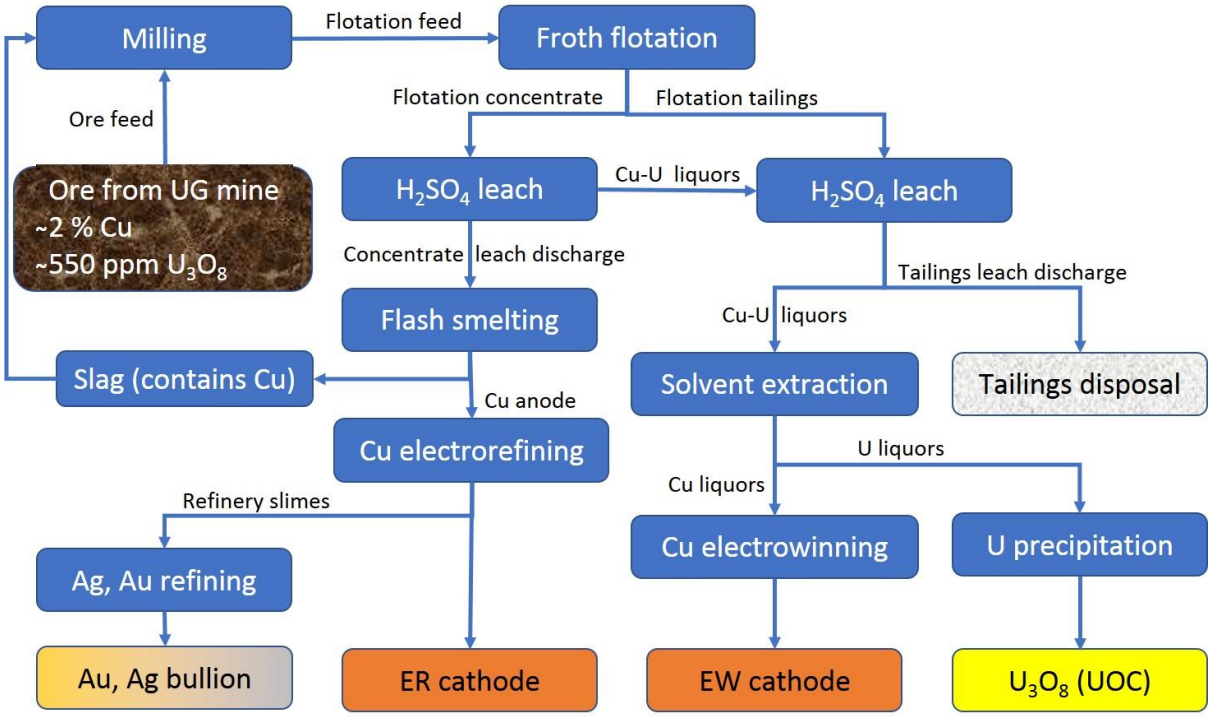

Figure 1.2. Simplified flowsheet for Olympic Dam copper processing. Created from data provided by BHP Olympic Dam.

1.3 Previous work

Due to the specific nature of this issue, previous research in this area is quite limited, or better said, there is very limited information available in the public domain. BHP Olympic Dam has conducted significant prior research regarding the mobility and removal of RNs from their

concentrates in conjunction with the Australian Nuclear Science and Technology Organisation (ANSTO), although this work remains largely confidential and unpublished. Access to much of these data was granted exclusively to Hub researchers to provide a foundation for future work – and to avoid experimental repetition. Although previous work found only limited success in reducing radionuclide activities in smelter feed, it raised questions about the roles played by mineralogy, chemical speciation and physical location of radionuclides at micro- to nanometre scales, and hinted at both the complexity of radionuclide distributions in Olympic Dam ore and the need to identify means to visualise those distributions down to the smallest scales. These are among the questions which the ARC Research Hub for Australian Copper-Uranium has sought to answer.

A broader literature overview reveals many seemingly tangential publications which provide valuable insight and direction relating to our specific objective. Papers regarding general principles of radioactivity; the geochemistry of uranium and its decay products in mining, processing and tailings disposal; and the distributions of radionuclides in the environment, ranging from volcanic activity to active hydrothermal systems, sediments and waters, to plant and animal life, food and the atmosphere (see review in Cook et al., 2018) – some dating back over 100 years – have provided a wealth of geochemical information. The most valuable resource has been the anthology regarding chemical and physical characteristics of the individual radionuclides themselves.

Published research on polonium chemistry has been limited since its discovery in 1898 (Curie et al., 1898) due to its high radioactivity and scarcity. Significant research occurred during and immediately after World War II resulting from its use as a trigger for early-generation nuclear weapons. Military interest declined after the war with the development of alternative, safer triggers; consequently, research interest had virtually disappeared by 1960. Currently, most Po research addresses environmental issues (at environmental concentrations)

with limited published work related to elevated Po activities seen in the mining industry (Roessler, 1990; Cook et al., 2018). There are, however, a few studies relating to elevated Po levels in the environment as a result of uranium mining. Although not directly relevant from a minerals processing perspective, they do provide insight into the interactions between Po and geologic materials such as ground water (Carvalho et al., 2005), rivers (Carvalho et al., 2007), and soils (Maity et al., 2011; Michel and Champion, 2019). A few comprehensive studies of polonium chemistry are worthy of note, however, including Maxwell, 1946; Haring and Yalman, 1949; Moyer, 1956; Bagnall, 1957, 1973; Weigel, 1959; Figgins, 1961; Zikovsky, 1998; and Ram et al., 2019.

Similar to ^{210}Po, the current focus of most ^{210}Pb research is environmental in nature. Since ^{210}Pb chemistry is virtually indistinguishable from $Pb_{(total)}$ chemistry, there are few publications specific to the *chemistry* of this isotope. There are, however, many excellent resources which address overall inorganic Pb chemistry including general reference (e.g., Swadźba-Kwaśny, 2015; Rumble, 2017) and academic texts (e.g., Cotton et al., 1999). Importantly, there are also a small number which relate specifically to ^{210}Pb in mining operations or waste handling (e.g., Bonczyk, 2013; Bister et al., 2015; Vaasma et al., 2016). Increasingly, ^{210}Pb is being used for dating sedimentation and soil erosion rates (e.g., Pheiffer Madsen and Sørensen, 1979; Oldfield and Appleby, 1984; Appleby et al., 1986).

A review of radium research has by far been the most fruitful for this project, having provided detailed investigations involving Ra in natural minerals, boiler scale, oil and gas pipelines, coal production, and mining and ore processing – to name a few. The two common themes among these are: Ra behaviour correlating to that of other Group 2A elements (Mg, Ca, and especially Sr and Ba); and Ra behaviour as a water- and acid-insoluble sulphate.

Radium uptake into baryte has been known for almost a century (Germann, 1921; Doerner and Hoskins, 1925). Investigation of this phenomenon continues today with, for example, detailed nanoscale observation of (Ba, Ra)SO_4 replacement of $BaSO_4$ aided by internal porosity (Weber et al., 2017), or how uptake in baryte is affected by the presence of Sr (Vinograd et al., 2018a, 2018b). Recrystallisation experiments under various conditions, backed by thermodynamic calculations, have shown significant potential for Ra uptake in (Ba,Sr,Ra)SO_4 + H_2O systems (Curti et al., 2010; Brandt et al., 2015). Notably relevant to our research are reports on the Taiwanese natural hot spring mineral hokutolite (plumbian barite) which has a remarkable capacity for incorporating Ra during formation (Momoshima et al., 1997; Chao et al., 2009).

Although anthropogenic in nature, boiler scale (Poggi et al., 2015), reactor scale, and sludge from oil and gas production (Hamlat et al., 2003; Gazineu and Hazin, 2008; Zhang et al., 2014) are all analogues of natural mineral systems. Sulphate or carbonate precipitation of Sr, Ba, or Pb may quantitatively incorporate available Ra^{2+} within their crystal lattices, either directly during crystallisation or during subsequent coupled dissolution-reprecipitation (CDR) alteration. Mechanisms are similar to those in natural systems, only environmental conditions may be more extreme. Coal ash may also contain radionuclides, including ^{226}Ra (Baba, 2002; Janković et al., 2011), but the chemical form of the Ra is unknown. Long term release of coal ash may pose a threat when exposed to ground water, as it is likely that Ra may precipitate out as a complex sulphate or carbonate which may then be transported long distances from the source (Pluta, 2001).

Equally relevant to our objective, research regarding Ra in mining production and waste handling has produced a few applicable papers. Radionuclide contamination around former (e.g., Carvalho et al., 2007, 2014), current (Osmanlioglu et al., 2017), and pending (Suman et al., 2017) U and Ra mining sites has been investigated. Uranium-238 also occurs in phosphate

rock; its decay products (including ^{226}Ra) must therefore be monitored in waste materials (phosphogypsum) remaining after fertiliser production (Roessler, 1990).

1.4 Aims, objectives, and project progression

One of the objectives of the ARC Research Hub for Australian Copper-Uranium – and by association the aim of this Ph.D. – is to locate, characterise, and (ideally) quantify RNs in copper concentrates. As a member of the mineralogical assessment and characterisation group, the primary objective was to determine RN distributions in copper concentrate minerals at the micro- or nanoscale using multiple complementary techniques. Expected output from this research included a list of proven RN host minerals with estimated RN loads in each stage of processing, and recommendations to the minerals processing group regarding their removal.

This project evolved throughout its course to benefit from, complement, and feed into other projects within the Hub. From commencement, it was anticipated that nanoscale techniques would play a major role in identifying and characterising RN-bearing nanoparticles in materials from various stages of processing. It was also believed that ^{206}Pb could be considered a proxy that could help unravel the complex behaviour of ^{210}Pb and ^{210}Po and ideally determine the cause for the disruption of secular equilibrium following acid leaching.

It was determined fairly early on, however, that ^{206}Pb was in no way a proxy for ^{210}Pb, so an alternative technique had to be found to directly observe ^{210}RN distributions. After being shown examples of nanoscale secondary ion mass spectrometry (nanoSIMS) isotope maps of ^{13}C-labeled bacterial clusters (Onetto Carvallo, 2018), this technique was proposed as a possible investigative avenue and initial tests run on the CAMECA nanoSIMS 50L in Perth in February 2017 returned excellent results. From that point forward, nanoSIMS became the primary analytical technique employed due to its ability to (qualitatively) map very low

concentrations of ^{238}U, ^{234}U, ^{230}Th, ^{226}Ra, ^{210}RN, and ^{206}Pb in mineral grains at very high (<1 μm) lateral resolution.

In response to many discussions and evidence provided by other research groups, the focus of the project shifted from ^{210}Pb-^{210}Po to ^{226}Ra-^{210}Pb. This was in part due to the inability of nanoSIMS to distinguish the respective 210 isotopes (or to convincingly see ^{210}Po at all), as well as taking into consideration the shorter half-life of ^{210}Po. Technically, stockpiling copper concentrate for 18 months would result in a sufficiently low ^{210}Po activity product – but only if the ^{210}Pb had been removed to prevent ingrowth. This would not be an ideal solution for BHP Olympic Dam, but a possible solution nonetheless.

Focus thus shifted to Pb removal, with additional effort spent studying Ra due to the similar insolubilites of Ra and Pb as sulphates. If Ra could be minimised in a sulphate-rich environment, then Pb (including ^{210}Pb) should be correspondingly reduced. To this end, investigation of various processing samples was supplemented with diffusion experiments on pure mineral separates using solutions of isolated RNs. Natural mineral separates were eventually superseded by synthetic mineral analogues, grown in the lab to control purity. A solution containing 100 Bq/ml Ra was acquired from the Environmental Protection Authority South Australia, and the mineral proxies were exposed to Ra solution under various conditions.

Chalcogenides were also prepared in the lab, consisting of Ag, Bi, and Pb sulphides, selenides, and tellurides. Po solution (~300 Bq/ml) was produced from Au-plated Ag/Po foil. The chalcogenides were exposed to Po solution and a selection of the crystals were subsequently analysed by scanning electron microscopy (SEM) and nanoSIMS. The results were, however, somewhat tainted by excessive Au in the Po solution and these data are only briefly mentioned in Chapter 2.

1.5 Structure of the thesis

This research has involved analyses using a range of qualitative and quantitative microanalytical techniques capable of characterisation at different scales of observation. These techniques are summarised in Chapter 2, together with information on the sample suite.

The application of nanoSIMS to directly observe radionuclide distribution in natural samples had previously only been attempted once, by a group investigating the transport of plutonium on amorphous iron oxide colloids (Novikov et al., 2006). Verification of this technique, and its novel application to mineral grains, is presented in Chapter 3. Individual grains of Olympic Dam copper concentrate were mapped which show clear and logical distributions of ^{238}U, ^{234}U, ^{230}Th, ^{226}Ra, ^{210}RN (predominantly ^{210}Pb), and ^{206}Pb. Issues regarding possible isobaric mass interferences and other issues are discussed. Verification and publication of this method justified continuation of nanoSIMS isotope mapping, leading to the results presented in Chapters 4 through 7.

NanoSIMS mapping of mineral grains has proven valuable not only for specific radionuclides, but for trace elements and isotopes in general. Chapter 4 presents nanoSIMS capabilities for locating precious metals, rare earth elements, penalty elements (e.g., As, Sb, Pb), as well as radionuclides in copper concentrates. Despite its current inability to quantify observed concentrations, nanoSIMS provides spatial distribution information at a scale not achievable by most other instrumentation. The quantification shortcoming does not, however, apply to isotope ratios which are sound (e.g. Winterholler et al., 2007) as long as all measured isotopes are the same element (e.g., $^{13}C/^{12}C$, $^{65}Cu/^{63}Cu$, $^{207}Pb/^{206}Pb$ – but *not* $^{87}Rb/^{86}Sr$). The

examples presented illustrate the significant potential for nanoSIMS to complement other microanalytical methods in micron- to nanoscale investigations.

Some elemental distributions – especially those of Sr, Ba, Ra and Pb – are radically altered during sulphuric acid leaching. To understand the possible mechanisms responsible, a series of experiments was established to observe the mobility of Sr, Ba, and Pb in various high-sulphate activity conditions – the results of which are presented in Chapter 5. Lab-grown mineral analogues were exposed to sulphate and/or chloride solutions under different pH conditions. NanoSIMS maps and LA-ICP-MS transects collected after exposure revealed dissolution and reprecipitation potentials for celestite ($SrSO_4$), baryte ($BaSO_4$), and anglesite ($PbSO_4$). Correlations between mineral analogues and natural minerals became clear. Calculations of supersaturation factors and nucleation rates support the observed results.

After mapping radionuclides in hundreds of sample grains by nanoSIMS, patterns began to emerge. It became clear that some minerals were consistent RN hosts, some were occasional RN hosts, and the remainder were not capable of incorporating RNs at all. Chapter 6 presents nanoSIMS isotope maps for those minerals determined to be major hosts of either some or all of the ^{238}U decay chain. These minerals are either highly enriched in some or all RNs, or are only moderately enriched but comprise a significant proportion of the concentrate. Residual uranium minerals, U- and Th-bearing minerals, most sulphates and some phosphates all make the list. The insolubilities of certain members of the decay chain in sulphate form (Ra, Pb, Po) and phosphate form (Th) offer a likely explanation.

In addition to the major hosts described in Chapter 6, a large number of minor hosts became apparent. Some mineral phases were either highly enriched but very sparse in the deposit (e.g., euxenite), or contained low accumulations of RNs but were significant components of the concentrate (e.g., hematite). These are presented in Chapter 7. The total RN load for any of

these individual examples would not amount to much, but cumulatively this entire group of minerals may significantly add to the overall RN budget. NanoSIMS maps also revealed distinct surface enrichment of ^{226}Ra and ^{210}Pb on virtually every mineral in the concentrate – except quartz. Sulphate-insoluble nanoparticles formed during the acid leach are likely adhering to charge-imbalanced surfaces, a phenomenon which was particularly evident on electronegative sulphides. Surface features are hereby classified as a "host" moving forward and will be added to RN budget calculations.

Building on the excellent results from the Sr, Ba, and Pb diffusion experiments presented in Chapter 5, the experiments were modified and repeated using Ra solution. In Chapter 8, analogue mineral crystals were exposed to Ra solution under various conditions, followed by LA-ICP-MS analysis. Radium incorporation was observed in celestite, baryte, and anglesite, but uptake potentials for each changed with conditions. Three mechanisms (overgrowth, coupled dissolution-reprecipitation, and diffusion) were observed. Results not only complemented those seen in Chapter 5, but also paralleled observations made by nanoSIMS mapping of ^{226}Ra and ^{210}Pb in real mineral samples. A clearer understanding of the mechanisms at work, especially during the sulphuric acid leach, may provide the minerals processing group the means to engineer an efficient solution for ^{226}Ra and ^{210}Pb reduction in copper concentrates.

Chapter 9 summarises application of several additional microanalytical techniques that were used in the course of the research but are not otherwise described in Chapters 2-7.

Chapter 10 provides a summary of key findings and implications of this research. The chapter concludes with a critical evaluation of results and a discussion of the practical implications of the research as well as emphasising a number of outstanding research gaps and suggestions for future research.

Supplementary information (Appendix A for Chapter 2) and additional material (conference abstracts and co-authored papers) are given in Chapter 11. A full bibliography is provided in Chapter 12.

1.6 References

Allen, S.R., McPhie, J., Ferris, G., Simpson, C., 2008. Evolution and architecture of a large felsic igneous province in western Laurentia: The 1.6 Ga Gawler Range Volcanics, South Australia. Journal of Volcanology and Geothermal Research 172, 132-147.

Appleby, P.G., Nolan, P.J., Gifford, D.W., Godfrey, M.J., Oldfield, F.J.A.N., Anderson, N.J., Battarbee, R.W., 1986. 210 Pb dating by low background gamma counting. Hydrobiologia 143, 21-27.

Apukhtina, O.B., 2016. Distribution, petrology, geochemistry and geochronology of carbonate assemblages at the Olympic Dam deposit, University of Tasmania, Hobart, unpublished Ph.D. thesis. 240 pp. https://eprints.utas.edu.au/23013/.

Baba, A., 2002. Assessment of radioactive contaminants in by-products from Yatagan (Mugla, Turkey) coal-fired power plant. Environmental Geology 41, 916-921.

Bagnall, K.W., 1957. The chemistry of polonium. Quarterly Reviews, Chemical Society 11, 30-48.

Bagnall, K.W., 1973. The Chemistry of Sulphur, Selenium, Tellurium and Polonium. Pergamon Press, NY, 935-1008.

Barton, M., 2014. Iron oxide (–Cu–Au–REE–P–Ag–U–Co) systems. In: Holland, H.D., Turekian, K.K., (Eds.), Treatise on Geochemistry 2nd ed., vol. 13, Elsevier, Amsterdam, 515–541.

BHP Billiton, 2009. Olympic Dam Expansion. Draft Environmental Impact Statement 2009. Appendix S. Uranium and Radiation. www.bhp.com. Accessed 30 July 2019.

BHP Billiton, 2011. Olympic Dam Expansion Supplementary Environmental Impact Statement, Chapter 26, p. 689–758. www.bhp.com. Accessed 30 July 2019.

BHP, 2018. Annual Report 2018. www.bhp.com/investor-centre/annual-report-2018. Accessed 16 August 2019.

Bister, S., Birkhan, J., Lüllau, T., Bunka, M., Solle, A., Stieghorst, C., Riebe, B., Michel, R., Walther, C., 2015. Impact of former uranium mining activities on the floodplains of the Mulde River, Saxony, Germany. Journal of Environmental Radioactivity 144, 21-31.

Bonczyk, M., 2013. A Determination of the Concentration Level of Lead ^{210}Pb Isotope in Solid Samples for the Assessment of Radiation Risk Occurring in Coal Mines. Journal of Sustainable Mining, 12, 1-7.

Brandt, F., Curti, E., Klinkenberg, M., Rozov, K., Bosbach, D., 2015. Replacement of barite by a (Ba,Ra)SO_4 solid solution at close-to-equilibrium conditions: A combined experimental and theoretical study. Geochimica et Cosmochimica Acta 155, 1-15.

Carvalho, F.P., Madruga, M.J., Reis, M.C., Alves, J.G., Oliveira, J.M., Gouveia, J., Silva, L., 2007. Radioactivity in the environment around past radium and uranium mining sites of Portugal. Journal of Environmental Radioactivity 96, 39-46.

Carvalho, F.P., Oliveira, J.M., Libânio, A., Lopes, I., Ferrador, G., Madruga, M.J., 2005. Radioactivity in public water supplies in the uranium mining regions of Portugal. In: Environmental contamination from uranium production facilities and their remediation. Proceedings of an International Workshop, Lisbon, Portugal, February 11-13, 2004. International Atomic Energy Agency. pp. 29-40.

Carvalho, F.P., Oliveira, J.M., Malta, M., 2014. Radioactivity in soils and vegetables from uranium mining regions. Procedia Earth and Planetary Science 8, 38-42.

Chao, J.H., Chuang, C.Y., Yeh, S.A., Wu, J.M., 2009. Relationship between radioactivity of radium and concentrations of barium and lead in hokutolite. Applied Radiation and Isotopes 67, 650-653.

Cherry, A.R., Ehrig, K., Kamenetsky, V.S., Ehrig, K., McPhie, J., Crowley, J.L., Kamenetsky, M.B., 2018. Precise geochronological constraints on the origin, setting and incorporation of ca. 1.59 Ga surficial facies into the Olympic Dam Breccia Complex, South Australia. Precambrian Research 315, 162-178.

Cherry, A., Kamenetsky, V., McPhie, J., Kamenetsky, M., Ehrig, K., Keeling, J., 2017. Post-1590 Ma modification of the supergiant Olympic Dam deposit: links with regional tectonothermal events. Proceedings of the 14th SGA Biennial Meeting, Quebec City, QC, Canada, 20–23 August 2017. 847-850.

Ciobanu, C.L., Wade, B.P., Cook, N.J., Schmidt Mumm, A., Giles, D., 2013. Uranium-bearing hematite from the Olympic Dam Cu-U-Au deposit, South Australia: a geochemical tracer and reconnaissance Pb-Pb geochronometer. Precambrian Research 238, 129-147.

Ciobanu, C.L., Cook, N.J., Ehrig, K., 2017a. Ore minerals down to the nanoscale: Cu-(Fe)-sulphides from the iron oxide copper gold deposit at Olympic Dam, South Australia. Ore Geology Reviews 81, 1218-1235.

Ciobanu, C.L., Kontonikas-Charos, A., Slattery, A., Cook, N.J., Ehrig. K., Wade, B.P., 2017b. Short-range stacking disorder in mixed-layer compounds: a HAADF STEM study of bastnäsite-parisite intergrowths. Minerals 7, 227. doi:10.3390/min7110227.

Ciobanu, C.L., Verdugo-Ihl, M.R., Slattery, A., Cook, N.J., Ehrig, K., Courtney-Davies, L., Wade, B.P., 2019. Silician magnetite: Si–Fe-nanoprecipitates and other mineral inclusions in magnetite from the Olympic Dam deposit, South Australia. Minerals 9, 311. doi:10.3390/min9050311.

Cook, N.J., Ehrig, K.J., Rollog, M., Ciobanu, C.L., Lane, D.J., Schmandt, D.S., Owen, N.D., Hamilton, T., Grano, S., 2018. ^{210}Pb and ^{210}Po in geological and related anthropogenic materials: implications for their mineralogical distribution in base metal ores. Minerals 8(5), 211. doi:10.3390/min8050211

Cotton, F.A., Wilkinson, G., Murillo, C.A., Bochmann, M., 1999. Advanced Inorganic Chemistry. John Wiley and Sons, Hoboken NJ. 1376 pp.

Courtney-Davies, L., Tapster, S.R., Ciobanu, C.L., Cook, N.J., Verdugo-Ihl, M.R., Ehrig, K.J., Kennedy, A.K., Gilbert, S.E., Condon, D.J., Wade, B.P., 2019. A multi-technique evaluation of hydrothermal hematite U-Pb isotope systematics: Implications for ore deposit geochronology. Chemical Geology 513, 54-72.

Creaser, R.A., Cooper, J.A., 1993. U-Pb geochronology of middle Proterozoic felsic magmatism surrounding the Olympic Dam Cu-U-Au-Ag and Moonta Cu-Au-Ag deposits, South Australia. Economic Geology 88, 186-197.

Curie, P., Curie, M., Becquerel, H., 1898. Sur une substance nouvelle radio-active, contenue dans la pechblende. Comptes Rendus 127, 1215-1217.

Curti, E., Fujiwara, K., Iijima, K., Tits, J., Cuesta, C., Kitamura, A., Glaus, M.A., Müller, W., 2010. Radium uptake during barite recrystallization at 23±2 ºC as a function of solution composition: An experimental ^{133}Ba and ^{226}Ra tracer study. Geochimica et Cosmochimica Acta, 74, 3553-3570.

Dmitrijeva, M., Ehrig, K.J., Ciobanu, C.L., Cook, N.J., Verdugo-Ihl, M.R., Metcalfe, A.V., 2019. Defining IOCG signatures through compositional data analysis: a case study of lithogeochemical zoning at Olympic Dam, South Australia. Ore Geology Reviews 105, 86-101.

Doerner, H.A., Hoskins, W.M., 1925. Co-Precipitation of Radium and Barium Sulphates 1. Journal of the American Chemical Society 47, 662-675.

Ehrig, K., McPhie, J., Kamenetsky, V., 2012. Geology and mineralogical zonation of the Olympic Dam iron oxide Cu-U-Au-Ag deposit, South Australia. In: Hedenquist, J.W., Harris, M., Camus, F. (Eds.), Geology and Genesis of Major Copper Deposits and Districts of the World, a Tribute to Richard Sillitoe. SEG Special Publication 16, 237-268.

Ehrig, K., Kamenetsky, V., McPhie, J., Cook, N.J., Ciobanu, C.L., 2017. Olympic Dam iron-oxide Cu-U-Au-Ag deposit. In: G.N. Phillips, (Ed.), Australian Ore Deposits. AusIMM, Melbourne, pp. 601-610.

Fanning, C.M., Flint, R.B., Parker, A.J., Ludwig, K.R., Blissett, A.H., 1988. Refined Proterozoic evolution of the Gawler craton, South Australia, through U-Pb zircon geochronology. Precambrian Research 40, 363-386.

Figgins, P.E., 1961. The radiochemistry of polonium. National Research Council's Nuclear Science Series Vol. 3037, National Academy of Sciences. 74 pp.

Flint, R.B., 1993. Hiltaba suite. In: Drexel, J.F., Preiss, W.V., Parker, A.J., (Eds.), The Geology of South Australia 1, pp. 127-131.

Foden, J., Elburg, M.A., Dougherty-Page, J., Burtt, A., 2006. The timing and duration of the Delamerian Orogeny: correlation with the Ross Orogen and implications for Gondwana assembly. The Journal of Geology 114, 189-210.

Gazineu, M.H.P., Hazin, C.A., 2008. Radium and potassium-40 in solid wastes from the oil industry. Applied Radiation and Isotopes 66, 90-94.

Hamlat, M.S., Kadi, H., Fellag, H., 2003. Precipitate containing NORM in the oil industry: modelling and laboratory experiments. Applied Radiation and Isotopes 59, 95-99.

Haring, M.M., Yalman, R.G., 1949. Solution chemistry of polonium. (Interim Report). No. MLM-211. Mound Laboratory, Miamisburg, Ohio. 12 pp.

Hitzman, M.W., Oreskes, N., Einaudi, M.T., 1992. Geological characteristics and tectonic setting of Proterozoic iron-oxide (Cu–U–Au–REE) deposits. Precambrian Research 58, 241–287.

Hondros, J., 2014. Background Radiation Briefing presentation. Unpublished document. 69 pp.

Huang, Q., Kamenetsky, V.S., McPhie, J., Ehrig, K., Meffre, S., Maas, R., Thompson, J., Kamenetsky, M., Chambefort, I., Apukhtina, O., Hu, Y., 2015. Neoproterozoic (ca. 820–830 Ma) mafic dykes at Olympic Dam, South Australia: links with the Gairdner Large Igneous Province. Precambrian Research 271, 160–172.

International Atomic Energy Agency, 2004. Application of the Concepts of Exclusion, Exemption and Clearance. International Atomic Energy Agency, Vienna. IAEA Safety Standards Series: Safety Guide No. RS-G-1.7

Janković, M.M., Todorović, D.J., Nikolić, J.D., 2011. Analysis of natural radionuclides in coal, slag and ash in coal-fired power plants in Serbia. Journal of Mining and Metallurgy Section B: Metallurgy 47, 149-155.

Johnson, J.P., Cross, K.C., 1995. U-Pb geochronological constraints on the genesis of the Olympic Dam Cu-U-Au-Ag deposit, South Australia. Economic Geology 90, 1046–1063.

Kirchenbaur, M., Maas, R., Ehrig, K., Kamenetsky, V.S., Strub, E., Ballhaus, C., Münker, C., 2016. Uranium and Sm isotope studies of the supergiant Olympic Dam Cu-Au-U-Ag deposit, South Australia. Geochimica et Cosmochimica Acta 180, 15-32.

Kontonikas-Charos, A., Ciobanu, C.L., Cook, N.J., Ehrig, K., Krneta, S., Kamenetsky, V.S., 2017. Feldspar evolution in the Roxby Downs Granite, host to Fe-oxide Cu-Au-(U) mineralisation at Olympic Dam, South Australia. Ore Geology Reviews 80, 838-859.

Krneta, S., Ciobanu, C.L., Cook, N.J., Ehrig, K., Kontonikas-Charos, A., 2016. Apatite at Olympic Dam, South Australia: A petrogenetic tool. Lithos 262, 470–485.

Krneta, S., Ciobanu, C.L., Cook, N.J., Ehrig, K., Kontonikas-Charos, A., 2017. Rare earth element behaviour in apatite from the Olympic Dam Cu–U–Au–Ag deposit, South Australia. Minerals, 7, 135.

Lane, D.J., Cook, N.J., Grano, S.R., Ehrig, K., 2016. Selective leaching of penalty elements from copper concentrates: A review. Minerals Engineering 98, 110-121.

Macmillan, E., Cook, N.J., Ehrig, K., Ciobanu, C.L., Pring, A., 2016. Uraninite from the Olympic Dam IOCG-U-Ag deposit: linking textural and compositional variation to temporal evolution. American Mineralogist 101, 1295–1320.

Macmillan, E., Cook, N.J., Ehrig, K., Pring, A., 2017. Chemical and textural interpretation of late-stage coffinite and brannerite from the Olympic Dam IOCG-Ag-U deposit. Mineralogical Magazine 81, 1323-1366.

Maity, S., Mishra, S., Bhalke, S., Pandit, G., Puranik, V., Kushwaha, H., 2011. Estimation of distribution coefficient of polonium in geological matrices around uranium mining site. Journal of Radioanalytical and Nuclear Chemistry 290, 75-79.

Martland, H.S., Conlon, P., Knef, J.P., 1925. Some unrecognized dangers in the use and handling of radioactive substances: with especial reference to the storage of insoluble products of radium and mesothorium in the reticulo-endothelial system. Journal of the American Medical Association 85, 1769-1776.

Maxwell, C.R., 1946. Physical properties and crystal structure of polonium, Retrospective Theses and Dissertations, Iowa State University, Paper 13649. 71 pp.

Michel, H., Champion, J., 2019. ^{210}Po sequential extraction applied to wetland soils at uranium mining sites. Journal of Environmental Radioactivity 199, 1-6.

Momoshima, N., Nita, J., Maeda, Y., Sugihara, S., Shinno, I., Matsuoka, N., Huang, C.W., 1997. Chemical composition and radioactivity in hokutolite (plumbian barite) collected at Peito hot spring, Taiwan. Journal of Environmental Radioactivity 37, 85-99.

Moyer, H.V., 1956. Chemical Properties of Polonium. Mound Laboratory, Dayton, OH. 401 pp.

Novikov, A.P., Kalmykov, S.N., Utsunomiya, S., Ewing, R.C., Horreard, F., Merkulov, A., Myasoedov, B.F., 2006. Colloid transport of plutonium in the far-field of the Mayak Production Association, Russia. Science 314(5799), 638-641.

Oldfield, F., Appleby, P.G., 1984. Empirical testing of 210 Pb-dating models for lake sediments. In: Haworth, E., Lund, J.W.G., (Eds.), Lake sediments and environmental history. Leicester University Press, Leicester, U.K., pp. 93-124.

Onetto Carvallo, C., 2018. Identity and physiology of glycogen accumulating organisms in activated sludge. Unpublished Ph.D. thesis, The University of Adelaide, Adelaide, Australia. 129 pp. http://hdl.handle.net/2440/114264

Osmanlioglu, A.E., Adiguzel, D., Tuylu, S., Bascetin, A., 2017. Acid mine drainage and environmental impacts of uranium deposits. International Multidisciplinary Scientific GeoConference: SGEM: Surveying Geology & Mining Ecology Management 17, 9-14.

Owen, N.D., Cook, N.J., Rollog, M., Ehrig, K.J., Schmandt, D.S., Ram, R., Brugger, J., Ciobanu, C.L., Wade, B., Guagliardo, P., 2019. REE-, Sr- Ca-aluminum-phosphate-sulfate minerals of the alunite supergroup and their role as hosts for radionuclides. American Mineralogist, (in press).

Pheiffer Madsen, P., Sørensen, J., 1979. Validation of the lead-210 dating method. Journal of Radioanalytical and Nuclear Chemistry 54, 39-48.

Pluta, I., 2001. Barium and radium discharged from coal mines in the Upper Silesia, Poland. Environmental Geology 40, 345-348.

Poggi, C.M.B., de Farias, E.E.G., Silveira, P.B., Silva Filho, C.A., De França, E.J., Gazineu, M.H.P. Hazin, C.A., 2015. ^{226}Ra, ^{228}Ra and ^{40}K in scales from boilers of industrial installations. Journal of Radioanalytical and Nuclear Chemistry 306, 667-672.

Ragozzini, R.J., Sparrow, G.J., 1987. Selective dissolution of uranium from Olympic Dam copper concentrates. Hydrometallurgy 18, 367-382.

Ram, R., Vaughan, J., Etschmann, B., Brugger, J., 2019. The aqueous chemistry of Polonium (Po) in environmental and anthropogenic processes. Journal of Hazardous Materials 380, 120725, 1-17.

Reeve, J.S., Cross, K.C., Smith, R.N., Oreskes, N., 1990. Olympic Dam copper-uranium-gold-silver deposit. In: Hughes, F.E., (Ed.), Geology of the Mineral Deposits of Australia and Papua New Guinea. The Australasian Institute of Mining and Metallurgy, Melbourne, pp. 1009–1035.

Reid, A., 2019. The Olympic Cu-Au Province, Gawler Craton: A Review of the Lithospheric Architecture, Geodynamic Setting, Alteration Systems, Cover Successions and Prospectivity. Minerals 9, 371. doi:10.3390/min9060371.

Roberts, D.E., Hudson, G.R.T., 1983. The Olympic Dam copper-uranium-gold deposit, Roxby Downs, South Australia. Economic Geology 78, 799-822.

Roessler, C.E., 1990. Control of radium in phosphate mining, beneficiation and chemical processing. The environmental behaviour of radium vol. 2, Technical Report Series 310, International Atomic Energy Agency, pp. 270-279.

Rumble, J., 2017. CRC Handbook of Chemistry and Physics. CRC press. 1532 pp.

Schmandt, D.S., 2019. Mineralogical distribution of radionuclides in copper-uranium ores, Olympic Dam, South Australia. Unpublished Ph.D. thesis, The University of Adelaide, Adelaide, Australia. 371 pp. http://hdl.handle.net/2440/120092.

Schmandt, D.S., Cook, N.J., Ciobanu, C.L., Ehrig, K., Wade, B.P., Gilbert, S., Kamenetsky, V.S., 2017. Rare earth element fluorocarbonate minerals from the Olympic Dam Cu-U-Au-Ag deposit, South Australia. Minerals 7, 202. doi:10.3390/min7100202.

Schmandt, D.S., Cook, N.J., Ciobanu, C.L., Ehrig, K., Wade, B.P., Gilbert, S., Kamenetsky, V.S., 2019a. Rare earth element phosphate minerals from the Olympic Dam Cu-U-Au-Ag deposit, South Australia: Recognizing temporal-spatial controls on REE mineralogy in an evolved IOCG systems. Canadian Mineralogist 57, 3-24.

Schmandt, D.S., Cook, N.J., Ehrig, K., Gilbert, S., Wade, B.P., Rollog, M., Ciobanu, C.L., Kamenetsky, V.S., 2019b. Uptake of trace elements by baryte during copper ore processing: A case study from Olympic Dam, South Australia. Minerals Engineering 135, 83-94.

Skirrow, R.G., Bastrakov, E.N., Baroncii, K., Fraser, G.L., Creaser, R.A., Fanning, C.M., Raymond, O.L., Davidson, G.J., 2007. Timing of iron oxide Cu-Au-(U) hydrothermal activity and Nd isotope

constraints on metal sources in the Gawler craton, South Australia.: Economic Geology 102, 1441–1470.

www.statista.com/topics/1409/copper. Updated 23 November 2018, accessed 26 July 2019.

Suman, G., Sreenath, R., Gopal, R., Yadagiri, R., Rama, R., 2017. Preliminary data of radiation levels near the proposed uranium mining site, Dasarlapally, Nalgonda, Telangana. In: Proceedings of the twentieth national conference on solid state nuclear track detectors and their applications: abstracts. Mysuru, India, October 26-28, 2017. Vidya Vikas Institute of Engineering and Technology, Mysuru, India. p. 106.

Swadźba-Kwaśny, M., 2015. Lead: Inorganic Chemistry. In: King, B. (Ed.), Encyclopedia of Inorganic and Bioinorganic Chemistry. John Wiley & Sons, pp. 1-24.

Vaasma, T., Bityukova, L., Kiisk, M., Özden, B., Tkaczyk, A.H., 2016. Behavior mechanisms and correlation between lead (Pb) and its isotope ^{210}Pb in industrial residue as an indicator for waste characterization. Environmental Technology 37, 3208-3218.

Verdugo-Ihl, M.R., Ciobanu, C.L., Cook, N.J., Ehrig, K., Courtney-Davies, L., Gilbert, S., 2017. Textures and U-W-Sn-Mo signatures in hematite from the Cu-U-Au-Ag orebody at Olympic Dam, South Australia: defining the archetype for IOCG deposits. Ore Geology Reviews 91, 173–195.

Verdugo-Ihl, M.R., Ciobanu, C.L., Cook, N.J., Ehrig, K.J., Courtney-Davies, L., 2019a. Defining early stages of IOCG systems: evidence from iron-oxides in the outer shell of the Olympic Dam deposit, South Australia. Mineralium Deposita, 1-24. doi:10.1007/s00126-019-00896-2.

Verdugo-Ihl, M.R., Ciobanu, C.L., Slattery, A., Cook, N.J., Ehrig, K., Courtney-Davies, L., 2019b. Copper-arsenic nanoparticles in hematite: fingerprinting fluid-mineral interaction. Minerals 9, 388. doi:10.3390/min9070388.

Vinograd, V.L., Kulik, D.A., Brandt, F., Klinkenberg, M., Weber, J., Winkler, B., Bosbach, D., 2018a. Thermodynamics of the solid solution-aqueous solution system (Ba, Sr, Ra) SO_4 + H2O: I. The effect of strontium content on radium uptake by barite. Applied Geochemistry 89, 59-74.

Vinograd, V.L., Kulik, D.A., Brandt, F., Klinkenberg, M., Weber, J., Winkler, B., Bosbach, D., 2018b. Thermodynamics of the solid solution-Aqueous solution system (Ba,Sr,Ra)SO_4 + H_2O: II. Radium retention in barite-type minerals at elevated temperatures. Applied Geochemistry 93, 190-208.

Weber, J., Barthel, J., Klinkenberg, M., Bosbach, D., Kruth, M., Brandt, F., 2017. Retention of ^{226}Ra by barite: The role of internal porosity. Chemical Geology 466, 722-732.

Weigel, F., 1959. Chemistry of Polonium. Angewandte Chemie 71, 289-299.

Winterholler, B., Hoppe, P., Foley, S., Andreae, M.O., 2008. Sulfur isotope ratio measurements of individual sulfate particles by NanoSIMS. International Journal of Mass Spectrometry 272, 63-77.

Zhang, T., Gregory, K., Hammack, R.W., Vidic, R.D., 2014. Co-precipitation of radium with barium and strontium sulfate and its impact on the fate of radium during treatment of produced water from unconventional gas extraction. Environmental Science & Technology 48, 4596-4603.

Zikovsky, L., 1998. Precipitation and solubility of some polonium compounds. Journal of Radioanalytical and Nuclear Chemistry 227, 171-172.

Chapter 2

Methodology

2. Methodology

This chapter provides a summary of the samples analysed during the project, as well as a brief introduction to the primary analytical techniques employed. Sample selection, as well as mineral grain selection within each sample, is discussed and tabulated. Descriptions, standards, and running conditions are provided for each of the primary means of investigation for this project: optical microscopy, scanning electron microscopy (SEM), nanoscale secondary ion mass spectrometry (nanoSIMS), laser ablation inductively coupled plasma mass spectrometry (LA-ICP-MS), solution ICP-MS, and alpha track radiography (alpha tracking). Additional information regarding supplementary analytical techniques, including focussed ion beam scanning electron microscopy (FIB-SEM), transmission electron microscopy (TEM), atom probe tomography (APT), and electron backscatter diffraction (EBSD), is provided in Chapter 9.

2.1 Sample suite

2.1.1 Samples provided by BHP Olympic Dam

Six primary sample types from the Olympic Dam mine and processing plant were investigated in the course of this project: core samples from selected diamond drill holes; flotation feed (ore feed); flotation concentrate; flotation tailings; acid-leached copper concentrate (hereafter concentrate leach discharge); and tailings leach discharge. These are listed in Table 2.1. Additional (non-BHP) samples listed in Table 2.1 are described in Section 2.1.3. All samples provided/made were 1-inch round epoxy resin blocks.

Note: The cyclosized C1 (~27 µm) size fraction samples proved to be too difficult to work with (e.g., finding individual specific grains of interest repeatedly), so all subsequent analyses for

all sample types were performed on the +53 µm size fraction, with each mount containing roughly 100,000 exposed grains.

Table 2.1. Samples received/made/analysed during this project.

Sample name	#	Type	Particle size	Coll. date	Recd. date	Analyses
0815_CLD	3	CLD	+53	08/2015	11/2016	OM, SEM, NS, LA, EB
0815_CLD	3	CLD	+C1	08/2015	11/2016	OM, SEM
0815_FC	3	FC	+53	08/2015	11/2016	OM, SEM, NS, LA
0815_FC	3	FC	+C1	08/2015	11/2016	OM, SEM
0815_FF	1	FF	+75	08/2015	11/2016	OM, SEM
0815_FF	1	FF	+53	08/2015	11/2016	OM, SEM
0815_FF	1	FF	+C1	08/2015	11/2016	OM
0815_FT	1	FT	+75	08/2015	11/2016	OM, SEM
0815_FT	1	FT	+53	08/2015	11/2016	OM, SEM
0815_FT	1	FT	+C1	08/2015	11/2016	OM
0815_TLD	1	TLD	+75	08/2015	11/2016	OM, SEM
0815_TLD	1	TLD	+53	08/2015	11/2016	OM, SEM
0815_TLD	1	TLD	+C1	08/2015	11/2016	OM
GR003	3	OF	+75	08/2015	11/2016	OM, SEM
GR003	3	OF	+53	08/2015	11/2016	OM, SEM
GR003	3	OF	+C1	08/2015	11/2016	OM
See appendix	16	DC	N/A	11/2016	12/2016	OM, SEM, NS
1216_CLD	3	CLD	+53	12/2016	02/2017	OM, SEM, NS, LA
1216_FC	3	FC	+53	12/2016	02/2017	OM, SEM, NS, LA, EB
1217_CLD	3	CLD	+53	12/2017	01/2018	OM, SEM, NS, LA
1217_FC	3	FC	+53	12/2017	01/2018	OM, SEM, NS, LA
MR_Sulph_1	1	Syn	N/A	01/2018	01/2018	OM, SEM, NS
MR_Sulph_2	2	Syn	N/A	05/2018	05/2018	OM, SEM, NS, LA
MR_Ra	2	Syn	N/A	11/2018	11/2018	OM, SEM, LA
MR_Po	2	Syn	N/A	01/2018	01/2018	OM, SEM, NS
TMS	1	NC	N/A	08/2017	09/2017	OM, SEM, NS, LA
Uran-std	1	NC	N/A	08/2017	09/2017	OM, SEM, NS, LA

Sample names in italics were provided by BHP Olympic Dam. Sample types: concentrate leach discharge (CLD); flotation concentrate (FC); flotation feed (FF); flotation tailings (FT); tailings leach discharge (TLD); ore feed (OF); drill core fragments (DC); synthetic minerals (Syn); and single, natural crystals (NC).

"Size" refers to size fraction of concentrate (if applicable), mounted in 1" round epoxy resin blocks, polished.

refers to number of polished blocks prepared from each sample.

Analytical methods: optical microscopy (OM); scanning electron microscopy (SEM); nanoSIMS (NS); laser ablation inductively coupled plasma mass spectrometry (LA); electron backscatter diffraction (EB).

2.1.1.1 Diamond Drill Core (DC)

Drill core samples were collected from the core yard at BHP Olympic Dam in November 2016. After examination of several hundred metres of drill core representative of hematite breccia-hosted copper mineralisation, sixteen samples were chosen based on their potential for interesting chemical compositions or structural features. Small sections, roughly 2x2 cm in size, were cut, mounted, and polished down to 0.25 µm in 1-inch epoxy rounds at Adelaide Petrographics. Figure 2.1 shows a reflected light optical petrographic microscope image of drill core sample MR05. Table 11.1 in Appendix A provides details of the drill core samples.

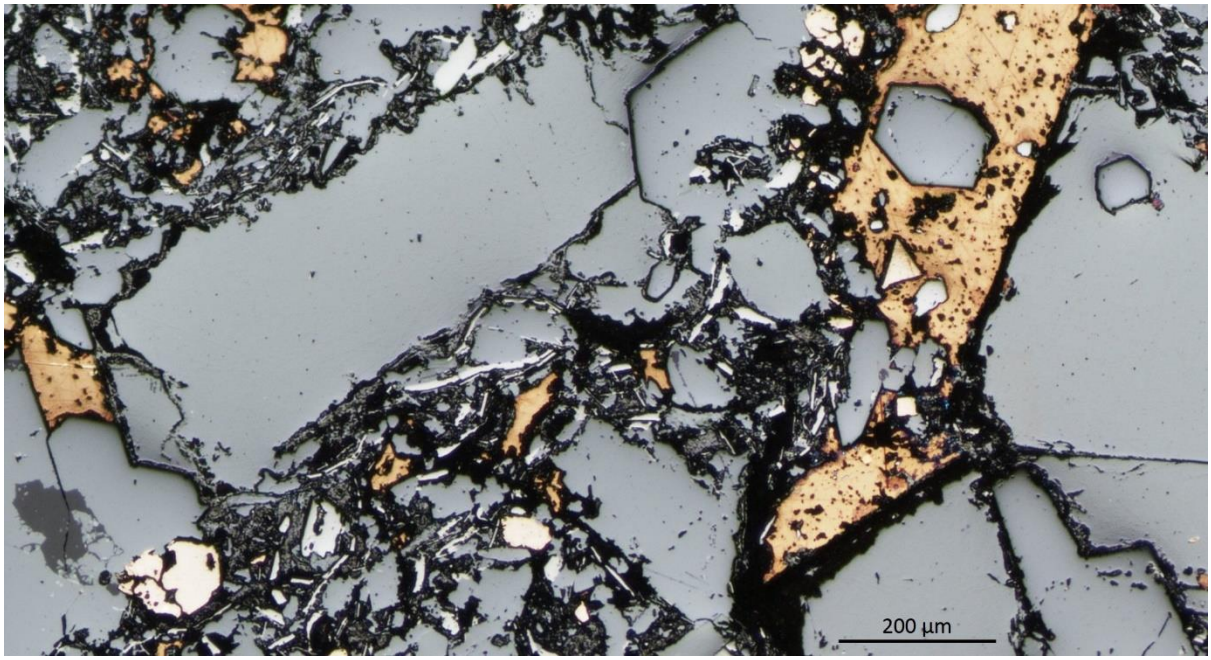

Figure 2.1. Optical reflected light microscope image of drill core sample MR05 (depth of 569 m, drill hole RD2316). Chalcopyrite is pale orange; pyrite is creamy white. All other minerals are various shades of grey. Full mineral identifications for this image are listed in Figure 2.6.

2.1.1.2 Flotation Feed (FF)

After ore is brought to the surface it is milled to a P_{80} of 75 µm and sent for froth flotation. At this point the FF still represents the original mineral composition of the ore body. Examination of FF provides insight into ore composition, mineralisation mechanisms, redox potential, and elemental distributions before any chemical or mechanical processes (other than grinding) can modify ore composition or mineralogy. Samples provided include 0815_FF and GR003

(labelled "ore feed"), representing three different size fractions (Table 2.1). These samples were surveyed by optical microscopy and briefly examined by SEM, but focus soon shifted to FC and CLD samples due to their significantly higher proportion of economic minerals.

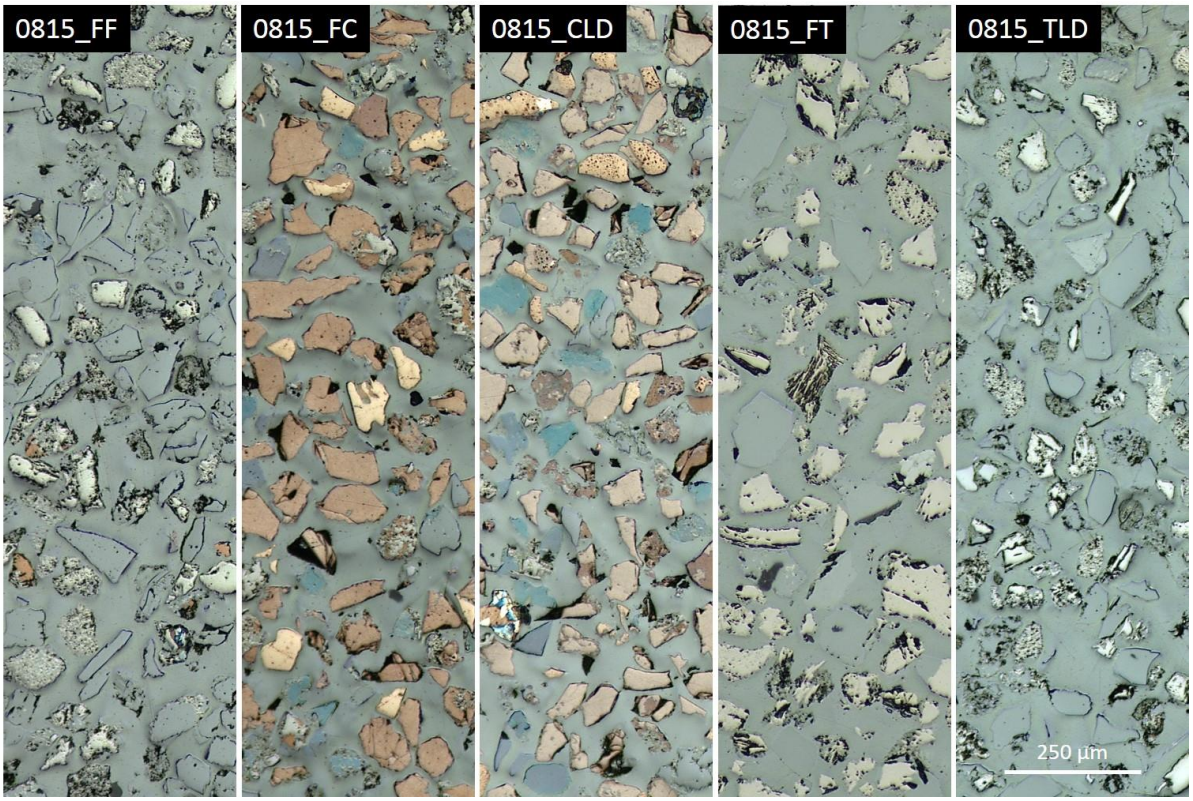

Figure 2.2. Optical, reflected light microscope image of examples of the five ore concentrate types (+53 size fractions) provided by BHP Olympic Dam. Material mounted in epoxy resin and polished by Adelaide Petrographics. More detailed images of each concentrate type, with partial mineral labels and proportions, are provided in Chapter 11, Appendix A. Copper minerals and pyrite are coloured, all other minerals are various shades of grey.

2.1.1.3 Flotation Concentrate (FC)

The froth flotation process involves bubbling large quantities of air (as microbubbles) through a slurry of FF suspended in a solution of surfactants and other proprietary chemicals. Desired minerals statically adhere to the bubbles and float to the surface, while gangue minerals sink and may be separated. The formulation of the flotation fluid may be manipulated to favour or disfavour certain minerals, depending on the FF composition and the desired end-products. No significant chemical reactions occur, and the resulting FC contains the same minerals as in the FF, only in proportions which now greatly favour commodity minerals (Figure 2.2). Copper

has been upgraded from 2 wt.% to ca. 35 wt.%. FC samples provide invaluable information regarding the mobility of RNs during processing, as they represent the precursor (control) to acid-leached samples. Material was collected from the processing stream on three occasions: August 2015; December 2016; and December 2017. Samples were prepared in triplicate by Adelaide Petrographics and were labelled 0815_FC, 1216_FC, and 1217_FC (Table 2.1).

2.1.1.4 Concentrate Leach Discharge (CLD)

Since the primary objective of this project was to investigate radionuclides in final copper concentrates (smelter feed) from Olympic Dam, the majority of analyses were performed on CLD samples. These samples consist of FC samples which have been leached in <1.6 M sulphuric acid for 8-12 hours at 60 ºC. Exact conditions are dependent on FC composition. Most uranium minerals, carbonates, and fluorite have been removed, with rare earth minerals, phyllosilicates, and hematite significantly reduced. Copper has been further upgraded to ca. 40 wt.%. Covellite and digenite ($Cu_{1.8}S$) are created through metathesis reactions (Dunn et al., 2017; Byrne et al., 2018). Sulphate minerals such as anglesite and jarosite – not found in the ore – are created during the leach. Samples were collected on the same dates as the FC samples and labelled 0815_CLD, 1216_CLD, and 1217_CLD (Table 2.1).

2.1.1.5 Flotation Tailings (FT)

After froth flotation, sulphides and other economic minerals (now labelled FC) are sent for 8-12 hours of sulphuric acid leaching to recover residual U and Cu and then sent to the smelter. Gangue minerals such as quartz, hematite, feldspars, carbonates, fluorite, baryte and sericite have settled to the bottom of the tank as tailings. These FT still contain appreciable Cu and U and are therefore leached in a separate 6 to 10-hour sulphuric acid/sodium chlorate leach cycle.

Minimal effort was spent on these samples initially, due to most of the minerals of interest having been removed. For calculations of overall mineral (and RN) budgets, however, these

samples will eventually be characterised by MLA and alpha, beta, and/or gamma counting. Detailed mineralogical analysis may also highlight areas of possible improvement in the froth flotation procedure.

2.1.1.6 Tailings Leach Discharge (TLD)

Following sulphuric acid leaching of FT, the Cu- and U-rich solution is sent for solvent-exchange recovery of Cu and U. The remaining solids are economically spent and are separated into: slimes which are thickened and released into tailings ponds; and sands (TLD) which are mixed with crushed dolomite, water, and a binding component and used as backfill for exhausted stopes.

As with FT samples, minimal initial effort was spent on these samples, being completely devoid of minerals of interest for this project. Processing efficiencies may be investigated in the future, however, by surveying and assaying TLD solids.

2.1.2 Grain selection

Sample grain selection initially centred around a list of minerals that were predicted to be potential hosts for RNs, based on published precedents or principles of crystal structures and geochemistry. These included lead minerals, uranium and thorium minerals, baryte, rare earth element (REE) minerals, apatite-group minerals and iron oxides – namely mineral groups capable of, or proven to, host radionuclides (e.g., Doerner and Hoskins, 1925; Gramaccioli and Segalstad, 1978; Ciobanu et al., 2013). Additionally, silver and bismuth chalcogenides were included on the assumption that Po may mimic Bi, Se, or Te in its behaviour (Curie et al., 1898; Bagnall, 1973).

Once nanoSIMS mapping commenced, it was realised that RN distributions are not always predictable and that fractures, pores and inter-grain margins in almost any mineral can host RNs. The objective then became the development of an extended database of *all* possible host

minerals, regardless of economic value or relative abundance. Mineral grain selection subsequently broadened to include as diverse a range of major, minor and trace minerals from Olympic Dam as possible (Table 2.2).

Table 2.2. Olympic Dam minerals analysed by nanoSIMS

Abbr	Mineral name	**Abbr**	Mineral name	**Abbr**	Mineral name
alt	altaite	**cos**	cosalite	**Ni-cob**	Ni-cobaltite
ang	anglesite	**cov**	covellite	**petz**	petzite
anh	anhydrite	**cpy**	chalcopyrite	**qz**	quartz
apa	apatite	**Cu**	native copper	**rut**	rutile
APS	woodhouseite-svanbergite grp	**dol**	dolomite	**sch**	scheelite
bab	babkinite	**ele**	electrum	**sel**	sellaite
bar	barite	**eux**	euxenite	**ser**	sericite
bast	bastnäsite	**flu**	fluorite	**sph**	sphalerite
Bi	native bismuth	**fnc**	florencite	**Sr-bar**	Sr-barite (to 1:1)
bn	bornite	**gal**	galena	**syn**	synchysite
bran	brannerite	**hess**	hessite	**tbi**	tellurobismuthite
cal	calcite	**hem**	hematite	**ten**	tenorite
car	carrollite	**jar**	jarosite	**tet**	tetradymite
cat	cattierite	**kaw**	kawazulite	**thd**	tetrahedrite
cc	chalcocite	**mel**	melonite	**thor**	thorite
chal	chalcanthite	**mly**	molybdenite	**uran**	uraninite
chl	chlorite	**Mn-dol**	Mn-dolomite	**vol**	volynskite
cls	clausthalite	**Mn-sid**	Mn-siderite	**wit**	wittichenite
cob	cobaltite	**mon**	monazite	**xen**	xenotime
coff	coffinite	**nev**	nevskite	**zir**	zircon

2.1.3 Additional samples

2.1.3.1 Synthetic analogues of minerals

To better understand the mobility of radionuclides in certain minerals, mineral analogues were created to be used in diffusion experiments. Various sulphates (including Sr, Ba, and Pb) were grown by the silica gel method (Henisch 1996). The method involves dissolving the cation of

choice (M^{2+}) in a basic sodium metasilicate solution, adding acid, and letting the solution set into a semi-firm gel which takes a few days. A solution of sodium sulphate is then carefully poured on top of the gel, and diffusion of sulphate solution into the gel over 1-2 weeks results in small, euhedral MSO_4 crystals up to 500 µm in maximum dimension. A comprehensive description of sulphate synthesis may be found in Chapter 5 (Experimental Methods section). These crystals were used for a variety of diffusion experiments involving solutions of Sr, Ba, Pb, and Ra under varying conditions. After diffusions, the crystals were mounted in epoxy resin, polished, and imaged by SEM (Samples labelled MR_Sulph_1, MR_Sulph_2, and MR_Ra; Table 2.1). Examples of these crystals may be seen in Chapter 8, Figure 8.1.

Additionally, chalcogenides including Ag-, Pb-, and Bi-selenides, sulphides, and tellurides were created by fusion of the pure elements in evacuated sealed glass tubes. These crystals were reacted with a ~300 Bq/ml Po solution then mounted in epoxy resin, polished, and imaged by SEM (sample labelled MR_Po; Table 2.1). Unfortunately, the solution contained excess gold as a by-product of the Po extraction process and was not clean enough to give meaningful results, so the experiment was de-prioritised in favour of the Ra diffusions. Some sample grains were mapped on the nanoSIMS and showed promise as candidates for Po uptake (Figure 2.3).

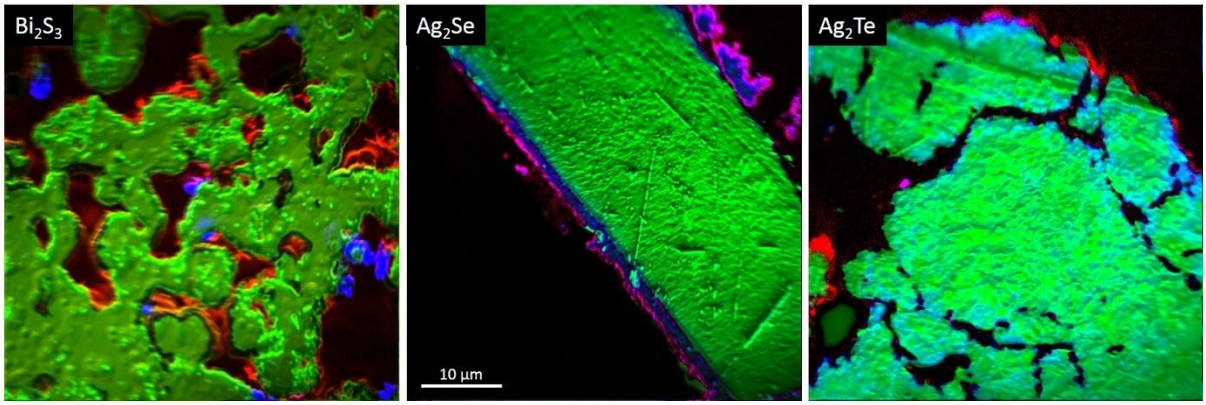

Figure 2.3. NanoSIMS composites of three chalcogenides which had been exposed to Po solution. Bi or Ag in green, Au in blue, ^{210}Po in red/purple. Po appears to co-precipitate with Au, so a low-Au solution will be produced for future experiments.

2.1.3.2 Tate Museum samples

Any attempts at nanoSIMS quantification requires known standards. Although the nanoSIMS facility in Perth had adequate elemental standards, very few mineral standards were available. With the assistance of Dr. Tony Milnes, samples of pure minerals were collected from the Tate Mineral Museum located in the Mawson Laboratories, The University of Adelaide. Small (1-2 mm) chips of 103 mineral samples were collected and mounted in three 1-inch epoxy resin mounts, containing roughly 34 samples each. The mounts were polished and each mineral imaged by SEM to determine suitability as a standard. Some grains showed extensive heterogeneity and were discounted from further study; others appeared to be homogeneous with low trace elements and minimal structural features (Figure 2.4).

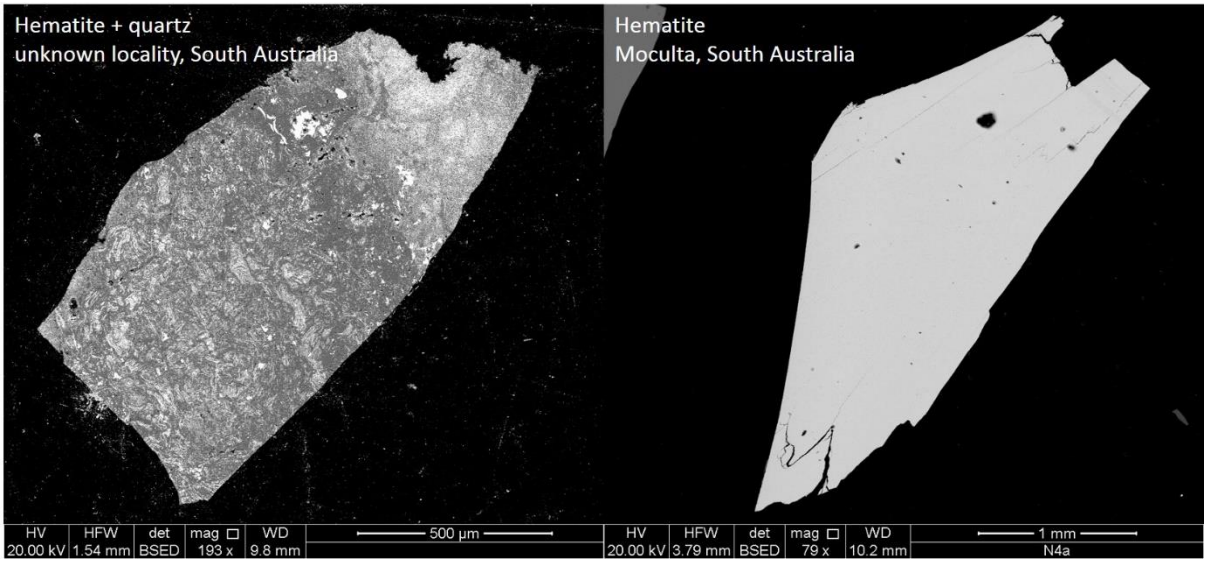

Figure 2.4. BSE images of two South Australian hematite samples from the Tate Museum. Only clean, homogeneous minerals like the sample on the right were selected for the Tate mineral standard mount.

Of the 103 original mineral samples, 32 were chosen for our Tate Mineral Standard (TMS). In a few instances, heterogeneous samples of important minerals were selected if homogeneous examples were not available. These 32 grains were mounted in a single epoxy mount, polished, and imaged by SEM in BSE mode. Ideally, this standard would be used to quantify major, minor, and possibly trace elements by nanoSIMS, at least for the 32 minerals represented.

Initial results are discussed in Chapter 3. Information on the mineral samples included in TMS is provided in Table 11.2 in Chapter 11, Appendix A.

2.1.3.3 Uranium decay chain standard

Quantification of RN elements is complicated by the lack of standards for ^{234}U, ^{230}Th, ^{226}Ra, and ^{210}RN. Even for methods which provide accurate isotopic concentrations (to ppb levels) such as LA-ICP-MS, a lack of RN standards makes quantification difficult. There is an alternative method, however, which involves calculating the concentration of RNs based on secular equilibrium. If a radioactive sample is in secular equilibrium, and the parent isotope can be accurately measured, then all daughter isotope concentrations can be calculated (Prince, 1979).

Three uraninite samples and one thorianite sample were mounted in epoxy resin, polished, and imaged by SEM (Uran_std; Table 2.1). Replicate LA-ICP-MS analyses of these samples revealed that three were at or near secular equilibrium while the fourth, uraninite 3, was not. Concentration estimates based on calibrated ^{238}U data were used for Ra concentration calculations, and are detailed in Chapter 8, Section 8.4.

2.2 Instrumentation and analytical methodology

2.2.1 Optical microscopy

The first step before any experimentation or analytical investigation commenced was to fully survey, characterise, and image the samples of interest – allowing optimal selection of grains for further work, recognition of minerals present, and identification of inclusions, fractures, or grain-scale zoning that might impact on results. Initial sample surveys were conducted using optical microscopy, predominantly in reflected light mode using a Nikon Eclipse LV100 POL petrographic microscope, located at Adelaide Microscopy, The University of Adelaide. Images of some, but not all, samples were digitally captured for general mineralogical characterisation

and future position referencing to aid navigation on other analytical platforms. Optical microscopy is suitable for initial surveys but is limited in its ability to distinguish most minerals in reflected light. Detailed petrographic analysis is usually performed on thin sections so that cross-polarised transmitted light may be used (e.g., Pracejus, 2015). For polished epoxy resin blocks, however, reflected light is the only option. Examples may be seen in Figure 2.2.

2.2.2 Scanning electron microscopy

For accurate mineral identification down to the scale of a few microns, a more powerful microscope is needed. The SEM platform is a workhorse, providing fast, spatially resolved semi-quantitative information on mineral composition and detailed, high-resolution images of mineral grains when used in combination with a back-scatter electron (BSE) detector and energy-dispersive X-ray spectroscopy (EDS) (e.g., Ludwig, 1998). Finding individual grains of interest (among tens of thousands) would have been impossible without the BSE ability to highlight Pb-, Bi-, Ag-, REE-, and U-bearing minerals (higher atomic mass = brighter BSE signal) which comprised a majority of the initial target mineral list. Grain selection and location with X-Y coordinates, high-resolution imaging, spot elemental analyses and occasionally large-scale elemental mapping were performed before all subsequent analyses including nanoSIMS, FIB, TEM, EBSD, and APT. Imaging sample grains after analyses was also quite useful to observe the amount of damage incurred during procedures (Figure 2.5).

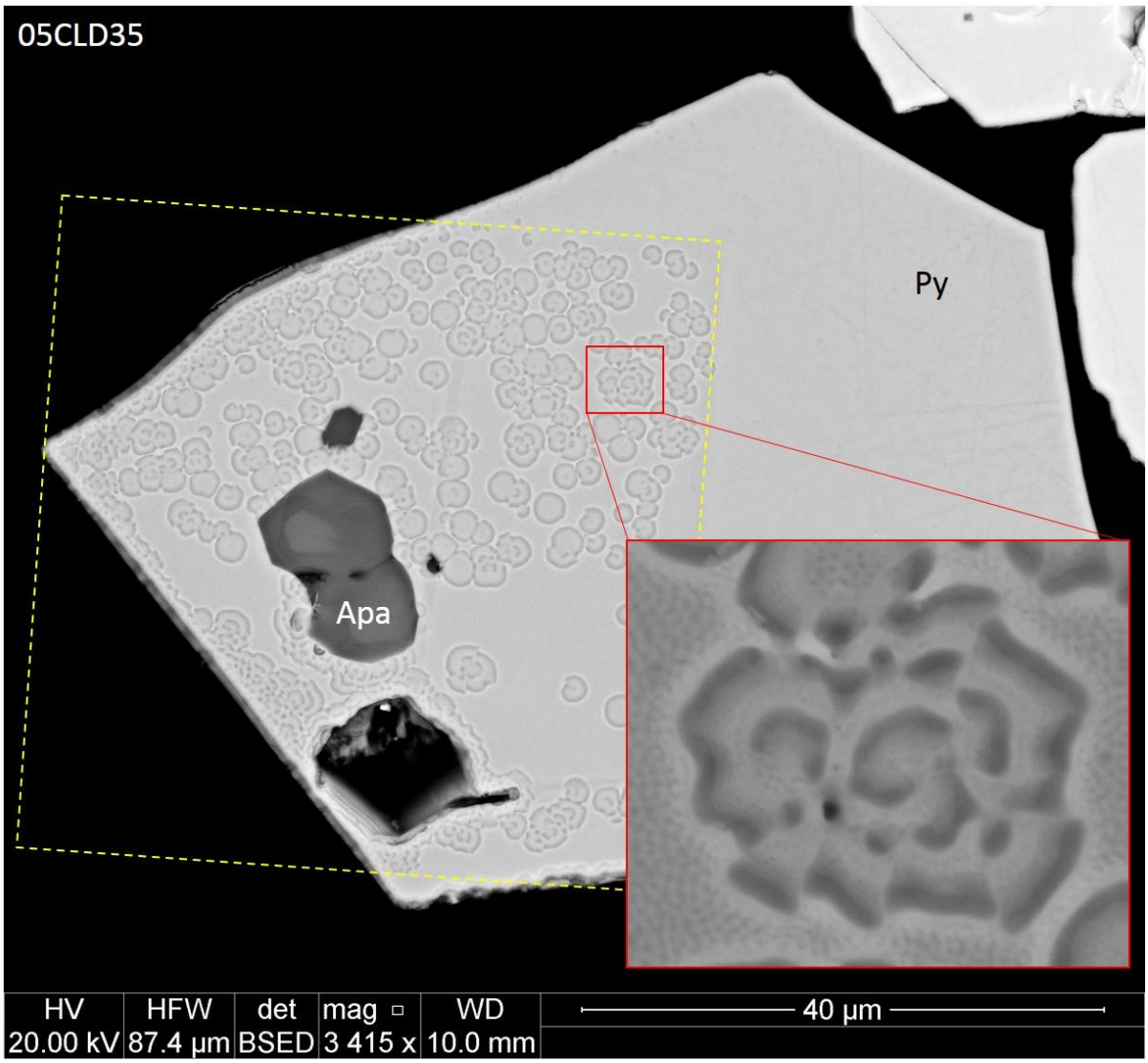

Figure 2.5. BSE image of a pyrite/apatite grain after nanoSIMS mapping. NanoSIMS map area outlined in yellow. Surface alteration is evident in pyrite, but the (previously) zoned apatite appears unaffected.

Adelaide Microscopy offers five SEM platforms, differing in terms of resolution and fitted spectrometers for ancillary purposes. The vast majority of characterisation and imaging for this project was performed on an FEI Quanta 450 field emission gun scanning electron microscope (FEG-SEM) with an EDAX EDS system (operative until December 2017), or a silicon drift detector (SDD) EDX system that was installed in early 2018. Figure 2.6 shows an example of a core sample from Olympic Dam, mapped with the new SDD EDX system. A few samples were analysed using a FEI Quanta 600 SEM, also equipped with an EDAX EDS system, or

using the FEI Helios Nanolab dual beam focused ion beam scanning electron microscope (FIB-SEM) equipped with an EDAX system.

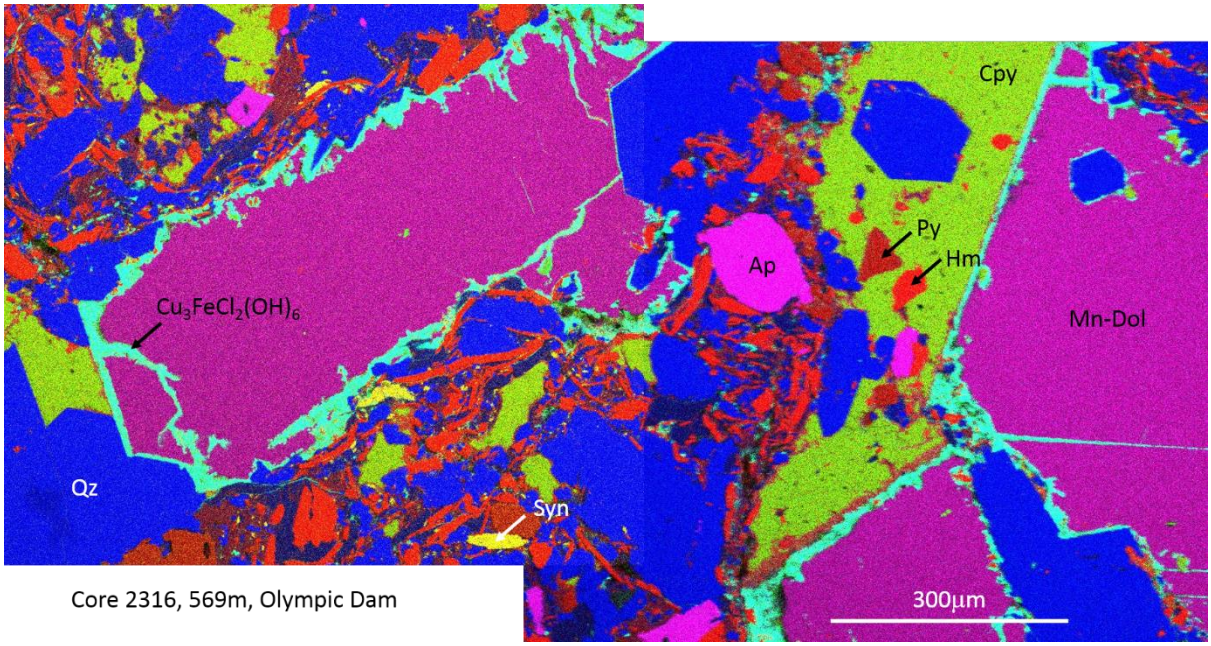

Figure 2.6. Elemental (mineral) mapping capabilities of the FEI Quanta 450 FEG-SEM with SDD EDS system exemplified by a multi-mineral assemblage within Olympic Dam drill core. Region imaged is the same as in Figure 2.1. Colours represent Cu (green), Si (blue), Ca (magenta), Nd (yellow), Fe (red), Mn (purple), and Cl (cyan). Minerals present within the mapped area are chalcopyrite (Cpy), manganoan dolomite (Mn-Dol), quartz (Qz), apatite (Ap), pyrite (Py), hematite (Hm), synchysite (syn), and unknown phase ($Cu_3FeCl_2(OH)_6$).

2.2.3 Nanoscale secondary ion mass spectrometry

Early in the project it was unclear which instrumentation, if any, would be able to provide the necessary combination of sub-micron resolution and lowest possible detection limits to identify the spatial distribution of RNs of interest within mounted grains. After seeing some examples of ^{13}C-labeled bacterial clusters analysed on the CAMECA nanoSIMS 50 in Perth (Onetto Carvallo, 2018), it became evident that this could be a suitable analytical platform, even if nanoSIMS mapping of elemental Ra or Po, or of minor isotopes such as ^{234}U, ^{230}Th, or ^{210}Pb had never, to our knowledge, been previously attempted. Beginning in February of 2017, the nanoSIMS 50L (produced by CAMECA in Gennevilliers, France, and located at the Centre for Microscopy, Characterisation, and Analysis (CMCA) at the University of Western Australia in

Perth) became the primary analytical tool for this Ph.D. project and provided pivotal results of major significance for the overarching ARC Research Hub for Australian Copper-Uranium. During 12 weeks of mapping over five separate trips to Perth, over 4000 nanoSIMS isotope maps were collected on the various sample types listed above.

The general theory behind SIMS involves bombarding a sample with an ion beam and then sending the secondary ions ejected from the sample into a mass spectrometer. The advantage of nanoSIMS over other SIMS platforms lies in the design, which sends the ion beam (usually either O^- or Cs^+) along the same path as the returning secondary ions. This geometry affords extremely short working distances (400 µm) which in turn results in high efficiency in terms of secondary ions reaching the detectors (Stadermann et al., 1999). Conventional systems use either an angled beam source or an angled detector, which results in longer working distances (4-20 mm) and lower efficiencies (Kilburn and Wacey, 2014). The nanoSIMS provides excellent spatial resolution (ideally down to 50 nm) and excellent detection capabilities (to low ppb) albeit without accurate quantification, at least for minerals. A schematic of the CAMECA nanoSIMS 50L is presented in Figure 2.7, reproduced from Hauri et al. (2016).

Unique complications were encountered while attempting to analyse ultra-low concentration isotopes at significantly higher-than-normal currents, without proper standards, in complex mineral matrices (Rollog et al., 2019; Chapter 3). Issues such as detector tuning, isobaric mass interferences, and sample damage are addressed. Examples of nanoSIMS isotope maps of different mineral grains may be seen throughout Chapters 3 through 7.

2.2.4 Laser ablation inductively coupled plasma mass spectrometry

LA-ICP-MS is a valuable technique to accurately determine low (typically ppm) levels of multiple minor and trace elements and isotope ratios in mineral matrices at resolution down to ~10 microns (e.g., Arrowsmith, 1987; Walder et al., 1993; Russo et al., 2002). The technique

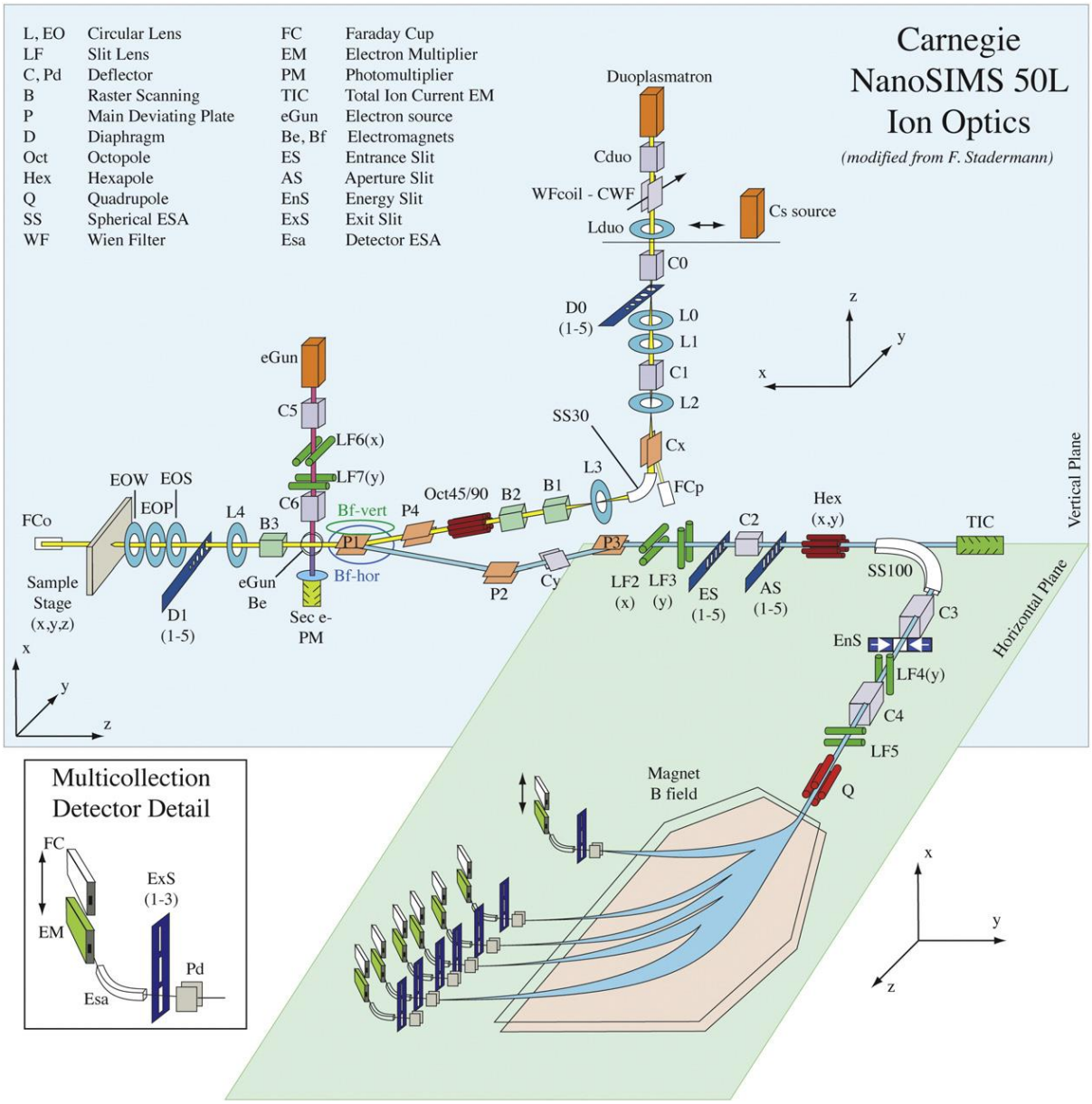

Figure 2.7. "Schematic diagram of the ion optical elements of the DTM Cameca NanoSIMS 50L, modified from the NanoSIMS 50 drawing by Frank Stadermann. The primary ion column is oriented in the vertical plane, while the mass spectrometer is oriented in the horizontal plane. Light-blue elements are circular lenses, red elements are multi-pole lenses, dark-green elements are slit lenses, grey elements are deflectors, light-green elements are used for synchronized rastering of the primary and secondary ions (dynamic transfer). Dark blue elements are user-positioned circular apertures for the primary beam (D0, D1) and slits for the mass spectrometer (ES, AS, EnS, ExS). The co-axial lens stack near the sample (EOW, EOP, EOS, L4) acts on both the primary and secondary ion beams and requires the primary and secondary ions be of opposite polarity and equal energy." Image and caption from Hauri et al. (2016).

is a three-step process: pulsing an ultra-fine laser onto a solid sample to create fine particles; ionising the liberated particles in a plasma torch; and accelerating the ions into a mass spectrometer for analysis. Adjustable laser beam widths and depths, pulse rates, and energies

provide flexibility for variable sample types and research objectives. The method has played an integral part of this Ph.D. project, providing a link between micron-scale observation of textures and assemblages and nanoscale information on element and isotope distributions.

Adelaide Microscopy is equipped with an ASI RESOlution-LR ArF excimer laser ablation system with a large format S155 sample chamber (Laurin Technic Inc.), coupled to an Agilent 7900x ICP-MS. Single-spot analyses (51, 74 or 110 µm spot size) were run on synthetic minerals, all of the Tate Museum Standard minerals, and the uranium decay chain standard minerals, with isotopic concentrations calculated from single spot measurements (74 µm) of standards NIST-610 and NIST-612. Elemental concentrations (except Pb and Ra) were calculated from measured isotope concentrations using global isotopic ratios reported in Haynes (2014). Additionally, laser transects using a small (6 µm-diameter) beam width were performed across synthetic grains from diffusion experiments. Details including instrument settings, concentration calculations, and transect data are presented in Chapters 5 and 8.

2.2.5 Solution ICP-MS

Solution ICP-MS combines the flexibility and accuracy of ICP-MS with ultra-low detection limits (theoretically to ppq). Similar to the ICP-MS measurements above, the only difference is the sample introduction method which involves aspirating a dilute acid solution containing the sample into the plasma torch. Although only briefly mentioned in one chapter (Chapter 8, Figure 8.2), solution ICP-MS has played an integral role in monitoring progress and results of the diffusion experiments. Sample solutions collected during various stages of experimentation were analysed on an Agilent 8900x triple-quad (QQQ-ICP-MS) system (Adelaide Microscopy); concentrations were calculated using various dilutions of calibrated in-house standard solutions containing most of the periodic table.

2.2.6 Alpha track radiography

It could be argued that the first experiment ever performed regarding RNs was autoradiography, resulting in the discovery of radioactivity (Becquerel, 1896). Briefly, alpha radiation reacts with silver (and other metals) suspended in photographic emulsions which results in their reduction to the metal upon development (Herschel, 1843). Although traditional photographic paper still works well, modern techniques involve specially formulated alpha-track gel which may be applied directly on a sample (Kalnins et al., 2019), or a plastic polymer (CR-39) which reacts specifically to alpha radiation (Fews and Henshaw, 1982).

Samples of all types were frequently subjected to alpha-tracking gel or CR-39 plastic in order to determine whether RNs were present. Alpha tracking gel consists of activated silver compound nanoparticles in a thin gel matrix which may be "painted" on a sample and left to react. As alpha particles pass into the gel, they leave a trail of reduced silver nanoparticles. After developing the sample (a process similar to photographic development; Kalnins et al., 2019), the silver particle trails become visible to optical or scanning electron microscopy (Figure 2.8c). In similar fashion, CR-39 plastic is a polymer with a narrow range of bond strengths which are broken by passing alpha particles. The 0.5 mm-thick plastic is left in contact with the sample for a measured period of time and then etched, usually using the "666" system – 6 M NaOH at 60 °C for 6 hours. The NaOH preferentially dissolves the polymer where bonds were broken, leaving small, oblong voids representing individual alpha decay events (Figure 2.8d). Shorter etch times resulted in smaller etch pores, which facilitated counting in higher alpha-density samples (Figure 2.8b).

If the density of tracks in the gel or pores in the CR-39 plastic allows, then a rough calculation of total activity – and therefore concentration – can be made. For natural samples, assumptions must be made as to the RNs present, as all alpha tracks look roughly the same

with these methods. However, the sample grain in Figure 2.8 was exposed only to Po, so an estimate of 200 ppt Po (whole grain) could be calculated quite easily.

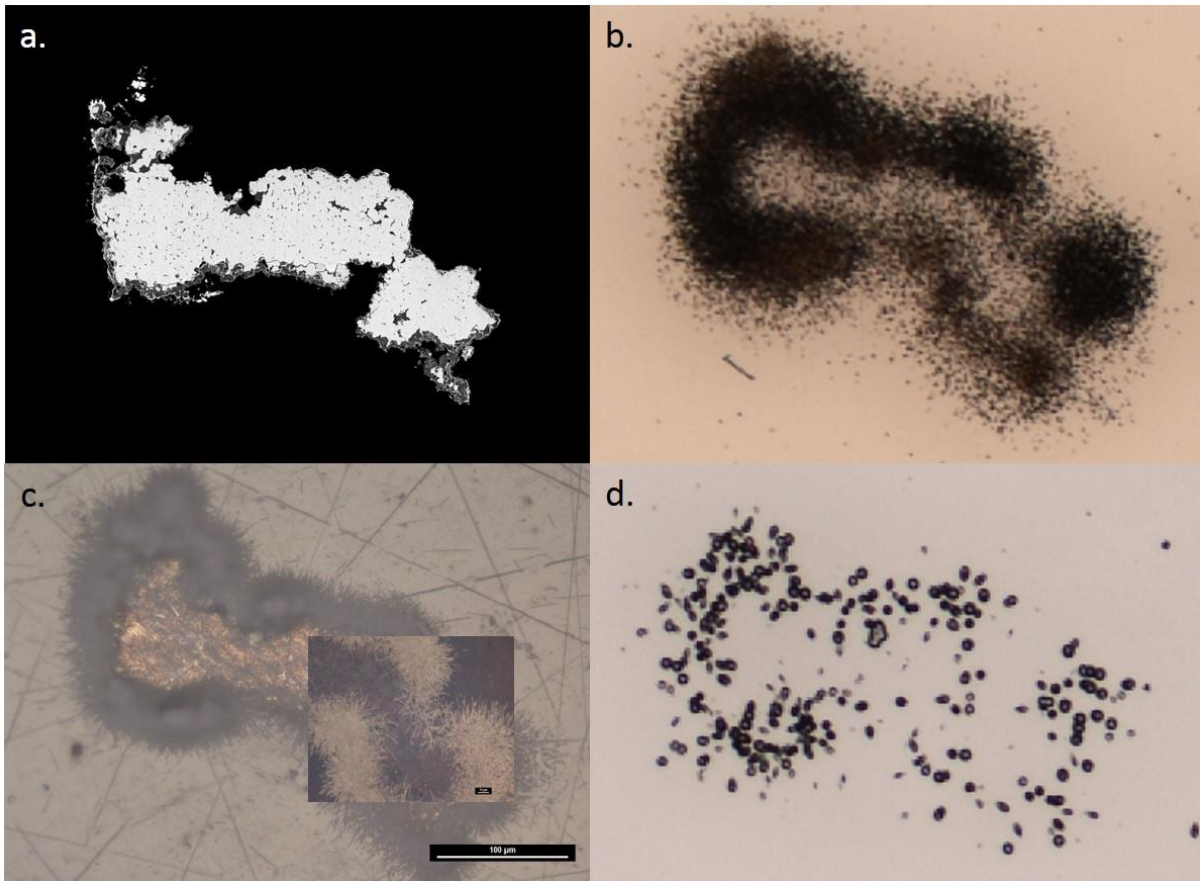

Figure 2.8. Alpha-track images of a synthetic grain of clausthalite (PbSe) which had been exposed to Po solution. BSE image (a); CR-39 plastic, 168-hour exposure time, 3-hour etch (b); alpha-track gel (c, courtesy of Chris Kalnins); and CR-39 plastic, 45-minute exposure time, 6-hour etch (d). The overlay in frame (c) employed top-lighting, the rest of the frame is back-lit. Polonium concentration is estimated to be 200 parts-per-trillion (whole grain) and up to 20 ppb (rim).

2.3 References

Arrowsmith, P., 1987. Laser ablation of solids for elemental analysis by inductively coupled plasma mass spectrometry. Analytical Chemistry 59, 1437-1444.

Bagnall, K.W., 1973. The Chemistry of Sulphur, Selenium, Tellurium and Polonium. Pergamon Press, NY. pp. 935-1008.

Becquerel, A.H., 1896. Sur les radiations invisibles émises par les corps phosphorescents. Comptes Rendus de l'Academie des Science 122, 501.

Byrne, K., Hawker, W., Vaughan, J., 2018. Deportment of radionuclides during copper concentrate metathesis reactions. Proceedings ALTA 2018, 19-26 May 2018, Perth, WA, 12 pp.

Ciobanu, C.L., Wade, B.P., Cook, N.J., Mumm, A.S., Giles, D., 2013. Uranium-bearing hematite from the Olympic Dam Cu–U–Au deposit, South Australia: A geochemical tracer and reconnaissance Pb–Pb geochronometer. Precambrian Research 238, 129-147.

Curie, P., Curie, M., Becquerel, H., 1898. Sur une substance nouvelle radio-active, contenue dans la pechblende. Comptes Rendus de l'Academie des Science 127, 1215-1217.

Doerner, H.A., Hoskins, W.M., 1925. Co-Precipitation of Radium and Barium Sulfates 1. Journal of the American Chemical Society 47, 662-675.

Dunn, G.M., Saich, S., Bartsch, P.J., 2017. Hydrometallurgical method for the removal of radionuclides from radioactive copper concentrates. United States Orway Mineral Consultants Pty. Ltd. Patent no. US9587290B2.

Fews, A.P., Henshaw, D.L., 1982. High resolution alpha particle spectroscopy using CR-39 plastic track detector. Nuclear Instruments and Methods in Physics Research 197, 517-529.

Gramaccioli, C.M., Segalstad, T.V., 1978. A uranium-and thorium-rich monazite from a south-alpine pegmatite at Piona, Italy. American Mineralogist 63, 757-761.

Hauri, E.H., Papineau, D., Wang, J., Hillion, F., 2016. High-precision analysis of multiple sulfur isotopes using NanoSIMS. Chemical Geology 420, 148-161.

Haynes, W.M., 2014. CRC Handbook of Chemistry and Physics. CRC Press, Boca Raton, FL, 2643 pp.

Henisch, H.K., 1996. Crystal growth in gels. Pennsylvania State University Press, University Park, PA, 107 pp.

Herschel, J.F.W., 1843. Note on the Art of Photography, or the Application of the Chemical Rays of Light to the Purposes of Pictorial Representation. In: Abstracts of the Papers Printed in the Philosophical Transactions of the Royal Society of London 4, pp. 131-133.

Kalnins, C.A., Spooner, N.A., Clarke, M.J., Ottaway, D., 2019. Alpha particle autoradiography for high spatial resolution mapping of radionuclides. Journal of Environmental Radioactivity 197, 9-15.

Kilburn, M.R., Wacey, D., 2014. Nanoscale secondary ion mass spectrometry (NanoSIMS) as an analytical tool in the geosciences. In: Fay, L.B., Kussmann, M. (Eds.), Principles and Practice of Analytical Techniques in Geosciences. Royal Society of Chemistry, pp. 1-34.

Ludwig, R., 1998. Scanning electron microscopy. Springer, Berlin, Germany. 529 pp.

Onetto Carvallo, C.A., 2018. Identity and physiology of glycogen accumulating organisms in activated sludge Unpublished Ph.D. thesis, The University of Adelaide, Adelaide, Australia. 71 pp.

Pracejus, B., 2015. The ore minerals under the microscope – an optical guide, 2nd Edition. Elsevier Publishing. 1118 pp.

Prince, J.R., 1979. Comments on equilibrium, transient equilibrium, and secular equilibrium in serial radioactive decay. Journal of Nuclear Medicine 20, 162-164.

Rollog, M., Cook, N.J., Guagliardo, P., Ehrig, K., Kilburn, M., 2019. *In situ* spatial distribution mapping of radionuclides in minerals by nanoSIMS. Geochemistry: Exploration, Environment, Analysis 19, 245-254. doi:10.1144/geochem2018-038.

Russo, R.E., Mao, X., Gonzalez, J.J., Mao, S.S., 2002. Femtosecond laser ablation ICP-MS. Journal of Analytical Atomic Spectrometry 17(9), 1072-1075.

Stadermann, F.J., Walker, R.M., Zinner, E., 1999. NanoSIMS: The next generation ion probe for the microanalysis of extra-terrestrial material. Meteoritics and Planetary Science Supplement 34, A111-A112.

Walder, A.J., Abell, I.D., Platzner, I., Freedman, P.A., 1993. Lead isotope ratio measurement of NIST 610 glass by laser ablation inductively coupled plasma mass spectrometry. Spectrochimica Acta Part B: Atomic Spectroscopy 48(3), 397-402.

Chapter 3

In situ spatial distribution mapping of radionuclides in minerals by nanoSIMS

Mark Rollog [a,*], Nigel J. Cook [a], Paul Guagliardo [b], Kathy Ehrig [c], Matt Kilburn [b]

[a] *School of Chemical Engineering, University of Adelaide, Adelaide, 5005 S.A., Australia*

[b] *Centre for Microscopy, Characterisation, and Analysis, University of Western Australia, 35 Stirling Highway, Crawley, 6009 W.A., Australia*

[c] *BHP Olympic Dam, 55 Grenfell St., Adelaide, 5000 S.A., Australia*

Article published in *Geochemistry: Exploration, Environment, Analysis 19, 245-254*.

Statement of Authorship

Title of Paper	In situ spatial distribution mapping of radionuclides in minerals by nanoSIMS
Publication Status	☑ Published ☐ Accepted for Publication ☐ Submitted for Publication ☐ Unpublished and Unsubmitted work written in manuscript style
Publication Details	Submitted for publication to Geochemistry: Exploration, Environment, Analysis 26 April 2018 Accepted for publication 30 June 2018, https://doi.org/10.1144/geochem2018-038

Principal Author

Name of Principal Author (Candidate)	Mark Rollog
Contribution to the Paper	Designed experimentation, performed sample analysis and data interpretation, wrote manuscript
Overall percentage (%)	70
Certification:	This paper reports on original research I conducted during the period of my Higher Degree by Research candidature and is not subject to any obligations or contractual agreements with a third party that would constrain its inclusion in this thesis. I am the primary author of this paper.
Signature	Date 23.08.19

Co-Author Contributions

By signing the Statement of Authorship, each author certifies that:

i. the candidate's stated contribution to the publication is accurate (as detailed above);

ii. permission is granted for the candidate in include the publication in the thesis; and

iii. the sum of all co-author contributions is equal to 100% less the candidate's stated contribution.

Name of Co-Author	Nigel J. Cook
Contribution to the Paper	Supervised direction and progress of work, helped evaluate and edit manuscript
Overall percentage (%)	10
Signature	Date 1/8/19

Name of Co-Author	Paul Guagliardo
Contribution to the Paper	Oversaw sample analyses, provided training regarding data handling and interpretation, and helped evaluate and edit the manuscript
Overall percentage (%)	10

Signature	Paul Guagliardo	Date	25 Jul 2019

Name of Co-Author	Kathy Ehrig		
Contribution to the Paper	Provided samples and helped evaluate and edit the manuscript		
Overall percentage (%)	5		
Signature		Date	31 July 19

Name of Co-Author	Matt Kilburn		
Contribution to the Paper	Oversaw the facility where the samples were analysed, provided insight and assistance with initial instrument operation and data interpretation		
Overall percentage (%)	5		
Signature		Date	25 Jul 2019

GEEA

Research article

Geochemistry: Exploration, Environment, Analysis

Published online November 19, 2018

https://doi.org/10.1144/geochem2018-038 | Vol. 19 | 2019 | pp. 245–254

In situ spatial distribution mapping of radionuclides in minerals by nanoSIMS

Mark Rollog[1]*, Nigel J. Cook[1], Paul Guagliardo[2], Kathy Ehrig[3] & Matt Kilburn[2]

[1] School of Chemical Engineering, University of Adelaide, Adelaide 5005 S.A., Australia
[2] Centre for Microscopy, Characterisation, and Analysis, University of Western Australia, 35 Stirling Highway, Crawley, 6009 W.A., Australia
[3] BHP Olympic Dam, 55 Grenfell St., Adelaide 5000 S.A., Australia
M.R., 0000-0001-6719-2586; K.E., 0000-0002-5381-9445; M.K., 0000-0002-1858-8485
* Correspondence: mark.rollog@adelaide.edu.au

Abstract: The nanoSIMS (nanometre-resolution secondary ion mass spectrometry) microanalytical platform is used, for the first time, for direct *in situ* visualization of medium half-life radionuclide (RN) distributions (^{226}Ra – 1602y; ^{210}Pb – 22.3y) in copper sulphide-bearing ore and copper sulphide flotation concentrate samples. More than 200 grains have been mapped, all with an Hyperion (H200) RF plasma oxygen ion source. Sufficient counts for masses of interest allowed the generation of maps that stand as a proof of concept for further detailed work to address the physical locations of radionuclides of main interest. The issue of potential isobaric interfering masses has been addressed and partially resolved. The distribution of the studied radionuclides, both in relation to host minerals and in relation to each other, is logical and clearly supported by well-established theories of deportment, diffusion, and redistribution. Isotope maps for ^{210}RN (^{210}Pb, ^{210}Po and ^{210}Bi) and ^{226}Ra maps tended to show RN distribution either within minerals (evenly distributed or zoned), as 'hot spots' on grain surfaces/mineral boundaries, or between cleavage planes of micaceous minerals. NanoSIMS element mapping of radionuclides may have widespread application for the disposal and long-term storage of nuclear waste, radioisotope monitoring, forensic science, nuclear and materials science, nuclear medicine, minerals engineering, and isotope geochemistry.

Keywords: *in situ* spatial distribution mapping; radionuclides; ^{210}Pb; polonium; radium; thorium; uranium; nanoSIMS

Received 26 April 2018; **revised** 18 June 2018; **accepted** 30 June 2018

Uranium and thorium and their daughter isotopes occur naturally throughout the environment, from soils and streams to mountains and oceans. Brick and concrete, copper and steel, even the food we grow and the water we drink contain ultra-trace amounts of these elements. Measurements of uranium, thorium, radium, radon, lead and polonium radionuclides (RN) in various media have been undertaken since their discovery more than a century ago (Becquerel 1901; Borkowski 1949; Solomon & Estes 1948).

Certain sectors have advanced monitoring methods for radionuclides of the ^{238}U, ^{235}U and ^{232}Th decay chains, such as nuclear medicine (Cherry *et al.* 1995), environmental studies (Cowart & Burnett 1994; Clayton & Bradley 1995; von Gunten & Beneš 1995; Jia *et al.* 2007; Matthews *et al.* 2007; Skwarzec 2009; Hu *et al.* 2010), nuclear energy production and waste storage (Godbee *et al.* 1969; Weber & Roberts 1983), and mining (Bettencourt *et al.* 1990; Landa & Gray 1995). Currently, ^{210}Pb, ^{210}Po, and to a lesser extent ^{210}Bi (here collectively referred to as ^{210}RN) and ^{226}Ra are measured routinely in environmental studies as well as activities associated with the nuclear fuel cycle. Methods are varied and include solvent extraction (Case & McDowell 1982; Beklemishev *et al.* 1994; Law *et al.* 1999), co-precipitation (Zhang *et al.* 2014), ion-exchange (Gleason 1980; Case & McDowell 1982; Oliveira & Carvalho 2006), chelation (Henriksen *et al.* 2002; Aaseth *et al.* 2015), electrodeposition (Vesterbacka & Ikäheimonen 2005; Oliveira & Carvalho 2006), chromatography (Dickey 1953), and radon emanation (^{226}Ra only) (Liatsou & Pashalidis 2016; Krupp *et al.* 2017). These methods are only used for isolation and concentration of radionuclides of interest; quantification relies on alpha (Skwarzec *et al.* 2016), beta (Hansen *et al.* 2014), gamma spectroscopy (Adams & Dams 1970) – or a combination thereof (Schuster 2015).

Although advancements in separation and extraction methods have allowed minimum detection limits of ^{210}RN and ^{226}Ra to drop exponentially, many methods still rely on the dissolution or digestion of samples which necessitate averaged bulk analyses. For many applications, this is perfectly acceptable and gives excellent results. There are, however, certain scenarios where passive detection is not ideal, and where spatially resolved radionuclide distributions are desired. *In situ* determination of isotopic distributions, at sub-micrometre resolution, is of utmost importance for unravelling the complex mineralogical behaviour of radionuclides as they progress down the decay chain. The Cameca line of nanoSIMS instruments (Hillion *et al.* 1993; Kilburn & Wacey 2014) are well-suited to fulfil these requirements. Complementary to nanoSIMS, high-resolution alpha track methods are also in development to pinpoint regions of high alpha and beta activity within natural mineral samples. With the advantages of a simple procedure, high throughput, and quick turnaround, alpha tracking can highlight regions of interest for detailed nanoSIMS analyses, reducing instrument time lost on inactive grains.

Mining industry procedures for radionuclide monitoring involve measuring activity levels of samples from various stages of processing (Fukuma *et al.* 2000; Martin 2000). This approach is not appropriate for determining the mineralogical hosts of RN, especially for those deposits which exhibit fine to extremely fine-grained mineral textures. In South Australian iron-oxide-copper-gold-uranium (IOCG-U) deposits, for example, ores comprise nano- to micrometre-scale intergrowths which can only be characterized by careful scanning electron microscopy. It is not uncommon for 50 µm-sized particles in ore feed or flotation

concentrate to contain a dozen or more minerals, with some occurring as disseminated nanoparticles only visible with transmission electron microscopy. This complexity hinders efforts to resolve the mineralogical pathways of radionuclides, as the exact host minerals (or surface features, in the case of nanoparticles) are unknown.

Analyses of radionuclides at these facilities has, to this point, been limited to bulk analyses. While extremely sensitive, they offer limited information as to the specific chemical or physical processes involved at the mineral scale. These samples necessitate an intermediate step by which radionuclides must first be located before activities can be measured. The Cameca nanoSIMS platform provides an alternative approach which can provide detailed, sensitive spatial distributions of trace-level isotopes *in situ,* on individual grains.

Some advancements have been made in the direct detection of low-concentration radionuclides using various ICP-based instruments. Becker (2005) states '… ICP-MS coupled with a laser ablation system (LA) to create LA-ICP-MS opens up the possibility of direct isotope analysis on solid samples, mostly without additional sample preparation steps', and indeed, a few studies have been performed (Boulyga *et al.* 2003, 2004; Didier *et al.* 2015), although not analysing for radium or ^{210}RN. The Cameca nanoSIMS systems provide a new approach to moderate half-life radionuclide research with application to sectors where spatial resolution of radionuclide distributions is paramount. NanoSIMS has been underutilized to this point regarding radionuclide analyses, although a few actinide and caesium studies have yielded excellent results (Cantrell & Felmy 2012; Kalmykov *et al.* 2007; Kersting 2013, 2017).

This contribution reports a proof of concept that nanoSIMS can be applied to the direct *in situ* visualization of moderate half-life radionuclide distributions (^{226}Ra and ^{210}Pb) in copper sulphide-bearing ore and copper sulphide flotation concentrate samples. These radionuclides represent non-target components of some ores. Knowledge of their physical distributions is essential for efforts to reduce or remove them. The same methodologies applied to other moderate half-life isotopes – both natural and anthropogenic – will, we believe, have implications for the disposal and long-term storage of nuclear waste, for radioisotope monitoring, in forensic science, and will likely also be a valuable complement to existing techniques in nuclear and materials science, minerals engineering, isotope geochemistry and geochronology.

Methods

Investigated sample mounts are one-inch diameter polished epoxy mounts, each containing on the order of 100 000 exposed grains (*c.* 200 grains per mm^2), representing specific stages of the mining and mineral processing operation at Olympic Dam, South Australia (Ehrig *et al.* 2012). Sample mounts included copper sulphide flotation concentrates (FC), diamond drill core samples, and sulphuric acid leached concentrates subsequent to flotation to remove the majority of uranium (concentrate leach discharge, CLD). Sample mounts were surveyed at Adelaide Microscopy (The University of Adelaide) using scanning electron microscopy (SEM) to locate and identify grains of interest. Targeted minerals were those considered known or likely RN-carriers and included Pb-, Ag, Bi-chalcogenides and uranium minerals (uraninite, coffinite and brannerite), but also included various REE-Y minerals (bastnäsite, xenotime, florencite) apatite, fluorite, hematite, and zircon, as well as various carbonates and other gangue minerals (Ciobanu *et al.* 2013; Macmillan *et al.* 2016, 2017; Krneta *et al.* 2016, 2017; Schmandt *et al.* 2017; Verdugo-Ihl *et al.* 2017). Grains were imaged, location coordinates recorded, and major components identified using energy-dispersive X-ray spectroscopy (EDS). Using the Helios NanoLab focused ion-beam SEM (FIB/SEM) at Adelaide Microscopy, additional thin-slice samples were prepared from some grains that were appropriate for transmission electron microscopy (TEM), measuring *c.* 20 × 10 × 0.1 μm mounted on 3-mm copper foil mounts.

Isotope distribution mapping was performed on a Cameca NanoSIMS 50 L, hosted by the Centre for Microscopy, Characterisation, and Analysis (CMCA) at the University of Western Australia in Perth. Sample mounts were sent to the facility two weeks in advance for degassing in the instrument's antechamber. More than 200 grains of interest were mapped in total, using various instrument settings, but all with the Hyperion (H200) RF plasma oxygen ion source. Seven isotopes may be mapped at once, and most grains were mapped two or three times. Copper and/or iron isotopes were included in each run as baseline isotopes, to which all other maps may be compared.

The first 13 grains mapped were all located on a single sample mount consisting of a copper sulphide concentrate from Olympic Dam. The concentrates were produced via separation of copper sulphides from gangue minerals by the froth flotation process. Prior to mapping, the area of interest was pre-sputtered with the primary beam to a dose of *c.* 3 × 10^{17} ions/cm^2 in order to remove the carbon coating and any surface contamination, and to implant oxygen into the analysis area to enhance secondary ion emission.

The instrument was tuned to most of the isotopes of interest using a 40-element standard mount, supplied by Astimex. An additional rare earth standard mount, produced in-house, was used for rare earth elements. Barium was not included on either standard mount, so tuning was performed while scanning a barite grain on the sample mount. Initial instrument settings (50 × 50 μm raster area, 100 pA ion current, ES = 2, AS = 0, D1 = 2, 256 × 256 px, 6 planes, 10 ms/px) proved unsuccessful, as there was no discernible signal on mass 210 when mapping a barite grain (a suspected host for ^{226}Ra and its decay products). Repeating the analysis with an increase in beam current from 100 to 250 pA resulted in a low signal on mass 210 correlating with the barite grain, and only the barite grain. All further ^{210}RN analyses were performed using these settings. The seven isotopes mapped during each run changed each day to address as many isobaric interfering mass issues as possible within a limited timeframe. Since ^{208}Pb and ^{209}Bi were considered to be primary candidates for mass 210 interference, seven grains were mapped for all three masses. Because nanoSIMS cannot simultaneously analyse for species differing by <*c.* 4 atomic mass units at high mass, these were mapped in three separate runs.

After detailed analysis of results from the first nanoSIMS session, an additional 125 grains of CLD, 59 grains of FC, and select areas from 9 drill core samples from Olympic Dam were mapped. A more uniform approach was applied to these analyses. Each grain was first mapped for ^{54}Fe$^+$, ^{63}Cu$^+$, ^{138}Ba$^+$, ^{142}Nd$^+$, ^{169}Tm$^+$, ^{206}Pb$^+$ and ^{238}U$^+$ (50 × 50 μm raster area, 50 pA ion current, D1 = 2, ES = 2, AS = 0, 512 × 512 px, 3 planes, 5 ms/px, effective beam diameter ≈500 nm). In some instances, ^{144}Nd$^+$ was substituted for ^{142}Nd$^+$. Grains were pre-sputtered with the primary beam to a dose >3 × 10^{17} ions/cm^2. Three frames were generated for each isotope for each grain; analysis time (including the presputter) was 87 min per grain.

The grains were then mapped again, without presputtering, for ^{42}Ca$^+$, ^{46}Ti$^+$, ^{54}Fe$^+$, ^{88}Sr$^+$, ^{210}RN$^+$, ^{226}Ra$^+$, and ^{230}Th$^+$ (50 × 50 μm raster area, 250 pA ion current, D1 = 2, ES = 2, AS = 0, 512 × 512 px, 6 planes, 5 ms/px, effective beam diameter ≈700 nm). For some grains, ^{47}Ti$^+$ and ^{87}Sr$^+$ were determined instead of the above. Six frames were generated for each isotope for each grain; analysis time was 131 min per grain.

Image processing was carried out using the OpenMIMS plugin (Poczatek *et al.* 2009) for ImageJ (Schindelin *et al.* 2012, 2015). Maps for each isotope were corrected for dead time, aligned to account for instrument drift, and the total counts compiled in sum

maps. These are the maps used for image presentation (adjusted for brightness/contrast, colorized) and statistical analyses.

It is important to note that this method is (currently) not quantifiable, due to differences in ionization probabilities for each element/isotope as well as variations in sputtering rates for different minerals in each grain. Efforts are currently underway to produce matrix-matched standards to allow at least semi-quantification of like material.

Results

Isobaric mass interferences

When employing any form of mass spectrometry, it is of paramount importance to ensure that the mass signal observed is due to the isotope(s) of interest and not from interference. Isobaric mass interference may be from a single element with the same isotopic mass or a combination of elements. Fortunately, the only elemental possibilities for mass 210 include ^{210}Po, ^{210}Bi, and ^{210}Pb, all of which are relevant to this project. It is not necessary to distinguish between elemental contributions to the total mass 210 signal, although this can be estimated with the assumption of secular equilibrium (98.26% Pb, 1.68% Po, and 0.06% Bi). However, regarding di- and tri-atomic compounds there are theoretically hundreds of possible isobaric mass interferences for mass 210 (or 226). Conveniently, the overwhelming majority of those may be immediately discounted due to either a lack of one (or both) of the elements in the sample (e.g. ^{78}Kr^{132}Xe), or the scarcity of one of the isotopes of interest (e.g. ^{196}Pt^{14}C). All combinations involving a cosmogenic isotope were discounted. Rationally, the most likely interferences would be compounds either involving two elements of high abundance in the sample, or a high abundance element in combination with a component of residual atmosphere found in the nanoSIMS sample chamber. Oxides and nitrides are of particular interest, since an oxygen source was used as the ion beam for these analyses and the sample chamber is flushed with dry nitrogen prior to evacuation.

Efforts focused on the most likely mass 210 interferences for these specific mineral assemblages, which include ^{209}Bi^{1}H, ^{208}Pb^{1}H^{1}H, ^{194}Pt^{16}O, ^{196}Pt^{14}N, and ^{130}Te^{80}Se. For ^{226}Ra, the two likeliest candidates are ^{194}Pt^{32}S and ^{138}Ba^{88}Sr – the oxide having been ruled out (^{210}RN^{16}O) due to distinctly different distributions observed between mass 210 and mass 226. Three criteria were used for determining whether a mass interference was an issue: measuring the ratio of interfering mass to the major mass peak while analysing a standard; comparing distribution maps of the individual isotopic components to look for overlap; calculating a 'theoretical maximum interference' by analysing a worst-case scenario.

After tuning the instrument to mass 208 using a pure lead standard, the detector was shifted up by 2.016 mass units to where ^{208}Pb^{1}H^{1}H would be expected. There was a signal, but it was four orders of magnitude lower than the mass 208 signal. Assuming that atmospheric interferences (hydrides, nitrides, oxides) are instrument-dependent and will therefore be the same for sample and standard alike, it suggests that this represented a near-maximum interference based on the standard being 100% lead. A similar response was observed for mass 209 on the bismuth standard and the subsequent shift to ^{209}Bi^{1}H.

Commonly, the term 'isobaric' mass is not accurate, as di- or triatomic molecules tend to have slightly higher or lower masses than a single element. For example, polonium is a chalcogen and would therefore behave like sulphur, selenium and tellurium. Consequently, polonium liberated in the acid leach tank may eventuate in association with selenium and/or tellurium in a mineral containing those elements. This is complicated by ^{82}Se^{128}Te and ^{80}Se^{130}Te, which combined account for 19.7% of all SeTe, and each has an apparent mass of 210. More precisely, however, the masses are 209.8225 and 209.8227, respectively. The individual detectors of the nanoSIMS are able to distinguish these from ^{210}Po (209.9829) and ^{210}Pb (209.9842), although the peaks may not be completely resolved.

Figure 1 shows the distribution of ^{208}Pb, ^{209}Bi, and ^{210}RN in a uraninite-bearing chalcopyrite grain. If the ^{210}RN signal was the result of mass interference from a hydride, we would expect to see a near-exact correlation between the ^{208}Pb or ^{209}Bi map (or a combination thereof) and the ^{210}RN map. No such correlation is apparent. Similar results were evident in many other grains. The ^{210}RN distribution observed is logical and expected, with clear correlations between ^{238}U and ^{226}Ra and a complete lack of correlation between ^{210}RN and Fe, Cu, etc. Likewise, overlays of distribution maps for ^{138}Ba and ^{88}Sr do not correlate directly to ^{226}Ra maps, although there is substantial overlap. This is to be expected, as it is well known that both Sr and Ra substitute easily into barite (Hedström *et al.* 2013; Weber *et al.* 2017). There is sufficient difference, however, to state with confidence that the ^{226}Ra signal is not *caused* by a ^{138}Ba^{88}Sr interference but is instead coincident with Ba and Sr in the sample.

As a potential worst-case scenario, a sample grain was mapped which had been previously subjected to FIB/SEM trenching. This sample grain had a 25 × 20-μm trench cut on one edge of the grain, with a 2 × 2 × 25-μm deposited platinum strip still in place, as seen in Figure 2a. The reasoning was that pure platinum metal in combination with the oxygen source beam would provide the likeliest possible chance of observing a mass 210 signal (^{194}Pt^{16}O, which represents 33% of all PtO) which was *not* due to ^{210}Pb, ^{210}Bi, or ^{210}Po. Additionally, 25% of all PtN, another possible interference, also has a mass of 210, increasing the likelihood that interference caused by platinum approaches a maximum. Figure 2b shows the distribution of ^{210}RN in the sample grain, and at first glance it appeared that the platinum strip was the cause of the strong signal in the lower left of the map. Upon more detailed analysis, it was discovered that the highest signal intensity was, in fact, the chalcocite/barite and siderite/barite grain boundaries and not the platinum strip, which was visible as a uniform shadow just to the left of the boundary. The platinum oxide/nitride did give a positive response which had little to no influence from ^{210}Pb, ^{210}Bi, or ^{210}Po. The response in question, however, was very low with an average intensity of only one count per pixel per hour of measurement time, and the counts which can be directly attributed to platinum interference represent less than 6% of the total counts in the map. When considering the average platinum concentration in Olympic Dam ore is <1 ppb, it would be difficult to argue a significant contribution to the mass 210 signal from either ^{194}Pt^{16}O or ^{196}Pt^{14}N.

A second example of a worst-case interfering mass involves ^{169}Tm. Of the rare earths, there are four which are ideal for SIMS analyses because they have only one isotope, and that isotope is unique to that element. Of the four (^{141}Pr, ^{159}Tb, ^{165}Ho, and ^{169}Tm) the last was chosen to represent the heavy rare earth elements (HREE) in the samples. In addition to the previously mentioned methods of ensuring thulium was being determined, including tuning the instrument using a pure thulium standard material, mass 169 distribution was mapped in barites. Isobaric mass interference at 169 in barite would not be unexpected as ^{137}Ba^{32}S or ^{137}Ba^{16}O^{16}O, considering ^{137}Ba, ^{16}O, and ^{32}S are all important isotopic contributors (11.23%, 99.76%, and 94.93%, respectively) of major elements in the mineral. Mass 170 may have provided a stronger response due to the higher abundance of ^{138}Ba (71.70% of all barium); however, mass 170 may represent either erbium or terbium and preference was given to the uniqueness of ^{169}Tm. Although this would make little difference in natural samples, where Er, Tm, and Tb all generally occur together, when verifying

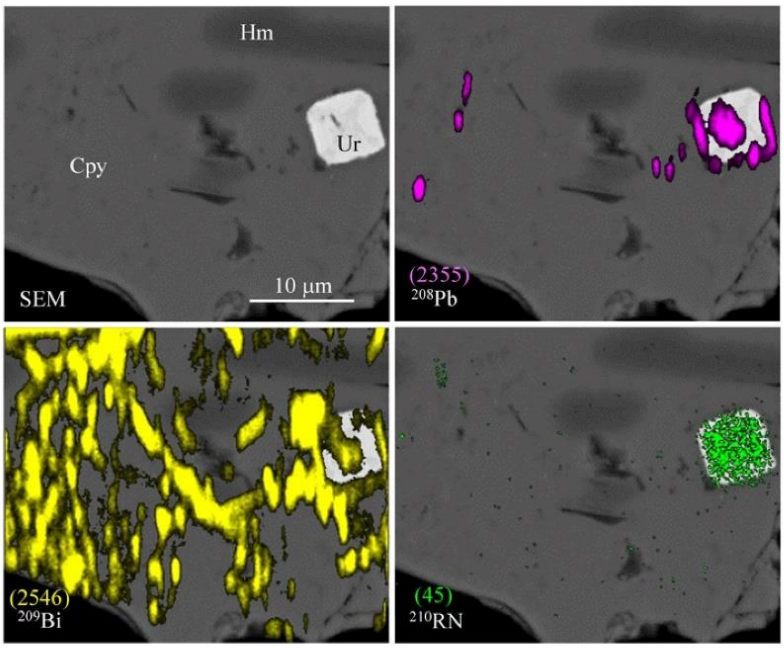

Fig. 1. Isotopic distribution maps for a grain consisting of a small, cross-zoned uraninite (Ur) in a chalcopyrite (Cpy) hematite (Hm) matrix. The ^{210}RN spatial distribution bears little resemblance to that of ^{209}Bi or ^{208}Pb, suggesting that ^{209}Bi^{1}H and ^{208}Pb^{1}H$_2$ are not significant contributors to the ^{210}RN signal. Similarly, only minimal correlation exists between ^{208}Pb and ^{209}Bi, suggesting that ^{208}Pb^{1}H is likewise not responsible for the ^{209}Bi response. Maximum intensities are indicated in parentheses (counts/pixel/s, 1pixel ≈200 × 200 nm).

masses using pure elemental standards the benefit of choosing a unique isotope/element becomes evident.

Many natural barites analysed did, in fact, have elevated counts for mass 169; however, most also had elevated counts (with identical, or at least similar, spatial distribution) for neodymium and thorium. When comparing counts per area (nm^2) per second (c/a/s), the strongest element pair correlations for all minerals analysed were those for Nd-Tm and Tm-Th, so it could be said that a signal on mass 169 in barite represents, at least in part, the real presence of thulium in that barite in association with neodymium and thorium.

There was, however, one exception: a sample grain showing a faint shadow on mass 169 correlating with barite, in addition to a few hot spots throughout the mapped area (Fig. 3). The ^{142}Nd and ^{230}Th distributions did not correlate with the barite but did overlap the hotspots. In this situation, it is more likely that the 169 signal is caused by isobaric mass interference from barium/sulphur/oxygen, as opposed to Tm existing in the grain alone with no corresponding Nd or Th. Although this may seem discouraging, the (c/a/s) for barium was >300 000 times greater than those for mass 169. This is in excellent agreement with other mass interference tests, with a maximum observed interference signal four to five orders of magnitude lower than the signal for the element of interest.

While not absolute, these examples provide substantial evidence that the mass 210 and mass 226 signals observed are in fact due to the presence of ^{210}RN and ^{226}Ra.

Distribution maps

The ^{210}RN and ^{226}Ra maps for the 65 sample grains analysed by nanoSIMS tended to fall into one (or more) of five general categories.

1. Even distribution throughout a host mineral
2. Zoned distribution in a host mineral
3. Preference of one textural type over another
4. Independent 'hot spots'
5. Minerals which exhibited no significant response.

Figure 4 displays an example of a host mineral, in this case a Sr-bearing phosphate-sulphate with empirical composition (Sr,Ca)$Al_3(PO_4,SO_4)(OH)_6$ which may contain up to 14 wt% REY. The

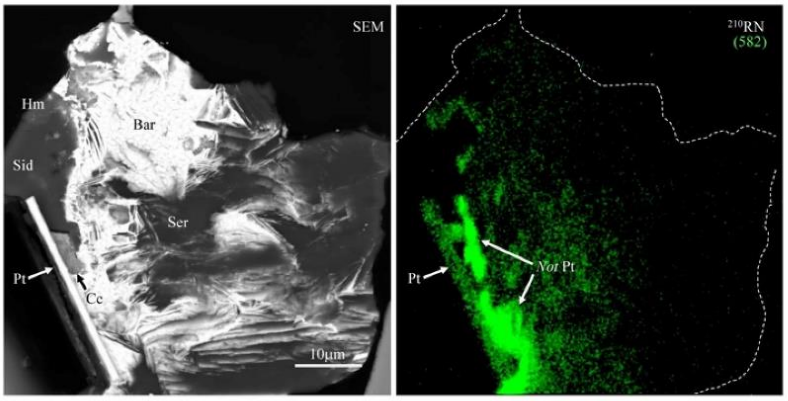

Fig. 2. BSE image and ^{210}RN intensity map for a grain of blocky barite (Bar), interleaved barite/sericite (Ser), siderite (Sid), chalcocite (Cc) and hematite (Hm). Isobaric mass interference from platinum oxide/nitride can be seen but is not the primary contributor. Maximum intensity is indicated in parentheses (counts/pixel/s, 1pixel ≈200 × 200 nm).

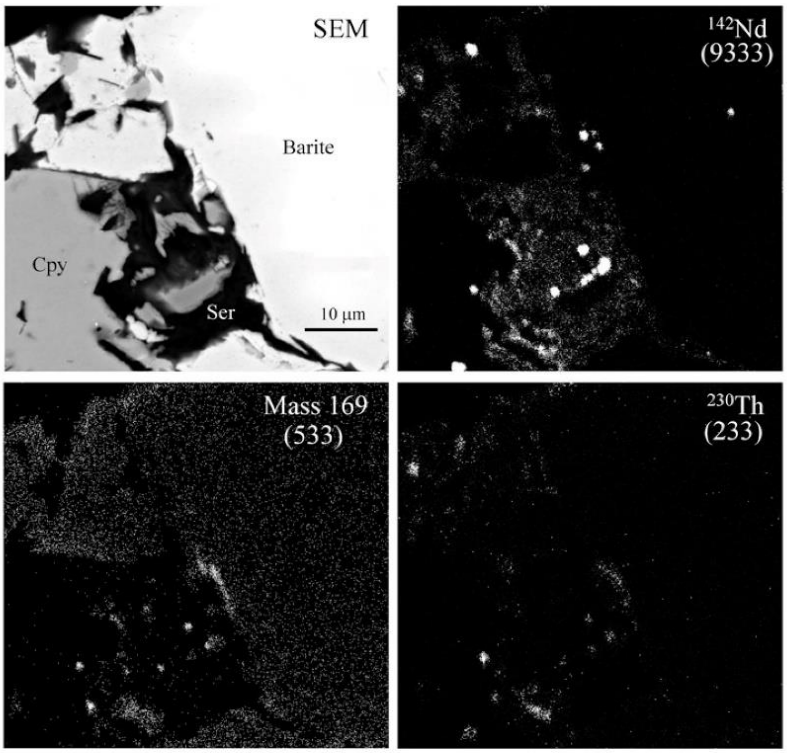

Fig. 3. Isotopic distribution maps for a grain of blocky barite with chalcopyrite (Cpy) and sericite (Ser). Overlap between '^{169}Tm' and barite, but not between '^{169}Tm', ^{142}Nd, and ^{230}Th suggests that the mass 169 signal is predominantly $^{137}Ba^{16}O_2$ or $^{137}Ba^{32}S$ and *not* ^{169}Tm. Maximum intensities are in parentheses (counts/pixel/s, 1pixel ≈100 × 100 nm).

phosphate-sulphate is associated with brannerite (U^{4+},REE,Th,Ca)(Ti,Fe^{3+},Nb)$_2$(O,OH)$_6$ and is entrained in a chalcopyrite matrix. It is no surprise that the ^{238}U and ^{230}Th are both found almost exclusively in the brannerite, as it is a uranium/thorium mineral. Further down the decay chain, however, it appears that radium has begun migrating into the phosphate-sulphate, concentrating around the mineral edges. The ^{210}RN map shows a more pronounced influx, with nearly uniform distribution throughout the phosphate-sulphate grains. At the end of the decay chain, ^{206}Pb shows an even distribution throughout the phosphate-sulphate, as well as elevated concentrations in the brannerite. Aside from a few pinpoints, the chalcopyrite remains largely barren regarding the entire ^{238}U chain.

Figure 5 represents a subset of host minerals which display zoning, indicating at least two genetic events. This area of interest consists of a large (20 × 17 µm) euhedral grain of apatite within a pyrite/chalcopyrite matrix. Two smaller apatites are also present, as is a large mass of bladed hematite. The dark areas of the SEM map are epoxy resin. Of the 12 isotopes mapped only two exhibited an

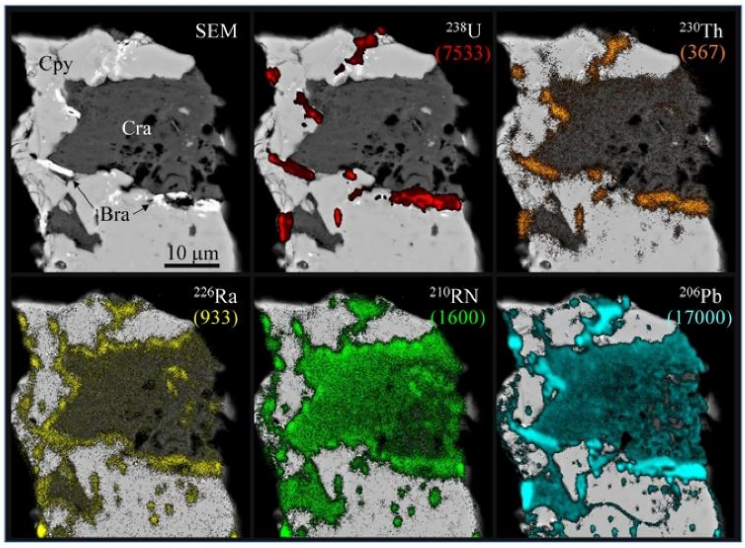

Grain 27, CLD, Olympic Dam

Fig. 4. Isotopic distribution maps for a grain of Sr-bearing phosphate-sulphate likely related to crandallite (Cra) and brannerite (Bra) in chalcopyrite (Cpy). All radionuclides and lead are found in brannerite, whereas only ^{226}Ra, ^{210}RN, and ^{206}Pb concentrate in the Sr-phosphate-sulphate. The chalcopyrite shows only minimal enrichment. Maximum intensities are in parentheses (counts/pixel/s, 1pixel ≈100 × 100 nm).

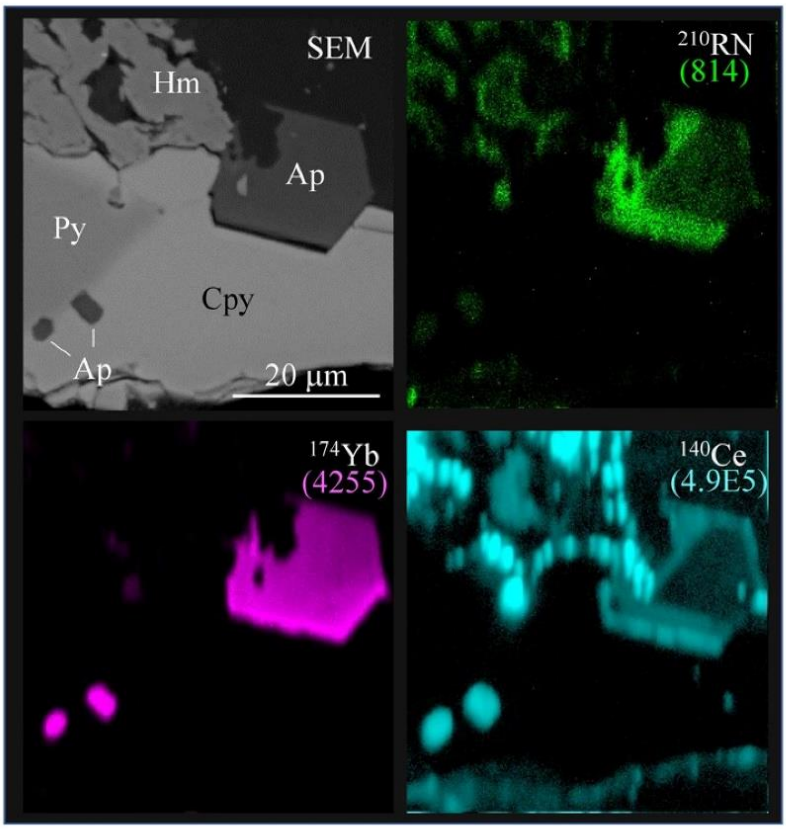

Fig. 5. Isotopic distribution maps for a composite grain including one large and two small euhedral apatite (Ap) grains in a pyrite (Py)/chalcopyrite (Cpy) matrix, with hematite (Hm). Only ^{210}RN and ^{140}Ce showed oscillatory zonation in the apatite, ^{174}Yb and the nine other isotopes measured exhibited no such patterning. Colour intensity scales are qualitative only and are not calibrated. Maximum intensities are indicated in parentheses (counts/pixel/s, 1pixel ≈200 × 200 nm).

oscillatory zonation pattern in the large apatite, ^{140}Ce and ^{210}RN. No zoning was evident in the smaller apatites, although that may be the result of a loss of resolution at high ion currents. The smaller apatites did contain a much higher concentration of ^{140}Ce than the larger apatite, and the hematite (or inclusions therein) also appears to contain a substantial amount, although a direct comparison between the two is not possible due to matrix effects. In comparison, the ^{174}Yb exhibits even distribution throughout the large and small apatites, with lower concentrations evident in the hematite. For this grain, ^{230}Th, ^{226}Ra, and ^{206}Pb were not mapped.

Figure 6 shows a textural difference, in which radionuclides preferentially adhere to the micaceous texture of covellite. The mapped particle consists of bornite, covellite replacing bornite, chalcopyrite, and two inclusions of wittichenite, Cu_3BiS_3. The fresh bornite exhibits a cross-hatch fracturing, a typical texture for this location. The surface of the replacement areas shows a clear affinity

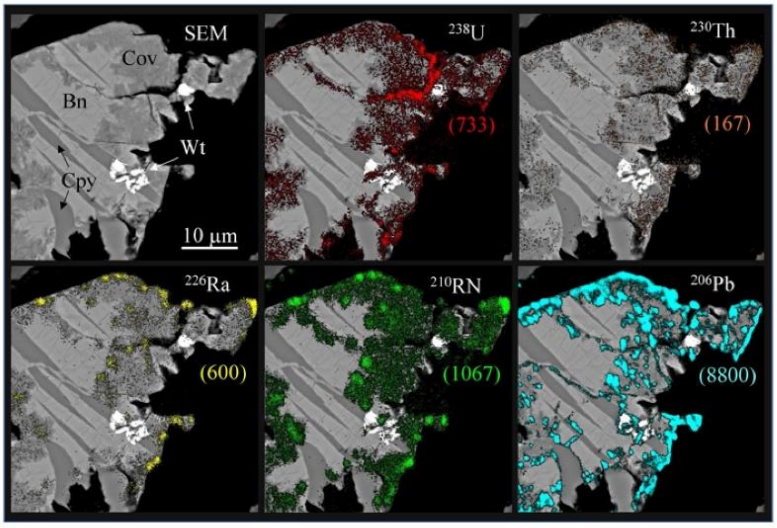

Fig. 6. Isotopic distribution maps for a grain consisting of bornite (Bn), replacement covellite (Cov), chalcopyrite (Cpy) and wittichenite (Wt). Radionuclides, especially ^{210}RN, show a clear preference for areas of the grain replaced by covellite. Maximum intensities are in parentheses (counts/pixel/s, 1pixel ≈100 × 100 nm).

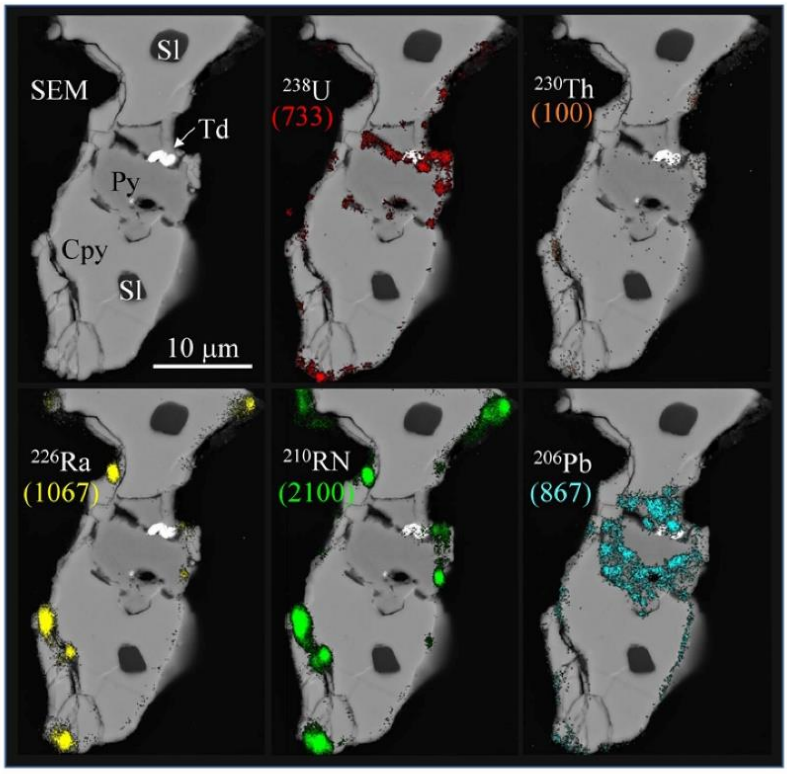

Fig. 7. Isotopic distribution maps of a composite grain comprising sellaite (Sl), tetradymite (Td), pyrite (Py) and chalcopyrite (Cpy). Although the ^{206}Pb seems to correlate with pyrite, ^{226}Ra and ^{210}RN instead accumulate as small 'hot spots' on grain boundaries, possibly resulting from the formation of nanoclusters. Maximum intensities are in parentheses (counts/pixel/s, 1pixel ≈100 × 100 nm).

for radionuclides, particularly ^{210}RN and ^{238}U, and to a lesser extent ^{226}Ra and ^{230}Th. Chalcopyrite and fresh bornite remain barren, as does the wittichenite. Similar RN enrichments are present in all molybdenites as well as sericite/chlorite when in proximity to an RN source (such as uraninite) which suggests that mineral texture or surface area may be of equal or greater importance than mineral chemistry.

Figure 7 represents the last two categories, although there have been examples of barren minerals in previous sample grain maps. The particle is a small grain of chalcopyrite with a core of pyrite, two small crystals of sellaite (MgF_2), and a couple of tiny inclusions of tetradymite (Bi_2Te_2S). Although the ^{206}Pb clearly favours pyrite, the radionuclides show no preference for any one mineral host. Instead, the ^{226}Ra and ^{210}RN appear as 'hot spots', with intensities (in counts nm^{-2} s^{-1}) two orders of magnitude higher than the surrounding matrix. Occurrences seem to coincide with grain boundaries, fractures, pores, or other physical features. Smooth boundaries display a lower response than rough or highly fractured boundaries, indicating the phenomenon may be related to surface area. The sellaite and virtually all the chalcopyrite is barren, except around fractures. There is minor overlap between tetradymite and ^{238}U and ^{206}Pb, but these relationships appear to be tenuous and do not overlap with each other. This phenomenon is rarely seen on flotation concentrate sample grains but is prevalent on acid-leached sample grains.

Discussion

The issue of isobaric interfering masses has been addressed but is by no means resolved. It is promising, however, that for every example of a possible interfering mass (e.g. $^{56}Fe^{138}Ba^{16}O$ on mass 210 in barite) a complementary example with similar chemistry which shows little to no correlation has been observed. Importantly, the true mass of most possible interferences is >0.1 amu removed from our isotopes of interest. Every isotope of every element on the Periodic Table between oxygen and lead has a mass slightly less than its sum of protons and neutrons (e.g. $^{56}Fe = 55.9383$). One possible isobaric mass interference for mass 210 would be Y_2O_2, as would be found in fergusonite, xenotime, or euxenite. The true mass of Y_2O_2, however, is 209.8015 – more than 0.18 amu removed from ^{210}Po (209.9824) or ^{210}Pb (209.9842). This difference is distinguishable on the nanoSIMS detectors and would appear as two peaks, although not always completely resolvable. As a result, the only possible diatomic isobaric mass interferences for elements beyond lead would necessarily have to include a positive differential element such as ^{1}H (1.00783), ^{11}B (11.0093), or ^{14}N (14.0031) to offset the mass depletion. When considering that only hydrides, borides, and nitrides may threaten to interfere with analyses for heavier elements, the possibility of such is drastically reduced.

A theoretical calculation of how much ^{210}RN would be expected yields promising results. The uraninite in Figure 1 measures *c.* 6.5 × 7 μm. Using the unit cell volume for uraninite of 163.5 $Å^3$, it can be estimated, assuming secular equilibrium, that ablating the uraninite to a depth of 500 nm (total volume 22.75 $μm^3$) would release *c.* 1.4×10^{11} atoms of uranium, and 500–1000 atoms of ^{210}RN. The total counts of mass 210 for the crystal was *c.* 800. Although 100% ionization may not be assumed, and some isobaric mass interference is certain, these are offset by the fact that the effective spot size is less than the pixel area resulting in a true analysis volume <22.75 $μm^3$. The calculated result is close enough to warrant further investigation.

First step towards quantification

At present, the spatial distribution maps presented above are qualitative only. The images are created by rastering the area of

interest with an ion beam, collecting data from all seven collectors every 5 ms, and representing those data as a single pixel with an intensity value corresponding to the counts on each detector. There have been attempts to associate counts per pixel to concentration, some quite successfully (Wilson & Novak 1991); however, little has been accomplished regarding natural mineral samples. Quantification is dependent on relative sensitivity factors (RSF) (Wilson *et al.* 1989), represented by the equation:

$$\mathrm{RSF} = \left(\frac{\gamma_m}{\gamma_i}\right)\rho_i/a_\mathrm{m}$$

where i denotes impurity, m denotes matrix, γ is the secondary-ion intensity, ρ_i is a known impurity density in the matrix, and a_m is the abundance of the matrix isotope chosen for reference (Wilson & Novak 1991). The nanoSIMS seven-detector array limits the number of minerals which may be analysed during a run, as at least one major component of each mineral must be included (a_m), leaving only six for trace elements. Sputtering rate is also an issue, as SEM images of minerals pre- and post-nanoSIMS analyses has shown. Chalcocite and uraninite decay rather quickly, while barite and pyrite appear untouched.

Although all the above variables are obtainable, there is no database of RSFs for any mineral matrix. The task of determining an RSF for each element/isotope (six at a time), for each mineral phase, for each ion current used, for each ion source, represents potentially thousands of analyses on the nanoSIMS as well as a complete set of independent analyses (LA-ICP-MS, for example) to confirm the results. In light of this, quantification of minerals has generally been left to other means. There is an argument, however, for attempting to at least semi-quantify certain elements/isotopes in a limited selection of minerals under specific conditions.

Using ImageJ, it was possible to highlight regions of interest (ROIs) and perform data analyses on single minerals within the image. Information gathered includes area of the ROI (in pixels, 1 pixel ≈10 000 nm^2), total counts, minimum and maximum counts, standard deviation of counts, and other basic statistics. These data were then normalized, accounting for measurement time and the difference in ion current used for different maps. The resulting values for each isotope, converted to counts per area (nm^2) per second, hereafter (c/a/s), were then back-calculated to a total elemental estimate based on the isotope measured, assuming natural isotopic abundances. For example, the ^{54}Fe value was divided by 0.05845 to arrive at a total Fe value, given that only 5.845% of all iron is ^{54}Fe. Radionuclide data (^{210}RN, ^{226}Ra, ^{230}Th, and ^{238}U) were not adjusted, and an estimate was applied to ^{206}Pb based on data from Olympic Dam samples (Švedkauskaitė-LeGore *et al.* 2008). From the last 50 sample grains analysed, 175 mineral ROIs consisting of at least 40 mineral types were selected for analysis in this manner, and the data were analysed for trends.

Understanding, of course, that without accounting for matrix effects, the data are of only limited usefulness, but trends appeared nonetheless. To more easily compare major elements and trace elements on the same charts, values are presented as log(c/a/s). There was remarkable similarity in log(c/a/s) values from the same mineral type in different sample grains. For example, the log(c/a/s) values for Fe (all minerals) ranged from −0.1 to +5.7, but for hematite (10 ROIs from 8 grains), the range narrowed to +5.1 to +5.2. For 35 chalcopyrite ROIs (from 32 grains) the values for Fe ranged from +5.3 to +5.6. The same 35 chalcopyrite ROIs had a slightly larger range of +3.7 to +4.2 for Cu, in comparison to an overall range of −0.6 to +5 for all minerals. Some variability does occur, but much of the variation in these values can be attributed to inclusions, or to overlap with neighboring grains, and a smaller subset of large, clean mineral ROIs give more reproducible results than small, complex, fractured minerals. Figure 8 shows an example of the data analyses. All minerals analysed are represented, ore and gangue, which offsets the burden of matrix effect to some extent. It

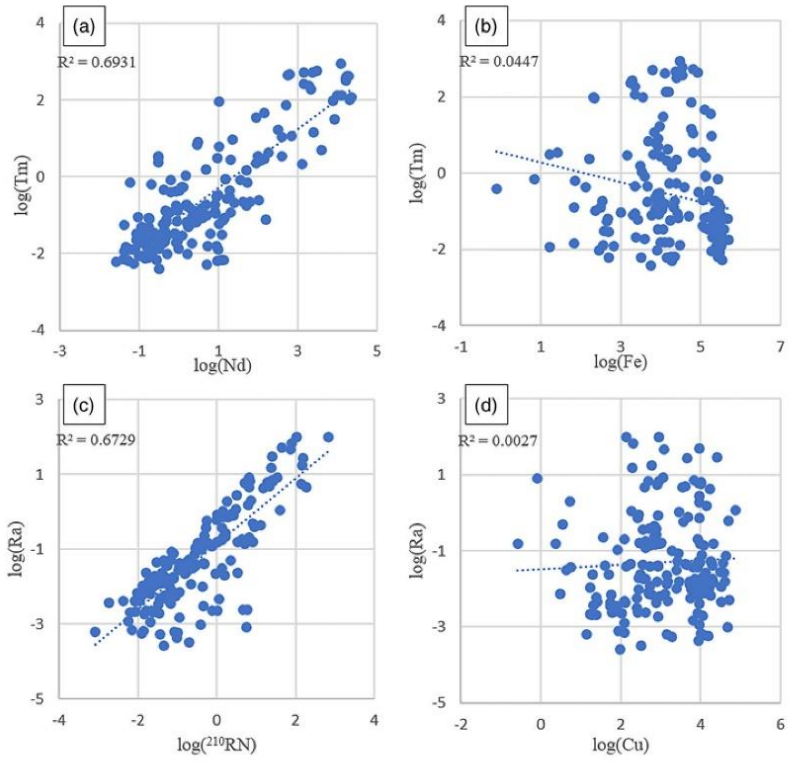

Fig. 8. Elemental correlations, expressed as log(counts·nm^{-2} s^{-1}). Nd:Tm and Ra:^{210}RN show strong correlations as expected, whereas Fe:Tm and Cu:Ra show virtually no correlation.

is unlikely that the additional consideration of matrix effect in calculating these values would diminish such trends, although further studies are needed to verify this. For expected correlative trends, such as Nd:Tm, U:Th, Ba:Ra, ^{210}RN:Ra, and Fe:Cu, R-squared values are significantly higher than for element pairs not expected to correlate, such as Sr:Cu or Ra:Ti. This agreement with expected results lends credence to the possibility of quantifying these data. Efforts are currently underway to create and calibrate a multiple-mineral matrix-matched standard, which will allow at least semi-quantification of even low concentration elements in natural minerals. Although quantification results will not even approach those of ICP-AES or AMS, there is an enormous advantage in being able to measure these isotopes *in situ,* even at the expense of precision.

The distribution of radionuclides, both in relation to host minerals and in relation to each other, is logical and easily explained by well-established theories of deportment, diffusion, and redistribution (Klinkenberg *et al.* 2014; Anvia 2015; Boujrhal & Sabbani 2015; MacMillan *et al.* 2016). The maps and data presented represent a valid proof-of-concept for this new approach. Further studies, already in progress, will address additional isobaric mass interference issues, establish detection limits, emulate hydrothermal diffusion, and attempt semi-quantification through the calibration of matrix-matched mineral standards.

Implications and outlook

The first results presented here illustrate a simple and effective avenue for investigation of moderate half-life radionuclides and their presence, deportment, and/or mobility in virtually any solid media. The maps are a proof-of-concept for the routine spatially resolved investigation of radionuclide-bearing materials and identification of the physical sites for moderate half-life radionuclides. A detailed documentation of which minerals are the optimal hosts for ^{226}Rn and ^{210}RN, and in what textural context, will be prepared following ongoing investigation of a larger volume of mineral grains.

The capability of mapping RN distributions by nanoSIMS has broad application well beyond the metallurgical context of our study, both within and beyond the earth and environmental sciences. For example, in geochronology, an understanding of the physical pathways of radioactive decay, potential isotopic decoupling, and the resultant distributions of daughter radionuclides is critical for interpretation of measured isotopic ratios and their application as geologically meaningful ages. Remobilization in present-day seafloor hydrothermal environments, leading to redistribution of Ra isotopes and impacting on ^{226}Ra/Ba dating, was demonstrated by Ditchburn & de Ronde (2017). The ability to identify pathways of radioisotope migration in ancient, geologically complex mineralized systems carries major significance for understanding deportment of radionuclides, and implicitly, for geochronology.

It is important to note that the nanoSIMS platform is an *imaging* technique and is not currently useful for quantification. We are not suggesting that nanoSIMS replace existing methods for measuring activities, but instead provides a valuable complement to these methods to ensure their quality.

Conclusions

For over a century, moderate half-life radionuclides have been measured exclusively by the trail of alpha particles, electrons, and gamma rays left in their wake. Although these time-tested *ex situ* methods provide excellent precision and accuracy with minimum detection limits less than 1 mBq, they often require laborious sample preparation and extraction procedures. The Cameca nanoSIMS instruments provide a unique perspective to this field of research, enabling the user to actively map spatial distributions of low-concentration isotopes *in situ* in a wide range of solid media, albeit (currently) at the expense of quantification. Uranium mining, nuclear fuel cycle and storage, forensics, and environmental remediation are but a few of the fields which may benefit from direct observation of isotopes, naturally occurring or anthropogenic, with half-lives in the 100-day to 100 000-year range.

Acknowledgements This is a contribution to the ARC Research Hub for Australian Copper-Uranium, co-supported by BHP Olympic Dam and the South Australian Mining and Petroleum Services Centre of Excellence. We acknowledge valuable comments from an anonymous reviewer and Editor Gwendy Hall.

Funding This work was funded by the Australian Research Council, BHP Billiton and University of Adelaide Research Training Program Scholarship.

Scientific editing by Gwendy Hall

References

Aaseth, J., Skaug, M.A., Cao, Y. & Andersen, O. 2015. Chelation in metal intoxication—principles and paradigms. *Journal of Trace Elements in Medicine and Biology*, **31**, 260–266.

Adams, F. & Dams, R. 1970. Semiconductor gamma detectors. *In:* Belcher, R. & Freiser, H. (eds) *Applied Gamma-Ray Spectrometry. International Series of Monographs in Analytical Chemistry*, **41**, 69–110.

Anvia, M. 2015. *Radionuclide Deportment in Rare Earth Processing from Monazite and Bastnasite using Conventional and Alternative Processing Routes*. Unpublished PhD thesis, The University of Sydney, http://hdl.handle.net/2123/13886

Becker, J.S. 2005. Inductively coupled plasma mass spectrometry (ICP-MS) and laser ablation ICP-MS for isotope analysis of long-lived radionuclides. *International Journal of Mass Spectrometry*, **242**, 183–195.

Becquerel, H. 1901. The radio-activity of matter. *Nature*, **63**, 396–398.

Beklemishev, M.K., Elshani, S. & Wai, C.M. 1994. Solvent extraction of radium with crown ether carboxylic acids. *Analytical Chemistry*, **66**, 3521–3524.

Bettencourt, A.O., Teixeira, M.M., Elias, M.D. & Madruga, M.J. 1990. Environmental monitoring in uranium mining areas. *The Environmental Behaviour of Radium*, IAEA Technical Reports Series 310, **2**, 281–294.

Borkowski, C.J. 1949. Instruments for measuring radioactivity. *Analytical Chemistry*, **21**, 348–352.

Boujrhal, F.Z. & Sabbani, H. 2015. Radon diffusion in rocks and minerals. *In:* Merkel, B.J. & Arab, A. (eds) *Uranium-Past and Future Challenges, Proceedings, 7th International Conference on Uranium Mining and Hydrogeology*. Springer, Cham, 545–552.

Boulyga, S.F., Desideri, D., Meli, M.A., Testa, C. & Becker, J.S. 2003. Plutonium and americium determination in mosses by laser ablation ICP-MS combined with isotope dilution technique. *International Journal of Mass Spectrometry*, **226**, 329–339.

Boulyga, S.F., Tibi, M. & Heumann, K.G. 2004. Application of isotope-dilution laser ablation ICP–MS for direct determination of Pu concentrations in soils at pg g(−1) levels. *Analytical and Bioanalytical Chemistry*, **378**, 342–347.

Cantrell, K.J. & Felmy, A.R. 2012. Plutonium and americium geochemistry at Hanford: a site-wide review. *Pacific Northwest National Laboratory, Report PNNL-21651*, 1–32.

Case, G.N. & McDowell, W.J. 1982. An improved sensitive assay for polonium-210 by use of a background-rejecting extractive liquid-scintillation method. *Talanta*, **29**, 845–848.

Cherry, S.R., Sorenson, J.A. & Phelps, M.E. 1995. *Physics in Nuclear Medicine*. 4th edn. Elsevier Health Sciences.

Ciobanu, C.L., Wade, B., Cook, N.J., Schmidt Mumm, A. & Giles, D. 2013. Uranium-bearing hematite from the Olympic Dam Cu-U-Au deposit, South Australia; a geochemical tracer and reconnaissance Pb-Pb geochronometer. *Precambrian Research*, **238**, 129–147.

Clayton, R.F. & Bradley, E.J. 1995. A cost effective method for the determination of 210 Po and 210 Pb in environmental materials. *Science of the Total Environment*, **173**, 23–28.

Cowart, J.B. & Burnett, W.C. 1994. The distribution of uranium and thorium decay-series radionuclides in the environment—a review. *Journal of Environmental Quality*, **23**, 651–662.

Dickey, E.E. 1953. Separation of radium D, E, and F by paper chromatography. *Journal of Chemical Education*, **30**, 525–526.

Didier, A., Bosse, V. *et al.* 2015. NanoSIMS mapping and LA-ICP-MS chemical and U–Th–Pb data in monazite from a xenolith enclosed in andesite (Central Slovakia Volcanic Field). *Contributions to Mineralogy and Petrology*, **170:45**, 1–23.

Ditchburn, R.G. & de Ronde, C.E.J. 2017. Evidence for Remobilization of Barite Affecting Radiometric Dating Using ^{228}Ra, ^{228}Th, and ^{226}Ra/Ba Values: Implications for the Evolution of Sea-Floor Volcanogenic Massive Sulfides. *Economic Geology*, **112**, 1231–1246.

Ehrig, K., McPhie, J. & Kamenetsky, V.S. 2012. Geology and mineralogical zonation of the Olympic Dam iron oxide Cu-U-Au-Ag deposit, South Australia. *In:* Hedenquist, J.W., Harris, M. & Camus, F. (eds) *Geology and Genesis of Major Copper Deposits and Districts of the World, a Tribute to Richard Sillitoe*. Society of Economic Geologists Special Publication, **16**, 237–268.

Fukuma, H.T., Fernandes, E.A.N. & Quinelato, A.L. 2000. Distribution of natural radionuclides during the processing of phosphate rock from Itataia-Brazil for production of phosphoric acid and uranium concentrate. *Radiochimica Acta*, **88**, 809–814.

Gleason, G. 1980. Improved ion exchange procedure for the separation of barium from radium. *In:* Lyons, W.S. (ed.) *Radioelement analysis: progress and problems*. Ann Arbor Science Publishers, Inc, Ann Arbor, Michigan.

Godbee, H.W., Fitzgerald, C.L., Blomeke, J.O. & Blanco, R.E. 1969. Diffusion of radioisotopes through waste solids. *Transactions of the American Nuclear Society*, **12**, 450–451.

Hansen, E., Peatross, J., Bergeson, S. & Ware, M. 2014. Precision Measurements of Beta-Decay Rates. *Bulletin of the American Physical Society*, **59**.

Hedström, H., Ramebäck, H. & Ekberg, C. 2013. A study of the Arrhenius behaviour of the co-precipitation of radium, barium and strontium sulphate. *Journal of Radioanalytical and Nuclear Chemistry*, **298**, 847–852.

Henriksen, G., Hoff, P. & Larsen, R.H. 2002. Evaluation of potential chelating agents for radium. *Applied Radiation and Isotopes*, **56**, 667–671.

Hillion, F., Daigne, B., Girard, F., Slodzian, G. & Schuhmacher, M. 1993. A new high-performance instrument: the CAMECA NanoSIMS 50. *Secondary Ion Mass Spectrometry: SIMS*, **IX**, 254–257.

Hu, Q.H., Weng, J.Q. & Wang, J.S. 2010. Sources of anthropogenic radionuclides in the environment: a review. *Journal of Environmental Radioactivity*, **101**, 426–437.

Jia, G., Torri, G. & Ocone, R. 2007. Determination of radium isotopes in soil samples by alpha-spectrometry. *Journal of Radioanalytical and Nuclear Chemistry*, **273**, 779–783.

Kalmykov, S.N., Kriventsov, V.V., Teterin, Y.A. & Novikov, A.P. 2007. Plutonium and neptunium speciation bound to hydrous ferric oxide colloids. *Comptes Rendus Chimie*, **10**, 1060–1066.

Kersting, A.B. 2013. Plutonium transport in the environment. *Inorganic Chemistry*, **52**, 3533–3546.

Kersting, A.B. 2017. *LLNL SFA OBER SBR FY17 Program Management and Performance Report: Subsurface Biogeochemistry of Actinides* (No. LLNL-TR-733899). Lawrence Livermore National Lab (LLNL), Livermore, CA, USA.

Kilburn, M.R. & Wacey, D. 2014. Nanoscale secondary ion mass spectrometry (NanoSIMS) as an analytical tool in the geosciences. *In:* Fay, L.B. & Kussmann, M. (eds) *Principles and Practice of Analytical Techniques in Geosciences.* Royal Society of Chemistry, 1–34.

Klinkenberg, M., Brandt, F., Breuer, U. & Bosbach, D. 2014. Uptake of Ra during the recrystallization of barite: a microscopic and time of flight-secondary ion mass spectrometry study. *Environmental Science & Technology*, **48**, 6620–6627.

Krneta, S., Ciobanu, C.L., Cook, N.J., Ehrig, K. & Kontonikas-Charos, A. 2016. Apatite at Olympic Dam, South Australia: a petrogenetic tool. *Lithos*, **262**, 470–485.

Krneta, S., Ciobanu, C.L., Cook, N.J., Ehrig, K. & Kontonikas-Charos, A. 2017. Rare earth element behaviour in apatite from the Olympic Dam Cu-U-Au-Ag deposit, South Australia. *Minerals*, **7**, 135, https://doi.org/10.3390/min7080135

Krupp, K., Baskaran, M. & Brownlee, S.J. 2017. Radon emanation coefficients of several minerals: How they vary with physical and mineralogical properties. *American Minerals*, **102**, 1375–1383.

Landa, E.R. & Gray, J.R. 1995. US Geological Survey research on the environmental fate of uranium mining and milling wastes. *Environmental Geology*, **26**, 19–31.

Law, J.D., Brewer, K.N., Herbst, R.S., Todd, T.A. & Wood, D.J. 1999. Development and demonstration of solvent extraction processes for the separation of radionuclides from acidic radioactive waste. *Waste Management*, **19**, 27–37.

Liatsou, I. & Pashalidis, I. 2016. Radium concentration in uranium-bearing rocks and minerals by radon emanation after acidic sample dissolution. *Journal of Radioanalytical and Nuclear Chemistry*, **309**, 1327–1332.

Macmillan, E., Ciobanu, C.L., Ehrig, K., Cook, N.J. & Pring, A. 2016. Chemical zoning and lattice distortion: Uraninite from Olympic Dam, South Australia. *American Minerals*, **101**, 2351–2354.

Macmillan, E., Cook, N.J., Ehrig, K. & Pring, A. 2017. Chemical and textural interpretation of late-stage coffinite and brannerite from the Olympic Dam IOCG-Ag-U deposit. *Mineralogical Magazine*, **81**, 1323–1366.

Martin, P. 2000. *Radiological impact assessment of uranium mining and milling*. Unpublished PhD thesis, Queensland University of Technology, Brisbane, QLD, Australia.

Matthews, K.M., Kim, C.K. & Martin, P. 2007. Determination of 210 Po in environmental materials: a review of analytical methodology. *Applied Radiation and Isotopes*, **65**, 267–279.

Oliveira, J.M. & Carvalho, F.P. 2006. Sequential extraction procedure for determination of uranium, thorium, radium, lead and polonium radionuclides by alpha spectrometry in environmental samples. *Czechoslovak Journal of Physics*, **56**, D545–D555.

Poczatek, C., Kaufman, Z. & Lechene, C. 2009. *OpenMIMS ImageJ Plugin Guide*. Harvard Medical School, Boston, USA.

Schindelin, J., Arganda-Carreras, I., *et al.* 2012. Fiji: an open-source platform for biological-image analysis. *Nature Methods*, **9**, 676–682.

Schindelin, J., Rueden, C.T., Hiner, M.C. & Eliceiri, K.W. 2015. The ImageJ ecosystem: An open platform for biomedical image analysis. *Molecular Reproduction and Development*, **82**, 518–529.

Schmandt, D.S., Cook, N.J., Ciobanu, C.L., Ehrig, K., Wade, B.P., Gilbert, S. & Kamenetsky, V.S. 2017. Rare Earth Element Fluorocarbonate Minerals from the Olympic Dam Cu-U-Au-Ag Deposit, South Australia. *Minerals*, **7**, 202, https://doi.org/10.3390/min7100202

Schuster, M. 2015. *Entwicklung und Validierung einer kombinierten Schnellanalysenmethode zur Bestimmung der natürlichen Radionuklide ^{210}Pb, ^{210}Po, ^{226}Ra, ^{228}Ra, ^{234}U und ^{238}U in Trinkwasser*. Unpublished PhD thesis, Universität Regensburg, Germany. http://epub.uni-regensburg.de/32890/1/Diss_Schuster.pdf

Skwarzec, B. 2009. Determination of Radionuclides in the Aquatic Environment. *In:* Namiesnik, J. & Szefer, P. (eds) *Analytical Measurements in Aquatic Environments*, CRC Press, Boca Raton, FL, 241–256.

Skwarzec, B., Boryło, A. & Strumińska-Parulska, D. 2016. Alpha spectrometry in radiochemical analysis and its application in the study of the natural environment. *Annales Universitatis Mariae Curie-Sklodowska, sectio AA–Chemia*, **71**, 151–167.

Solomon, A.K. & Estes, H.D. 1948. The measurement of radioactivity in solution. *Review of Scientific Instruments*, **19**, 47–50.

Švedkauskaitė-LeGore, J., Rasmussen, G., Abousahl, S. & Van Belle, P. 2008. Investigation of the sample characteristics needed for the determination of the origin of uranium-bearing materials. *Journal of Radioanalytical and Nuclear Chemistry*, **278**, 201–209.

Verdugo-Ihl, M.R., Ciobanu, C.L., Cook, N.J., Ehrig, K.J., Courtney-Davies, L. & Gilbert, S. 2017. Textures and U-W-Sn-Mo signatures in hematite from the Olympic Dam Cu- U-Au-Ag deposit, South Australia: Defining the archetype for IOCG deposits. *Ore Geology Reviews*, **91**, 173–195.

Vesterbacka, P. & Ikäheimonen, T.K. 2005. Optimization of ^{210}Pb determination via spontaneous deposition of ^{210}Po on a silver disk. *Analytica Chimica Acta*, **545**, 252–261.

von Gunten, H.R. & Beneš, P. 1995. Speciation of radionuclides in the environment. *Radiochimica Acta*, **69**, 1–30.

Weber, W.J. & Roberts, F.P. 1983. A review of radiation effects in solid nuclear waste forms. *Nuclear Technology*, **60**, 178–198.

Weber, J., Barthel, J., Klinkenberg, M., Bosbach, D., Kruth, M. & Brandt, F. 2017. Retention of ^{226}Ra by barite: The role of internal porosity. *Chemical Geology*, **466**, 722–732.

Wilson, R.G. & Novak, S.W. 1991. Systematics of secondary-ion-mass spectrometry relative sensitivity factors v. electron affinity and ionization potential for a variety of matrices determined from implanted standards of more than 70 elements. *Journal of Applied Physics*, **69**, 466–474.

Wilson, R.G., Stevie, F.A. & Magee, C.W. 1989. *Secondary ion mass spectrometry: a practical handbook for depth profiling and bulk impurity analysis*. Wiley-Interscience, New York.

Zhang, T., Gregory, K., Hammack, R.W. & Vidic, R.D. 2014. Co-precipitation of radium with barium and strontium sulphate and its impact on the fate of radium during treatment of produced water from unconventional gas extraction. *Environmental Science & Technology*, **48**, 4596–4603.

Chapter 4

Detection of trace elements/isotopes in Olympic Dam copper concentrates by nanoSIMS

Mark Rollog [a,*], Nigel J. Cook [a], Paul Guagliardo [b], Kathy Ehrig [c], Cristiana L. Ciobanu [a], and Matt Kilburn [b]

[a] *School of Chemical Engineering, University of Adelaide, Adelaide, 5005 S.A., Australia*

[b] *Centre for Microscopy, Characterisation, and Analysis, University of Western Australia, 35 Stirling Highway, Crawley, 6009 W.A., Australia*

[c] *BHP Olympic Dam, 55 Grenfell St., Adelaide, 5000 S.A., Australia*

Article published in *Minerals* 9(6), 336.

Statement of Authorship

Title of Paper	Detection of Trace Elements/Isotopes in Olympic Dam Copper Concentrates by nanoSIMS
Publication Status	☑ Published ☐ Accepted for Publication ☐ Submitted for Publication ☐ Unpublished and Unsubmitted work written in manuscript style
Publication Details	Submitted to *Minerals* special issue: Minerals Down to the Nanoscale: A Glimpse at Ore Forming Processes 28 April 2019. Accepted for publication 30 May 2019. Available online 31 May 2019. https://doi.org/10.3390/min9060336

Principal Author

Name of Principal Author (Candidate)	Mark Rollog
Contribution to the Paper	Designed experimentation, performed sample analysis and data interpretation, wrote manuscript
Overall percentage (%)	70
Certification:	This paper reports on original research I conducted during the period of my Higher Degree by Research candidature and is not subject to any obligations or contractual agreements with a third party that would constrain its inclusion in this thesis. I am the primary author of this paper.
Signature	Date 23.08.19

Co-Author Contributions

By signing the Statement of Authorship, each author certifies that:

i. the candidate's stated contribution to the publication is accurate (as detailed above);

ii. permission is granted for the candidate in include the publication in the thesis; and

iii. the sum of all co-author contributions is equal to 100% less the candidate's stated contribution.

Name of Co-Author	Nigel J. Cook
Contribution to the Paper	Supervised direction and progress of work, helped evaluate and edit manuscript
Overall percentage (%)	10
Signature	Date 1/8/19

Name of Co-Author	Paul Guagliardo
Contribution to the Paper	Oversaw sample analyses and helped evaluate and edit the manuscript

Overall percentage (%)	10		
Signature		Date	25 Jul 2019

Name of Co-Author	Kathy Ehrig		
Contribution to the Paper	Provided samples and helped evaluate and edit the manuscript		
Overall percentage (%)	5		
Signature		Date	31 July 2019

Name of Co-Author	Cristiana L. Ciobanu		
Contribution to the Paper	Provided direction and insightful editing of the manuscript		
Overall percentage (%)	3		
Signature		Date	21.08.2019

Name of Co-Author	Matt Kilburn		
Contribution to the Paper	Oversaw the facility where the samples were analysed		
Overall percentage (%)	2		
Signature		Date	25 Jul 2019

minerals

MDPI

Article

Detection of Trace Elements/Isotopes in Olympic Dam Copper Concentrates by nanoSIMS

Mark Rollog [1,*], Nigel J. Cook [1], Paul Guagliardo [2], Kathy Ehrig [3], Cristiana L. Ciobanu [1] and Matt Kilburn [2]

1 School of Chemical Engineering, The University of Adelaide, Adelaide, 5005 SA, Australia; nigel.cook@adelaide.edu.au (N.J.C.); cristiana.ciobanu@adelaide.edu.au (C.L.C.)
2 Centre for Microscopy, Characterisation and Analysis, The University of Western Australia, 35 Stirling Highway, Crawley, 6009 WA, Australia; paul.guagliardo@uwa.edu.au (P.G.); matt.kilburn@uwa.edu.au (M.K.)
3 BHP Olympic Dam, 55 Grenfell St., Adelaide, 5000 SA, Australia; kathy.ehrig@bhp.com
* Correspondence: mark.rollog@adelaide.edu.au; Tel.: +61-466-848-699

Received: 30 April 2019; Accepted: 28 May 2019; Published: 30 May 2019

Abstract: Many analytical techniques for trace element analysis are available to the geochemist and geometallurgist to understand and, ideally, quantify the distribution of trace and minor components in a mineral deposit. Bulk trace element data are useful, but do not provide information regarding specific host minerals—or lack thereof, in cases of surface adherence or fracture fill—for each element. The CAMECA nanoscale secondary ion mass spectrometer (nanoSIMS) 50 and 50L instruments feature ultra-low minimum detection limits (to parts-per-billion) and sub-micron spatial resolution, a combination not found in any other analytical platform. Using ore and copper concentrate samples from the Olympic Dam mining-processing operation, South Australia, we demonstrate the application of nanoSIMS to understand the mineralogical distribution of potential by-product and detrimental elements. Results show previously undetected mineral host assemblages and elemental associations, providing geochemists with insight into mineral formation and elemental remobilization—and metallurgists with critical information necessary for optimizing ore processing techniques. Gold and Te may be seen associated with brannerite, and Ag prefers chalcocite over bornite. Rare earth elements may be found in trace quantities in fluorapatite and fluorite, which may report to final concentrates as entrained liberated or gangue-sulfide composite particles. Selenium, As, and Te reside in sulfides, commonly in association with Pb, Bi, Ag, and Au. Radionuclide daughters of the ^{238}U decay chain may be located using nanoSIMS, providing critical information on these trace components that is unavailable using other microanalytical techniques. These radionuclides are observed in many minerals but seem particularly enriched in uranium minerals, some phosphates and sulfates, and within high surface area minerals. The nanoSIMS has proven a valuable tool in determining the spatial distribution of trace elements and isotopes in fine-grained copper ore, providing researchers with crucial evidence needed to answer questions of ore formation, ore alteration, and ore processing.

Keywords: radionuclides; trace elements; isotopes; nanoSIMS; copper concentrate; Olympic Dam

1. Introduction

Systematic analysis of trace elements (or isotopes) in ore samples is beneficial on multiple fronts. Valuable geochemical insight may be gained by detailed analysis of ore deposits at every scale, from regional trends useful for mineral exploration down to the nanoscale deportment of trace elements. The association of certain trace elemental or isotopic components in a mineralized system may aid

in determining ore genesis timelines, mineralization conditions, source rocks, and subsequent alteration via interaction with hydrothermal fluids or metamorphism—just to name a few. Trace element/isotope analyses may also provide economic advantages. Many mining operations employ complex processing flowsheets and monitoring strategies which take into account variable ore compositions, particle sizing, wash water chemistry, acid or base leach compositions and concentrations, oxidation/reduction potentials, and temperature—all optimized through cost-benefit analysis algorithms. Detailed monitoring of each component of the ore, not just the economic ones, may eventuate into lowering the unit costs of production. To this end, measuring concentrations of trace elements *not* currently recovered, and determining their mineralogical distributions, has become routine for many mine operations. Although a comprehensive review of trace element methods and applications is far beyond the scope of this study, our intention is simply to emphasize the importance of such analyses and to demonstrate the utility of an alternative analytical technique which offers significant advantages over other instrumentation.

To process engineers, trace components nominally fall into one of three categories—benign, beneficial or deleterious. Benign elements are of little economic interest and do not, in low concentrations, affect the recovery of economic elements. Beneficial components may either be elements not currently marketable in quantities available, but which may be in the future (notably certain 'strategic' elements increasingly applied in high-tech applications such as rare earth elements (REE), Ni, Co, Te, Sc, and Nb); or elements which are currently recovered through secondary processes (e.g., Au, Ag, and platinum group elements from electrorefining slimes, V from coal/oil production, Re from molybdenum ores, or Ga, Ge, and In from zinc production). The provenance or deportment of these elements in the deposit may be poorly or incompletely understood. Deleterious components are generally either penalty elements (e.g., Pb, Bi, Sb, or As in copper concentrate [1]), elements which cause issues with processing (e.g., halogens), or environmentally sensitive elements (e.g., Hg).

Regardless of its beneficial/deleterious/benign classification, a robust understanding of the behavior, as well as concentration, of the component in question is critical knowledge to the geologist, mineralogist, and metallurgist alike. Bulk analyses of trace elements (and isotopes) are available via many well-established methods [2], but crucial information may be lost when measuring homogenized aliquots. In situ analysis of specific minerals eliminates this uncertainty to some extent but may be difficult at the resolution and minimum detection limits required for certain elements or isotopes. Few currently available instruments provide the resolution and sensitivity necessary for these in situ analyses.

One such analytical platform is nanoscale secondary ion mass spectrometry (nanoSIMS) manufactured by CAMECA. As with other instruments, it has both positive and negative characteristics [3]. Drawbacks include expense, rarity (currently ~45 worldwide), isobaric mass interferences (inherent in all mass spectrometry), and the inability to quantify isotope or element concentrations in complex matrices—including most minerals. Advantages include multicollection capabilities (seven detectors on the 50L instrument at the Centre for Microscopy, Characterisation, and Analysis (CMCA) in Perth, Western Australia); interchangeable ion sources (Cs^+ for organics and anions, O^- for most cations); mass resolution to 0.1 atomic mass unit (amu); low minimum detection limits; and excellent spatial resolution (ultimately to 40 nm). The pairing of these last two points is arguably its greatest advantage over other instruments.

NanoSIMS has provided valuable insight in such diverse fields as cell metabolism [4,5], cosmochemistry (e.g., Reference [6]), metallurgy (e.g., Reference [7]), nanoelectronics (e.g., Reference [8]), and geosciences [3]). In ore deposit research, nanoSIMS mapping has proven invaluable for unraveling the internal compositional heterogeneity of ore minerals, notably with respect to extending understanding of the location and speciation of Au in pyrite and arsenopyrite and how sulfide minerals form in nature (e.g., References [9–11], and not least, to provide critical constraints on interpretation of geochronological data [12]. Although generally not quantifiable for trace elements—at least in complex mineral assemblages—isotope ratio analyses are robust. Applications include $^{34}S/^{32}S$ in sulfides and

sulfates (e.g., References [13,14], $^{18}O/^{16}O$ in meteorites (e.g., Reference [15]), $^{13}C/^{12}C$ and $^{15}N/^{14}N$ in biological samples (e.g., Reference [16]), and $^{207}Pb/^{206}Pb$ dating of zircon and baddeleyite [17].

In this contribution, we document how nanoSIMS mapping represents a scale-appropriate analytical technique that can provide an advanced understanding of the physical state of trace elements of interest in complex ores and their processing materials. Drawing on selected examples from the Olympic Dam (OD) mining-processing operation, South Australia, we discuss the utility of nanoSIMS mapping for investigation of trace element and radionuclide (isotope) distributions and how correlations between different elements relate to mineralogy. Although only about 20 elements were mapped for this study, the nanoSIMS platform is capable of in situ analysis of virtually the entire periodic table at a resolution well-suited to complex, fine-grained ores and processing materials generated from them. NanoSIMS capabilities used together with complementary microanalytical techniques represent an important contribution towards the development of semi-quantitative deportment models for trace components of the ore. These are, in turn, a necessary pre-requisite for future extraction of potential by-products and for efforts to reduce or eliminate deleterious components in final concentrates.

2. Background

The Olympic Cu-Au province is located along the eastern margin of the Gawler Craton, South Australia [18,19] and hosts numerous Cu-Au-(U) deposits of iron oxide copper gold (IOCG) type, in which hematite is the most abundant mineral. The Olympic Dam Cu-U-Au-Ag deposit is by far the largest of these. Olympic Dam ores are mineralogically complex, characteristically fine-grained and feature mineral intergrowths down to the sub-micron-scale [20,21]. Although the deposit is exploited for Cu, U, Au, and Ag, it is also enriched in many other elements, including REE, Y, W, Mo, Sn, As, Co, Nb, Se, Te, F, Ba, and Sr [20]. Although the complexity of Olympic Dam ores was recognized early on [22,23], research over the past decade has been able to take advantage of the array of modern microanalytical instrumentation to systematically document the mineralogy of the deposit and element distributions in processing streams. These studies have used scanning electron microscopy (SEM), electron probe microanalysis (EPMA), laser ablation inductively coupled plasma mass spectrometry (LA-ICP-MS), focused ion beam SEM (FIB-SEM) and transmission electron microscopy (TEM), often on the same sample material. Outcomes have emphasized the fine-scale intergrowths and also relationships between ore and gangue minerals, the latter also playing a significant role in concentrating trace elements of interest or concern.

Ores and their component minerals display evidence of multiple cycles of in situ replacement and phase transformation but also remobilization and recrystallization (e.g., [20,24–28]. Copper concentrates produced by froth flotation contain ca. 80% Cu-(Fe)-sulfides but are also enriched in many minor and trace metals (Ag, As, Bi, Au, Co, etc.) relative to ore feed; in many cases, those trace elements mostly occur in solid solution in the host sulfides or as included grains of discrete minerals. Uranium is recovered by sulfuric acid leaching of both flotation tailings and copper concentrates.

One critical aspect of the overarching approach in the present study is the characterization of distinct distributions and behaviors of some elements/isotopes/minerals in samples taken from different stages of mineral processing. The sample suite encompasses a few drill core specimens but is largely focused on flotation concentrates (FC) and concentrate leach discharge (CLD) samples. Drill core samples provide a snapshot into the naturally formed deposit. Flotation concentrates are produced via ore comminution followed by froth flotation, upgrading sulfides and potentially remobilizing nanoparticulates. Concentrate leach discharges are flotation concentrates which have undergone sulfuric acid leaching; extensively altering mineralogy on the nano-, micro-, and macroscales and redistributing trace elements and isotopes at anthropogenic conditions. A simplified flow sheet of ore processing at Olympic Dam may be found in Schmandt et al. [29]. This study presents just a few examples of beneficial trace element/isotope analyses, including examples of both geochemical and economic interest.

Chalcopyrite, bornite and chalcocite are the predominant copper minerals in Olympic Dam ore [20,28]. These sulfides are commonly intergrown with one another (notably bornite-chalcocite symplectites) and with U- and REE-bearing phases. Uranium-bearing minerals are uraninite, coffinite and brannerite [24–27], with significant concentrations also present in solid solution and as nanoparticles within hematite [30–32]. Gangue minerals are dominantly hematite, sericite, quartz, feldspars, pyrite, siderite, chlorite, baryte and several dozen other minor and trace minerals [20].

Rare earth elements are abundant and ubiquitous within the Olympic Dam ore [20] but are not recovered. The two major REE minerals at Olympic Dam are bastnäsite, $REE(CO_3)F$ [33] and florencite, $REEAl_3(PO_4)_2(OH)_6$ [34]; these plus minor xenotime (YPO_4), synchysite [$CaREE(CO_3)_2F$], monazite [$REE(PO_4)$], and parisite [$CaREE_2(CO_3)_3F_2$] comprise ~0.2 wt.% of the ore [20]. Additionally, woodhouseite-svanbergite group minerals, fluorapatite, zircon, fluorite, and uranium/thorium minerals are known to host low quantities of REE [35–37].

Precious metals within the Olympic Dam resource grade at an average of 0.30 g/t Au and 1.3 g/t Ag [38]. Assays of various processing stream concentrates show platinum group elements to be insignificant (<3 ppb). Most of the gold at Olympic Dam is either present in the native form or electrum [20] and is recovered efficiently from refinery slimes after electrorefining. Silver at Olympic Dam is rarely native and is either incorporated within Cu-(Fe)-sulfides or as discrete minerals combined with Pb, Bi, Se, and/or Te [20].

Uranium-bearing copper ore from iron oxide-copper-gold deposits such as Olympic Dam requires the additional consideration of daughter radionuclides (RNs) from ^{238}U, ^{235}U, and ^{232}Th decay. Most of these daughters have either very long (^{234}U = 245,500 years) or very short (^{214}Po = 164 µs) half-lives and therefore have either specific activities or concentrations that are too low to be of any concern. There are, however, three radionuclides which require routine monitoring due to their combination of measurable concentrations and high specific activities: ^{226}Ra (1601 years), ^{210}Pb (22.3 years), and ^{210}Po (138.3 days). These radionuclides constitute most of the activity in Olympic Dam copper concentrates [39].

3. Methods

The strategy for selecting samples for analysis was based on building a broad database of isotope distribution maps containing data for as many Olympic Dam minerals as possible. Priority was given to minerals predicted to host radionuclides, such as U-, REE-, and Pb-bearing phases, and baryte. Most ore minerals (e.g., chalcopyrite, bornite, chalcocite) and gangue minerals (e.g., quartz, hematite, white mica (e.g. sericite), fluorite, carbonates) were not targeted as such, but the finely-intergrown nature of the ore guaranteed that prevalent minerals were peripherally sampled many times each. For example, individual 50 µm-diameter grains may contain 10+ unique mineral phases. The images presented here represent typical examples for the topics discussed, selected from over 3200 isotope maps collected from 205 sample grains.

Samples were analyzed as described in Rollog et al. [40]. Briefly, copper concentrates from Olympic Dam were mounted in 25 mm-diameter epoxy resin rounds which were then polished. Both FC and CLD samples were prepared. Drill core pieces were mounted in epoxy resin, ground flat, and polished. Mounts were surveyed using an FEI Quanta450 field emission gun scanning electron microscope (FEG-SEM) equipped with a backscatter secondary electron (BSE) detector and an EDAX electron dispersive spectroscopy (EDS) detector, located at Adelaide Microscopy, The University of Adelaide. Grains of interest were located, imaged, characterized for mineralogy, and select grains were mapped for elemental distributions.

Isotopic maps were produced on CAMECA 50 and 50L nanoSIMS instruments (CAMECA, Gennevilliers, France) at the Centre for Microscopy, Characterisation, and Analysis, located at The University of Western Australia, Perth, Western Australia. Both the nanoSIMS 50 (5 detectors, Cs^+ ion source) and nanoSIMS 50L (7 detectors, O^- ion source) were used. For analyses on the nanoSIMS 50L, the seven detectors were carefully tuned to the desired isotopes and grains of interest were presputtered, then mapped (50 × 50 µm raster area, 50 pA ion current, D1 = 2, ES = 2, AS = 0, 512 × 512 pixels (px),

3 planes, 5 ms/px, effective beam diameter ≈ 400 nm). Following this round of mapping, the instrument was retuned to six different isotopes and one redundant isotope, usually ^{54}Fe (for comparison and alignment between runs), and the grains were mapped a second time (50 × 50 µm raster area, 250 pA ion current, D1 = 2, ES = 2, AS = 0, 512 × 512 px, 5 or 6 planes, 5 ms/px, effective beam diameter ≈ 700 nm). A similar procedure was used for the nanoSIMS 50, although most grains were mapped only once (50 x 50 µm raster area, 2 pA ion current, D1 = 2, ES = 2, AS = 2, 512 × 512 px, 1-3 planes, 15 ms/px, egun on, effective beam diameter ≈ 400 nm). There are two exceptions to the above; maps of samples 01FC58 and 01FC13 shown as Figures 2 and 3 were mapped at a resolution of 256 × 256 px.

Images presented in this contribution represent samples from six distinct batches of copper concentrate, mounted independently (Table 1). No significant differences in mineralogy were reported between collection dates, per sample type. NanoSIMS images were collected over three visits to CMCA in Perth during 2017.

Table 1. The particles (sample grains) analyzed by nanoSIMS, per concentrate type and collection date. Between 7 and 26 isotope maps were collected for each, averaging ~14. A selected subset of these analyses is presented in this study.

	Collection Date			
Sample Type	**08/2015**	**11/2016**	**12/2016**	**12/2017**
Flotation concentrate (FC)	13		43	16
Acid-leached concentrate (CLD)	51		31	44
Drill core samples		7		

Images were processed with ImageJ [41,42] and the OpenMIMS plugin [43]. Dead-time corrections were applied, and multiple image-planes were summed. Occasionally, second runs did not overlap perfectly with initial runs. Images were cropped accordingly to remove non-overlapping regions. Color composite images of 3 or 4 major isotopes were generated to more easily associate faint, nebulous trace element patterns with grain-scale features in the BSE images.

To verify what was seen in nanoSIMS maps, LA-ICP-MS spot analyses were performed on selected samples using an ASI RESOlution-LR ArF excimer laser ablation system (Adelaide Microscopy, The University of Adelaide) with a large format S155 sample chamber (Laurin Technic Inc.) coupled to an Agilent 7900× ICP-MS. Instrument specifics include a 13 µm spot diameter, fluence 3.5 Jcm^{-2}, and repetition rate of 10 Hz. Counts-per-second (isotopic) were converted to counts-per-second (elemental) using global isotopic abundances [44]. RN concentrations were not quantifiable due to a lack of radionuclide standards so the traces presented are for comparison only. In this study, however, the *lack* of signal is a significant result.

4. Results and Discussion

Since they are easily detectable in bulk samples, trace elements can be tracked (and in most cases recovered or removed, if desired) during processing, but details of their micro- or nanoscale deportment are not easily discerned by low-resolution techniques. Close inspection of nanoSIMS maps revealed a number of associations that may be largely undetectable using other methods due to extremely low concentrations and/or the scale of mineral intergrowths.

4.1. Precious Metals

Although methods of precious metal recovery from electrorefining slimes are well established, they are not necessarily efficient if the mineralogical balance for those elements is inadequately studied. Hidden associations revealed by nanoSIMS mapping may offer pathways to more cost-effective recovery solutions. The presence of Au and Ag can be seen in various sulfide and non-sulfide minerals on

nanoSIMS maps of Olympic Dam samples, likely as nanoscale inclusions. Gold and Ag are recovered only from the copper concentrates, not flotation tailings where the Au-Ag grades are sub-economic.

Gold concentrations average approximately 10 ppm in copper concentrates. Although most Au at the Olympic Dam is found as micron-sized native gold or electrum, there is evidence of remobilization of Au throughout the deposit and at a range of scales. Hydrothermal fluids containing many (likely complexed) cations have circulated through the deposit multiple times [20], depositing their metal load when conditions are appropriate. One mechanism for brannerite formation involves U-rich fluids interacting with rutile [27]. It is not unreasonable to think that the U-rich fluids may contain other elements, such as Au and Te, which precipitate simultaneously as nanoparticles (Figure 1). The ability of brannerite to incorporate Au and Te has been observed in Buryatian placer nuggets up to 50 g in weight [45].

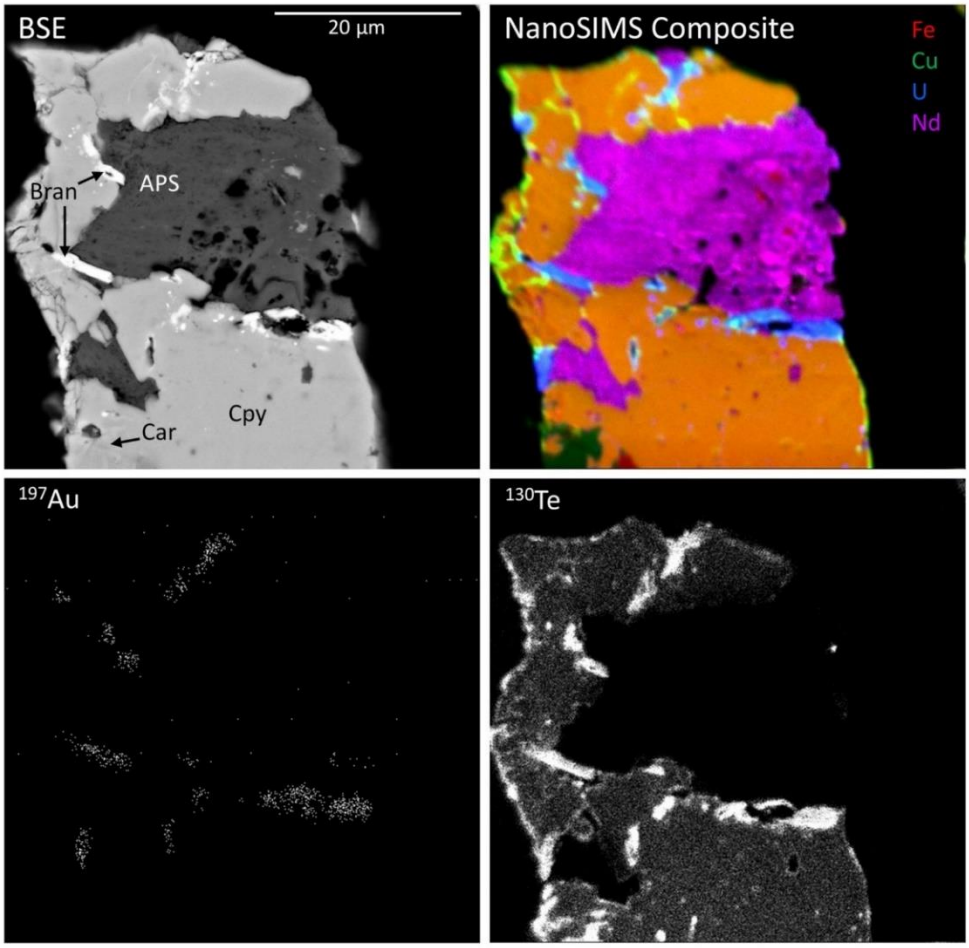

Figure 1. The backscatter secondary electron detector (BSE) image and nanoSIMS images of grain 05CLD27. The composite image contains nanoSIMS overlays of Fe (red), Cu (green), U (blue), and Nd (magenta). Note that orange is the result of a red and green overlap (chalcopyrite in this sample). Abbreviations: (Bran) = brannerite; (Cpy) = chalcopyrite; (Car) = carrollite; (APS) = aluminum phosphate-sulfate phase. Trace levels of Au can be seen coincident with Te, likely as cogenetic nanoparticles in brannerite.

Silver grades average 1.3 ppm in the Olympic Dam resource [38] but can upgrade to >80 ppm during flotation. It is predominantly found as hessite (Ag_2Te) inclusions in sulfides or at concentrations of tens to hundreds of ppm in bornite and chalcocite [20]. Two samples were selected for analyses to determine the distribution and associations of Ag in copper sulfides. The first sample is comprised of coarsely intergrown bornite-chalcocite (Bn-Cc) with a uraninite-dolomite vein fill (Figure 2). The nanoSIMS composite image reproduces the BSE image, but additionally reveals high levels of heavy rare earth elements (HREE) in the uraninite. The Ag is concentrated in chalcocite, but to a lesser extent between the uraninite-dolomite veins. Highly enriched zones are found where chalcocite borders the grain edge. In contrast, Bi favors bornite and is more enriched between the uraninite-dolomite veins. A possible mass interference exists, as $^{1}H^{208}Pb$ is indistinguishable from ^{209}Bi on the nanoSIMS. The example in Figure 3 illustrates that this interference is minor. A survey of multiple lead minerals shows a variable 209 signal, suggesting that this is due to real variable amounts of ^{209}Bi, which would be expected, and not an inconsistent $^{1}H^{208}Pb$ signal response. Additionally, scanning mass 209 while focusing the nanoSIMS on a pure Pb standard gives a response four orders of magnitude lower than that of mass 208, suggesting that the $^{1}H^{208}Pb$ interference is inconsequential.

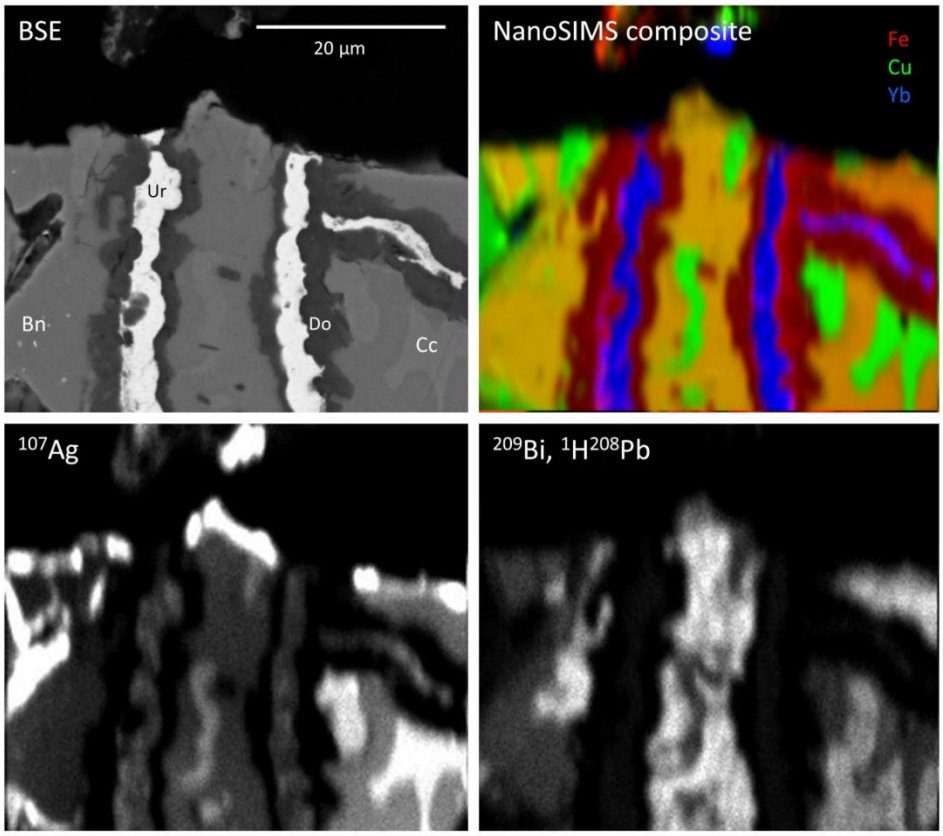

Figure 2. The BSE (top left) and nanoSIMS images of sample 01FC58 showing fracture fill uraninite (Ur) and dolomite (Do) within host bornite (Bn) and chalcocite (Cc). The nanoSIMS composite image combines Fe (red), Cu (green), and Yb (blue) maps. Note that orange is the result of a red and green overlap (bornite in this sample).

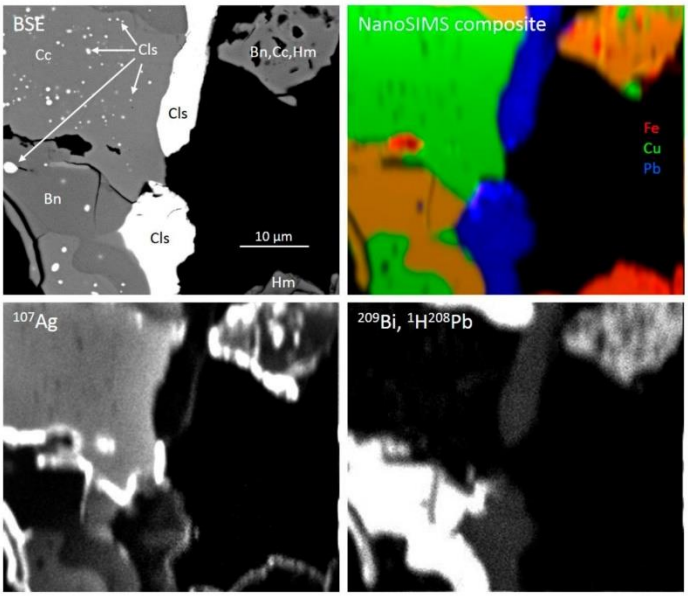

Figure 3. The BSE (top left) and nanoSIMS images of sample 01FC13 showing two large clausthalites (Cls) in bornite/chalcocite. Sub-micron clausthalite inclusions are found throughout the chalcocite, and—to a lesser extent—in bornite. The composite image represents overlapping nanoSIMS maps of Fe (red), Cu (green), and Pb (blue). Note that orange is the result of a red and green overlap (bornite in this sample). Silver shows a clear preference for chalcocite whereas Bi is more readily incorporated into bornite. Silver also appears at grain boundaries and in fractures. Isobaric mass interference for mass ^{209}Bi can barely be seen coinciding with the clausthalite grains, partially caused by $^{1}H^{208}Pb$.

The second sample analyzed for Ag distribution consists of coarsely intergrown chalcocite and bornite, both containing sub-micron inclusions of clausthalite (Figure 3). Two large clausthalites are bound to the grain margin. Smaller grains of hematite (lower right) and clausthalite-free bornite with chalcocite and hematite inclusions (upper right) are peripheral to the main grain. Silver is once again concentrated in chalcocite, consistent with Reference [46], with highly enriched zones at Bn-Cc grain boundaries. The peripheral bornite also has elevated Ag, predominantly on the edges and around inclusions. Bismuth distribution mimics that of the first sample, concentrating in bornite. Little to no Bi is found in chalcocite or hematite. The faint signal of mass 209 in the large clausthalites is likely (at least in part) to be the result of mass interference from $^{1}H^{208}Pb$, although Bi substitution into Pb minerals is certainly possible [47].

Precious metals at Olympic Dam are well-characterized and recovered via established methods. Gold or Ag associated with copper ore minerals are destined for recovery regardless of their mineralogy, and nanoSIMS maps only serve to verify what is already understood. Trace amounts of Au and Ag can also be seen in various non-ore minerals, but not to levels which are economically inducive to incorporate additional extraction techniques. This information may be useful, however, to geochemists in the form of previously unknown associations or the abundance of nanoinclusions.

4.2. Rare Earth Elements

Fluorapatite comprises only 0.1 wt.% of the Olympic Dam deposit [20] but is known to host up to 70 ppm Th and >1.8 wt.% ΣREE [32]. Substitution of REE^{3+} (or Th^{4+}) for Ca^{2+} in apatite-group minerals can be extensive. Euhedral fluorapatite grains are frequently found associated with pyrite, as shown in Figure 4. Enriched cores contain primarily light rare earth elements (LREE), although HREE, Ra, and Th also show elevated concentrations. Three of the zoned grains are exposed at

the pyrite grain surface and feature high-Pb zones in the visibly corroded internal grain boundaries. The fourth fluorapatite grain is completely entrained in pyrite and has no corresponding boundary Pb enrichment. Neodymium, Ra, Th, and particularly Tm, also show enrichment at these three grain boundaries, suggesting exposure to REE- and RN-rich solution which did not have access to the entrained crystal. Small aluminum phosphate-sulfate (APS) inclusions exhibit high REE—and moderate RN—enrichment.

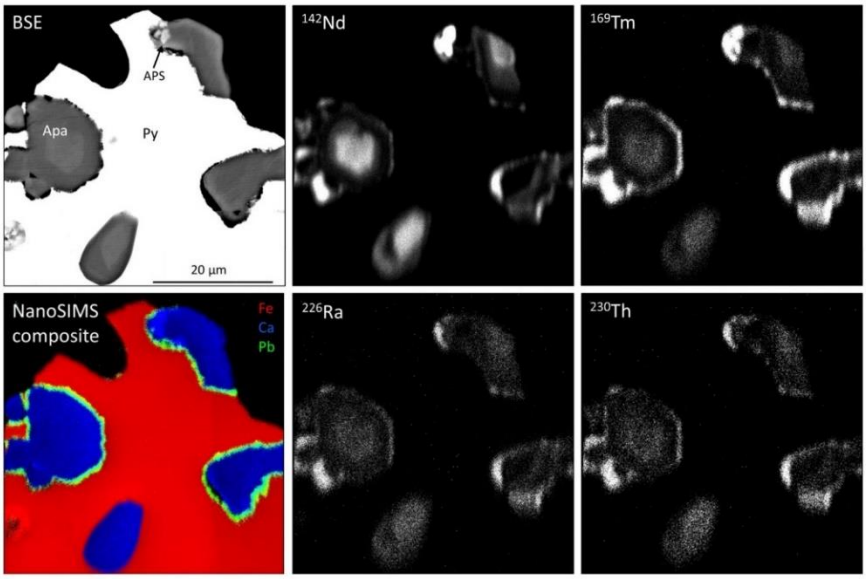

Figure 4. The BSE (top left) and nanoSIMS images of sample 10FC41b, showing inclusions of fluorapatite (Apa) within pyrite (Py). The composite image represents overlapping nanoSIMS maps of Fe (red), Ca (blue), and Pb (green). Rare earth elements (represented by ^{142}Nd and ^{169}Tm), Ra, and Th are present (and frequently show zoning) in the fluorapatite.

Unzoned fluorapatite associated with sericite-hematite alteration behaves similarly, with even more distinct dissociation between HREE and LREE (Figure 5). The nanoSIMS composite faithfully reproduces the BSE image, with Sr in blue representing fluorapatite (Ca was not mapped). The ^{144}Nd map highlights enriched areas of LREE not visible in the BSE image, possibly representing florencite, which has roughly the same gray-scale response. Lead is absent from around the apatite and is contained entirely within the chalcopyrite. As in the previous example, the HREE distribution is coincident with RNs.

Fluorite is prevalent at OD, representing approximately1 wt.% of the ore body [20]. Nonetheless, most fluorapatite and fluorite recover to flotation tailings along with the other REE-bearing minerals. Although most of the fluorite that survives froth flotation is removed during sulfuric acid leaching, residual fluorite has the capability of hosting not only elements such as Mg, Sr, and REE, but also Th—at least in concentrations high enough for thermochronology [48]. The comminution process does not always fully liberate gangue minerals, as illustrated by a fluorite grain completely entrained in bornite-chalcocite symplectite (Figure 6). Despite having gone through the sulfuric acid leach tank, this 18 x 25 µm fluorite grain survived. The Sr^{2+} replacement of Ca^{2+} is expected and observed, although there is a Sr-depleted region in the fluorite. The high Sr concentration on the symplectite grain edges is attributed to insoluble $SrSO_4$ formed during the sulfuric acid leach. LREE are also present in trace concentrations, represented by Nd; Tm is absent. Thorium-230 shows a very slight enrichment in the fluorite grain, with additional hot spots correlating to both Nd and Tm—likely due to sub-micron REE-phase (possibly APS-phase) inclusions.

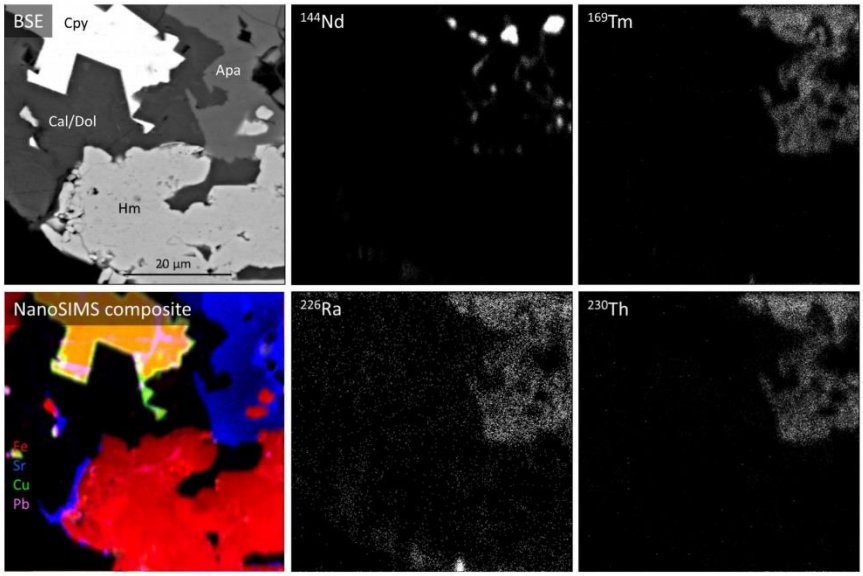

Figure 5. The BSE (top left) and nanoSIMS images of sample 10FC68 comprising an assemblage of apatite, calcite/dolomite (Cal/Dol), chalcopyrite, and hematite (Hm). The composite image represents overlapping nanoSIMS maps of Fe (red), Sr (blue), and Cu (green). Note that orange is the result of a red and green overlap (chalcopyrite in this sample). Rare earth elements (represented by ^{144}Nd and ^{169}Tm), Ra, and Th are found throughout the apatite (and only the apatite), though no zoning is evident.

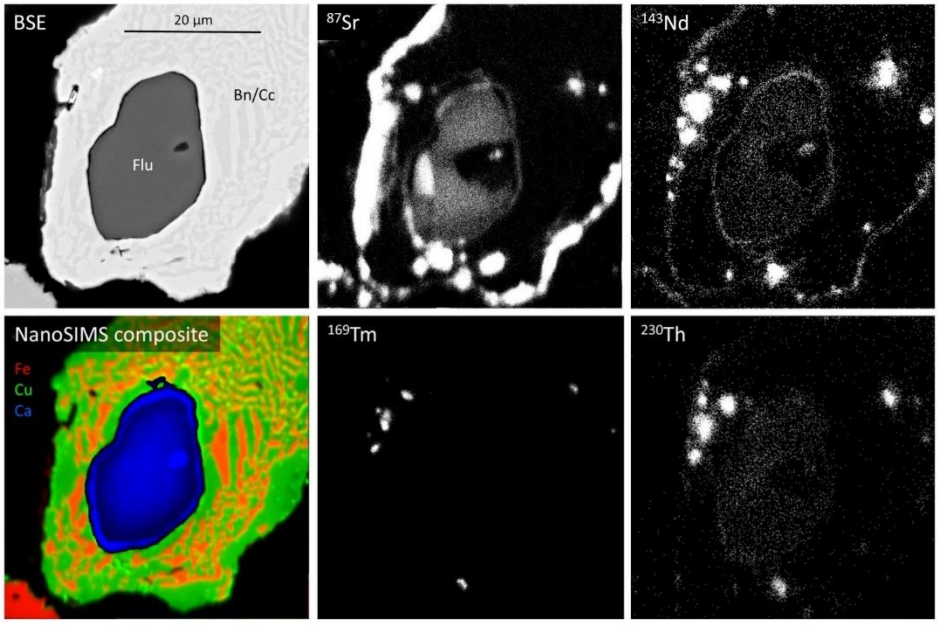

Figure 6. The BSE and nanoSIMS images of sample 05CLD86 showing corroded/resorbed fluorite (Flu) within the symplectitic intergrowth of chalcopyrite and bornite. The composite image represents overlapping nanoSIMS maps of Fe (red), Cu (green), and Ca (blue). Note that orange is the result of a red and green overlap (in this case, bornite). Sr^{2+} commonly substitutes for Ca^{2+} in fluorite, frequently resulting in intricate zoning patterns. LREE, represented here by ^{143}Nd, is associated positively with Sr in the fluorite, but HREE is absent.

Occasionally, a relatively coarse grain of fluorite survives both froth flotation and acid leaching (Figure 7). Compositional zoning with respect to Sr within the crystal is distinct, and correlates to the zoning patterns of Nd and Tm. Thorium-230 is completely absent (not pictured) and ^{206}Pb is found only as a thin layer of (most likely) insoluble $PbSO_4$ as a result of the sulfuric acid leach process. For verification, a single LA-ICP-MS spot analysis was performed (represented by the dashed yellow circle) and returned La and Ce concentrations above 100 ppm.

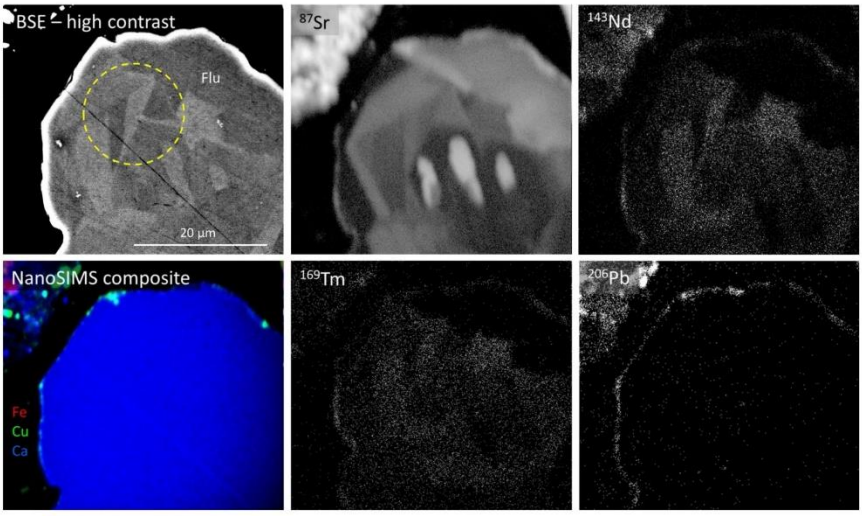

Figure 7. The high-contrast BSE (top left) and nanoSIMS images of sample 02CLD39 (coarse fluorite grain). The nanoSIMS composite image represents overlapping nanoSIMS maps of Fe (red), Cu (green), and Ca (blue). Sr^{2+} commonly substitutes for Ca^{2+} in fluorite, frequently resulting in intricate zoning patterns. REE, represented here by ^{143}Nd and ^{169}Tm, are associated somewhat negatively with Sr. Lead-206 is found only on the grain surface, likely as insoluble $PbSO_4$. The dashed yellow circle represents the location and relative size of a single 15 µm-diameter LA-ICP-MS spot analysis.

One minor, but important host for REE is the Sr-Ca-dominant aluminum phosphate-sulfates of the woodhouseite-svanbergite group. Detailed investigation of these minerals in OD samples has revealed several distinct members [37]. These phases belong to the alunite supergroup with the general formula $[AB_3(XO_4)_2(OH)_6]$, where [A] may be a wide variety of mono-, bi-, or trivalent cations, [B] is almost always Al, and (XO_4) may be phosphate, sulfate, or a mixture thereof [49]. At the Olympic Dam, these APS minerals have the A-site dominantly populated by (Sr, Ca, REE), and may contain up to 15 wt.% REE (Figure 8). NanoSIMS maps confirm high levels of Sr, Ba, and Nd, and lesser amounts of Tm, exclusively in the APS phase. This phase is also included by about a dozen small xenotimes, difficult to see in the BSE image but highlighted clearly in the ^{169}Tm nanoSIMS map. Xenotime is well known to host heavy REE [50,51] but rarely incorporates light REE—as seen in the ^{143}Nd map. Lead-206 is found throughout both the APS phase and chalcopyrite, although the distribution in APS seems relatively uniform while the host of cracks and fissures in chalcopyrite preferentially accumulate Pb. A single time-resolved laser ablation spot yields high Ca, Sr, La, and Ce, with lesser amounts of Ba and Pb. Thulium is lower in concentration and irregular, suggesting the presence of small inclusions.

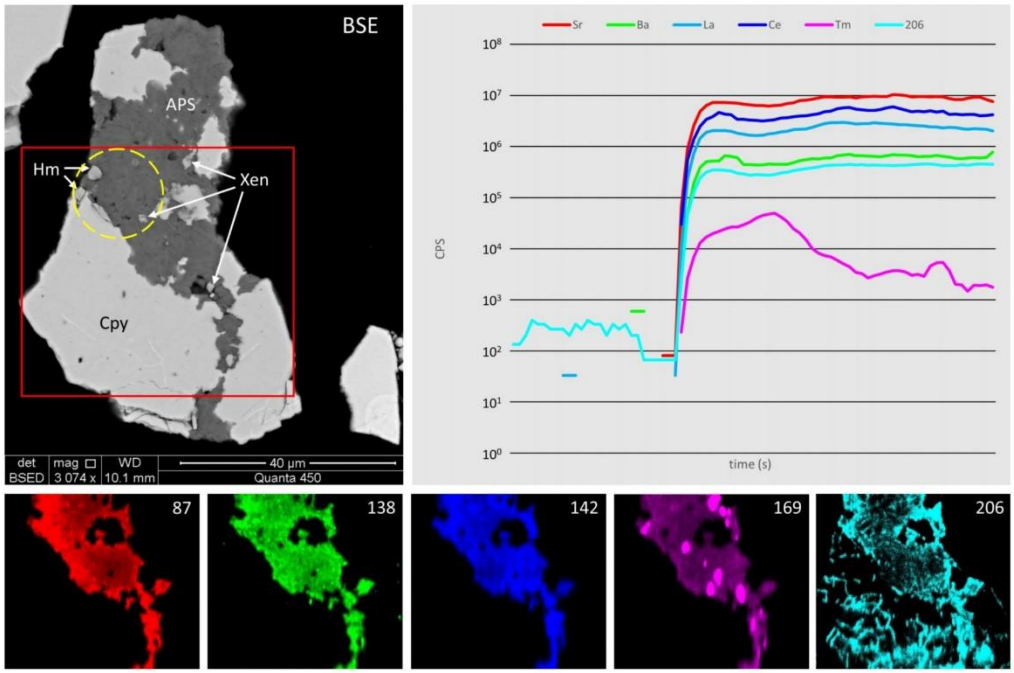

Figure 8. The BSE image (top left), single time-resolved laser ablation inductively coupled plasma mass spectrometry (LA-ICP-MS) depth profile data (top right, CPS: counts-per-second), and nanoSIMS images (bottom) of an assemblage of aluminum-phosphate-sulfate (APS) phase(s) with chalcopyrite, hematite, and xenotime in sample 10CLD42. Maps of ^{87}Sr, ^{138}Ba, ^{142}Nd, ^{169}Tm, and ^{206}Pb are presented. The red square outline is nanoSIMS mapping area, dashed yellow circle is 15 µm-diameter LA-ICP-MS spot location. Significantly more spatial detail is attainable through nanoSIMS compared to LA-ICP-MS mapping or BSE imaging, although it remains non-quantifiable.

4.3. Penalty Elements

Monitoring trace elements may have potential benefits on the other end of the economic spectrum as well. As opposed to payable elements, "penalty elements" may have a negative effect on a saleable product if concentrations are too high. Copper concentrates sold into the global concentrate pool are monitored for concentrations of F, Hg, As, Sb, Bi, Se, Te, and Pb to name a few. Excessive amounts of these may result in penalties, so every effort is made to minimize these in final products. Copper concentrates produced at Olympic Dam are smelted on site, therefore, the spatial locations of smelter deleterious or payable elements within the concentrates are shown here for illustrative purposes only.

Figures 9 and 10 display BSE and nanoSIMS images for selected deleterious elements in different assemblages from four CLD and three FC samples. Arsenic occurs in association with many metals including Fe, Co, Ni, Cu, and Tl, so finding As in pyrite is unsurprising as is the fine oscillatory zoning shown by sample 10FC35. It is more interesting, and less expected, however, that As also appears associated with molybdenite (10CLD24). There are only a few minerals containing both As and Mo, and most of those are in the oxoanionic forms of AsO_4^{3-} and MoO_4^{2-} and are unlikely to be found in sulfide ores. Selenium and Te (also associated with Mo) are frequently found together, both representing group VIa of the periodic table. Molybdenite is known as a suitable trap for various minor minerals, including fine-grained gold and Bi-tellurides, within cleavage domains [52].

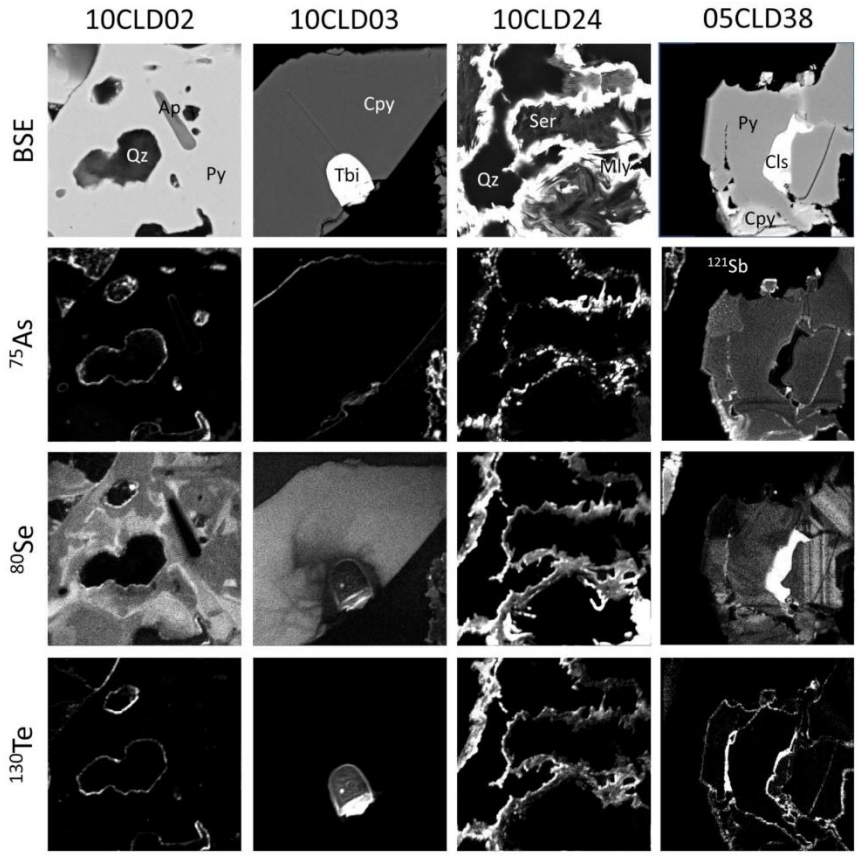

Figure 9. The BSE (top row) and nanoSIMS images of potentially deleterious elements (^{75}As, ^{80}Se, ^{121}Sb, and ^{130}Te) in different assemblages from the four sulfide concentrate leach discharge (CLD) samples. Abbreviations: Ap-apatite; Cls-clausthalite; Cpy-chalcopyrite; Mly-molybdenite; Py-pyrite; Qz-quartz; Ser-sericite; Tbi-tellurobismuthite. Note that ^{121}Sb was analyzed instead of ^{75}As for sample 05CLD38. Previously undetected zoning may be seen with respect to Se in samples 10CLD02, 10CLD03, and 05CLD38.

Commonly associated with Fe, Cu, Ag, Ag, Pd, Bi, and Pb, the chalcogens are found in varying amounts in most pyrite and copper sulfide ore minerals at Olympic Dam. NanoSIMS reveals intricate zoning with respect to Se (10CLD02 and 05CLD38), which is not apparent for Te (or S). Grains 10CLD02 and 05CLD38 illustrate the elusive nature of Te, with high concentrations limited to grain boundaries and microfractures.

One critical penalty element that must be considered during copper concentrate production is Pb. Flotation circuits may be optimized for galena rejection, which solves the bulk of the problem, but Pb in combination with other elements such as Se, Te, Sb, Ag, Cu, or Bi may not behave similarly. Additionally, Olympic Dam ore is well known for extremely fine heterogeneous textures [20], with many minerals occurring as nanosized inclusions (similar to those described in Reference [53]) or fracture fill—also immune to flotation. The deportation of Pb takes on further importance at Olympic Dam where ^{210}Pb is also a radionuclide. Although low in concentration (only around 13 kg in the entire 10,700 Mt deposit) an activity limit of 1 Bq/g in final concentrates equates to only 380 parts-per-quadrillion (ppq) of ^{210}Pb. Since targeting ^{210}Pb specifically by hydrometallurgy is currently not possible, the overall reduction of total Pb in final concentrates is the only reasonable approach to minimizing ^{210}Pb.

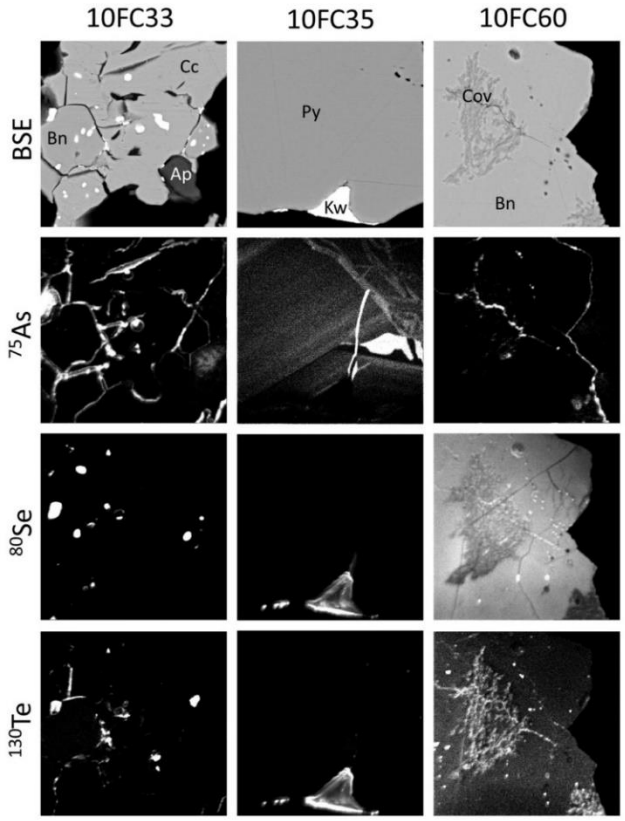

Figure 10. The BSE (top row) and nanoSIMS images of potentially deleterious elements (^{75}As, ^{80}Se, and ^{130}Te) in different assemblages from three sulfide flotation concentrate (FC) samples. Abbreviations: Ap-apatite; Bn-bornite; Cc-chalcocite; Cov-covellite; Kw-kawazulite; Py-pyrite. Zoning with respect to As is evident in sample 10FC35.

In some chalcopyrite and bornite, networks containing elevated concentrations of Pb crosscut individual sulfide grains (Figure 11). These are interpreted as healed microfractures and/or boundaries between sub-grains. Sub-micron zones of a yet-to-be-characterized Pb-bearing component appear at boundaries between minerals, frequently between chalcopyrite and other sulfides. Sample 02FC41 shows such a feature following the mutual boundary between pyrite and chalcopyrite.

Similar features can also be seen on the maps of sample 05CLD85. Sample 02FC44 has more diffuse boundaries, with gradual transitions from chalcopyrite to bornite to chalcocite. In this case, these features appear throughout the bornite, which probably represents an annealed aggregate of small grains rather than a larger single grain, and never extends into adjacent chalcocite or chalcopyrite. Samples 05CLD85 (lower right sector) and 10FC52 show traces of Pb in completely annealed fractures in chalcopyrite, with occasional forays into bornite. During (re-)crystallization, trace amounts of Pb may accumulate in these zones to avoid incorporation into incompatible crystal structures, or the Pb may have been filled in microfractures which have since annealed.

Identifying and characterizing all components within ore-forming hydrothermal fluids may aid in reconstructing ore formation and alteration profiles, and for defining the geochemical signature of the deposit [54]. To the metallurgist, greater interest lies in the ability of nanoSIMS to track trace amounts of potentially economic elements, including Co, Ni, V, In, and REE during various stages of ore processing. Monitoring the fate of these elements after each stage of processing enables metallurgists to classify discrete tailings streams as potential reservoirs for future recovery.

The distributions of potentially deleterious elements are often complex, split between discrete minerals and in solid solution at trace to minor concentrations within multiple host phases. Many of the potential hosts for common elements of concern can be readily predicted on the basis of known geochemical behaviors and published studies from other locations. For example, the relative enrichment of Cd in sphalerite, As in pyrite, or of Bi in bornite are well documented in the literature and supported by quantitative microanalysis (e.g., LA-ICP-MS). Other patterns may, however, be less obvious and can only be picked up by qualitative mapping at appropriate scales.

4.4. Radionuclide Distributions

Most IOCG deposits contain some U, with OD being at the higher-concentration end of the spectrum. Fortunately, neither the ^{235}U and ^{232}Th decay chains contain any isotopes with the right combination of high activity and a long enough half-life to accumulate in concentrates (months to years); the ^{238}U chain is more complicated. Efficient removal of ^{238}U, combined with its long half-life, results in very low activity of ^{238}U in the final concentrate. The shorter half-lives of a few of the daughter radionuclides, however, create the additional challenge of removing ppb-quantities of these daughters economically, and without a corresponding loss of Cu by co-dissolution. Principal among these daughters is ^{210}Pb, along with ^{226}Ra and ^{210}Po. Our initial hypothesis at the commencement of this project was that by reducing Pb (total) during processing, the ^{210}Pb concentrations should drop accordingly. This, however, has proven not to be quite as simple as it seemed. NanoSIMS data have confirmed the dissociation between ^{206}Pb and ^{210}Pb observed in direct measurements on bulk materials, likely the result of extremely dissimilar residence times.

Six members of the ^{238}U decay chain can be detected by nanoSIMS; ^{238}U, ^{234}U, ^{230}Th, ^{226}Ra, ^{210}Pb, and ^{206}Pb. A crucial facet of this study is the determination of host minerals for these RNs and any dissociations which may occur. Four examples of RN distributions are presented in Figure 12. All members of the chain are present, to some extent, in most uranium and thorium minerals—especially uraninite (10FC20). Radionuclides in coffinite (10FC06) and brannerite (10FC48) are frequently dissociated from one another at the mineral scale, with variable concentrations and distributions throughout the grains. Although the ^{238}U in 10FC06 is clearly concentrated in the coffinite, ^{234}U and ^{230}Th appear approximately evenly distributed between the coffinite and the surrounding xenotime. Lead-210 and ^{226}Ra are almost exclusively found in xenotime, and ^{206}Pb is primarily found as tiny blebs of galena in the center of the coffinite. The ^{206}Pb-^{210}Pb dissociation can be seen in 10FC06, 02FC40, and to a lesser extent in 10FC48.

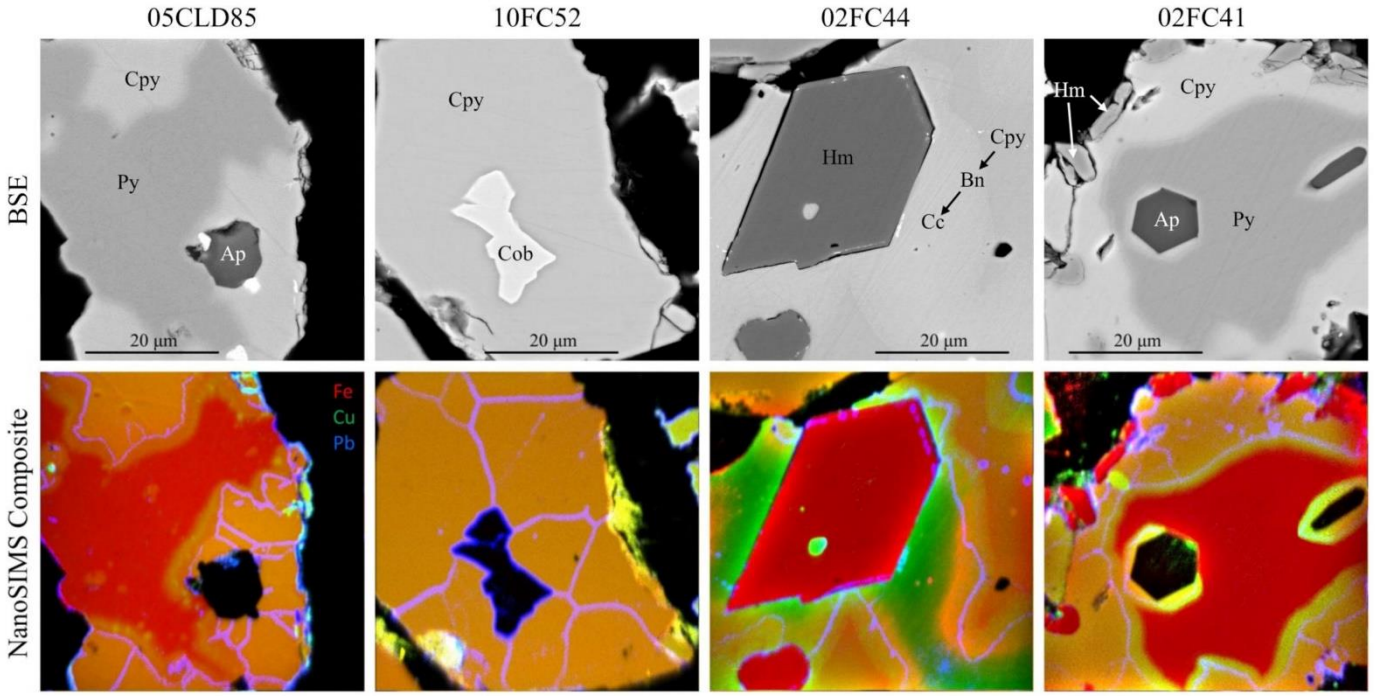

Figure 11. The BSE image (upper row) and nanoSIMS composite images of sulfide assemblages in samples 05CLD85, 10FC52, 02FC44, and 02FC41. Abbreviations: Cpy-chalcopyrite; Py-pyrite; Ap-apatite; Cob-cobaltite; Hm-hematite; Bn-bornite; Cc-chalcocite. The composites represent overlapping nanoSIMS maps of Fe (red), Cu (green), and Pb (blue)—the color scheme is uniform for all four composites. Note that orange is the result of a red and green overlap and magenta is the result of a blue and orange overlap. Lead-206 lines/spots are pervasive throughout chalcopyrite and bornite, but are virtually absent in hematite, chalcocite, and pyrite.

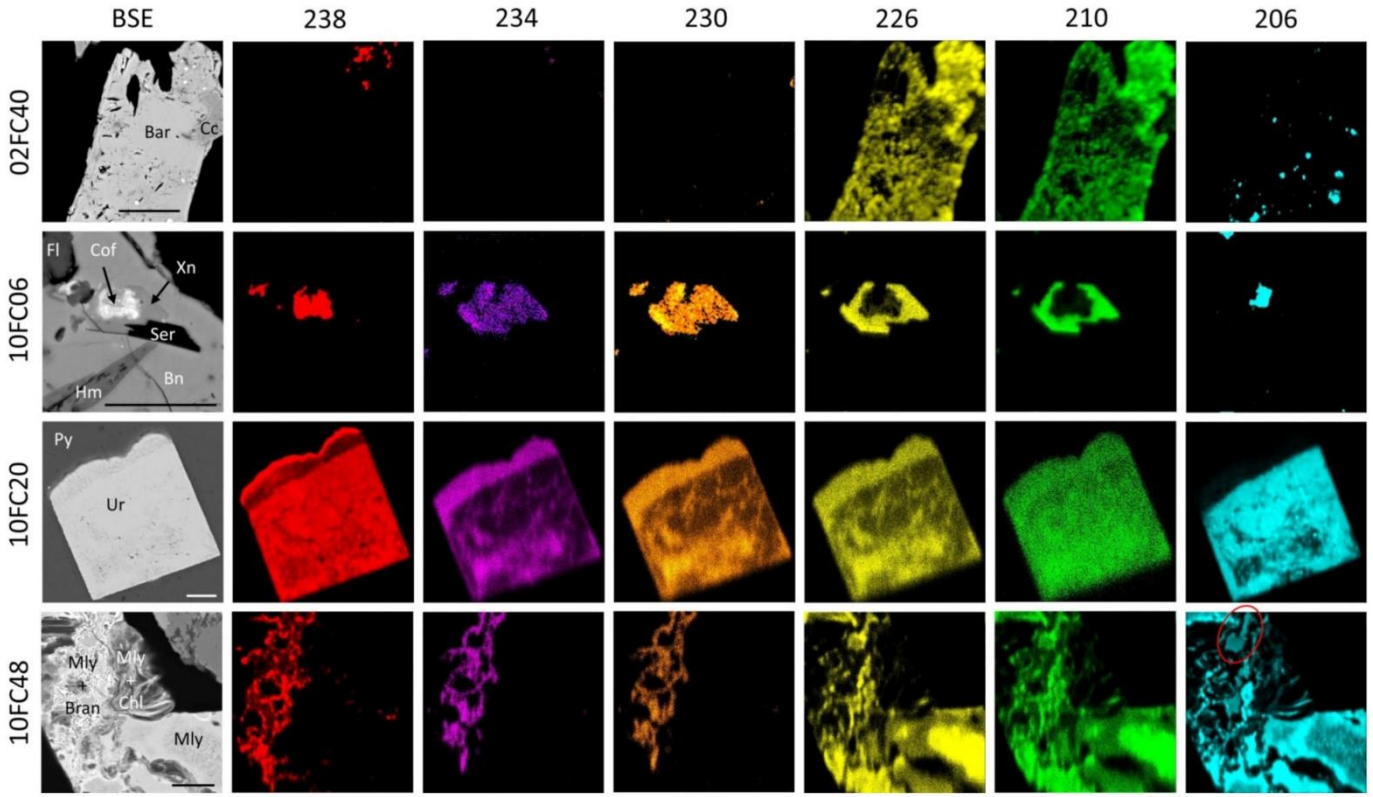

Figure 12. The BSE (left column) and nanoSIMS maps of members of the ^{238}U decay chain from selected areas in samples 02FC40, 10FC06, 10FC20, and 10FC48. Bar-baryte; Bn-bornite; Bran-brannerite; Chl-chlorite; Cof-coffinite; Fl-fluorite; Hm-hematite; Mly-molybdenite; Py-pyrite; Ser-sericite; Ur-uraninite; Xn-xenotime. Scale bars represent 10 μm. Retention of daughter isotopes is strong in uranium minerals (notably uraninite in 10FC20), but dissociation may be prevalent in other minerals without essential U. In sample 10FC48, note the "quarter note" (crotchet) shape in the red oval on the 206 map. Although a complicated pattern, it can be seen that the maps for masses 206, 210, and 226 are in fact the *inverse* of the 230, 234, and 238 maps. In Olympic Dam copper concentrates, the ^{230}Th/^{226}Ra decay transition appears to be the most common point of dissociation amongst RNs.

Baryte (Figure 12, 02FC40; Figure 13) and other sulfate-bearing minerals (e.g., APS phases) are excellent repositories for ^{210}Pb and ^{226}Ra, but much less so for RNs from further up the chain. Here, sulfate activity is the controlling factor since both $PbSO_4$ and $RaSO_4$ are extremely insoluble in both water and acids, and baryte is well known as a scavenger of Ra [55–57]. Molybdenite (in sample 10FC48) also seems to only host RN from ^{226}Ra down the chain, with very little Th or U present. Enrichment of Ra and ^{210}Pb in the entire molybdenite grain, with higher concentrations in areas of platy textures (lower left) suggest that high surface area cleavage planes may act as a mechanical trap for sulfate-insoluble RNs. The fact that U and Th seem to be immune to this indicates the possibility that nanoparticles of sulfate precipitates are the true host of Ra and Pb and are simply being filtered out of the solution or are adhering to the extensive surface area of molybdenite cleavage planes via electrokinetics.

There are many forms and mineralization stages of baryte at Olympic Dam [29]. Two such types are "dirty" baryte containing a high density of inclusions, and clean, largely homogeneous baryte—both visible in Figure 13. Near the chalcocite/chlorite vein, dirty baryte predominates. Concentrations of ^{226}Ra and ^{210}Pb are elevated, and although ^{230}Th appears to correlate with these, it actually appears to fill boundaries around the chalcocite/chlorite grains. Both U isotopes are confined to the chalcocite/chlorite vein and correlate with REE. Not surprisingly, ^{206}Pb occurs to some extent everywhere in the mapped area, both coinciding with ^{238}U and occurring as tiny inclusions (likely galena) within dirty baryte. Interestingly, the "clean" baryte (lowest center-to-left portions of the nanoSIMS maps) is nearly devoid of RNs and ^{206}Pb. This difference would suggest either two stages of baryte growth or the corrosion/replacement of a pristine baryte crystal by coupled dissolution-reprecipitation processes. The semi-porous nature of the corroded baryte would suggest the latter [58].

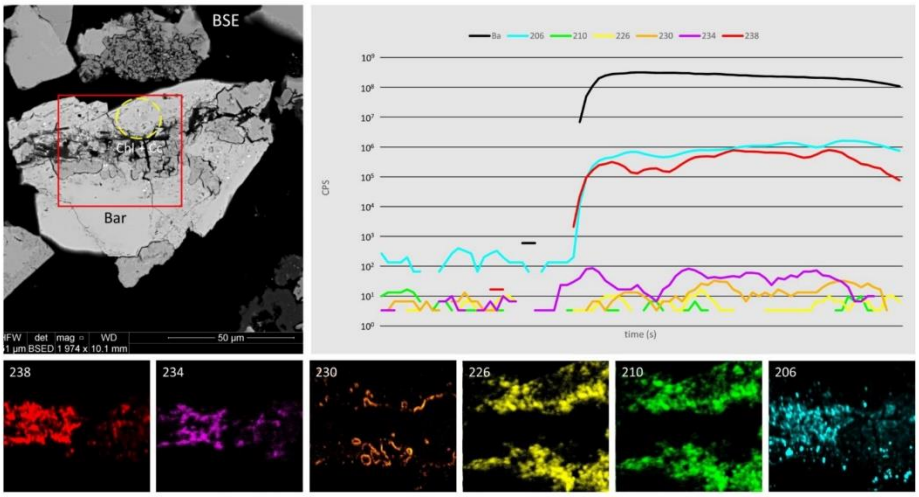

Figure 13. The BSE image (top left), single time-resolved LA-ICP-MS depth profile data (top right), and nanoSIMS images (bottom) of assemblage in sample 02CLD29 (chalcocite/chlorite 'vein' crosscutting baryte (Bar) with abundant inclusions). Maps of ^{206}Pb, ^{210}Pb, ^{226}Ra, ^{230}Th, ^{234}U, and ^{238}U are presented. The red outline is the nanoSIMS mapping area, the yellow circle represents the location of the 15 µm-diameter LA-ICP-MS spot. Uranium is concentrated within the vein, whereas ^{210}Pb, Ra, and Th appear preferentially enriched in baryte containing abundant, dense inclusions. Lead-206 likely has multiple origins and is found throughout. Pristine baryte (lower left of the nanoSIMS maps) contains virtually no RNs.

As opposed to baryte, APS minerals do not seem to display the decoupling of the ^{238}U chain at the Th-Ra boundary, although there is some considerable variability in the grains observed (e.g., Figure 14). Most RNs seem to reside in small inclusions of xenotime within the APS. What is worthy of note,

however, is the consistent background of all RNs throughout the APS. Although not an overly enriched host, this family of minerals represents approximately 0.1 wt.% of the deposit [20]. When considering concentration limits of certain RNs in the parts-per-trillion range, their relative significance increases.

Exploring the distributions of radionuclides in various minerals from different assemblages from multiple samples raises several questions. Diverse distributions of Pb, Ra, Th, and U may be rationalized by disparities in the chemical behaviors of these elements during fluid-assisted remobilization, but why the apparent dissociation between ^{238}U and ^{234}U, and ^{210}Pb and ^{206}Pb? Isotopic fractionation will be present, of course, but cannot explain the complete isotopic decoupling of Pb or U. The answers lie at the ends of the decay chain, with the stability of ^{206}Pb and the exceptionally long half-life of ^{238}U. Lead-206 is stable and has been produced at Olympic Dam over the past 1.6 billion years, adding to the ^{206}Pb already present in precursor rocks and ore-forming fluids. It has had sufficient time and exposure to tectonothermal events to mobilize and remobilize multiple times, eventually forming galena or other Pb-chalcogenides [53] and attaining the stability necessary to remain relatively static for millions of years. Lead-210, on the other hand, has a half-life of only 138 days. It is effectively a slave to Ra chemistry since the ingrowth of ^{210}Pb through the ^{226}Ra-^{222}Rn-^{218}Po-^{214}Pb-^{214}Bi-^{214}Po-^{210}Pb chain only takes a few days. There is insufficient time for ^{210}Pb to form Pb minerals as such, though it may augment existing minerals if proximity, time, conditions and growth kinetics allow for it. It is significantly more likely that ^{226}Ra (half-life ~1600 years) finds stability in accommodating minerals such as sulfates [29], and the ^{210}Pb simply decays in situ. Although logical, this dissociation has disappointingly nullified attempts to use (readily measurable) ^{206}Pb as a proxy for (parts-per-trillion-level or less) ^{210}Pb. Fortunately, however, the nanoSIMS platform eliminates the need for such a proxy.

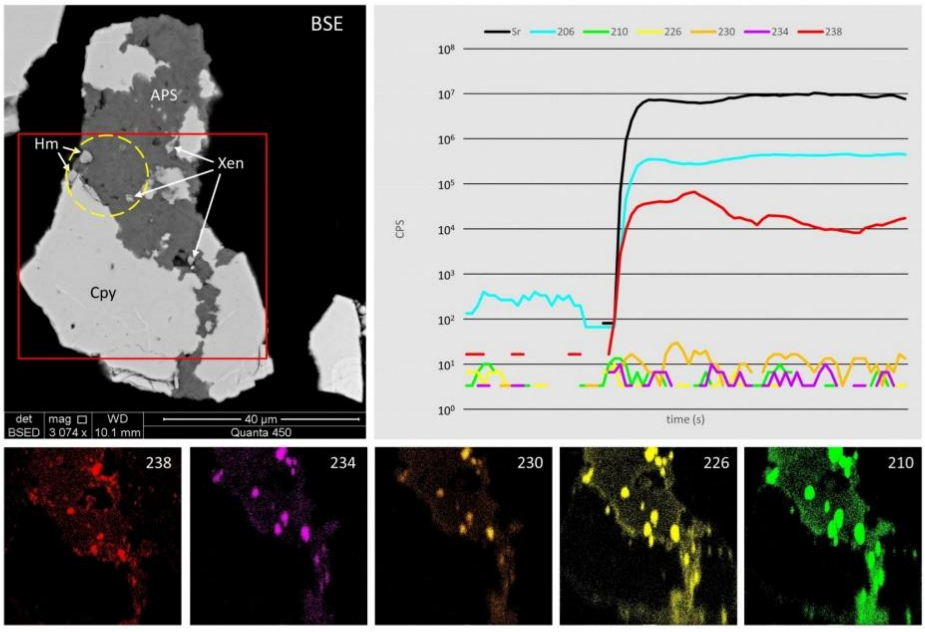

Figure 14. The BSE image (top left), single time-resolved LA-ICP-MS depth profile data (top right), and nanoSIMS images (bottom) of an assemblage of APS phase(s) with chalcopyrite (Cpy), hematite (Hm), and xenotime (Xen) in sample 10CLD42. Maps of ^{238}U, ^{234}U, ^{230}Th, ^{226}Ra, and ^{210}Pb are presented. The red outline is the nanoSIMS mapping area, the yellow circle is the location of a 15 µm-diameter LA-ICP-MS spot. Only ^{238}U gives a convincing response by LA-ICP-MS, but all five RNs are clearly present on the nanoSIMS maps with elevated backgrounds in the APS phases and xenotime but not in chalcopyrite.

Uranium pseudo-fractionation is a slightly different mechanism by which fluids containing mostly ^{238}U (possibly naturally fractionated) infiltrate and begin replacing a crystal already containing the ^{238}U decay chain in secular equilibrium. The late-stage coffinite replacement of xenotime in 10FC06 (Figure 12), for example, has artificially enriched the grain in ^{238}U. The top crust of ^{238}U enrichment on the uraninite grain in 10FC20 is likely the result of a similar mechanism. In short, these apparent "fractionations" between ^{234}U and ^{238}U are the result of multiple sources of U in different combinations, rather than the result of a linear chemical process favoring lighter or heavier mass isotopes.

4.5. Instrument Capabilities and Future Development

Laser ablation ICP-MS is a remarkably powerful tool which has proven invaluable for detailed characterization of a range of minerals [59]. It has found wide application in mineral characterization of Olympic Dam ores, for hematite [30,32], apatite [35], feldspars [60], rare earth minerals [33,34], and baryte [29], among others. Moreover, microbeam techniques have proven invaluable for the development of new methodologies for dating oxide-dominant ores [61] from Olympic Dam. There are instances, however, when the spatial resolution of LA-ICP-MS is simply inadequate, or where detection limits are not low enough for a given application.

The laser ablation data in Figures 8, 13 and 14 serve to highlight the primary comparative advantage of nanoSIMS for in situ detection of trace elements and isotopes in very fine-grained mineral samples. Lead-206 and ^{238}U are readily measured and quantified by LA-ICP-MS, but the ^{210}RN, ^{226}Ra, ^{230}Th, and ^{234}U signals are all barely above the background. It is clear from the laser spot size that even if the signals for these four isotopes were large enough to quantify, all spatial information would be lost.

Equal-scale representations of a 15 μm single time-resolved LA-ICP-MS spot (2500 μm^3) and a 50 × 50 × 1 μm nanoSIMS map (also 2500 μm^3) clearly illustrate the resolution advantage of nanoSIMS (Figure 15). Granted, though laser ablation spots may be as little as 3 μm in diameter, this dramatically reduces the analyzed volume and usually results in trace elements – especially those with lighter masses–falling below minimum detection limits. A 15 μm-diameter spot size provides higher signals, gives more depth information and is quantifiable (given appropriate matrix-matched standards) but the spatial resolution is clearly limited. For ultra-trace elements, spot diameters of 50 or even 100 μm are not unusual. The nanoSIMS mapped area in the figure assumes an effective spot size of 700 nm, resulting in roughly a 71 × 71 spot grid (pictured). This actually represents the *lowest* resolution for the images above (at 250 pA); running at lower currents can reduce the effective spot size to below 100 nm, resulting in a similar-sized mapped area containing 500 × 500 spots. Ablation depth is estimated at ~1 μm but may be significantly less. The actual depth of ablation is unknown, but it is clear from the BSE images of samples taken after nanoSIMS analyses that different minerals do ablate at different rates.

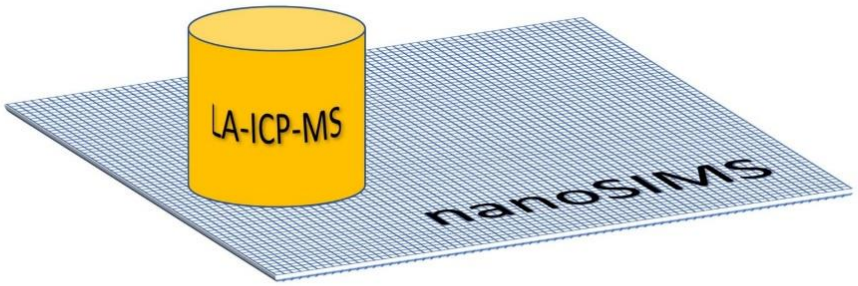

Figure 15. The equal-volume representations of a 15 μm single time-resolved LA-ICP-MS crater and a nanoSIMS 50x50x1 μm mapped area. Scales and analysis volumes are equivalent.

As for the greatest shortcoming of nanoSIMS—quantification—we believe this to be both a non-critical and a temporary deficiency. Measuring concentrations of trace elements and isotopes

is always of great interest, but this is impossibly complicated by textures which routinely extend below the micron-scale. LA-ICP-MS spot analysis can provide precise, spatially-resolved concentration data [59], but only as an average of the laser spot volume (at least a few thousands of cubic microns). Judging from the extremely detailed mineral textures presented here, this would be informative yet nevertheless, still a bulk analysis.

The unique information provided by nanoSIMS lies in its spatial resolution without loss of sensitivity, allowing researchers to determine the host minerals—or the lack thereof, wherever boundary domains or surface adherence play a significant role—for trace elements and isotopes in the sub-micron range. Once located, fragments can be extracted in situ for subsequent nanoscale study using techniques such as atom probe tomography [62], or transmission electron microscopy [63], to characterize the materials down to the Ångstrom-scale. Such an approach has been necessary to adequately capture the nanoscale heterogeneity present in several mineral groups from Olympic Dam [28,64–66].

Regarding the longer-term potential for quantification of nanoSIMS analysis, isotope ratios have been measured routinely for over 15 years [67] and relative sensitivity factors have been successfully measured for most elements within uniform matrices [68]. As expected, minerals have proven to be more difficult to quantify, a problem compounded by grain-scale heterogeneity in many natural minerals. Initial tests by the first author have nevertheless shown promising results, with consistent response intensities observed for selected major and minor elements.

5. Conclusions

(1) The combined sensitivity and resolution of the nanoSIMS analytical platform provides invaluable information regarding the deportment of trace elements and isotopes and the ultimate destination of components that have been remobilized or reconcentrated, both within the orebody and during mineral processing.
(2) Precious metal extraction may benefit from identifying previously unknown host minerals.
(3) Potentially economic elements may be monitored and archived for future extraction if commodity prices become favorable or game-changing processing methods are developed.
(4) Deleterious "penalty" elements may be closely monitored and reduction/elimination techniques optimized based on new information, especially with respect to hitherto unrecognized host minerals.
(5) Radionuclide daughters of the ^{238}U decay chain may be located in situ within ores and concentrates and this information used to develop models of their behavior during copper ore processing that will be useful for optimization of extraction.
(6) The nanoSIMS has proven a valuable tool in determining the spatial distribution of trace elements and isotopes in fine-grained copper ores. It complements observations and qualitative data obtained from other methods and offers unique insights into element/isotope distributions in cases where these are too low in absolute concentration and/or too fine to be resolved by other methods. NanoSIMS data can provide researchers with crucial evidence needed to answer questions of ore formation and ore processing.

Author Contributions: M.R. and P.G. performed the work presented here. M.R. processed results and made interpretations, supervised by N.J.C. K.J.E. supplied sample material and, together with C.L.C., provided extensive advice. M.R. wrote the manuscript assisted by N.J.C. and all other co-authors.

Funding: This is a contribution to the ARC Research Hub for Australian Copper-Uranium (Grant IH130200033), co-supported by BHP Olympic Dam.

Acknowledgments: Special thanks are extended to Sarah Gilbert (Adelaide Microscopy) for assistance with laser-ablation ICP-MS analyses.

Conflicts of Interest: The authors declare no conflict of interest.

References

1. Lane, D.J.; Cook, N.J.; Grano, S.R.; Ehrig, K. Selective leaching of penalty elements from copper concentrates: A review. *Miner. Eng.* **2016**, *98*, 110–121. [CrossRef]
2. Brown, R.J.; Milton, M.J. Analytical techniques for trace element analysis: An overview. *TrAC Trends Anal. Chem.* **2005**, *24*, 266–274. [CrossRef]
3. Kilburn, M.R.; Wacey, D. Nanoscale secondary ion mass spectrometry (NanoSIMS) as an analytical tool in the geosciences. In *Principles and Practice of Analytical Techniques in Geosciences*; Royal Society of Chemistry: London, UK, 2015; pp. 1–34.
4. Kilburn, M.R.; Clode, P.L. Elemental and isotopic imaging of biological samples using NanoSIMS. In *Electron Microscopy*; Humana Press: Totowa, NJ, USA, 2014; pp. 733–755.
5. Gao, D.; Huang, X.; Tao, Y. A critical review of NanoSIMS in analysis of microbial metabolic activities at single-cell level. *Crit. Rev. Biotechnol.* **2016**, *36*, 884–890. [CrossRef]
6. Hoppe, P. NanoSIMS: A new tool in cosmochemistry. *Appl. Surf. Sci.* **2006**, *252*, 7102–7106. [CrossRef]
7. Valle, N.; Drillet, J.; Perlade, A.; Migeon, H.N. Application of SIMS nano-analysis to the development of new metallurgical solutions. *Appl. Surf. Sci.* **2008**, *255*, 1569–1571. [CrossRef]
8. Yardley, S.S.; Moore, K.L.; Ni, N.; Wei, J.F.; Lyon, S.; Preuss, M.; Lozano-Perez, S.; Grovenor, C.R. An investigation of the oxidation behaviour of zirconium alloys using isotopic tracers and high resolution SIMS. *J. Nucl. Mater.* **2013**, *443*, 436–443. [CrossRef]
9. Barker, S.L.L.; Hickey, K.A.; Cline, J.S.; Dipple, G.M.; Kilburn, M.; Vaughan, J.R.; Longo, A.A. Uncloaking invisible gold: Use of nanoSIMS to evaluate gold, trace elements, and sulfur isotopes in pyrite from Carlin-type gold deposits. *Econ. Geol.* **2009**, *104*, 897–904. [CrossRef]
10. Fougerouse, D.; Micklethwaite, S.; Halfpenny, A.; Reddy, S.M.; Cliff, J.B.; Martin, L.A.J.; Kilburn, M.; Guagliardo, P.; Ulrich, S. The golden ark: Arsenopyrite crystal plasticity and the retention of gold through high strain and metamorphism. *Terra Nova* **2016**, *28*, 181–187. [CrossRef]
11. Fougerouse, D.; Micklethwaite, S.; Tomkins, A.G.; Mei, Y.; Kilburn, M.; Guagliardo, P.; Fisher, L.A.; Halfpenny, A.; Gee, M.; Paterson, D.; et al. Gold remobilization and formation of high-grade ore shoots driven by dissolution-reprecipitation replacement and Ni substitution into auriferous arsenopyrite. *Geochim. Cosmochim. Acta* **2016**, *178*, 143–159. [CrossRef]
12. Didier, A.; Bosse, V.; Bouloton, J.; Mostefaoui, S.; Viala, M.; Paquette, J.L.; Devidal, J.L.; Duhamel, R. NanoSIMS mapping and LA-ICP-MS chemical and U-Th-Pb data in monazite from a xenolith enclosed in andesite (Central Slovakia Volcanic Field). *Contrib. Mineral. Petrol.* **2016**, *170*, 45. [CrossRef]
13. Zhang, J.; Lin, Y.; Yang, W.; Shen, W.; Hao, J.; Hu, S.; Cao, M. Improved precision and spatial resolution of sulfur isotope analysis using NanoSIMS. *J. Anal. At. Spectrom.* **2014**, *29*, 1934–1943. [CrossRef]
14. Hauri, E.H.; Papineau, D.; Wang, J.; Hillion, F. High-precision analysis of multiple sulfur isotopes using NanoSIMS. *Chem. Geol.* **2016**, *420*, 148–161. [CrossRef]
15. Ito, M.; Messenger, S. Isotopic imaging of refractory inclusions in meteorites with the NanoSIMS 50L. *Appl. Surf. Sci.* **2008**, *255*, 1446–1450. [CrossRef]
16. Peteranderl, R.; Lechene, C. Measure of carbon and nitrogen stable isotope ratios in cultured cells. *J. Am. Soc. Mass Spectrom.* **2004**, *15*, 478–485. [CrossRef]
17. Yang, W.; Lin, Y.T.; Zhang, J.C.; Hao, J.L.; Shen, W.J.; Hu, S. Precise micrometre-sized Pb-Pb and U-Pb dating with NanoSIMS. *J. Anal. At. Spectrom.* **2012**, *27*, 479–487. [CrossRef]
18. Skirrow, R.G.; Bastrakov, E.; Davidson, G.J.; Raymond, O.L.; Heithersay, P. The Geological Framework, Distribution and Controls of Fe-oxide Cu-Au Mineralisation in the Gawler Craton, South Australia. Part II—Alteration and Mineralisation. In *Hydrothermal Iron Oxide Copper-Gold & Related Deposits: A Global Perspective*; Porter, T.M., Ed.; PGC Publishing: Adelaide, Australia, 2002; pp. 33–47.
19. Skirrow, R.G.; Bastrakov, E.N.; Barovich, K.; Fraser, G.L.; Creaser, R.A.; Fanning, C.M.; Raymond, O.L.; Davidson, G.J. Timing of iron oxide Cu-Au-(U) hydrothermal activity and Nd isotope constraints on metal sources in the Gawler craton, South Australia. *Econ. Geol.* **2007**, *102*, 1441–1470. [CrossRef]
20. Ehrig, K.; McPhie, J.; Kamenetsky, V.S. Geology and Mineralogical Zonation of the Olympic Dam Iron Oxide Cu-U-Au-Ag Deposit, South Australia. In *Geology and Genesis of Major Copper Deposits and Districts of the World, a Tribute to Richard Sillitoe*; Hedenquist, J.W., Harris, M., Camus, F., Eds.; Society of Economic Geologists Special Publication 16: Littleton, CO, USA, 2012; pp. 237–267.

21. Ehrig, K.; Kamenetsky, V.; McPhie, J.; Cook, N.J.; Ciobanu, C.L. Olympic Dam iron-oxide Cu-U-Au-Ag deposit. In *Australian Ore Deposits*; Phillips, G.N., Ed.; AusIMM: Melbourne, Australian, 2017; pp. 601–610.
22. Roberts, D.E.; Hudson, G.R.T. The Olympic Dam copper-uranium-gold deposit, Roxby Downs, South Australia. *Econ. Geol.* **1983**, *78*, 799–822. [CrossRef]
23. Reeve, J.S.; Cross, K.C.; Smith, R.N.; Oreskes, N. Olympic Dam copper-uranium-gold-silver deposit. In *Geology of the Mineral Deposits of Australia and Papua New Guinea*; Hughes, F.E., Ed.; AusIMM: Melbourne, Australian, 1990; pp. 1009–1035.
24. Macmillan, E.; Cook, N.J.; Ehrig, K.; Ciobanu, C.L.; Pring, A. Uraninite from the Olympic Dam IOCG-U-Ag deposit: Linking textural and compositional variation to temporal evolution. *Am. Mineral.* **2016**, *101*, 1295–1320. [CrossRef]
25. Macmillan, E.; Ciobanu, C.L.; Ehrig, K.; Cook, N.J.; Pring, A. Chemical zoning and lattice distortion in uraninite from Olympic Dam, South Australia. *Am. Mineral.* **2016**, *101*, 2351–2354. [CrossRef]
26. Macmillan, E.; Ciobanu, C.L.; Ehrig, K.; Cook, N.J.; Pring, A. Replacement of uraninite by bornite via coupled dissolution-reprecipitation: Evidence from texture and microstructure. *Can. Mineral.* **2016**, *54*, 1369–1383. [CrossRef]
27. Macmillan, E.; Cook, N.J.; Ehrig, K.; Pring, A. Chemical and textural interpretation of late-stage coffinite and brannerite from the Olympic Dam IOCG-Ag-U deposit. *Mineral. Mag.* **2017**, *81*, 1323–1366. [CrossRef]
28. Ciobanu, C.L.; Cook, N.J.; Ehrig, K. Ore minerals down to the nanoscale: Cu-(Fe)-sulphides from the iron oxide copper gold deposit at Olympic Dam, South Australia. *Ore Geol. Rev.* **2017**, *81*, 1218–1235. [CrossRef]
29. Schmandt, D.S.; Cook, N.J.; Ehrig, K.; Gilbert, S.; Wade, B.P.; Rollog, M.; Ciobanu, C.L.; Kamenetsky, V.S. Uptake of trace elements by baryte during copper ore processing: A case study from Olympic Dam, South Australia. *Miner. Eng.* **2019**, *135*, 83–94. [CrossRef]
30. Ciobanu, C.L.; Wade, B.P.; Cook, N.J.; Schmidt Mumm, A.; Giles, D. Uranium-bearing hematite from the Olympic Dam Cu-U-Au deposit, South Australia: A geochemical tracer and reconnaissance Pb-Pb geochronometer. *Precambrina Res.* **2013**, *238*, 129–147. [CrossRef]
31. Cook, N.J.; Ciobanu, C.L.; Ehrig, K.; Slattery, A.; Verdugo-Ihl, M.R.; Courtney-Davies, L.; Gao, W. Advances and opportunities in ore mineralogy. *Minerals* **2017**, *7*, 233. [CrossRef]
32. Verdugo-Ihl, M.R.; Ciobanu, C.L.; Cook, N.J.; Ehrig, K.; Courtney-Davies, L.; Gilbert, S. Textures and U-W-Sn-Mo signatures in hematite from the Cu-U-Au-Ag orebody at Olympic Dam, South Australia: Defining the archetype for IOCG deposits. *Ore Geol. Rev.* **2017**, *91*, 173–195. [CrossRef]
33. Schmandt, D.S.; Cook, N.J.; Ciobanu, C.L.; Ehrig, K.; Wade, B.P.; Gilbert, S.; Kamenetsky, V.S. Rare Earth Element Fluorocarbonate Minerals from the Olympic Dam Cu-U-Au-Ag Deposit, South Australia. *Minerals* **2017**, *7*, 202. [CrossRef]
34. Schmandt, D.S.; Cook, N.J.; Ciobanu, C.L.; Ehrig, K.; Wade, B.P.; Gilbert, S.; Kametetsky, V.S. Rare earth element phosphate minerals from the Olympic Dam Cu-U-Au-Ag deposit, South Australia: Recognizing temporal-spatial controls on REE mineralogy in an evolved IOCG systems. *Can. Mineral.* **2019**, *57*, 3–24. [CrossRef]
35. Krneta, S.; Ciobanu, C.L.; Cook, N.J.; Ehrig, K.; Kontonikas-Charos, A. Rare Earth Element Behaviour in Apatite from the Olympic Dam Cu-U-Au-Ag Deposit, South Australia. *Minerals* **2017**, *7*, 135. [CrossRef]
36. Schmandt, D.S. Mineralogical Distribution of Radionuclides in Copper-Uranium Ores, Olympic Dam, South Australia. Ph.D. Thesis, The University of Adelaide, Adelaide, Australia, 2019; 371p.
37. Owen, N.D.; Cook, N.J.; Rollog, M.; Ehrig, K.J.; Schmandt, D.S.; Ram, R.; Brugger, J.; Ciobanu, C.L.; Wade, B.; Guagliardo, P. REE-, Sr- Ca-aluminum-phosphate-sulfate minerals of the alunite supergroup and their role as hosts for radionuclides. *Am. Mineral.* **2019**. in review.
38. BHP Annual Report 2018. Section 6. 2018, p. 259. Available online: www.bhp.com (accessed on 25 March 2019).
39. BHP Billiton Olympic Dam Expansion Supplementary Environmental Impact Statement. Chapter 26. 2011, pp. 689–758. Available online: www.bhp.com (accessed on 25 May 2019).
40. Rollog, M.; Cook, N.J.; Guagliardo, P.; Ehrig, K.; Kilburn, M. *In Situ* spatial distribution mapping of radionuclides in minerals by nanoSIMS. *Geochem. Explor. Environ. Anal.* **2019**. [CrossRef]
41. Schindelin, J.; Arganda-Carreras, I.; Frise, E.; Kaynig, V.; Longair, M.; Pietzsch, T.; Preibisch, S.; Rueden, C.; Saalfeld, S.; Schmid, B.; et al. Fiji: An open-source platform for biological-image analysis. *Nat. Methods* **2012**, *9*, 676–682. [CrossRef]

42. Schindelin, J.; Rueden, C.T.; Hiner, M.C.; Eliceiri, K.W. The ImageJ ecosystem: An open platform for biomedical image analysis. *Mol. Reprod. Dev.* **2015**, *82*, 518–529. [CrossRef]
43. Poczatek, C.; Kaufman, Z.; Lechene, C. *OpenMIMS ImageJ Plugin Guide*; Harvard Medical School: Boston, MA, USA, 2009.
44. Haynes, W.M. *CRC Handbook of Chemistry and Physics*; CRC Press: Boca Raton, FL, USA, 1988.
45. Mironov, A.G.; Karmanov, N.S.; Mironov, A.A.; Khodyreva, E.V. Gold-brannerite nuggets in placers of the Ozernoe ore cluster (Buryatia). *Russ. Geol. Geophys.* **2008**, *49*, 743–748. [CrossRef]
46. Cook, N.J.; Ciobanu, C.L.; Danyushevsky, L.V.; Gilbert, S. Minor elements in bornite and associated Cu-(Fe)-sulfides: A LA-ICPMS study. *Geochim. Cosmochim. Acta* **2011**, *73*, 4761–4791. [CrossRef]
47. Wasserstein, B. Precision lattice measurements of galena. *Am. Mineral.* **1951**, *36*, 102–115.
48. Evans, N.J.; Byrne, J.P.; Keegan, J.T.; Dotter, L.E. Determination of uranium and thorium in zircon, apatite, and fluorite: Application to laser (U-Th)/He thermochronology. *J. Anal. Chem.* **2005**, *60*, 1159–1165. [CrossRef]
49. Dill, H.G. The geology of aluminum phosphates and sulfates of the alunite group minerals: A review. *Earth-Sci. Rev.* **2001**, *53*, 35–93. [CrossRef]
50. Palache, C.; Berman, H.; Frondel, C.; Dana, E.S. *The System of Mineralogy of James Dwight Dana and Edward Salisbury Dana, Yale University, 1837–1892: Halides, Nitrates, Borates, Carbonates, Sulfates, Phosphates, Arsenates, Tungstates, Molybdates, etc*; John Wiley and Sons: Hoboken, NJ, USA, 1951.
51. Åmli, R. Mineralogy and-Rare Earth Geochemistry of Apatite and Xenotime from the Gloserheia Granite Pegmatite, Froland, Southern Norway. *Am. Mineral.* **1975**, *60*, 607–620.
52. Ciobanu, C.L.; Cook, N.J.; Kelson, C.R.; Guerin, R.; Kalleske, N.; Danyushevsky, L. Trace element heterogeneity in molybdenite fingerprints stages of mineralization. *Chem. Geol.* **2013**, *347*, 175–189. [CrossRef]
53. Owen, N.D.; Ciobanu, C.L.; Cook, N.J.; Slattery, A.; Basak, A. Nanoscale study of clausthalite-bearing symplectites in Cu-Au-(U) ores: Implications for ore genesis. *Minerals* **2018**, *8*, 67. [CrossRef]
54. Dmitrijeva, M.; Ehrig, K.J.; Ciobanu, C.L.; Cook, N.J.; Verdugo-Ihl, M.R.; Metcalfe, A.V. Defining IOCG signatures through compositional data analysis: A case study of lithogeochemical zoning from the Olympic Dam deposit, South Australia. *Ore Geol. Rev.* **2019**, *105*, 86–101. [CrossRef]
55. Doerner, H.A.; Hoskins, W.M. Co-precipitation of radium and barium sulphates. *J. Am. Chem. Soc.* **1925**, *47*, 662–715. [CrossRef]
56. Itzkovitch, I.J.; Ritcey, G.M. *Removal of Radionuclides from Process Streams—A Survey*; CANMET Report 79-21; Energy, Mines, and Resources Canada: Ottawa, ON, Canada, 1979; 171p.
57. Smith, A.L. Radioactive-scale formation. *J. Pet. Technol.* **1987**, *39*, 697–706. [CrossRef]
58. Putnis, A. Mineral replacement reactions. *Rev. Mineral. Geochem.* **2009**, *70*, 87–124. [CrossRef]
59. Cook, N.J.; Ciobanu, C.L.; George, L.; Ehrig, K. Trace element analysis of minerals in magmatic-hydrothermal ores by laser ablation inductively-coupled plasma mass spectrometry: Approaches and opportunities. *Minerals* **2016**, *6*, 111. [CrossRef]
60. Kontonikas-Charos, A.; Ciobanu, C.L.; Cook, N.J.; Ehrig, K.; Krneta, S.; Kamenetsky, V.S. Feldspar evolution in the Roxby Downs Granite, host to Fe-oxide Cu-Au-(U) mineralisation at Olympic Dam, South Australia. *Ore Geol. Rev.* **2017**, *80*, 838–859. [CrossRef]
61. Courtney-Davies, L.; Tapster, S.R.; Ciobanu, C.L.; Cook, N.J.; Verdugo-Ihl, M.R.; Ehrig, K.J.; Kennedy, A.K.; Gilbert, S.E.; Condon, D.J.; Wade, B.P. A multi-technique evaluation of hydrothermal hematite U-Pb isotope systematics: Implications for ore deposit geochronology. *Chem. Geol.* **2019**, *513*, 54–72. [CrossRef]
62. Miller, M.K. *Atom Probe Tomography: Analysis at the Atomic Level*; Springer Science & Business Media: New York, NY, USA, 2012; 239p.
63. Ayache, J.; Beaunier, L.; Boumendil, J.; Ehret, G.; Laub, D. *Sample Preparation Handbook for Transmission Electron Microscopy: Techniques*; Springer Science & Business Media: New York, NY, USA, 2010; Volume 2.
64. Ciobanu, C.L.; Kontonikas-Charos, A.; Slattery, A.; Cook, N.J.; Ehrig, K.; Wade, B.P. Short-range stacking disorder in mixed-layer compounds: A HAADF STEM study of bastnäsite-parisite intergrowths. *Minerals* **2017**, *7*, 227. [CrossRef]
65. Kontonikas-Charos, A.; Ciobanu, C.L.; Cook, N.J.; Ehrig, K.; Ismail, R.; Krneta, S.; Basak, A. Feldspar mineralogy and rare earth element (re)mobilization in iron-oxide copper gold systems from South Australia: A nanoscale study. *Mineral. Mag.* **2018**, *82*, S173–S197. [CrossRef]

66. Ciobanu, C.L.; Verdugo-Ihl, M.R.; Slattery, A.; Cook, N.J.; Ehrig, K.; Courtney-Davies, L.; Wade, B.P. Silician magnetite: Si-Fe-nanoprecipitates and other mineral inclusions in magnetite from the Olympic Dam deposit, South Australia. *Minerals* **2019**, *9*, 311. [CrossRef]
67. Slodzian, G.; Hillion, F.; Stadermann, F.J.; Horreard, F. Oxygen isotopic measurements on the CAMECA NanoSIMS 50. *Appl. Surf. Sci.* **2003**, *203*, 798–801. [CrossRef]
68. Wilson, R.G.; Novak, S.W. Systematics of secondary-ion-mass spectrometry relative sensitivity factors versus electron affinity and ionization potential for a variety of matrices determined from implanted standards of more than 70 elements. *J. Appl. Phys.* **1991**, *69*, 466–474. [CrossRef]

Chapter 5

Intermobility of barium, strontium, and lead in chloride and sulphate leach solutions

Mark Rollog [a,*], Nigel J. Cook [a], Paul Guagliardo [b], Kathy Ehrig [c], Sarah E. Gilbert [d], and Matt Kilburn [b]

[a] *School of Chemical Engineering, University of Adelaide, Adelaide, 5005 S.A., Australia*

[b] *Centre for Microscopy, Characterisation, and Analysis, University of Western Australia, 35 Stirling Highway, Crawley, 6009 W.A., Australia*

[c] *BHP Olympic Dam, 55 Grenfell St., Adelaide, 5000 S.A., Australia*

[d] *Adelaide Microscopy, The University of Adelaide, 5005 S.A., Australia*

(sarah.gilbert@adelaide.edu.au)

Article published in *Geochemical Transactions* 20(4), 1-23.

Statement of Authorship

Title of Paper	Intermobility of barium, strontium, and lead in chloride and sulfate leach solutions
Publication Status	☑ Published ☐ Accepted for Publication ☐ Submitted for Publication ☐ Unpublished and Unsubmitted work written in manuscript style
Publication Details	Submitted to *Geochemical Transactions* 4 March 2019. Available online 6 September 2019.

Principal Author

Name of Principal Author (Candidate)	Mark Rollog
Contribution to the Paper	Designed experimentation, performed sample analysis and data interpretation, wrote manuscript
Overall percentage (%)	75
Certification:	This paper reports on original research I conducted during the period of my Higher Degree by Research candidature and is not subject to any obligations or contractual agreements with a third party that would constrain its inclusion in this thesis. I am the primary author of this paper.
Signature	Date 23.08.19

Co-Author Contributions

By signing the Statement of Authorship, each author certifies that:

i. the candidate's stated contribution to the publication is accurate (as detailed above);
ii. permission is granted for the candidate in include the publication in the thesis; and
iii. the sum of all co-author contributions is equal to 100% less the candidate's stated contribution.

Name of Co-Author	Nigel J. Cook
Contribution to the Paper	Supervised direction and progress of work, helped evaluate and edit manuscript
Overall percentage (%)	5
Signature	Date 1/8/19

Name of Co-Author	Paul Guagliardo
Contribution to the Paper	Oversaw sample analyses and helped evaluate and edit the manuscript
Overall percentage (%)	5

24

Signature	Paul Guagliardo	Date	25 Jul 2019

Name of Co-Author	Kathy Ehrig
Contribution to the Paper	Provided samples and helped evaluate and edit the manuscript
Overall percentage (%)	-
Signature	Date: 31 July 2019

Name of Co-Author	Sarah E. Gilbert
Contribution to the Paper	Oversaw sample analyses and helped evaluate and edit the manuscript
Overall percentage (%)	5
Signature	Date: 5/8/19

Name of Co-Author	Matt Kilburn
Contribution to the Paper	Oversaw one of the facilities where samples were analysed
Overall percentage (%)	5
Signature	Date: 25 Jul 2019

25

26

Rollog et al. Geochem Trans (2019) 20:4
https://doi.org/10.1186/s12932-019-0064-0

Geochemical Transactions

RESEARCH ARTICLE Open Access

Intermobility of barium, strontium, and lead in chloride and sulfate leach solutions

Mark Rollog[1*], Nigel J. Cook[1], Paul Guagliardo[2], Kathy Ehrig[3], Sarah E. Gilbert[4] and Matt Kilburn[2]

Abstract

Production of radionuclide-free copper concentrates is dependent on understanding and controlling the deportment of daughter radionuclides (RNs) produced from ^{238}U decay, specifically ^{226}Ra, ^{210}Pb, and ^{210}Po. Sulfuric acid leaching is currently employed in the Olympic Dam processing plant (South Australia) to remove U and fluorine from copper concentrates prior to smelting but does not adequately remove the aforementioned RN. Due to chemical similarities between lead and alkaline earth metals (including Ra), two sets of experiments were designed to understand solution interactions between Sr, Ba, and Pb at various conditions. Nanoscale secondary ion mass spectrometry (NanoSIMS) isotopic spatial distribution maps and laser ablation inductively coupled-plasma mass spectrometry transects were performed on laboratory-grown crystals of baryte, celestite, and anglesite which had been exposed to different solutions under different pH and reaction time conditions. Analysis of experimental products reveals three uptake mechanisms: overgrowth of nearly pure $SrSO_4$ and $PbSO_4$ on baryte; incorporation of minor of Pb and Ba into celestite due to diffusion; and extensive replacement of Pb by Sr (and less extensive replacement of Pb by Ba) in anglesite via coupled dissolution-reprecipitation reactions. The presence of H_2SO_4 either enhanced or inhibited these reactions. Kinetic modelling supports the experimental results, showing potential for extrapolating the (Sr, Ba, Pb)SO_4 system to encompass $RaSO_4$. Direct observation of grain-scale element distributions by nanoSIMS aids understanding of the controlling conditions and mechanisms of replacement that may be critical steps for Pb and Ra removal from concentrates by allowing construction of a cationic replacement scenario targeting Pb or Ra, or ideally all insoluble sulfates. Experimental results provide a foundation for further investigation of RN uptake during minerals processing, especially during acid leaching. The new evidence enhances understanding of micro- to nanoscale chemical interactions and not only aids determination of where radionuclides reside during each processing stage but also guides development of flowsheets targeting their removal.

Keywords: Alkali earth sulfates, Sulfate leaching, NanoSIMS analysis, Cation intermobility, Radionuclides

Introduction

Uranium-bearing mineral deposits, such as the Olympic Dam iron oxide-copper-gold-uranium (IOCG-U) orebody, South Australia, contain not only appreciable amounts of uranium and thorium, but also all daughter isotopes produced by radioactive decay. Elimination or reduction of some daughter radionuclides (RNs) during processing represents a unique metallurgical challenge. As examples, ^{226}Ra, ^{210}Pb, and ^{210}Po are all found in Olympic Dam ore feed at sub-ppb concentrations. To achieve activities of < 1 Bq/g per radionuclide in the final copper concentrate, concentrations of roughly 27 parts-per-trillion (ppt), 370 parts-per-quadrillion (ppq), and 6 ppq, respectively, are required. Since these concentration values fall below the minimum detection limits of most conventional instrumentation for analysis of samples in situ, it is simpler to use proxies, where possible, to predict the behavior of these elements during processing.

Understanding hydrothermal mobility of cations in ore deposits is important for the study of ore genesis, but this information may be of limited usefulness on the processing floor. Hydrometallurgy involving high-temperature leach solutions containing acids, alkalis, complexing

*Correspondence: mark.rollog@adelaide.edu.au
[1] School of Chemical Engineering, The University of Adelaide, Adelaide, SA 5005, Australia
Full list of author information is available at the end of the article

27

agents, organic solvents, redox reagents, or more likely a combination of the above, can completely rearrange the chemical composition of ore material—preferentially to the operator's benefit. Sulfuric acid leaching is a key solution currently employed in the Olympic Dam plant to reduce U and RNs in copper concentrates prior to smelting (8 to 12-h leach time at ~ 60 °C and pH of ~ 1–1.5). A simplified Olympic Dam processing flowsheet is presented in Schmandt et al. [38]. Since the chlorides and nitrates of Ra, Po, and to some extent Pb, are all water- and acid-soluble, these are not of primary concern. Sulfates of these cations, however, are of great interest due to their insolubility and potential for radionuclide sequestration.

Before attempting to determine the deportment of Ra, Po or ^{210}Pb, it is vital to understand intermobility of Ba, Sr and Pb among their insoluble sulfates—the minerals baryte, celestite, and anglesite. A significant amount of work has been done in this field, primarily on individual compounds. Strontium sulfate solubility in water [16, 20, 32], in chloride solutions [5, 20, 32], and in sulfate solutions [20] has been determined, as has extraction and biosorption of Sr in the environment [14, 43]. Barium sulfate solubility in water [16, 31], chloride solutions [4, 5, 7, 31], and sulfate solutions [7] has likewise been covered, notably from researchers interested in boiler scale. Lead sulfate solubility greatly affects lead-acid battery performance and has therefore been extensively measured in water [18], and in chloride [21] and sulfate solutions [17, 18, 21]. Radium solubilities have also been determined [3, 44]. These are but a few of the studies addressing solubilities in the entire Sr-Ba-Pb-Ra-Cl-SO_4-H^+-H_2O system. Current consensus is that solubility of the alkali metal (and lead) sulfates in water at 60 °C is Mg > Ca > Sr > Pb > Ba > Ra. Generally, solubilities positively correlate with chloride activity (through complexation), although $SrSO_4$ solubility reaches a maximum between 2 and 3 N NaCl or HCl, decreasing at higher concentrations [20]. This would suggest a simple chloride leach may be a potential approach to removal of selected RNs, but the system is far more complex than it initially appears.

Process waters at Olympic Dam contain chloride (e.g., flotation water is 2.5 to 4 g/L Cl^-), as does the ore itself, but the sulfuric acid leach process (involving up to 150 g/L sulfate) overwhelmingly dictates solution activity and pH. From a RN standpoint, sulfuric acid would be the least favorable reactant due to the insolubility of $RaSO_4$, $PbSO_4$, and $PoSO_4$. Nonetheless, efficiency in removal of fluorine as well as dissolution of most uranium/thorium and rare earth species—coupled with low cost—makes sulfuric acid the logical, practical choice. To that end, optimizing the process already in place is preferential to redesigning the entire system. With additional information about nanoscale mineral-fluid reactions and the behavior of RN-sulfate nanoparticles, it may be possible to modify existing industrial processes to minimize their accumulation in economic products.

To elicit this information, two methods were employed. Laser ablation inductively coupled-plasma mass spectrometry (LA-ICP-MS) is a powerful, well-established tool for generating quantitative compositional data in solids, and is accordingly widely applied across the earth sciences and in mineral processing research [6]. It has, however, several drawbacks. Quadrupole mass spectrometry generally has a mass resolution of 1 atomic mass unit (amu), which prevents distinction between the mass of interest and isobaric mass interferences. Additionally, the finest spatial resolution available is limited by a minimum 3 μm-diameter spot (commonly resulting in a much larger pit, depending on the mineral). For quantitative trace element analysis, much larger spot sizes are required. The Cameca nanoscale secondary ion mass spectrometry (nanoSIMS) platform is an imaging technique which offers solutions to both the above problems. Each of seven detectors on the nanoSIMS has mass resolution approaching 0.1 amu, which is very useful in distinguishing, for example, ^{226}Ra (226.0254) from ^{88}Sr^{138}Ba (225.811). Additionally, the effective spot size for high concentration elements can be < 100 nm, although for trace elements may approach 700 nm. This still represents a significant improvement over LA-ICP-MS for the resolution of nanoscale features. NanoSIMS, however, is not currently quantifiable - at least not for mineral analyses. Although each is independently limited, the complementary use of both methods provides the quantification and spatial resolution necessary for the results required in this investigation.

Through the combined analyses provided by these two analytical platforms, we strive to better understand the deportment of Sr, Ba, Pb, and by extension, also Ra, throughout ore processing at Olympic Dam. Process methods are ever-changing; optimization is achieved via complex formulae based on mineral abundances, elemental compositions, operating costs, and time—weighed against the constantly moving targets of commodity prices. Even slight adjustments in certain mathematical expressions may result in significant benefit to the operators, so it is crucial to understand (to the extent possible and/or realistically implementable) the intimate mechanisms responsible for the behavior of selected elements—either beneficial or detrimental—during processing. Beyond minerals processing, these results provide valuable insight regarding mechanisms involved in natural processes such as ore formation, hydrothermal alteration, and weathering—and anthropogenic processes including

soil reclamation, boiler scale prevention, and nuclear waste storage.

Experimental methods

Raw material synthesis and characterization

Crystal growth

To control purity, synthetic mineral crystals were produced using a gel-growth method [13, 22]. A ~ 0.5 M sodium metasilicate stock solution was prepared by adding 100 g $Na_2SiO_3{\cdot}5H_2O$ to 1 L of reverse osmosis (RO) water (boiled and cooled to remove CO_2). One drop of bromophenol blue indicator was added to 20 mL of stock solution, with stirring, and 3 M HCl was added in small portions until the loss of blue color indicated a pH of < 4.5. $SrCl_2$, $BaCl_2$ or $Pb(acetate)_2$ solution (0.5 mL, 1 M) was added dropwise, with stirring. The solutions were quickly poured into glass test tubes, 2.5 cm in diameter and 15 cm long, lightly covered, and allowed to set for 1 week. A K_2SO_4 solution (10 mL, 1 M) was added slowly to the top of the semi-firm gels, taking care not to disrupt the surface. Crystals grew by diffusion within 1–2 weeks and were well-formed, ranging from < 100 µm to > 500 µm in length.

Characterization methods

Samples from each batch were analyzed using a FEI Quanta 450 field emission gun scanning electron microscope (FEG-SEM) equipped with an EDAX energy- dispersive X-ray (EDS) detector (Adelaide Microscopy, The University of Adelaide) to verify composition and quality.

Leaching/recrystallization tests

Reactions in simple solutions

To elicit information regarding the uptake of competing cations, crystals were exposed to solutions of single cations under various anionic activity and time conditions. Table 1 lists the contents and conditions of the 24 vials. Half of these were run with only MCl_2 solution (M = Sr, Ba, or Pb) while the other half also included 1.6 M H_2SO_4 to more closely represent the conditions found in a typical acid leach tank. As expected, white sulfate precipitated immediately in all reaction experiments containing sulfuric acid, resulting in reduced effective concentrations of all three cation solutions. The reduced concentrations should reasonably reproduce actual activities present during processing in a 1.6 M H_2SO_4 acid leach solution.

Vials were capped and heated to 60 °C (typical for Olympic Dam hydrometallurgical processes) for either 40 or 210 h. Without cooling, the surviving crystals were rinsed with 60 °C RO water three times, dried, individually selected and embedded in 2.5 cm-round epoxy resin mounts. The mounts were polished, carbon-coated, and imaged in backscatter electron (BSE) mode by SEM. The primary distinction between this experiment and the one below is that these crystals were isolated and only exposed to one additional cation at a time, in great excess.

Crystal analysis by LA-ICP-MS

Samples from the above set of experiments were analyzed by LA-ICP-MS using an ASI RESOlution-LR ArF excimer laser ablation system equipped with a large format S155 sample chamber (Laurin Technic Inc.) and coupled to an Agilent 7900 × ICP-MS. Transects were performed across each crystal, including at least an extra 10 µm on either side in the epoxy to establish a blank. Instrument conditions for the transects were set using a 6 µm spot size, fluence 3.5 J/cm^2, repetition rate 10 Hz. The NIST-610 reference standard was analyzed in replicate at the beginning, middle, and end of the run, with two sections of 24 transects in-between. Standards were run using a 74 µm spot size, fluence 3.5 J/cm^2, repetition rate 10 Hz. Isotopes analyzed were limited to ^{35}Cl, ^{88}Sr, ^{138}Ba, $^{204, 206,}$

Table 1 Experimental conditions for reactions in simple solutions

Experiment/vial	Crystals	a. 40 h	b. 40 h	c. 210 h	d. 210 h
5(a–d)	$BaSO_4$	0.07 M $PbCl_2$	0.07 M $PbCl_2$* 1.6 M H_2SO_4	0.07 M $PbCl_2$	0.07 M $PbCl_2$* 1.6 M H_2SO_4
6(a–d)	$BaSO_4$	0.1 M $SrCl_2$	0.1 M $SrCl_2$* 1.6 M H_2SO_4	0.1 M $SrCl_2$	0.1 M $SrCl_2$* 1.6 M H_2SO_4
7(a–d)	$SrSO_4$	0.1 M $BaCl_2$	0.1 M $BaCl_2$* 1.6 M H_2SO_4	0.1 M $BaCl_2$	0.1 M $BaCl_2$* 1.6 M H_2SO_4
8(a–d)	$SrSO_4$	0.07 M $PbCl_2$	0.07 M $PbCl_2$* 1.6 M H_2SO_4	0.07 M $PbCl_2$	0.07 M $PbCl_2$* 1.6 M H_2SO_4
9(a–d)	$PbSO_4$	0.1 M $SrCl_2$	0.1 M $SrCl_2$* 1.6 M H_2SO_4	0.1 M $SrCl_2$	0.1 M $SrCl_2$* 1.6 M H_2SO_4
10(a–d)	$PbSO_4$	0.1 M $BaCl_2$	0.1 M $BaCl_2$* 1.6 M H_2SO_4	0.1 M $BaCl_2$	0.1 M $BaCl_2$* 1.6 M H_2SO_4

*Estimated

29

^{207}, ^{208}Pb, and ^{226}Ra. Due to the simple, stoichiometric composition of the crystals, elemental concentration data (in ppm) was calculated using a modified version of the internal standard method [19] with an additional minor drift correction. To avoid irregularities at grain edges, concentration values were calculated in ppm normalized to 1,000,000 instead of $ppm_{(total\ count)}$. Isotopic concentrations were converted to elemental concentrations using global isotopic abundances [12]. The time-resolved transect data from the ICP-MS (in seconds) was converted to distance (μm) by direct comparison between transect traces and their corresponding BSE image, and are therefore estimates. Calculated concentration data was smoothed using a 3-period moving average to minimize electronic spikes.

Despite clean EDS spectra, LA-ICP-MS analyses revealed that the crystals were slightly contaminated with other cations. As a result, the baryte crystals contained approximately 10 ppm Pb and 140 ppm Sr; the celestite contained approximately 10 ppm each of Ba and Pb; and the anglesite contained around 165 ppm Ba and 115 ppm Sr. The $SrCl_2$, $BaCl_2$, and $PbCl_2$ solutions also contained ppm quantities of contaminants, but analysis of the data suggests that contamination of both crystals and solutions proved to be many orders of magnitude lower in concentration than the effects observed in crystalline reaction zones and therefore had only a minimal effect on the experiments.

Supersaturation and nucleation rate calculations

Using the equations from Söhnel [40], Sangwal [35], and Pina and Putnis [23], supersaturation and nucleation rates were calculated for the above experiments. Briefly, the equation for supersaturation $S(x)$ is:

$$S(x) = \sqrt{\frac{a\left(C^{2+}\right)^{1-x} a\left(B^{2+}\right)^{x} a\left(A^{2-}\right)}{\left(K_{CA} a_{CA}\right)^{1-x} \left(K_{BA} a_{BA}\right)^{x}}}$$

where B represents Sr, Ba, or Pb of the crystal matrix; C represents Sr, Ba, or Pb in the added chloride solution, $A = (SO_4^{2-})$; K_{CA} and K_{BA} represent the appropriate solubility product constants at 60 °C; and x and $(1 - x)$ represent the mole fractions of B and C, respectively. Solid solutions are assumed to be complete and ideal, simplifying the activity fractions a_{CA} and a_{BA} to 1. Concentrations, and subsequently activities, were estimated from the extrapolation/interpolation of data from various sources including Linke and Seidell [18], Krumgalz [16], initial experimental concentrations, and solubility products listed in Table 2. Experimental conditions prevented the possibility of measuring actual concentrations, mostly due to size constraints, so estimates were made based on solubilities of $BaSO_4$, $SrSO_4$, and $PbSO_4$ in neutral chloride, acid chloride, neutral sulfate, and acid sulfate conditions at 60 °C. Although this does introduce some error, variation of the activities resulted in only minor changes in the trend curves produced—and even then, only in magnitude. The shape of the trend curves as well as the maximum X_{BA} values remained consistent.

Table 2 Solubility data for selected sulfates

Compound	K_{sp} (60 °C)	V_{mol} (m^3)[d]	CIR[a] (Å)	Sol (kg^{-1} H_2O)
$BaSO_4$[b]	2.216×10^{-10}	8.67×10^{-29}	1.75	3.62 mg (60 °C)
$CaSO_4 2\,H_2O$[b]	2.137×10^{-5}	12.38×10^{-29}	1.26	2559 mg (60 °C)
$CaSO_4 0.5\,H_2O$[b]	4.971×10^{-5}	8.80×10^{-29}	1.26	421.2 mg (60 °C)
$CaSO_4$[b]	1.674×10^{-5}	7.64×10^{-29}	1.26	1670 mg (60 °C)
$SrSO_4$[b]	1.775×10^{-7}	7.68×10^{-29}	1.58	100 mg (60 °C)
$PbSO_4$[c]	2.53×10^{-8}	7.94×10^{-29}	1.63	63.4 mg (60 °C)
$RaSO_4$[c]	1.78×10^{-10}	9.24×10^{-29}	1.84	~4 mg (60 °C)

CIR crystal ionic radius of the cation (XII coordination) except Ca (VIII coordination)

Data sources: [a]Haynes [12]; [b]Krumgalz [16]; [c]Brown et al. [3]; [d]https://www.mindat.org, and references within; [e]Shannon [39]

The nucleation rate function $J(x)$ is calculated by:

$$J(x) = \Gamma(x) \exp\left[\frac{-B\sigma^3(x)\Omega^2(x)}{k^3 T^3 (\ln S(x))^2}\right]$$

where $\Gamma(x)$ is the preexponential factor, estimated from molecular volume (Table 2); $\Omega(x)$ is molecular volume (Table 2); $\sigma(x)$ is the interfacial free energy, estimated from K_{sp} values (Table 2); B represents a geometric factor dependent on nucleus shape; k is Boltzmann's constant (1.38×10^{-23} J/K); T is temperature in Kelvin; and $S(x)$ is the supersaturation factor from the equation above. A full description of these equations and their derivations can be found in Pina and Putnis [23] and references within. The reasoning behind these calculations is that thermodynamics alone do not always reproduce the observed results. Nucleation rates may significantly outweigh supersaturation ratios, and crystallization products may form contrary to solubility products [29].

Reactions in the presence of different sulfates

Two to five crystals of each compound (~200 μg) were placed together in 4.5 mL Exetainer glass screw-top vials. More or fewer crystals were added depending on size to roughly balance representation, but the samples were not weighed. Solutions (50 μL) were added to each vial. Table 3 lists the contents of the vials from experiments 1-4. Vials were capped and placed in a 60 °C oven for 30 h. After the allotted time, remaining crystals were rinsed while hot and sample preparation was completed in the same manner as above. Note that for this experiment all

Table 3 Experimental conditions for reaction experiments in the presence of different sulfates

Experiment/vial	Crystals	Solution	Approx. pH
1	Sr, Ba, Pb sulfates	0.1 M K_2SO_4	7
2	Sr, Ba, Pb sulfates	0.08 M H_2SO_4	1
3	Sr, Ba, Pb sulfates	0.1 M NaCl	7
4	Sr, Ba, Pb sulfates	0.12 M HCl	1

three cations are in direct competition in the same vials, and that the only source of Sr^{2+}, Ba^{2+}, and Pb^{2+} are from material dissolved from the crystals themselves.

Crystal analysis using NanoSIMS

Samples were analyzed on the Cameca NanoSIMs 50L at the Centre for Microscopy, Characterisation, and Analysis (CMCA), located at the University of Western Australia, Perth, using previously established settings [33]. To best explore surface addition, replacement, or diffusive activity, sites near the edges of grains were mapped. A Hyperion (H200) RF plasma oxygen ion source was used for all analyses. The instrument was operated in multicollection mode, with five of the seven available detectors tuned to ^{28}Si, ^{40}Ca, ^{88}Sr, ^{138}Ba, and ^{206}Pb. The additional two detectors were tuned to rare-earth element isotopes used in a separate experiment (and will thus not be referenced here). Maps of ^{28}Si and ^{40}Ca were included as quality control and to confirm that the silicon and calcium contribution to crystal growth was minimal. Similar instrument settings were used for all mapping (50×50 µm raster area, 50 pA ion current, D1 = 2, ES = 2, AS = 0, 512×512 px, 3 planes, 5 ms/px, effective beam diameter ≈ 400 nm).

Images were processed using ImageJ [36, 37] and the OpenMIMS plugin [25]. The color convention of Sr (in red), Ba (green), and Pb (blue) has been adopted for all images.

Results and discussion

Crystal characteristics

All three sulfates crystallize in the orthorhombic crystal system, dipyrimidal ($2/m\ 2/m\ 2/m$) crystal class. $SrSO_4$ formed slightly rounded orthorhombic prisms with dipyrimidal (chisel) terminations. Many crystals exhibited additional symmetric lateral growths (ears) near the prism/dipyramid interface. $BaSO_4$ formed as double orthorhombic blades, centrally attached in bow-tie fashion. $PbSO_4$ grew in well-formed euhedral prisms with varying dipyrimidal terminations. Figure 1 shows examples of the crystals produced from gel growth. Spectra of all three compounds were clean and sharp, with minimal traces of silicon found in the center of some of the grains but very little near the edges. This is not uncommon in crystals grown in a silica gel matrix, but nanoSIMS imaging revealed that this was not a factor in the experiment.

Although these synthetic crystals do not adhere to the strict definition of a mineral [8], the terms celestite, baryte, and anglesite are used interchangeably with $SrSO_4$, $BaSO_4$, and $PbSO_4$, respectively, in the following sections. These crystals are designed to be simple but accurate proxies for the natural minerals in question, and evidence suggests that behaviors of the natural and artificial—with respect to these experiments—are aligned and would therefore apply equally to both.

Leaching/recrystallization in simplified media

Figure 2 shows transects from barytes exposed to $PbCl_2$ solution (experiments 5a–d), The BSE image of experiment 5d shows the typical bowtie morphology of the baryte crystals. The crystal in experiment 5b has tipped over and the bottom surface has been broken off. Thin,

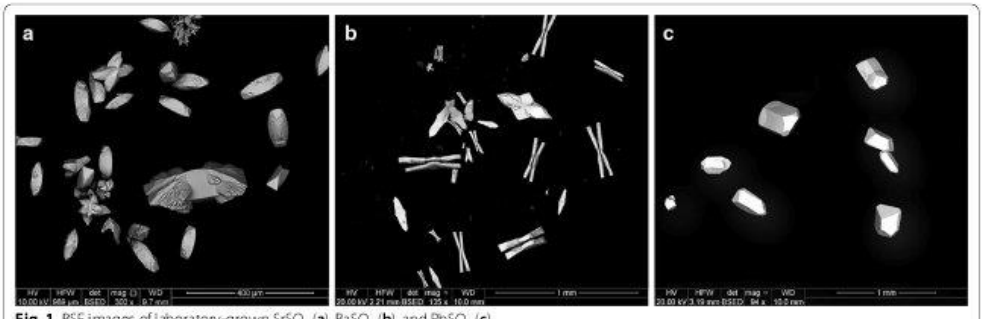

Fig. 1 BSE images of laboratory-grown $SrSO_4$ (**a**), $BaSO_4$ (**b**), and $PbSO_4$ (**c**)

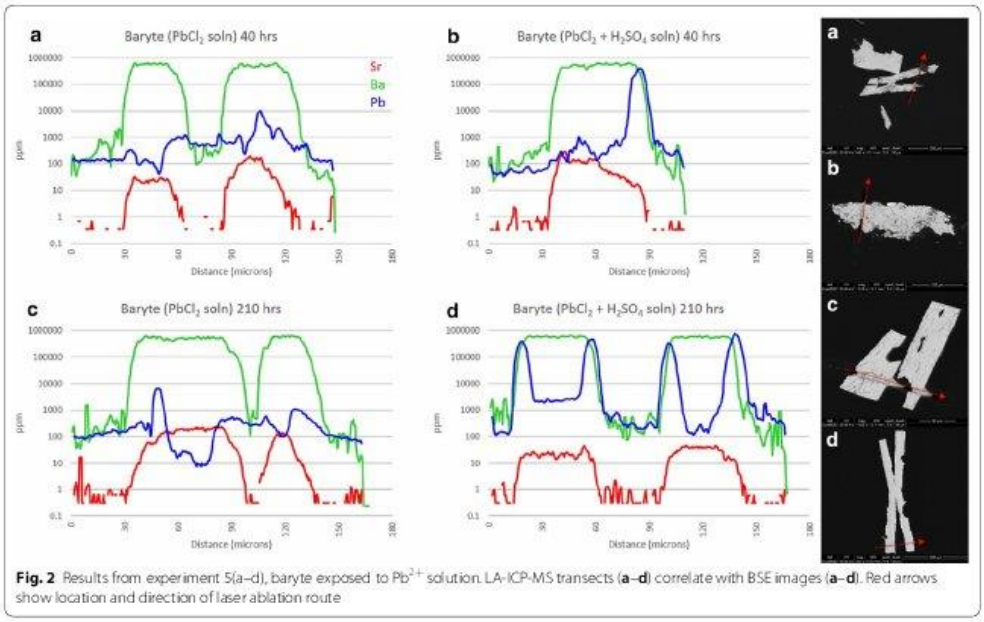

Fig. 2 Results from experiment 5(a–d), baryte exposed to Pb^{2+} solution. LA-ICP-MS transects (**a**–**d**) correlate with BSE images (**a**–**d**). Red arrows show location and direction of laser ablation route

bright overgrowths of Pb-rich sulfate can be clearly seen in experiment 5b and d, with no visible surface effects in experiment 5a and c. The Sr background in the crystals is evident (everywhere < 200 ppm), with lower concentration areas the result of partial leaching.

Although reaction time seems to have had little effect on the experiment, the presence of sulfate has had a profound effect. Overgrowth of $PbSO_4$ in experiment 5b and 5d occurs almost universally, though non-uniformly, up to 6 µm-thick in some areas. In transects, overgrowth is represented where the minor trace (Pb—blue) crosses over the major trace (Ba—green). All four surfaces of 5d show overgrowth in both BSE and LA-ICP-MS. Only one surface of experiment 5b shows the same, as the bottom surface was clearly broken during mounting. The roughly parabolic Pb traces appear wider than the overgrowth layers visible in the BSE image due to the relatively large beam width, with the increased Pb intensity beginning with the leading edge of the beam and ending with the trailing edge. The resulting width displayed by ICP-MS is the overgrowth layer plus the beam width plus any diffusive zone of the crystal face. Since the edge zones appear to be roughly symmetric (surface vs. interior), it is likely that diffusion of Pb into the $BaSO_4$ structure was minimal. Crystals from experiment 5a and c show no evidence of Pb in BSE images, with relatively clean, sharp crystal surfaces. Transects of the same crystals indicate little to no uptake of Pb either as overgrowth on, or diffusion into, the crystal surfaces. The few enriched regions which are present may represent either limited uptake or surface contamination due to polishing, but the Pb concentrations there are nearly two orders of magnitude lower than those in the sulfate-available experiments.

Barytes exposed to $SrCl_2$ solution (experiments 6a, c, and d) are shown in Fig. 3. Unfortunately, the crystal from experiment 6b was lost. The Pb background in all crystals was consistently low, around 10 ppm, and had little impact on the experiment. The second laser transect visible in 6a was a test of instrument conditions. Although 6b is missing, it appears that the overall result of experiment 6(a-d) is similar to experiment 5(a–d), with reaction time having little effect but sulfate activity having a pronounced effect on the uptake of Sr. A dark overgrowth layer in 6d is clearly visible in the BSE image (to 15 µm-thick), although the ICP-MS data confirms that this layer is not pure $SrSO_4$ but is predominantly $BaSO_4$ with up to 20% Sr on a metals basis (m.b.). Consistent sloping of both Ba and Sr traces on the right side of both leaves indicates that the entire crystal is mounted in the epoxy at an angle, sloping upwards towards the "northwest" into the frame. No visible or measured Sr-rich edge

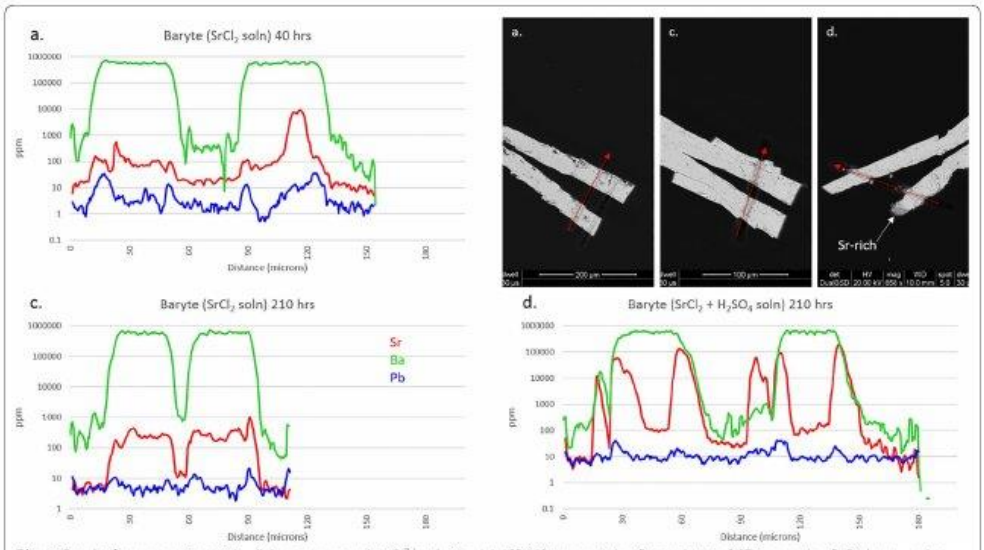

Fig. 3 Results from experiment 6(a–d), baryte exposed to Sr^{2+} solution. LA-ICP-MS transects (**a**–**d**) correlate to BSE images (**a**–**d**). Red arrows show location and direction of laser ablation route. The baryte from vial 6b was lost

zones are evident in either 6a or 6c, although one spot on the interior of 6a approaches 2% Sr.

Figure 4 shows the results of experiment 7a–d (celestite exposed to $BaCl_2$ solution). Pb in the crystal interiors generally ranges from 10 to 50 ppm, although it is suggested from edge zone concentrations (to 400 ppm Pb) that the $BaCl_2$ solution probably contained some Pb. Uptake of Pb into grain edges mimics uptake of Ba but remains 1–3 orders of magnitude lower in concentration. All celestite crystals show visible porosity, the result of growth in a silica gel matrix. Slight enrichments in both Ba and Pb in grain centers are likely a result of this. Unlike the baryte experiments, it appears that reaction time does have some effect on the uptake of Ba by celestite, although this may only apply to low-sulfate activity conditions. Incorporation of Ba remains low at 40 h (< 1%, m.b.) but increases to > 70% in thin edge zones at 210 h. This may actually approach 100%, but ICP-MS resolution is limited by spot size. Crystals 7a and 7c maintain sharp features, and a bright Ba-rich replacement zone can be seen on BSE images for 7c although this rarely exceeds 1 µm in thickness. This is confirmed by ICP-MS as the Ba trace overlaps the Sr trace on both grain edges, with the right edge appearing more pronounced. This is likely from crystal mounting angle, suggested by the trailing edge of the laser transect on the right side of the crystal. Crystals 7b and 7d show signs of surface dissolution, amplified at terminations. Unlike the acid sulfate experiment from Phase 1, no overgrowth layers are visible. Independent of time, Ba uptake in high-sulfate activity conditions appears to stabilize around 2–2.5% (m.b.). Ba concentration appears to positively correlate with porosity in 7(b, d) but not 7(a, c), suggesting that freshly precipitated $BaSO_4$ may be trapped in crystal pores.

Transects of celestite exposed to $PbCl_2$ solution (experiments 8a–d) are presented in Fig. 5. The impact of extraneous Ba is minimal, with slightly higher concentrations in crystal centers which is likely the result of porosity. All crystal faces are primarily sharp with little evidence of surface dissolution, although 8b has both clean and rough surfaces. Pb-rich sites are evident in all four BSE images, primarily as nucleated spots as opposed to uniform layers (although both exist). These spots may be freshly precipitated $PbSO_4$ adhering to crystal surfaces or Pb-rich sulfates which grew during the experiment—it is very difficult to distinguish. Pb concentrations appear to be higher in longer experiments, with an increase from 3.5% Pb at 40 h to > 90% Pb at 210 h. Realistically, however, this may be the result of the laser transect crossing—or not crossing—a precipitated $PbSO_4$ surface particle, so any broad statements about the effect of reaction time would be unsupported. In comparison, porosity clearly has a pronounced influence on Pb uptake, as seen from 8c. The left half of the crystal is enriched in Pb, which correlates

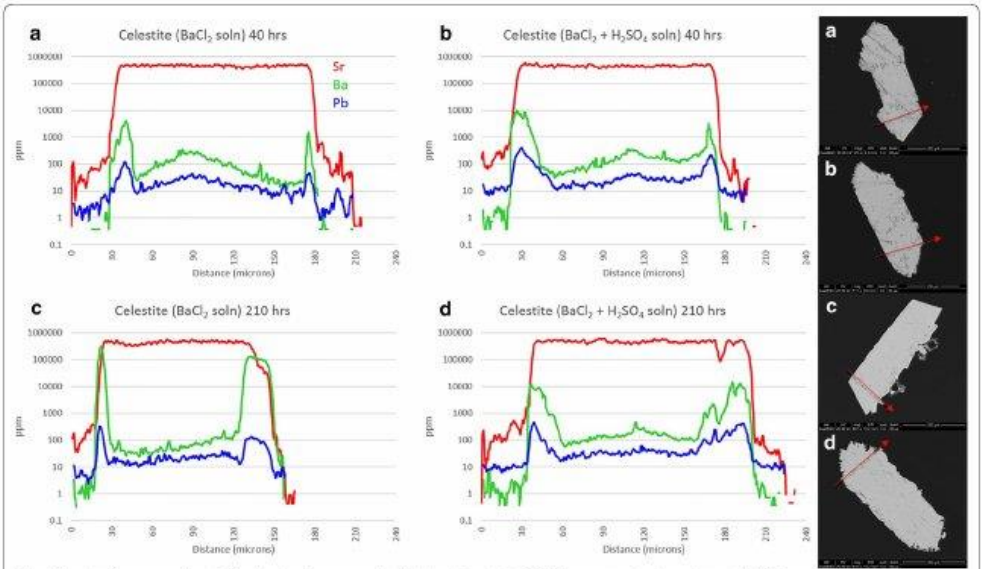

Fig. 4 Results from experiment 7(a–d), celestite exposed to Ba^{2+} solution. LA-ICP-MS transects (**a**–**d**) correlate with BSE images (**a**–**d**). Red arrows show location and direction of laser ablation route

perfectly with the high porosity region as seen in the BSE image. This is likely the result of enhanced incorporation of Pb due to increased surface area (and not the result of ineffective rinsing of residual $PbCl_2$ solution from pores) as the ^{35}Cl concentration remains minimal across both regions. With the exception of Pb-rich spots, it appears that maximum uptake of Pb remains around 2% regardless of reaction time or sulfate activity.

Anglesite reactions with $SrCl_2$ solution (experiments 9a-d) are presented in Fig. 6. The crystals remained euhedral, although some porosity is evident in 9a and 9b. This is likely due to growth rate, as the crystals which grew quickly (3–4 days) tended to have higher porosity than those which took 2 weeks or longer to form in the silica gel. Consistent concentrations of Sr in the center of all 4 grains is clear evidence that the extent of porosity had no effect on uptake here, in contradiction to the celestite experiments. Dark, Sr -rich rims are visible to some extent on all four crystals: on 9a and 9c as a thin, irregular layer (< 1 μm) on all surfaces; on 9b as thick (10 μm) replacement zones on the lower left and upper right surfaces $\{\mathbf{101}, \bar{\mathbf{1}}\mathbf{0}\bar{\mathbf{1}}\}$ with an overlying 2 μm layer of very high-Sr sulfate covering every surface except {**101**}; and on 9d as very patchy Sr-rich replacement zones to 25 μm thick in some areas, but completely absent in others. As for the preferential reaction zones of sample 9b, anisotropic growth based on crystallographic orientation has been noted in baryte [24], and likely extends to the entire class of similar sulfates.

Neutral uptake of Sr into anglesite (9a, 9c) is sharp and thin, with the outer 1 μm layer surpassing Sr:Pb of 1.2. The Sr-rich zones of 9b also reach 1.2, but the ubiquitous thin overgrowth layer approaches 2.8. On 9d, however, the diffuse Sr-rich regions only contain about 30% Sr (m.b.). Interestingly, Sr concentrations in grain edges seem to stabilize around 100,000 ppm independent of sulfate activity, reaction time, or reaction zone width.

Figure 7 shows anglesite reactions in Ba solutions (experiments 10a-d). Background Sr concentrations remain a consistent 100 ppm and do not affect the results. Crystals from experiments 10a and 10c are still euhedral and sharp, with no uptake or overgrowth of Ba visible in BSE images. Acid-leached crystals, however, show signs of significant surface reactions with rounded edges and dissolution/recrystallization textures extending up to 40 μm deep. LA-ICP-MS transects show Ba uptake in these reaction zones, but only to about 3 wt%. Time seems to have played a minor role, with Ba concentrations only slightly increased in 210-h experiments.

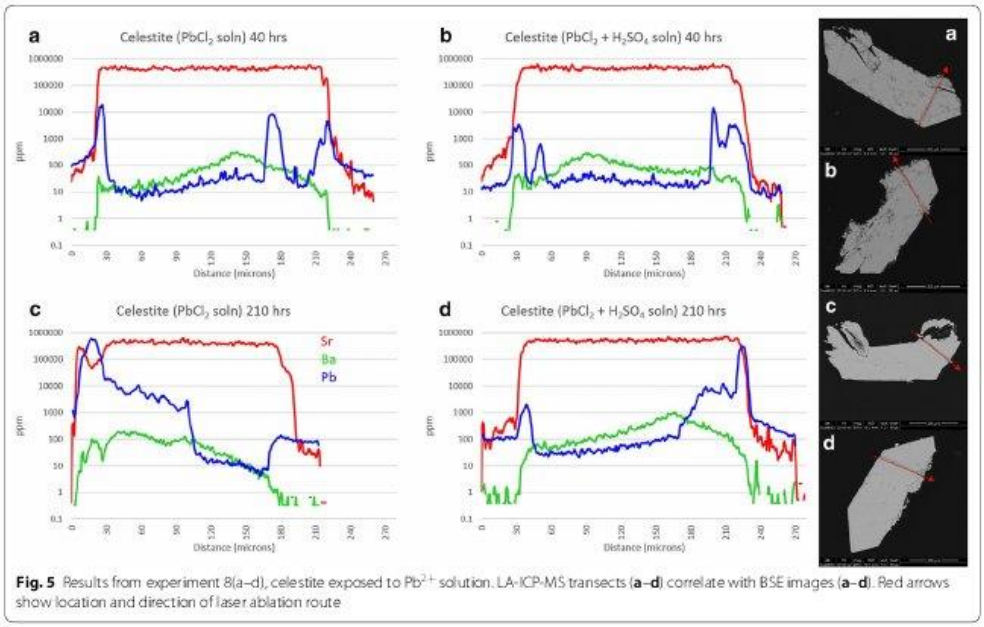

Fig. 5 Results from experiment 8(a–d), celestite exposed to Pb^{2+} solution. LA-ICP-MS transects (**a**–**d**) correlate with BSE images (**a**–**d**). Red arrows show location and direction of laser ablation route

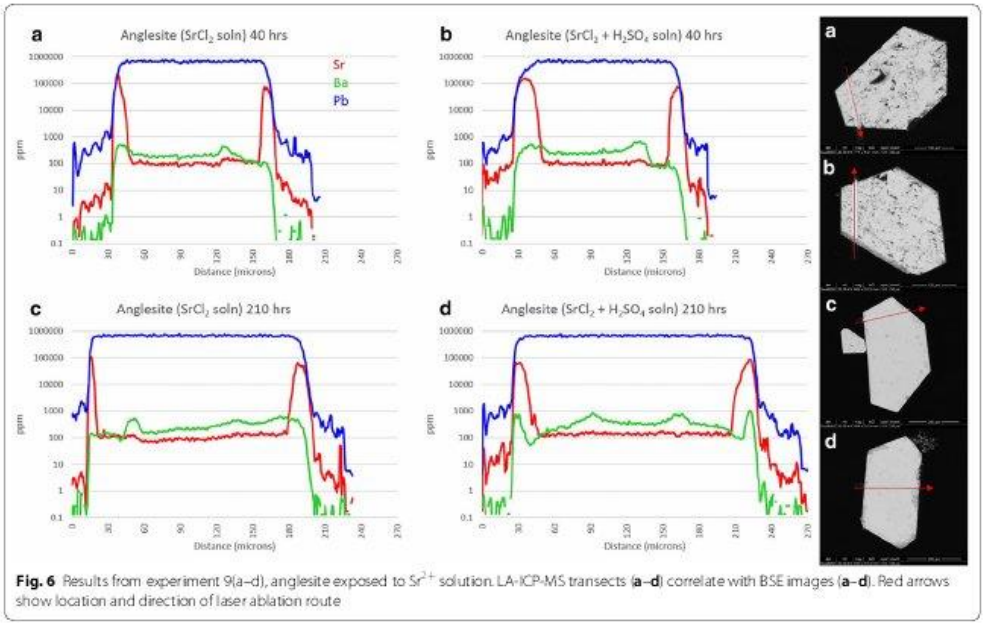

Fig. 6 Results from experiment 9(a–d), anglesite exposed to Sr^{2+} solution. LA-ICP-MS transects (**a**–**d**) correlate with BSE images (**a**–**d**). Red arrows show location and direction of laser ablation route

35

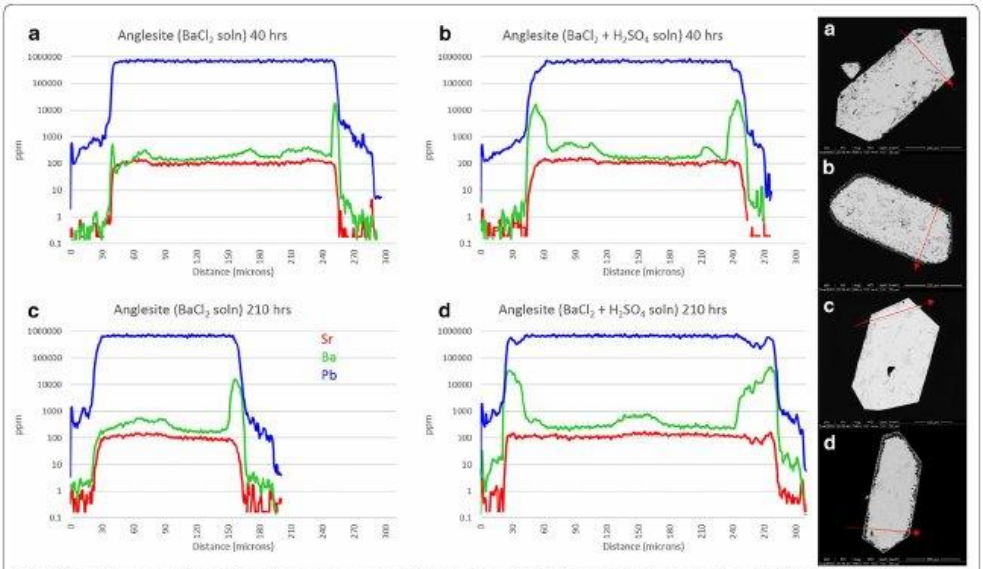

Fig. 7 Results from experiment 10(a–d), anglesite exposed to Ba^{2+} solution. LA-ICP-MS transects (**a**–**d**) correlate with BSE images (**a**–**d**). Red arrows show location and direction of laser ablation route

Interpretation and discussion

For baryte in experiment 5a–d, the $S(x)$ and $J(x)$ calculations are in agreement with experimental observations. With access to only $PbCl_2$, supersaturation remains low and nucleation rate is so low as to be effectively zero. Accordingly, virtually no Pb is diffused into, or crystallized on the surface of, baryte (Fig. 2a, c). In $PbCl_2 + H_2SO_4$, however, the supersaturation function is significantly higher with a maximum of 100 at $X_{BaSO4} = 0.66$. Although this may imply that $BaSO_4$ crystallization would be slightly favored, the nucleation rate maximum of $\sim 1.2 \times 10^{14}$ nuclei/cm^{3}s is actually found at $X_{PbSO4} = 0.9$ indicating that $PbSO_4$ nucleation is heavily favored. Figure 2b, d shows precisely this with thick, nearly pure $PbSO_4$ layers grown (albeit unevenly) on baryte surfaces.

Barytes from experiment 6a-d also correlate to the models, with similarly low $S(x)$ and $J(x)$ values for sulfate-free environments and significantly higher $S(x)$ and $J(x)$ values in sulfuric acid solutions. Correspondingly, thick zones of Sr-rich sulfate can be seen on baryte surfaces in Fig. 3d.

Celestite models behaved somewhat differently from baryte, although similarities can be seen between the high-sulfate (Ba, Sr)SO_4 trends and (Sr, Ba)SO_4 trends. With exposure to $BaCl_2$, higher supersaturation functions occur for both solutions, both heavily favoring $BaSO_4$. Nucleation rates are split, with sulfate-free solutions favoring $BaSO_4$ precipitation and sulfuric acid solutions preferring $SrSO_4$ precipitation. Experimentally, Ba remains low in celestite with < 1% (m.b.) being common although thin $BaSO_4$-rich overgrowth zones are seen in Fig. 4c. Nucleation rates would suggest that in sulfate-rich environments $SrSO_4$ is more likely to precipitate than $BaSO_4$, although some Ba uptake is inevitable providing there is some Ba^{2+} available. Opposite inclinations exist in sulfate-poor environments. The former is counter-intuitive considering the higher solubility of celestite, but is confirmed experimentally by the presence of an irregular $BaSO_4$ layer on the celestite surface in Fig. 4c—and the complete lack of the same in Fig. 4b, d, with the minimal Ba signal in the latter being due to diffusion, rather than an overgrowth of $BaSO_4$.

Lead and Sr sulfate have similar solubility products; therefore, it is expected that nucleation rates will be similar. Celestite exposed to $PbCl_2$ solution exhibits favorability towards $PbSO_4$ in both the $S(x)$ and $J(x)$ functions, but the addition of H_2SO_4 not only greatly increases the nucleation rate but also shifts the $J(x)$ maximum from pure $PbSO_4$ to a more predictable $X_{PbSO4} = X_{SrSO4}$. Figure 5c clearly shows a few microns of $PbSO_4$ overgrowth on the celestite surface, although the same cannot be

seen in Fig. 5a. Pb uptake by celestite in sulfate solutions seems to remain low, although there are a few $PbSO_4$ particles on the crystal surface in Fig. 5d. These are likely to be precipitates from the initial solution mixing which became lodged in the porous surface of the celestite, as no layering or adhesion to the surface is apparent.

Not surprisingly, $S(x)$ and $J(x)$ trends for the (Pb,Sr)SO_4 system is similar to the (Sr,Pb)SO_4 system. With less Pb^{2+} available, the $S(x)$ and $J(x)$ values for the Pb endmembers have been reduced to nearly zero in the sulfate-free solution. $S(x)_{max}$ and $J(x)_{max}$ in sulfuric acid solution remain the same, at $X_{PbSO4} \approx 0.8$ and 0.5, respectively, although the nucleation rate is somewhat reduced. From the LA-ICP-MS data, it can be seen that Sr^{2+} uptake by anglesite occurs in both systems, but different mechanisms may be responsible depending on SO_4^{2-} availability. [Sr] seems stable at ~ 10 wt% in all four crystals in Fig. 6a–d, but the sulfate-free samples show little to no surface alteration in the BSE images, whereas the sulfuric acid samples are clearly altered in zones up to 30 µm thick. The simplest explanation is that—despite very low nucleation rates—very thin zones of high-Sr sulfate is forming on anglesite in sulfate-free solutions (overgrowth), whereas thick, porous zones of mixed Pb,Sr sulfates are replacing anglesite in sulfate-rich solutions (CDR).

Keeping with the trend, $S(x)$ and $J(x)$ curves for (Ba,Pb)SO_4 are similar to those for (Pb,Ba)SO_4. Although supersaturation seems to favor $BaSO_4$ precipitation, nucleation rates suggest nearly pure $PbSO_4$ will occur instead. This effect presents as thick layers of $PbSO_4$ on baryte but exhibits as a lack of any precipitation (or a reprecipitation of Ba-doped $PbSO_4$) on anglesite. Little to no Ba is present in the crystals shown in Fig. 7a, c, achieving only 1 wt% in very thin zones not visible in BSE images. With H_2SO_4, there is clearly a CDR reaction occurring, but the precipitation rate seems to be lagging significantly behind the dissolution rate. Porosity is very high, with most of the sparse replacement sulfate being Pb-dominant.

These are obviously simplified models and although nucleation rate predictions seem to parallel experimental results there are other factors to consider. Chloride complexation amplifies Sr-, Ba-, and $PbSO_4$ solubilities by many orders of magnitude, and are only passively included in the kinetics calculations in the form of sulfate solubility estimates in Cl^- solutions. It is also well known that both thermodynamic and kinetic properties tend to diverge between bulk systems and nanoscale structures such as fractures [41, 42], pores [28], and ultrathin fluid–solid reaction interfaces [1].

Leaching/recrystallization in experiments involving multiple sulfates

Experimental results

Most of the crystals from experiment 1 (neutral sulfate solution) were still clear and euhedral after the experiment. One $PbSO_4$ crystal suffered damage during removal from the vial which resulted in a detrital coating on the undamaged $PbSO_4$ crystal, visible in the BSE image. Figure 8 shows BSE images of the crystals (top) as well as color composites of the ^{88}Sr, ^{138}Ba, and ^{206}Pb nanoSIMS distribution maps overlying zoomed-in sections of the BSE images (bottom). Red squares indicate the area of mapping. The crystals appear to be internally clean, although small amounts of Pb are seen filling near-edge gaps in both the $SrSO_4$ and $BaSO_4$ crystals. Small patches of Ba can be seen within a few microns of the edge of the $SrSO_4$, and a trace amount of Sr can be seen on the inside edge of the left crystal of $BaSO_4$ (appears as orange). Virtually no Sr or Ba was detected in or on the surface of the $PbSO_4$.

Figure 9 shows the resulting crystals from experiment 2 (acidic sulfate solution). These crystals were also in very good condition visually, although the normally transparent $PbSO_4$ had become translucent. The $BaSO_4$ crystal shattered during polishing. BSE images show a thin veneer of overgrowth on all three crystals, consisting of the other two sulfates. NanoSIMS images confirm this, and clearly show a thin (< 2 µm) layer of recrystallization. A comparison of signal intensities of the rim on $SrSO_4$ produces an estimated Sr:Ba:Pb ratio of 15:1:10; for the $BaSO_4$ rim the ratio is 4:6:9; for the $PbSO_4$ rim the ratio is 8:11:2.

The $BaSO_4$ and $PbSO_4$ crystals from experiment 3 (neutral chloride solution) were noticeably corroded and opaque, and thin layers of overgrowth could be seen flaking off even under low magnification. $SrSO_4$ appears to have survived quite well, although surface pitting was visible under magnification. BSE images (Fig. 10) show some etching of $BaSO_4$ and significant dissolution of $PbSO_4$. NanoSIMS mapping revealed very little recrystallization on the $SrSO_4$ and $PbSO_4$ but showed what appeared to be Sr diffusion up to ~ 6 µm into the $BaSO_4$ crystal with a thin, pure $PbSO_4$ layer on the surface.

The surviving crystals from experiment 4 (acid chloride solution) were significantly corroded and opaque. No $BaSO_4$ crystals were found, having presumably complexed with excess chloride and dissolved. NanoSIMS maps show little to no deposition on the surface of the corroded $SrSO_4$, but the $PbSO_4$ shows significant dissolution and replacement by both $BaSO_4$ and $SrSO_4$. Despite extensive Pb removal, the crystal clearly retained its original shape and the $PbSO_4$ core remains intact. Figure 11 illustrates the extent of replacement, as the original

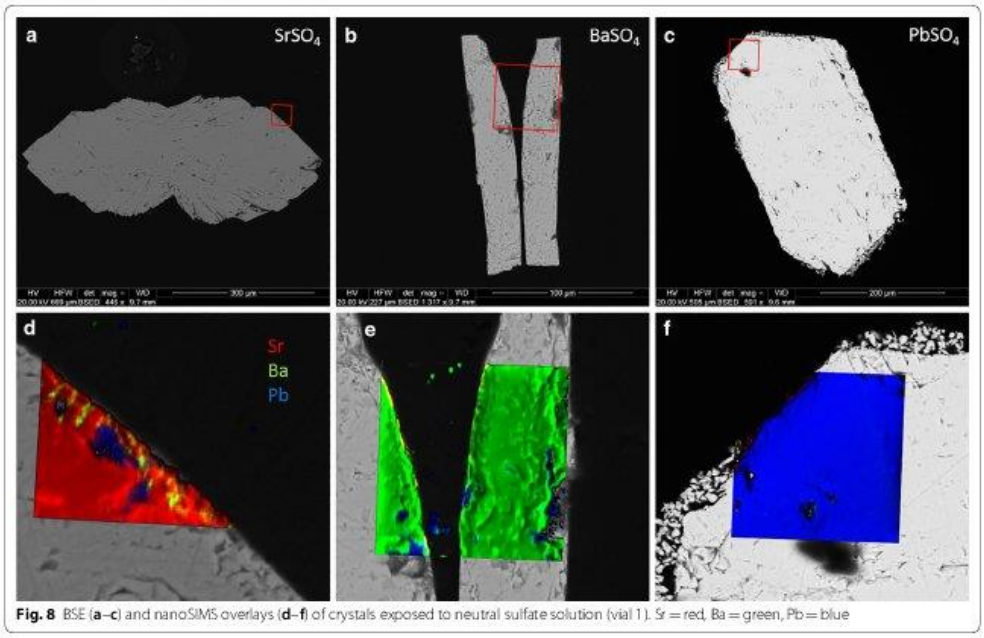

Fig. 8 BSE (**a**–**c**) and nanoSIMS overlays (**d**–**f**) of crystals exposed to neutral sulfate solution (vial 1). Sr = red, Ba = green, Pb = blue

$PbSO_4$ (blue) is virtually gone with Sr (red) nearly completely replacing Pb, and imported Ba (green, but displays as yellow-orange where overlapping red color) highlighting the edges of exposed surfaces.

Figure 12 contains a montage of 18 nanoSIMS images of the same grain, B4. The extent of Sr replacement is evident, as is the remaining untouched core of pure $PbSO_4$. A remnant strip of $PbSO_4$ can also be seen near the left edge of the grain (circled). The inset image shows detail of the boundary between the original $PbSO_4$ and invasive Sr. Despite appearances, regions of Sr replacement still contain lead, and semi-quantification shows this material to be close to 3:1 in Sr:Pb. The 3:1 ratio holds for replacement regions near the edge as well as in the interior of the crystal. Similar analyses of blue regions reveal nearly pure $PbSO_4$, with Pb:Sr being > 100. Figure 13 shows a small area of grain B4, with BSE (a), color-composite map (b), and log-scale distribution map of Pb:Sr (c). Although the color composite seems to indicate great variation in composition, the Pb:Sr map shows that there are primarily three distinct classifications: high-Pb (red to white); high-Sr, low-Pb (blue); and epoxy (black). Boundaries between the relatively pure $PbSO_4$ regions and the Sr:Pb ≈ 3 regions are quite sharp, and the thin green perimeters are likely to be a result of a relatively large beam width (~ 400 nm) compared to pixel size (~ 100 nm) and not true gradients. Barium contribution is minimal, with the brightest area on the image representing only about 25% Ba content (total cations).

Figure 14 contains Sr:Ba:Pb ratios (in wt%, normalized to 100%) for 225 point analyses of nanoSIMS data from throughout the composite image in Fig. 12. Three classifications appear here, as well, with most of the points clustering around a rough composition of $Sr_3Pb(SO_4)_4$. A second cluster represents samples of nearly pure lead sulfate, with some samples trailing into the "Sr-bearing" zone. Again, this is quite possibly due to beam-width overlap as the true boundaries appear to be distinct and sharp. The third classification of points represents areas containing > 5% Ba, found almost exclusively near exposed surfaces. These regions likely crystallized last and contain mostly $SrSO_4$ but may contain up to 55% $(Pb+Ba)SO_4$.

Interpretation and discussion

The results shown in Fig. 8 (experiments containing neutral sulfate solution), are no surprise. Of the entire periodic table, only Ba, Ca, Pb, Ra, and Sr form insoluble sulfates in their most common oxidation state, with

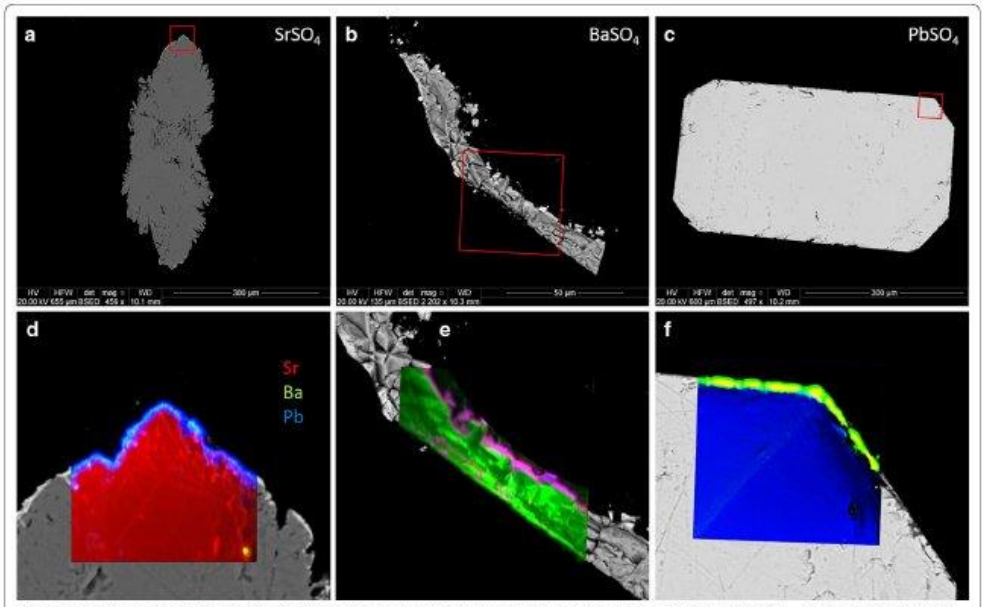

Fig. 9 BSE (**a**–**c**) and nanoSIMS overlays (**d**–**f**) of crystals exposed to acid sulfate solution (vial 2). Sr = red, Ba = green, Pb = blue. The thin magenta edge in (**e**) indicates Sr–Pb overlap

minor species including Hg^{+}, Ag^{+}, and Po^{4+} [11]. The lack of available H^{+} and of any complexing agent results in low activity and therefore virtually no mobility, with the compounds' solubility in water being the effective limiting factors. For a 200 µg sample, the most soluble of these, $SrSO_4$, should only lose a maximum of 3% to dissolution at 60 °C.

In Fig. 9, crystals from experiment 2 (0.08 M acid sulfate solution) show increased surface activity, with movement between all three compounds. A thin veneer of overgrowth < 2 µm thick can be seen in the BSE images, especially around the $SrSO_4$. Slight pitting and etching can also be seen, although this does not penetrate the crystal surfaces more than a micron or two. NanoSIMS images confirm that a thin layer of $(Sr,Ba,Pb)SO_4$ has deposited on the surface of all three crystals, although the Sr:Ba:Pb ratio differs between the three. From these ratios, it appears that Sr mostly either precipitates back on the $SrSO_4$ as a mixed Sr-Pb sulfate, with little Ba, or it precipitates on the $PbSO_4$ as a Sr-Ba mixed sulfate, with very little Pb. Lead mobility seems to be one-directional, with liberated Pb^{2+} preferring to recrystallize on the other two sulfates but not back on the $PbSO_4$.

LA-ICP-MS results seem to differ here from the nanoSIMS maps, with thin overgrowths evident in experiments 1-4 but only on both barytes and one anglesite in the simple reaction experiments. Although both sets of experiments were under acid sulfate conditions, those in the simple reaction experiments also contained significant chloride from the added 0.1 M MCl_2 solutions. In effect, experiment 2 contained only H_2SO_4 whereas the "b" and "d" sub-set of experiments 5 through 10 contained $[H^{+}]+[SO_4^{2-}]+[Cl^{-}]$. Chloride is well known as a strong complexing agent with Sr, Ba, and Pb which appears to have subdued the formation of overgrowth layers in some cases, especially on celestite.

Results for crystals of $BaSO_4$ and $PbSO_4$ in Fig. 10 from experiment 3 (0.1 M neutral chloride solution) were similarly unsurprising, as it is well known that alkali earths and lead form soluble chloride complexes. Visible etching of the $SrSO_4$ was surprisingly low, however Lucchesi and Whitney [20] show that for < 1 M NaCl, solubility of $SrSO_4$ decreases with temperature, with values of 185 mg/L at 0 °C and 170 mg/L at 25 °C. An estimate of 150 mg/L for 60 °C would result in < 4% solubility for a 200 µg sample. The $BaSO_4$ shows noticeable etching and pitting on the surface. The small amount of Sr^{2+} liberated

39

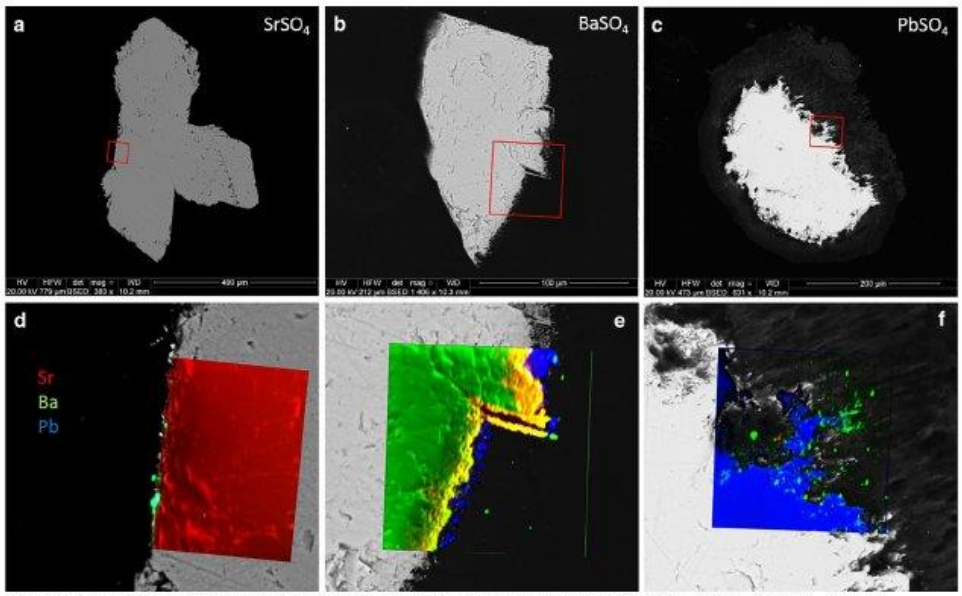

Fig. 10 BSE (**a**–**c**) and nanoSIMS overlays (**d**–**f**) of crystals exposed to neutral chloride solution (vial 3). Sr = red, Ba = green, Pb = blue. The yellow-orange band in (**e**) denotes Sr–Ba overlap

seems to have ended up entirely in the $BaSO_4$, appearing as a diffuse boundary extending up to 6 µm in from the surface. Although a substantial amount of Ba^{2+} has been liberated from the sulfate, none of this is found in the $SrSO_4$—although a few tiny blebs can be seen on the surface. With crystal ionic radii (CIR) of 1.58 Å for Sr^{2+} and 1.75 Å for Ba^{2+} [39], it makes sense that $BaSO_4$ could incorporate Sr^{2+} while $SrSO_4$ would not accommodate the larger Ba^{2+}. Pb^{2+} is very similar in size to Sr^{2+}, having a CIR of 1.63 Å (ibid.). There is a thin, patchy layer of pure $PbSO_4$ on the surface of the $BaSO_4$. It is logical that most of the Pb and Ba liberated by complexation with chloride remained in solution and was rinsed away when the crystals were washed.

Laser ablation results from the "a" and "c" sub-sets of experiments (also neutral chloride conditions) expand on these results. Thin Ba and Pb overgrowth layers are seen on celestite but only in the 210-h experiments, indicating sluggish kinetics. Baryte crystals showed little uptake of either Sr or Pb, but independent spots did reach 1 wt% in both cases. Anglesite showed an affinity towards Sr, incorporating over 100,000 ppm in thin edge zones. This was not apparent from the nanoSIMS results, the primary difference being that the only source of Sr^{2+} in that experiment was the $SrSO_4$ crystal itself—which showed virtually no signs of dissolution. When Sr^{2+} is in great excess, however, anglesite readily accommodates thin Sr-rich overgrowth layers. Barium uptake in anglesite is negligible with Ba:Pb never exceeding 0.25, and then only in sub-micron patchy layers.

Experiment 4 (0.12 M acid chloride solution) gave the most impressive results. $BaSO_4$ had completely complexed with chloride and was removed with the rinse. This was surprising considering the relatively moderate removal of $BaSO_4$ in the neutral chloride solution. Little work has been done comparing neutral vs. acidic solutions of the same anion, but Lucchesi and Whitney [20] show for $SrSO_4$ that pH has little effect on solubility in sulfate solutions but that HCl can dissolve 3–3.5 times as much $SrSO_4$ as similar concentrations of NaCl. For baryte, the K_{sp} would have to increase by more than 3 orders of magnitude to account for complete removal. The crystal ionic radius of Ba^{2+} would prevent diffusive uptake into either $PbSO_4$ or $SrSO_4$, although some late-stage replacement (co-crystallization with Sr) of $PbSO_4$ seems apparent from the nanoSIMS images.

Liberated Sr^{2+} appears to have predominantly replaced Pb^{2+} in the $PbSO_4$ crystal. Thin $BaSO_4$-rich

40

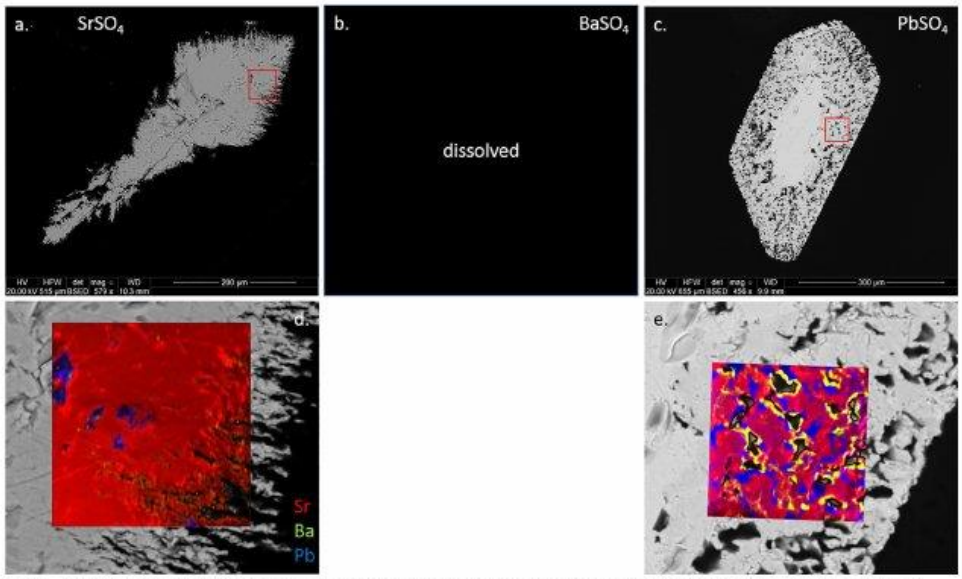

Fig. 11 BSE (**a**–**c**) and nanoSIMS overlays (**d**–**e**) of crystals exposed to acid chloride solution (vial 4). Sr = red, Ba = green, Pb = blue. The yellow edging in (**e**) indicates Sr–Ba overlap

rims are found on most surfaces (Fig. 13b), indicating either a local (fluid-crystal interface) or "global" increase in $[Ba^{2+}]/([Pb^{2+}]+[Sr^{2+}])$. Local concentration gradients may exist due to a lack of convection, with interfacial fluid chemistry following different thermodynamic properties from bulk fluids [10, 15, 34]. Global concentration changes would imply precipitation of sufficient Pb and Sr from the overall solution to trigger favorable kinetics for $BaSO_4$ (or at least Ba-rich sulfate) precipitation. Visible textures suggest coupled dissolution/reprecipitation (CDR), a mechanism of pseudomorphic replacement [26, 27, 30] with the possible end-result (if given sufficient time) being a celestite pseudomorph after anglesite. Future experiments will test this pathway further.

Synthesis and comparison of results

Laser ablation results from the "b" and "d" sub-set of experiments 5-10 show remarkably similar patterns to those in experiment 4—at least for celestite and anglesite. Incorporation of Ba and Pb into celestite is minimal, topping out at 1.2 wt% and 1.4 wt%, respectively. Etching of surface material is visible. Baryte showed more uptake, with thick overgrowth layers of nearly pure $SrSO_4$ (Sr:Ba approaching 7) and $PbSO_4$ (Pb:Ba surpassing 150). Baryte dissolution in experiment 4 is likely the result of that vial containing HCl with no added (SO_4^{2-}), whereas experiments 5(b,d) and 6(b,d) contained H^+, Cl^-, and excess (SO_4^{2-}). Excess sulfate will affect activity factors as well as inhibit dissolution, even in the presence of chloride. Anglesite once again showed the most impressive results, with thick, visible zones of dissolution and recrystallization in both Sr^{2+} and Ba^{2+} solutions. Although the Sr:Pb did reach 2.7 on one edge, in agreement with the nanoSIMS results, most areas showed lower—but still significant—concentrations of Sr. This is likely due to excess sulfate in in the simple reaction experiments, while experiment 4 contained excess acid chloride only. Additionally, dissolution of all three was more significant in the multi-sulfate experiments for the same reason.

These results indicate there are three distinct mechanisms at work, depending on conditions: overgrowth, diffusion, and CDR. Overgrowth refers to the addition of crystalline sulfate on the surface of an existing crystal which has a different composition than the host. The pure $PbSO_4$ layer on the surface of baryte in Fig. 2d is an excellent example. In this case, the $BaSO_4$ structure acts as a template for $PbSO_4$ crystallization, but there appears to be no dissolution of baryte or significant incorporation of Ba^{2+} in the fresh $PbSO_4$ layer. The morphology of the

41

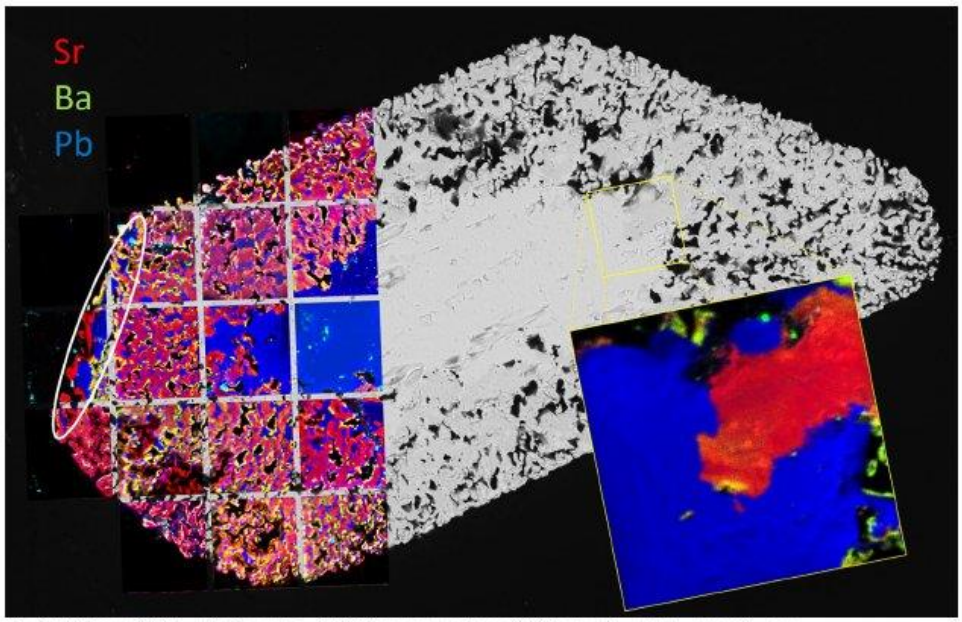

Fig. 12 BSE image of $PbSO_4$ grain B4, overlain with 19 tri-color composite nanoSIMS images. Sr = red, Ba = green, Pb = blue

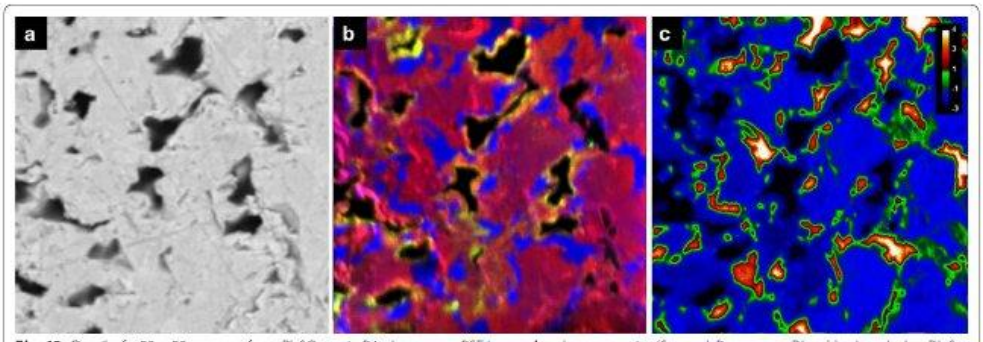

Fig. 13 Detail of a 50 × 50 µm area from $PbSO_4$ grain B4, shown as **a** BSE image, **b** color composite (Sr = red, Ba = green, Pb = blue), and **c** log Pb/Sr. The yellow edging in **b** represents Sr–Ba overlap

parent crystal is not maintained, with the $PbSO_4$ clearly a surficial addition. There is also no porosity visible in the $PbSO_4$.

Diffusion exists when there is no visible change to the crystal surfaces, although low but measurable concentrations of contaminant elements are present near grain edges. Concentrations tend to decrease with increased depth, as implied in Fig. 15 (experiment 9d). Diffusion may be aided by porosity, as in Fig. 5c, or may be dictated by crystallographic orientation. It

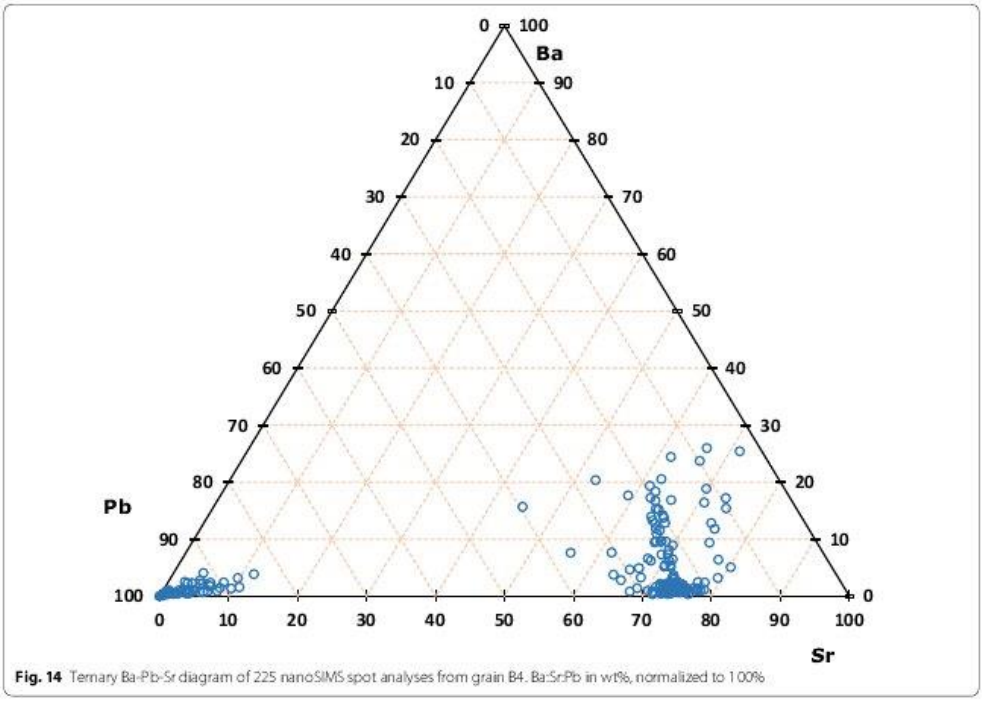

Fig. 14 Ternary Ba-Pb-Sr diagram of 225 nanoSIMS spot analyses from grain B4. Ba:Sr:Pb in wt%, normalized to 100%

is possible, however, for CDR to resemble diffusion, depending on the difference in dissolution and precipitation rates and the amount of resulting porosity. Putnis [26] states "Although volume diffusion is of course always operating, it is doubtful whether it plays a significant role when fluids are present and dissolution–precipitation is another available mechanism". The key phrase in that statement is "significant role", although strong evidence exists for a diffusive mechanism. Figure 16 shows nanoSIMS results from a tangential experiment in which diffusion fronts can be seen mimicking crystallographic planes. Concentrations are low, however, and it is unlikely that diffusion (at only 60 °C) was significant in these experiments or will be influential in any future (Ra^{2+}, Pb^{2+}) removal scenarios.

CDR is a complex mechanism by which a dry-stable compound will undergo dissolution and replacement by an alternatively stable compound when exposed to fluids. Five criteria for identifying CDR have been suggested [27]:

1. Dissolution and precipitation fronts are spatially close. This is crucial for the preservation of morphology of the parent mineral.
2. Sharp reaction fronts dominate, with minimal evidence of solid-state diffusion fronts.
3. The recrystallization product is porous and permeable, allowing continuous fluid contact.
4. Fractures are common ahead of the reaction front, associated with a sufficient increase or decrease in molecular volume.
5. Epitaxial continuity exists across the reaction interface for dissolution/precipitation pairs with similar crystal structures. For dissimilar pairs, a polycrystalline product is observed.

Mineral pseudomorphs are classic examples of this [27, 30]. Figures 12 and 13 show a clear example of anglesite being replaced primarily by (Sr, Pb)SO_4, with later (Ba, Sr)SO_4. Data in Fig. 14 suggest temporary stability around Sr:Pb = 3, although the system is clearly not in equilibrium. Reprecipitation lags slightly behind dissolution, with the resultant porosity exceeding 30%—not

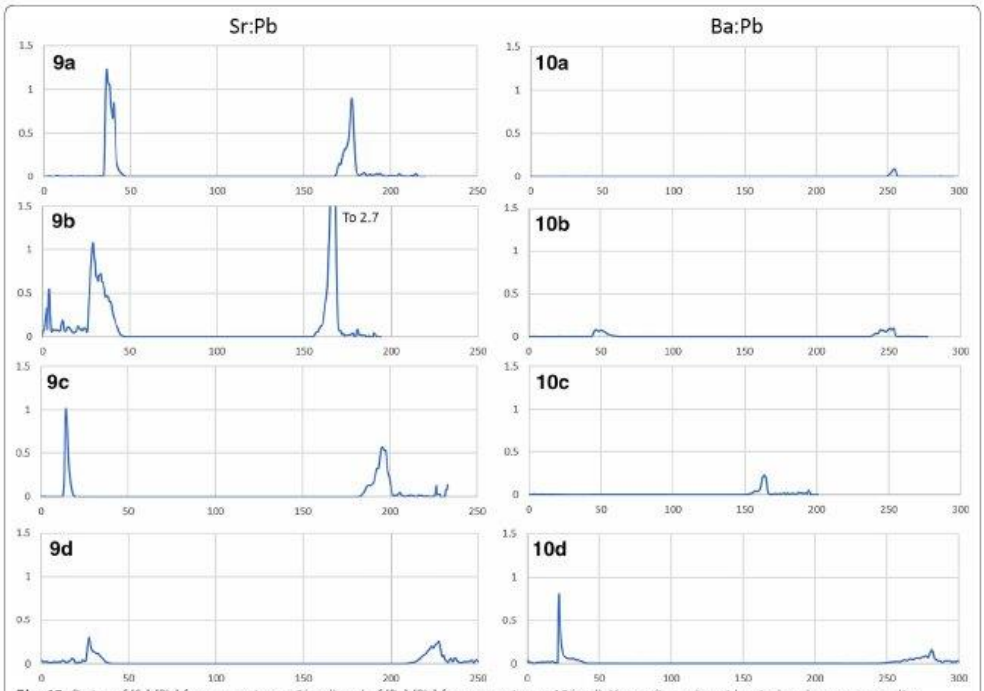

Fig. 15 Ratios of [Sr]:[Pb] from experiment 9(a–d) and of [Ba]:[Pb] from experiment 10(a–d). X-axes (in μm) are identical to the corresponding LA-ICP-MS transects above (Figs. 6 and 7)

achievable by molecular volume difference alone. Figures 6b, d and 7b, d confirm these results. With 40 h of low pH $SrCl_2$ exposure (Fig. 6b), anglesite shows thick replacement zones on prismatic faces (parallel to b axis) consisting of roughly $PbSr(SO_4)_2$. After 210 h under the same conditions (Fig. 6d), the Sr:Pb dropped to 0.25 but the resulting patchy zones are up to 4 times thicker. Reprecipitation nearly matches dissolution, with porosity of only ~ 10%. Figure 7b, d shows advanced dissolution rims, with Ba-rich $PbSO_4$ precipitation lagging. Porosity exceeds 85% at 40 h but is reduced to 70% at 210 h, though the reaction zone has not increased in width. It has been suggested that dissolution and precipitation rates must be necessarily equal to maintain parent crystal morphology [26], yet these timed results suggest there may some room for inequality.

Figure 15 shows the [Sr]/[Pb] for experiments 9(a-d) and [Ba]/[Pb] for experiments 10(a-d). The difference between overgrowth and other uptake methods becomes clear, with thin, nearly pure layers of overgrowth presenting as sharp, symmetric peaks, as seen in the left grain edge of 9c. The right edge of grain 9c is shorter, wider, and asymmetric indicating either diffusion or CDR. Both grain edges of 9d appear to be diffusion but are known to be CDR from textural observations, as are both edges of 10b. The left edge of grain 10d appears to be a hybrid, with a sharp overgrowth peak (or more likely a single particle of $BaSO_4$ precipitate adhered to the grain surface) with a much lower concentration of Ba within the grain, decreasing to zero with depth. Naturally, grain orientation in the mount and angle of transect intercept will impart some bias to the shape and amplitude of these peaks, but these ratios can reveal features that are not obvious from transects alone. They emphasize, for example, the preference of Sr uptake over Ba uptake in anglesite.

Similar to diffusion, concentration of contaminants in CDR examples tends to be higher near the original grain surface and decrease with depth. As dissolution progresses, followed by reprecipitation of the new solution components on fresh surfaces, there will be an increase in concentration of the sulfate host cation and a decrease in concentration of the fluid cationic component. As the

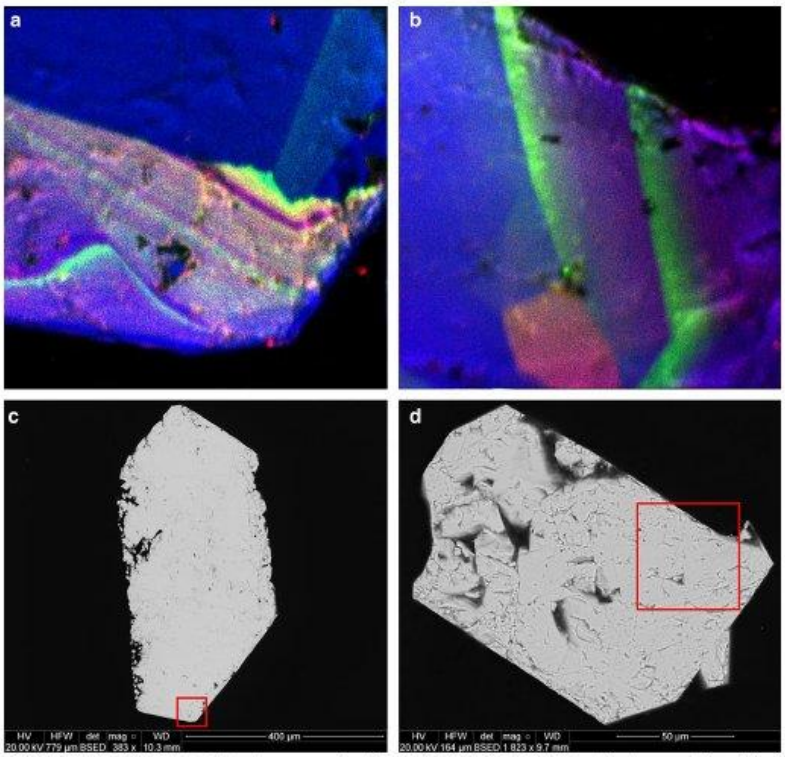

Fig. 16 NanoSIMS color composite images (**a**, **b**) and corresponding BSE images (**c**, **d**) of anglesite crystals. Red squares indicate 50 × 50 µm nanoSIMS mapped areas. Diffusion fronts of Ba (green) and Sr (red) can be clearly seen, apparently emulating crystallographic structures of the $PbSO_4$ (blue)

reaction progresses deeper into the crystal, the solution composition will, to some extent, approach the host end member. This would not apply for well-mixed, endless reservoir systems, but for stagnant limited reservoir systems where diffusion kinetics outperform convection kinetics (as tested here) the effect is evident.

LA-ICP-MS transects show this, with both diffusion fronts and CDR reaction zones recognizable as decreasing product/parent cation ratios towards the center of the crystal (Fig. 15). The relatively large laser spot size, however, results in an averaging effect which swamps finer detail. NanoSIMS images (Figs. 12 and 13) show a general decrease in Ba concentration towards the center of the crystal on a large scale but reveal sharp reaction fronts at high resolution. For this example, four of the five criteria above are met with only Δ_{vol}-induced fracturing absent. In this case, fracturing would not be expected as the molecular volume of $(Sr_{0.75}\ Pb_{0.25})SO_4$ is only 2.4% less than the molecular volume of $PbSO_4$.

Porosity is not only a by-product but also a crucial component in CDR [34]. Anglesites in Figs. 6, 7, and 11, 12, 13 show classic CDR textures, similar to those in other published works (Figs. 1a–g and 10a, b in [34]. The rates at which crystals dissolve and reprecipitate (or more accurately, the difference between these rates) will determine not only their new composition, but also the homogeneity and depth of alteration. Based on these rates, minerals may dissolve completely, undergo partial alteration along surfaces and fractures, pseudomorph into an entirely new mineral, or be completely unaffected. Given enough time and preferential metasomatic conditions, mineral grains may be entirely replaced by new minerals with little trace remaining of the original grain other than its shape. Replacement mechanisms are varied, and parent/product

45

compositions may be similar (azurite after malachite, goethite after hematite, etc.), or entirely different (petrified wood, pyrite after aragonite bivalve and gastropod shells; [2]. Judging from the porosity observed in these experiments, replacement of anglesite by celestite (or at least $(Sr,Pb)SO_4$) was underway, and was interrupted upon conclusion of the experiment. The same cannot be said for baryte replacement of anglesite, as the porosity seems far too high to sustain complete regrowth. Molecular volume also must be considered, as it is much more difficult to substitute a Ba^{2+} (1.75 Å) into a site normally held by Pb^{2+} (1.63 Å), whereas swapping in a Sr^{2+} (1.58 Å) would be energetically effortless. Porosity would therefore be critical in the incorporation of Ba into $PbSO_4$, or Ra (1.84 Å) into any other sulfate, as the increase in molecular volume would necessarily have to be alleviated by pore spaces [34], or substitution pairing with smaller-radii ions (e.g. Mg^{2+}, Ca^{2+}). Crystal radii from [39]. From starting conditions, it should be possible to predict crystallization products based solely on thermodynamics, but kinetic effects profoundly complicate this. Figure 17 presents the models of all 12 ionic combinations (ignoring the reaction time aspect of the experiments).

Processing implications

Projecting the above results forward, controlling conditions to maximize replacement mechanisms may be the key for Pb and Ra removal from copper concentrates. Knowing the composition and abundance of non-economic minerals present in the concentrate, and the conditions of acid leaching and subsequent washing, it may be possible to construct a cationic replacement scenario targeting Pb or Ra, or ideally all "insoluble" sulfates.

What sets this study apart from others is that previously, most solubility experiments were performed on isolated compounds. The benefits of this, of course, were simpler data analysis and more accurate data. What was missed, however, was the potential for seeing movement *between* compounds—with no corresponding increase or decrease in overall solubility. With simplistic experiments, it may be assumed that once Sr^{2+}, Ba^{2+}, or Pb^{2+} ends up in solution, an equilibrium state is met. Once this occurs, the same concentration of ions remains in solution, and is removed during rinsing. During the experiment, liberated ions have nowhere to go other than recrystallizing back on the crystal or remaining in solution. Multiple phases, however, result in multiple potentials which may manifest as mobility between phases (reduction in entropy) with no change in ionic strength of the solution. NanoSIMS images show that there is significant potential for movement between sulfates although solubilities remain low; LA-ICP-MS transects support this hypothesis.

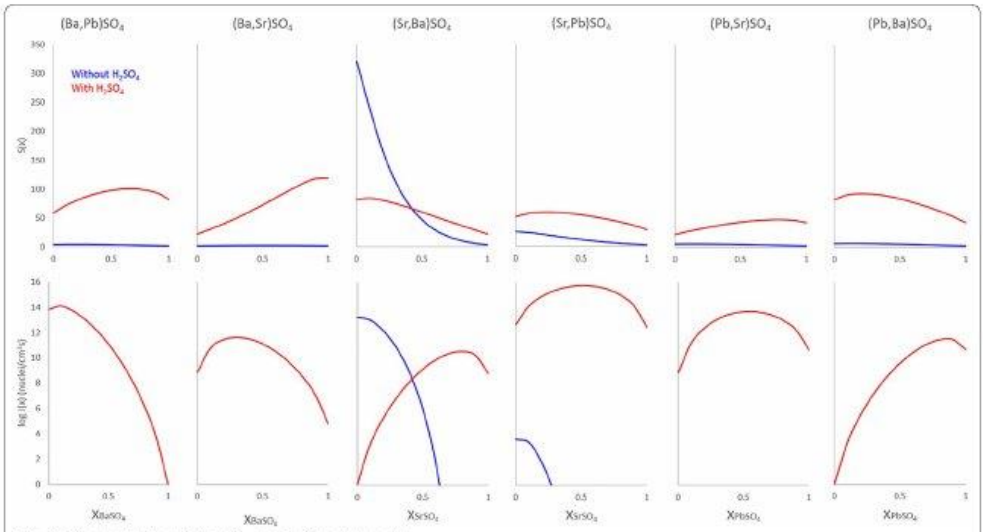

Fig. 17 Supersaturation *S(x)* and Nucleation Rate *J(x)* models

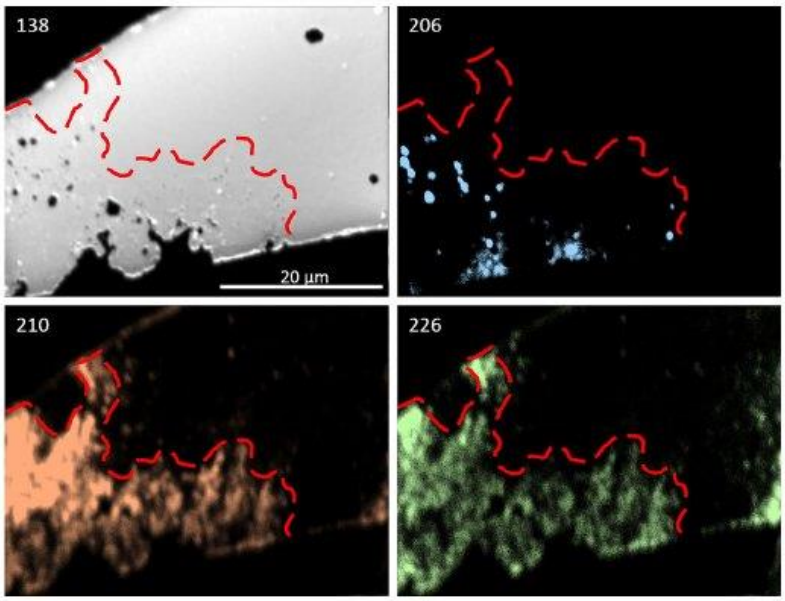

Fig. 18 NanoSIMS images of baryte in leached concentrate sample 05CLD 13 from Olympic Dam. The estimated reaction front is marked in red. The non-correlation between ^{206}Pb and ^{210}Pb indicate multiple pathways; coeval incorporation of old lead into the baryte, uptake of ^{210}Pb by the baryte during acid-leaching, and decay of ^{210}Pb from ^{226}Ra previously taken in by the baryte

Given these results, the question arises: how would they apply to real-world examples? The purpose of this research is to find a practical and efficient pathway for the removal of Ra and lead-210 from copper concentrates. Celestite and anglesite are rare in Olympic Dam ore, although some replacement $PbSO_4$ has been found on sulfuric acid-treated galena. Baryte, however, comprises 1.2% of the total orebody [9] and represents the optimal vehicle for an engineered CDR solution. Evidence exists from LA-ICP-MS data of naturally occurring lead uptake in baryte, which increases greatly in the sulfuric acid leach bath [38]. Figure 18 shows nanoSIMS images of baryte exhibiting (CDR-induced?) porosity correlating with ^{206}Pb, ^{210}Pb, and ^{226}Ra concentrations. If CDR is already taking place in the leach tank to some extent, optimizing the process for maximum Pb and Ra removal becomes an achievable goal.

Results from these experiments set the stage for further investigation of radionuclide uptake during minerals processing, especially during acid leaching. At Olympic Dam, the primary RNs of concern during processing are ^{226}Ra, ^{210}Pb, and ^{210}Po. These elements, along with Sr and Ba, represent the entire suite of acid-insoluble sulfates. Considering the commonplace use of sulfuric acid for leaching, understanding the behavior of these sulfates is paramount to controlling their deportment. The evidence provided here enhances our knowledge of this family of micro- to nanoscale chemical interactions and will not only aid in determining where RNs reside during each stage of processing but will also establish the foundation for a plan targeting their removal.

Conclusions

Results suggest that three distinct mechanisms are involved: overgrowth; diffusion; and CDR. Overgrowth is common for both Pb- and $SrSO_4$ on barytes (in low pH, high sulfate solutions), with little evidence that significant amounts of Pb or Sr are incorporated into the baryte structure. Celestite hosts only small amounts of Ba or Pb (generally up to 1 wt%) through porosity-driven diffusion, though very thin overgrowth zones or spots appear sporadically in both cases. Anglesite is readily dissolved and replaced through CDR at low pH conditions, although the effect is somewhat dampened by the presence of excess sulfate. Strontium replacement of Pb averages ~ 75% (m.b.) in acid chloride solution but is reduced

47

to 10 wt% in neutral chloride or acid sulfate solutions. Barium substitution through CDR increases in high-sulfate conditions, but never exceeds 4 wt%. Diffusion of both Ba and Sr into anglesite does occur along crystallographic axes, but only at very low concentrations.

Abbreviations

amu: atomic mass units; BSE: back scatter electron; CDR: coupled dissolution/reprecipitation; CIR: crystal ionic radius; CMCA: Centre for Microscopy, Characterisation, and Analysis; EDS: electron dispersive spectroscopy; FEG: field emission gun; IOCG-U: iron oxide-copper-gold-uranium; LA-ICP-MS: laser ablation inductively coupled plasma mass spectrometry; m.b.: metals basis; nanoSIMS: nanoscale secondary ion mass spectrometry; ppm: parts per million; ppq: parts per quadrillion; ppt: parts per trillion; RN: radionuclide; RO: reverse osmosis; SEM: scanning electron microscopy.

List of symbols

B: geometric factor; J(x): nucleation rate; k: Boltzmann's constant; K_{sp}: solubility product; S(x): supersaturation function; T: temperature (in Kelvin); Γ(x): preexponential factor; Σ(x): interfacial free energy; Ω(x): molecular volume.

Acknowledgements

The authors thank Ken Neubauer and Dr. Alec Walsh for additional analytical support, Dr. Jon Tyler for laboratory access, and Dr. Ruth Shaw and Prof. Stephen Grano for project management support. We would also like to thank the editors and reviewers for their valuable insight and suggestions, which helped make this a stronger and clearer manuscript.

Authors' contributions

MR, SG, and PG performed the work presented here. MR processed results and made interpretations, supervised by NJC. KE supplied sample material and provided extensive advice. MR wrote the manuscript assisted by NJC and other co-authors. All authors read and approved the final manuscript.

Funding

This is a contribution to the ARC Research Hub for Australian Copper-Uranium (Grant IH130200033), co-supported by BHP Olympic Dam.

Availability of data and materials

The data presented above remain the property of, and will only be dispersed at the discretion of, BHP.

Competing interests

The authors declare that they have no competing interests.

Author details

[1] School of Chemical Engineering, The University of Adelaide, Adelaide, SA 5005, Australia. [2] Centre for Microscopy, Characterisation, and Analysis, The University of Western Australia, 35 Stirling Highway, Crawley, WA 6009, Australia. [3] BHP Olympic Dam, 55 Grenfell St., Adelaide, SA 5000, Australia. [4] Adelaide Microscopy, The University of Adelaide, Adelaide, SA 5005, Australia.

Received: 3 March 2019 Accepted: 26 August 2019
Published online: 05 September 2019

References

1. Anderson JG, Larson MA, Doraiswamy LK (1998) Microphase-assisted "autocatalysis" in a solid–liquid reaction with a precipitating product—II. Experimental. Chem Eng Sci. 53(13):2459–2468
2. Blazek MC (1979) Classification of pseudomorphs. Rocks Miner. 54(5):194–197
3. Brown PL, Ekberg C, Ramebäck H, Hedström H, Matyskin A. Solubility of radium and strontium sulfate across the temperature range of 0 to 300 C. In: Merkel BJ, Arab A, editors. Uranium-past and future challenges—proceedings of the 7th international conference on uranium mining and hydrogeology. Springer, Cham; 2015. pp 553–564
4. Christy AG, Putnis A (1993) The kinetics of barite dissolution and precipitation in water and sodium chloride brines at 44–85 C. Geochim Cosmochim Acta 57(10):2161–2168
5. Collins AG, Davis JW (1971) Solubility of barium and strontium sulfates in strong electrolyte solutions. Environ Sci Technol 5(10):1039–1043
6. Cook NJ, Ciobanu CL, George L, Zhu ZY, Wade B, Ehrig K (2016) Trace element analysis of minerals in magmatic-hydrothermal ores by laser ablation inductively-coupled plasma mass spectrometry: approaches and opportunities. Minerals 6(4):111
7. Dai Z, Kan AT, Shi W, Yan F, Zhang F, Bhandari N, Ruan G, Zhang Z, Liu Y, Alsaiari HA, Lu YT (2017) Calcite and barite solubility measurements in mixed electrolyte solutions and development of a comprehensive model for water-mineral-gas equilibrium of the Na-K-Mg-Ca-Ba-Sr-Cl-SO_4-CO_3-HCO_3-CO_2-(aq)-H_2O system up to 250 °C and 1500 bar. Ind Eng Chem Res 56(23):6548–6561
8. Dyar MD, Gunter ME, Tasa D (2008) Mineralogy and optical mineralogy. Mineral Soc Am, Chantilly
9. Ehrig K, McPhie J, Kamenetsky VS. Geology and mineralogical zonation of the Olympic Dam iron oxide Cu-U-Au-Ag deposit, South Australia. In: Hedenquist JW, Harris M, Camus F, editors. Geology and genesis of major copper deposits and districts of the world, a tribute to Richard Sillitoe. Society of Economic Geologists Special Publication 16, Littleton, USA; 2012. pp 237–267
10. Fenter P, Sturchio NC (2004) Mineral–water interfacial structures revealed by synchrotron X-ray scattering. Prog Surf Sci 77(5–8):171–258
11. Figgins PE (1961) The radiochemistry of polonium. Mound Lab, Miamisburg
12. Haynes WM (2014) CRC Handbook of chemistry and physics. CRC Press, Baco Raton
13. Henisch HK (1996) Crystal growth in gels. Courier Corporation, North Chelmsford
14. Ilyas S, Srivastava RR, Ilyas N (2020) Biosorption of strontium from aqueous solutions. In: Pathak P, Gupta DK (eds) Strontium contamination in the environment. The handbook of environmental chemistry, 88th edn. Springer Nature, Berlin, pp 65–83
15. Kerisit S, Liu C (2009) Molecular simulations of water and ion diffusion in nanosized mineral fractures. Environ Sci Technol 43(3):777–782
16. Krumgalz BS (2018) Temperature dependence of mineral solubility in water. Part 3. Alkaline and alkaline earth sulfates. J Phys Chem Ref Data 47(2):023101
17. Lehman TA, Everett WW (1982) Solubility of lead sulfate in water and in sodium sulfate solutions: an experiment in atomic absorption spectrophotometry. J Chem Educ 59(9):797
18. Linke WF, Seidell A (1965) Solubilities, inorganic and metal-organic compounds, K-Z: a compilation of solubility data from the periodical literature. A revision and continuation of the compilation originated by Atherton Seidell. American Chemical Society, Washington
19. Longerich HP, Jackson SE, Günther D (1996) Inter-laboratory note. Laser ablation inductively coupled plasma mass spectrometric transient signal data acquisition and analyte concentration calculation. J Anal At Spectrom. 11(9):899–904
20. Lucchesi PJ, Whitney ED (1962) Solubility of strontium sulphate in water and aqueous solutions of hydrogen chloride, sodium chloride, sulphuric acid and sodium sulphate by the radiotracer method. J Appl Chem 12(6):277–279
21. Nguyen CK, Clark BN, Stone KR, Edwards MA (2011) Role of chloride, sulfate, and alkalinity on galvanic lead corrosion. Corrosion 67(6):065005
22. Patel AR, Bhat HL (1984) Gel growth of lead sulfate single crystals. In: Рост Кристаллов/Rost Kristallov/growth of crystals. Springer, Boston. pp 122–125
23. Pina CM, Putnis A (2002) The kinetics of nucleation of solid solutions from aqueous solutions: a new model for calculating non-equilibrium distribution coefficients. Geochim Cosmochim Acta 66(2):185–192
24. Pina CM, Becker U, Risthaus P, Bosbach D, Putnis A (1998) Molecular-scale mechanisms of crystal growth in barite. Nature 395(6701):483–486
25. Poczatek C, Kaufman Z, Lechene C (2009) OpenMIMS ImageJ Plugin Guide. Harvard Medical School (Boston, Massachusetts, USA)
26. Putnis A (2002) Mineral replacement reactions: from macroscopic observations to microscopic mechanisms. Miner Mag 66(5):689–708
27. Putnis A (2009) Mineral replacement reactions. Rev Miner Geochem 70(1):87–124

28. Putnis A, Mauthe G (2001) The effect of pore size on cementation in porous rocks. Geofluids 1(1):37–41
29. Putnis A, Fernandez-Diaz L, Prieto M (1992) Experimentally produced oscillatory zoning in the (Ba, Sr)SO_4 solid solution. Nature 358(6389):743–745
30. Putnis CV, Tsukamoto K, Nishimura Y (2005) Direct observations of pseudomorphism: compositional and textural evolution at a fluid-solid interface. Am Mineral 90:1909–1912
31. Raju K, Atkinson G (1988) Thermodynamics of" scale" mineral solubilities. 1. Barium sulfate (s) in water and aqueous sodium chloride. J Chem Eng Data 33(4):490–495
32. Raju K, Atkinson G (1989) Thermodynamics of" scale" mineral solubilities. 2. Strontium sulfate (s) in aqueous sodium chloride. J Chem Eng Data 34(3):361–364
33. Rollog M, Cook NJ, Guagliardo P, Ehrig K, Kilburn M (2019) In situ spatial distribution mapping of radionuclides in minerals by nanoSIMS. Geochem Explor Environ Anal 19:245–254. https://doi.org/10.1144/geochem2018-038
34. Ruiz-Agudo E, Putnis CV, Putnis A (2014) Coupled dissolution and precipitation at mineral–fluid interfaces. Chem Geol 383:132–146
35. Sangwal K (1989) On the estimation of surface entropy factor, interfacial tension, dissolution enthalpy and metastable zone-width for substances crystallizing from solution. J Cryst Growth 97(2):393–405
36. Schindelin J, Arganda-Carreras I, Frise E, Kaynig V, Longair M, Pietzsch T, Preibisch S, Rueden C, Saalfeld S, Schmid B, Tinevez JY (2012) Fiji: an open-source platform for biological-image analysis. Nat Methods 9(7):676
37. Schindelin J, Rueden CT, Hiner MC, Eliceiri KW (2015) The ImageJ ecosystem: an open platform for biomedical image analysis. Mol Reprod Dev 82(7–8):518–529
38. Schmandt DS, Cook NJ, Ehrig K, Gilbert S, Wade BP, Rollog M, Ciobanu CL, Kamenetsky VS (2019) Uptake of trace elements by baryte during copper ore processing: a case study from Olympic Dam, South Australia. Miner Eng 135:83–94
39. Shannon RD (1976) Revised effective ionic radii and systematic studies of interatomic distances in halides and chalcogenides. Acta Crystallogr Sect A 32(5):751–767
40. Söhnel O (1982) Electrolyte crystal-aqueous solution interfacial tensions from crystallization data. J Cryst Growth 57(1):101–108
41. Steefel CI, Lichtner PC (1998) Multicomponent reactive transport in discrete fractures: I. Controls on reaction front geometry. J Hydrol. 209(1–4):186–199
42. Steefel CI, Lichtner PC (1998) Multicomponent reactive transport in discrete fractures: II: Infiltration of hyperalkaline groundwater at Maqarin, Jordan, a natural analogue site. J Hydrol 209(1–4):200–224
43. Srivastava RR, Ilyas S (2020) Strontium extraction from the Geo-environment. In: Pathak P, Gupta DK (eds) Strontium contamination in the environment. The handbook of environmental chemistry, 88th edn. Springer Nature, Berlin, pp 43–63
44. Zhang T, Gregory K, Hammack RW, Vidic RD (2014) Co-precipitation of radium with barium and strontium sulfate and its impact on the fate of radium during treatment of produced water from unconventional gas extraction. Environ Sci Technol 48(8):4596–4603

Publisher's Note

Chapter 6

Radionuclide-bearing minerals in Olympic Dam copper concentrates

Mark Rollog [a,*], Nigel J. Cook [a], Paul Guagliardo [b], Kathy Ehrig [c], and Matt Kilburn [b]

[a] *School of Chemical Engineering, University of Adelaide, Adelaide, 5005 S.A., Australia*

[b] *Centre for Microscopy, Characterisation, and Analysis, University of Western Australia, 35 Stirling Highway, Crawley, 6009 W.A., Australia*

[c] *BHP Olympic Dam, 55 Grenfell St., Adelaide, 5000 S.A., Australia*

Article published in *Hydrometallurgy* 190, 105153.

Statement of Authorship

Title of Paper	Radionuclide-bearing minerals in Olympic Dam copper concentrates
Publication Status	☑ Published ☐ Accepted for Publication ☐ Submitted for Publication ☐ Unpublished and Unsubmitted work written in manuscript style
Publication Details	Submitted to *Hydrometallurgy* May 9 2019. Available online 11 October 2019.

Principal Author

Name of Principal Author (Candidate)	Mark Rollog
Contribution to the Paper	Designed experimentation, performed sample analysis and data interpretation, wrote manuscript
Overall percentage (%)	70
Certification:	This paper reports on original research I conducted during the period of my Higher Degree by Research candidature and is not subject to any obligations or contractual agreements with a third party that would constrain its inclusion in this thesis. I am the primary author of this paper.
Signature	Date 23.08.19

Co-Author Contributions

By signing the Statement of Authorship, each author certifies that:

i. the candidate's stated contribution to the publication is accurate (as detailed above);

ii. permission is granted for the candidate in include the publication in the thesis; and

iii. the sum of all co-author contributions is equal to 100% less the candidate's stated contribution.

Name of Co-Author	Nigel J. Cook
Contribution to the Paper	Supervised direction and progress of work, helped evaluate and edit manuscript
Overall percentage (%)	10
Signature	Date 1/8/19

Name of Co-Author	Paul Guagliardo
Contribution to the Paper	Oversaw sample analyses and helped evaluate and edit the manuscript
Overall percentage (%)	10

73

Signature		Date	25 Jul 2019

Name of Co-Author	Kathy Ehrig
Contribution to the Paper	Provided samples and helped evaluate and edit the manuscript
Overall percentage (%)	5
Signature	Date: 31 July 2019

Name of Co-Author	Matt Kilburn
Contribution to the Paper	Oversaw the facility where samples were run
Overall percentage (%)	5
Signature	Date: 25 Jul 2019

74

75

Hydrometallurgy 190 (2019) 105153

Contents lists available at ScienceDirect

Hydrometallurgy

journal homepage: www.elsevier.com/locate/hydromet

Radionuclide-bearing minerals in Olympic Dam copper concentrates

Mark Rollog[a,*], Nigel J. Cook[a], Paul Guagliardo[b], Kathy J. Ehrig[c], Matt Kilburn[b]

[a] School of Chemical Engineering, The University of Adelaide, Adelaide, 5005, SA, Australia
[b] Centre for Microscopy, Characterisation, and Analysis, The University of Western Australia, 35 Stirling Highway, Crawley, 6009, WA, Australia
[c] BHP Olympic Dam, 55 Grenfell St., Adelaide, 5000, SA, Australia

ARTICLE INFO

Keywords:
Uranium
Thorium
Polonium
Radium
Lead
Radionuclides
Baryte
nanoSIMS

ABSTRACT

Olympic Dam hosts > 80 million tonnes of copper, as copper-iron sulphides, within hematite-dominant gangue. Processing of the relatively fine-grained copper ore is complicated by the presence of by-product uranium and its radiogenic isotopes, in particular ^{226}Ra, ^{210}Pb and ^{210}Po, which partially recover to the final copper sulphide concentrates. Although the majority (~85%) of the U-bearing minerals (uraninite, coffinite, brannerite, thorianite, thorite) are recovered to flotation tailings, the remaining ~15% occurs in copper concentrates as sulphide-gangue composite particles and micron- to nanoscale grains occluded within sulphide minerals. Sulphuric acid leaching of copper concentrates significantly reduces the concentration of U but has only a minor impact on the daughter isotopes. Further reduction of these isotopes may be achieved through selective targeting and removal of specific minerals known to be radionuclide (RN) hosts, but fine-grained, micro- to nanoscale ore textures preclude easy direct identification of these RN host phases.

Nanoscale secondary ion mass spectrometry (nanoSIMS) has proven to be an excellent platform for in situ mapping of ultra-trace RN distributions, with sub-micron spatial resolution, in individual mineral grains. Uranium and thorium minerals are, as expected, the major hosts and display significant concentrations of the entire ^{238}U decay chain. Although the majority of these minerals are removed via acid leaching of copper concentrate, sufficient RNs remain in the concentrate as micron- to nanoscale grains within sulphides and gangue minerals or along particle microfractures. Results show that brannerite, potentially more problematic due to its lower solubility in sulphuric acid than uraninite, does not appear to contain appreciable amounts of daughter isotopes. The insolubility of $ThPO_4$ produces the potential for sequestration of ^{232}Th and ^{230}Th in rare earth phosphates such as xenotime, which then retain the respective decay chains. Likewise, the insolubility of certain sulphates (Sr, Ba, Pb, Ra) provides a mechanism for precipitation and entrapment of RNs. Baryte was shown to accumulate Ra and Pb naturally in the deposit, and it can upgrade its RN content substantially during sulphuric acid leaching through coupled dissolution-reprecipitation mechanisms involving Pb^{2+} and Ra^{2+} liberated from dissolved uranium minerals. Identification and prioritization of RN host minerals is crucial for the development of a more efficient processing flowsheet.

1. Introduction

South Australia is host to at least 23% of the World's uranium resources (and ~80% of the Australian total), with the larger part of that endowment within copper deposits that are generally classified as iron oxide-copper-gold (IOCG ± U) type (Hitzman et al., 1992; Hitzman and Valenta, 2005). Located on the eastern margin of the Gawler Craton, Olympic Dam (OD) is by far the largest among these deposits with current resources estimated to be 10,100 Mt. at 0.78% Cu, 250 ppm U_3O_8, 0.3 g/t Au, and 1 g/t Ag (BHP, 2018). The deposit is hosted within a breccia complex itself enclosed by the Roxby Downs Granite (RDG; 1593.87 ± 0.21 Ma; Cherry et al., 2018), and consists of hematite-dominant ores containing copper-iron sulphides, grading from high-S, low-Cu (pyrite-chalcopyrite) at the base to low-S, high-Cu (bornite-chalcocite) near the top (Roberts and Hudson, 1983; Ehrig et al., 2012). Although primary hypogene mineralisation is roughly cogenetic with RDG emplacement (Ciobanu et al., 2013; Ehrig et al., 2017; Courtney-Davies et al., 2019), multiple subsequent phases of remobilisation are recognised that have impacted on the ores as seen today, potentially also introducing additional metals into the system (e.g., Maas et al., 2011; Ciobanu et al., 2013; Huang et al., 2015; Kirchenbaur et al., 2016; McPhie et al., 2016; Apukhtina et al., 2017).

* Corresponding author.
E-mail addresses: mark.rollog@adelaide.edu.au (M. Rollog), nigel.cook@adelaide.edu.au (N.J. Cook), paul.guagliardo@uwa.edu.au (P. Guagliardo), kathy.ehrig@bhp.com (K.J. Ehrig), matt.kilburn@uwa.edu.au (M. Kilburn).

https://doi.org/10.1016/j.hydromet.2019.105153
Received 9 May 2019; Received in revised form 8 September 2019; Accepted 13 September 2019
Available online 15 September 2019
0304-386X/

76

Ores at Olympic Dam are characteristically fine-grained, exhibiting complex mineralogy with heterogeneity extending to the nanoscale (Ehrig et al., 2012; Ciobanu et al., 2013). Processing of these ores entails producing copper sulphide concentrates for onsite smelting and refining, including sulphuric acid leaching of flotation concentrates to reduce fluorine and uranium prior to smelting. Alongside copper, the Olympic Dam resource contains sufficient uranium for economic recovery, producing an average of approximately 3700 t U_3O_8 annually from 2006 to 2018 (World Nuclear Association: Information Library, 2018). A consequence of uranium enrichment in copper ore is the persistence of all radioactive daughter isotopes resulting from the natural decay of ^{238}U. Reduction of smelter deleterious elements, such as fluorine, to below appropriate threshold concentrations is achieved through relatively straightforward hydrometallurgy, but the reduction of radionuclide (RN) activities in final concentrates presents an extraordinary challenge. The concentration of uranium is significantly reduced during acid leaching, but ^{226}Ra, ^{210}Pb, and ^{210}Po activities are not as readily reduced – even though these RNs are only present in tiny quantities. Achieving an aspirational activity of < 1 Bq/g per isotope (International Atomic Energy Agency, 2004) would require concentration limits of 27 parts-per-trillion (ppt), 0.38 ppt, and 6 parts-per-quadrillion (ppq) for ^{226}Ra, ^{210}Pb and ^{210}Po, respectively, in smelter feed.

Accurate concentration measurements (at the mineral scale) at these orders of magnitude are problematic for most microanalytical techniques and become even more so when considering the spatial resolution required for in situ analysis of such a fine-grained ore. Laser ablation inductively coupled plasma mass spectrometry (LA-ICP-MS) is a powerful tool and has greatly advanced understanding the deportment of trace elements, including uranium, in Olympic Dam apatite (Krneta et al., 2017), hematite (Ciobanu et al., 2013; Verdugo-Ihl et al., 2017), feldspar (Kontonikas-Charos et al., 2017), rare earth fluorocarbonates and -phosphates (Schmandt et al., 2017, 2019a) and baryte (Schmandt et al., 2019b). However, the best resolution available utilises a 3 μm diameter spot size and can generally only measure at sensitivities of parts-per-million or above at that spatial resolution. To increase sensitivity, laser spot size must also increase. For trace element analyses, spot diameters of 50 to 100 μm are not unusual – effectively destroying any micron-scale spatial information. The CAMECA nanoSIMS platform offers an excellent alternative, combining high sensitivity with submicron spatial resolution. Although nanoSIMS is a non-quantifiable imaging technique – at least for complex mineral matrices – the exceptional lateral resolution (ideally to 40 nm) provides a wealth of information regarding trace element and isotope dissemination at the mineral scale. To develop an efficient removal plan, only the *identification* of RN host minerals is necessary; an elevated RN signal (compared to surrounding minerals) indicates a potential target for removal – regardless of exact concentrations of the isotopes in question.

A significant part of the RN budget at Olympic Dam is hosted within the three main uranium minerals (uraninite, brannerite and coffinite; Macmillan et al., 2016a, 2016b, 2017). Daughter isotopes do not escape the host structure, even if no longer structurally bound. Several other major (and minor) host minerals for radionuclides at Olympic Dam can be predicted on the basis of geochemistry and readily confirmed by microanalysis; these include baryte and other sulphates (Schmandt, 2019), some phosphates, and a range of uranium- and thorium-bearing minerals present in trace amounts (e.g., euxenite).

The overarching objective of the Australian Research Council Research Hub for Australian Copper-Uranium – of which this study is only one facet – is to undertake a comprehensive evaluation of all potential host minerals for RN in Olympic Dam ore and copper concentrate. This information, along with weighted estimates based on rough RN concentrations and proportions of each mineral in the ore or concentrates, may be used by the hydrometallurgy team to devise and optimise a flowsheet for efficiently minimising the overall RN activity in final concentrates. To this end, identification of the dominant radionuclide-bearing minerals at Olympic Dam based on > 3200 individual nanoSIMS isotope maps is reported here. The ability of certain minerals to retain some, or all, members of the ^{238}U decay chain is discussed. Dissociation of isotopes in the ^{238}U decay chain at the grain scale is common, and explanations are provided for the preference – or, in some cases, exclusion – of individual radionuclides in specific mineral hosts based on thermodynamic, kinetic, chemical, and crystallographic considerations. A sister paper (Rollog et al., 2019d) examines the importance of minor RN hosts, likely incorporation mechanisms, and the role of mineral surfaces.

2. Methods

Samples were analysed as described in Rollog et al., 2019a. Briefly, aliquots of flotation concentrate (FC) and concentrate leach discharge (CLD), both of the +53 μm fraction, were collected on three different dates (August 2015, December 2016, and December 2017). A simplified processing flowsheet relating these samples to the overall processing circuit at Olympic Dam was given by Schmandt et al. (2019b). In addition, selected drill core samples were analysed in a similar manner, representing unprocessed ore.

The +53 μm size fractions were used to ensure that a sufficient number (~100,000) of suitably-sized particles were present within each 1-in. round mounted block. Samples of each were fixed in epoxy resin, polished, and carbon coated. General surveys were performed on a FEI Quanta 450 field emission gun scanning electron microscope (FEG-SEM) equipped with a back-scatter electron (BSE) detector and an EDAX electron dispersive spectrometry (EDS) system at Adelaide Microscopy, The University of Adelaide. Grains of interest were located, characterised, imaged, and in some cases mapped for elemental distributions.

NanoSIMS analyses were performed on a CAMECA NanoSIMS 50 L at the Centre for Microscopy, Characterisation, and Analysis (CMCA) at the University of Western Australia, Perth. A Hyperion (H200) RF plasma O^- source was used for all analyses. Prior to imaging, each area was presputtered with the primary beam to a dose of > 1×10^{17} ions/cm^2. Grains of interest were typically mapped twice, at 50 pA and 250 pA, targeting major and minor elements/isotopes, respectively. The instrument was operated in multicollection mode, allowing the simultaneous detection of up to seven isotopes. For the 50 pA analyses, the multicollection was set to detect ^{46}Ti, ^{54}Fe, ^{65}Cu, ^{87}Sr, ^{138}Ba, ^{206}Pb, and ^{238}U. For the 250 pA analyses, the multicollection was set to ^{54}Fe (repeated for alignment between runs), ^{142}Nd, ^{169}Tm, ^{210}RN (predominantly ^{210}Pb plus minor ^{210}Po and ^{210}Bi), ^{226}Ra, ^{230}Th, and ^{234}U. The ratio of ^{210}Pb:^{210}Po (assuming secular equilibrium) is ~60, and this likely increases when nanoSIMS analysis is undertaken using the oxygen source. For this study, ^{210}RN is assumed to almost exclusively represent ^{210}Pb.

Detector substitutions were occasionally made based on tuning efficiency and minerals analysed and included ^{42}Ca, ^{47,48}Ti, ^{57}Fe, ^{86,88}Sr, ^{137}Ba, ^{143,144}Nd, ^{230}Th^{16}O, ^{234}U^{16}O, and ^{238}U^{16}O. Images were recorded with a raster size of (50 um)^2, a dwell time of 5 ms/px and at a resolution of (512 pixels)^2; up to six planes were recorded for each area. Images were analysed using ImageJ (Schindelin et al., 2012, 2015) and the OpenMIMS plugin (Poczatek et al., 2009). Dead time corrections were applied, and images were aligned, summed, and adjusted for brightness/contrast. Colorisation (linear in scale to the original black and white intensities) aids in isotopic distinction and visualisation. For clarity, figure images have been labelled with mass and element (e.g. ^{238}U) although technically mass spectrometers are mass-specific but not element-specific. Isobaric mass interference issues were examined and addressed in Rollog et al. (2019a).

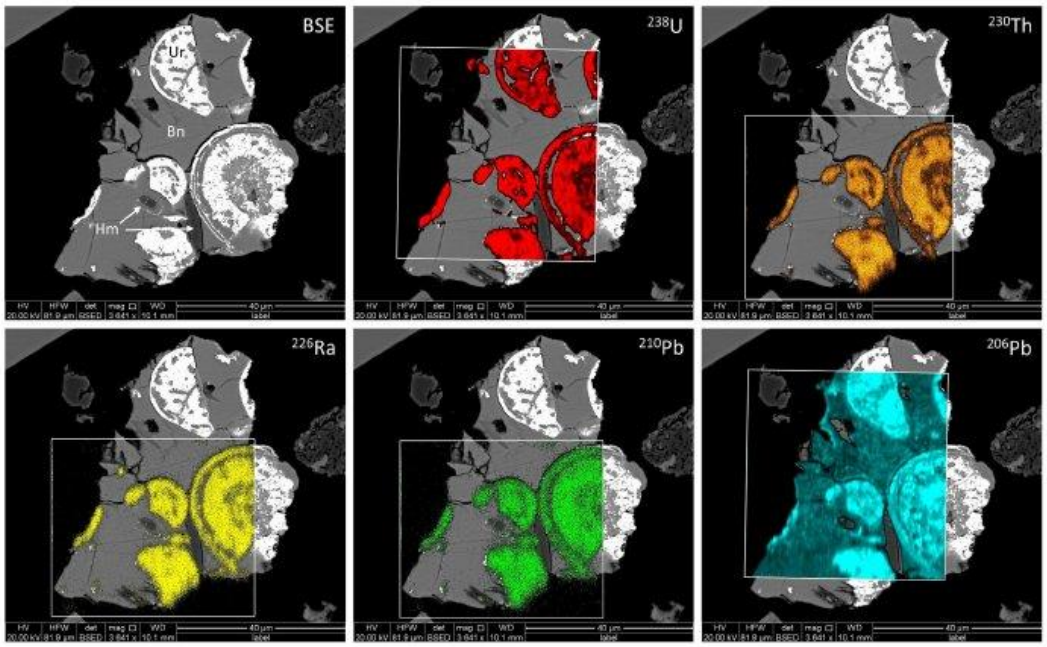

Fig. 1. BSE images with overlays of nanoSIMS isotope maps (masses 238, 230, 226, 210 and 206) for grain 10FC25 (flotation concentrate), consisting of bornite (Bn) containing colloform uraninite (Ur) and small inclusions of hematite (Hm). The entire decay chain is retained within uraninite. Only ^{206}Pb is observed - at low concentration levels - in bornite.

3. Results

3.1. Uranium and thorium minerals

The primary uranium minerals at Olympic Dam are uraninite, brannerite, and coffinite (Roberts and Hudson, 1983; Ehrig et al., 2012). Although these each naturally contain uranium, their ability to retain daughter isotopes varies. Colloform uraninite (Fig. 1) is considered late-stage and typically contains < 7 wt% Pb (Macmillan et al., 2016a). Distributions of all radionuclide members of the decay chain correlate exactly with those of uranium. ^{206}Pb is present in uraninite, suggesting the persistence of the entire chain, but is also found in low concentration throughout the host bornite.

Coffinite and brannerite (nominally $USiO_4$ and UTi_2O_6) account for roughly 46% and 26%, respectively, of uranium in the deposit. The abundance of brannerite is inversely related to Fe concentration (less common in ores containing > 20 wt% Fe) whereas coffinite abundance remains constant across the deposit (Ehrig et al., 2012). Commonly found together, brannerite and coffinite display markedly disparate abilities to retain daughter isotopes of the ^{238}U decay chain. In Fig. 2, globular coffinite (Macmillan et al., 2017) has nucleated on the quartz-sericite boundary and is associated with brannerite, rutile, monazite, and chalcopyrite. Like uraninite it also retains the entire decay chain, but the Pb content is greatly reduced relative to the other daughter isotopes. Brannerite can be observed replacing rutile at its margins. Although trace amounts of daughter isotopes are evident, the brannerite is mostly devoid of any members of the ^{238}U decay chain - except ^{238}U itself. ^{206}Pb appears distributed throughout the rutile, including the associated brannerite, but at concentrations below the minimum detection limits of energy-dispersive spectrometry (EDS).

Brannerite is also frequently found associated with molybdenite (Rollog et al., 2019c, 2019d), or with heavily substituted members of the AB_2O_6 group (A = Ca, Y, U, Th, or REY; B = Nb, Ta, or Ti) such as euxenite $[(Y,Ca,Ce,U,Th)(Nb,Ta,Ti)_2O_6]$ (Fig. 3). The brannerite hosts ^{238}U, but only insignificant amounts of ^{230}Th, ^{226}Ra or ^{210}Pb are present. ^{206}Pb levels are higher in brannerite than in euxenite, highlighted by sub-micron inclusions of galena, but still below the detection limit of EDS. Euxenite efficiently hosts the entire decay chain but is not considered a primary target mineral due to its limited abundance in the ore.

3.2. Phosphates

Some, but not all, phosphate minerals exhibit significant amounts of RNs, generally from the lighter end of the decay chain but also commonly including thorium. Apatite and monazite, for example, are known to host trace Th and other RNs, but are not considered major hosts at Olympic Dam (Krneta et al., 2017; Rollog et al., 2019c, 2019d). Fig. 3 above contains two grains of xenotime which clearly show the presence of ^{226}Ra and ^{210}Pb, but do not appear to host any other radionuclides.

In parallel with ^{232}Th (Krneta et al., 2017), xenotime from Olympic Dam consistently hosts ^{230}Th and daughter isotopes thereof. Fig. 4 displays a 20 × 20 μm magnified region of grain 10FC06, centred on a euhedral xenotime crystal undergoing replacement by uraninite/coffinite containing tiny blebs of galena. The assemblage is hosted in bornite with associated hematite, sericite, and florencite. ^{230}Th, ^{226}Ra, and ^{210}Pb all accumulate within the xenotime relative to other minerals, but only the ^{230}Th is also found in uraninite/coffinite. ^{238}U occurs only in uraninite/coffinite, and ^{206}Pb is represented entirely by tiny galena blebs within the replacement zone. Despite also being a phosphate, this particular florencite $[REE^{3+}Al_3(PO_4)_2(OH)_6]$ shows no sign of

78

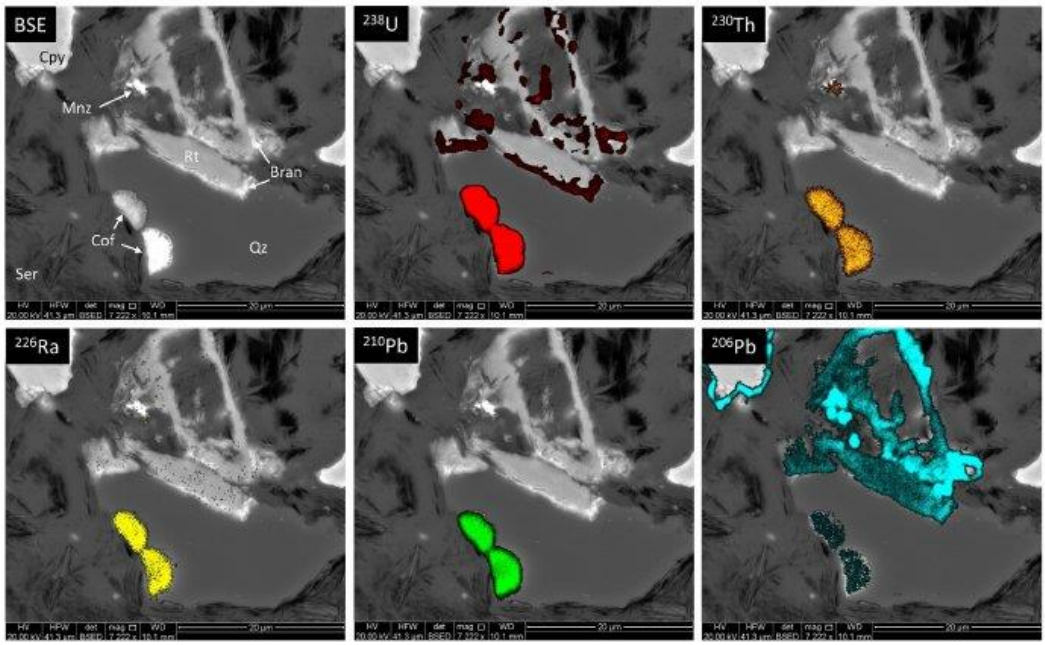

Fig. 2. BSE images with overlays of nanoSIMS isotope maps (masses 238, 230, 226, 210 and 206) for grain 05CLD25 (leached flotation concentrate). Rutile (Rt) with surficial alteration to brannerite (Bran) and globular coffinite (Cof) are hosted in a matrix of quartz (Qz) and sericitic mica (Ser). One small inclusion of monazite (Mnz) abuts the rutile. Coffinite hosts the entire ^{238}U decay chain, although the ^{206}Pb concentration is quite low. Brannerite, however, contains only ^{238}U and ^{206}Pb, excluding the rest of the chain. Monazite shows elevated ^{230}Th and ^{206}Pb; the lead also resides throughout the rutile and along grain boundaries between chalcopyrite (Cpy) and sericite.

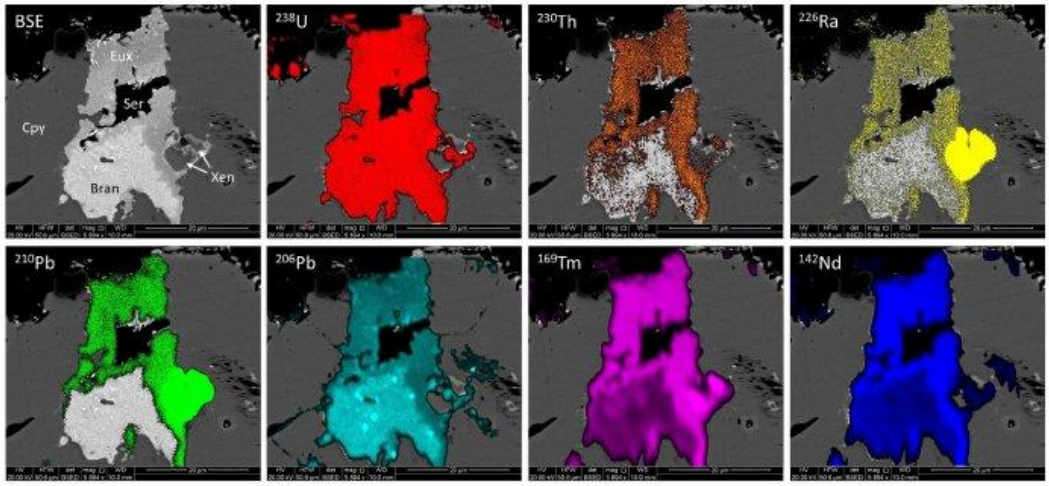

Fig. 3. BSE images with overlays of nanoSIMS isotope maps (masses 238, 230, 226, 210, 206, 169 and 142) for grain 10FC76 (flotation concentrate). Mottled euxenite/brannerite (Eux, Bran) fill within chalcopyrite (Cpy), associated with sericite (Ser) and xenotime (Xen). Brannerite hosts ^{238}U and ^{206}Pb (with sub-micron inclusions of galena), as well as minor rare earth metals. Euxenite accomodates the entire ^{238}U chain and substantial rare earths, both LREE and HREE. Xenotime (enriched in ^{169}Tm but devoid of ^{142}Nd) preferentially hosts ^{226}Ra and ^{210}Pb and is barren with respect to the rest of the decay chain.

79

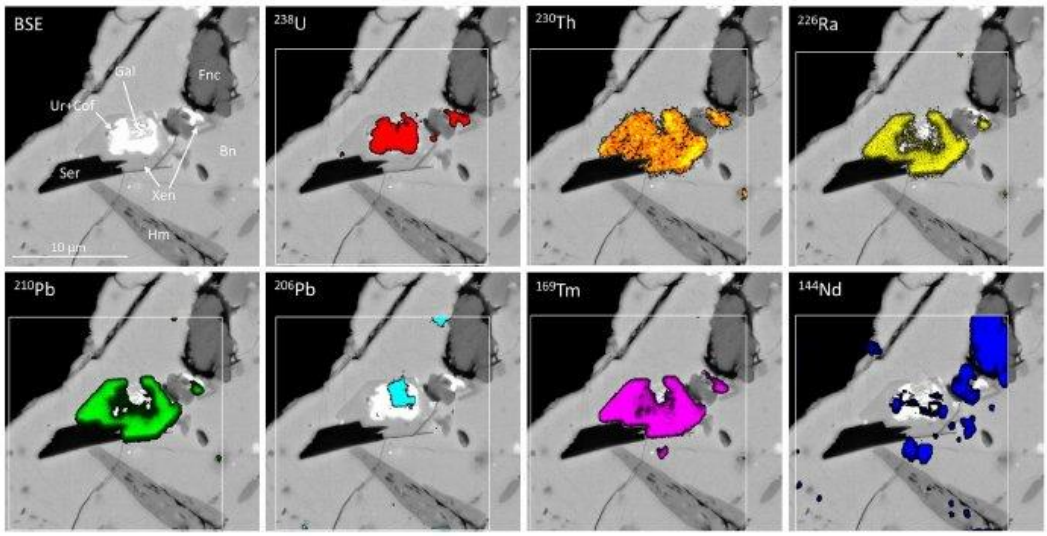

Fig. 4. BSE images with low energy nanoSIMS isotope overlays (masses 238, 230, 226, 210, 206, 169 and 144) for grain 10FC06 (flotation concentrate). NanoSIMS maps are 20 × 20 µm in size instead of the usual 50 × 50 µm, and a 12 pA ion current was used for all maps. Euhedral xenotime (Xen) is replaced by an intergrowth of coffinite/uraninite/galena (Cof, Ur, Gal) in a matrix of bornite (Bn), with associated hematite (Hm), sericite (Ser), and florencite (Fnc). Dissociation among radionucludes is observed, with only ^{226}Ra and ^{210}Pb exhibiting coincident behaviour in favouring xenotime. ^{238}U is almost exclusively found in the replacement uraninite/coffinite. ^{230}Th resides throughout the uraninite/coffinite and in xenotime. ^{206}Pb is most enriched in the sub-micron galena blebs inside the zone of replacement, but is also found at low concentrations throughout the xenotime and bornite (below contrast limit of image). Xenotime demonstrates a clear preference for HREE over other phases present. Xenotime is highly enriched in ^{169}Tm but virtually devoid of ^{144}Nd.

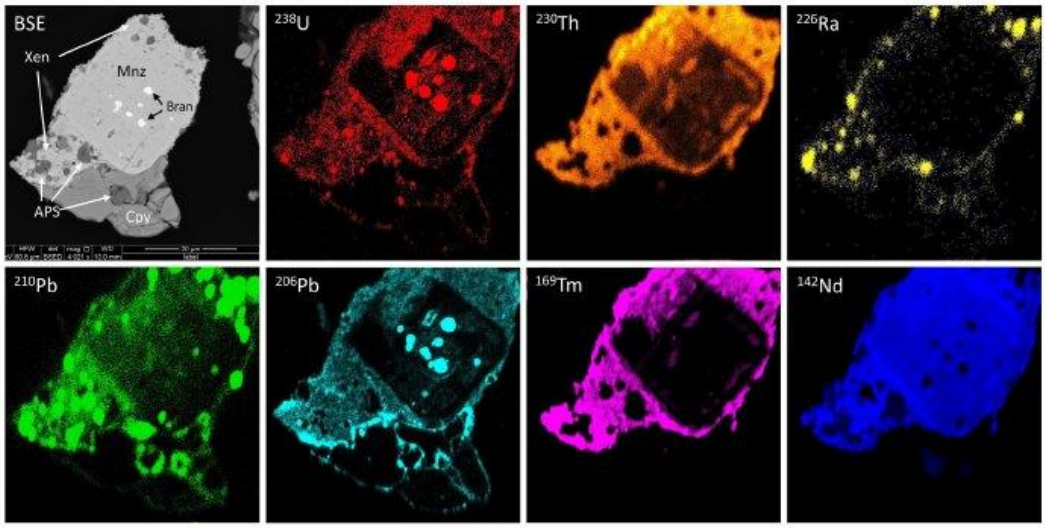

Fig. 5. BSE image and correlated nanoSIMS isotope maps (masses 238, 230, 226, 210, 206, 169 and 142) for grain 05CLD58 (leached flotation concentrate). Relatively coarse monazite (Mnz) with inclusions of brannerite (Bran) has accumulated a complex xenotime/chalcopyrite (Cpy)/APS/hematite (Hm) agglomerate coating. The nearly-square core monazite crystal contains little RN other than ^{238}U, likely the result of effusion from included brannerite. In comparison, the agglomerated xenotime is relatively enriched in U, Th, Pb, and HREE. Small granules of an APS-phase have accumulated a majority of the Ra and ^{210}Pb.

80

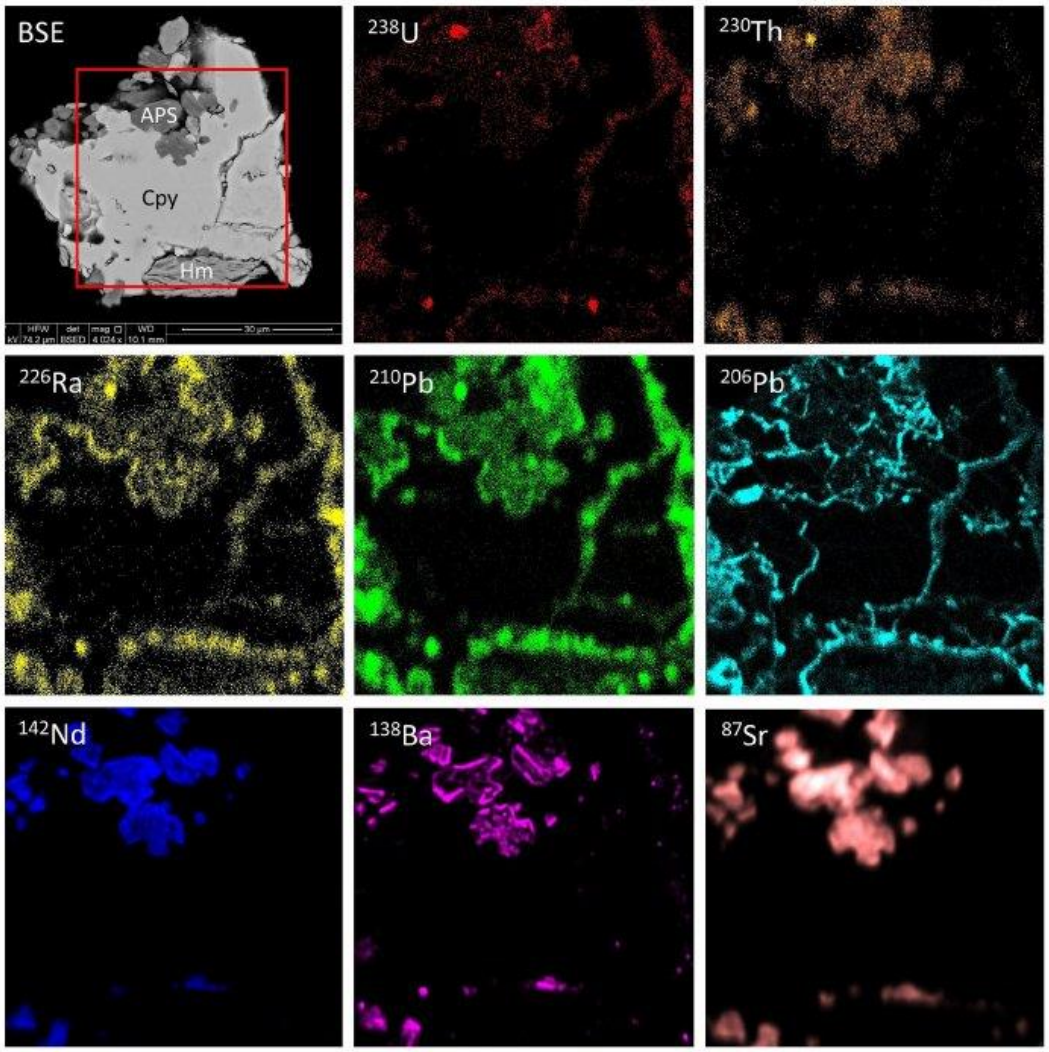

Fig. 6. BSE image and nanoSIMS isotope maps (masses 238, 230, 226, 210, 206, 142, 138, 87) for grain 05CLD19 (leached flotation concentrate). The zoned aluminum sulphate-phosphate (APS) phases at Olympic Dam commonly contain dominant Sr (mass 87) but are also markedly enriched in Ba (mass 138) and REE (represented here by mass 142). A few sub-micron, uranium-bearing phases can be seen in the ^{238}U map, but there appears to be no U within the APS phase. ^{230}Th, ^{226}Ra, and ^{210}Pb are all enriched in the APS. ^{206}Pb shows evidence of an association with annealed fracturing in chalcopyrite (Cpy) and is also found at grain boundaries. ^{206}Pb has not, however, accumulated within any phase in the mapped area. Hm-hematite.

accumulating RNs.

REE-bearing phases are commonly found together (although not necessarily in equilibrium) at OD, but do not appear to sequester RNs to the same extent. A relatively coarse (25 × 25 μm), roughly euhedral monazite (included by a half-dozen brannerites) has accumulated an agglomerate coating comprised of xenotime and aluminum-sulphate-phosphate (APS) phases (Fig. 5). Several APS phases exist at Olympic Dam and can be classified as Ca-, Sr-, and REE-enriched members of the alunite series (Owen et al., 2019). Of similar grayscale tones in the BSE image, the two REE phases may easily be distinguished by their ability to incorporate RNs as well as HREEs, represented by ^{169}Tm. There is a clear preference for xenotime by ^{238}U, ^{230}Th, and ^{206}Pb, whereas the monazite contains only ultra-trace amounts of ^{230}Th and ^{210}Pb. The RNs ^{226}Ra and ^{210}Pb are found predominantly in the APS minerals, with lower (but still elevated) concentrations also present throughout the xenotime – but little to none in monazite. Brannerite again hosts only the two end members of the decay chain.

Although comprising only ~0.1 wt% of the overall deposit (Ehrig et al., 2012), a proportion of APS phases report to concentrate – and are even augmented by formation of new material during the sulphuric acid

81

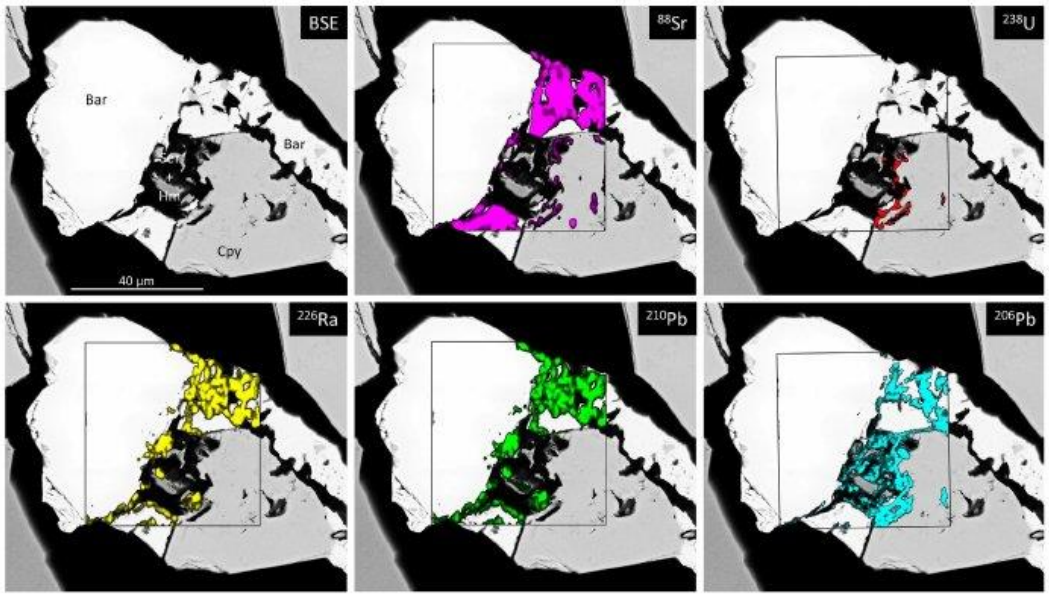

Fig. 7. BSE images with nanoSIMS isotope overlays (masses 88, 238, 226, 210, 206) for grain 05CLD23 (leached flotation concentrate). Coarse baryte (Bar) and chalcopyrite (Cpy) grains are cemented by a finer-grained, secondary baryte with hematite/sericite (Hm, Ser). Although the coarser baryte is barren of Sr and RNs, the secondary baryte is enriched in ^{226}Ra, ^{210}Pb, and ^{88}Sr. Evidence of coupled dissolution-reprecipitation (abundant porosity) is observed in the baryte fill, which has experienced uptake of other sulphate-insoluble cations. ^{206}Pb is also found in edges and grain boundaries of the secondary baryte, but preferentially resides in chalcopyrite and fractures within.

leach stage – and can attain > 0.80 wt% in final concentrates. The conspicuous ability of these phases to host RNs has been presented previously (Owen et al., 2019; Rollog et al., 2019a, 2019c), but deserves mention here among other major RN hosts. The compositionally heterogeneous, zoned APS phases are REE- and alkaline earth metal-rich, as shown in the ^{142}Nd, ^{138}Ba, and ^{87}Sr maps (Fig. 6). A few submicron grains of uraninite can be seen in the ^{238}U map, and correlate with similar spots of enrichment for the daughter isotopes. ^{230}Th, ^{226}Ra, and ^{210}Pb show a clear preference for the APS phase, and also appear as spotty concentrations in fracture fill and along grain boundaries. ^{206}Pb shows possible evidence of annealed fractures in chalcopyrite and can be observed along APS grain edges, but not within the APS crystals.

3.3. Sulphates

In addition to APS minerals, simple sulphates are commonly found associated with copper-iron sulphides. Baryte is prevalent at Olympic Dam, representing ~1.2 wt% of the deposit (Ehrig et al., 2012), with an average 0.3 wt% remaining in concentrate after flotation and acid-leaching. Significant fracturing is common in barytes examined in this study due to grinding-induced breakage along cleavage planes.

Two types of baryte predominate: large, inclusion-free, roughly euhedral grains, and porous, anhedral baryte containing abundant inclusions of other minerals. Examples of both are present in Fig. 7, showing large baryte and chalcopyrite crystals cemented with secondary baryte, sericite, and hematite. The secondary baryte shows a history of coupled dissolution-reprecipitation (CDR) in the form of porosity, and contains significant amounts of ^{226}Ra, ^{210}Pb, ^{206}Pb, and Sr (to 3 wt%, per EDS analysis). The small spots of ^{226}Ra and ^{210}Pb which appear to be in the hematite/sericite are in fact small inclusions of baryte. Uranium appears only in fractures in the chalcopyrite, and ^{230}Th has no presence at all (not pictured).

It may be expected that grains which have undergone sulphuric acid leaching, as in Fig. 7, exhibit characteristics resulting from the leach, and not from natural processes in the deposit. It can be seen in Fig. 8, however, that similar processes do in fact occur within the deposit. MR11-4b is a polished core sample, analysed in similar fashion to the concentrate samples, which clearly shows elevated concentrations of ^{226}Ra and ^{210}Pb in baryte with no correlating signals from other members of the decay chain. Inclusions in the baryte fill are concentrated around the edges, as can be seen on both the BSE image and in the ^{206}Pb nanoSIMS map. Porosity accompanies these inclusions, suggesting that CDR has affected the outer regions of these grains but left the interiors relatively pore- and inclusion-free. Although the ^{226}Ra and ^{210}Pb distributions do not closely mimic those of ^{206}Pb, all three show elevated responses only near interior edges of the baryte. Coffinite, in contrast, only hosts the top of the decay chain here, with daughters below ^{230}Th absent.

A key component of this research is the distinction between FC samples and CLD samples, which aids metallurgists in determining which chemical mechanisms occur naturally in the deposit and which are a result of processing. The sulphuric acid leach has a profound effect on mineral chemistry (Bhargava et al., 2015; Gilligan and Nikoloski, 2015) and may both help and hinder the removal of RNs from copper concentrate. Significant reduction of U and Th by sulphuric acid leaching is inexpensive and efficient, but sulphate-dominated kinetics may trigger the simultaneous precipitation of Ra- and Pb-bearing phases. Anglesite is absent in the Olympic Dam deposit and is therefore missing in earlier overviews of ore mineralogy (Ehrig et al., 2012). It is, however, observed as an (anthropogenic) by-product of sulphuric acid leaching. In Fig. 9, the presence of substantial ^{238}U in the heavily corroded-looking anglesite suggests it may have been a uranium phase

82

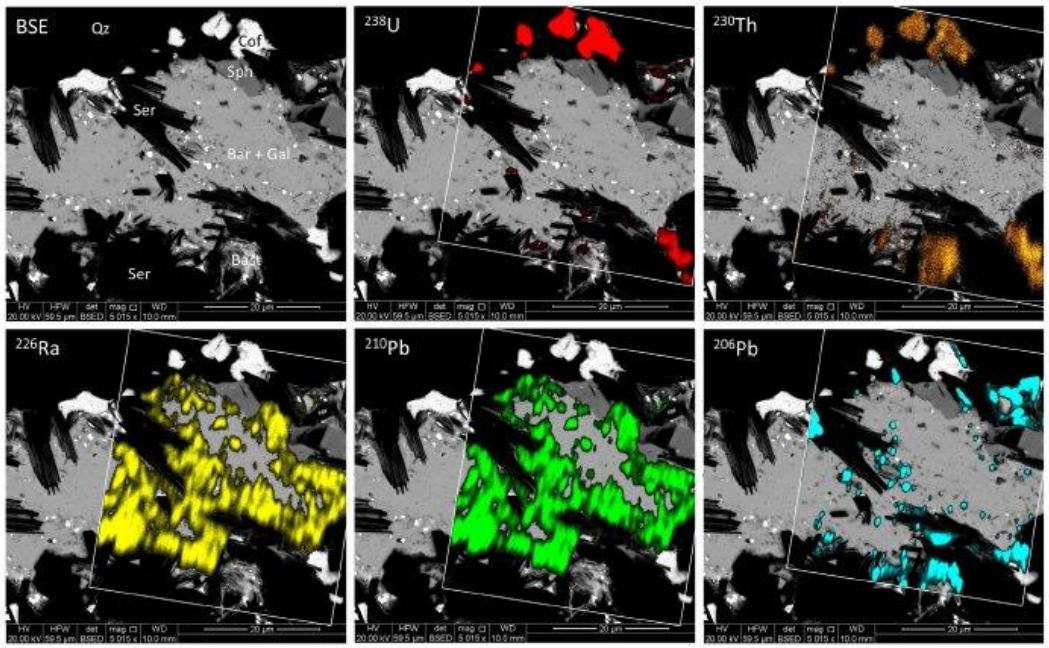

Fig. 8. BSE images with nanoSIMS isotopic overlays (masses 238, 230, 226, 210, 206) for drill core sample MR11-4b. Porous baryte (Bar)with abundant inclusions fills a predominantly quartz-sericite (Qz, Ser) matrix. Minor sphalerite (Sph), coffinite (Cof) and bastnäsite (Bast) are associated phases, with numerous galena (Gal) inclusions throughout the baryte. Coffinite hosts only the upper part of the decay chain, whilst baryte contains only ^{226}Ra and ^{210}Pb.

which has dissolved away, leaving behind sulphate-insoluble ^{206}Pb with incorporated residual U. The correlation between ^{226}Ra and ^{210}Pb distributions and anglesite supports this argument, as do the nearly identical distributions for other insoluble sulphate-forming alkali earths, Sr and Ba. The lack of ^{230}Th in acid-formed anglesite would be expected, as is it neither sulphate insoluble nor sufficiently abundant in uranium phases (^{238}U:^{230}Th ≈ 60,000, assuming secular equilibrium) to be trapped by precipitating sulphates. Note also that ^{206}Pb intensity is significantly higher in the "new" anglesite than in "old" galena, indicating a ^{206}Pb-rich lead source (i.e. ^{238}U-derived) during anglesite formation, compared to ^{206}Pb-poor lead isotope ratios during galena formation – reminiscent of *global* lead isotope ratios of which ^{206}Pb represents < 25%.

4. Discussion

The presence of radionuclides in uranium minerals or of radium in baryte is of no great surprise. Even at Olympic Dam, where fine-grained textures prevent conventional radionuclide analyses of mineral separates and at the grain scale, the deportment of daughter isotopes may be largely predicted with a high degree of accuracy by chemistry alone. Practical experience, however, is that behaviour predicted is not always behaviour observed. Although U and Th are significantly separated from copper minerals during acid leaching of flotation concentrates, ^{226}Ra, ^{210}Pb and ^{210}Po are still found at relatively elevated concentrations in the final leached concentrates. "Elevated", in this case, refers to above the aforementioned 27 ppt, 380 ppq and 6 ppq, respectively, diminishing any chance of detection except through bulk analyses. The value of this study lies in the ability of the nanoSIMS platform to detect low (to ppb) levels of ^{210}RN in individual mineral grains, thereby informing metallurgists which minerals should be given additional consideration when engineering a strategy to generate concentrates with extremely low concentrations of ^{210}RN.

Sulphide minerals are, obviously, by far the dominant minerals within copper concentrates. The crystal structures of Cu-(Fe)-sulphides do not support incorporation of lattice-bound U, daughter RNs, or lead – whether radiogenic or not (Moggi-Cecchi et al., 2002; Cook et al., 2011; George et al., 2018). Traces of lead may nevertheless be routinely measured although this would appear to be from nanoparticles of discrete minerals rather than lattice-bound substitution (Cook et al., 2011; George et al., 2018). This important observation that Cu-(Fe)-sulphides are not, in themselves, hosts for RNs is backed up by extensive NanoSIMS mapping of Cu-(Fe)-sulphides in the present study. Cu-(Fe)-sulphides can, however 'host' RNs within pores, sealed microfractures and at grain boundaries (Rollog et al., 2019d), a phenomenon critical to understanding RN deportment in copper concentrates, and an important consideration when developing processing strategies designed to remove them. Furthermore, most Cu-(Fe)-sulphides also contain low levels of ^{206}Pb (e.g., Figs. 1 and 6). This can be readily related to remobilisation of radiogenic lead from their primary hosts and reaction with available S or Se to form new, nanoscale Pb-chalcogenide phases (Owen et al., 2018).

Nearly all uraninites in this study retained the entire decay chain, regardless of morphology or age. This seems to be at odds with uraninite solubility, which has been shown to be significant (Grandstaff, 1976; Ram et al., 2013; Bhargava et al., 2015). Dissociation within uraninites has been reported (Ludwig, 1977, 1978; Martz et al., 2019), indicating a high potential for mobility of daughter isotopes independent of the parent. Age is a critical factor, however, as secular equilibrium between ^{238}U and all daughter isotopes is approximated after only 500 ky and attained by about 1.2 My. Since only the presence or absence – and not exact concentrations – of radionuclides are

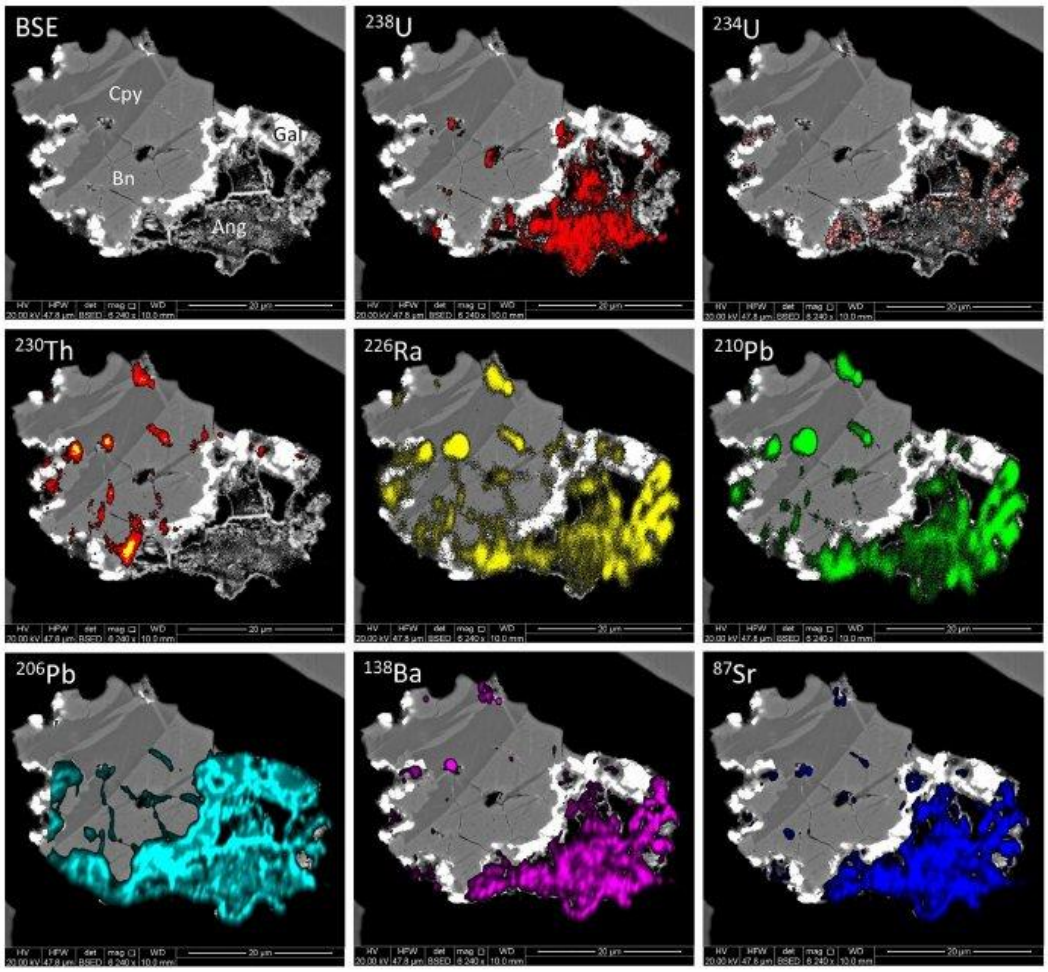

Fig. 9. BSE images with nanoSIMS isotope overlays (masses 238, 234, 230, 226, 210, 206, 138, 87) for grain 10CLD61 (leached flotation concentrate). As a result of sulphuric acid leaching, galena (Gal) and possibly a uranium-bearing phase have been partially replaced by anglesite (Ang), associated with chalcopyrite (Cpy) and highly fractured bornite (Bn). No radionuclides are found in the unaffected galena, but the new-formed anglesite, as well as fractures in the bornite, are relatively enriched in ^{226}Ra and ^{210}Pb, and to a lesser extent, also ^{230}Th. Residual ^{238}U and ^{234}U in the anglesite may be the result of incomplete dissolution of a U-bearing phase, or incorporation of trace amounts of U from the leach solution into anglesite during precipitation. Note that the galena is actually less enriched in ^{206}Pb than anglesite, indicating a difference between an isotopically balanced source of Pb during galena formation, and a ^{206}Pb-enriched source during anglesite formation.

provided by nanoSIMS, slight differences in, for instance, ^{234}U/^{238}U ratios are not obvious. Deviations from secular equilibrium in uraninites from the ~1590 Ma Olympic Dam deposit are more likely to be caused by hydrothermal alteration or oxidative ground waters than by extreme youth.

The major portion of RNs in the ore is contained within minerals containing essential U and is removed during acid leaching, even if the three uranium minerals dissolve at vastly different rates, brannerite being the most difficult (e.g. Gilligan, 2017). NanoSIMS maps show that most uranium minerals (except brannerite) retain all members of the ^{238}U decay chain. This is also true of several other refractory minerals in Olympic Dam containing minor concentrations of uranium, notably hematite, apatite and zircon, a phenomenon facilitating direct application of precise U-Pb geochronology to date these hydrothermal minerals in order to establish the age of the deposit (Ciobanu et al., 2013; Courtney-Davies et al., 2016, Courtney-Davies et al., 2019; Apukhtina et al., 2017). Isotopic heterogeneity within some mineral grains is nevertheless evidence for isotope migration within the mineral lattice (e.g., grain-scale isotope ratio maps for hematite in Courtney-Davies et al., 2019). The same applies to many other minerals which easily incorporate minor amounts of uranium (e.g., euxenite, thorianite, HREE minerals); these also generally host the entire decay chain.

During ore processing, however, the acid leach process resets the equilibrium clock to zero and allows the eight primary (and three secondary) elements in the decay chain to obey their own individual thermodynamic rules. The high solubility of uraninite in sulphuric acid

84

precludes survival of residual, partially leached uraninite, in which some decay chain isotopes have been selectively removed, effectively rendering "acid-derived dissociation" moot; uraninite and other primary uranium minerals identified in CLD samples are assumed to have been fully locked (e.g. not accessible) from the acid solution (e.g. coffinite in Fig. 2). This does not exonerate *(re)-precipitation*-derived dissociation, however, as there is significant evidence for separation of decay chain elements through chemical precipitation processes. Some phosphates can accumulate members of the chain, frequently from ^{230}Th down, likely driven by the insolubility of $ThPO_4$. Similarly, sulphates tend to retain only sulphate-insoluble members (Ra, Pb, Po), with the upper part of the decay chain pointedly absent.

It should be noted that other REE minerals (bastnäsite, synchysite), other phosphates (florencite), and sulphates (anhydrite) were also analysed but were found to contain negligible radionuclides, suggesting that the presence of these specific cations or oxyanions alone is insufficient to promote significant accumulation of RNs.

4.1. Host minerals for daughter products of uranium decay

The literature provides some insights into the presence of individual daughter isotopes in specific minerals, but virtually none relates specifically to the mineral assemblages present in Olympic Dam ores and processing products due to difficulties in obtaining mineral separates on such fine-grained ore. In-depth studies of Olympic Dam uraninite, coffinite, and brannerite have been done (Ehrig et al., 2012; Macmillan et al., 2016a, 2016b, 2017) but only total U, Pb and Th were analysed, without isotopic abundances. Much work has been done regarding deviations from secular equilibrium in the ^{238}U chain in geological samples, predominantly from an age dating perspective. Uranium ratios in bulk sediments (DePaolo et al., 2006; Dosseto et al., 2008), crystalline rocks (Rosholt, 1983), and of irradiated minerals (Fleischer, 1980) have been investigated revealing slight dissociative effects resulting from alpha recoil or selective leaching through alpha-track etched pathways, but these mechanisms are usually limited to grain-surface or near-grain-surface boundaries. While slight deviations from secular equilibrium may have a significant effect on calculated ages, they are minor compared to the dissociations seen by nanoSIMS mapping whereby members of the decay chain are entirely present or absent in the minerals observed. With regard to nanoparticles, however, recoil effects may be considerable (Rollog et al., 2019d).

Investigation of radium uptake by baryte began almost a century ago (Germann, 1921; Doerner and Hoskins, 1925) and continues today as rapid advances in micro- and nano-analytical techniques provide insight into the complex mechanisms at work at the molecular level (e.g. Ceccarello et al., 2004; Curti et al., 2010; Hedström et al., 2013; Klinkenberg et al., 2014; Zhang et al., 2014; Brandt et al., 2015; Brandt et al., 2018; Vinograd et al., 2018a,b). Cationic substitution (e.g. Sr) in baryte has been shown to promote Ra uptake (Vinograd et al., 2018b), and has also been shown to inhibit Ra uptake (Ceccarello et al., 2004; Brandt et al., 2018). This discrepancy can be explained by the concentration of Sr^{2+} incorporated into the baryte and activity of Sr^{2+} in the solution. A high Sr/Ba ratio in the crystal structure can shrink the overall molar volume, making accommodation of the large Ra^{2+} ion increasingly difficult. Low Sr/Ba ratio, however, can actually promote uptake by creating gaps in the $BaSO_4$ structure into which Ra^{2+} may fit. Modelling studies have determined that optimal Ra uptake occurs in baryte with 5–10 mol% $SrSO_4$ (Vinograd et al., 2018a,b). Fig. 7 clearly shows a correlation between ^{226}Ra uptake and the presence of Sr in baryte, with the Sr-rich baryte high in ^{226}Ra (and ^{210}Pb, either through similar processes or via decay only) while the Sr-free baryte is barren of RNs.

Lead substitution into the baryte structure also affects Ra uptake. Hokutolite is a natural plumbian baryte which – in Japanese and Taiwanese hot spring samples – ranges from 0.87 to 24.4 mol% Pb and 0.21 to 4.8 mol% Sr (Sasaki and Minato, 1982). The Pb-enriched samples (Ba/Pb mol ratio 1–2.7) can incorporate ~30–85 Bq/g of both ^{226}Ra and ^{210}Pb, the average activity ratios of which roughly suggest secular equilibrium (Momoshima et al., 1997). Ra activity in hokutolite is positively correlated with $(Ba/Pb)_{molar}$ ratios (Chao et al., 2009), suggesting that the optimal Ra incorporation in $(Ba,Pb)SO_4$ may occur at very low Pb concentrations – although the lowest Pb concentration of the samples measured was 0.31 mol%.

LA-ICP-MS analyses of 34 FC samples and 38 CLD baryte samples from Olympic Dam yielded concentrations averaging 0.78 mol% $SrSO_4$ and 0.011 mol% $PbSO_4$ (Schmandt et al., 2019a, 2019b). Although low on average, respective *maximum* values were in fact 4.6 mol% and 0.68 mol%, with $SrSO_4$ in vein baryte exceeding 7.5 mol%. Both ranges for [Sr] and [Pb] in Olympic Dam baryte overlap the calculated ideal windows for high uptake of Ra.

Pure anglesite can uptake significant amounts of Ra in low-pH, low $[SO_4^{2-}]$ conditions through CDR (Rollog et al., 2019e) and has been calculated to hypothetically enrich Ra up to 35 times more than baryte and > 11,000 times more than celestite (Langmuir and Riese, 1985). Anglesite is rare in the Olympic Dam system (Ehrig et al., 2012) but is fairly common as a replacement product in acid-leached concentrate (Fig. 9). Dissolution of a uranium phase (likely containing significant lead) followed by precipitation of $PbSO_4$ in its place occurred in just a matter of hours in the sulphuric acid leach tank. The presence of residual U is likely due to the trapping of it (and other major solutes) during the very quick precipitation of anglesite. Both ^{226}Ra and ^{210}Pb are elevated, as are Ba and Sr. The Pb maps are of particular interest, as they show the newly formed anglesite to be much higher in ^{206}Pb compared to the neighbouring galena, while the galena is barren of ^{210}Pb. This would make sense if the primary galena had formed from a lead source representative of global abundances (currently ~24% ^{206}Pb, ~22% ^{207}Pb, and ~52% ^{208}Pb, but would have been lower in ^{206}Pb 1600 Ma ago during initial ore formation), and had lost all of its ^{210}Pb through decay. Such a hypothesis is also consistent with the presence of both radiogenic and non-radiogenic lead at Olympic Dam (Schmandt, 2019). The newly formed anglesite, in contrast, precipitated from a high-^{206}Pb solution (from U-phase dissolution) and incorporated other insoluble sulphates such as Sr, Ba, Ra and ^{210}Pb during crystallization.

Tetragonal xenotime and orthorhombic monazite are both known to host Th (Ault et al., 2016; Agarwal et al., 2017) and can contain U (Vallini et al., 2007), although only xenotime shows RN enrichment in Olympic Dam samples. Some OD xenotimes show enrichment in only ^{226}Ra and ^{210}Pb (Fig. 3, similar to the uptake seen in sulphates) while others are also high in Th (Figs. 4 and 5). Monazite in igneous and metamorphic rocks preferentially accumulate Th, with xenotime hosting significantly less (Hetherington et al., 2010). The exact opposite seems to be the case for OD sulphide ore, as seen in Fig. 5.

4.2. Retention mechanisms

The ability of a mineral to retain daughter radionuclides, or trace elements of any sort, depends on crystal structure and lattice energies, microfractures or other lattice imperfections, local or global charge imbalances, the extent of cationic and anionic substitution (discussed above), particle or crystal size and shape, and recoil mechanisms relating to specific isotopic decays.

Estimated lattice energies for uraninite, coffinite, and brannerite are 12,199, 24,931, and 38,648 kJ/mol, respectively (Institute of Experimental Mineralogy: Internet Database, 2019). Although coffinite and brannerite should be less accessible than uraninite, they are almost always found in a metamict state (Zhang et al., 2006; Charalambous et al., 2012; Lumpkin et al., 2012) which renders them more susceptible to acid decomposition. Although the most soluble of the three, uraninite has the ability of rapid self-annealing (Eyal and Fleischer, 1985) which minimises the effects of radiation damage-induced leaching. Alpha and beta decay not only directly cause damage to crystal lattices but may

also create local charge imbalances which alter stability potentials. During the decay of $^{238}U^{6+}$, for example, the newly formed $^{234}Th^{4+}$ may travel around 30 nm through a coffinite matrix (Hashimoto et al., 1985) before coming to rest. The force and speed of this relocation causes electrons to be stripped off the formerly complete $6s^2\ 5p^6\ 5d^{10}\ 4f^{14}$ outer shell, resulting in an electron-deficient ion and an electron-enriched region (i.e. lattice damage) along the path of recoil. Stabilising this ion by commandeering electrons from the surrounding electron field causes local charge imbalances and reorganisation of the crystal lattice to a non-ideal arrangement (metamictisation).

Metamict textures are generally less stable than ordered crystalline matrices. Six primary rock-forming minerals showed a decrease in density when converted to a metamict state by electron bombardment (Maruyama and Muto, 2016). Natural zircons showed a 10% loss in density from natural alpha decay damage (Murakami et al., 1991), and theoretically may reach 16% reduction (Holland and Gottfried, 1955). The decrease in density results in an increase in average bond length, and consequently a decrease in average bond strength. Dissociation energies are reduced as it becomes easier to break bonds, and solubility increases. As fluids pass over metamict or alpha-track-etched samples, the leaching of some RNs but not others due to the stability of individual elements with respect to the given fluid composition may result in RN imbalances.

4.3. Behaviour of different minerals and causes of fractionation

Detection of the entire ^{238}U decay chain in uranium minerals – regardless of age – is of no surprise due to the relatively quick re-establishment of secular equilibrium (< 2.5 Ma), but there exist subtle differences in the ability of the crystal structures of the various uranium- and thorium-bearing minerals to retain individual daughter products. For short half-life daughters (e.g., ^{210}Bi, half-life 5 days), mobilisation and relocation to another host mineral may not be possible, regardless of the compatibility of the host structure (the exception being gaseous ^{222}Rn which can readily escape from highly fractured or porous structures; Baskaran, 2016). In contrast, there is ample opportunity for longer-lived radionuclides to be remobilised following their incompatibility-related expulsion from the parent structure, selectively leached out in the presence of fluids, or via other means of fractionation through alpha recoil, coupled dissolution-reprecipitation, and/or diffusion.

In most cases where the full decay chain is not represented on the nanoSIMS images, a simple explanation exists for the dissociation. For example, baryte hosting only Ra, Pb, and (likely) Po (Figs. 7 and 8) may be attributed to sulphate insolubility. Coffinite, which sometimes contains only U and Th but no lower members of the chain (Fig. 8), may be charge-dependant; as RN-rich fluids flowed through a quartz-sericite-baryte matrix the $U^{+4,+6}$ and Th^{+4} combined with quartz to form coffinite and thorianite and all of the M^{+2} elements accumulated in the much more accommodating baryte.

One pertinent finding of the present work is that brannerite generally contains only U (sometimes trace ^{230}Th) and ^{206}Pb and is frequently 'missing' many intermediate members of the decay chain. Brannerite at Olympic Dam ranges from uraniferous rutile to nearly stoichiometric UTi_2O_6. Petrographic and compositional data suggest that at least some brannerite is the result of alteration of primary uraninite at some stage after deposit formation with much of the remainder forming from U-rich fluids interacting with rutile (Macmillan et al., 2017). The crystal structure of brannerite resembles that of anatase (Szymanski and Scott, 1982) and has been shown to contain < 2 wt% Pb (Macmillan et al., 2017). Thorium concentrations in brannerite can vary, with reports of 8–10 wt% indicating solid solution between brannerite and thorutite (Charalambous et al., 2012); however, Macmillan et al. (2017) found a maximum of only 1.38% in 395 analyses from 17 Olympic Dam samples. NanoSIMS maps generally show only ^{238}U and ^{206}Pb in mapped brannerites, with occasional traces of ^{230}Th (Figs. 2, 3, and 6). Alpha recoil alone cannot explain the conspicuous lack of intermediate isotopes throughout the crystals, which are generally larger than 1 μm. Selective leaching via alpha-track etched pathways is possible but does not fully explain the presence of ^{206}Pb but lack of ^{210}Pb, or, indeed, the uniform distributions of the isotopes which remain. Relatively recent formation of brannerite via reaction between mobilised uranium with rutile or ilmenite, and incorporation of modest amounts of mobilised Pb (present along with U), may explain this anomaly. Logic dictates that the incorporation of U, trace Th, and ^{206}Pb into newly-formed brannerite would be simpler than removal of ^{230}Th, ^{226}Ra, and ^{210}Pb from old brannerite. Mobilisation and removal of Pb and Ra would require a complexing agent (e.g., Cl^- or an organic ligand) – which would likely also complex with U and Th. Dissolution of uraninite would release both U and Pb (overwhelmingly ^{206}Pb) into solution. Primary uraninites from Olympic Dam commonly contain 17–18 wt% Pb, although as little as 2 wt% has been found in younger, massive uraninite (Macmillan et al., 2016a). Incorporation of Pb would likely occur, at least to some extent, in newly-formed brannerite. Even if other RNs are solubilized with the U and ^{206}Pb, they may either remain in solution or incorporate into the brannerite in such low concentrations as to be below the detection limits of nanoSIMS.

Coffinite, like brannerite, has been inferred to be of various ages and often the result of either late-stage replacement of uraninite, or 'new' coffinite formed after uranium remobilisation (Macmillan et al., 2017). Examples illustrated here reflect this heterogeneity in composition and age, showing either the entire decay chain (Fig. 2), or just U and Th, without the lower members (Figs. 5 and 8). The distinction here may largely be time-related, with older coffinite replacing quartz as a secondary process but still having occurred on a geological timescale of millions of years. Secular equilibrium is re-established, and as long as the coffinite grains exceed 1 μm in diameter they should retain the majority of daughter isotopes. In contrast, new coffinite would likely not contain much, if any, Ra or Pb since these do not comfortably fit into the silicate structure.

4.4. Time constraints, kinetics and diffusion during processing

The three types of sample analysed (drill core samples, flotation concentrate, concentrate leach discharge) provide information related to chemical processes occurring on different time scales. Diamond drill core samples are relatively fresh and uncorrupted other than during cutting and polishing, and should retain signatures of natural ore-forming processes and evolution thereof over geological time. Flotation samples have been milled, ground, and have undergone sulphide upgrading by froth flotation. Any impact on these samples from interaction with flotation agents should be minimal, with RNs remaining in secular equilibrium during froth flotation.

The greatest change, by far, is seen in the acid-leached flotation concentrates (CLD). Partial to complete dissolution of uranium species, rare earth minerals, carbonates, fluorite, hematite, and various other acid-soluble minerals occurs in a matter of hours. Precipitation of acid-insoluble sulphates occurs either simultaneously as nanoparticles or within a very short time window through coupled dissolution-reprecipitation. Dissociation of radionuclides becomes commonplace, as even short-lived radionuclides will behave according to their elemental thermodynamic properties – and not reside solely where the parent isotope accumulates. Release of gaseous ^{222}Rn should be facilitated, as escape into solution is far less energetic than forcing its way out of (even heavily damaged) crystal matrices.

Uranium and thorium sulphates are acid-soluble and are therefore removed quite efficiently during this process. Radium, lead, and polonium, however, form sulphates which are insoluble in sulphuric acid and immediately seek out a mechanically or chemically stable environment. Mechanical processes may include electrostatic "filtration" through high surface-area or high-cleavage minerals (e.g. chlorite,

Table 1
Data for selected minerals from Olympic Dam. % ore = concentration in the deposit (10,000 sample MLA dataset; Ehrig et al., 2012). Columns % FC and % CLD represent mineral proportions in the +53 μm size fraction of flotation concentrate (FC) and concentrate leach discharge (CLD) as determined by MLA. Data for specific isotopes are qualitative only, with "+" representing a major host, "+" representing a minor host, and "v" representing variable hosting capabilities. Empty cells represent little to no hosting capability.

Mineral	% ore	% FC	% CLD	^{238}U	^{230}Th	^{226}Ra	^{210}Pb	^{206}Pb
Uraninite	0.0049	0.446	0.053	+	+	+	+	+
Brannerite	0.0119	0.272	0.144	+	v			+
Coffinite	0.0159	0.321	0.086	+	+	+	+	v
Xenotime	0.0045	0.023	0.030		+	v	v	
Monazite	0.0184	0.058	0.123		+	+	+	
APS phases	0.1097	0.958	0.879			+	+	+
Baryte	1.2252	0.909	1.303			+	+	+
Anglesite	N/A	0.0	Unknown			+	+	+

sericite, molybdenite, covellite), trapping within microfractures or micropores (^{206}Pb in Figs. 6 and 9), or accumulating on mineral surfaces (especially sulphides) which have experienced a surficial charge-imbalance caused by the acid solution (^{206}Pb on the surface of chalcopyrite in Fig. 5, and Rollog et al., 2019d). Chemical sequestration of these lower members of the decay chain is also possible through CDR mechanisms. In acid-sulphate conditions, mobility of Ba, Sr, and Pb between sulphates is extremely rapid and is dependant predominantly on kinetics and not solubility products (Pina and Putnis, 2001; Rollog et al., 2019b). Radium also follows this trend, and significant uptake into baryte and anglesite occurs within hours at elevated temperatures (Rollog et al., 2019e).

Bulk solid-state diffusion is always present, and increases relative to temperature, but the overall bulk transport of material by diffusion is dwarfed by other mechanisms such as CDR (Putnis, 2002).

4.5. Processing implications

The objective of this study is to provide process engineers with critical information regarding which minerals (or structural features) to target to most efficiently reduce the overall radionuclide load in final concentrates. The results from nanoSIMS analysis of many dozens of mineral types from Olympic Dam ore, including those reported here, will be compiled, classified, and weighted to create an approximate RN budget for the final concentrates. Once complete, this budget will be scrutinised to determine a course of action for potentially modifying and/or adjusting the hydrometallurgy cycle to maximise removal of those minerals deemed to host substantial proportions of RNs based on estimated RN concentrations and mineral abundances. RN removal at Olympic Dam is already quite efficient, with very effective removal of U and Th as well as significant reductions in Ra and Pb. The identification of previously unknown hosts, however, may enable economically feasible modifications to the processing flowsheet that will result in lowering the current RN levels to below the target activities of 1 Bq/g per isotope in final concentrates.

The data in Table 1 are indicative of the results gathered so far in this study. They do, however, also highlight the complexities involved in producing an overall radionuclide budget for Olympic Dam ore or concentrate, as well as the limitations that may need to be placed on the results. The qualitative nature of the nanoSIMS maps precludes accurate calculations of total RN loads for any particular mineral. Mineral concentration data presented were measured by mineral liberation analysis (MLA) on a single size fraction (+ 53 μm), on which the nanoSIMS data were collected, from one sampling date (August 2015). Calculated mineral proportions from MLA data are accurate only above a certain size threshold, so the mineral concentrations in smaller size fractions may be less reliable. Additionally, not all minerals may be accurately identified by MLA, potentially leaving gaps in the budget. Moreover, such a deportment model doesn't readily account for RNs hosted at boundaries between minerals or adsorbed onto mineral surfaces. Last but not least, the geochemical and mineralogical nature of the ore being mined changes constantly, demanding a dynamic budget structure. Despite these obstacles, this study represents a critical first step in accumulating the data necessary for eventual (semi) quantification of radionuclides in Olympic Dam ore for the purposes of process monitoring and control.

Once identified, target RN host minerals may be reduced using standard techniques, customised to the specific mineral constituents in the concentrate being processed. If, for example, there is sufficient evidence for the reduction of sulphates, then a secondary leach involving the complexation of sulphate-insoluble cations (Sr, Ba, Pb, Ra) could be employed. Many possible chelating and complexing agents exist, such as Cl^-, acetate, ethylenediamine tetraacetic acid (EDTA), or any of dozens of other organic compounds – each with variable efficiencies based on temperature, reaction time, and pH. Of course, minimising the loss of copper will also be paramount, so a balance may need to be struck between chemical potentials.

5. Conclusions

NanoSIMS mapping has proven an excellent tool in verifying predicted behaviours of RNs as well as revealing some previously unknown associations. Older (primary) uranium minerals tend to retain daughter radionuclides to varying degrees; maximizing efficient removal during processing will reduce the RN activity of final concentrates and reduce subsequent ingrowth of lighter daughter isotopes. Some uranium minerals are, however, geologically young and may have not yet achieved secular equilibrium. Uranium- and thorium-bearing phases (e.g. xenotime, APS phases) behave similarly to minerals containing essential U and Th and should not be underestimated; minimising these minerals will also reduce the overall RN budget in final concentrates. Sulphate chemistry dominates the uptake mechanisms of Ra and Pb (and likely Po), with baryte and newly-formed anglesite capable of accommodating significant amounts of these RNs. Enrichment of Ra and Pb in sulphates is greatly accelerated during the acid leach stage of processing. Suppression of sulphate precipitation, for example via addition of EDTA or similar complexants, may appreciably reduce ^{226}Ra, ^{210}Pb, and ^{210}Po retention in concentrates.

Declaration of Competing Interest

The authors declare no competing interests.

Acknowledgements

This research is a contribution of the ARC Research Hub for Australian Copper-Uranium (Grant IH130200033), co-supported by BHP Olympic Dam and the South Australian Mining and Petroleum Services Centre of Excellence.

References

Agarwal, S., Kim, H.I., Park, K.H., Lee, J.Y., 2017. Monazite Mineral Processing. In: Mineral Processing Methods, Applications and Technology, Geology, and Mineralogy Research Development. Nova Science, New York, NY, pp. 39–56.
Apukhtina, O.B., Kamenetsky, V.S., Ehrig, K., Kamenetsky, M.B., Maas, R., Thompson, J., McPhie, J., Ciobanu, C.L., Cook, N.J., 2017. Early, deep magnetite-fluorapatite mineralization at the Olympic dam cu-U-au-ag deposit, South Australia. Econ. Geol. 112 (6), 1531–1542.
Ault, T., Gosen, B.V., Krahn, S., Croff, A., 2016. Natural thorium resources and recovery: options and impacts. Nucl. Technol. 194 (2), 136–151.
Baskaran, M., 2016. Mechanisms of radon emanation and long-term radon flux studies. In: Radon: A Tracer for Geological, Geophysical and Geochemical Studies. Springer, Cham, pp. 37–62.
Bhargava, S.K., Ram, R., Pownceby, M., Grocott, S., Ring, B., Tardio, J., Jones, L., 2015. A review of acid leaching of uraninite. Hydrometallurgy 151, 10–24.
BHP, 2018. Annual Report 2018. https://www.bhp.com/investor-centre/annual-report-

2018.
Brandt, F., Curti, E., Klinkenberg, M., Rozov, K., Bosbach, D., 2015. Replacement of barite by a (Ba, Ra) SO4 solid solution at close-to-equilibrium conditions: a combined experimental and theoretical study. Geochim. Cosmochim. Acta 155, 1–15.
Brandt, F., Klinkenberg, M., Poonoosamy, J., Weber, J., Bosbach, D., 2018. The effect of ionic strength and Sr_{aq} upon the uptake of Ra during the recrystallization of barite. Minerals 8 (11), 502. https://doi.org/10.3390/min8110502.
Ceccarello, S., Black, S., Read, D., Hodson, M.E., 2004. Industrial radioactive barite scale: suppression of radium uptake by introduction of competing ions. Miner. Eng. 17 (2), 323–330.
Chao, J.H., Chuang, C.Y., Yeh, S.A., Wu, J.M., 2009. Relationship between radioactivity of radium and concentrations of barium and lead in hokutolite. Appl. Radiat. Isot. 67 (4), 650–653.
Charalambous, F.A., Ram, R., Pownceby, M.I., Tardio, J., Bhargava, S.K., 2012. Chemical and microstructural characterisation studies on natural and heat treated brannerite samples. Miner. Eng. 39, 276–288.
Cherry, A.R., Ehrig, K., Kamenetsky, V.S., McPhie, J., Crowley, J.L., Kamenetsky, M.B., 2018. Precise geochronological constraints on the origin, setting and incorporation of ca. 1.59 Ga surficial facies into the Olympic dam breccia complex, South Australia. Precambrian Res. 315, 162–178.
Ciobanu, C.L., Wade, B.P., Cook, N.J., Schmidt Mumm, A., Giles, D., 2013. Uranium-bearing hematite from the Olympic dam cu–U–au deposit, South Australia: a geochemical tracer and reconnaissance Pb–Pb geochronometer. Precambrian Res. 238, 129–147.
Cook, N.J., Ciobanu, C.L., Danyushevsky, L.V., Gilbert, S., 2011. Minor elements in bornite and associated cu-(Fe)-sulfides: a LA-ICPMS study. Geochim. Cosmochim. Acta 73, 4761–4791.
Courtney-Davies, L., Zhu, Z., Ciobanu, C., Wade, B., Cook, N., Ehrig, K., Cabral, A., Kennedy, A., 2016. Matrix-matched iron-oxide laser ablation ICP-MS U–Pb geochronology using mixed solution standards. Minerals 6 (3), 85.
Courtney-Davies, L., Tapster, S.R., Ciobanu, C.L., Cook, N.J., Verdugo-Ihl, M.R., Ehrig, K.J., Kennedy, A.K., Gilbert, S.E., Condon, D.J., Wade, B.P., 2019. A multi-technique evaluation of hydrothermal hematite U-Pb isotope systematics: implications for ore deposit geochronology. Chem. Geol. 513, 54–72.
Curti, E., Fujiwara, K., Iijima, K., Tits, J., Cuesta, C., Kitamura, A., Glaus, M.A., Müller, W., 2010. Radium uptake during barite recrystallization at 23 ± 2 C as a function of solution composition: an experimental ^{133}Ba and ^{226}Ra tracer study. Geochim. Cosmochim. Acta 74 (12), 3553–3570.
DePaolo, D.J., Maher, K., Christensen, J.N., McManus, J., 2006. Sediment transport time measured with U-series isotopes: results from ODP North Atlantic drift site 984. Earth Planet. Sci. Lett. 248 (1–2), 394–410.
Doerner, H.A., Hoskins, W.M., 1925. Co-precipitation of radium and barium Sulfates1. J. Am. Chem. Soc. 47 (3), 662–675.
Dosseto, A., Bourdon, B., Turner, S.P., 2008. Uranium-series isotopes in river materials: insights into the timescales of erosion and sediment transport. Earth Planet. Sci. Lett. 265 (1–2), 1–17.
Ehrig, K., McPhie, J., Kamenetsky, V.S., 2012. Geology and mineralogical zonation of the Olympic dam Iron oxide cu-U-au-ag deposit, South Australia. In: Hedenquist, J.W., Harris, M., Camus, F. (Eds.), Geology and Genesis of Major Copper Deposits and Districts of the World, a Tribute to Richard Sillitoe. Vol. 16. Society of Economic Geologists Special Publication, Littleton, USA, pp. 237–267.
Ehrig, K., Kamenetsky, V.S., McPhie, J., Cook, N.J., Ciobanu, C.L., 2017. Olympic dam iron oxide Cu-U-Au-ag deposit. In: Phillips, G.N. (Ed.), Australian Ore Deposits. AusIMM, Melbourne, pp. 601–610.
Eyal, Y., Fleischer, R.L., 1985. Timescale of natural annealing in radioactive minerals affects retardation of radiation-damage-induced leaching. Nature 314, 518–520.
Fleischer, R.L., 1980. Isotopic disequilibrium of uranium: alpha-recoil damage and preferential solution effects. Science 207 (4434), 979–981.
George, L.L., Cook, N.J., Crowe, B.B.P., Ciobanu, C.L., 2018. Trace elements in hydrothermal chalcopyrite. Mineral. Mag. 82, 59–88.
Germann, F.E., 1921. Adsorption of radium by barium sulfate. J. Am. Chem. Soc. 43 (7), 1615–1621.
Gilligan, R., 2017. The Extractive Metallurgy of Brannerite: Leaching Kinetics, Reaction Mechanisms and Mineralogical Transformations (Doctoral dissertation). Murdoch University.
Gilligan, R., Nikoloski, A.N., 2015. The extraction of uranium from brannerite-a literature review. Miner. Eng. 71, 34–48.
Grandstaff, D.E., 1976. A kinetic study of the dissolution of uraninite. Econ. Geol. 71 (8), 1493–1506.
Hashimoto, T., Aoyagi, Y., Kudo, H., Sotobayashi, T., 1985. Range calculation of alpha-recoil atoms in some minerals using LSS theory. J. Radioanal. Nucl. Chem. 90 (2), 415–438.
Hedström, H., Ramebäck, H., Ekberg, C., 2013. A study of the Arrhenius behavior of the co-precipitation of radium, barium and strontium sulfate. J. Radioanal. Nucl. Chem. 298 (2), 847–852.
Hetherington, C.J., Harlov, D.E., Budzyń, B., 2010. Experimental metasomatism of monazite and xenotime: mineral stability, REE mobility and fluid composition. Mineral. Petrol. 99 (3–4), 165–184.
Hitzman, M.W., Valenta, R.K., 2005. Uranium in iron oxide-copper-gold (IOCG) systems. Econ. Geol. 100, 1657–1661.
Hitzman, M.W., Oreskes, N., Einaudi, M.T., 1992. Geological characteristics and tectonic setting of Proterozoic iron oxide (cu-U-au-REE) deposits. Precambrian Res. 58, 241–287.
Holland, H.D., Gottfried, D., 1955. The effect of nuclear radiation on the structure of zircon. Acta Crystallogr. 8 (6), 291–300.
Huang, Q., Kamenetsky, V.S., McPhie, J., Ehrig, K., Meffre, S., Maas, R., Thompson, J., Kamenetsky, M., Chambefort, I., Apukhtina, O., Hu, Y., 2015. Neoproterozoic (ca. 820–830 ma) mafic dykes at Olympic dam, South Australia: links with the Gairdner large igneous province. Precambrian Res. 271, 160–172.
Institute of Experimental Mineralogy, 2019. Internet database. http://database.iem.ac.ru/mincryst Updated 01 March. Accessed 21 March 2019.
International Atomic Energy Agency, 2004. Application of the Concepts of Exclusion, Exemption and Clearance. International Atomic Energy Agency, Vienna (IAEA Safety Standards Series: Safety Guide No. RS-G-1.7).
Kirchenbaur, M., Maas, R., Ehrig, K., Kamenetsky, V.S., Strub, E., Ballhaus, C., Münker, C., 2016. Uranium and Sm isotope studies of the supergiant Olympic dam cu–au–U–ag deposit, South Australia. Geochim. Cosmochim. Acta 180, 15–32.
Klinkenberg, M., Brandt, F., Breuer, U., Bosbach, D., 2014. Uptake of Ra during the recrystallization of barite: a microscopic and time of flight-secondary ion mass spectrometry study. Environ. Sci. Technol. 48 (12), 6620–6627.
Kontonikas-Charos, A., Ciobanu, C.L., Cook, N.J., Ehrig, K., Krneta, S., Kamenetsky, V.S., 2017. Feldspar evolution in the Roxby downs granite, host to Fe-oxide cu-au-(U) mineralisation at Olympic dam, South Australia. Ore Geol. Rev. 80, 838–859.
Krneta, S., Ciobanu, C.L., Cook, N.J., Ehrig, K., Kontonikas-Charos, A., 2017. Rare earth element behaviour in apatite from the Olympic dam cu–U–au–ag deposit, South Australia. Minerals 7 (8), 135. https://doi.org/10.3390/min7080135.
Langmuir, D., Riese, A.C., 1985. The thermodynamic properties of radium. Geochim. Cosmochim. Acta 49 (7), 1593–1601.
Ludwig, K.R., 1977. Effect of initial radioactive daughter disequilibrium on U-Pb isotope apparent ages of young minerals. J. Res. US Geol. Surv 5, 663–667.
Ludwig, K.R., 1978. Uranium-daughter migration and U/Pb isotope apparent ages of uranium ores, Shirley Basin, Wyoming. Econ. Geol. 73 (1), 29–49.
Lumpkin, G.R., Leung, S.H.F., Ferenczy, J., 2012. Chemistry, microstructure, and alpha decay damage of natural brannerite. Chem. Geol. 291, 55–68.
Maas, R., Kamenetsky, V., Ehrig, K., Meffre, S., McPhie, J., Diemar, G., 2011. Olympic dam U-cu-au deposit, Australia: new age constraints. Mineral. Mag. 75, 1375.
Macmillan, E., Cook, N.J., Ehrig, K., Ciobanu, C.L., Pring, A., 2016a. Uraninite from the Olympic dam IOCG-U-ag deposit: linking textural and compositional variation to temporal evolution. Am. Mineral. 101, 1295–1320.
Macmillan, E., Ciobanu, C.L., Ehrig, K., Cook, N.J., Pring, A., 2016b. Chemical zoning and lattice distortion in uraninite from Olympic dam, South Australia. Am. Mineral. 101 (10), 2351–2354.
Macmillan, E., Cook, N.J., Ehrig, K., Pring, A., 2017. Chemical and textural interpretation of late-stage coffinite and brannerite from the Olympic dam IOCG-ag-U deposit. Mineral. Mag. 81 (6), 1323–1366.
Martz, P., Mercadier, J., Perret, J., Villeneuve, J., Deloule, E., Cathelineau, M., Quirt, D., Doney, A., Ledru, P., 2019. Post-crystallization alteration of natural uraninites: implications for dating, tracing, and nuclear forensics. Geochim. Cosmochim. Acta 249, 138–159.
Maruyama, I., Muto, S., 2016. Change in relative density of natural rock minerals due to electron irradiation. J. Adv. Concr. Technol. 14 (11), 706–716.
McPhie, J., Orth, K., Kamenetsky, V., Kamenetsky, M., Ehrig, K., 2016. Characteristics, origin and significance of Mesoproterozoic bedded clastic facies at the Olympic dam cu–U–au–ag deposit, South Australia. Precambrian Res. 276, 85–100.
Meggi-Cecchi, V., Cipriani, C., Rossi, P., Ceccato, D., Rudello, V., Somacal, H., 2002. Trace element contents and distribution maps of chalcopyrite: a micro-PIXE study. Periodico di Mineral. 71, 101–109.
Momoshima, N., Nita, J., Maeda, Y., Sugihara, S., Shinno, I., Matsuoka, N., Huang, C.W., 1997. Chemical composition and radioactivity in hokutolite (plumbian barite) collected at Peito hot spring, Taiwan. J. Environ. Radioact. 37 (1), 85–99.
Murakami, T., Chakoumakos, B.C., Ewing, R.C., Lumpkin, G.R., Weber, W.J., 1991. Alpha-decay event damage in zircon. Am. Mineral. 76 (9–10), 1510–1532.
Owen, N.D., Ciobanu, C.L., Cook, N.J., Slattery, A., Basak, A., 2018. Nanoscale study of clausthalite-bearing symplectites in cu-au-(U) ores: implications for ore genesis. Minerals 8 (2), 67. https://doi.org/10.3390/min8020067.
Owen, N.D., Cook, N.J., Rollog, M., Ehrig, K.J., Schmandt, D.S., Ram, R., Brugger, J., Ciobanu, C.L., Wade, B., Guagliardo, P., 2019. REE-, Sr- ca-Aluminum-Phosphate-Sulfate Minerals of the Woodhouseite Series and their Role as Hosts for Radionuclides. In: American Mineralogist, https://doi.org/10.2138/am-2019-7116. **in press.**
Pina, C.M., Putnis, A., 2001. The kinetics of nucleation of solid solutions from aqueous solutions: a new model for calculating non-equilibrium distribution coefficients. Geochim. Cosmochim. Acta 66 (2), 185–192.
Poczatek, C., Kaufman, Z., Lechene, C., 2009. OpenMIMS ImageJ Plugin Guide. Harvard Medical School, Boston, Massachusetts, USA.
Putnis, A., 2002. Mineral replacement reactions: from macroscopic observations to microscopic mechanisms. Mineral. Mag. 66 (5), 689–708.
Ram, R., Charalambous, F.A., McMaster, S., Pownceby, M.I., Tardio, J., Bhargava, S.K., 2013. An investigation on the dissolution of natural uraninite ores. Miner. Eng. 50, 83–92.
Roberts, D.E., Hudson, G.R.T., 1983. The Olympic dam copper-uranium-gold deposit, Roxby downs, South Australia. Econ. Geol. 78 (5), 799–822.
Rollog, M., Cook, N.J., Guagliardo, P., Ehrig, K.J., Kilburn, M., 2019a. In situ spatial distribution mapping of radionuclides in minerals by nanoSIMS. Geochemistry. https://doi.org/10.1144/geochem2018-038. **(in print).**
Rollog, M., Cook, N.J., Guagliardo, P., Gilbert, S.E., Ehrig, K.J., Kilburn, M., 2019b. Intermobility of barium, strontium, and lead in chloride and sulfate leach solutions. Geochem. Trans. 20: 4. https://doi.org/10.1186/s12932-019-0064-0.
Rollog, M., Cook, N.J., Guagliardo, P., Ehrig, K.J., Ciobanu, C., Kilburn, M., 2019c. Detection of trace elements/isotopes in Olympic dam copper concentrates by nanoSIMS. Minerals 9 (6), 336. https://doi.org/10.3390/min9060336.
Rollog, M., Cook, N.J., Guagliardo, P., Ehrig, K.J., Kilburn, M., 2019d. Radionuclide

distributions in Olympic dam copper concentrates: the importance of minor hosts, incorporation mechanisms, and mineral surfaces. Miner. Eng (in review, submitted 19th June 2019).
Rollog, M., Cook, N.J., Ehrig, K., Gilbert, S.E., 2019e. Rapid, competitive radium uptake in strontium, barium, and lead sulfates during sulfuric acid leaching. Appl. Geochem (in review, submitted 18th July 2019).
Rosholt, J.N., 1983. Isotopic composition of uranium and thorium in crystalline rocks. J. Geophys. Res. 88 (B9), 7315–7330.
Sasaki, N., Minato, H., 1982. Relationship between lattice constants and strontium and calcium contents of hokutolite. Mineral. J. 11 (2), 62–71.
Schindelin, J., Arganda-Carreras, I., Frise, E., Kaynig, V., Longair, M., Pietzsch, T., Preibisch, S., Rueden, C., Saalfeld, S., Schmid, B., Tinevez, J.Y., 2012. Fiji: an open-source platform for biological-image analysis. Nat. Methods 9, 676–682.
Schindelin, J., Rueden, C.T., Hiner, M.C., Eliceiri, K.W., 2015. The ImageJ ecosystem: an open platform for biomedical image analysis. Mol. Reprod. Dev. 82, 518–529.
Schmandt, D., 2019. Mineralogical distributions of radionuclides in copper-uranium ores. In: Olympic Dam, South Australia. University of Adelaide, Adelaide, Australia PhD thesis.
Schmandt, D., Cook, N., Ciobanu, C., Ehrig, K., Wade, B., Gilbert, S., Kamenetsky, V., 2017. Rare earth element Fluorocarbonate minerals from the Olympic dam cu-U-au-ag deposit, South Australia. Minerals 7 (10), 202.
Schmandt, D.S., Cook, N.J., Ciobanu, C.L., Ehrig, K., Wade, B.P., Gilbert, S., Kamenetsky, V.S., 2019a. Rare earth element phosphate minerals from the Olympic dam cu-U-au-ag deposit, South Australia: recognizing temporal-spatial controls on REE mineralogy in an evolved IOCG system. Can. Mineral. 57 (1), 3–24.
Schmandt, D.S., Cook, N.J., Ehrig, K., Gilbert, S., Wade, B.P., Rollog, M., Ciobanu, C.L., Kamenetsky, V.S., 2019b. Uptake of trace elements by baryte during copper ore processing: a case study from Olympic dam, South Australia. Miner. Eng. 135, 83–94.
Szymański, J.T., Scott, J.D., 1982. A crystal structure refinement of synthetic brannerite, UTi_2O_6, and its bearing on rate of alkaline-carbonate leaching of brannerite in ore. Can. Mineral. 20 (2), 271–280.
Vallini, D.A., Groves, D.I., McNaughton, N.J., Fletcher, I.R., 2007. Uraniferous diagenetic xenotime in northern Australia and its relationship to unconformity-associated uranium mineralisation. Mineral. Deposita 42 (1–2), 51–64.
Verdugo-Ihl, M.R., Ciobanu, C.L., Cook, N.J., Ehrig, K., Courtney-Davies, L., Gilbert, S., 2017. Textures and U-W-Sn-Mo signatures in hematite from the cu-U-au-ag orebody at Olympic dam, South Australia: defining the archetype for IOCG deposits. Ore Geol. Rev. 91, 173–195.
Vinograd, V.L., Kulik, D.A., Brandt, F., Klinkenberg, M., Weber, J., Winkler, B., Bosbach, D., 2018a. Thermodynamics of the solid solution-aqueous solution system (Ba,Sr,Ra) SO_4 + H_2O: I. the effect of strontium content on radium uptake by barite. Appl. Geochem. 89, 59–74.
Vinograd, V.L., Kulik, D.A., Brandt, F., Klinkenberg, M., Weber, J., Winkler, B., Bosbach, D., 2018b. Thermodynamics of the solid solution-aqueous solution system (Ba,Sr,Ra) SO_4 + H_2O: II. Radium retention in barite-type minerals at elevated temperatures. Appl. Geochem. 93, 190–208.
World Nuclear Association, 2018. Information Library. http://www.world-nuclear.org **updated. Accessed 15 Feb 2019.**
Zhang, Y., Lumpkin, G.R., Li, H., Blackford, M.G., Colella, M., Carter, M.L., Vance, E.R., 2006. Recrystallisation of amorphous natural brannerite through annealing: the effect of radiation damage on the chemical durability of brannerite. J. Nucl. Mater. 350 (3), 293–300.
Zhang, T., Gregory, K., Hammack, R.W., Vidic, R.D., 2014. Co-precipitation of radium with barium and strontium sulfate and its impact on the fate of radium during treatment of produced water from unconventional gas extraction. Environ.Sci. Technol. 48 (8), 4596–4603.

Chapter 7

Radionuclide distributions in Olympic Dam copper concentrates: the significance of minor hosts, incorporation mechanisms, and the role of mineral surfaces

Mark Rollog [a,*], Nigel J. Cook [a], Paul Guagliardo [b], Kathy Ehrig [c], and Matt Kilburn [b]

[a] *School of Chemical Engineering, University of Adelaide, Adelaide, 5005 S.A., Australia*

[b] *Centre for Microscopy, Characterisation, and Analysis, University of Western Australia, 35 Stirling Highway, Crawley, 6009 W.A., Australia*

[c] *BHP Olympic Dam, 55 Grenfell St., Adelaide, 5000 S.A., Australia*

Article accepted for publication in *Minerals Engineering* on 6 November 2019

Statement of Authorship

Title of Paper	Radionuclide distributions in Olympic Dam copper concentrates: the significance of minor hosts, incorporation mechanisms, and the role of mineral surfaces
Publication Status	☐ Published ☑ Accepted for Publication ☐ Submitted for Publication ☐ Unpublished and Unsubmitted work written in manuscript style
Publication Details	Submitted to *Minerals Engineering* 19 June 2019, accepted 6 November 2019.

Principal Author

Name of Principal Author (Candidate)	Mark Rollog
Contribution to the Paper	Designed experimentation, performed sample analysis and data interpretation, wrote manuscript
Overall percentage (%)	70
Certification:	This paper reports on original research I conducted during the period of my Higher Degree by Research candidature and is not subject to any obligations or contractual agreements with a third party that would constrain its inclusion in this thesis. I am the primary author of this paper.
Signature	Date 23.08.19

Co-Author Contributions

By signing the Statement of Authorship, each author certifies that:

i. the candidate's stated contribution to the publication is accurate (as detailed above);
ii. permission is granted for the candidate in include the publication in the thesis; and
iii. the sum of all co-author contributions is equal to 100% less the candidate's stated contribution.

Name of Co-Author	Nigel J. Cook
Contribution to the Paper	Supervised direction and progress of work, helped evaluate and edit manuscript
Overall percentage (%)	10
Signature	Date 1/8/19

Name of Co-Author	Paul Guagliardo
Contribution to the Paper	Oversaw sample analyses and helped evaluate and edit the manuscript
Overall percentage (%)	10

112

Signature		Date	25 Jul 2019

Name of Co-Author	Kathy Ehrig
Contribution to the Paper	Provided samples and helped evaluate and edit the manuscript
Overall percentage (%)	5
Signature	Date 31 July 2019

Name of Co-Author	Matt Kilburn
Contribution to the Paper	Oversaw facility where samples were analysed
Overall percentage (%)	5
Signature	Date 25 Jul 2019

113

114

Abstract

Some iron oxide-copper-gold (IOCG) deposits contain variable amounts of uranium. Developing mineral deportment models for the radiogenic isotopes resulting from decay of ^{238}U presents a singular technical challenge, as concentrations of ^{226}Ra, ^{210}Pb, and ^{210}Po fall far below the detection limits achievable for most *in situ* analytical methodologies. The nanoscale secondary ion mass spectrometry (nanoSIMS) platform combines low detection limits with sub-micron resolution, revealing previously unseen spatial distribution patterns of radionuclides (RNs) in (and on) particles of copper sulphide concentrates. Many potential host minerals for these radionuclides can be readily predicted based on chemical behaviour, periodic table trends, and published studies documenting likely host minerals. Using nanoSIMS data for ores and metallurgical products from the Olympic Dam IOCG deposit and associated processing facilities, we present compelling evidence for the ability of certain minerals within the copper concentrates to host daughter radionuclides derived from uranium decay. Many of these minerals had not traditionally been considered or previously documented as such. These include high-abundance minerals hosting low concentrations of radionuclides, and several relatively low abundance minerals exhibiting remarkable radionuclide enrichment. Rutile, fluorapatite, fluorite, hematite, zircon, covellite, and molybdenite are all proven to be minor hosts of at least some members of the ^{238}U decay chain, and are, collectively, important for establishing the overall RN budget. Surface effects are found to play a significant role, with elevated levels of ^{226}Ra and ^{210}Pb found on most available surfaces, irrespective of mineral, in acid-leached concentrate. Some radionuclides, particularly ^{226}Ra and ^{210}Pb liberated from uranium minerals during sulphuric acid leaching, can become extensively redistributed throughout the concentrate, creating newly-formed RN hosts. This new mineralogical deportment information can be used in developing new flowsheets to enhance radionuclide removal without a corresponding loss of Cu. NanoSIMS has proven invaluable for elucidating

the mineral-scale deportment of ultra-trace radionuclides throughout the processing circuit at Olympic Dam.

Keywords: radium, lead, polonium, surface charge, nanoparticles, nanoSIMS.

1. Introduction

Olympic Dam is by far the largest of many iron oxide-copper-gold deposits in the Olympic Cu-Au province, South Australia. Copper, U, Au, and Ag are recovered at Olympic Dam, with nearly 40 additional elements exhibiting enrichment – albeit below economic viability (Ehrig et al., 2012). Grinding/flotation, concentrate and flotation tailings leach, Cu-U solvent extraction, smelting, electrorefining/electrowinning and precious metals refining circuits operate as a fully integrated circuit at Olympic Dam. Process engineers must not only upgrade desired elements, but also minimise deleterious components which may interfere with downstream processing (e.g. smelting or refining) or impact on final product (Cu-cathode, uranium oxide concentrate, Au-Ag bullion) quality.

Radionuclides (RNs) from the decay of ^{235}U, ^{232}Th, and most importantly ^{238}U are present in mineralisation at OD and report to the processing plant. Deportment of ^{226}Ra, ^{210}Pb, and ^{210}Po within the deposit is not well understood at the mineral scale – this is further complicated during processing by a redistribution of RNs, inducing secular disequilibrium during sulphuric acid leaching. Monitoring RN activities in bulk samples (i.e. not on mineral separates) from various process streams over the past 30 years of operation at Olympic Dam is required for RN control and eventual removal. However, efforts to further reduce RN concentrations prior to smelting and refining are limited without a detailed understanding of specific mineral and non-mineral RN hosts. The ability of some minerals to incorporate and retain RNs (e.g., uraninite) has been established (e.g. Grandstaff, 1976; Bowles, 1990); other minerals have the ability to remove specific RNs from solution - e.g., uptake of Ra by baryte (Curti et al., 2010;

Klinkenberg et al., 2014; Vinograd et al., 2018). However, several other minerals with relatively low concentrations may also host RNs (e.g. zircon, apatite, rare earth element minerals).

When considering the overall RN budget, mineral hosts fall into one of four categories: High RN, high % (where % represents the proportion of a given mineral in the ore or concentrate); high RN, low %; low RN, high %; and low RN, low %. The U-minerals uraninite, coffinite and brannerite fall within the first category and are largely reduced during concentrate and flotation tailings leach (Rollog et al., 2019a, 2019b). The last category has minimal impact on the RN budget and is therefore of limited practical relevance to process engineers. However, high abundance/low RN concentration and low abundance/high RN concentration minerals require extra consideration as the total RN contribution of these minerals is unknown – and may, collectively, be significant. Within the scope of this research, "minor" hosts are defined as minerals which contain (within the crystal structure or attached to the mineral surface) either: ultra-trace amounts of radionuclides but have ~>0.1% abundance in the concentrates; or which have measurable RN concentrations but are rare.

Sample analyses from various stages of the processing circuit provide different, yet complementary observations into the changing deportment and upgrading of RNs during froth flotation and concentrate acid leaching at Olympic Dam (simplified processing flowsheet presented in Schmandt et al., 2019). Flotation concentrate (FC) and concentrate leach discharge (CLD) samples each provide unique insight into RN distributions within unleached copper concentrates and H_2SO_4-leached concentrates, respectively. Acid leaching is an aggressive process and alters the chemistry of some minerals (Bhargava et al., 2015), including those at Olympic Dam (Ragozzini and Sparrow, 1987; Lane et al., 2016). Thus, RNs may be liberated from their original hosts in the ore and redistributed in response to rapidly changing thermodynamic and kinetic conditions.

189 Olympic Dam ore consists of >100 different mineral types which are typically intergrown
190 at the nanometre scale. Hence it is very time consuming and impractical to produce pure
191 mineral separates from Olympic Dam ore. Routinely utilised *in situ* microanalytical techniques
192 such as laser ablation inductively-coupled plasma mass spectrometry (LA-ICP-MS) provide
193 neither the spatial resolution nor the sensitivity needed to distinguish RN hosts from non-RN
194 hosts at the micron or sub-micron scale. The sensitivity of LA-ICP-MS (parts-per-million to
195 parts-per-billion for some elements) is inadequate for some RN detection. LA-ICP-MS can
196 provide quantification of lower ultra-trace concentrations but only at the expense of spatial
197 resolution, usually requiring spot diameters and ablation depth of >50 μm, or even >100 μm.
198 The CAMECA nanoSIMS platform provides an excellent compromise well-suited to
199 determination of RN distributions in ores and concentrates, as it combines ultra-low (albeit
200 non-quantifiable) detection with sub-micron rastering resolution.
201 In this study, we present compelling evidence of the ability of a number of minerals to host
202 RNs derived from uranium decay. Some of these can be predicted to contain daughter RNs on
203 the basis of structurally-bound trace levels of U and robust, refractory structures. Others
204 documented here are neither traditional, previously documented, or even predicted hosts (Cook
205 et al., 2018). The article concludes with a discussion of the potential pathways for structural or
206 surficial RN enrichment.

207 **2. Methods**

208 All samples were processed and analysed as described in Rollog et al. (2019a). In brief, 53
209 μm size fractions of FC and CLD were collected at Olympic Dam in August 2015, December
210 2016, and December 2017. Samples of each were mounted in 1" epoxy resin rounds (in
211 triplicate), polished, and carbon coated. Grains of interest were identified, characterised, and
212 imaged through an extensive survey using back scatter electron (BSE) detection on a FEI
213 Quanta450 field emission gun scanning electron microscope (FEG-SEM) equipped with an

EDAX electron dispersive spectroscopy (EDS) detector at Adelaide Microscopy, The University of Adelaide.

Selected grains were subsequently mapped on the CAMECA NanoSIMS 50L at the Centre for Microscopy, Characterisation, and Analysis (CMCA), The University of Western Australia, Perth. A Hyperion (H200) RF plasma O_2 source was used for all analyses. Samples were mapped twice each in multicollection mode with detectors typically set to ^{46}Ti, ^{54}Fe, ^{65}Cu, ^{87}Sr, ^{137}Ba, ^{206}Pb, and ^{238}U for the first analysis (50x50 μm raster area, 50 pA ion current, D1=2, ES=2, AS=0, 512x512 pixels (px), 3 planes, 5 ms/px, effective beam diameter ≈400 nm) and ^{54}Fe, ^{143}Nd, ^{169}Tm, ^{210}RN (predominantly ^{210}Pb plus minor ^{210}Po and ^{210}Bi), ^{226}Ra, ^{230}Th, and ^{234}U for the second analysis (50x50 μm raster area, 250 pA ion current, D1=2, ES=2, AS=0, 512x512 px, 5 or 6 planes, 5 ms/px, effective beam diameter ≈700 nm). Alternative isotopes occasionally chosen (based on sample mineralogy and tuning efficiency) included ^{42}Ca, ^{47}Ti, ^{57}Fe, ^{86,88}Sr, ^{138}Ba, ^{142,144}Nd, ^{204}Pb, ^{230}Th^{16}O, ^{234}U^{16}O, and ^{238}U^{16}O. Actual masses analysed are noted on the maps presented. NanoSIMS images were processed through ImageJ software (Schindelin et al., 2012, 2015) utilising the OpenMIMS plugin (Poczatek et al., 2009). Dead-time corrections were applied, and planes were aligned, summed, and adjusted for brightness/contrast. Colorisation (linear in scale to the original black and white intensities) aids in isotopic distinction and visualisation.

Note: The ratio of ^{210}Pb:^{210}Po:^{210}Bi (assuming secular equilibrium) is ~1625:28:1, and it is likely that ^{210}Pb is favoured even further in nanoSIMS analyses where the O_2 source is used. Po is predicted to behave like Se and Te, which are more sensitive when analysed with a Cs primary ion beam; Pb is more sensitive when measured with a O_2 primary ion beam. In this study, ^{210}RN is thus assumed to almost exclusively represent ^{210}Pb.

3. Results

Over 3,200 nanoSIMS isotopic distribution maps collected for this study have provided a wealth of information regarding RN deportment in Olympic Dam copper concentrates. Within the 'minor-host' category, minerals may be further classified as either "incorporating hosts", in which RNs are found either within the crystal structure of the host or as unbound nanoinclusions, or "surficial hosts", where RNs have adhered to electrically-charged surfaces or are mechanically sequestered in pores, fractures, or cleavage planes. Where appropriate, both FC and CLD examples are presented. In some instances, it is demonstrable that H_2SO_4 leaching mobilises and redistributes certain cations, creating new RN hosts where none previously existed.

3.1. Incorporating hosts

The term "incorporating" in this study refers to minerals in which RNs are either structurally bound or present as nanoinclusions. Minerals presented from this category include several phosphates and sulphates, as well as hematite, rutile, zircon, and fluorite. This list is by no means exhaustive; the nanoSIMS data suggest "minor host" status may also be applied to bastnäsite, florencite, parisite, and several sulphides, sulpharsenides and antimonides, tellurides and selenides.

Euxenite $[(Y,Ca,Ce,U,Th)(Nb,Ta,Ti)_2O_6]$ is a member of the euxenite-polycrase series and is associated with U-thorianite, sericite, and chalcocite at Olympic Dam (Figure 1). NanoSIMS maps show that euxenite can host the entire decay chain, although the ^{206}Pb concentration is quite low (present, but below the contrast limit of the nanoSIMS image) compared to that in associated chalcocite. Within the U-thorianite, the Th:U ranges from 5:1 to 2:1. This variation can be seen in the ^{238}U map (Figure 1), with high-Th zones darker than mid-Th zones. The darkest regions of the ^{238}U map represent euxenite, which also contains some Th. Thorium-230, ^{226}Ra, and ^{210}Pb are observed to reside relatively equally in both euxenite and U-thorianite,

but the ^{206}Pb distribution is distinct from the rest of the decay chain and resides predominantly within the associated chalcocite.

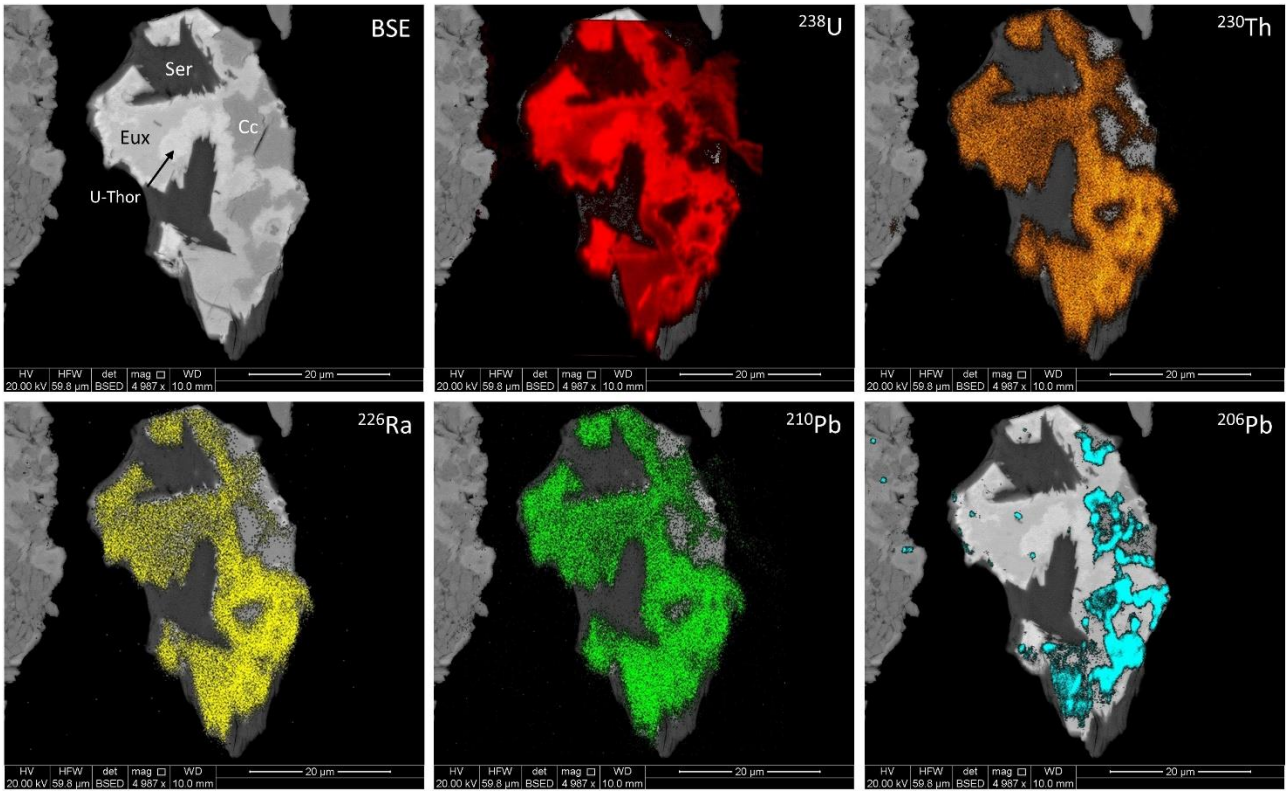

Figure 1. BSE images with nanoSIMS isotopic overlays for grain 10FC65. The particle consists of a small fragment of U-thorianite (U-Thor) with euxenite (Eux), sericite (Ser) and chalcocite (Cc). Maps of ^{238}U, ^{230}Th, ^{226}Ra, ^{210}Pb, and ^{206}Pb are presented. Both U-thorianite and euxenite host all radionuclides in the ^{238}U decay chain, with a slight preference for euxenite from ^{230}Th down.

Fluorapatite is a minor hydrothermal mineral at Olympic Dam, present at a little over 0.1 wt.% of the deposit (Ehrig et al., 2012); after flotation, 0.04 % remains in the concentrate. Apatite is a known host for rare earth elements (REE) and Th at Olympic Dam (Krneta et al., 2017; Rollog et al., 2019c), and may also host other radionuclides (Figure 2). Uranium-234, ^{230}Th, ^{226}Ra, and ^{210}Pb are all abundant within the oscillatory-zoned apatite and are enriched within the grain cores. Lead-206, however, resides exclusively in grain boundaries surrounding the apatite grains.

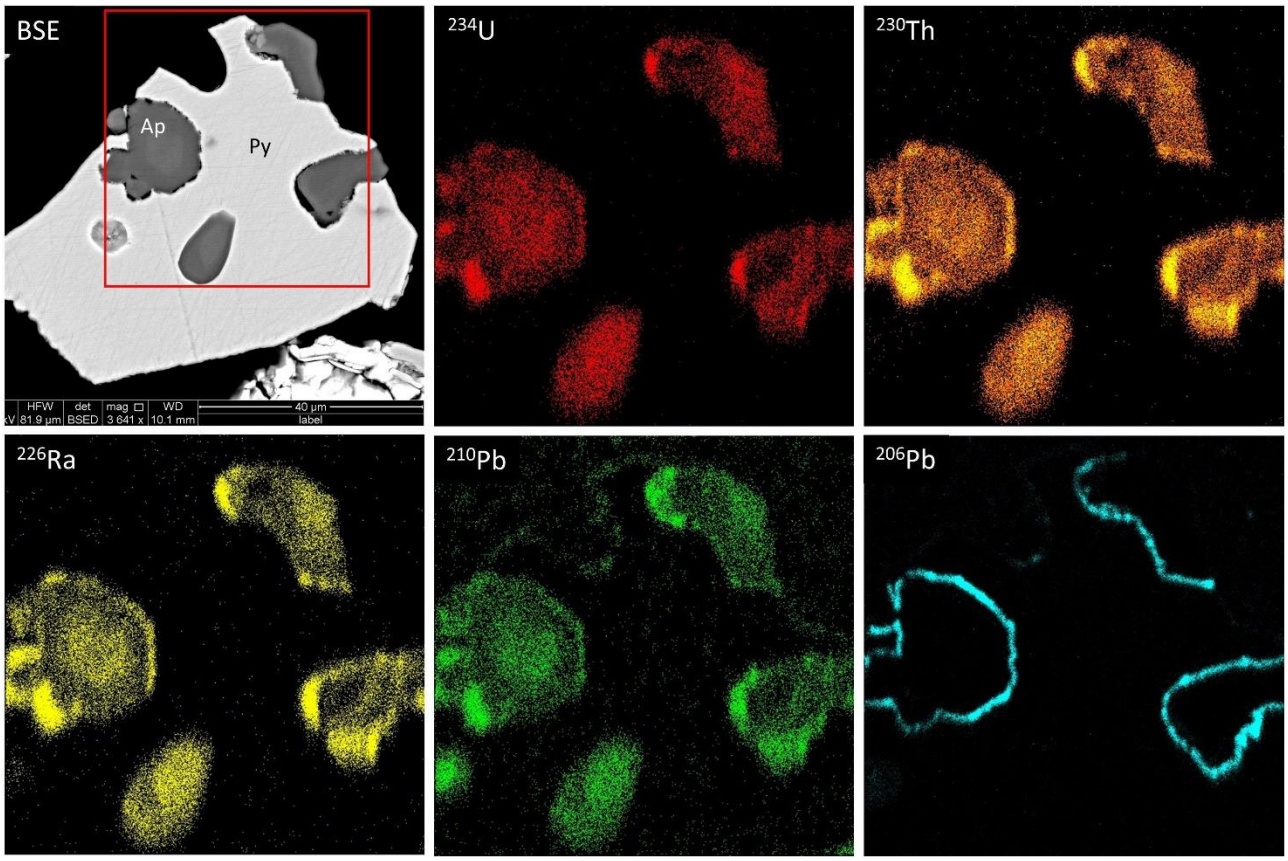

Figure 2. BSE image with nanoSIMS overlays for grain 10FC41, oscillatory-zoned fluorapatite (Ap) crystals in pyrite (Py). Maps of ^{234}U, ^{230}Th, ^{226}Ra, ^{210}Pb, and ^{206}Pb are presented. All radionuclides of the ^{238}U decay chain are present throughout the apatites and are enriched in the grain cores.

Rutile is typically associated with (and may alter into or be replaced by) brannerite at Olympic Dam (Macmillan et al., 2017), and accounts for 0.2 wt.% of the deposit (Ehrig et al., 2012). It maintains 0.2 wt.% in FC and CLD. Although the intensity of RN signals in the accompanying coffinite tends to drown out weaker signals elsewhere in the maps (Figure 3), adjusting the contrast reveals that rutile contains low, uniform amounts of every member of the ^{238}U decay chain. Two small included grains of monazite are enriched in all members of the chain from ^{230}Th down. Uranium is predominantly hosted within brannerite which shares grain boundaries with rutile but is also found at lower concentration throughout the rutile itself.

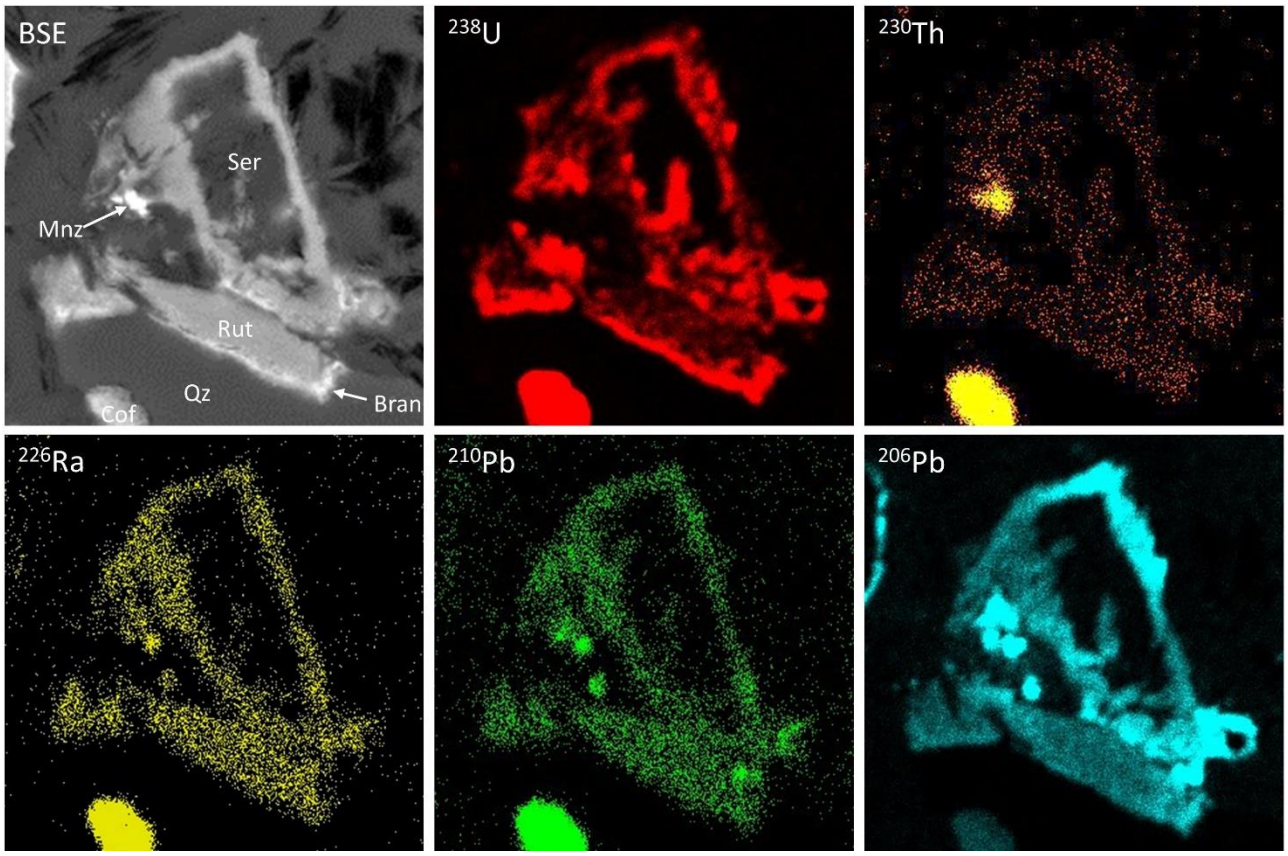

Figure 3. BSE and nanoSIMS isotope distribution maps for sample 05CLD25 – rutile (Rut) in quartz (Qz) and sericite (Ser) with minor brannerite (Bran) replacement, coffinite (Cof), and small monazite (Mnz). Maps of ^{238}U, ^{230}Th, ^{226}Ra, ^{210}Pb, and ^{206}Pb are presented.

Fluorite is a significant accessory mineral and comprises 1.2% of the deposit (Ehrig et al., 2012). The primary function of concentrate leach using H_2SO_4 leaching is to remove F^-; however, fully entrained grains of fluorine-bearing minerals (primarily fluorite but also fluorapatite and REE-fluorocarbonates) may survive (Figure 4). Shielded within a complex bornite/chalcocite symplectite (micron-scale intergrowth of two mineral phases), the fluorite is barren with respect to most of the ^{238}U decay chain but there is a low, uniform background ^{210}Pb signal throughout the grain, and a slightly elevated signal surrounding the grain. The fluorite-symplectite grain boundary is also visible in the ^{226}Ra map, as are hot spots on the grain's outer surface. A few tiny inclusions of uraninite can be seen in the symplectite in the BSE image and the ^{238}U nanoSIMS map. Although signal intensities suggest very low RN concentrations, and almost all fluorite is removed from the process circuit during acid leaching,

the remaining fluorite may contribute measurably to the overall RN budget in final concentrates.

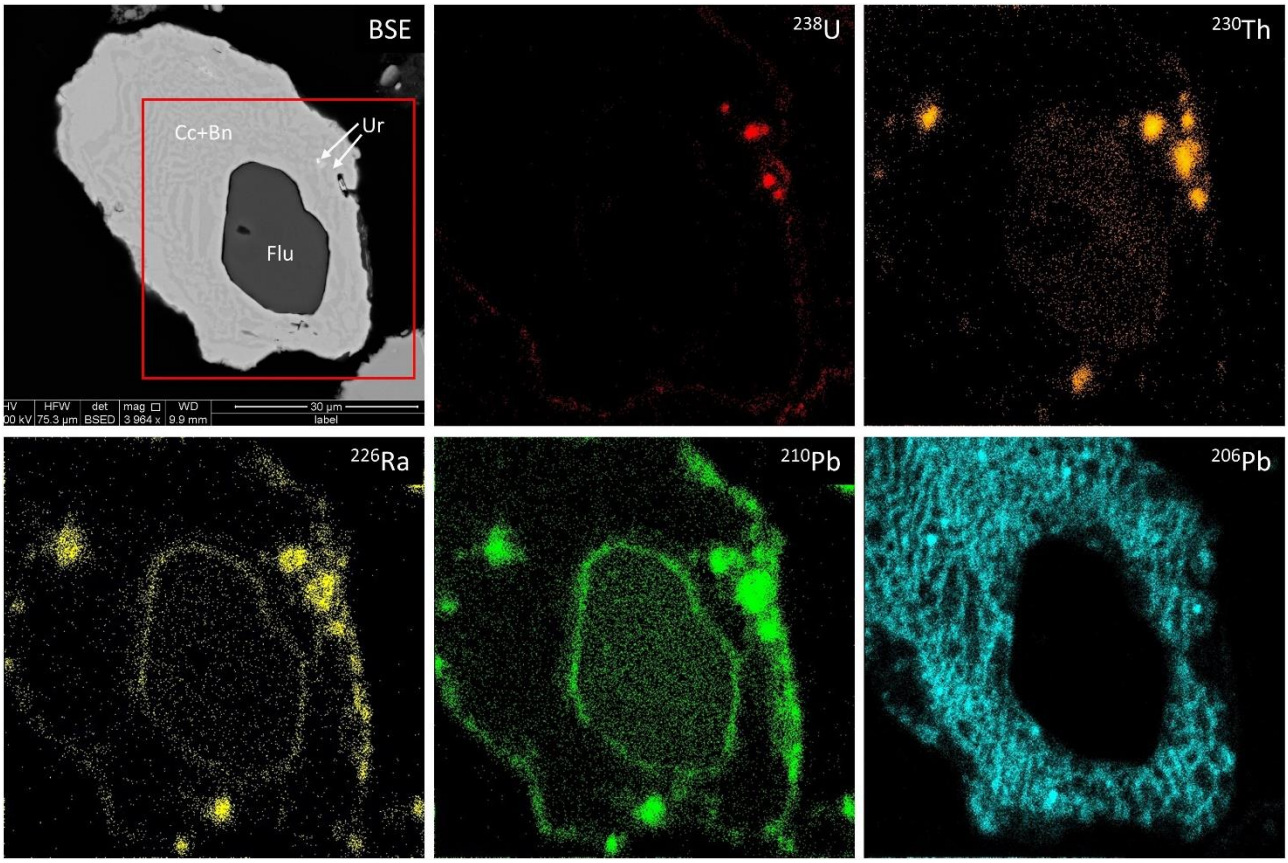

Figure 4. BSE image and nanoSIMS isotopic distribution maps for grain 05CLD86 – fluorite (Flu) in a fine symplectite of chalcocite (Cc) and bornite (Bn). Maps of ^{238}U, ^{230}Th, ^{226}Ra, ^{210}Pb, and ^{206}Pb are presented. Only ^{210}Pb is slightly elevated within the fluorite, although signals for ^{226}Ra and ^{230}Th are suggestive of very low enrichment.

Radionuclides in zircon have been studied and utilised for dating methods since the 1950s (e.g. Hurley and Fairbairn, 1953), and have been used to date rocks hosting the Olympic Dam deposit (Cherry et al., 2018). Although comprising only ~0.05 wt.% in the deposit (Ehrig et al., 2012), more than half of the zircon remains in the concentrate after flotation and acid leaching. Typically found with other end members of the zircon-thorite-coffinite-xenotime system (Förster, 2006), two small RN-bearing zircons can be seen associated with uraniferous thorite in Figure 5. All members of the ^{238}U decay chain appear to be present in the thorite and, to a lesser extent, the zircons.

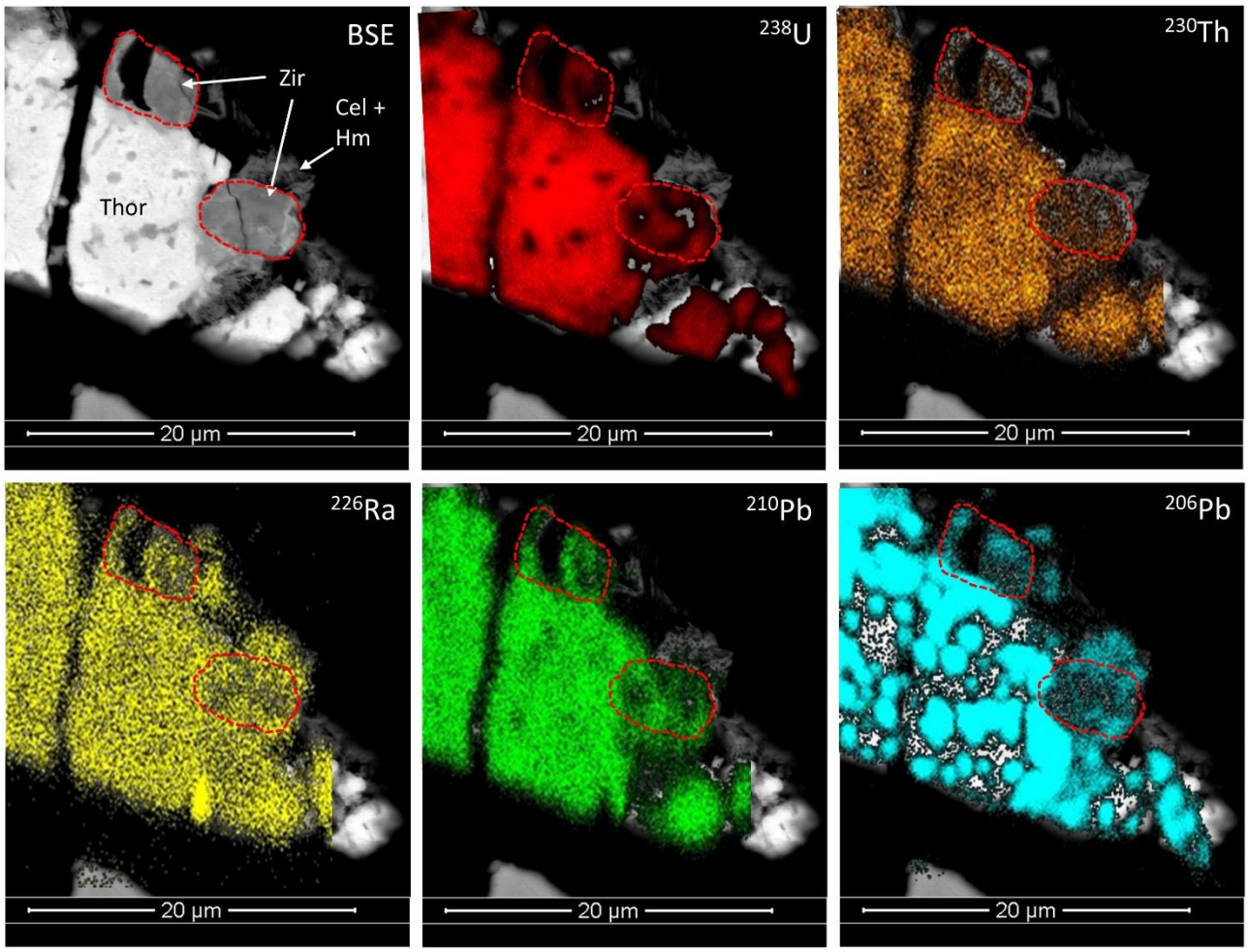

Figure 5. BSE image and nanoSIMS isotope distribution maps for grain 10FC71 – zircon (Zir, outlined in red) in uraniferous thorite (Thor) with intergrown celestite (Cel) and hematite (Hm). Maps of ^{238}U, ^{230}Th, ^{226}Ra, ^{210}Pb, and ^{206}Pb are presented. Radionuclide concentrations in thorite dominate, but two small zircons also host the entire ^{238}U decay chain.

Hematite acts as both a structural host and a surficial host for RNs and is the fourth most significant uranium-bearing mineral at Olympic Dam after brannerite, coffinite, and uraninite (Ehrig et al., 2012). Hematite comprises at least 30 wt.% of the deposit and makes up as much as 80% of some ores, therefore even low U concentrations can contribute a substantial part to the U budget. Uranium can occur in oscillatory-zoned Olympic Dam hematite in up to wt.% concentrations and the presence of U and ^{206}Pb been well characterised by LA-ICP-MS mapping (Ciobanu et al., 2013a; Verdugo-Ihl et al., 2017), also allowing for development of U-Pb hematite geochronology (Courtney-Davies et al., 2019). Although the isotope chemistry

of hematite has been discussed extensively elsewhere (above references), the present contribution would be incomplete without a brief discussion of this critically important mineral component. Figure 6 shows two examples of hematite: the first (a) is a euhedral hematite in a Cu-(Fe)-sulphide matrix in flotation concentrate; the second (b) is an acid-leached grain comprised of bladed hematite with chalcocite containing inclusions of uraninite and monazite. The unzoned, trigonal hematite in (a) appears to be devoid of RNs, which shows that although hematite may contain up to wt.% U - it may also contain very little (Verdugo-Ihl et al., 2017). Lead-206 and ^{238}U are found only at grain boundaries, and ^{210}Pb, ^{226}Ra, and ^{230}Th are absent. The bladed hematite in (b) shows high, but irregular, concentrations of ^{226}Ra, ^{210}Pb, and ^{206}Pb, with no RNs in the accompanying chalcocite (although minor ^{238}U and ^{230}Th spots correlate to sub-micron uraninite and monazite inclusions).

3.2. Surficial hosts

Grain surfaces (especially of sulphides) exhibit elevated amounts of sulphate-insoluble RNs (Ra, ^{210}Pb, and likely ^{210}Po) and ^{206}Pb. Sulphides which exhibit basal cleavage (e.g., molybdenite and covellite) are found to be high in RNs, likely due to the large exposed (charged) surface areas. Microfractures and grain boundaries may also accumulate RNs, either as thin, uniform ribbons or as discrete loci. Although these RN concentrations are generally quite low, consideration of the total surface area of finely ground (~regrind size of P80 = 35 microns) copper concentrates emphasises their significant potential as a hitherto unrecognised RN reservoir.

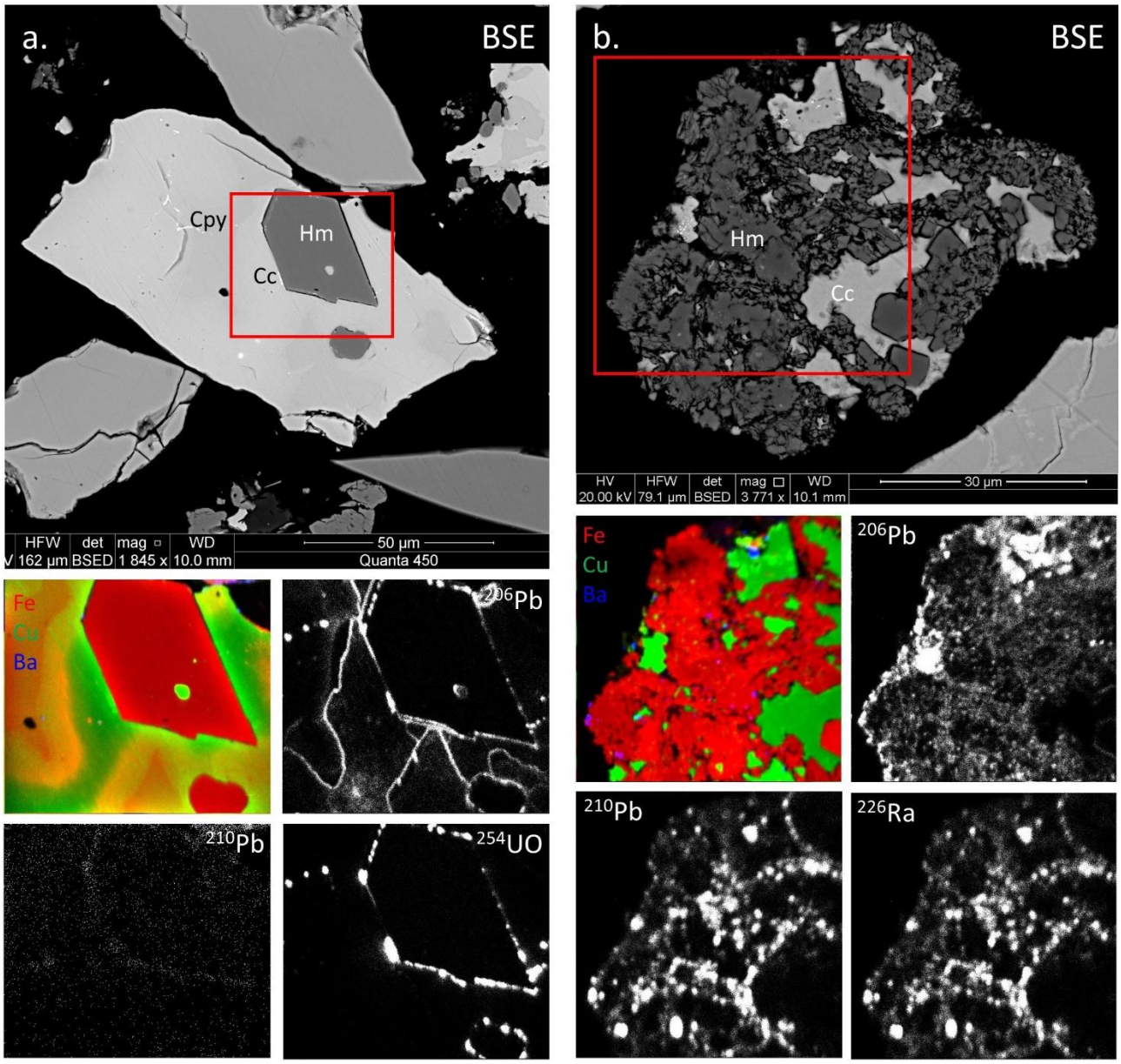

353

354 **Figure 6.** BSE images, nanoSIMS color composites, and nanoSIMS isotopic distribution
355 maps for grains 02FC44 (a) and 05CLD29 (b). Maps of ^{254}UO, ^{226}Ra, ^{210}Pb, and ^{206}Pb are
356 presented. The flotation concentrate example (a) is a large, euhedral hematite (Hm) in a
357 diffusely graded matrix of chalcopyrite→bornite→chalcocite. The acid-leached example (b)
358 consists of bladed hematite with a high surface area together with chalcocite, and with sub-
359 micron inclusions of Pb-rich uraninite and monazite. The hematite has appreciable irregular
360 accumulations of ^{226}Ra, ^{210}Pb, and ^{206}Pb.

361 Molybdenite is a minor mineral at Olympic Dam; on average Mo comprises <60 ppm of the
362 orebody but may approach 1,000 ppm in some mineralised zones (Ehrig et al., 2012). A
363 significant part of the total Mo may be found within hematite. Due to being insoluble in acid,

slight upgrading of Mo during processing is observed and final concentrates may average around 300 ppm. Molybdenite is the only recorded mineral at OD containing essential Mo; it is almost always intimately associated with brannerite and gives a similar signal response (greyscale) in BSE images. However, due to it being a mass-dependant analysis, nanoSIMS can easily distinguish the two. Targeted for study due to its high surface area potential, molybdenite exhibits planar, micaceous cleavage and is quite friable. Figure 7 shows a complex aggregate of fine-grained molybdenite intergrown with monazite, rutile, brannerite, quartz, and sericite.

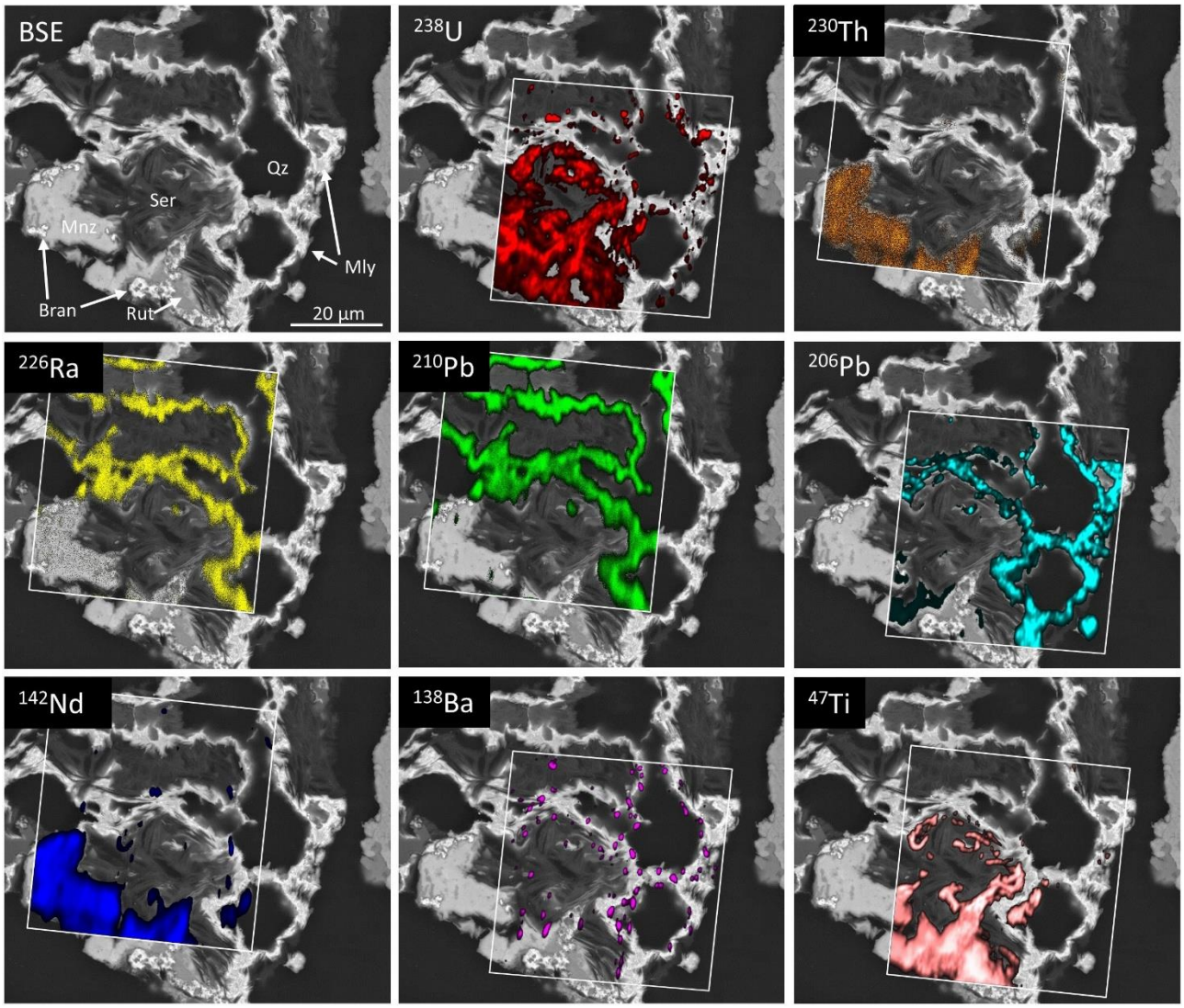

Figure 7. BSE images with nanoSIMS isotopic distribution overlays for grain 10CLD24, complex molybdenite (Mly) intergrown with brannerite (Bran), rutile (Rut), monazite (Mnz), sericite (Ser), quartz (Qz), and sub-micron baryte. Maps of ^{238}U, ^{230}Th, ^{226}Ra, ^{210}Pb, ^{206}Pb,

^{142}Nd, ^{138}Ba, and ^{47}Ti are presented. Uranium-238 appears primarily in brannerite (where ^{238}U and ^{47}Ti overlap). Thorium-230 resides exclusively in the monazite, coincident with REE (^{142}Nd). Radium-226, ^{210}Pb, and ^{206}Pb accumulate in significant amounts in molybdenite.

The molybdenite in Figure 7 contains significant amounts of ^{226}Ra and ^{210}Pb, with trace levels of ^{206}Pb also noted. The quantity of lighter RNs found in molybdenite qualifies it as a borderline major RN host, despite its scarcity in the orebody. Associated brannerite (generally where ^{238}U and ^{47}Ti overlap) contains only ^{238}U and very minor ^{206}Pb, but negligible evidence of RNs in-between – in agreement with other nanoSIMS analysis of brannerite (Rollog et al., 2019b). Thorium-230 resides exclusively in monazite, correlating with ^{142}Nd. Barium-138 appears only as tiny spots on or near molybdenite grain boundaries, apparently independent of ^{226}Ra or ^{210}Pb.

Covellite is another high surface area sulphide due to its planar cleavage. Although a relatively scarce hypogene mineral at Olympic Dam, covellite is a major mineral in leached concentrates. It is produced by removal of Cu from chalcocite and removal of Fe from bornite during H_2SO_4 leaching. Figure 8 shows two examples of covellite, one from flotation concentrate (a) and the other acid-leached material (b). The bornite in Figure 8a, partially replaced by covellite, also contains sub-micron blebs of galena, visible on the ^{206}Pb distribution map. The sample in Figure 8b consists of hematite, covellite replacing bornite, sericite, and minor wittichenite (Cu_3BiS_3). Although industrially-induced metathesis is at least partially responsible for the replacement of bornite by covellite in the CLD grain, it cannot fully explain the replacement observed in the FC sample. Limited amounts of covellite are observed in ores and are best interpreted as hypogene rather than secondary, possibly induced by late fluid circulation. The result of this different origin presents itself in the ^{210}Pb and ^{226}Ra distribution maps. Deposit-formed covellite contains no RNs but is elevated in ^{206}Pb (which may be of any age). In comparison, covellite which either formed during, or was merely exposed to, H_2SO_4

401 leaching contains considerable ^{206}Pb, ^{210}Pb and ^{226}Ra. Neither grain contains appreciable ^{230}Th
402 or ^{238}U.

403 In addition to micaceous cleavage, high surface areas may be achieved through interlinked
404 porosity or fracturing. There are many reasons minerals may become porous or fractured, both
405 by geological processes and during metallurgical processing. Selective leaching, coupled
406 dissolution/reprecipitation (CDR, a phenomenon widely reported from Olympic Dam ores),
407 radiation damage, stress release, shearing, or mechanical grinding during processing may all
408 contribute to crystal damage. Figure 9 shows a representative area of drill core (unprocessed
409 ore) consisting of an assemblage of fluorite, quartz, galena, hematite, and chalcopyrite enclosed
410 within massive sphalerite. Both the chalcopyrite and sphalerite exhibit variable degrees of
411 porosity, especially for the former. The ^{138}Ba (and to a lesser extent, ^{87}Sr) map shows erratic
412 spots of enrichment throughout the porous area, but none in the non-porous region. Maps of
413 ^{226}Ra and ^{210}Pb show the same in chalcopyrite, but signals drop off abruptly at the chalcopyrite-
414 sphalerite boundary with no signals present in sphalerite. Lead-206 is naturally found in galena
415 but can also be observed as thin veneers along chalcopyrite-sphalerite grain boundaries.

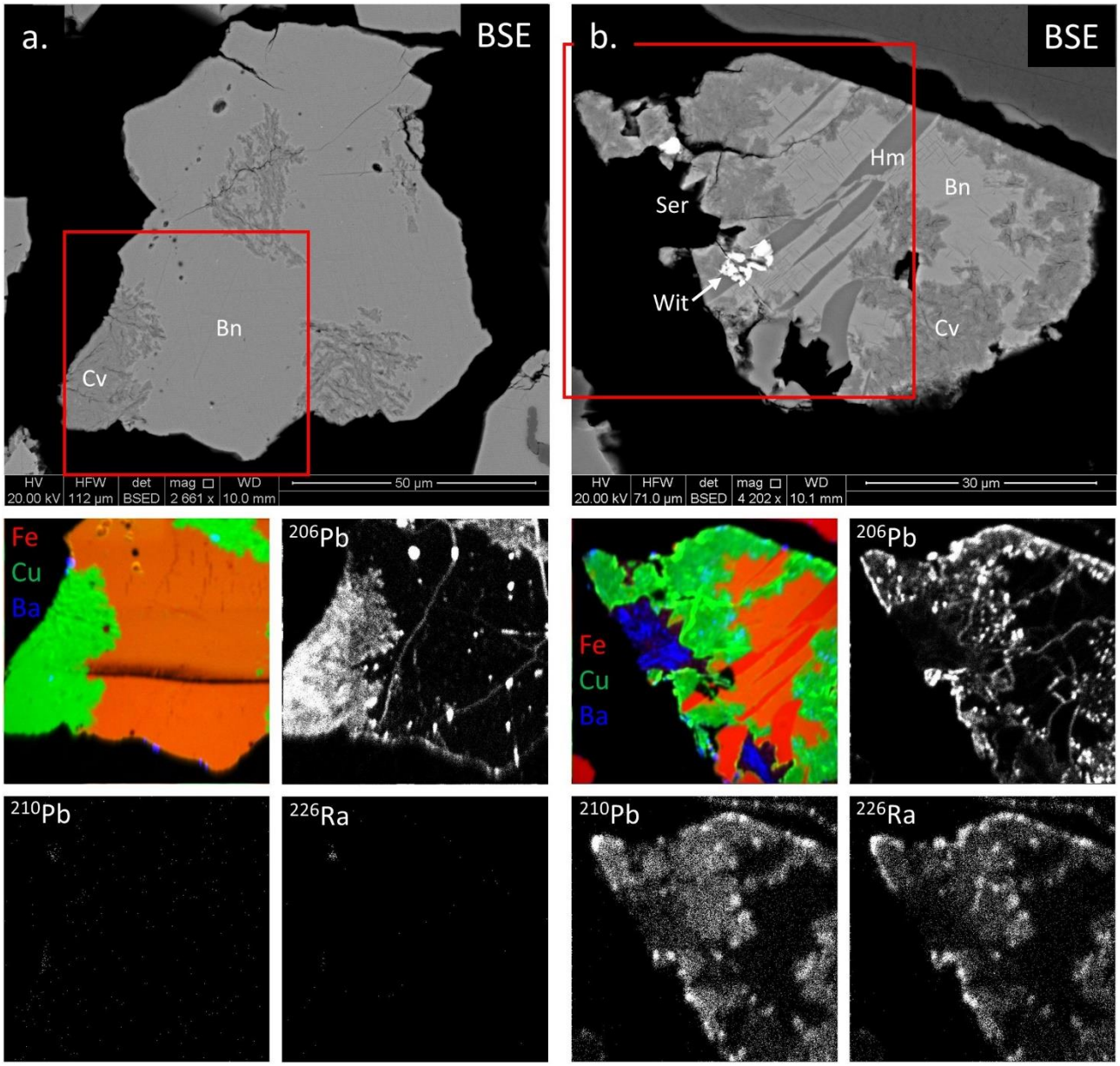

Figure 8. BSE images, nanoSIMS color composites, and nanoSIMs isotopic distribution maps for grains 10FC60 (a) and 05CLD28 (b). The former is covellite (Cv) replacing bornite, the latter is the same with associated hematite and a few small grains of wittichenite (Wit). Maps of ^{226}Ra, ^{210}Pb, and ^{206}Pb are presented. Covellite which formed naturally in the deposit (a) is barren of RNs, but post-acid leach covellite (b) hosts significant ^{226}Ra, ^{210}Pb, and ^{206}Pb. Note: The black anomaly running through the nanoSIMS color composite (a) is a surface crack which developed after the BSE image was taken.

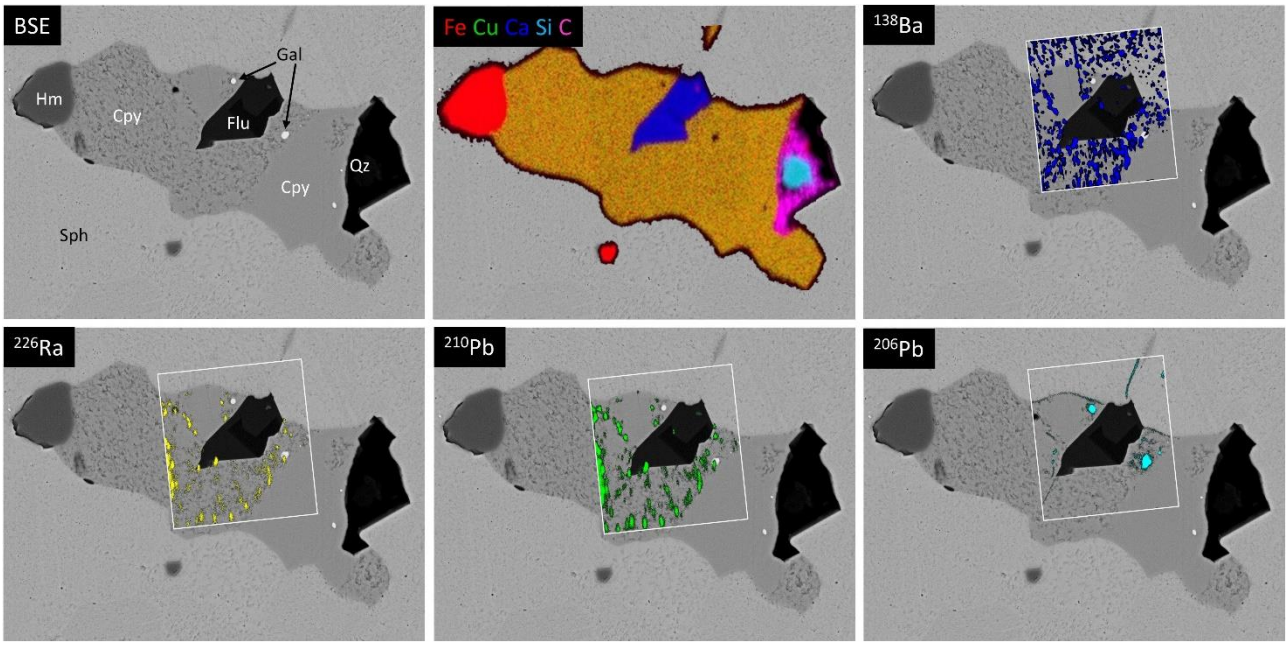

Figure 9. BSE images with an EDS color composite (top, center) and nanoSIMS overlays for grain MR11-4b. Maps of ^{138}Ba, ^{226}Ra, ^{210}Pb, and ^{206}Pb are presented. This unprocessed drill core sample consists of quartz (Qz), fluorite (Flu), sub-micron-scale galena (Gal), and hematite (Hm) hosted in both porous and non-porous chalcopyrite (Cpy) and massive sphalerite (Sph). Porous regions of both sphalerite and chalcopyrite have accumulated spotty Ba, but only porous chalcopyrite hosts ^{226}Ra and ^{210}Pb. Non-porous chalcopyrite is barren of Ba, RNs and ^{206}Pb.

Agglomerates of fine particles present in the +53 µm sized sample formed during laboratory screening/cyclosizing. These agglomerates contain particles that represent a wide range in mineralogical diversity, they have extremely high surface areas compared to surrounding grains. Two agglomerates, (a) from flotation concentrate and (b) representing acid-leached concentrate are presented in Figure 10. NanoSIMS mapping reveals slight differences in RN-hosting potential. There are foci of ^{226}Ra, ^{210}Pb, and ^{206}Pb activity in the FC sample. Comparison with other isotopic maps for the same sample confirms that these points entirely coincide with spots of either ^{238}U, ^{138}Ba, or ^{169}Tm - suggesting that these signals are simply sub-micron grains of uraninite, coffinite, baryte, xenotime, etc. which are known RN hosts. The acid-leached sample also shows foci of activity, but these overlie a nebulous background of ^{210}Pb, ^{226}Ra, and ^{238}U present throughout the entire map, excluding large grains of non-RN-

443 bearing minerals. Surface area may act as an independent RN host, accumulating sulphate-
444 insoluble components of the leach solution on almost all surfaces.

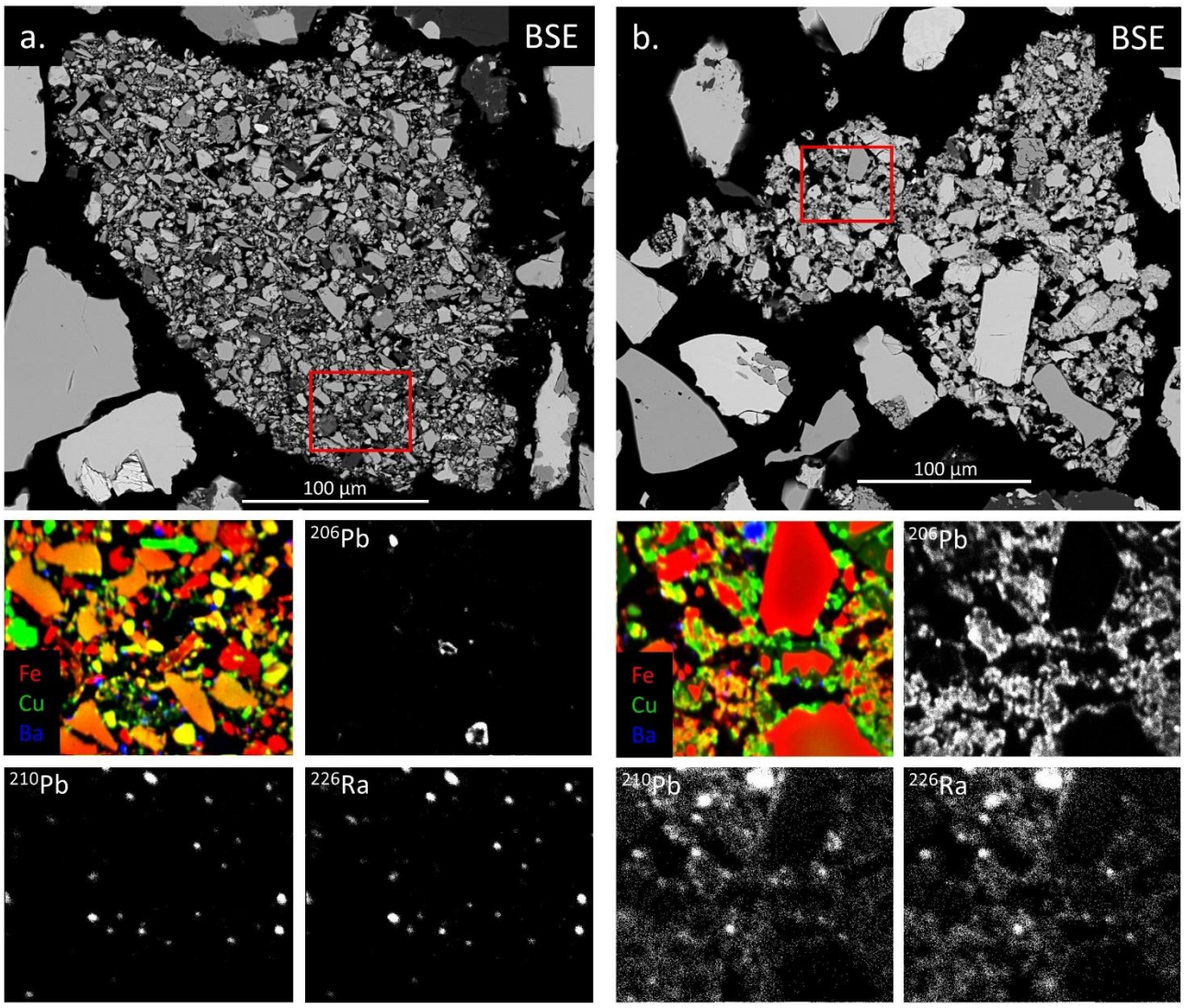

445

446 **Figure 10.** BSE images, nanoSIMS color composites, and nanoSIMS isotopic distribution
447 maps for "grains" 02FC27 (a) and 02CLD65 (b), agglomerates. Maps of ^{226}Ra, ^{210}Pb, and
448 ^{206}Pb are presented. In the flotation concentrate agglomerate (left) tiny spots of ^{210}Pb and ^{226}Ra
449 can be seen, but have a direct correlation with signals of either ^{238}U, ^{138}Ba, or ^{169}Tm.

450 *3.3. Recycled smelter slags*

451 Olympic Dam electric furnace slags contain Cu and are routinely reprocessed in the
452 concentrator to recover the Cu. Figure 11 presents ^{226}Ra and ^{210}Pb distributions in two slag
453 samples: (a) from flotation concentrate; and (b) from acid-leached concentrate. Both grains
454 consist of Fe-Cu-oxides and -silicates of varying compositions. Thorium-230 and ^{238}U have

distributions similar to Pb in both grains, but at insignificant concentrations. The small inset in Figure 11b highlights a 5 µm-sized glass bead inclusion, itself containing 10-50 nm-diameter clustered nanoparticles of unknown composition. Radium-226 seems to be enriched at the centre of these glass beads, correlating with Ba. These unique images vividly emphasise the extraordinary capabilities of nanoSIMS mapping and underscore the near impossibility of accurate detailed *in situ* RN analyses by most other techniques.

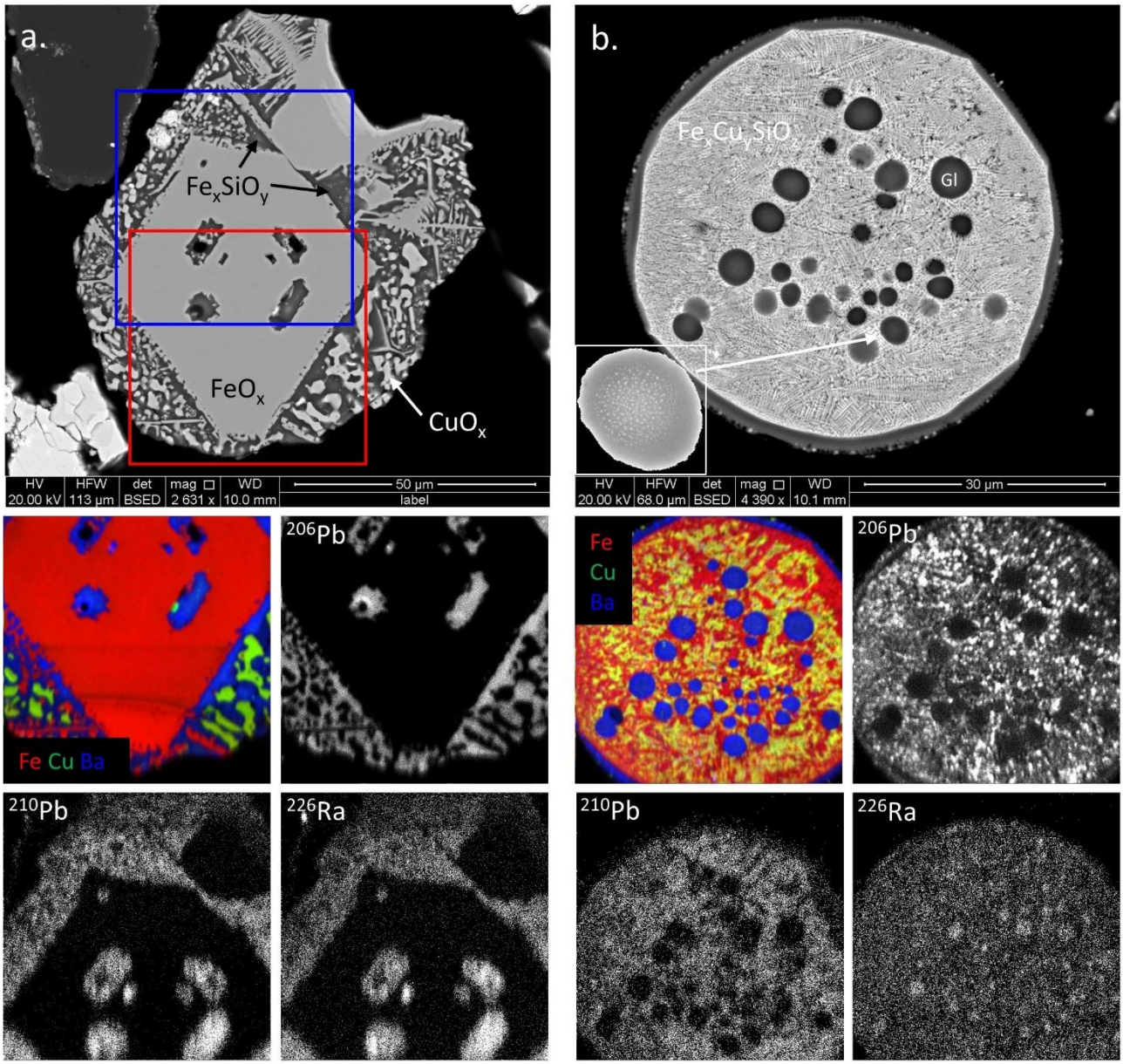

Figure 11. BSE images, nanoSIMS color composites, and nanoSIMS isotopic distribution maps for slag grains 10FC47 (a) and 05CLD40 (b). Maps of ^{226}Ra and ^{210}Pb (blue outline), and ^{206}Pb (red outline) are presented. Compositions for both are Fe-Cu-oxides-silicates in

various proportions. Slag textures include symplectites, fine crystalline aggregates, large euhedral crystals, and glassy inclusions (Gl). The inset in BSE image (b) shows nanometer-sized inclusions within the glassy spherule.

4. Discussion

4.1. Radionuclides hosted within minerals

Due to the variable chemical characteristics of each radionuclide in the ^{238}U decay chain, a large number of RN mineral hosts have been identified. The presence of an RN within a given mineral may result from at least one (or more) of six distinct pathways: crystallisation, *in situ* enrichment, CDR, fracture annealing, aggregate incorporation, or diffusion.

Crystallisation refers to incorporation of the element of interest during initial formation. Uranium and Th minerals are the most obvious examples, but this category also include minerals which readily adopt U and Th into their crystal structures, such as U in zircon or Th in monazite. Zoned apatite grains in Figure 2 and rutile in Figure 3 both exhibit traces of U throughout, likely incorporated during initial crystal formation. Thorium content in apatite is predominantly primary but is also the result of *in situ* ^{238}U decay. Apatite has thus been proposed as an efficient repository for radioactive waste (Rigali et al., 2016). Radionuclides are well known in rutile and have been measured previously, including U (Dostal and Capedri, 1978; Jackson et al., 1994; Radhamani et al., 2010), Th (Jackson et al., 1994) and Ra (Morawska and Jeffries, 1994).

In situ enrichment is the accumulation of a daughter isotope in a mineral originally containing the parent isotope. The parent may have incorporated into the crystal structure during mineral formation or may itself be the result of *in situ* enrichment. The association between ^{226}Ra and ^{210}Pb, shown in several figures here (Figures 1-5, 6b, 7, 8b, 9, 10, and 11a) is an excellent example of this, and is strongly time dependent. Although ^{238}U (half-life 4.47 Ga), ^{234}U (245,500 yrs.), and ^{230}Th (75,350 yrs.) have sufficiently long half-lives for

490 independent dissolution, mobilisation, and recrystallisation – at least in a buried deposit with
491 near continuous groundwater circulation buffered by a high fluoride content (McPhie et al.,
492 2011) – it is very unlikely that ^{210}Pb (22.3 yrs.) would have enough time to accumulate
493 sufficiently to form independent mineral grains, even at the micron-scale. Under natural
494 conditions, ^{210}Pb is linked to Ra chemistry and can only possibly exist in significant quantities
495 where Ra resides.

496 During metal extraction, however, dissociation can occur. Figure 11b shows ^{210}Pb and ^{226}Ra
497 in smelter slag. When chemical reactions progress at extreme temperatures over hours instead
498 of millennia (or longer), half-lives become irrelevant and ^{210}Pb can follow its own
499 thermodynamic path and behave similarly to ^{206}Pb. Instead of concentrating in the Ba-rich glass
500 bead inclusions which host much of the Ra, both Pb-isotopes are found only in the Fe-Cu-
501 silicate matrix.

502 Coupled dissolution/reprecipitation involves the dissolution of a mineral, initially at the
503 surface but propagating as a reaction front into the mineral, frequently accompanied by a
504 complexing agent such as F^- or Cl^-, and precipitation of a replacement mineral (or same mineral
505 with modified chemistry) in its place (Putnis, 2002). As dissolution continues and porosity
506 increases, a replacement front can work its way deep beneath the mineral surface. Advanced
507 CDR may result in the complete replacement of one mineral by another, usually with retention
508 of the original crystal morphology (pseudomorphism).

509 One of the identifying characteristics of CDR is preserved porosity (Putnis, 2009), which
510 can be caused by the volume differential between parent and product minerals, or the rate
511 differential between dissolution and precipitation. Figure 9 shows Ba and RN uptake into
512 porous areas of chalcopyrite with no uptake in non-porous regions. This may represent limited
513 CDR, with only thin veneers of what is likely Ra- and Pb-bearing baryte coating the inner pore
514 surfaces. An alternative explanation exists, however. The porosity may have existed

515 previously, and Ba and Ra were deposited during subsequent mineralised fluid circulation.
516 Although still a surface-driven mechanism, this would qualify as simple crystallisation.
517 Replacement of bornite by covellite (Figure 8) is also via CDR, though it is possible in this
518 case that the 'new' covellite is not directly hosting RNs within its crystal structure but is instead
519 attracting RN nanoparticles to its extensive surface area.

520 Fractures exist in most samples in this study as an unfortunate side-effect of mechanical
521 grinding. Observations from core samples, however, verify the existence of abundant
522 microfracturing in most minerals within the deposit, consistent with the protracted geological
523 history (Ehrig et al., 2017). Saturated fluids readily deposit minerals in fractures and pores
524 (Bekri et al., 1997; Dijk and Berkowitz, 1998; Tartakovsky et al., 2007). Over time, defects in
525 mineral structures may anneal, resulting in what appears to be a continuous, uniform crystal
526 structure. If mineralisation occurred in the fractures prior to annealing, the trapped phase would
527 be incorporated within the host phase. Alternatively, foreign-element uptake may be possible
528 via the mechanically similar process of aggregate incorporation.

529 If a change in the source or composition of a mineralising fluid occurs during mineral
530 crystallisation, elements that are incompatible within the structure of that mineral may become
531 trapped. An initial generation of mineral growth, defined by multiple isolated nucleation points,
532 is followed by fluid interaction and surface deposition of a second mineral. Crystal growth of
533 the primary mineral then continues, merging around the secondary surficial crust. Annealing
534 incorporates the secondary phase as thin zones into what outwardly appears to be a single
535 crystal of the primary mineral (Figure 12). Further evidence of fluid-assisted remobilization
536 and redeposition of Pb can be seen in Figure 2, which shows ^{206}Pb-filled grain boundaries
537 between apatite and pyrite.

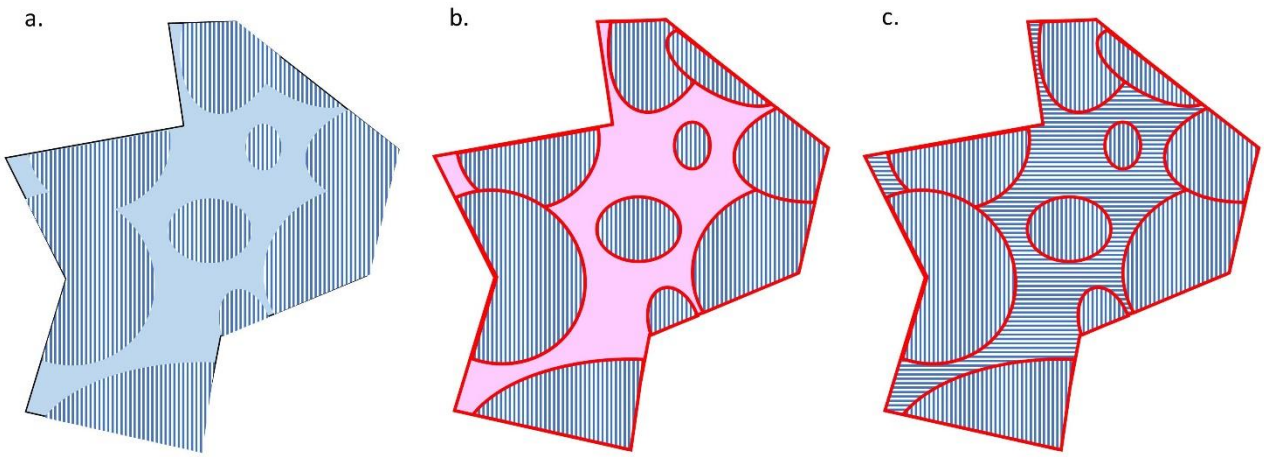

Figure 12. Schematic illustration of aggregate incorporation. The sequence would be: (a) primary crystal growth (blue vertical lines) from solution (light blue); (b) thin deposition of Pb-phase (red) from different mineralising fluid (pink), covering every surface; (c) continuation of chalcopyrite growth, with a different crystal orientation (blue horizontal lines), filling remaining voids. Thin veneers of a Pb-bearing phase now exist in what outwardly appears to be a single grain of chalcopyrite.

Electron backscatter diffraction (EBSD) can determine the crystal orientation of minerals. Figures 6a and 8a show thin, linear traces of ^{206}Pb in chalcopyrite and bornite, with some tracks corresponding to current microfractures and other tracks apparently independent of any visible structures. NanoSIMS maps of a seemingly uniform grain of chalcopyrite containing a large cobaltite inclusion reveal a network of ^{206}Pb throughout the chalcopyrite, aligning with no visible cracks or grain boundaries (Figure 13). EBSD mapping of the grain, however, reveals a complex crystal orientation pattern which aligns perfectly with the ^{206}Pb nanoSIMS map. Straight-line orientation boundaries on the EBSD image (with no incorporated Pb) represent twinning. Simultaneous growth of both twins would preclude incorporation of Pb.

Mineral deposits are, essentially, examples of non-equilibrium at a regional scale. Diffusion is – to some extent – ubiquitous in such an environment, even at low-T, low-fluid conditions (Atkinson, 1985). The Second Law of Thermodynamics suggests that any concentration imbalances will slowly approach equilibrium (given the mechanisms to do so) and when time

is in abundance (i.e. geologic time scales) processes of equilibration can be extensive (Brady, 1995). Fluid-rock interaction will generally accelerate the uptake of trace elements through alternative means (Putnis, 2014). Diffusion is considered to be an ever-present but minor mechanism which is generally eclipsed by processes such as CDR (Putnis, 2002). Figure 6a highlights the difference between mineral boundaries (hematite and enclosing minerals, which may not necessarily be in equilibrium) and diffuse boundaries (gradational from chalcopyrite→bornite→chalcocite). The chalcocite-bornite symplectite in Figure 4 is also the result of oriented diffusion.

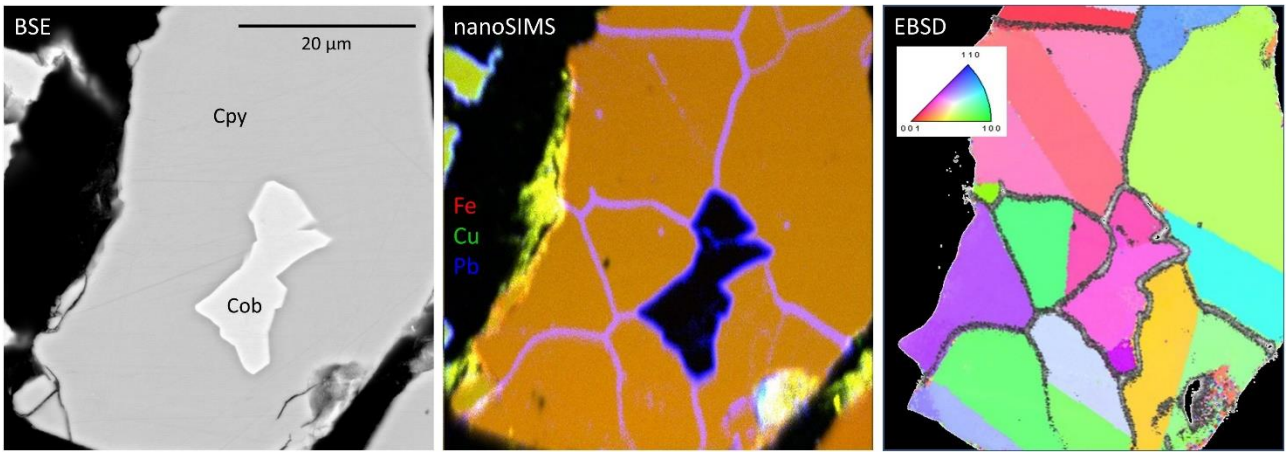

Figure 33. BSE, nanoSIMS composite, and EBSD images of grain 10FC52 – cobaltite (Cob) in chalcopyrite (Cpy). For the nanoSIMS composite, orange represents Fe + Cu (chalcopyrite in this instance) and light purple represents Pb overlapping Cpy. The colours in the EBSD image indicate different crystal orientations. The ^{206}Pb nanoSIMS map (grey stipple) overlays the EBSD map. Lead-206 has been clearly deposited and incorporated during aggregate chalcopyrite crystal growth, and not within annealed fractures in a single crystal.

4.2. The significance of mineral surfaces

One surprising fact resulting from nanoSIMS mapping – with major significance for RN removal from final concentrates – is the nearly ubiquitous presence of RNs on grain surfaces, along grain boundaries, and within fractures and cleavage planes. For the most part, samples of flotation concentrate show little-to-no surface enrichment in any of the isotopes mapped. Acid-leached samples, on the other hand, exhibit a nearly ubiquitous "coating" of ^{206}Pb, ^{210}Pb,

580 and ^{226}Ra, and Figures 4 and 8b illustrate these bright rims on grain surfaces. This surface
581 enrichment is variably smooth or spotty, with very high concentrations occurring where surface
582 damage has resulted in microfracturing or other topographic irregularities.

583 Sulphide surfaces shift away from their isoelectric points during acid leaching (Bebie et al.,
584 1998), creating potential for surface adherence of charged particles. This effect is amplified for
585 sulphides of extremely high surface areas – for example, the micaceous cleavage exhibited by
586 molybdenite and covellite (Figures 7, 8). These minerals appear to act as electrostatic filters,
587 removing insoluble sulphates of Sr, Ba, Pb, and Ra as nanoparticles or nanoclusters.
588 Molybdenite is generally close to stoichiometric with only limited minor element components
589 (Palache et al., 1951); however, LA-ICP-MS analyses of samples from the Hilltop Au deposit
590 in Nevada, USA, and the Boddington Cu-Au-(Mo) deposit in Western Australia have revealed
591 concentrations >100 ppm of W, Re, Te, Bi, Pb, and Se (Ciobanu et al., 2013b). Up to 4.5 wt.%
592 Pb has been measured in molybdenite from Shanxi, China (Li et al., 2016), although it is
593 possible that this molybdenite only hosts Pb trapped at surfaces with little or none actually
594 located in the MoS_2 crystal structure. Covellite may also contain Pb (to <0.1 wt.%), possibly
595 in its structure, as recorded by LA-ICP-MS data (Melekestseva et al., 2017). It should be noted
596 that it is beyond nanoSIMS capabilities, or indeed the scope of the present contribution, to
597 distinguish between matrix-hosted RN cations and surficially-affixed RN-rich particles.

598 The most feasible explanation for surficial RN enrichment in acid-leached concentrates
599 begins with liberation of ^{226}Ra, ^{210}Pb, ^{210}Po, and ^{206}Pb from dissolved uranium minerals. Excess
600 sulphate immediately precipitates all four as nanoparticles onto available mineral surfaces, as
601 they (along with Ba and Sr) represent the only acid-insoluble sulphates on the periodic table.

602 Considering this phenomenon, exposure to H_2SO_4 may be viewed as non-ideal with respect
603 to RN removal, but the amount of sulphate already in the concentrate (chiefly as baryte) renders
604 this moot. Some of the newly-formed sulphates will complex with chloride or other ligands

and become available for CDR or diffusion. Uptake of RNs into baryte through CDR is substantial (Rollog et al., 2019b). Non-complexed RN-sulphate nanoparticles eventually accumulate by mechanical or electrostatic means, filtered out of suspension by contact with high surface area minerals or textures.

If RN-bearing nanoparticle formation and behaviour can be validated, for example by direct visualisation of the nanoparticles in question, this information may prove invaluable in attempts to engineer alternative strategies for RN removal. Liberation of RNs followed by deposition on all grain surfaces may seem problematic, but it may actually facilitate easy access in any remedial, post-leach removal process.

In contrast to RN retention, expulsion of isotopes is also a consideration when determining mechanisms for dissociation. The alpha decay recoil of ^{234}Th in coffinite, for example, has little influence on micron-sized grains and no influence on mm-sized grains. Researchers attempting to date sediments have noted that RN recoil out of small particles may cause a depleted zone near particle or crystal edges (DePaolo et al., 2006; Dosseto et al., 2008). Their solution is to apply a correction based on sediment-size distributions – or to simply use larger size fractions for their measurements. For process engineers, slightly depleted edges may affect ratio calculations but they would have little effect on overall retention of RNs in grains of interest – except for nanoparticles. If a 30 nm recoil is assumed for decay from ^{238}U to ^{234}Th in coffinite, then any nanoparticle <30 nm diameter would lose all of its ^{234}Th – and all of the daughters to follow, except for the small percentage which may then recoil back into the grain. Figure 14 was modelled using a fractional loss equation for a sphere (equation (2) from DePaolo et al., 2006) which details the potential of a spherical particle to lose a daughter ion to recoil.

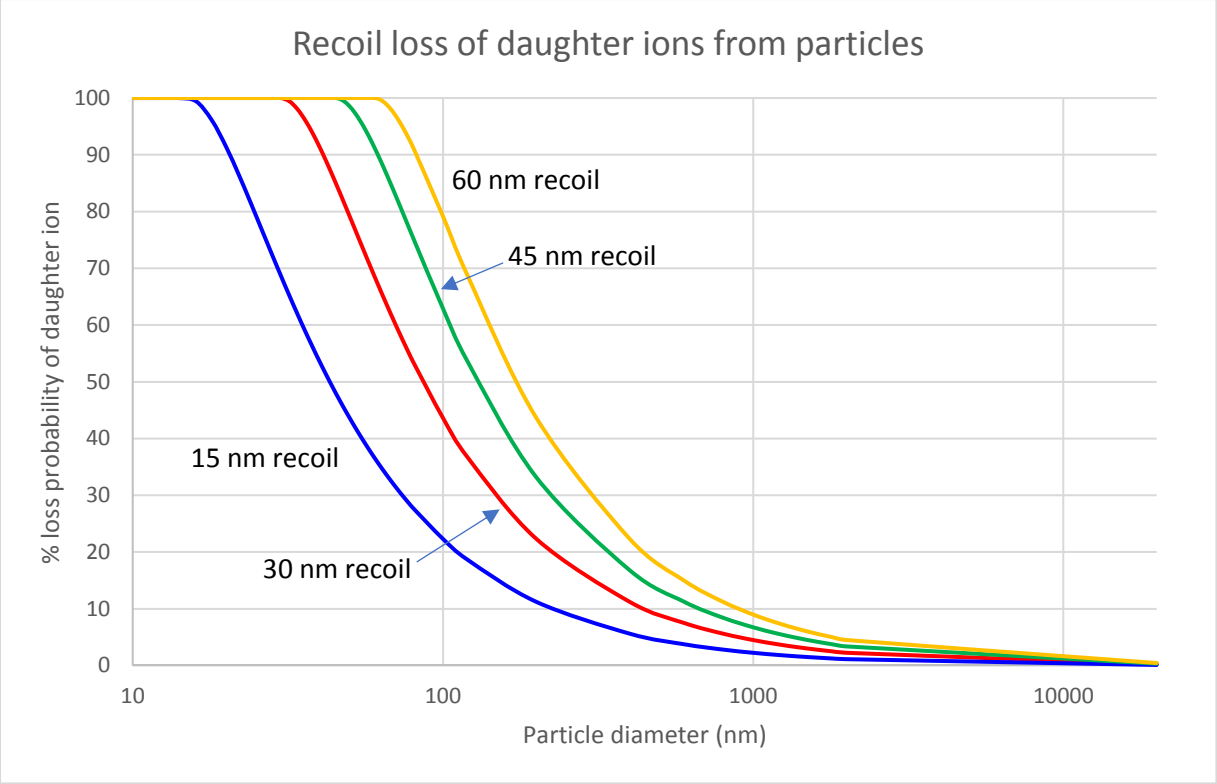

Figure 14. Probability of loss of daughter ions through recoil, modelled on spherical particles. The 30 nm recoil line (red) would be typical for ^{234}Th recoil in coffinite, suggesting nearly 100% loss of all daughter isotopes from coffinite particles/crystals smaller than 30 nm diameter or width.

This phenomenon might be seen as a mere curiosity given that it only affects the smallest (sub-micron) grains, but it is probable that nanoscale mechanisms play a primary role in the mobility and deportment of RNs at Olympic Dam. Nanoinclusions of U-bearing phases are nearly ubiquitous throughout the deposit, and are hosted in most minerals, including all main sulphides (e.g., Figures 4, 6a, 7). The 'new' insoluble Ra-, Pb-, and Po-bearing sulphates formed during the acid leach process are at least partly nanoparticulates (Rollog et al., 2019b). This has implications for processing and would explain why ^{210}Pb and ^{210}Po are frequently not observed together with ^{206}Pb (with a recoil energy 43% greater than ^{234}Th; Hashimoto et al., 1985). Although such separation is most marked in leached concentrates, it also occurs within the deposit as well; dissociation between ^{226}Ra and ^{210}Pb will be aided by four intermediate alpha decays if there is an available mode of removal for the expelled daughter ions.

5. Conclusions

- Minor host minerals may represent a significant, hitherto poorly constrained reservoir for radionuclides, especially ^{226}Ra and ^{210}Pb, within copper concentrates at Olympic Dam, and potentially other mineral deposits.
- Incorporating host minerals include apatite, fluorite, hematite, rutile, zircon, and likely also various REE fluorocarbonates and phosphates.
- Surficial hosts represent a significant RN reservoir in acid-leached copper concentrate, as sulphate-insoluble members are found on the surfaces of most grains. Surface area is a controlling factor, and nucleation on highly fractured or otherwise textured surfaces may result in significant localised RN activities.
- NanoSIMS mapping represents an efficient, high-resolution method to gain an understanding of RN distributions in complex ores and processing materials. Meaningful semi-quantitative distribution models can only be devised by a holistic investigation, incorporating likely, predictable hosts, less obvious potential mineral hosts, and non-mineral bound RNs.

Acknowledgements

This is a contribution to the ARC Research Hub for Australian Copper-Uranium (Grant IH130200033), co-supported by BHP Olympic Dam. The authors would also like to thank the editor and reviewers for their valuable contributions.

References

Atkinson, A., 1985. Grain boundary diffusion-structural effects and mechanisms. *Le Journal de Physique Colloques*, *46*(C4), C4-379.

665 Bebie, J., Schoonen, M.A., Fuhrmann, M. and Strongin, D.R., 1998. Surface charge development on
666 transition metal sulfides: an electrokinetic study. *Geochimica et Cosmochimica Acta*, *62*(4), 633-
667 642.
668 Bekri, S., Thovert, J.F. and Adler, P.M., 1997. Dissolution and deposition in fractures. *Engineering*
669 *Geology*, *48*(3-4), 283-308.
670 Bhargava, S.K., Ram, R., Pownceby, M., Grocott, S., Ring, B., Tardio, J. and Jones, L., 2015. A
671 review of acid leaching of uraninite. *Hydrometallurgy*, *151*, 10-24.
672 Bowles, J.F., 1990. Age dating of individual grains of uraninite in rocks from electron microprobe
673 analyses. *Chemical Geology*, *83*(1-2), 47-53.
674 Brady, J.B., 1995. Diffusion data for silicate minerals, glasses, and liquids. *Mineral Physics and*
675 *Crystallography: A Handbook of Physical Constants*, *2*, 269-290.
676 Cherry, A.R., Ehrig, K., Kamenetsky, V.S., McPhie, J., Crowley, J.L., Kamenetsky, M.B., 2018.
677 Precise geochronological constraints on the origin, setting and incorporation of ca. 1.59 Ga
678 surficial facies into the Olympic Dam Breccia Complex, South Australia. *Precambrian Research*,
679 *315*, 162-178.
680 Ciobanu, C.L., Cook, N.J., Kelson, C.R., Guerin, R., Kalleske, N. and Danyushevsky, L., 2013b.
681 Trace element heterogeneity in molybdenite fingerprints stages of mineralization. *Chemical*
682 *Geology*, *347*, 175-189.
683 Ciobanu, C.L., Wade, B.P., Cook, N.J., Schmidt Mumm, A. and Giles, D., 2013a. Uranium-bearing
684 hematite from the Olympic Dam Cu–U–Au deposit, South Australia: A geochemical tracer and
685 reconnaissance Pb–Pb geochronometer. *Precambrian Research*, *238*, 129-147.
686 Cook, N.J., Ehrig, K.J., Rollog, M., Ciobanu, C.L., Lane, D.J., Schmandt, D.S., Owen, N.D., Hamilton,
687 T. and Grano, S., 2018. ^{210}Pb and ^{210}Po in geological and related anthropogenic materials:
688 implications for their mineralogical distribution in base metal ores. *Minerals* 8(5), 211;
689 https://doi.org/10.3390/min8050211
690 Courtney-Davies, L., Tapster, S.R., Ciobanu, C.L., Cook, N.J., Kennedy, A.K., Ehrig, K., Condon,
691 D.J., Verdugo-Ihl, M.R., Wade, B.P. and Gilbert, S.E., 2019. Evaluating the U-Pb isotope

systematics of hydrothermal hematite and its implications for geochronology: insights from Olympic Dam, South Australia. *Chemical Geology*, 513, 54-72.

Curti, E., Fujiwara, K., Iijima, K., Tits, J., Cuesta, C., Kitamura, A., Glaus, M.A. and Müller, W., 2010. Radium uptake during barite recrystallization at 23±2 °C as a function of solution composition: An experimental ^{133}Ba and ^{226}Ra tracer study. *Geochimica et Cosmochimica Acta*, *74*(12), 3553-3570.

DePaolo, D.J., Maher, K., Christensen, J.N. and McManus, J., 2006. Sediment transport time measured with U-series isotopes: results from ODP North Atlantic drift site 984. *Earth and Planetary Science Letters*, *248*(1-2), pp.394-410.

Dijk, P. and Berkowitz, B., 1998. Precipitation and dissolution of reactive solutes in fractures. *Water Resources Research*, *34*(3), 457-470.

Dostal, J. and Capedri, S., 1978. Uranium in metamorphic rocks. *Contributions to Mineralogy and Petrology*, *66*(4), 409-414.

Dosseto, A., Bourdon, B. and Turner, S.P., 2008. Uranium-series isotopes in river materials: insights into the timescales of erosion and sediment transport. *Earth and Planetary Science Letters*, *265*(1-2), 1-17.

Ehrig, K., Kamenetsky, V.S., McPhie, J., Cook, N.J., Ciobanu, C.L., 2017. Olympic Dam iron oxide Cu-U-Au-Ag deposit. In G.N. Phillips, ed., *Australian Ore Deposits*. AusIMM, Melbourne, 601-610.

Ehrig, K., McPhie, J., Kamenetsky, V.S., 2012. Geology and Mineralogical Zonation of the Olympic Dam Iron Oxide Cu-U-Au-Ag Deposit, South Australia. In: J.W. Hedenquist, M. Harris, F. Camus (eds.), *Geology and Genesis of Major Copper Deposits and Districts of the World, a Tribute to Richard Sillitoe*. Society of Economic Geologists Special Publication 16, Littleton, USA, 237–267.

Förster, H.J., 2006. Composition and origin of intermediate solid solutions in the system thorite–xenotime–zircon–coffinite. *Lithos*, *88*(1-4), 35-55.

Grandstaff, D.E., 1976. A kinetic study of the dissolution of uraninite. *Economic Geology*, *71*(8), 1493-1506.

719 Hashimoto, T., Aoyagi, Y., Kudo, H. and Sotobayashi, T., 1985. Range calculation of alpha-recoil
720 atoms in some minerals using LSS-theory. *Journal of radioanalytical and nuclear chemistry*, *90*(2),
721 415-438.
722 Hurley, P.M. and Fairbairn, H.W., 1953. Radiation damage in zircon: a possible age method. *Geological*
723 *Society of America Bulletin*, *64*(6), 659-673.
724 Jackson, P.E., Carnevale, J., Fuping, H. and Haddad, P.R., 1994. Determination of thorium and uranium
725 in mineral sands by ion chromatography. *Journal of Chromatography A*, *671*(1-2), 181-191.
726 Klinkenberg, M., Brandt, F., Breuer, U. and Bosbach, D., 2014. Uptake of Ra during the
727 recrystallization of barite: a microscopic and time of flight-secondary ion mass spectrometry study.
728 *Environmental science & technology*, *48*(12), 6620-6627.
729 Krneta, S., Ciobanu, C.L., Cook, N.J., Ehrig, K. and Kontonikas-Charos, A., 2017. Rare Earth Element
730 Behaviour in Apatite from the Olympic Dam Cu–U–Au–Ag Deposit, South Australia. *Minerals*,
731 *7*(8), 135, 1-26
732 Lane, D.J., Cook, N.J., Grano, S.R. and Ehrig, K., 2016. Selective leaching of penalty elements from
733 copper concentrates: A review. *Minerals Engineering*, *98*, 110-121.
734 Li, G., You, Z., Sun, H., Sun, R., Peng, Z., Zhang, Y. and Jiang, T., 2016. Separation of rhenium from
735 lead-rich molybdenite concentrate via hydrochloric acid leaching followed by oxidative roasting.
736 *Metals*, *6*(11), 282, 1-12.
737 Macmillan, E., Cook, N.J., Ehrig, K., Pring, A., 2017. Chemical and textural interpretation of late-
738 stage coffinite and brannerite from the Olympic Dam IOCG-Ag-U deposit. *Mineralogical*
739 *Magazine*, *81*(6), 1323-1366.
740 McPhie, J., Kamenetsky, V., Allen, S., Ehrig, K., Agangi, A. and Bath, A., 2011. The fluorine link
741 between a supergiant ore deposit and a silicic large igneous province. *Geology*, *39*(11), 1003-1006.
742 Melekestseva, I.Y., Maslennikov, V.V., Maslennikova, S.P., Danyushevsky, L.V. and Large, R., 2017,
743 March. Covellite of the Semenov-2 hydrothermal field (13° 31.13′ N, Mid-Atlantic Ridge):
744 Enrichment in trace elements according to LA ICP MS analysis. In *Doklady Earth Sciences* (Vol.
745 473, No. 1, 291-295). Pleiades Publishing.

Morawska, L. and Jeffries, C., 1994. Distribution of radium in mineral sand grains and its potential effect on radon emanation. *Radiation Protection Dosimetry*, *56*(1-4), 199-200.

Palache, C., Berman, H., Frondel, C. and Dana, E.S., 1951. *The system of mineralogy of James Dwight Dana and Edward Salisbury Dana, Yale University, 1837-1892: Halides, nitrates, borates, carbonates, sulfates, phosphates, arsenates, tungstates, molybdates, etc*. J. Wiley and Sons.

Poczatek, C., Kaufman, Z., Lechene, C., 2009. OpenMIMS ImageJ Plugin Guide. *Harvard Medical School, Boston, Massachusetts, USA*.

Putnis, A., 2002. Mineral replacement reactions: from macroscopic observations to microscopic mechanisms. *Mineralogical Magazine*, *66*(5), 689-708.

Putnis, A., 2009. Mineral replacement reactions. *Reviews in Mineralogy and Geochemistry*, *70*(1), 87-124.

Putnis, A., 2014. Why mineral interfaces matter. *Science*, *343*(6178), 1441-1442.

Radhamani, R., Mahanta, P.L., Murugesan, P. and Chakrapani, G., 2010. Novel fusion method for direct determination of uranium in ilmenite, rutile, columbite, tantalite, and xenotime minerals by laser induced fluorimetry. *Journal of Radioanalytical and Nuclear Chemistry*, *285*(2), 287-292.

Ragozzini, R.J. and Sparrow, G.J., 1987. Selective dissolution of uranium from Olympic Dam copper concentrates. *Hydrometallurgy*, *18*(3), 367-382.

Rigali, M.J., Brady, P.V. and Moore, R.C., 2016. Radionuclide removal by apatite. *American Mineralogist*, *101*(12), 2611-2619.

Rollog, M., Cook, N.J., Guagliardo, P., Ehrig, K.J., and Kilburn, M., 2019a. In situ spatial distribution mapping of radionuclides in minerals by nanoSIMS. *Geochemistry: Exploration, Environment, Analysis*, (in print). http://doi.org/10.1144/geochem2018-038

Rollog, M., Cook, N.J., Guagliardo, P., Ehrig, K.J., Ciobanu, C.L., and Kilburn, M., 2019c. Detection of trace elements/isotopes in South Australian copper concentrates by nanoSIMS. *Minerals* (accepted)

Rollog, M., Cook, N.J., Guagliardo, P., Ehrig, K.J., and Kilburn, M., 2019b. Radionuclide-bearing minerals in Olympic Dam copper concentrates. (in revision).

773 Schindelin, J., Arganda-Carreras, I., Frise, E., Kaynig, V., Longair, M., Pietzsch, T., Preibisch S.,
774 Rueden C., Saalfeld, S., Schmid, B., Tinevez, J.Y., 2012. Fiji: an open-source platform for
775 biological-image analysis. *Nature Methods*, *9*, 676-682.
776 Schindelin, J., Rueden, C.T., Hiner, M.C., Eliceiri, K.W., 2015. The ImageJ ecosystem: An open
777 platform for biomedical image analysis. *Molecular Reproduction and Development, 82*, 518-529.
778 Schmandt, D.S., Cook, N.J., Ehrig, K., Gilbert, S., Wade, B.P., Rollog, M., Ciobanu, C.L., Kamenetsky,
779 V.S., 2019. Uptake of trace elements by baryte during copper ore processing: a case study from
780 Olympic Dam, South Australia. *Minerals Engineering*, *135*, 83-94.
781 Tartakovsky, A.M., Meakin, P., Scheibe, T.D. and Wood, B.D., 2007. A smoothed particle
782 hydrodynamics model for reactive transport and mineral precipitation in porous and fractured porous
783 media. *Water Resources Research*, *43*(5). W05437, 1-18
784 Verdugo-Ihl, M.R., Ciobanu, C.L., Cook, N.J., Ehrig, K., Courtney-Davies, L. and Gilbert, S., 2017.
785 Textures and U-W-Sn-Mo signatures in hematite from the Cu-U-Au-Ag orebody at Olympic Dam,
786 South Australia: defining the archetype for IOCG deposits. *Ore Geology Reviews* 91, 173-195.
787 Vinograd, V.L., Kulik, D.A., Brandt, F., Klinkenberg, M., Weber, J., Winkler, B. and Bosbach, D.,
788 2018. Thermodynamics of the solid solution - Aqueous solution system (Ba, Sr, Ra) SO_4 + H_2O: II.
789 Radium retention in barite-type minerals at elevated temperatures. *Applied Geochemistry*, *93*, 190-
790 208.

791

792

793

Chapter 8

Rapid, competitive radium uptake in strontium, barium, and lead sulphates during sulphuric acid leaching

Mark Rollog [a,*], Nigel J. Cook [a], Kathy Ehrig [b], and Sarah E. Gilbert [c]

[a] *School of Chemical Engineering, University of Adelaide, Adelaide, 5005 S.A., Australia*

[b] *BHP Olympic Dam, 55 Grenfell St., Adelaide, 5000 S.A., Australia*

[c] *Adelaide Microscopy, The University of Adelaide, SA, 5005, Australia*

Article accepted for publication in *Applied Geochemistry* on 27 September 2019

Statement of Authorship

Title of Paper	Rapid, Competitive Radium Uptake in Strontium, Barium, and Lead Sulfates During Sulfuric Acid Leaching
Publication Status	☐ Published ☑ Accepted for Publication ☐ Submitted for Publication ☐ Unpublished and Unsubmitted work written in manuscript style
Publication Details	Submitted to *Applied Geochemistry* 20 July 2019, accepted 27 September 2019.

Principal Author

Name of Principal Author (Candidate)	Mark Rollog
Contribution to the Paper	Performed analytical work, carried out data corrections and interpretation, wrote and edited manuscript
Overall percentage (%)	80
Certification:	This paper reports on original research I conducted during the period of my Higher Degree by Research candidature and is not subject to any obligations or contractual agreements with a third party that would constrain its inclusion in this thesis. I am the primary author of this paper.
Signature	Date 23.08.19

Co-Author Contributions

By signing the Statement of Authorship, each author certifies that:

i. the candidate's stated contribution to the publication is accurate (as detailed above);
ii. permission is granted for the candidate in include the publication in the thesis; and
iii. the sum of all co-author contributions is equal to 100% less the candidate's stated contribution.

Name of Co-Author	Nigel J. Cook
Contribution to the Paper	Supervised direction of research, edited manuscript
Overall percentage (%)	10
Signature	Date 1/8/19

Name of Co-Author	Kathy Ehrig
Contribution to the Paper	Helped evaluate and edit manuscript
Overall percentage (%)	5
Signature	Date 31 July 2019

817

Name of Co-Author	Sarah E. Gilbert		
Contribution to the Paper	Oversaw sample analyses, helped evaluate and edit manuscript		
Overall percentage (%)	5		
Signature		Date	5/8/19

818

819

820

Abstract

Uranium- and thorium-bearing base metal mineral deposits contain daughter radionuclides which must be monitored and preferably removed or reduced during the process of generating base metal sulfide concentrates. Understanding the behavior of these radionuclides (focusing on ^{226}Ra in this study) is critical for minimizing their concentrations in final economic products. To this end, Ra uptake into Sr, Ba, and Pb sulfates was evaluated experimentally under various conditions, including those approximating processing plant environments. Lead activity was also monitored, as ^{210}Pb is also a radionuclide of concern. To simplify experiments, synthetic crystals of celestine ($SrSO_4$), baryte ($BaSO_4$), and anglesite ($PbSO_4$) were grown in silica gel and subsequently exposed to $RaCl_2$ solution at both low and neutral pH, for both 40 and 210 hours. Laser ablation inductively coupled plasma mass spectrometry (LA-ICP-MS) transects were performed across the grains to determine uptake of Ra (as well as trace Sr, Ba, and Pb) in the sulfates. Results indicate that Ra uptake in celestine is efficient when Ba and Pb are absent but is reduced to nearly zero when competing with baryte and anglesite. High acid sulfate activity inhibits uptake. Baryte incorporates significant Ra under all conditions. Anglesite is affected by coupled dissolution-reprecipitation mechanisms, resulting in dissolution of $PbSO_4$ followed by precipitation of a mixed $(Pb,Ba,Sr,Ra)SO_4$ phase in its place. Again, high sulfate activity inhibits this reaction. With this knowledge, it may be possible for process engineers to purposefully stimulate precipitation of Ra (and possibly Pb) onto a sulfate matrix, given the right conditions. Precipitation of $RaSO_4$ (and $^{210}PbSO_4$) onto a removable phase during processing would result in sulfide concentrates with natural background concentrations of radionuclides. Results from this study, including semi-quantitative Ra concentration data obtained via *in situ* LA-ICP-MS analysis add to data pertinent to management of Ra in boiler scales, oil and gas pipelines, environmental remediation, nuclear medicine, nuclear fuel processing and waste storage, among other industrial and research applications.

1. Introduction

Radium management is a continuing issue in a number of industries and research disciplines including mining and ore treatment (Roessler, 1990; Pluta, 2001; Carvalho et al., 2007), environmental monitoring (Puch et al., 2005), boiler operations (Poggi et al., 2015), oil (Gazineau & Hazin, 2008) and gas pipelines (Zhang et al., 2014), energy production from coal (Baba, 2002; Janković et al., 2011), nuclear medicine (e.g., Parker et al., 2013), nuclear energy production and waste management (Ojovan et al., 2019), and the few remaining industrial applications using Ra (Pratt, 1993; Halmshaw, 1996). Regardless of whether Ra is being minimized (environmental concerns) or maximized (Ra production for medical or industrial applications), the behavior of Ra and Ra-bearing compounds needs to be comprehensively understood, especially where that behavior is modified during a given industrial process, or under varying conditions.

Given that the most common isotope ^{226}Ra is around 3 million times less abundant than its distant parent isotope ^{238}U, detailed research into this element has only progressed as quickly as have advances in nanoscale analytical techniques that can accurately pinpoint host phases and provide qualitative or semi-quantitative data on activities/concentrations. Much research into Ra isotopes focuses either on natural abundances in environmental samples, or the handling of Ra-enriched products from nuclear fuel and other industrial uses.

This study highlights the importance of Ra management in the minerals industry where Ra concentrations in ores and intermediate processing materials may be elevated compared to natural background values but are not isolated within specific Ra-bearing products. Operators of mining-processing-smelting operations – including those exploiting ores that contain uranium and/or thorium – are tasked with isolating and purifying the elements or products with economic value from those without. Whether U or Th is economically recovered or not, these operators have the additional burden of managing daughter radionuclides (RNs) produced via

isotopic decay. Generally, daughter isotopes of the ^{235}U and ^{232}Th decay chains do not cause a problem during ore processing due to their extremely low concentrations or low activities. There are, however, a few members of the ^{238}U decay chain which may accumulate to above-acceptable activity levels during processing – yet remain below detection limits for most *in situ* analytical methods. Radium-226, ^{210}Pb, and ^{210}Po are such daughters, and additional steps must be taken to remove, or at least reduce, them in products to be sold on world markets or destined for further processing. Radium, Pb, and Po all form insoluble sulfates (along with Sr and Ba) and therefore the deportment of these elements in the deposit, and during ore processing, tends to be defined by sulfate activity.

Research into radium uptake in baryte began nearly a century ago (Doerner and Hoskins, 1925) and continues today (e.g., Curti et al., 2010; Weber et al., 2017; Vinograd et al., 2018a, 2018b). Similar mechanisms have been recognized in $PbSO_4$ (Langmuir and Riese, 1985), $SrSO_4$ (Brown et al., 2015), and mixed sulfates (e.g., Momoshima et al., 1997; Chao et al., 2009; Hedstrom et al., 2013; Vinograd et al., 2018a/b). Most existing literature focuses on Ra uptake over long periods of time under relatively benign conditions. This study aims to illuminate the mechanisms of Ra uptake into sulfates under more trying conditions – those which may be found in hydrometallurgical facilities at mine sites, in boiler operations, or in gas and oil production pipelines. Short exposure times (40 and 210 hours), elevated temperatures (60 °C), and harsh pH conditions (H_2SO_4, ca. 1.5 M), result in thermodynamic and kinetic conditions which may not exist under milder circumstances and may significantly accelerate reactions.

Chloride aids in dissolution of $SrSO_4$, $BaSO_4$, and $PbSO_4$ (Lucchesi and Whitney, 1962; Linke and Seidell, 1965; Raju and Atkinson, 1988, 1989; Nguyen et al., 2011) and is predicted to do the same for $RaSO_4$. In contrast, high sulfate activity should inhibit solubilities by causing precipitation at much lower concentrations, therefore reducing residence times of Sr^{2+}, Ba^{2+},

Pb^{2+}, and Ra^{2+} in solution. Reduced cationic residence times are predicted to translate into less uptake of Ra into the host crystals, although the adherence of freshly precipitated Ra-bearing sulfate nanoparticles onto crystal surfaces is a possibility.

Three primary methods of uptake are investigated, although these may not be comprehensive. Coupled dissolution-reprecipitation (CDR) involves the dissolution of a host phase and precipitation of a new phase in its place, usually retaining the original crystal morphology but exhibiting increased porosity (Putnis, 2002, 2009). Overgrowth involves the precipitation of a new phase on the surface of a host crystal without significant dissolution of the host phase. Diffusion refers to solid-state diffusion of a species into the surface of a host crystal without either significant dissolution of the host, or precipitation of a new phase.

This study has focused on ^{226}Ra and Pb with specific regard to the potential implications for effective treatment of ores and concentrates composed of minerals, although applications may extend to any industry or research application challenged with either the management of Ra or the removal of unwanted Ra.

2. Experimental Methods

2.1. Crystal growth

To better understand the behavior of insoluble sulfates, crystals of synthetic celestine ($SrSO_4$), baryte ($BaSO_4$), and anglesite ($PbSO_4$) were prepared by the silica gel method (Patel and Bhat, 1972; Henisch, 1996). Briefly, sodium metasilicate solutions were prepared containing either Sr^{2+}, Ba^{2+}, or Pb^{2+} (0.01-0.02 M) which were poured into individual 75 mL test tubes (to about 1/2 full) and allowed to set for one week into a semi-firm gel. Once firm, a solution of sodium sulfate (0.1 M) was carefully poured on top of the gel and was allowed to diffuse into the gel for 1-2 weeks. $SrSO_4$, $BaSO_4$, or $PbSO_4$ crystals grew by the slow interaction of reagents. The gel was scraped into a beaker and a jet of RO water from a squeeze bottle was used to break

920 up the gel and dislodge the crystals. Gentle swirling with multiple rinses of RO water resulted
921 in the crystals settling on the bottom of the beaker. The crystals were then removed with a
922 disposable pipette. Crystals were rinsed only with RO water, but SEM imaging of the crystals
923 showed nearly complete removal of the silica gel. It was decided that the tiny spots of
924 remaining silica gel would not affect the overall results, as chemical cleaning of the crystals
925 might.

926 A detailed description of the exact crystal growth method may be found in Rollog et al.
927 (2019). Celestine, baryte, and anglesite all crystallize in the orthorhombic crystal system,
928 dipyrimidal (2/*m* 2/*m* 2/*m*) crystal class. Crystals ranged in size from 50 to >500 µm in
929 maximum dimension. The $PbSO_4$ specimens were euhedral and transparent, generally adopting
930 a roughly tetragonal prism with variable dipyrimidal (bladed) terminations (Figure 1).
931 Strontium sulfate crystals were similar, though translucent, with slightly rounded prisms.
932 Twinning was frequent, as were additional lateral growths ("ears") near the prism/termination
933 interface. The $BaSO_4$ almost always formed translucent twin blades, joined at their centers in
934 "bowtie" fashion.

935 Crystals were imaged on an FEI Quanta450 field emission gun scanning electron
936 microscope (FEG-SEM), coupled with an Oxford Ultim Max energy-dispersive spectrometer
937 (EDS) at Adelaide Microscopy (The University of Adelaide). All EDS spectra were clean and
938 sharp, showing no contaminating cations above minimum limits of detection (~0.1 wt.%),
939 although small spots of silicon contamination (from the silica gel) could be seen on the surface
940 of some grains.

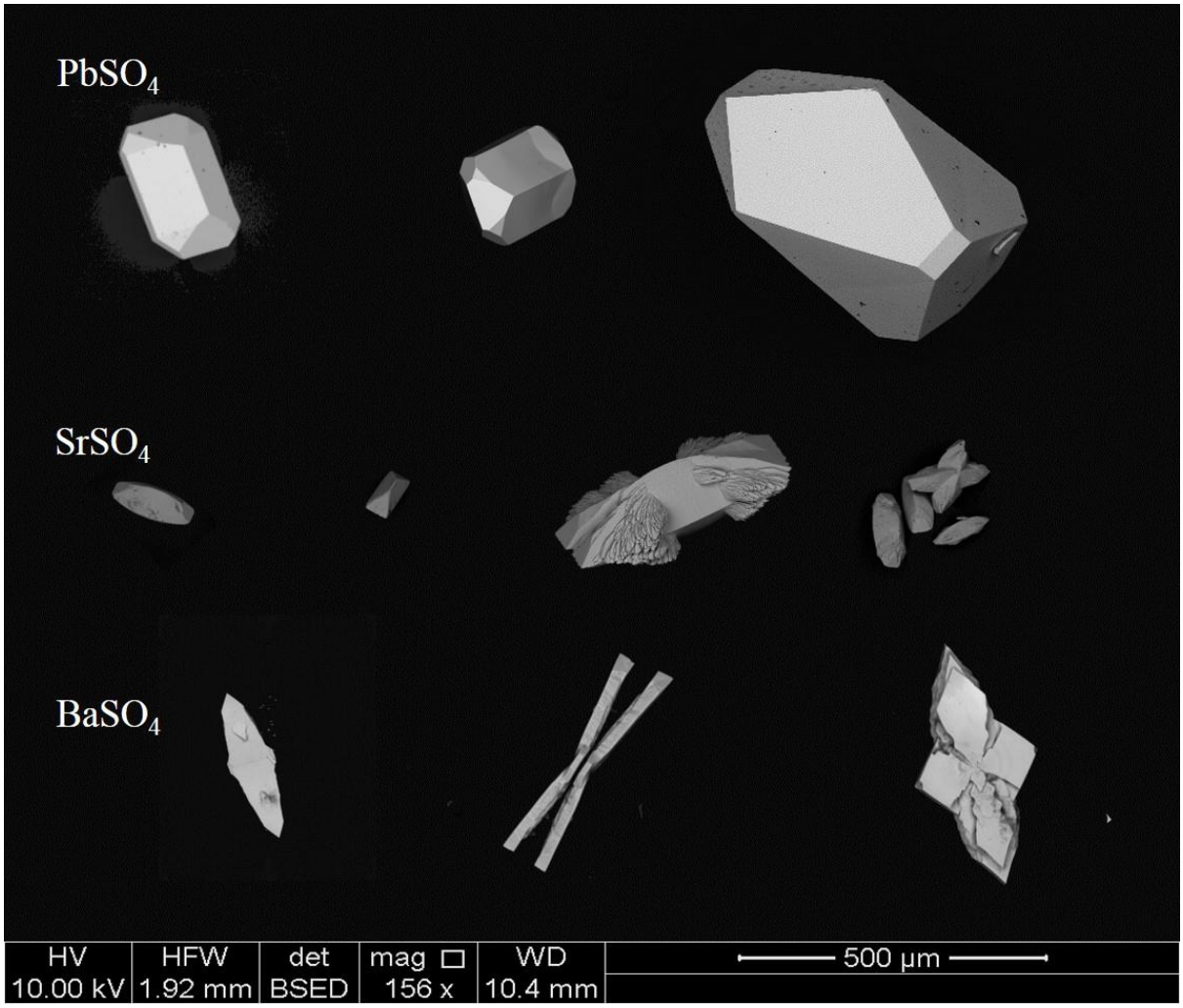

Figure 4. Backscatter electron (BSE) image of typical crystals of synthetic anglesite, celestine, and baryte crystals grown in silica gel.

It should be noted that although these synthetic crystals do not adhere to the strict definition of a mineral (Dyar et al., 2008), the terms baryte, celestine, and anglesite are used interchangeably with $BaSO_4$, $SrSO_4$, and $PbSO_4$, respectively, in this study. These synthetic crystals were created as clean, impurity-free proxies for the natural minerals that commonly contain up to wt% levels of other cations (e.g., Sr in baryte). Evidence suggests that their behaviors are similar enough that the results of these experiments would apply equally to synthetic phases and their mineral analogues.

2.2. Reactions

Four sets of experiments were performed using the crystals, with four reaction vials per set. The first three sets involved reacting isolated sulfates with $RaCl_2$ solution, both with and without additional sulfuric acid, both for 40 hours and for 210 hours. The final set repeated these conditions, but all three sulfates were together in the same vial. All reactions took place at 60 °C. The $RaCl_2$ solution used was provided by the South Australian Environmental Protection Authority (SA EPA) and was reported to be 100 Bq/mL. Solution ICP-MS analysis of the $RaCl_2$ solution revealed many other elements (Figure 2). Although the presence of trace amounts of Sr, Ba, and Pb in the $RaCl_2$ solution was not ideal, it does in fact represent conditions that more closely resemble those in natural environments.

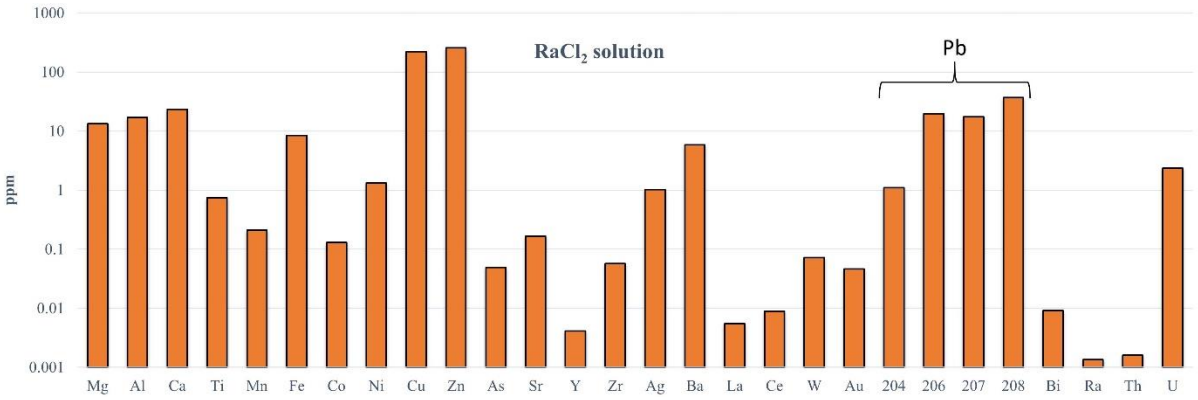

Figure 2. Solution ICP-MS analysis of the $RaCl_2$ solution provided by SA EPA. All values were calculated based on standard solutions except Ra, which is shown as 50 Bq/ml (~6 nM) – as reported by the SA EPA. Contaminants included 165 ppb Sr, 5.8 ppm Ba, and 75 ppm total Pb.

It should be noted that the addition of H_2SO_4 to some of the vials actually varies two parameters instead of one – an increase in sulfate activity and a decrease in pH. In the future, high-sulfate, neutral pH and sulfate-free, low pH experiments will also be performed. Acid

969 sulfate solutions were used to more closely represent the conditions experienced during mineral
970 processing.

971 Two to five crystals of each sulfate were selected for size and quality and added to the
972 appropriate vials (Table 1). Although the samples were not weighed, a rough visual estimate
973 was made to balance the amount of material in each vial (i.e., fewer large crystals, or more
974 smaller ones).

975 **Table 1.** Vial contents for the four experiments (experiment 1 = vials 1(a-d), experiment 2 =
976 vials 2(a-d), etc.) Values under the crystal types are the numbers of crystals added to each
977 vial. Solutions (150 g/L sulfate H_2SO_4, reverse osmosis (RO) filtered H_2O, and 50 Bq/mL =
978 ~6 nM $RaCl_2$) reported in µL.

Vial #s	n $SrSO_4$	n $BaSO_4$	n $PbSO_4$	H_2SO_4 (µL)	H_2O (µL)	$RaCl_2$ (µL)
1 (a,c)	2-3				50	50
1 (b,d)	2-3			50		50
2 (a,c)		4-5			50	50
2 (b,d)		4-5		50		50
3 (a,c)			2		50	50
3 (b,d)			2	50		50
4 (a,c)	2-3	4-5	2		50	50
4 (b,d)	2-3	4-5	2	50		50

979 The $RaCl_2$ solution was diluted by a factor of two (from 12 nM to 6 nM), and 50 µL was
980 added to each vial. Sulfuric acid (50 µL, 150 g/L sulfate ≈ 1.6 M) was added to half of the
981 vials, RO water (50 µL) was added to the other half to maintain consistent [Ra]; square brackets
982 designate concentrations/activities. Sample vials were placed in a 60 °C oven and left
983 undisturbed to react for either 40 or 210 hours. After the reactions were complete, crystals were
984 rinsed three times with 60 °C RO water and left to dry in the vials. Crystals from each vial were
985 individually selected under a microscope with a fine-tip paint brush and arranged on double-
986 sided tape, stuck to the base of a 1-inch round epoxy mold. Two identical epoxy mounts were
987 made, each with all 24 crystal experiments represented (one crystal each from vials 1a-3d, three

988 crystals each from vials 4a-4d). Mounts were polished and carbon-coated, after which grains
989 were imaged and analyzed by SEM-EDS.
990 EDS spectra of grain interiors were again shown to be clean and sharp, with the only
991 contamination coming from trace amounts of Si in some of the grain cores – a common
992 occurrence when growing crystals in silica gel. Since these experiments focused on surface
993 reactions, the slight Si enrichment in grain cores was considered irrelevant. Porosity was also
994 noted in some grains, especially in $SrSO_4$, but sharp and distinct surface reaction zones in LA-
995 ICP-MS transects suggest that this was also not an issue.

996 *2.3. Analysis*

997 Sample grains were analyzed by laser ablation inductively coupled plasma mass spectrometry
998 (LA-ICP-MS) using an ASI RESOlution-LR ArF excimer laser ablation system with a large
999 format S155 sample chamber (Laurin Technic Inc.), coupled to an Agilent 7900x ICP-MS.
1000 Transects were performed across each crystal (using a 6 µm-diameter laser spot size), with at
1001 least 10 µm on either side through the epoxy to establish a blank. Additionally, 110 µm-
1002 diameter single spot analyses were run (overlapping as much of the crystal edges as possible)
1003 to ensure a sufficiently large Ra signal was obtained. Fluence was set to 3.5 Jcm^{-2} and repetition
1004 rate was 10 Hz. Reference standard (NIST-610) was run in duplicate at the beginning, middle,
1005 and end of the run. Isotopes analyzed included ^{88}Sr, ^{138}Ba, $^{204, 206, 207, 208}Pb$, and ^{226}Ra. Elemental
1006 concentration data for single spots were calculated using the internal standard method
1007 (Longerich et al., 1996); transect concentration data (in ppm) were calculated using a modified
1008 version of the internal standard method with an additional minor drift correction. Ra
1009 concentration data were estimated using the method described in Section 4 below. Transect
1010 concentrations were normalized (in ppm) to 1,000,000 as measured in the center of the grain
1011 instead of $ppm_{(total\ count)}$ to avoid anomalous values across grain/epoxy boundaries. Isotopic
1012 abundances were converted to elemental abundances using global isotope ratios (Haynes,

2014). Time-resolved transect data from the ICP-MS (in seconds) were converted to distances (in µm) by directly comparing the isotope trace signals to grain dimensions on the BSE images, and are therefore estimates. Concentration data were smoothed using a 3-period moving average to minimize electrical spikes.

Analyses of unreacted material revealed that all three sulfates are slightly contaminated with other cations, although below EDS detection limits (Figure 3). Evident in the LA-ICP-MS transects, however was that the baryte contains approximately 10 ppm total Pb and 140 ppm Sr; celestine contains roughly 30 ppm of total Pb and 100 ppm of Ba; the anglesite contains up to 500 ppm Ba in the crystal centers, decreasing to around 100 ppm near the edges, and 100 ppm Sr. These contaminations were likely in the original solutions used to grow the crystals, but these traces and the [Sr], [Ba], and [Pb] in the Ra solution had only a minor effect on the results of the experiments, as addressed in the 'Results and Discussion' sections below.

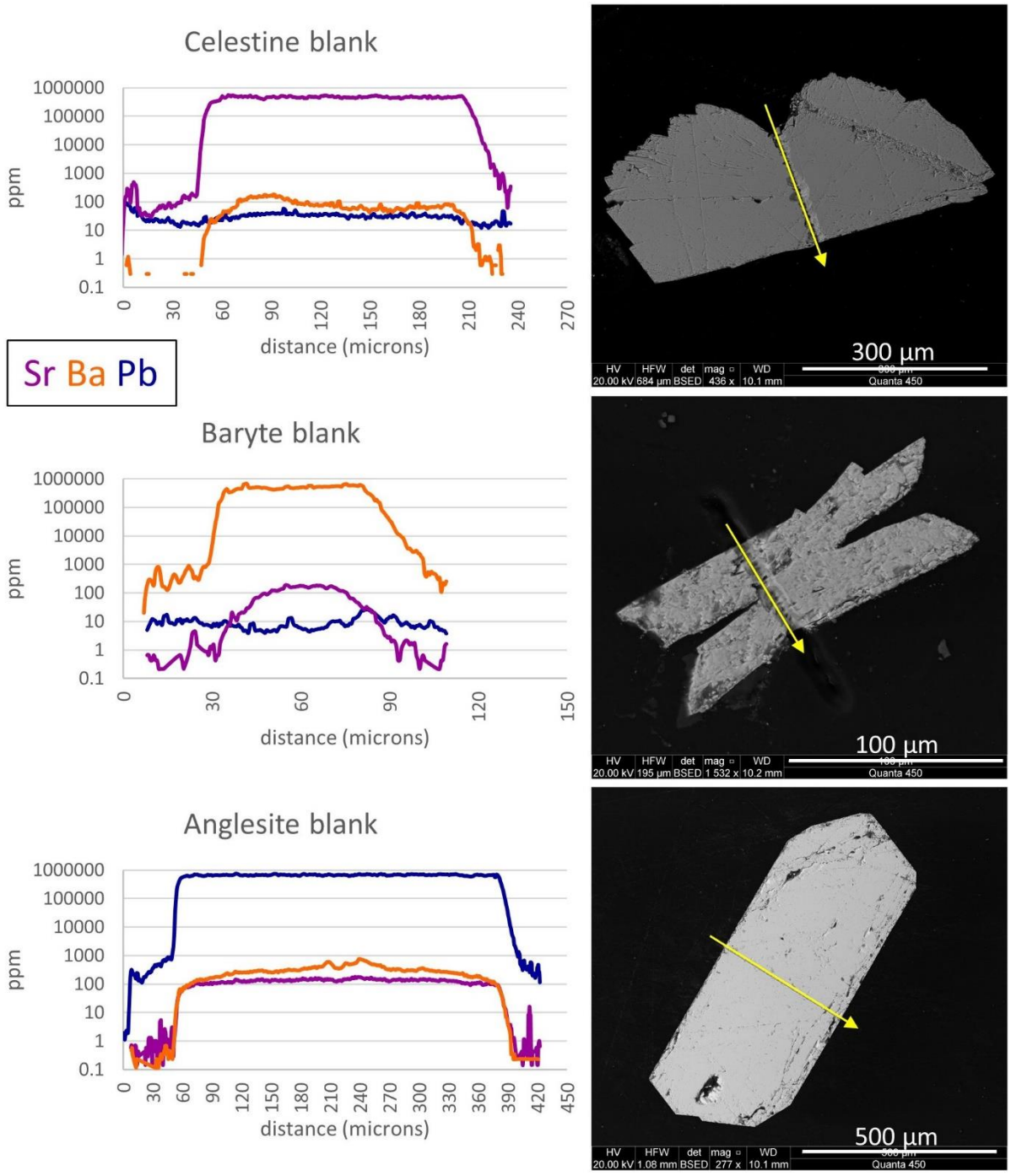

Figure 3. LA-ICP-MS transects and BSE images from unreacted crystals. Yellow arrows in the BSE images indicate locations and directions of laser transects. Radium measurements were below the detection limit.

3. Results and Discussion

3.1. Transects

Although experiments 1-4 were run sequentially, they will be presented here in slightly different order for clarity. Experiments 1-3 related to single sulfates, whereas experiment 4 involved all three sulfates in contact with one another. Each individual sulfate experiment will be presented, followed immediately by the same sulfate representative from experiment 4. By doing this, a simple comparison can be made between how these sulfates react with respect to Ra solution when alone, versus the reactions involved when they are in direct competition with the other two sulfates.

Experiment 1 involved isolated celestine crystals exposed to $RaCl_2$ solution under given conditions. The celestine crystals were euhedral to subhedral, with occasional twinning (Figure 4). Laser transects show sharp grain boundaries and stable Sr signals. Radium uptake by celestine in the sulfate-free vials was extensive, both at 40 and 210 hours. Concentration profiles of Ba and Pb parallel that of Ra., suggesting that even the minor concentrations in the $RaCl_2$ solution – along with chloride complexation – may have assisted in coupled dissolution-reprecipitation (CDR) reactions. Natural porosity in the crystals created during crystal growth may have accelerated the infiltration. However, the vials containing sulfate show very little Ra incursion into the crystals, despite the porosity. Radium uptake in these crystals still mimics those of Ba and Pb, but CDR was limited to within a few microns of the crystal surface, and total Ra uptake (and trace Ba and Pb uptake) was greatly reduced.

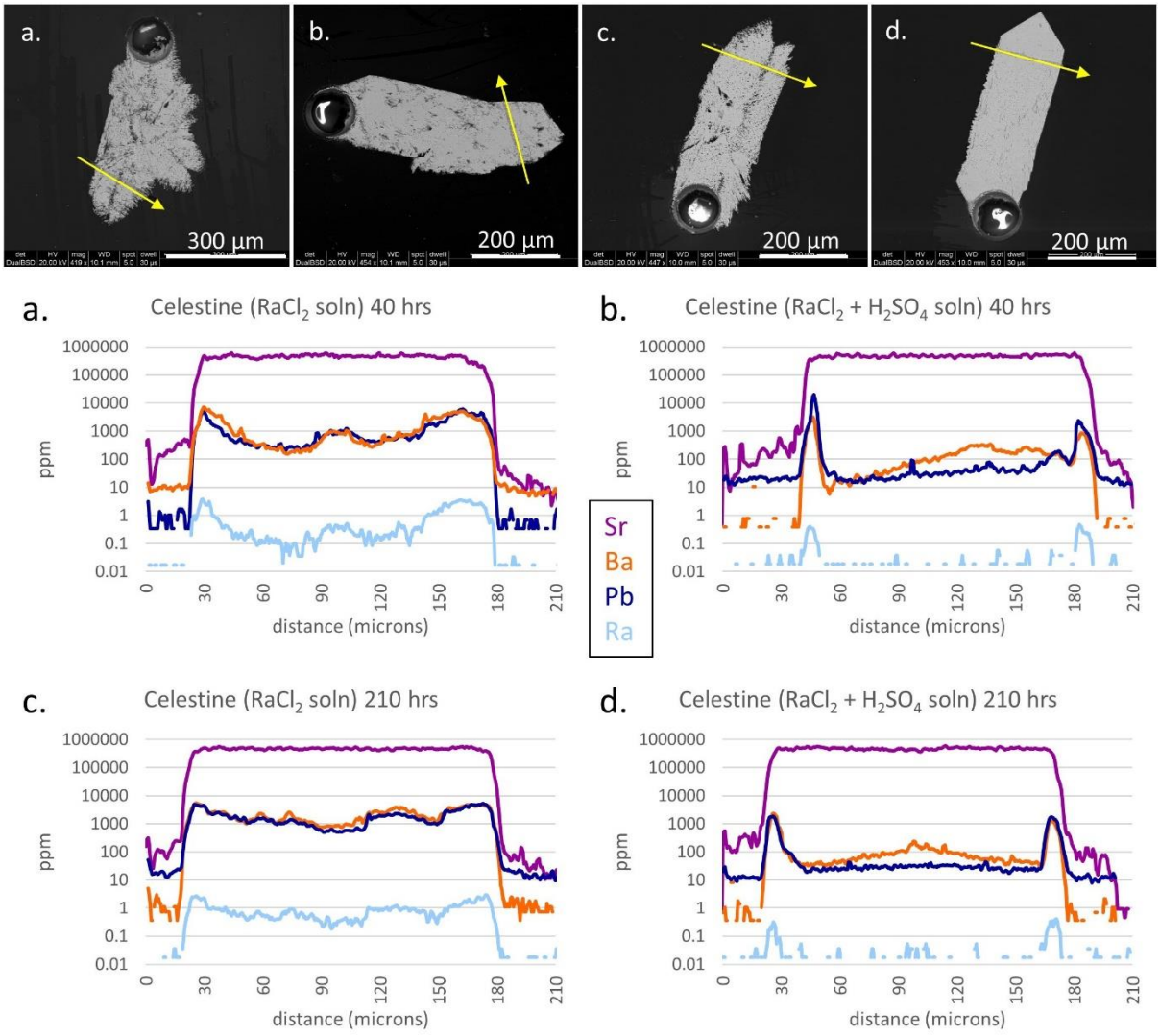

Figure 4. LA-ICP-MS transects and BSE images from experiment 1 with isolated $SrSO_4$ crystals and $RaCl_2$ solution: (a) without acid sulfate, 40 hours; (b) with acid sulfate, 40 hours; (c) without acid sulfate, 210 hours; and (d) with acid sulfate, 210 hours. Yellow arrows in the BSE images indicate locations and directions of laser transects. Radium concentrations (in yellow) are estimates.

Celestine crystals from experiment 4 showed very different results (Figure 5). When in direct competition with baryte and anglesite, virtually no Ra was incorporated into the celestine – regardless of sulfate activity. Porosity does play a minor role as seen in Figure 5a, where [Pb] increases and plateaus over a particularly porous region of the crystal. However, [Ba] and [Ra] in this region are unaffected. There is some increase in [Ba] and [Pb] in the high-sulfate vials, at grain surfaces, with a corresponding miniscule increase in [Ra].

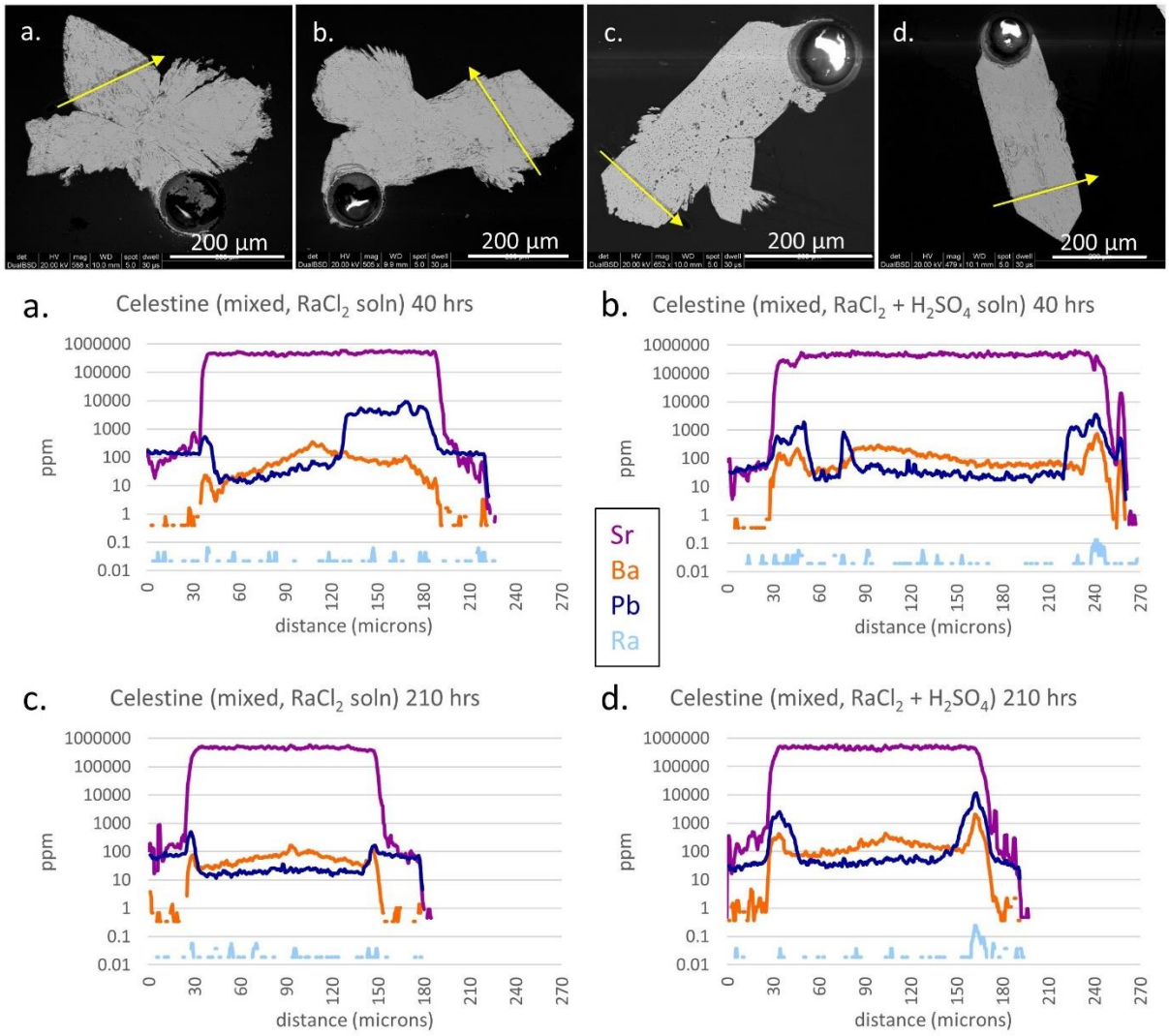

Figure 5. LA-ICP-MS transects and BSE images from experiment 4 with $SrSO_4$ crystals (in contact with $PbSO_4$ and $BaSO_4$ crystals) and $RaCl_2$ solution: (a) without acid sulfate, 40 hours; (b) with acid sulfate, 40 hours; (c) without acid sulfate, 210 hours; and (d) with acid sulfate, 210 hours. Yellow arrows in the BSE images indicate locations and directions of laser transects. Radium concentrations are estimates.

Experiment 2 focused on reactions of baryte crystals. An effort was made for the baryte "bowties" to be mounted upright in the epoxy resin so that both blades were visible, but the fragile (and microscopic) nature of these crystals occasionally resulted in broken or tilted samples (Figure 5). Laser transects from baryte resemble those of celestine, in that sulfate-free crystals incorporated very high amounts of Ra (to an estimated 6 ppm) throughout the entire crystal, whereas Ra uptake in the presence of sulfate was limited to grain surfaces. Once again,

chloride complexation in combination with CDR is a likely mechanism in both cases but is inhibited by high sulfate activity. Radium concentration profiles in all four grains parallel those of Pb but not Sr. Higher Sr concentrations in crystal centers suggest that higher concentrations of Sr were incorporated into the crystal structure early in the growth process, and the Sr contamination decreased as the crystals grew. Similar effects can be seen with Ba in Figure 5 above. pre-existing Sr may have been leached out during the experiment, whereas Pb was incorporated – along with Ra.

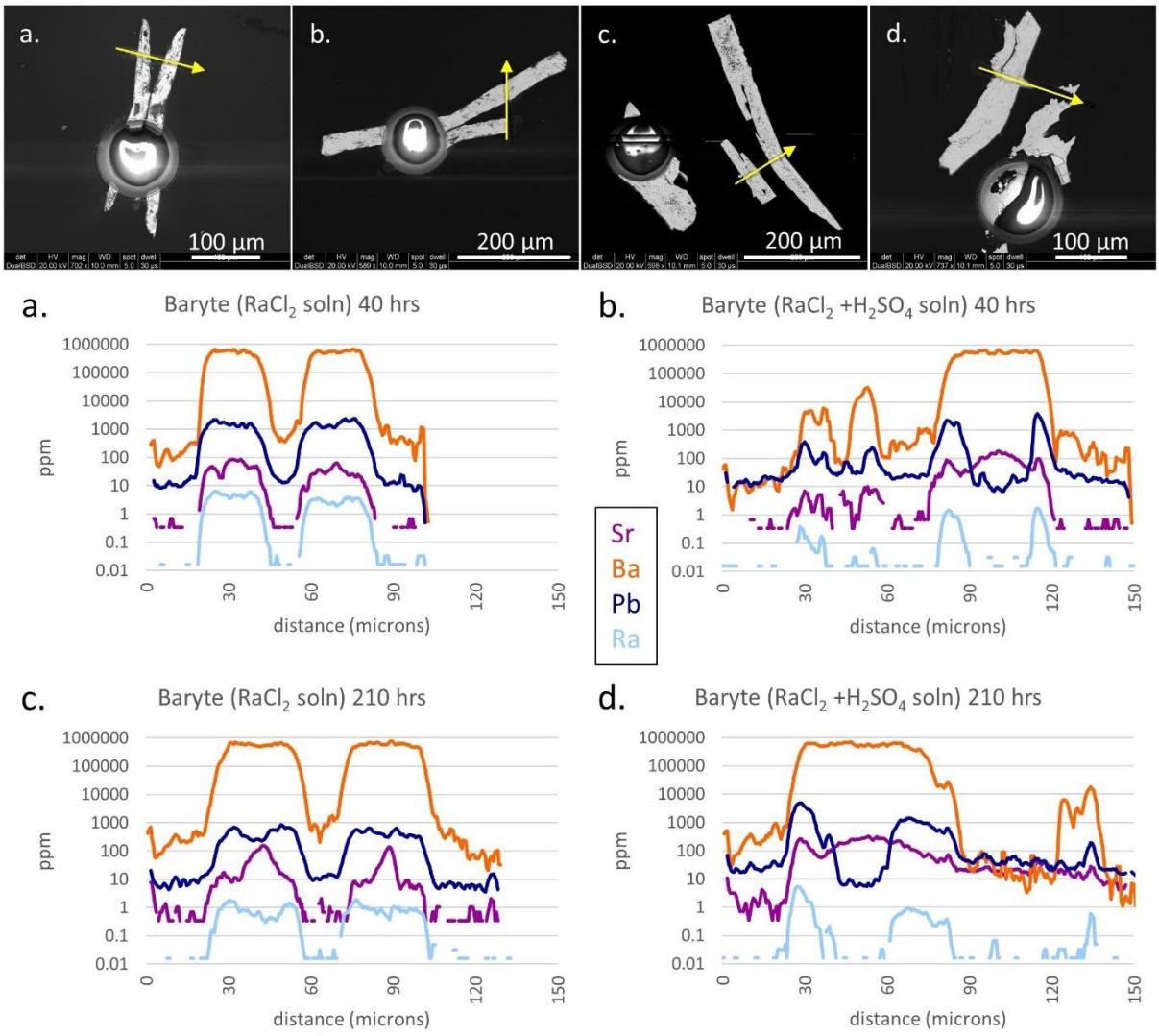

Figure 6. LA-ICP-MS transects and BSE images from experiment 2 with isolated $BaSO_4$ crystals and $RaCl_2$ solution: (a) without acid sulfate, 40 hours; (b) with acid sulfate, 40 hours; (c) without acid sulfate, 210 hours; and (d) with acid sulfate, 210 hours. Yellow arrows in the

BSE images indicate locations and directions of laser transects. Radium concentrations are estimates.

Baryte crystals from experiment 4 also showed significant Ra uptake, in both sulfate-free and sulfate-rich environments, but the CDR reaction fronts never penetrated more than about 20 µm in from the grain surface (Figure 7). The central feature in Figure 7d resulted from the laser sampling the bottom of a tipped-sideways crystal, visible as a "smear" in the BSE image. Overgrowth (predominantly $PbSO_4$) can be seen in BSE images as well as in the ICP-MS traces, where the Pb (blue) line exceeds the Ba (green) line (e.g., Figure 7c). Radium concentration profiles consistently parallel those of both Sr and Pb. Both [Pb] and [Sr] increased with time (the only experiment in which time had a marked effect) but [Ra] remained constant, suggesting that a kinetic equilibrium or saturation may be approached within 40 hours.

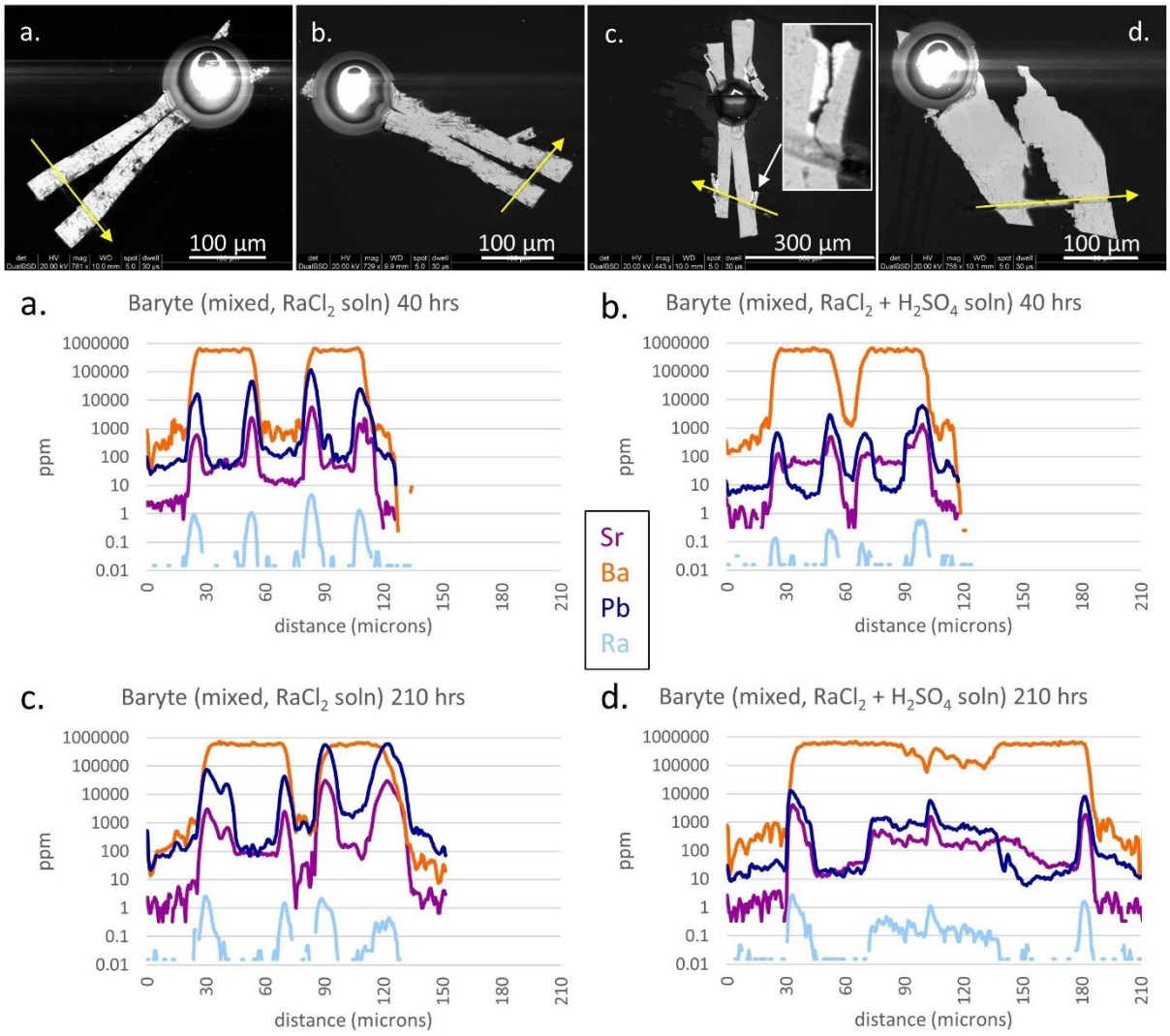

Figure 7. LA-ICP-MS transects and BSE images from experiment 4 with $BaSO_4$ crystals (in contact with $PbSO_4$ and $SrSO_4$ crystals) and $RaCl_2$ solution: (a) without acid sulfate, 40 hours; (b) with acid sulfate, 40 hours; (c) without acid sulfate, 210 hours; and (d) with acid sulfate, 210 hours. Yellow arrows in the BSE images indicate locations and directions of laser transects. Radium concentrations are estimates.

Large, euhedral anglesite crystals were exposed to $RaCl_2$ solution in experiment 3 (Figure 8). Crystals remained euhedral, with a majority of the grain edges remaining sharp and clean, although the grain in Figure 8a shows some surface dissolution. Some angular pitting was evident along grain edges and within grains due to damage from polishing. In contrast to the celestine and baryte results, anglesite incorporated very little Ra when isolated. A trace amount (generally <1 ppm) was integrated into grain edges, seemingly in concert with uptake of Ba

(but not Sr). Strontium traces remain constant throughout and represent the original ca. 100 ppm Sr contamination incorporated during crystal growth. Neither time nor sulfate activity had a noticeable effect.

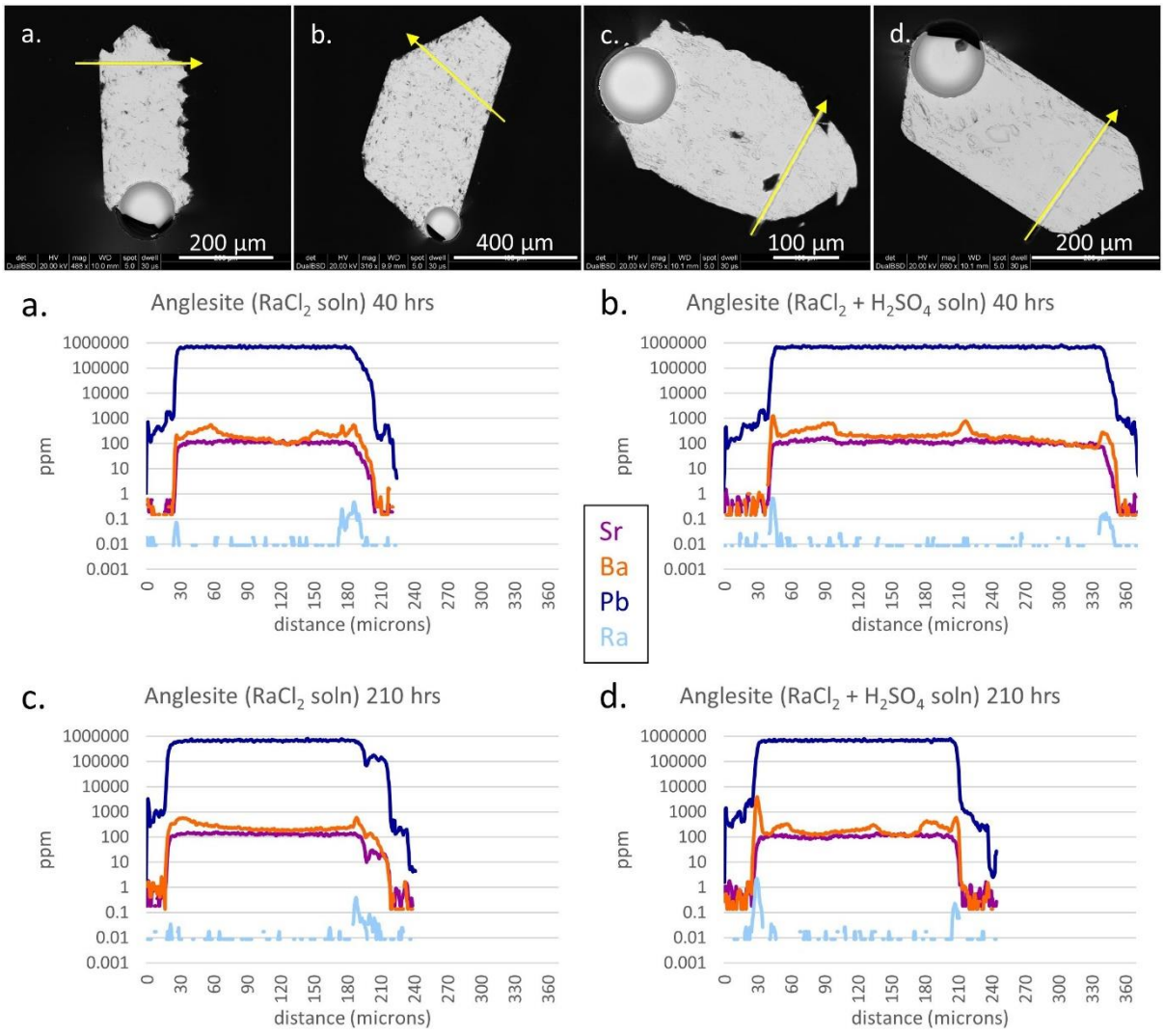

Figure 8. LA-ICP-MS transects and BSE images from experiment 3 with isolated $PbSO_4$ crystals and $RaCl_2$ solution: (a) without acid sulfate, 40 hours; (b) with acid sulfate, 40 hours; (c) without acid sulfate, 210 hours; and (d) with acid sulfate, 210 hours. Yellow arrows in the BSE images indicate locations and directions of laser transects. Radium concentrations are estimates.

Anglesite from experiment 4 showed distinct differences between the high-sulfate and sulfate-free vials (Figure 9). Crystals from the high-sulfate experiments remained in excellent shape, though the crystal in Figure 9b has slightly rounded corners and internal angular pitting. The sulfate-free experiment anglesites showed significant corrosion and replacement, visible

as darker patches (Sr- and Ba-rich sulfate) along grain edges. CDR is evident up to 60 µm deep into the crystal in Figure 9a, with significant loss of Pb and corresponding uptake of Sr, Ba, and Ra. As opposed to celestine, anglesite excels in incorporating Ra when in competition with other sulfates. Once again, Ra concentration profiles parallel those of Sr and Ba, indicating that CDR is driven by high [Sr] and [Ba] – released from their respective sulfates by chloride complexation. High sulfate activity inhibits complexation, and therefore inhibits CDR.

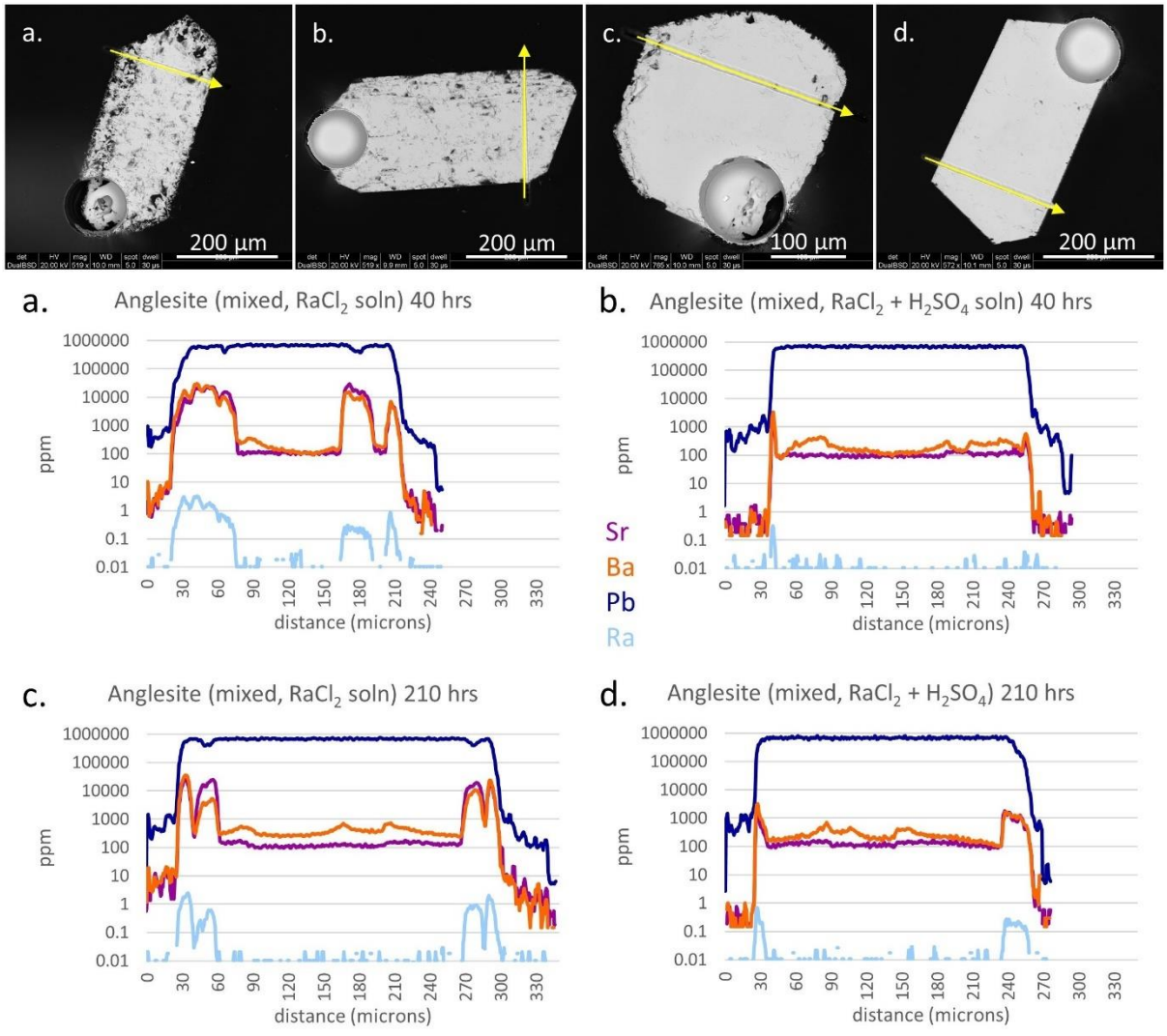

Figure 9. LA-ICP-MS transects and BSE images from experiment 4 with $PbSO_4$ crystals (in contact with $SrSO_4$ and $BaSO_4$ crystals) and $RaCl_2$ solution: (a) without acid sulfate, 40 hours; (b) with acid sulfate, 40 hours; (c) without acid sulfate, 210 hours; and (d) with acid sulfate, 210 hours. Yellow arrows in the BSE images indicate locations and directions of laser transects. Radium concentrations are estimates.

3.2. Single spot analyses

The 110 µm-diameter single spot analyses (visible craters in BSE images) were originally planned as a backup, in case the 6 µm-diameter spot size transects did not show any Ra. Fortunately, the transects provided excellent results regarding Ra uptake in these sulfates so the larger spot data were no longer required. A few examples are nonetheless fitting here, as these single spot analyses not only complement the transect results but also provided additional data needed for the semi-quantification of Ra as presented in Section 4 below.

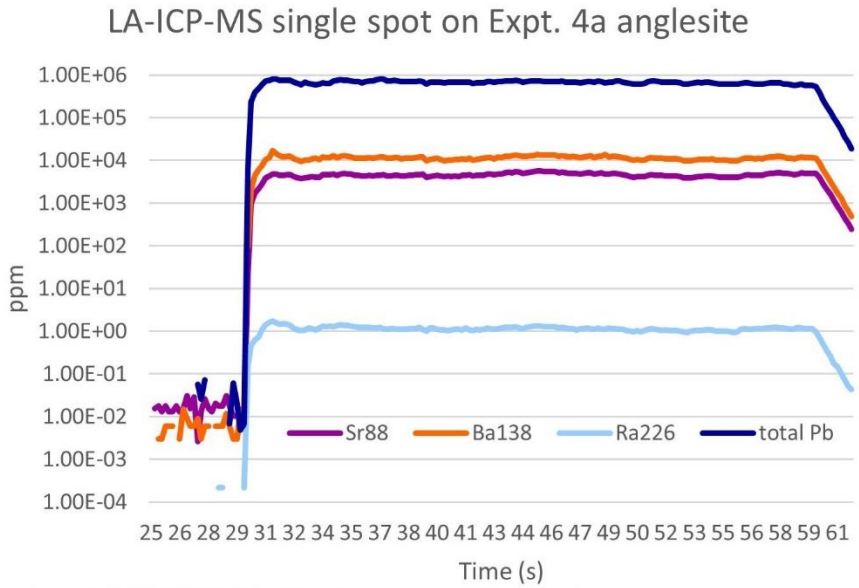
LA-ICP-MS single spot on Expt. 4a anglesite
ppm
1.00E+06
1.00E+05
1.00E+04
1.00E+03
1.00E+02
1.00E+01
1.00E+00
1.00E-01
1.00E-02
1.00E-03
1.00E-04
25 26 28 29 31 32 34 35 37 38 40 41 43 44 46 47 49 50 52 53 55 56 58 59 61
Time (s)
Sr88
Ba138
Ra226
total Pb

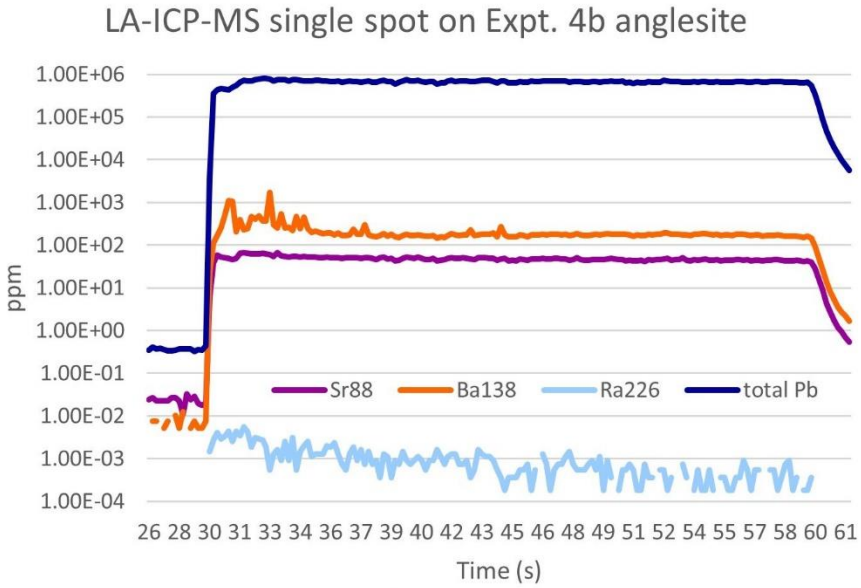
LA-ICP-MS single spot on Expt. 4b anglesite
ppm
1.00E+06
1.00E+05
1.00E+04
1.00E+03
1.00E+02
1.00E+01
1.00E+00
1.00E-01
1.00E-02
1.00E-03
1.00E-04
26 28 30 31 33 34 36 37 39 40 42 43 45 46 48 49 51 52 54 55 57 58 60 61
Time (s)
Sr88
Ba138
Ra226
total Pb

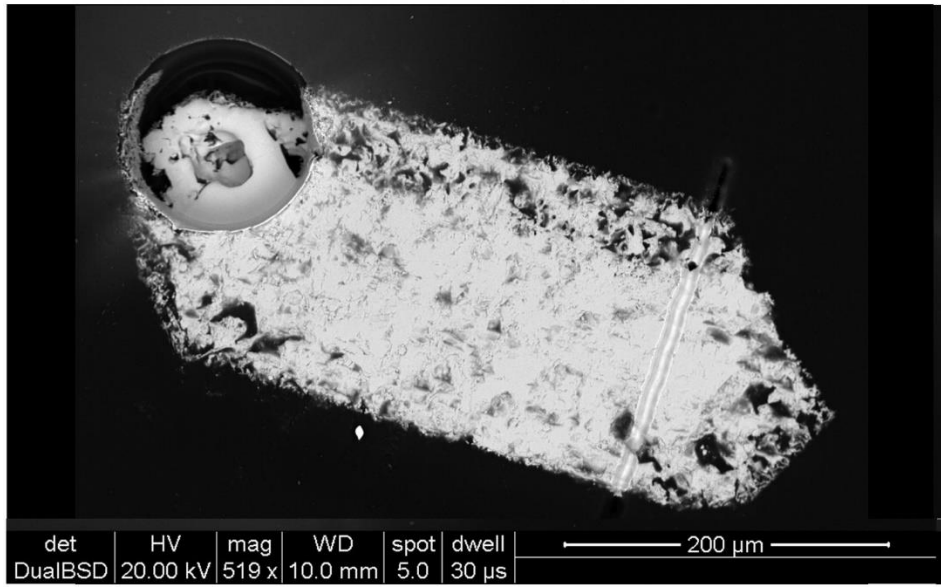
det
DualBSD
HV
20.00 kV
mag
519 x
WD
10.0 mm
spot
5.0
dwell
30 µs
200 µm

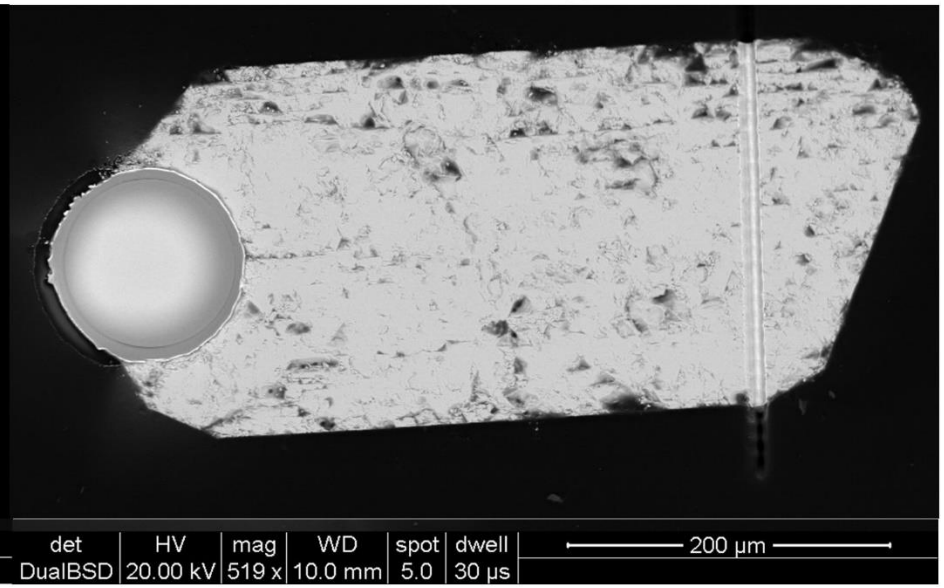
det
DualBSD
HV
20.00 kV
mag
519 x
WD
10.0 mm
spot
5.0
dwell
30 µs
200 µm

Figure 10. Single time-resolved LA-ICP-MS analyses of two lead sulfate grains. Radium, Sr, and Ba concentrations are elevated and consistent in the sulfate-free solution experiment (left) but 2-3 orders of magnitude lower in the high sulfate activity solution experiment (right).

The grain from experiment 4a shows high, consistent traces for Sr, Ba, and Ra (Figure 10). CDR reactions have clearly eroded much of the $PbSO_4$ (with increased porosity as a result) and replaced that material with $(Pb,Ba,Sr)SO_4$. Although Sr replacement of Pb in sulfates through CDR can be >75 wt.% (Rollog et al., 2019), this crystal only reports around 1 wt.% Ba and 0.5 wt.% Sr due to low concentrations of available, liberated Ba and Sr in the solution. Estimated Ra concentration hovers close to 1 ppm, although collateral inclusion of unreacted Ra-free core material in the laser analysis would likely indicate an elevated value in the rim. The anglesite from experiment 4b looks to be porous as well, but the ICP-MS spot analysis indicates very low uptake of Sr, Ba, and Ra in the crystal surface. Concentrations are quite consistent, with [Ba] and [Sr] leveling off at 200 ppm and 50 ppm, respectively. Considering the baseline contaminations in the anglesite crystal are roughly 165 ppm Ba and 115 ppm Sr, this represents little change – even a possible slight depletion in Sr. The Ra signal was at or below the detection limit of the ICP-MS, so the concentration is effectively zero.

3.3. Overall reactions

It is important to note here that these experiments differ from most previously published work in one critical aspect – time. The many excellent papers from the Institute for Energy and Climate Research in Jülich, Germany (and others) have also investigated Ra uptake by sulfates under various conditions, but their experiments were allowed to run for hundreds or even over one thousand days. Equilibrium may be assured in these timeframes. This information is critical in assessing the potential for loss of Ra from long-term waste storage facilities. The experiments presented here, however, run over the course of hours instead of years, have not reached (or in some cases even approached) equilibrium. The utility in such experiments lies

in the practicality of potential Ra removal from solutions in industrial settings, within an industrial timeframe. Future experiments by the authors will take this one step further, allowing reaction times from minutes to a few hours.

There are three primary means of Ra uptake presented here: overgrowth, diffusion, and CDR. Overgrowth in these (and similar; Rollog et al., 2019) experiments is commonly observed on baryte. Bright rims of Pb-dominated sulfate can easily be seen growing on the surface of baryte blades, with little visible indication of baryte dissolution. Naturally this only occurs when sufficient Pb is available, represented in this study solely by the sulfate-free mixed vials from experiment 4 (Figure 7a, c). Chloride complexation releases enough Pb from the anglesite (evidenced by high porosity in the BSE image) to precipitate on the baryte. Strontium shows no overgrowth on baryte, nor is overgrowth seen on celestine or anglesite. Overgrowth is, however, known to occur on celestine given the right conditions (Rollog et al., 2019).

Diffusion occurs to some extent in all of the crystals observed, aided by elevated temperatures and exposure to ionic solutions. Within a few microns of the surface, any cations in solution (or cation pairs) which will fit into the crystal structure will, given enough time, work their way in and replace the native species. Concentrations are generally low but can achieve wt.%. Although the mechanism may be similar to CDR, there is far less removal of the host cations. Crystal edges remain clean and sharp, with no signs of porosity or surface corrosion.

CDR reactions are evident in anglesite, especially in the absence of sulfate. Surface corrosion of sulfates in chloride-rich, sulfate-poor solutions may occur (e.g., Figures 6a, 8a), but there is no significant replacement by any other cation. True CDR requires dissolution of the host matrix resulting in high porosity and significant replacement of the host cation by foreign species (Putnis, 2009). The anglesite from experiment 4a in Figure 9a shows classic CDR texture with corresponding replacement of Pb in the reaction zone, matching previous

results (Rollog et al., 2019). Thick zones, to 50 µm wide, show significant porosity as well as up to 6 wt.% replacement of Pb by (Sr+Ba). This increase in Sr and Ba, assisted by porosity, is likely the reason for significant Ra incorporation into the replacement zones. The increase in cell dimensions caused by different crystal ionic radii (CIR) of 1.58 Å for Sr^{2+}, 1.63 Å for Pb^{2+}, and 1.75 Å for Ba^{2+} (Shannon, 1976), as well as the uninhibited porous structure, allows for accommodation of the larger Ra^{2+} (1.84 Å; Shannon, 1976). The baryte in Figure 6a also likely represents CDR. A rough calculation of total Ra uptake suggests the complete, or nearly complete, removal of Ra from solution in these two experiments – corresponding closely to the total Ra available.

Regarding Ra uptake, all three methods of incorporation seem to play a role. Thin diffusion zones can be seen near the surface of all three sulfates, but not under the same conditions. The overgrowth zone on baryte clearly hosts some Ra. CDR reactions incorporate Ra throughout the replacement zone in anglesite, up to 60 µm deep. Although there is no obvious preferential mechanism, it is abundantly clear that Ra does not act alone. In each instance above the Ra transect concentration profile parallels at least one non-host cation, suggesting a necessity for coupled precipitation. The crystal radius of Ra^{2+} in XII coordination is 1.84 Å (Shannon, 1976). Its substitution into baryte (Ba^{2+} radius = 1.75 Å) would be facilitated by co-incorporation with a smaller cation (Sr^{2+} = 1.58 Å; Pb^{2+} = 1.63 Å; Shannon, 1976) The correlation with Ba in anglesite and Pb in baryte – and the independence from Sr in both sulfates – indicates that Ra will incorporate easily into baryte or anglesite in conjunction with sufficient concentrations of the other cation. Alternatively, Ra will easily incorporate into plumbian baryte (hokutolite; Momoshima et al., 1997) or barian anglesite. In the absence of Pb, strontian baryte (10 ± 5 mol.% optimal Sr) has been theoretically calculated to uptake Ra (Vinograd et al., 2018a).

With regard to overgrowth, and to some extent the reprecipitation component of CDR, the minimization of volume mismatch during epitaxial growth (Klinkenberg et al., 2018) may also

play a role. The larger Ra^{2+} and smaller Pb^{2+} or Sr^{2+} ions may combine, in certain combinations, to mimic the cell dimensions of $BaSO_4$ which would promote growth on a baryte matrix. Even if this effect only enhanced – but was not critical to – the uptake of Ra in sulfate matrices, the affect on reaction rates may significantly improve Ra recoveries during short term industrial processes.

4. Radium concentration estimation

Radium concentrations (in ppm) given in the figures in the section above are estimated but are confidently within an order of magnitude of the true values. Relative sensitivity factors (RSFs) represent specific instrument responses and are unique to each element in each matrix. These can be used to directly convert counts per second (CPS) to ppm based on the internal standard method (Longerich et al., 1996). Since there was no Ra standard available, a series of proxy standards were analyzed to estimate the approximate RSF for Ra.

Uranium-bearing minerals in secular equilibrium should contain calculable concentrations of all decay chain radionuclides. Therefore, if the amount of ^{238}U is known (calibrated to an existing standard) then the rest of the decay chain should be estimable. Since radionuclide concentrations in secular equilibrium are inversely related to half-lives, it should be possible to compare half-life ratios to ratios of CPS directly from the ICP-MS to determine if a radioactive mineral is in secular equilibrium. One uraniferous thorianite (Madagascar) and three uraninites (Tsumeb, Namibia; Rum Jungle, NT, Australia; unknown deposit, North Carolina) were analyzed by LA-ICP-MS (Figure 11). Ratios indicate that the thorianite and two of the uraninite samples are at, or very near, secular equilibrium, and that the elements in the decay chain (U, Th, Ra, and Pb) all share very similar RSFs. In the fourth sample, uraninite 3 (North Carolina), decay chain radionuclides are clearly not in equilibrium.

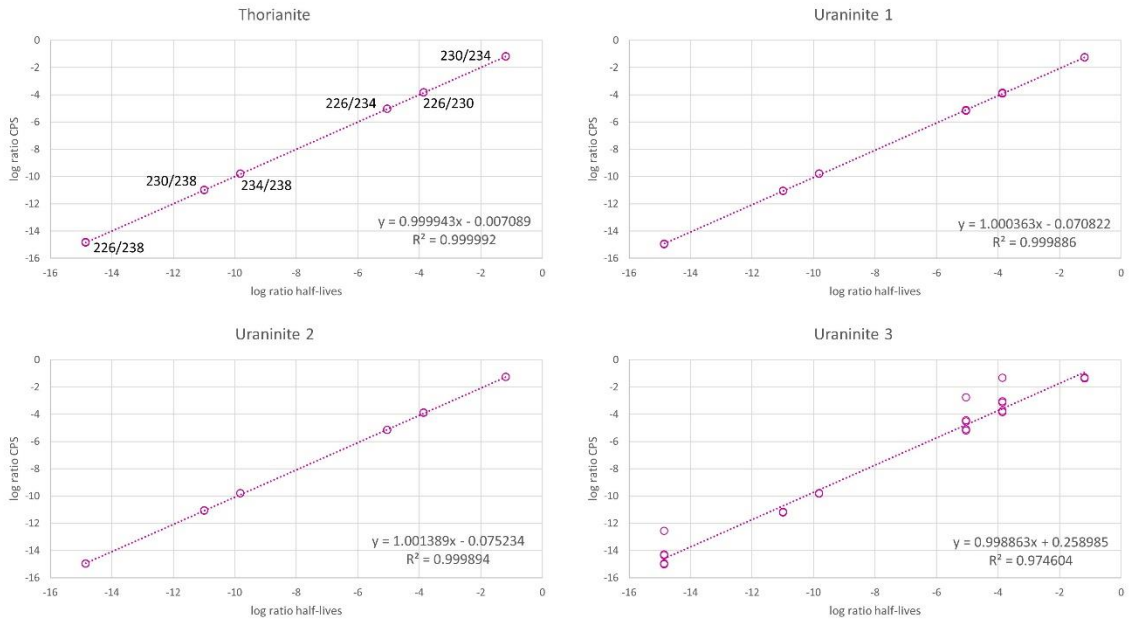

Figure 11. Log ratio charts demonstrating secular equilibrium potential in thorianite and three uraninite grains. Y-axes represent log ratios of counts per second (CPS) directly from the ICP-MS; X-axes represent log ratios of half-lives. Each mineral was analyzed 4-5 times. Ratios are labelled for thorianite and are consistent for all four charts. Secular equilibrium has been established for the first three samples; the third uraninite is clearly not in equilibrium.

By calculating the concentration of ^{238}U in each sample using the NIST-610 standard and estimating a CPS/ppm ratio for ^{226}Ra from the charts above, [Ra] could be estimated. Values were estimated separately for LA-ICP-MS data from transects and large single-spot analyses. Comparing results from transects and single spots for the anglesites in experiments 4a and 4b show very similar calculated Ra concentrations, within a factor of two. For sample 4a, the discrepancy is narrowed even more when considering that the single spot analysis overlaps some of the anglesite core, which is known to contain no Ra. Material ablated from the epoxy contains no members of the decay chain and therefore does not affect the calculations. Sample 4b shows concentrations approach zero, as the signals from ICP-MS were at or below the instrumental detection limit. Further quantification work is underway and will be published separately.

5. Implications for mineral processing and beyond

For mineral processing engineers targeting production of sulfide concentrates, with radionuclide activities/concentrations at or below natural background levels, from uranium-bearing copper ores, knowing the location and behavior of radionuclides is critical for effecting their removal. The information provided here not only offers insight into the behavior of Ra, a key intermediate member of the decay chain, but also provides a possible means of controlling this behavior to advantage. Depending on exact elemental activities within any given step in a processing circuit, it may be possible to stimulate precipitation of $RaSO_4$ onto an added, or pre-existing, matrix. It is unlikely, however, that any stage of a real-world processing stream would contain only one of the three minerals studied here, so the results from the "mixed" vial experiments would approximate conditions and guide efforts to sequester Ra in a processing circuit.

As a repository, celestine would not be efficient in removing Ra from solution, given the results shown in Figure 5. Anglesite looks very promising but would have to be used in concert with another mineral to remove liberated Pb (the latter also being a deleterious element in concentrates). Furthermore, since ^{210}Pb is likely to also be of equal if not greater concern, the build-up of total Pb in concentrates would necessarily result in the build-up of ^{210}Pb as well – resolving one problem but instigating another. Baryte, either in bulk or as a coating on a neutral (e.g. ceramic) matrix may be the best solution, as significant Ra uptake occurs regardless of sulfate activity. Baryte can also incorporate wt.% levels of Pb, also reducing available ^{210}Pb. Although Ra uptake seems to be linked with either Sr and/or Pb uptake, the [Sr] and [Pb] will likely be sufficient through dissolution of Pb- and Sr-bearing minerals already present in the concentrate. Alternatively, sulfate mixtures – either naturally occurring or manufactured – may represent the best possible Ra repositories. Assuming their ready availability close to the plant

site, they could represent a cost-effective solution that compares favorably with other recognized technologies for RN removal such as resin-in-pulp treatments or organic additives.

This knowledge may find application in other industries. Oil, gas, and coal production all involve complex chemical processing – and all need to deal with various degrees of radionuclide accumulation, depending on source. Minor adjustments in processing, customized using the knowledge provided here, may facilitate efficient, cost-effective radionuclide management and disposal. Environmental remediation of contaminated sites (whether natural, accidental, or intentional) may also benefit by establishing passive Ra traps. The treatment of Ra-bearing waste from medical and industrial applications may be made safer by creating low cost, leach-resistant media which may be stored or repurposed. In short, all disciplines which deal either directly or tangentially with Ra may benefit from the findings from this study and continuing research by the present authors and others cited above.

6. Conclusions

- Celestine removes Ra from solution efficiently, but only in the absence of baryte and anglesite.
- Baryte is an excellent Ra (and Pb) host and displays efficiency in both sulfate-free and sulfate-rich environments.
- Anglesite shows the greatest potential for Ra removal through rapid CDR reactions but high concentrations of Pb (and likely ^{210}Pb) re-enter the system and would need to be removed by a subsequent process.
- Radium uptake seems to be enhanced in conjunction with another cation, likely due to ionic size compensations and kinetic considerations.
- Radium removal from concentrate process streams may be affected by controlled exposure to an appropriate sulfate host mineral under specific conditions.

- Semi-quantitative information on Ra concentrations in solid materials can be readily achieved using LA-ICP-MS.

Declarations

Availability of data and material

The data forming the basis of the above remain the property of and will only be disseminated at the discretion of project sponsors, BHP Olympic Dam.

Competing interests

The authors declare that they have no competing interests. This manuscript has not been previously published and is not submitted for consideration anywhere else.

Funding

This is a contribution to the ARC Research Hub for Australian Copper-Uranium (Grant IH130200033), co-supported by BHP Olympic Dam.

Authors' contributions

M.R. and S.G. performed the work presented here. M.R. processed results and made interpretations, supervised by N.J.C. K.E. supplied sample material and provided extensive advice. M.R. wrote the manuscript assisted by N.J.C. and other co-authors. The material within has been approved by all authors.

Acknowledgements

The authors would like to acknowledge the editor and reviewers for providing invaluable comments and suggestions for the revision of this manuscript.

References

Baba, A., 2002. Assessment of radioactive contaminants in by-products from Yatagan (Mugla, Turkey) coal-fired power plant. Environmental Geology 41, 916-921.

Brown, P.L., Ekberg, C., Ramebäck, H., Hedström, H., Matyskin, A., 2015. Solubility of radium and strontium sulfate across the temperature range of 0 to 300 °C. In: Merkel, B.J., Arab, A., (Eds.) Uranium-Past and Future Challenges, Springer, Cham., pp. 553-564.

Carvalho, F.P., Madruga, M.J., Reis, M.C., Alves, J.G., Oliveira, J.M., Gouveia, J., Silva, L., 2007. Radioactivity in the environment around past radium and uranium mining sites of Portugal. Journal of Environmental Radioactivity 96, 39-46.

Chao, J.H., Chuang, C.Y., Yeh, S.A., Wu, J.M., 2009. Relationship between radioactivity of radium and concentrations of barium and lead in hokutolite. Applied Radiation and Isotopes 67, 650-653.

Curti, E., Fujiwara, K., Iijima, K., Tits, J., Cuesta, C., Kitamura, A., Glaus, M.A., Müller, W., 2010. Radium uptake during barite recrystallization at 23±2 ºC as a function of solution composition: An experimental ^{133}Ba and ^{226}Ra tracer study. Geochimica et Cosmochimica Acta 74, 3553-3570.

Doerner, H.A., Hoskins, W.M., 1925. Co-Precipitation of Radium and Barium Sulphates 1. Journal of the American Chemical Society 47, 662-675.

Dyar, M.D., Gunter, M.E., Tasa, D., 2008. Mineralogy and Optical Mineralogy. Mineralogical Society of America, Chantilly, VA. 708 pp.

Gazineu, M.H.P., Hazin, C.A., 2008. Radium and potassium-40 in solid wastes from the oil industry. Applied Radiation and Isotopes 66, 90-94.

Halmshaw, R., 1996. Introduction to the non-destructive testing of welded joints. Woodhead Publishing, Cambridge, UK. 124 pp.

Hedström, H., Ramebäck, H., Ekberg, C., 2013. A study of the Arrhenius behavior of the co-precipitation of radium, barium and strontium sulfate. Journal of Radioanalytical and Nuclear Chemistry 298, 847-852.

Henisch, H.K., 1996. Crystal growth in gels. Pennsylvania State University Press, University Park, PA. 107 pp.

Janković, M.M., Todorović, D.J., Nikolić, J.D., 2011. Analysis of natural radionuclides in coal, slag and ash in coal-fired power plants in Serbia. Journal of Mining and Metallurgy B: Metallurgy 47, 149-155.

Klinkenberg, M., Weber, J., Barthel, J., Vinograd, V., Poonoosamy, J., Kruth, M., Bosbach, D. Brandt, F., 2018. The solid solution–aqueous solution system (Sr, Ba, Ra) SO_4 + H_2O: A combined experimental and theoretical study of phase equilibria at Sr-rich compositions. Chemical Geology 497, 1-17.

Langmuir, D., Riese, A.C., 1985. The thermodynamic properties of radium. Geochimica et Cosmochimica Acta 49, 1593-1601.

Linke, W.F., Seidell, A., 1965. Solubilities, Inorganic and Metal-organic Compounds, K-Z: A Compilation of Solubility Data from the Periodical Literature. A Revision and Continuation of the Compilation Originated by Atherton Seidell. American Chemical Society, Van Nostrand, NY. 904 pp.

Longerich, H.P., Jackson, S.E., Günther, D., 1996. Inter-laboratory note. Laser ablation inductively coupled plasma mass spectrometric transient signal data acquisition and analyte concentration calculation. Journal of Analytical Atomic Spectrometry 11, 899-904.

Lucchesi, P.J., Whitney, E.D., 1962. Solubility of strontium sulphate in water and aqueous solutions of hydrogen chloride, sodium chloride, sulphuric acid and sodium sulphate by the radiotracer method. Journal of Applied Chemistry 12, 277-279.

Momoshima, N., Nita, J., Maeda, Y., Sugihara, S., Shinno, I., Matsuoka, N., Huang, C.W., 1997. Chemical composition and radioactivity in hokutolite (plumbian barite) collected at Peito hot spring, Taiwan. Journal of Environmental Radioactivity 37, 85-99.

Ojovan, M.I., Lee, W.E., Kalmykov, S.N., 2019. An Introduction to Nuclear Waste Immobilisation. Elsevier, 512 pp.

Nguyen, C.K., Clark, B.N., Stone, K.R., Edwards, M.A., 2011. Role of chloride, sulfate, and alkalinity on galvanic lead corrosion. Corrosion 67(6), 065005, 1-9.

Parker, C., Nilsson, S., Heinrich, D., Helle, S.I., O'Sullivan, J.M., Fosså, S.D., Chodacki, A., Wiechno, P., Logue, J., Seke, M.,Widmark, A. and 19 co-authors, 2013. Alpha emitter radium-223 and survival in metastatic prostate cancer. New England Journal of Medicine 369, 213-223.

Patel, A.R., Bhat, H.L., 1984. Gel growth of lead sulphate single crystals. InРост Кристаллоь/Rost Kristallov/Growth of Crystals. Springer, Boston, MA, 122-125.

Pluta, I., 2001. Barium and radium discharged from coal mines in the Upper Silesia, Poland. Environmental Geology 40, 345-348.

Poggi, C.M.B., de Farias, E.E.G., Silveira, P.B., Silva Filho, C.A., De França, E.J., Gazineu, M.H.P., Hazin, C.A., 2015. ^{226}Ra, ^{228}Ra and ^{40}K in scales from boilers of industrial installations. Journal of Radioanalytical and Nuclear Chemistry 306, 667-672.

Pratt, R.M., 1993. Review of radium hazards and regulation of radium in industry. Environment International 19, 475-489.

Puch, K.H., Bialucha, R., Keller, G., 2005. Naturally occurring radioactivity in industrial by-products from coal-fired power plants, from municipal waste incineration and from the iron-and steel-industry. Radioactivity in the Environment 7, 996-1008.

Putnis A., 2002. Mineral replacement reactions: from macroscopic observations to microscopic mechanisms. Mineralogical Magazine 66, 689-708.

Putnis A., 2009. Mineral replacement reactions. Reviews in Mineralogy and Geochemistry 70, 87-124.

Raju, K., Atkinson, G., 1988. Thermodynamics of “scale” mineral solubilities 1. Barium sulfate(s) in water and aqueous sodium chloride. Journal of Chemical and Engineering Data 33, 490-495.

Raju, K., Atkinson, G., 1989. Thermodynamics of “scale” mineral solubilities 2. Strontium sulfate(s) in aqueous sodium chloride. Journal of Chemical and Engineering Data 34, 361-364.

Roessler, C.E., 1990. Control of radium in phosphate mining, beneficiation and chemical processing. The environmental behaviour of radium vol. 2, Technical Report Series 310, International Atomic Energy Agency, pp.270-279.

Rollog, M., Cook, N.J., Guagliardo, P., Ehrig, K.J., Gilbert, S.E., Kilburn, M., 2019. Intermobility of barium, strontium, and lead in chloride and sulphate leach solution. Geochemical Transactions 20:4, 1-23.

Shannon, R.D., 1976. Revised effective ionic radii and systematic studies of interatomic distances in halides and chalcogenides. Acta Crystallographica section A: Crystal Physics, Diffraction, Theoretical and General Crystallography 32, 751-767.

Vinograd, V.L., Kulik, D.A., Brandt, F., Klinkenberg, M., Weber, J., Winkler, B., Bosbach, D., 2018a. Thermodynamics of the solid solution-aqueous solution system (Ba, Sr, Ra) SO_4 + H_2O: I. The effect of strontium content on radium uptake by barite. Applied Geochemistry 89, 59-74.

Vinograd, V.L., Kulik, D.A., Brandt, F., Klinkenberg, M., Weber, J., Winkler, B., Bosbach, D., 2018b. Thermodynamics of the solid solution-aqueous solution system (Ba,Sr,Ra)SO_4 + H_2O: II. Radium retention in barite-type minerals at elevated temperatures. Applied Geochemistry 93, 190-208.

Weber, J., Barthel, J., Klinkenberg, M., Bosbach, D., Kruth, M., Brandt, F., 2017. Retention of ^{226}Ra by barite: The role of internal porosity. Chemical Geology 466, 722-732.

Zhang, T., Gregory, K., Hammack, R.W., Vidic, R.D., 2014. Co-precipitation of radium with barium and strontium sulfate and its impact on the fate of radium during treatment of produced water from unconventional gas extraction. Environmental Science & Technology 48, 4596-4603.

Chapter 9

Supplementary analyses: Focussed ion beam SEM, transmission electron microscopy, atom probe tomography, and electron backscatter diffraction

Chapter 9: Supplementary methodologies

Upon commencement of this project, it was unclear exactly which instrumentation would be most beneficial and informative in the search for ultra-low concentration radionuclides. As a result some methods were tried and discounted, while others showed promising results and were earmarked for future development – but did not significantly contribute to the findings presented in Chapters 3 through 8. Four of these methods and preliminary results are included here since they represent potential avenues for future research to confirm and expand upon successful research outcomes presented elsewhere in this thesis. Moreover, undertaking each of them was critical to the overall thought process involved over the past three and a half years and contributed to the interpretations and conclusions reached.

9.1 Focussed ion beam SEM

Some analytical techniques involve extensive sample preparation; transmission electron microscopy requires sample foils <100 nm thick, and atom probe tomography only provides quality results for hemispherical needle tips with a ~100 nm diameter. Preparing samples of these dimensions can only efficiently be performed by focussed ion beam (FIB) technology. While intermediate sample preparation does constitute the majority of instrument usage, high-resolution FIB cross-section imaging may also be considered an independent analytical technique in its own right.

The FEI Helios Nanolab 600 dual beam focused ion beam scanning electron microscope (FIB-SEM) equipped with an EDAX system, located at Adelaide Microscopy, was used early in this Ph.D. project for preparation of TEM foils and nanoSIMS samples. The principle involves focussing a beam of ions (usually Ga but may also be Au, Ir, Xe, Ar, or He) at a sample which sputters atoms, ions, and electrons from the surface. The beam is only a few nm wide, and may be directed onto the sample with great precision. Secondary electrons or ions

may be detected and compiled for imaging surface features, analysing chemical compositions, or determining crystal orientations. The most useful aspect of FIB, however, was originally viewed as a detriment – its ability to remove material from the sample surface. High-precision milling may be performed on very specific regions of interest in a sample, for instance grain boundaries, micron-scale inclusions, crystal orientation boundaries, or reaction fronts (ThermoFisher Scientific 2019). At its simplest, milling may be used to create a trench, allowing the viewer to see a limited cross-section of the sample (Figure 9.1) but can also facilitate tomography to address 3-dimensional structures.

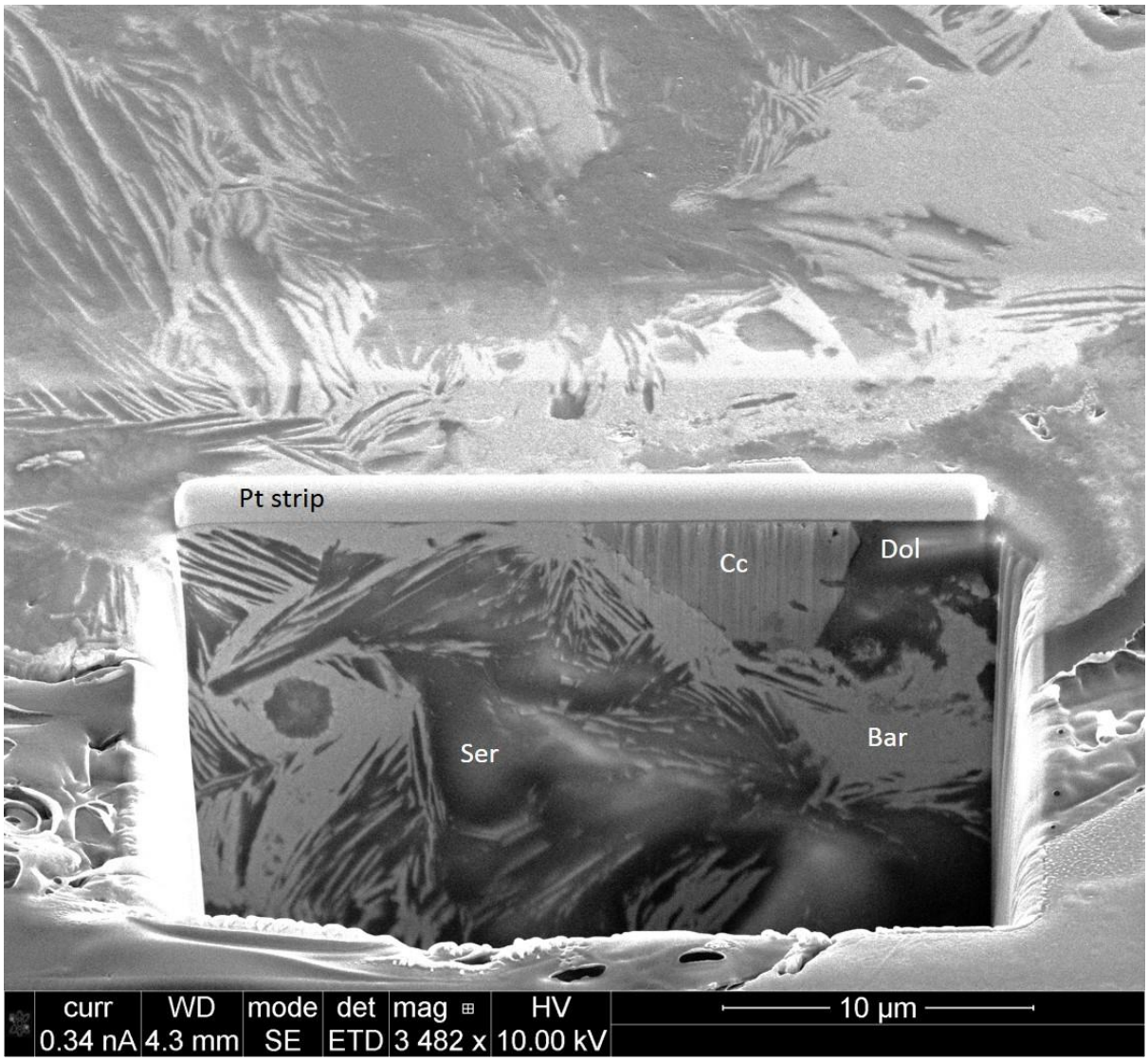

Figure 9.1. BSE image of a cross-sectional trench of sample 0815_FC_08. The protective Pt strip runs horizontally through the centre of the image. The same grain is featured in Chapter 3, Figure 2. Sericite (Ser); chalcocite (Cc); dolomite (Dol); baryte (Bar).

Trenches were milled in approximately two dozen grains from sample mounts 0815_FC and 0815_CLD, revealing 3-dimensional features not obvious from surface exposure alone. One universal observation was that heterogeneity extends to the nanoscale in every sample.

One advanced technique involves milling a thin slice (~2 µm thick) which may be removed from the sample and mounted on a suitable grid for further analyses (Figure 9.2). NanoSIMS analyses may be run on thicker slices (1-2 µm) whereas samples to be analysed by TEM require thinning to <100 nm. Alternatively, samples may be mounted on silicon supports and then shaped into a needle for atom probe tomography (Figure 9.4 a,b).

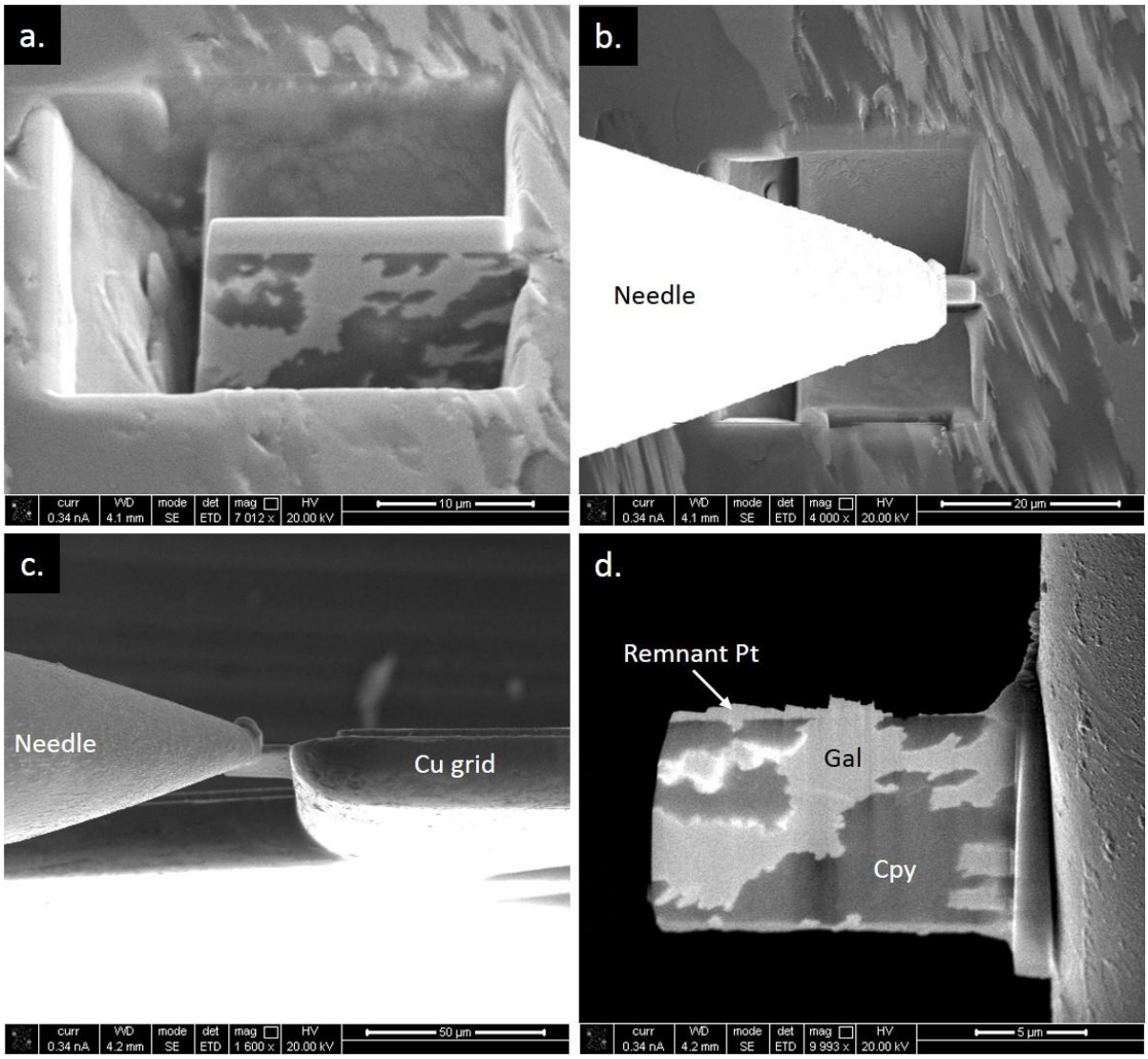

Figure 9.2. BSE images of the TEM sample mounting procedure for sample 0815_FC_61. The sample is milled (a), welded to a needle (b), transferred from needle to Cu grid (c), and thinned (d). Galena (Gal); chalcopyrite (Cpy).

9.2 Transmission electron microscopy

Transmission electron microscopy (TEM) and high-angle annular dark field scanning transmission electron microscopy (HAADF STEM) were expected to play a major contribution in the search for RN distributions at the nanoscale, particularly to follow-up and further constrain nanoSIMS observations, or to be used to characterise thinned foils representative of specific features prior to nanoSIMS analysis. The premise was to use the atomic-scale resolution FEI Titan Themis 80-200 TEM installed in 2016 at Adelaide Microscopy (AM). This instrument, and particularly high Z-contrast imaging in HAADF STEM mode has proven extraordinarily valuable for characterisation of some components of the Olympic Dam ore and host rocks, for example REE-fluorocarbonates (Ciobanu et al., 2017), Si-magnetite (Ciobanu et al., 2019), and zircons (Courtney-Davies et al., 2019), or for understanding geological processes after initial precipitation that have impacted on ore mineralogy and element distributions (e.g. Owen et al., 2018; Verdugo-Ihl et al., 2019). Routine use of HAADF STEM for this project ended up being supplanted by other instrumentation, but a number of samples were investigated by TEM early in the project.

Roughly a dozen foils were prepared, one from OZ Minerals sample CUUCO1aGB (with Danielle Schmandt), and the remainder from BHP samples 0815_FC and 0815_CLD, using the FEI dualbeam focused ion beam scanning electron microscope (FIB-SEM) at AM. Selected samples were then imaged using either the FEI Tecnai G2 Spirit or Philips CM200 instruments at AM. In Figure 9.3, uraninite nanoparticles were observed within a uraniferous carbonate matrix, possibly rutherfordine (UO_2CO_3). Another sample revealed complex intergrowths of phases in the system Pb-Ag-Bi-Te-Se-S, verifying the extremely fine-grained nature of ores and the necessity of including methods with sub-micron resolution to constrain RN distributions.

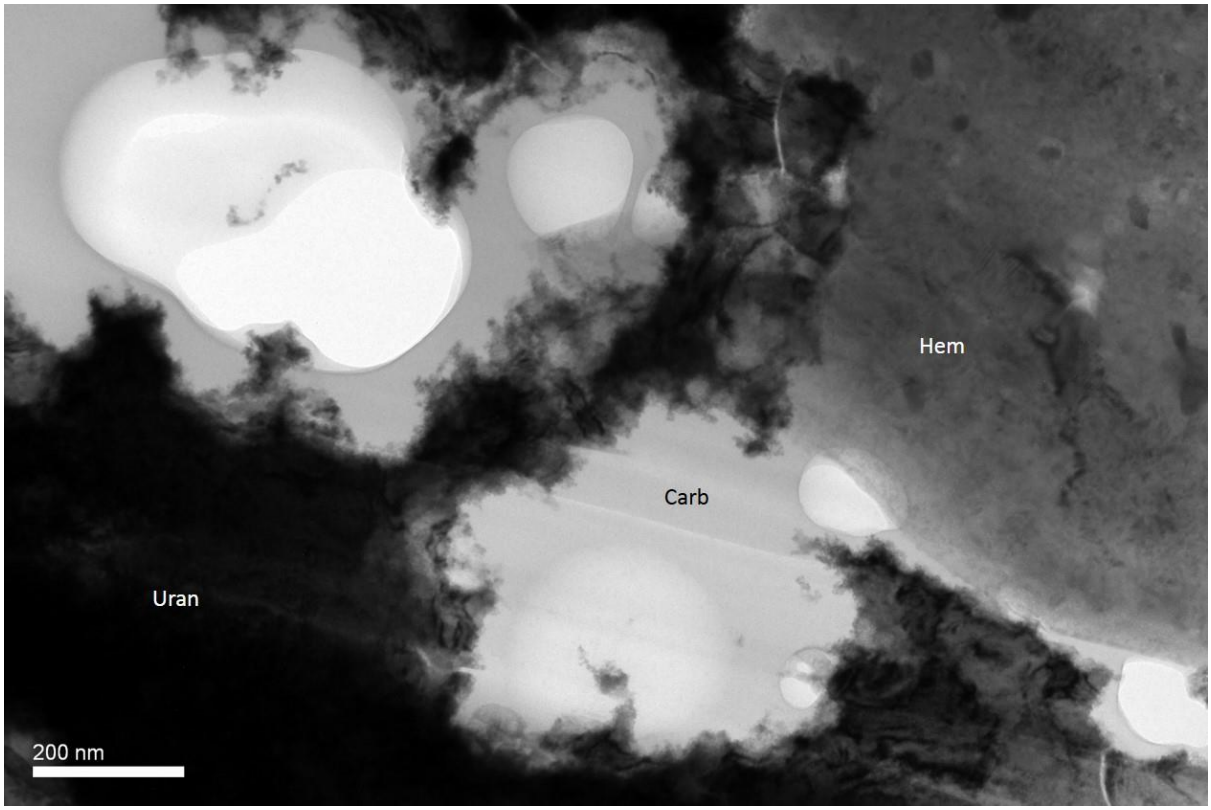

Figure 9.3. TEM image showing wispy nanoparticles of uraninite (Uran) in a carbonate (Carb) matrix with hematite (Hem), from sample CUUCO1aGB.

TEM has proven, and continues to prove, invaluable for many aspects of nanoscale characterisation of Olympic Dam ores and concentrates, within and beyond the overarching ARC Research Hub for Australian Copper-Uranium. Potential applications of HAADF STEM methods currently being addressed on samples from Olympic Dam within the wider research group include the grain-scale remobilisation of U and Pb within zircon and hematite, and the implications this carries for reliable U-Pb zircon dating, documentation of nanoscale coupled dissolution-reprecipitation reactions in pyrite and their impact on the distribution of previous metals, and further work documenting polysomatism among REE-fluorcarbonates of the bastnäsite-synchysite group.

9.3 Atom probe tomography

Commercially developed in the 1990's, atom probe tomography offers researchers a way to map the chemical or isotopic composition of a sample one atom at a time, in three dimensions.

APT provides specially-resolved chemical information in relation to specific nanoscale features of interest, such as the partitioning of elements or isotopes to a particular phase, grain boundary, or defect. Regions of interest can be targeted by preparation of needle-shaped specimens using a FIB-SEM.

Small samples (~100 nm diameter hemisphere) on the tip of a silicon support are inserted into the instrument and the chamber is evacuated to ultra-high vacuum. The samples are cryogenically cooled, and a large voltage (3-15 kV) is applied to the sample to just below the point at which it starts to evaporate. A pulsed laser provides the energy necessary for evaporation of atoms from the surface layer, ideally one at a time, which are then detected by position sensitive time-of-flight spectrometry (PoS TOFS), also known as a position sensitive detector (PSD). PoS TOFS records not only the mass of the atom but also its original position in the sample. Digital reconstruction of the sample in three dimensions, for any selected elements of interest, reveals nanostructures not detectable by any other instrumentation (Miller, 2012; Cameca, 2019).

APT has provided many advances in geochemical research, including insight regarding the homogeneity – and therefore suitability – of trace element standards (Reddy et al., 2016; Piazolo et al., 2017) and geochronology samples (e.g., Parman et al., 2015; Peterman et al., 2016). Mineral growth mechanisms may be determined by examining nanoinclusions and zoning patterns (e.g., Wu et al., 2019). Closely related to our research presented in Chapters 5 and 8, nanostructural features of barite have been mapped, including ordered inclusions of NaCl and H_2O (Weber et al., 2016).

A preliminary trial of APT was undertaken at the Geoscience Atom Probe Facility, John de Laeter Centre, Curtin University, Perth, Western Australia, using the LEAP 4000X HR Atom Probe Microscope. APT also employs FIB-SEM for sample preparation (Figure 9.4 a), but

instead of a thin slice, the ideal final form is a thin cone mounted on a silicon pedestal (Figure 9.4 b). Elemental concentrations down to ppm may be presented in 3-D format (Figure 9.4 c) and even displayed as rotating video.

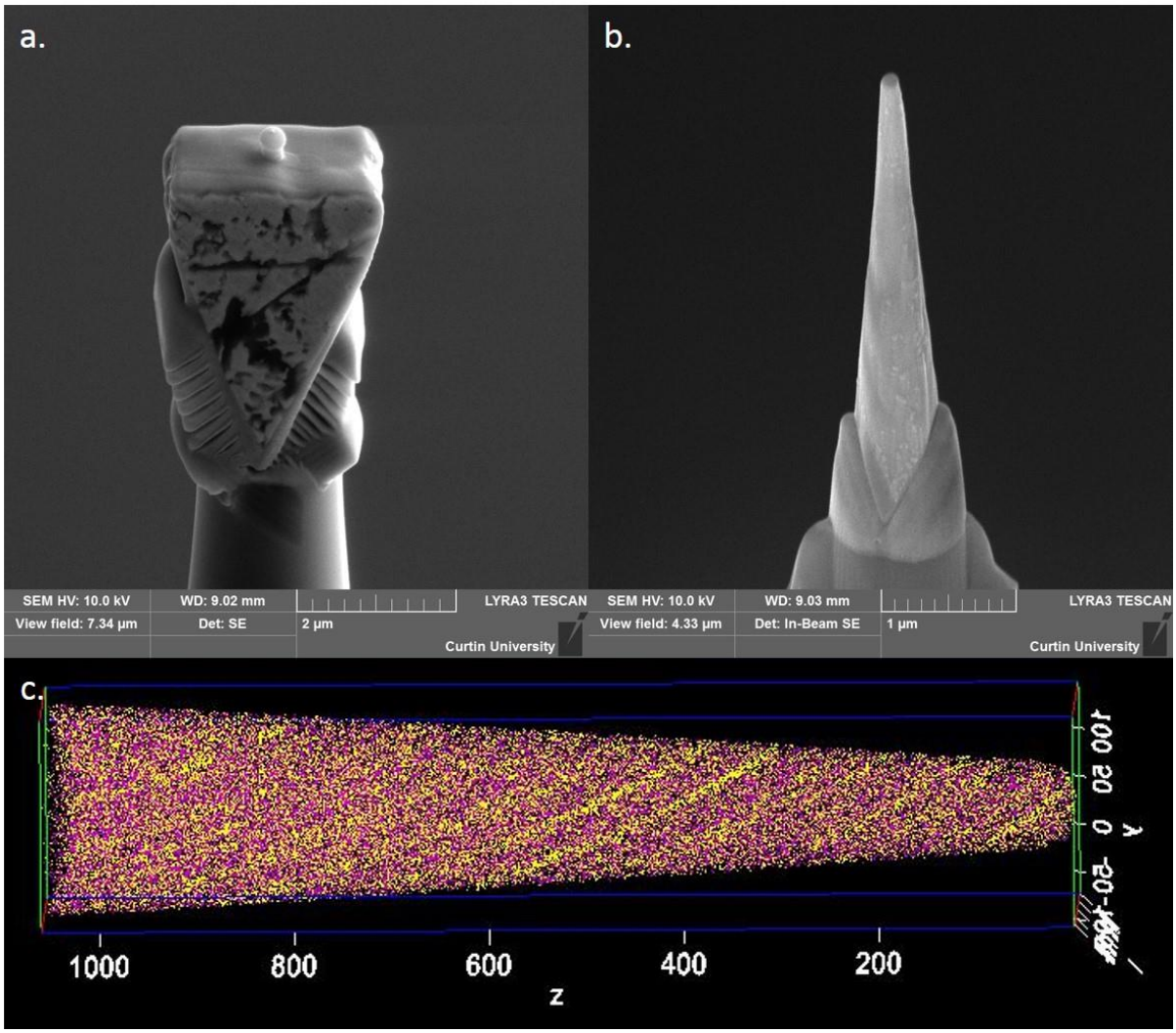

Figure 9.4. Atom probe tomography analysis of synthetic lead sulphate. Sample wedge milled from a grain using FIB-SEM, mounted on a silicon pedestal (a). Polished sample, ready for APT (b). Only the very tip will be analysed. Three-dimensional reconstruction of the data, with each point representing one atom recorded. Magenta represents Na, while yellow represents NO. Laminations can be seen alternating between Na and NO_3^-, likely formed during crystal growth.

APT is the only method which offers 3-D reconstructions of elemental data at the nanoscale. The initial analysis run for this project was very informative and provided an avenue for examining, for example, the uptake of Ra into baryte by CDR mechanisms on the atomic level, or the nanoscale dissociation of RNs within certain minerals under varying conditions. Although limited to ppm concentrations, investigation of U, Th, and Pb in natural samples as

well as Ra and ^{210}Pb (and potentially ^{210}Po) in laboratory samples would greatly expand our understanding of RN deportment on the atomic level. Unfortunately, the trial run on APT coincided too closely with the conclusion of this Ph.D. to warrant further studies at the time. Future projects have been proposed, however, using APT to unravel complicated diffusion mechanisms in both natural and lab-grown samples.

9.4 Electron backscatter diffraction

Electron backscatter diffraction (EBSD) is a complementary method to SEM and EDS and is commonly installed on the same microanalytical platform. Although EBSD is capable of determining multiple structural features of a crystal such as strain or phase, it is frequently used to map and compare crystallographic orientations (Kikuchi, 1928). Metallurgists and material scientists regularly use EBSD to determine how alloys and new materials crystallise, and how various parameters such as temperature and pressure, as well as defects, impact on crystallisation (Schwartz et al., 2009 and references therein; Wilkinson and Britton, 2012 and references therein; Perks et al., 2018). Increasingly used in mineralogy despite difficulties in obtaining sufficiently perfect polish (Nowell et al., 2005; Prior et al., 2009), information such as crystal strain and orientation of intergrowths (symplectites, twinning, exsolution lamellae) can help decipher complex growth histories of minerals and mineral assemblages. At Olympic Dam, growth processes have been investigated and constrained for uraninite, especially early uraninite replacing bornite through CDR reactions (Macmillan et al., 2016a, 2016b).

EBSD employs the principle of electrons escaping from a crystalline structure in a pattern determined by that structure. An electron beam is focussed on the sample, which is set ~70º off horizontal. A phosphor screen is placed horizontally in close proximity to the sample. Of the electrons entering the crystalline sample, a small number escape along low energy-derived paths determined by the atomic lattice of the crystal. Unique patterns are recorded on the

phosphor screen for each mineral, as well as the orientation of the crystal based on a Cartesian system.

During nanoSIMS analyses of Cu-(Fe)-sulphides from Olympic Dam samples, a conspicuous trend was revealed within chalcopyrite and occasionally also in bornite. Grains of seemingly clean, homogeneous chalcopyrite were criss-crossed by very thin lamellae displaying relative enrichment in ^{206}Pb. These lamellae did not correlate to any visible feature in or on the grain. Several alternative mechanisms were proposed for the inclusion of Pb in these grains either during or after crystallisation: Pb-rich solution flowed through the system during crystallisation of a chalcopyrite aggregate leaving a thin crust on existing crystal surfaces which later filled in; Pb-rich solution flowed through a single, clean chalcopyrite which had been fractured, followed by annealing; crystallisation of an aggregate from a Pb-bearing Cu-Fe-S melt, with incompatible Pb migrating towards grain margins and exsolved as what appears as isolated lamellae during cooling. To determine the responsible mechanism, samples containing what appeared as single grains of chalcopyrite were mapped by EBSD on a FEI Inspect F50 instrument at the Microscopy Australia facility, Flinders University, Adelaide, Australia. The example in Figure 9.5 shows the clear correlation between the Pb lamellae (in a seemingly uniform chalcopyrite grain) and crystal orientation boundaries, suggesting that the larger chalcopyrite is actually an aggregate of smaller crystals which was exposed to Pb-rich solution at some point during crystallisation.

While this information on crystal orientation may not seem to directly contribute to the overall objective of this project – the hunt for radionuclides in copper concentrates – it was extremely important in understanding how Pb could occur, seemingly "within" Cu-(Fe)-sulphides yet is neither visible on high-resolution BSE images nor measurable by LA-ICP-MS outside of the crosscutting features. Such Pb represents a previously invisible sink for contamination in concentrates, and even if the concentration of Pb is very low, given that

chalcopyrite comprises 40-50 wt.% of the final concentrate, the potential for lead accumulation is significant and would readily explain why Pb has proven hard or impossible to remove by any physical or hydrometallurgical treatment.

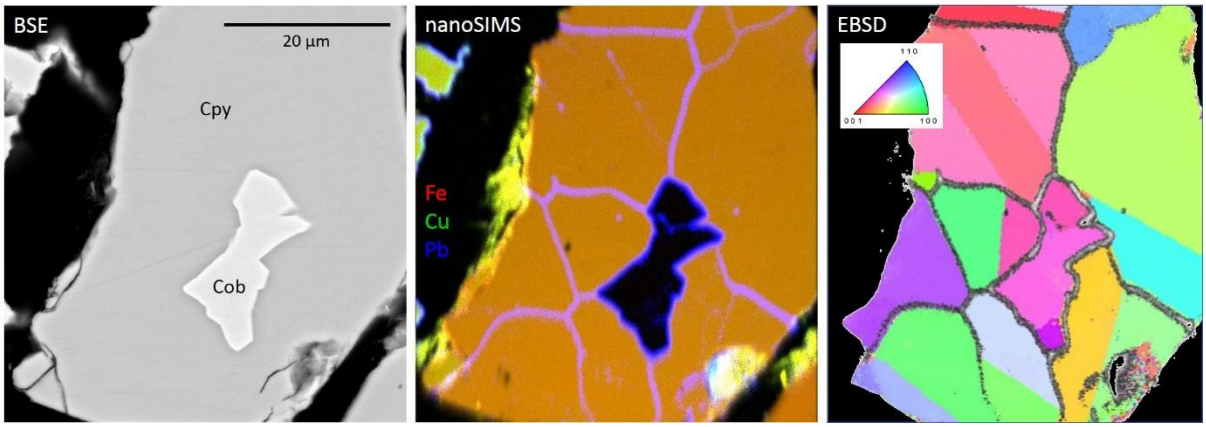

Figure 9.5. BSE, nanoSIMS compilation, and EBSD images of grain 10FC52 from Olympic Dam. Cpy = chalcopyrite, Cob = cobaltite. The ^{206}Pb lines (magenta on the nanoSIMS image, grey stipple on the EBSD image) correlate exactly with non-linear crystal orientation boundaries. The linear boundaries represent twinning, which would not allow Pb incorporation.

These observations also add to the general knowledge of hydrothermal processes within the Olympic Dam deposit at the time of initial precipitation and subsequent hydrothermal alteration. They carry implications for correct interpretation of Pb-isotope signatures and U-Pb dating of sulphides, and demonstrate, once again, that complementary techniques that can bridge scales of observation are necessary to correctly diagnose element distributions in Olympic Dam ores and concentrates.

9.5 References

Cameca, 2019. Introduction to APT. www.cameca.com/products/apt/technique. Accessed 13 August 2019.

Ciobanu, C., Kontonikas-Charos, A., Slattery, A., Cook, N., Wade, B., Ehrig, K., 2017. Short-range stacking disorder in mixed-layer compounds: A HAADF STEM study of bastnäsite-parisite intergrowths. Minerals 7, 227. doi:10.3390/min7110227.

Ciobanu, C.L., Verdugo-Ihl, M.R., Slattery, A., Cook, N.J., Ehrig, K., Courtney-Davies, L., Wade, B.P., 2019. Silician magnetite: Si–Fe-nanoprecipitates and other mineral inclusions in magnetite from the Olympic Dam deposit, South Australia. Minerals 9, 311.

Courtney-Davies, L., Ciobanu, C.L., Verdugo-Ihl, M.R., Slattery, A., Cook, N.J., Dmitrijeva, M., Keyser, W., Wade, B.P., Domnick, U.I., Ehrig, K., Xu, J., 2019. Zircon at the nanoscale records metasomatic processes leading to large magmatic–hydrothermal ore systems. Minerals 9, 364.

Kikuchi, S., 1928. Diffraction of cathode rays by mica. Proceedings of the Imperial Academy 4, 271-274.

Macmillan, E., Ciobanu, C.L., Ehrig, K., Cook, N.J., Pring, A., 2016a. Chemical zoning and lattice distortion in uraninite from Olympic Dam, South Australia. American Mineralogist 101, 2351–2354.

Macmillan, E., Ciobanu, C.L., Ehrig, K., Cook, N.J., Pring, A., 2016b. Replacement of uraninite by bornite via coupled dissolution-reprecipitation: Evidence from texture and microstructure. Canadian Mineralogist 54, 1369–1383.

Miller, M.K., 2012. Atom Probe Tomography: Analysis at the Atomic Level. Springer Science & Business Media, New York, NY. 239 pp.

Nowell, M.M., Witt, R.A., True, B.W., 2005. EBSD sample preparation: Techniques, tips, and tricks. Microscopy Today 13, 44-49.

Owen, N., Ciobanu, C., Cook, N., Slattery, A., Basak, A., 2018. Nanoscale study of clausthalite-bearing symplectites in Cu-Au-(U) ores: Implications for ore genesis. Minerals 8, 67.

Parman, S.W., 2015. Going small: Nanoscale geochronology using atom probe tomography. American Mineralogist 100, 1333-1334.

Perks, H., Cook, N.J., Ciobanu, C.L., Ehrig, K., Basak, A., 2018. Orientation maps for copper cathodes with defect growth: and EBSD study. Goldschmidt 2018, August 12-17, Boston, MA. Goldschmidt Conference Abstracts, 2005.

Peterman, E.M., Reddy, S.M., Saxey, D.W., Snoeyenbos, D.R., Rickard, W.D., Fougerouse, D., Kylander-Clark, A.R., 2016. Nanogeochronology of discordant zircon measured by atom probe microscopy of Pb-enriched dislocation loops. Science Advances 2, e1601318, 1-9.

Piazolo, S., Belousova, E., La Fontaine, A., Corcoran, C., Cairney, J.M., 2017. Trace element homogeneity from micron-to atomic scale: Implication for the suitability of the zircon GJ-1 as a trace element reference material. Chemical Geology 456, 10-18.

Prior, D.J., Mariani, E., Wheeler, J., 2009. EBSD in the earth sciences: applications, common practice, and challenges. In: Schwartz, A.J., Kumar, M., Adams, B.L., Field, D.P., (Eds.), Electron backscatter diffraction in materials science. Springer Science+Business Media, Boston, MA. pp. 345-360.

Reddy, S.M., van Riessen, A., Saxey, D.W., Johnson, T.E., Rickard, W.D., Fougerouse, D., Fischer, S., Prosa, T.J., Rice, K.P., Reinhard, D.A. Chen, Y., 2016. Mechanisms of deformation-induced trace element migration in zircon resolved by atom probe and correlative microscopy. Geochimica et Cosmochimica Acta 195, 158-170.

Schwartz, A.J., Kumar, M., Adams, B.L., Field, D.P. (Eds.), 2009. Electron backscatter diffraction in materials science. Springer Science+Business Media, Boston, MA. 403 pp.

ThermoFisher Scientific, 2019. Helios NanoLab DualBeam. www.fei.com/products/dualbeam/helios-nanolab. Accessed 13 August 2019.

Verdugo-Ihl, M.R., Ciobanu, C.L., Slattery, A., Cook, N.J., Ehrig, K., Courtney-Davies, L., 2019. Copper-Arsenic Nanoparticles in Hematite: Fingerprinting Fluid-Mineral Interaction. Minerals 9, 388.

Weber, J., Barthel, J., Brandt, F., Klinkenberg, M., Breuer, U., Kruth, M., Bosbach, D., 2016. Nano-structural features of barite crystals observed by electron microscopy and atom probe tomography. Chemical Geology 424, 51-59.

Wilkinson, A.J., Britton, T.B., 2012. Strains, planes, and EBSD in materials science. Materials Today 15, 366-376.

Wu, Y.F., Fougerouse, D., Evans, K., Reddy, S.M., Saxey, D.W., Guagliardo, P., Li, J.W., 2019. Gold, arsenic, and copper zoning in pyrite: A record of fluid chemistry and growth kinetics. Geology 47, 641-644.

Chapter 10

Summary, recommendations, and implications

Chapter 10: Summary, recommendations, and implications

10.1 Radionuclide deportment

10.1.1 Radionuclides in copper concentrates

Radionuclides at Olympic Dam follow complex, varied pathways from underground ore extraction through processing to final commodity production and disposal of waste materials. Current hydrometallurgical processes reduce concentrations of all radionuclides from decay of ^{238}U, ^{235}U, and ^{232}Th to below limits set for *chemical* contaminants, but the activities of some isotopes in smelter feed – notably ^{210}Pb and ^{210}Po – remain above the objective *radiological* limits of 1 Bq/g per radioisotope (International Atomic Energy Agency, 2004). Research described in this thesis, particularly nanoSIMS isotope mapping, has provided the foundation for a qualitative RN budget, based on mineralogical hosting preferences. Although not yet fully quantifiable, a preliminary list of minerals occurring in ores and concentrates at Olympic Dam has been compiled, along with their potential for hosting specific RNs (Table 10.1).

Table 20.1. Overview of RN host minerals present in ore/concentrate at Olympic Dam and their qualitative potential for hosting RNs. Enrichment levels represent total RN loads as determined by nanoSIMS. * % in the deposit (Ehrig et al., 2012).

Mineral	%*	Float Concentrate	Concentrate Leach Discharge
Thorite	0.0023	high enrichment	high enrichment
U-Thorite	0.0028	high enrichment	high enrichment
Uraninite	0.0049	high enrichment	high enrichment
Brannerite	0.0119	high enrichment	high enrichment
Coffinite	0.0159	high enrichment	high enrichment
Xenotime	0.0045	high enrichment	high enrichment
Molybdenite	0.0015	high enrichment within cleavage planes, 210 and 226	high enrichment within cleavage planes, 210 and 226
Baryte	1.2252	high enrichment, 210 and 226	very high enrichment, 210 and 226
APS phases	0.1097	variable enrichment	high enrichment
Synchysite	0.0124	low enrichment	low enrichment
Monazite	0.0184	low enrichment	low enrichment
Florencite	0.066	no enrichment	low enrichment
Bastnäsite	0.0833	low enrichment	low enrichment

Zircon	0.0549	low enrichment	low enrichment
Hematite	~30	low enrichment	low enrichment
Apatite	0.1029	low enrichment	low enrichment
Ilmenite	0.0447	low enrichment	low enrichment
Rutile	0.2411	low enrichment	low enrichment
slag		low enrichment	low enrichment
Chlorite group	1.324	low enrichment within cleavage planes	low enrichment within cleavage planes
Sericite	18.193	low enrichment within cleavage planes	low enrichment within cleavage planes
Anhydrite	0.0108	low enrichment, 210 and 226	unknown
Galena	0.0012	no enrichment	enrichment in alteration to $PbSO_4$
Covellite	0.0068	no enrichment	high enrichment possible within cleavage planes

NanoSIMS mapping revealed distinct trends in RN hosting capabilities among minerals in Olympic Dam ore. Generally, the list of RN hosts can be broken down into four categories: U and Th minerals; sulphates and phosphates; oxides; and surficial hosts.

Not surprisingly, uranium and thorium minerals all host RNs to some extent. Uraninite almost always contained the entire decay chain, indicating both sufficient age to allow for ingrowth and just enough stability to resist fractionation due to partial solubility (e.g., Chapter 6, Figure 6.1). Although uraninite is known to be quite soluble (Ram et al., 2013), it generally either dissolved entirely, or not at all due to complete encasement within another mineral. Coffinite usually contained the entire decay chain (e.g., Chapter 6, Figure 6.2) but was unpredictable, with consistent ^{238}U but occasionally variable amounts of other RNs present. Brannerite seems to behave counterintuitively, frequently containing only U and occasionally ^{230}Th and ^{206}Pb (Chapter 6, Figure 6.3); ^{226}Ra and ^{210}Pb were virtually never found in brannerite, either in FC or CLD material.

Most sulphates and phosphates have also been determined to accumulate RNs, although not always the entire decay chain. Solubility is a major factor, as sulphates tend to host sulphate-insoluble cations (Sr, Ba, Pb, Ra) whereas phosphates easily incorporate phosphate-insoluble

U and Th. Baryte (Chapter 6, Figure 6.8) and the woodhouseite-svanbergite series, referred to as aluminium phosphate-sulphate (APS) phases (Chapter 6, Figure 6.6) may contain significant Ra and ^{210}Pb. Anglesite is not found in the Olympic Dam deposit, but is formed during the sulphuric acid leach stage (Chapter 6, Figure 6.9), and is also enriched in ^{226}Ra, ^{210}Pb, and ^{206}Pb (relative to total Pb). Simple phosphates and APS phases tend to accumulate U and Th during formation (e.g., monazite is frequently up to 1 wt.% U and 3-12 wt.% ThO_2; Palache et al., 1951), and subsequent ingrowth of daughters results in the entire chain being present (Chapter 6, Figure 6.5). Apatite (Chapter 7, Figure 7.2) and florencite have also shown low RN enrichment in some samples.

Additional host minerals include zircon (Chapter 7, Figure 7.5) and some simple oxides: hematite, rutile, and ilmenite – all known as potential RN hosts (e.g., Davis et al., 2003 and references therein; Vandenborre et al., 2007; Radhamani et al., 2010; Ciobanu et al., 2013). Although all low enrichment hosts, zircon, ilmenite, rutile, (and ilmenorutile) essentially survive the acid leach intact, so any included RNs will report to final concentrates. Hematite is greatly reduced through flotation and acid leaching but 5 wt.% may still remain in final concentrates, representing a potentially significant RN sink (Chapter 7, Figure 7.6b).

Host minerals in the final category share a structural similarity as opposed to a chemical one. The surface area of minerals may increase due to fracturing from stress or shear, either in the deposit or during processing, or from micaceous cleavage. High surface area minerals consistently contain RNs, with more electronegative minerals (sulphides) and acid leached material showing the highest enrichment. Primary molybdenite and covellite, and covellite formed during acid leaching through metathesis reactions all host significant amounts of RNs – but usually only ^{226}Ra and ^{210}Pb.

Copper sulphides may not only host RNs within cleavage planes and fractures, and on charge-imbalanced surfaces, they can also contain trace amounts of U and Pb within seemingly solid grains. Chapter 7, Figures 7.12 and 7.13 detail the inclusion of thin lamellae of (predominantly) ^{206}Pb hosted within chalcopyrite, and rarely bornite, from both FC and CLD samples. This unexpected sink for Pb, caused by partial deposition of Pb during chalcopyrite formation and recrystallisation, complicates our ability to create a budget for Pb_{total} or ^{210}Pb. The surface adhesion of nanoparticles to, and the inclusion of trace Pb within, chalcopyrite/bornite grains also adds greatly to our uncertainty regarding RN deportment – especially in copper concentrate which is >50 wt.% copper sulphides.

10.1.2 The effect of processing

The information provided by different sample types, and the differences between types, allow a greater understanding of the geochemistry occurring in the Olympic Dam deposit and processing stream. Diamond drill core samples show a glimpse of the deposit unaffected by processing. Flotation concentrate samples have undergone Cu upgrading and milling, which tends to increase surface areas due to fracturing and cleavage but are still mineralogically representative of the ore deposit. Concentrate leach discharge samples are the most distinct, with a partial restructuring of mineralogy, including formation of covellite and anglesite, as well as trace element/isotope distribution. The primary results from this thesis regarding natural and chemically processed samples from Olympic Dam, as well as controlled lab experiments with mineral analogues, have provided not only a deeper understanding of deposit formation but also revealed detailed pathways of trace element and isotope deportment occurring at the nanoscale during copper concentrate processing.

The distinct differences in RN deportment between FC and CLD (for certain minerals) highlighted above emphasise the effect that the sulphuric acid leach has on this system.

Significant separation of parent and daughter RNs explains the measured secular disequilibrium. In drill core samples (i.e., within the deposit) and in FC samples, the majority of all RNs tend to reside with, or in the near vicinity of, parent U-bearing minerals – the exception being baryte which may or may not be locally enriched in ^{226}Ra and ^{210}Pb. Similarly, minerals which are known to host U and especially Th (e.g., xenotime or apatite) may contain significant amounts of the entire ^{238}U decay chain. Trace amounts of some RNs, particularly the sulphate-insoluble ones (^{226}Ra and ^{210}Pb), may be found in high surface area minerals such as chlorite, sericite, or molybdenite – but usually only within a few microns of the respective U-source mineral.

In contrast, acid-leached concentrate contains only very low concentrations of U- or Th-bearing minerals, most (all except the tiniest inclusions in sulphides and possibly some brannerite) having been dissolved and removed along with the carbonates, fluorite, some REE minerals, and some iron oxides. The remaining uranium minerals (primarily brannerite, some coffinite) do contain members of the ^{238}U decay chain, but, as shown in Chapter 4, not necessarily all members of the series.

One enigma revealed by nanoSIMS mapping was that almost all brannerite grains mapped showed only U and Th, or U, Th, and ^{206}Pb, with the remainder of the decay chain absent. There are a few possible mechanisms which may explain this observation. 1) It may be the result of partial dissolution resulting from some members of the decay chain not easily being accommodated by the brannerite crystal structure, and their expulsion facilitated by extensive fracturing. The brannerite structure is considered to be chemically flexible with regard to the U site, easily incorporating Th and Pb (Bailey et al., 2016) but not necessarily Ra or Rn. Fracturing due to alpha decay and subsequent fluid activity has been observed (Lumpkin et al., 2012). However, brannerite is almost always metamict (Smith, 1984) and amorphous (Zhang et al., 2006), the flexibility of which should actually facilitate retention of almost any element,

regardless of characteristics. 2) Youth, with abundant U ± ^{206}Pb crystallising in new brannerite without sufficient time for daughter ingrowth. This is possible, but unlikely, as a measurable amount of ^{230}Th should ingrow within decades, and ^{226}Ra within a millennium or so. 3) The most likely scenario involves brannerite formation by alteration and replacement of existing rutile (Macmillan et al., 2017), whereby rutile in contact with RN-bearing fluids will incorporate U and small amounts of Th and Pb (if available), likely through CDR mechanisms, but not Ra. Even if ^{210}Pb is incorporated along with ^{206}Pb it will decay out in a matter of decades if ^{226}Ra is not present, explaining its absence. Since (VI) coordinated U^{4+} has a crystal radius (CR) of 1.03 Å, (Th^{4+}: 1.08 Å, Ca^{2+}: 1.14 Å, Pb^{4+}: 0.92 Å, and Ce^{4+}: 1.01 Å) but Ra^{2+} has an estimated CR of 1.51 Å (all radii from Shannon, 1976), it may simply be a matter of size. Kinetics allows substitution of U, Ca, Pb, Th, and REE into the rutile structure, but oversized Ra^{2+} is unstable.

Baryte and other sulphate minerals (e.g., APS phases) mostly contained significant amounts of ^{226}Ra and ^{210}Pb, in all sample types, but frequently no other RNs. Moreover, some grains exhibited signs of RN uptake in progress, with porous, heavily substituted reaction rims containing RNs, surrounding a barren core. The baryte in Chapter 6, Figure 6.8 is heavily included and contains appreciable ^{226}Ra and ^{210}Pb, but a closer look reveals less-included, lower-RN-enrichment zones in the centre of the two baryte lobes. RN-bearing fluids passing through the surrounding sericite has likely altered the baryte rim, leaving the core as yet unaffected. The presence of significant RNs in baryte from drill core samples verifies that at least one mechanism of RN mobilisation and uptake is occurring in the deposit. Pristine baryte can be found, however, as shown in Chapter 6, Figure 6.7. A subhedral grain of baryte containing no RNs is cemented to a euhedral chalcopyrite by secondary baryte which is enriched in ^{226}Ra and ^{210}Pb. Early stages of RN encroachment into the pristine baryte can be

seen around the edges. The coincidental enrichment of Sr in the secondary baryte suggests CDR replacement with correlative uptake of Ra and Pb.

Anglesite ($PbSO_4$) is not found in the deposit but does constitute a small percentage of CLD material. During acid leaching, radiogenic Pb liberated from dissolving U and U-bearing minerals precipitates immediately as an insoluble sulphate – most likely as nanoparticles. In cases of high Pb liberation, anglesite aggregates (or nanoparticulate agglomerates) may form *in situ*, replacing the departing uranium mineral as a pseudomorph. One nanoSIMS map from Chapter 6, Figure 6.9 (Figure 10.1) Shows ^{206}Pb uptake in anglesite replacing a uranium phase. Note that the highest enrichment of ^{206}Pb is not in the galena (a pure Pb phase) but is in fact in the alteration zones immediately surrounding the galena. This suggests that the primary galena formed from a lower ^{206}Pb solution (e.g., global abundance, which is only ~24 % ^{206}Pb; Rumble, 2017) whereas the alteration zone was affected by high ^{206}Pb solution – as would be expected from the dissolution of a U phase.

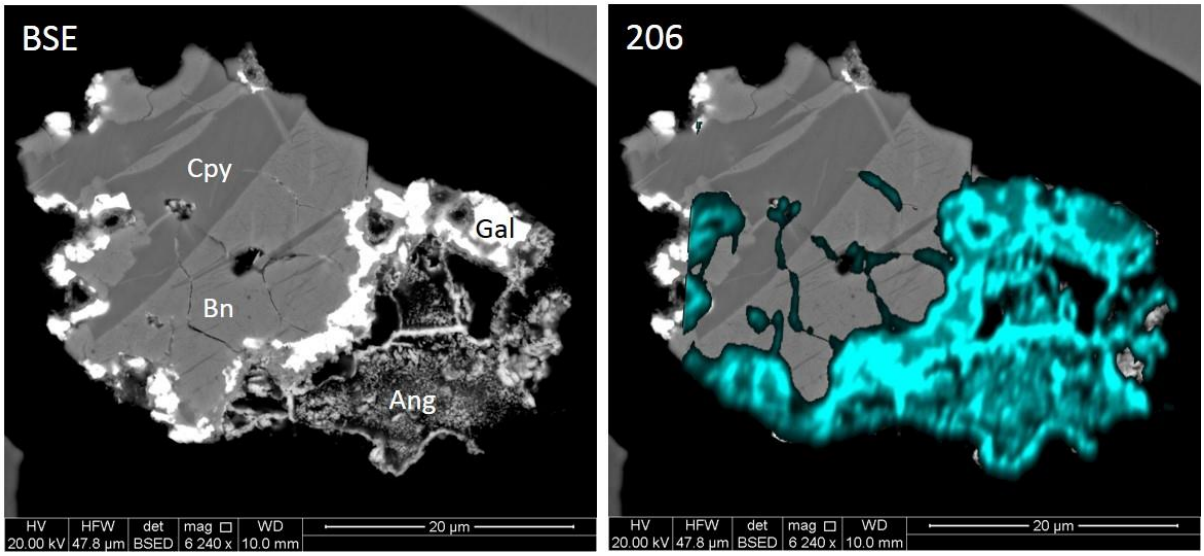

Figure 50.1. BSE and ^{206}Pb nanoSIMS image of grain 10CLD61. 206Pb is enriched in alteration zones around the existing galena.

These replacements were all quite enriched in both ^{226}Ra and ^{210}Pb, likely the result of a combination of trapping through rapid precipitation and coupled dissolution-reprecipitation

mechanisms (Ruiz-Agudo et al., 2014) occurring at the nanoscale (Figure 10.2; Chapter 6, Figure 6.9).

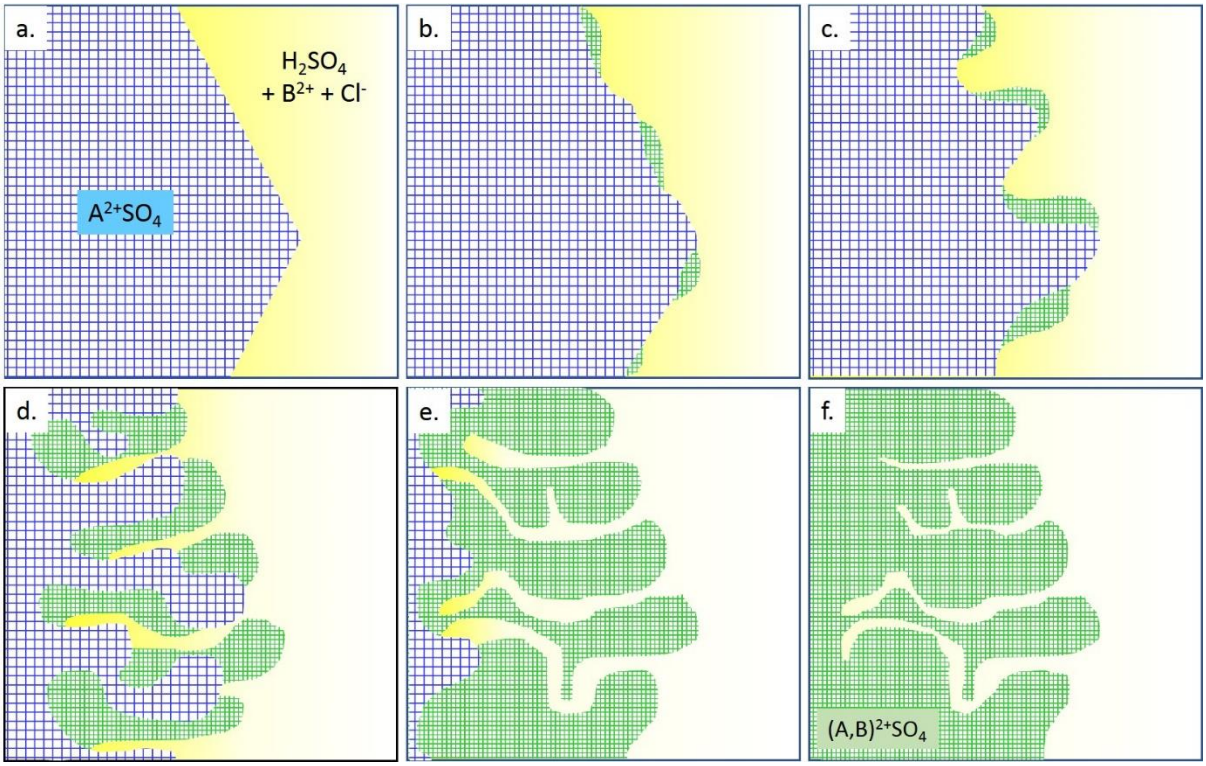

Figure 10.2. Schematic example of coupled dissolution-reprecipitation. (a): Crystal ASO_4 (blue) comes in contact with an H_2SO_4 solution (yellow) containing dissolved B^{2+} and a complexing agent such as Cl^-. (b) through (e): As the reaction progresses, ASO_4 irregularly dissolves while the hybrid $(A,B)SO_4$ (green) crystallises on nearby surfaces. (f): Eventually, ASO_4 is entirely replaced by $(A,B)SO_4$ while maintaining roughly the same crystal morphology, albeit exhibiting excessive porosity, and B^{2+} is depleted in the solution.

Appreciable concentrations of sulphate-insoluble RNs were observed in virtually all covellite and molybdenite from CLD samples. Covellite is rare in the deposit but may represent a few wt.% of CLD, having been created during the acid leach through metathesis reactions (Byrne et al., 2018). RN-bearing nanoparticles created in the leach tank may agglomerate immediately in the vicinity of formation (e.g., anglesite) or may be transported elsewhere. It is likely that the high surface area of covellite and molybdenite due to their planar, micaceous cleavage provides an ideal trap for filtering nanoparticulates out of passing fluids. Having been milled, the primary molybdenite and covellite would likely be friable due to shear and may have extremely high surface exposure. Secondary covellite may trap RN nanoparticles during

its formation and/or filter them out of solution afterwards. Furthermore, low but detectable concentrations could also be seen in other platy minerals with high surface area such as sericite and chlorite. These minerals appear to host RNs within their boundaries (as opposed to their outer surfaces), but it is unlikely that Ra is actually being incorporated into the crystal structures. As for brannerite's missing ^{226}Ra (and ingrown ^{210}Pb), assuming it had not already precipitated elsewhere, one possible explanation for this is the nearly universal pairing of brannerite and molybdenite. The high surface area cleavage planes of molybdenite would provide an excellent local trap for Ra- and Pb-sulphates, resulting in the entire ^{238}U decay chain being hosted in the brannerite-molybdenite pair (Chapter 4, Figure 12, sample 10FC48).

A phenomenon which was consistently observed in the CLD samples but was never encountered in any FC samples was surficial accumulation of RNs, particularly ^{226}Ra and ^{210}Pb. In this instance, the 'surface' referred to is limited to outer grain surfaces and does not include internal cleavage planes. The aforementioned Pb- and Ra-bearing nanoparticles, precipitated from liberated RNs in the sulphuric acid leach solution, may remain in colloidal suspension and transported if conditions allow. The low-pH conditions may cause surficial charge imbalances, especially on sulphides, which may then attract colloidal nanoparticles like an electrostatic filter (Bebie et al., 1998; Mikhlin and Romanchenko, 2007; Alonso et al., 2009). This electrostatic effect may also enhance the uptake within cleavage planes in molybdenite and covellite. Very low concentrations were also observed covering surfaces of almost all mineral types susceptible to surface charge (Figure 10.3). The only notable exception was inert quartz.

RN-bearing nanoparticles, both organic and inorganic, have been documented in geologic formations (Schäfer et al., 2012) and are responsible for at least some of the redistribution of RNs throughout the deposit. The actions of milling the ore and subsequent leaching with sulphuric acid seems to greatly exacerbate RN mobility. These phenomena, especially in an

acid-leached sulphide concentrate particularly susceptible to surface charge, greatly complicate any attempts to quantify RN deportment. These findings emphasise the importance of applying a holistic approach, as unexpected results have altered our overall perception of this issue.

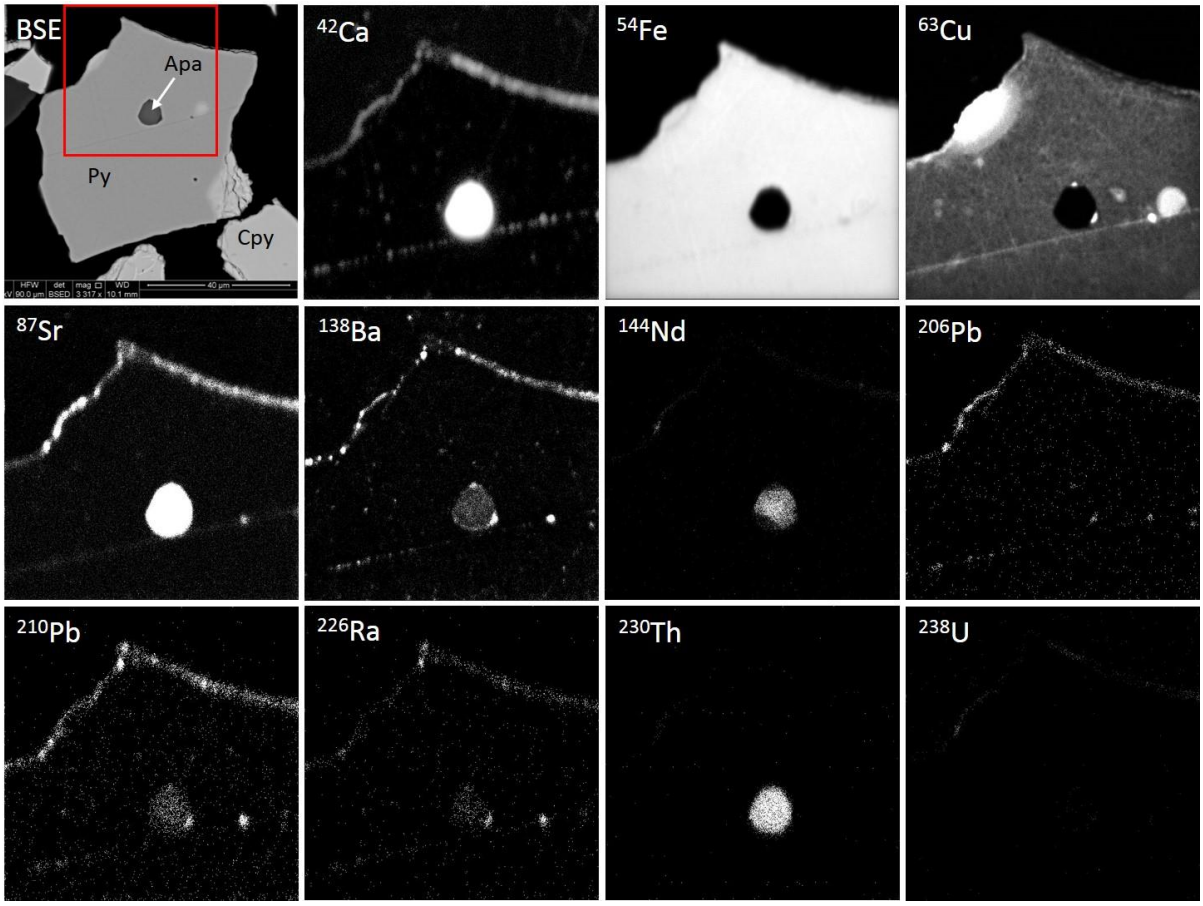

Figure 10.3. BSE and nanoSIMS images of grain 05CLD21, apatite (Apa) in pyrite (Py) with small zones of chalcopyrite (Cpy). Note the surface enrichment for sulphate-insoluble elements (Ca, Sr, Ba, Pb, and Ra) but not for sulphate-soluble elements (Fe, Cu, Nd, Th, and U).

10.1.3 Radionuclides in synthetic minerals

Diffusion experiments conducted on pure Sr, Ba, and Pb sulphates, followed by semi-quantitative LA-ICP-MS transects, revealed that multiple mechanisms are responsible for RN incorporation. Celestite ($SrSO_4$), baryte ($BaSO_4$), and anglesite ($PbSO_4$) are all capable of incorporating Ra, but not equally. Celestite may incorporate significant amounts of Ra, but only if Ba and Pb are absent. Baryte predominantly accumulates Ra through Ra-bearing overgrowth of $(Pb,Ba,Sr)SO_4$ on its surface. Anglesite is susceptible to coupled dissolution-

reprecipitation (CDR) which incorporates available Ra in the reprecipitation phase, but releases a large amount of Pb into solution. Generally, high chloride activity enhances these mechanisms, while high sulphate activity inhibits them. Diffusion of Ra^{2+} into the respective sulphate crystal structures is omnipresent but appears to be of minimal consequence compared to larger-scale overgrowth and CDR reactions.

10.2 Implications for generation of cleaner concentrates

Results detailed above have provided a detailed diagnosis of RN distributions, confirmed several predicted hosts, identified several that were less expected, and documented RN behaviour explaining the differences in RN activities between FC and CLD in both natural and synthetic samples. Based on this knowledge, it may seem a relatively simple hydrometallurgical task to reduce each radionuclide below 1 $Bq/g_{(concentrate)}$, but this is deceptive when considering that 1 Bq/g of ^{238}U represents a very manageable 80 ppm, while 1 Bq/g of ^{210}Pb is 400 parts-per-quadrillion (ppq; $1x10^{-15}$) and 1 Bq/g of ^{210}Po is only around 6 ppq. Even if Po concentrations are reduced to one ten-billionth of that of U, it will still remain above the target activity. When considering this, it is actually impressive that current processing techniques employed at Olympic Dam produce concentrates which are generally only 1-2 orders of magnitude above desired levels (Hondros, 2014).

The key to reducing these levels further lies in the targeted removal, or at least reduction, of specific minerals which have the greatest potential as an RN sink. It is likely, however, that there will be different mineral targets for different RNs, but that some overlap exists which may be utilised.

Results from both nanoSIMS mapping of copper concentrates and LA-ICP-MS analyses of synthetic minerals suggest that sulphate activity is a primary driving force for RN sequestration (at least for ^{210}Pb and ^{226}Ra). Since both Pb and Ra form insoluble sulphates (as Po is predicted

to do; Figgins, 1961; Ram et al., 2019 and references within) it makes sense for process engineers to investigate using this chemical correlation to their advantage. Uranium and Th levels in smelter feed (or final concentrates) are already quite low (Hondros, 2014) and can be brought close to or below the 1 Bq/g limit with little additional effort (Fu, 2019). This leaves sulphate manipulation as the most likely avenue for reduction of the remaining RNs.

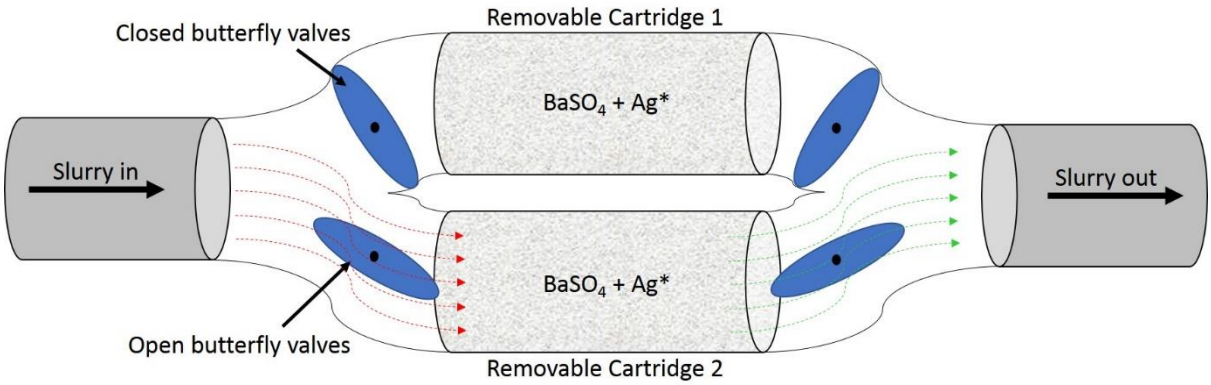

Figure 10.4. Proposal for passive RN removal system, to be spliced into a slurry transfer line. Switching system allows for cartridge replacement. Slurry thickness and $BaSO_4$ matrix size (i.e. pebbles or cobbles) would have to be adjusted to prevent clogging. Alternatively, the system could be mounted upright for gravity assist. Heating/cooling coils could be added to cartridges as appropriate. *Ag (or another suitable metal) could be added for removal of Po, Au, and platinum group elements, then processed for Au recovery and Po disposal.

Theoretical implementation on a processing plant scale might involve adding a reservoir of crystalline sulphate into the sulphuric acid leach tank or creating a filter cartridge arrangement which may be spliced into one of the slurry transfer lines. The optimal sulphate would probably be baryte, but a simple series of lab experiments should be able to determine the most effective candidate, whether it be a pure sulphate or a hybrid. A more complex mineral such as an APS phase (Owen et al., 2019) may be the ideal solution, containing both Ra- and Pb-scrubbing sulphate and U- and Th-scrubbing phosphate. Pure $SrSO_4$ would be ineffective for Ra removal in the presence of Ba and Pb, as shown in Chapter 8, Figure 8.4. CDR reactions induced in $PbSO_4$ have the potential for significant removal of Ra, but at the cost of introducing a significant amount of Pb back into the concentrate (likely including ^{210}Pb) as seen in Chapter 8, Figure 8.8a. Overgrowth of (Pb, Sr, Ba, Ra)SO_4 on baryte, however, works in both high and

low sulphate activity and high and low pH. Slight modifications to temperature, sulphate activity, or pH may improve efficacy, based on results from lab tests. Figure 10.4 shows a schematic of a possible Ra (and potentially Po) trap.

10.3 Implications for the evolution and development of Olympic Dam

NanoSIMS mapping of diamond drill core and flotation concentrate samples from Olympic Dam has provided a window into geochemical processes at work in the deposit, revealing information about ore formation and subsequent alteration due to local and regional geologic events. Hydrothermal alteration at Olympic Dam is well-established, albeit not entirely understood (e.g., Maas et al., 2011; Ehrig et al., 2012; Kirchenbaur et al., 2016; Apukhtina et al., 2017).

The BSE image of chalcopyrite, quartz, fluorite, galena, and hematite in sphalerite presented in Chapter 7, Figure 7.9 shows partial porosity – a clear textural indicator of hydrothermal activity. The nanoSIMS images augment this by showing sporadic enrichment of Ba, Ra, and ^{210}Pb in porous regions, with no enrichment in non-porous areas. From this we can deduce: 1) fluid activity has affected this sample; 2) alteration was likely minor, as only part of the chalcopyrite is affected and there are no classic replacement textures (other than porosity) or reaction rims visible; 3) chemical susceptibility to the particular fluid chemistry involved is sphalerite>chalcopyrite>fluorite, hematite, quartz; 4) intervening fluids contained at least Ba and Ra, the ^{210}Pb may be the result of ingrowth; 5) No ^{230}Th, ^{238}U, or ^{206}Pb was observed in the sample, except for the small galena inclusions, and were therefore either absent from the fluid or were not induced to precipitate; 6) conditions were appropriate for Ba precipitation in both sphalerite and chalcopyrite, but Ra precipitation only in chalcopyrite; and 7) ^{210}Pb and ^{206}Pb are driven by different mechanisms, given their complete dissociation. This highlights just one

example of the potential for unravelling geochemical conditions and complex histories of the ore prior to extraction, based on nanoSIMS mapping.

A second example providing evidence of the hydrothermal history of Olympic Dam is shown in Chapter 6, Figure 6.8. Ra-bearing fluid has clearly contacted a baryte grain, depositing a significant Ra load through what was likely a coupled dissolution-reprecipitation reaction. ^{210}Pb may have been incorporated in the same manner, but the current concentration in the grain is most likely from ingrowth.

These examples underline the complexity of the deposit, and the caution which must be exercised when interpreting what are effectively microscale bulk analyses from LA-ICP-MS, EPMA, TIMS, and similar instrumentation – without due attention to characterisation using techniques with appropriate sub-micron resolution. Geochronometric measurements, for example, commonly include a qualification to account for the inherent heterogeneity not only within the ore, but also within individual mineral grains (Courtney-Davies et al., 2019).

10.4 Broader applicability of findings

The hunt for radionuclides in Olympic Dam ore and copper concentrates may seem specialised, but the research output has much broader applications. The ability of nanoSIMS to map spatial distributions of not only RNs (Chapters 3, 6, and 7) but also trace elements (Chapter 4), may be applied to any number of research questions. *In situ* geoscience analytics are still dominated by ion microprobes such as the Australian Scientific Instruments sensitive high-resolution ion microprobe (SHRIMP and SHRIMP II) and CAMECA IMS 1280 microprobe (Kilburn and Wacey, 2014). The majority of nanoSIMS time, at least for the CAMECA 50 and 50L at CMCA in Perth, is spent on materials science and biological sciences (Paul Guagliardo, pers. comm.). But the advantages of nanoSIMS (e.g., spatial resolution, mass resolution, or sensitivity) over other methods are slowly being embraced by researchers investigating

geochemical reactions at the nanoscale; it is particularly well-suited to investigate mineral alteration, nanoinclusions, crystal formation, and trace element distributions. The results presented in the chapters above not only support this practice, but also strongly emphasise the importance of nanoSIMS data as complements to other techniques such as EPMA, TEM, ICP-MS, and APT.

Regardless of the analytical method used, monitoring RN deportment at ever-decreasing scales is a crucial facet of many disciplines beyond the mining industry. Natural radionuclides are ubiquitous in the environment (Kathren, 1998; Ram et al., 2019); both natural and anthropogenic RNs are having an increasingly widespread influence on industry (e.g., Crockett et al., 2003; Ram et al., 2019), technology (e.g., Emrich Jr., 2016), medicine (e.g., Kendi et al., 2017), and research (e.g., L'Annunziata, 1987; Quinto et al., 2017) – either as an active component or as a waste product. The diffusion experiments presented in Chapters 5 and 8 could be expanded upon to provide a broader understanding of RN interactions with soils, sediment, clays, construction materials, nuclear storage containment materials, etc., and the nanoSIMS would be indispensable for characterisation.

The incidents at Three Mile Island, Chernobyl, and Fukushima Daiichi, as well as the recent mysterious rocket explosion off Russia's north-west coast (and the associated spike in radioactive iodine) all provide sobering significance to the concept that even the most careful planning and execution may not prevent an accidental release of RNs into the environment. And the threat of intentional release should not be discounted. "*Scientia potentia est*", a quote often ascribed to Sir Francis Bacon, is a simple but potent concept which applies here, as our best efforts to monitor and control the interaction between radioactive elements and the biosphere hinge upon our intimate understanding of these interactions down to the atomic level.

10.5 Research gaps and potential future projects

Although the research documented in this thesis allowed significant progress in understanding RN distributions, several aspects of the work emerged that demand attention in the future to further constrain RN deportment, feed into continuing efforts to eliminate or reduce contaminants, and explain some of the more unexpected outcomes documented above. The following paragraphs are not intended to be a comprehensive overview of all outstanding research gaps, but include several of the primary avenues which deserve investigation – given the time and resources to do so.

The diffusion experiments presented in Chapters 5 and 8 were successful and provided understanding of Ra and Pb deportment in sulphates at the nanoscale. Similar experiments with other radionuclides (e.g., Th, Po) and other minerals (natural or synthetic) may also prove fruitful. Procedures would involve acquiring or making purified RN solutions, exposing a variety of appropriate natural and synthetic minerals to each RN solution under variable conditions, and analysing the results by SEM, nanoSIMS, LA-ICP-MS, and possibly TEM or APT. The benefits of expanding these experiments would extend beyond Olympic Dam and the mining industry in general, as it would complement the existing omnibus of information regarding the interaction between RNs and all natural and anthropogenic media including soil, sediment, flora and fauna (including foodstuffs), building materials, nuclear storage materials, industrial equipment, and ultimately humans.

As a complement to nanoSIMS analyses, atom probe tomography would literally add an extra dimension to our understanding of nanoscale mechanisms such as coupled dissolution-reprecipitation and solid-state diffusion. The ability to observe elemental and isotopic distributions at grain boundaries, reaction fronts, and in nanoinclusions at the atomic level – in three dimensions – would prove invaluable for research of this nature. A brief overview of the

benefits of, and research breakthroughs resulting from, APT is presented in Chapter 9, section 9.3. Investigation of natural minerals could easily be supplemented by results from diffusion experiments utilising synthetic mineral analogues, as proposed above.

Future analyses of RNs in any materials will be far more valuable given the ability to quantify the results. Few ^{226}Ra and/or ^{210}Pb standards are currently available, and those that are such as IAEA 385 sediment, IAEA 375 soil, IAEA-RGU-1 uranium ore (International Atomic Energy Agency, 2019), and the CANMET uranium ore standards BL-5, DL-1a, BL-4a, and DH-1a (Natural Resources Canada, 2019) are all provided as finely ground powders, suitable only for bulk analyses. With no assurances of homogeneity at the micron scale, virtually none of the available standards are appropriate for our proposed techniques. The location (or creation) and calibration of solid standards containing all members of the ^{238}U decay chain would prove greatly beneficial for nanoSIMS, APT, LA-ICP-MS, solution ICP-MS, EPMA, TIMS, TEM, and possibly other analytical platforms. Not all RNs would exist at concentrations measurable by all instruments, so limitations would have to be established. The MR_Uran standard was created with this in mind, and initial results (Chapter 8) have proven very promising. If successful, similar standards for the ^{235}U and ^{232}Th decay chains may also be created and calibrated.

As an extension of RN quantification, there also exists potential for quantifying at least minor, if not trace, elements in minerals by nanoSIMS. Quantification of trace elements with SIMS has been proven in solids with consistent chemical compositions (Wilson and Novak, 1991; Ganeev et al., 2016). Initial experiments with minerals have provided promising results (see Chapter 3), comparing nanoSIMS signal intensities to calibrated LA-ICP-MS concentration data. Although not suitable for every element in every matrix (mineral), an initial database of relative sensitivity factors (RSFs) for common elements in a selection of prevalent

rock- and ore-forming minerals would be an excellent start. The Tate Mineral Standard was created with this in mind, therefore this project could proceed directly to the analytical stage.

10.6 References

Alonso, U., Missana, T., Patelli, A., Ceccato, D., Albarran, N., Garcia-Gutierrez, M., Lopez-Torrubia, T., Rigato, V., 2009. Quantification of Au nanoparticles retention on a heterogeneous rock surface. Colloids and Surfaces A: Physicochemical and Engineering Aspects 347, 230-238.

Apukhtina, O.B., Kamenetsky, V.S., Ehrig, K., Kamenetsky, M.B., Maas, R., Thompson, J., McPhie, J., Ciobanu, C.L., Cook, N.J., 2017. Early, deep magnetite-fluorapatite mineralization at the Olympic Dam Cu-U-Au-Ag deposit, South Australia. Economic Geology 112, 1531-1542.

Bailey, D.J., Stennett, M.C., Hyatt, N.C., 2016. Synthesis and characterization of brannerite wasteforms for the immobilization of mixed oxide fuel residues. Procedia Chemistry 21, 371-377.

Bebie, J., Schoonen, M.A., Fuhrmann, M., Strongin, D.R., 1998. Surface charge development on 546 transition metal sulfides: an electrokinetic study. Geochimica et Cosmochimica Acta 62, 633-642.

Byrne, K., Hawker, W., Vaughan, J., 2018. Deportment of radionuclides during copper concentrate metathesis reactions. Proceedings ALTA 2018, 19-26 May 2018, Perth, WA, 12 pp.

Ciobanu, C.L., Wade, B.P., Cook, N.J., Schmidt Mumm, A., Giles, D., 2013. Uranium-bearing hematite from the Olympic Dam Cu-U-Au deposit, South Australia: A geochemical tracer and reconnaissance Pb-Pb geochronometer. Precambrian Research 238, 129–147.

Courtney-Davies, L., Tapster, S.R., Ciobanu, C.L., Cook, N.J., Verdugo-Ihl, M.R., Ehrig, K.J., Kennedy, A.K., Gilbert, S.E., Condon, D.J., Wade, B.P., 2019. A multi-technique evaluation of hydrothermal hematite U-Pb isotope systematics: Implications for ore deposit geochronology. Chemical Geology 513, 54-72.

Crockett, G.M., Smith, K.R., Oatway, W.B., Mobbs, S.F., 2003. Radiological Impact on the UK Population of Industries which Use or Produce Materials Containing Enhanced Levels of Naturally Occurring Radionuclides: The Steel Production Industry. National Radiological Protection Board Report R-327. 87 pp.

Davis, D.W., Krogh, T.E., Williams, I.S., 2003. Historical development of zircon geochronology. Reviews in Mineralogy and Geochemistry 53, 145-181.

Ehrig, K., McPhie, J., Kamenetsky, V.S., 2012. Geology and mineralogical zonation of the Olympic Dam iron oxide Cu-U-Au-Ag deposit, South Australia. In: Hedenquist, J.W., Harris, M., Camus, F., (eds.), Geology and Genesis of Major Copper Deposits and Districts of the World, a Tribute to Richard Sillitoe. Society of Economic Geologists Special Publication 16, Littleton, CO. 237–267.

Emrich Jr., W.J., 2016. Principles of Nuclear Rocket Propulsion. Butterworth-Heinemann. 344 pp.

Figgins, P.E., 1961. The radiochemistry of polonium. Mound Laboratory, Miamisburg, OH. 74 pp.

Fu, W., 2019. Node 3: Radionuclide Separation. Unpublished presentation, May 2019, 13 pp.

Ganeev, A.A., Gubal, A.R., Potapov, S.V.E., Agafonova, N.N., Nemets, V.M., 2016. Mass spectrometric methods for the direct elemental and isotopic analysis of solid material. Russian Chemical Reviews 85, 427-444.

Hondros, J., 2014. Background Radiation Briefing presentation. Unpublished document, 69 pp.

International Atomic Energy Agency, 2004. Application of the Concepts of Exclusion, Exemption and Clearance. International Atomic Energy Agency, Vienna. IAEA Safety Standards Series: Safety Guide No. RS-G-1.7

International Atomic Energy Agency, 2019. Reference products for Environment and Trade. https://nucleus.iaea.org/rpst/ReferenceProducts. Accessed 16 August 2019.

Kathren, R.L., 1998. NORM sources and their origins. Applied Radiation and Isotopes 49, 149-168.

Kendi, A.T., Moncayo, V.M., Nye, J.A., Galt, J.R., Halkar, R., Schuster, D.M., 2017. Radionuclide therapies in molecular imaging and precision medicine. PET Clinics 12, 93-103.

Kilburn, M.R., Wacey, D., 2014. Nanoscale secondary ion mass spectrometry (nanoSIMS) as an analytical tool in the geosciences. In: Grice, K. (Ed.), Principles and Practice of Analytical Techniques in Geosciences. Royal Society of Chemistry, London, UK, 1–34.

Kirchenbauer, M., Maas, R., Ehrig, K., Kamenetsky, V.S., Strub, E., Ballhaus, C., Münker, C., 2016. Uranium and Sm isotope studies of the supergiant Olympic Dam Cu–Au–U–Ag deposit, South Australia. Geochimica et Cosmochimica Acta 180, 15-32.

L'Annunziata, M.F., 1987. Radionuclide Tracers. Academic Press, London, UK. 505 pp.

Lumpkin, G.R., Leung, S.H.F., Ferenczy, J., 2012. Chemistry, microstructure, and alpha decay damage of natural brannerite. Chemical Geology 291, 55-68.

Maas, R., Kamenetsky, V., Ehrig, K., Meffre, S., McPhie, J., Diemar, G., 2011. Olympic Dam U–Cu–Au deposit, Australia: new age constraints. Mineralogical Magazine 75, 1375.

Macmillan, E., Cook, N.J., Ehrig, K., Pring, A., 2017. Chemical and textural interpretation of late-stage coffinite and brannerite from the Olympic Dam IOCG-Ag-U deposit. Mineralogical Magazine 81, 1323–1366.

Mikhlin, Y.L., Romanchenko, A.S., 2007. Gold deposition on pyrite and the common sulfide minerals: an STM/STS and SR-XPS study of surface reactions and Au nanoparticles. Geochimica et Cosmochimica Acta 71, 5985-6001.

Natural Resources Canada, 2019. https://www.nrcan.gc.ca/our-natural-resources/minerals-and-mining/mining-resources/certified-reference-materials. Updated 16 July 2019, Accessed 16 August 2019.

Owen, N.D., Cook, N.J., Rollog, M., Ehrig, K.J., Schmandt, D.S., Ram, R., Brugger, J., Ciobanu, C.L., Wade, B., Guagliardo, P., 2019. REE-, Sr- Ca-aluminum-phosphate-sulfate minerals of the alunite supergroup and their role as hosts for radionuclides. American Mineralogist, (in press).

Palache, C., Berman, H., Frondel, C., Dana, E.S., 1951. The System of Mineralogy of James Dwight Dana and Edward Salisbury Dana, Yale University, 1837–1892: Halides, Nitrates, Borates, Carbonates, Sulfates, Phosphates, Arsenates, Tungstates, Molybdates, etc., John Wiley and Sons, Hoboken, NJ. 688-696.

Quinto, F., Blechschmidt, I., Garcia Perez, C., Geckeis, H., Geyer, F., Golser, R., Huber, F., Lagos, M., Lanyon, B., Plaschke, M., Steier, P., 2017. Multiactinide Analysis with Accelerator Mass Spectrometry for Ultratrace Determination in Small Samples: Application to an *in situ* Radionuclide Tracer Test within the Colloid Formation and Migration Experiment at the Grimsel Test Site (Switzerland). Analytical Chemistry 89, 7182-7189.

Radhamani, R., Mahanta, P.L., Murugesan, P., Chakrapani, G., 2010. Novel fusion method for direct determination of uranium in ilmenite, rutile, columbite, tantalite, and xenotime minerals by laser induced fluorimetry. Journal of Radioanalytical and Nuclear Chemistry 285, 287-292.

Ram, R., Charalambous, F.A., McMaster, S., Pownceby, M.I., Tardio, J., Bhargava, S.K., 2013. An investigation on the dissolution of natural uraninite ores. Minerals Engineering 50, 83-92.

Ram, R., Vaughan, J., Etschmann, B., Brugger, J., 2019. The aqueous chemistry of Polonium (Po) in environmental and anthropogenic processes. Journal of Hazardous Materials 380, 120725, 1-17.

Ruiz-Agudo, E., Putnis, C.V., Putnis, A., 2014. Coupled dissolution and precipitation at mineral–fluid interfaces. Chemical Geology 383, 132-146.

Rumble, J., 2017. CRC handbook of chemistry and physics. CRC press. 1532 pp.

Schäfer, T., Huber, F., Seher, H., Missana, T., Alonso, U., Kumke, M., Eidner, S., Claret, F., Enzmann, F., 2012. Nanoparticles and their influence on radionuclide mobility in deep geological formations. Applied Geochemistry 27, 390-403.

Shannon, R.D., 1976. Revised effective ionic radii and systematic studies of interatomic distances in halides and chalcogenides. Acta Crystallographica section A: Crystal Physics, Diffraction, Theoretical and General Crystallography 32, 751-767.

Smith, D.K., 1984. Uranium mineralogy. In: de Vivo, B., (Ed.), Uranium geochemistry, mineralogy, geology, exploration and resources. Springer, Netherlands. pp. 43-88.

Vandenborre, J., Drot, R., Simoni, E., 2007. Interaction mechanisms between uranium (VI) and rutile titanium dioxide: From single crystal to powder. Inorganic Chemistry 46, 1291-1296.

Wilson, R.G., Novak, S.W., 1991. Systematics of secondary-ion-mass spectrometry relative sensitivity factors versus electron affinity and ionization potential for a variety of matrices determined from implanted standards of more than 70 elements. Journal of Applied Physics 69, 466-474.

Zhang, Y., Lumpkin, G.R., Li, H., Blackford, M.G., Colella, M., Carter, M.L., Vance, E.R., 2006. Recrystallisation of amorphous natural brannerite through annealing: The effect of radiation damage on the chemical durability of brannerite. Journal of Nuclear Materials 350, 293-300.

Chapter 11

Supplementary and Additional material

SUPPLEMENTARY MATERIAL A

Appendix A for Chapter 2

Table 11.1. Drill core samples collected from Olympic Dam. Information in italics was provided by BHP Olympic Dam before sample collection.

Sample #	Drill hole	Site	Depth(m)	Mineralogy	Features
MR01	RD2786A	OD	2290	qz, bast, hem, ser, mon, bran, zir, Mn-dol	*High magnetic susc., Cu, Au, Ag, Al, Te.* Small patch of Cu-mineralised red-black qz/hem in massive grey hem.
MR02	RD2786A	OD	2040	qz, hem, cpy, ser, mon, apa, flu, bar	*High magnetic susc., Au, Al, Mo.* Red-grey qz/hem breccia bordering red-black qz/hm breccia.
MR03	RD2786A	OD	1950	qz, cpy, py, flu, hem, uran, moly, sch, bran, syn	*High magnetic susc., Cu, Au, Ag, As, Mo, Te, Bi.* Cu-mineralised vein through banded red-grey hem matrix.
MR04	RD2786A	OD	1788	hem, qz, ser, bar, cpy, dol, sch	*High magnetic susc., Cu, Au, Ag, As, Mo, Te.* Reddish-grey qz/hem breccia, low visible Cu-mineralisation.
MR05	RD2316	OD	569	qz, ser, py, cpy, hem, syn, apa, bast, cls, gal, moly, Au	*Cu + Mo mineralisation 550-700m,* Cu-mineralised black Qz/Hm breccia.
MR06	RD2316	OD	587	qz, py, cpy, ser, bar, bast, apa, bran	*Cu + Mo mineralisation 550-700m.* Py/Cpy in black Hm matrix, bordering red qz/hem breccia.
MR07	RD2316	OD	668	qz, ser, py, cpy, syn, uran, coff	*Cu + Mo mineralisation 550-700m.* Zone between large-grained Cu-mineralised vein and finer-grained Cu-mineralised qz/hem breccia.
MR08	RD2316	OD	660	qz, dol, ser, hem, py, cpy, syn, gal, mon, uran, flu, coff	*Cu + Mo mineralisation 550-700m.* Cm-size cpy/py crystallisation in grey qz/hem matrix.
MR09	RU65-7976	OD	63	py, cpy, bran, bar, Mn-dol, hem	Massive py with cpy and hem inclusions.
MR10	RD3554	OD	988	qz, cpy, ser, bast, py, bar, U-thor, Au, dol, gal, hess mon, moly, mel	*High magnetic susc., U_3O_8, carbonate.* Cm-size cpy/py crystallisation in reddish-grey qz/hem/ser matrix.
MR11	RD3554	OD	540	qz, hem, sph, bast, cpy, cc,	*High magnetic susc., Zn, U_3O_8, carbonate.* Reddish-grey qz/hem/ser breccia,

				bar, dol, gal, coff, flu, uran	many visible spots of Cu-mineralisation.
MR12	WRD33	Wirrda Well	1600	qz, mag, chl, hem, ser, py, mon, apa, zir, cpy, bran, rut	Contact zone between Cu-mineralised vein and seemingly barren qz/mag/chl matrix.
MR13	ACD7	Acropolis	707	hem, cpy, py, mon, xen, apa, fnc, gal, thor	Visible Cu mineralisation, alteration haloes and other evidence of hydrothermal influence.
MR14	RD2366	OD	823	qz, hem, cpy, ser, flu, bar	*High magnetic susc., P, Cu.* Visible Cu-mineralisation in red/black qz-hem breccia.
MR15	IDD09	Island Dam	585		Sample missing or not received.
MR16A	RD2765	OD	712	hem, dol, Mn-dol, cal, flu, bar	Samples A and B cover the entire width of a purple/white fluorite vein, including its contact with black qz/hem host rock.
MR16B	RD2765	OD	712	hem, dol, Mn-dol, cal, flu, bar	See above.
MR16C	RD2765	OD	712	hem, dol, Mn-dol, cal, flu, bar	See above.

Abbreviations: apa-apatite; bar-baryte; bast-bastnäsite; bran-brannerite; cal-calcite; cc-chalcocite; chl-chlorite; cls-clausthalite; coff-coffinite; cpy-chalcopyrite; dol-dolomite; flu-fluorite; fnc-florencite; gal-galena; hem-hematite; hess-hessite; mag-magnetite; mel-melonite; moly-molybdenite; mon-monazite; py-pyrite; qz-quartz; rut-rutile; sch-scheelite; ser-sericite; sph-sphalerite; syn-synchysite; thor-thorite; uran-uraninite; xen-xenotime; zir-zircon.

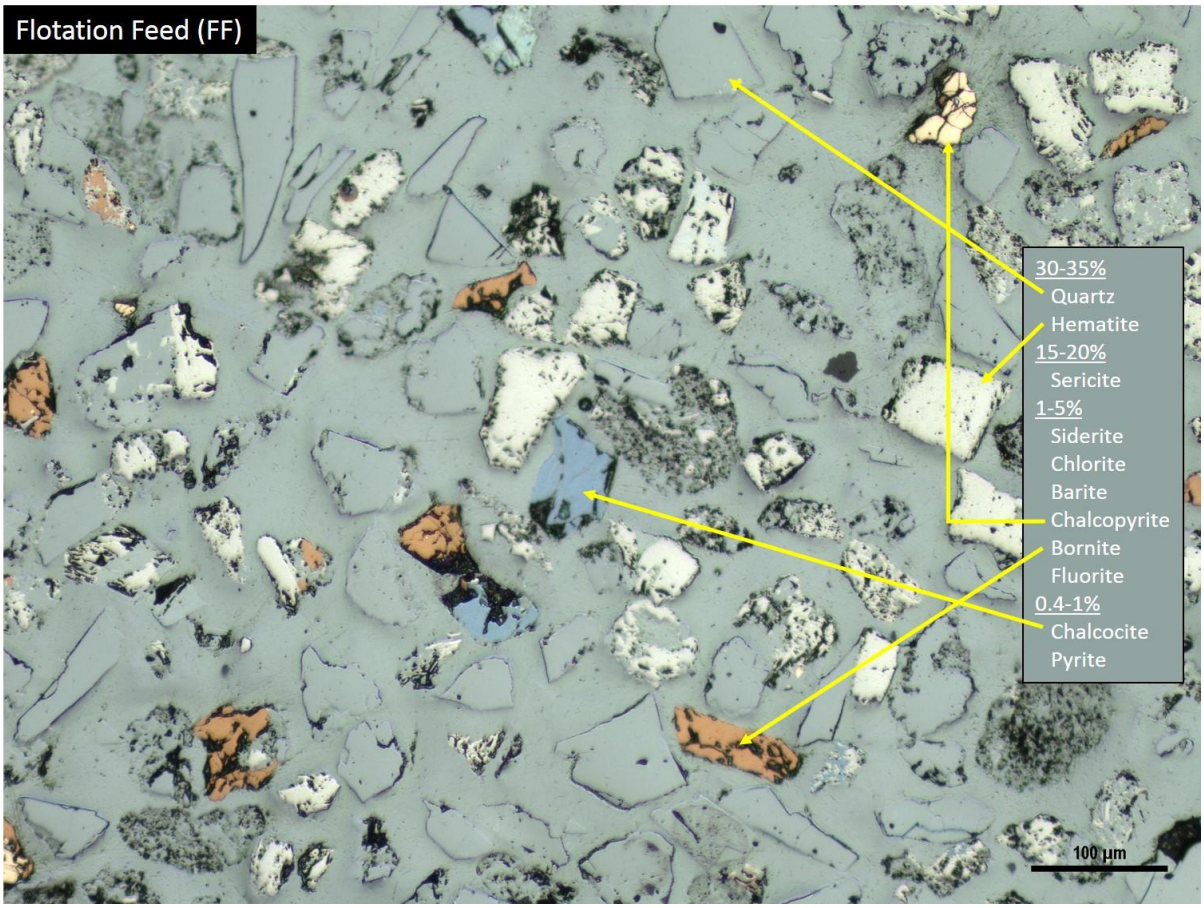

Figure 11.1. Optical microscope reflected light image of flotation feed, mounted in epoxy resin. Mineral abundances are provided, as are a few mineral identifications. Remaining minerals are various shades of grey and are difficult to identify in reflected light.

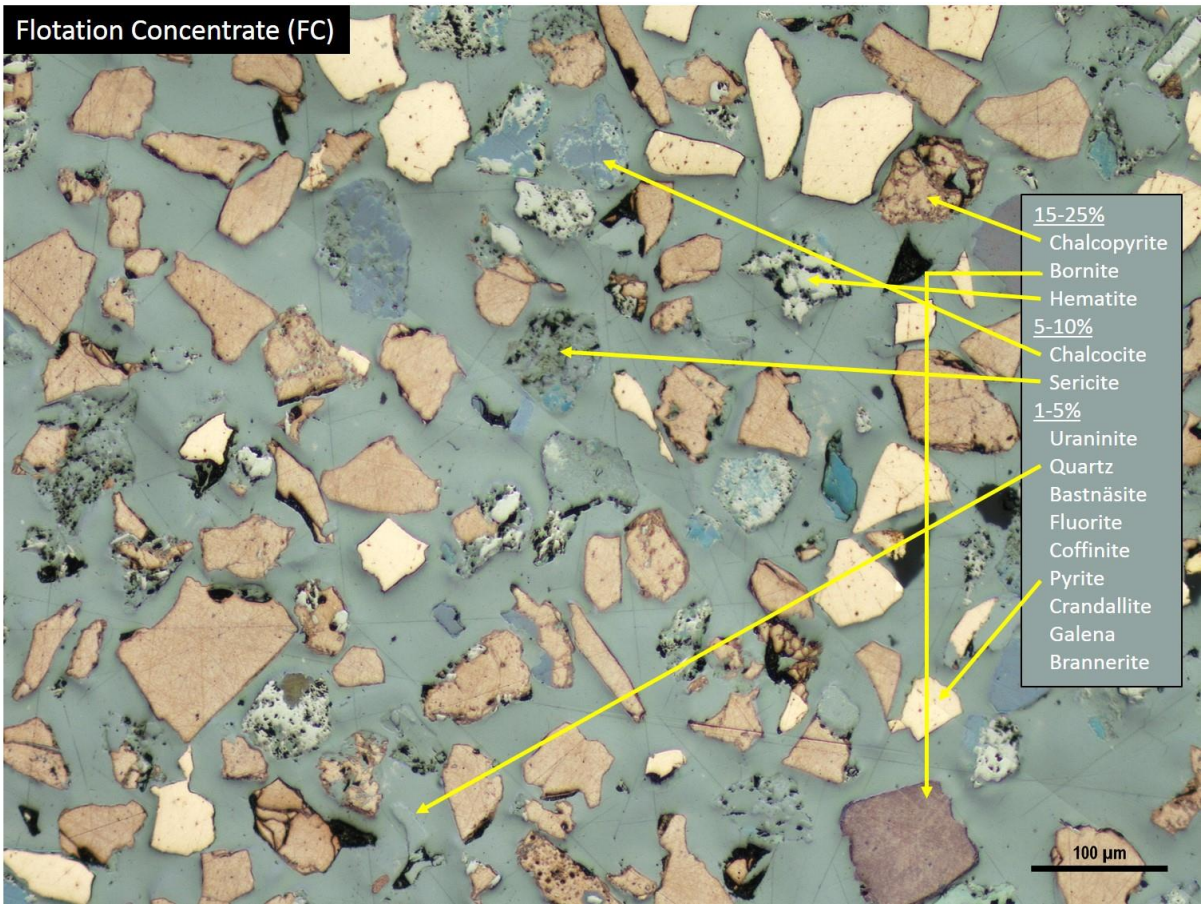

Figure 11.2. Optical microscope reflected light image of flotation concentrate, mounted in epoxy resin. Mineral abundances are provided, as are a few mineral identifications. Remaining minerals are various shades of grey and are difficult to identify in reflected light.

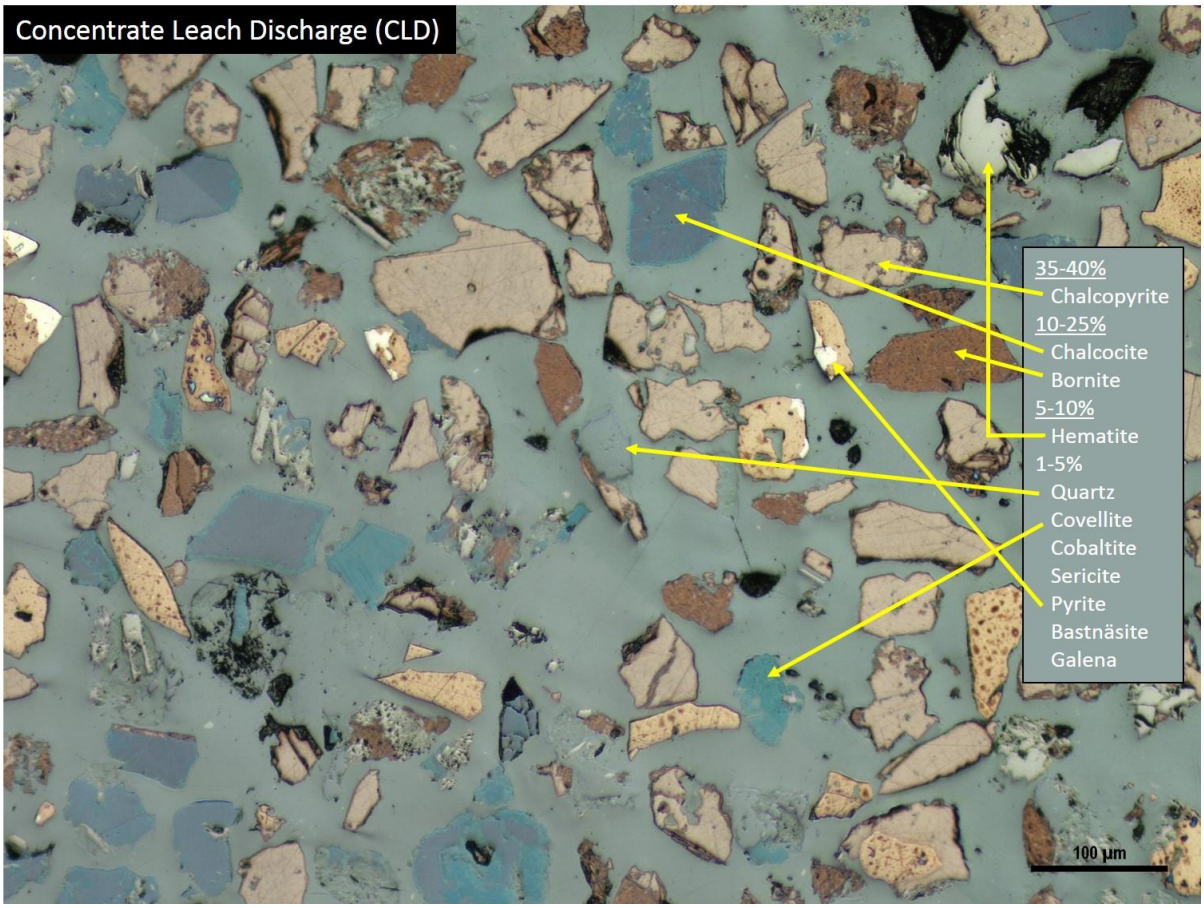

Figure 11.3. Optical microscope reflected light image of concentrate leach discharge, mounted in epoxy resin. Mineral abundances are provided, as are a few mineral identifications. Remaining minerals are various shades of grey and are difficult to identify in reflected light.

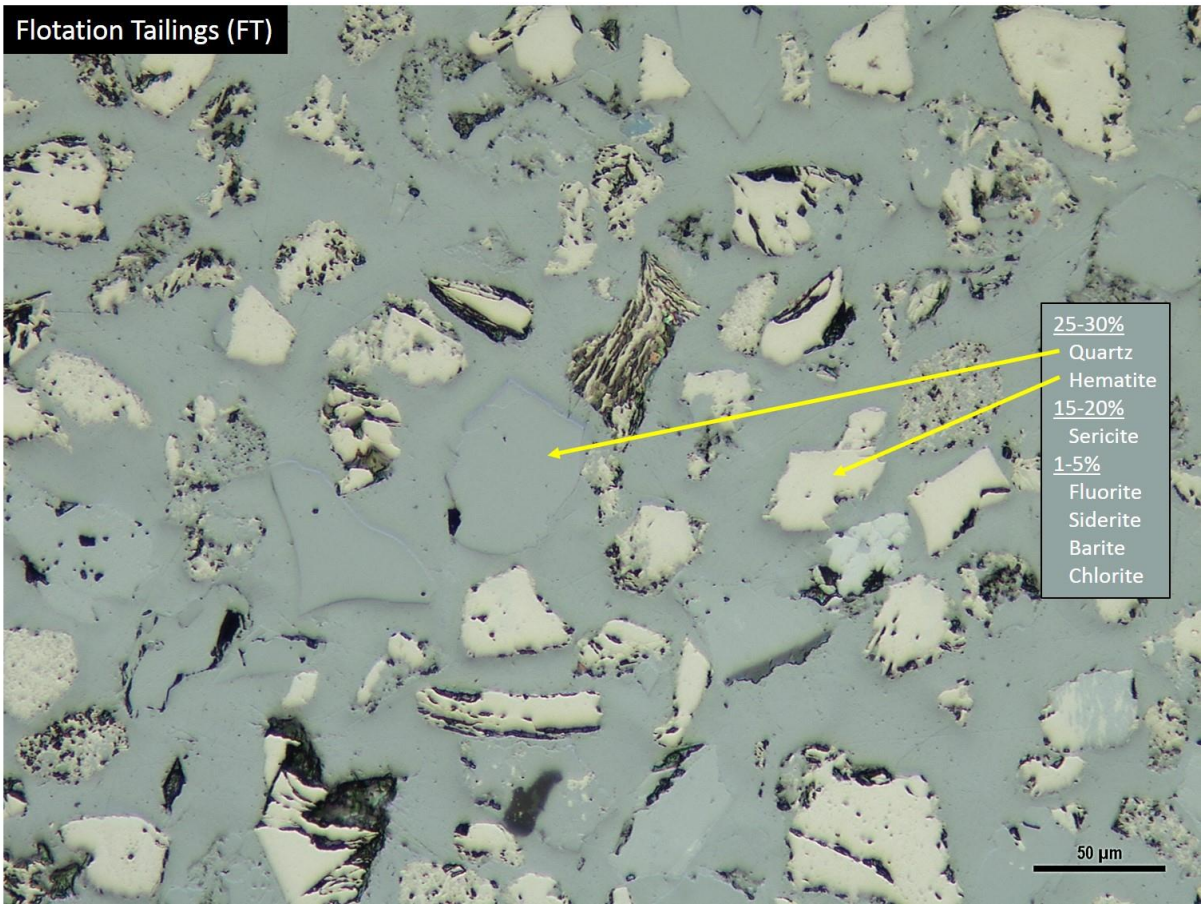

Figure 11.4. Optical microscope reflected light image of flotation tailings, mounted in epoxy resin. Mineral abundances are provided, as are a few mineral identifications. Most minerals are various shades of grey and are difficult to identify in reflected light.

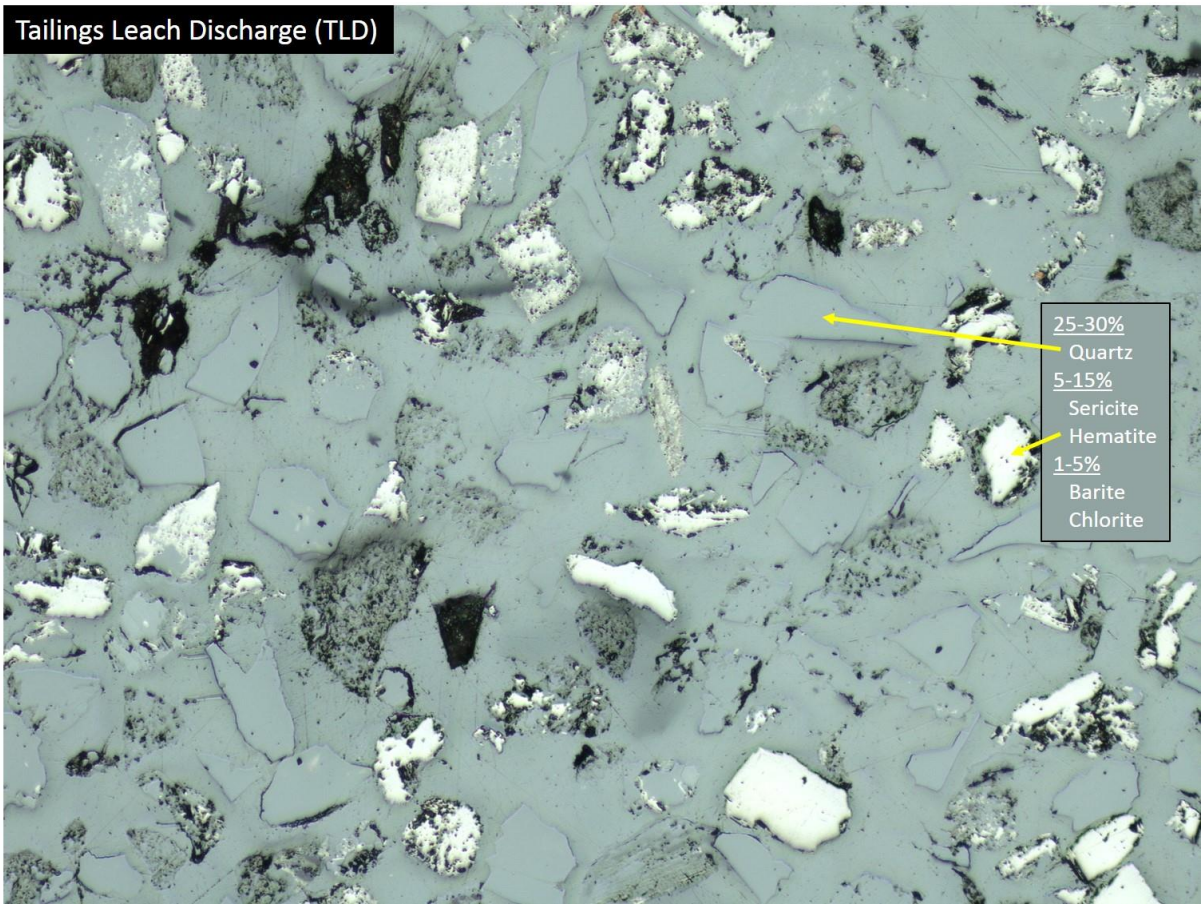

Figure 11.5. Optical microscope reflected light image of tailings leach discharge, mounted in epoxy resin. Mineral abundances are provided, as are a few mineral identifications. Most minerals are various shades of grey and are difficult to identify in reflected light.

Table 11.2. Mineral information for the Tate Museum Standard.

Mineral	#	Location	notes
Galena	1	Wallaroo, SA	
Sphalerite	2	Elmwood mine, Tenn., USA	
Bornite	3	Moonta, SA	
Chalcopyrite	4	Wallaroo, SA	
Argentian tetrahedrite	5	Austria	9 % Ag
Tennantite	6	Kalgoorlie, WA	Hm inclusion
Chalcocite	7	Anaconda mine, MT, USA	
Bismuthinite, Baksanite	8	Mt Freeling, SA	Var. Bi phases
Pyrite, Rhodonite	9	Broken Hill, NSW	
Molybdenite	10	Surprise mine, Dundee, NSW	
Hematite	11	Moculta, SA	
Spinel	12	Mittagong, NSW	
Rutile	13	South Australia	
Magnetite	14	Unk.	Qz incl.
Ilmenite	15	Mt. Pleasant, SA	
Fergusonite	16	Naegi district, Japan	Contains U
Euxenite	17	Støledalen, Norway	Var. w/coff., thor

Siderite	18	Broken Hill, NSW	
Witherite	19	Northumberland, UK	Var. Sr
Strontianite	20	Westphalia, Germany	Sr:Ca = 6:1
Cerussite	21	Broken Hill, NSW	
Celestite	22	Put-In Bay, OH, USA	
Baryte	23	Heath Cote, Vic.	
Anglesite	24	Broken Hill, NSW	
Anhydrite	25	Mound House, NV, USA	Calcite incl.
Monazite	26	Torrington, NSW	Small zircons
Apatite	27	Renfrew county, Ont., Canada	
Synchysite	28	Narssarssuk, Greenland	Variable comp.
Bastnäsite	29	Ampangabe, Madagascar	
Zircon	30	South Africa	Contains Nb
Thorianite	31	Alaska, USA	Th:U = 3:1
Monazite sand	top	Battia, Brazil	1-2% Th

Table 11.3. Mineral composition of selected concentrate samples, +53 µm size fraction, in ppm. Mineral Liberation Analysis data provided by BHP.

	0815_FC	0815_CLD	1216_FC	1216_CLD	1217_FC	1217_CLD
Al hydroxide	0	0	1	0	0	0
Albite	1	1	18	69	0	25
Altaite	0	0	1	0	0	0
Anhydrite	14	17	52	6	62	12
Ankerite	127	0	15	4	194	0
Apatite	242	5	446	7	295	7
Barite	1460	1404	1959	3031	3013	4202
Barite - Sr	37	65	54	47	55	95
Bastnäsite	1009	86	1423	334	1510	1087
Bismuthinite	0	1	0	0	0	0
Bornite	116250	124026	163687	181390	167274	158270
Brannerite	102	102	186	85	210	84
Carrollite	419	628	904	836	559	869
Chalcocite	47160	10729	65680	55618	89666	66289
Chalcopyrite	439101	516440	347421	419723	337170	399403
Chlorite	6289	0	10468	10	6820	83
Clausthalite	2	5	0	13	41	9
Cobaltite	133	296	265	558	238	352
Coffinite	154	11	149	52	195	85
Corundum	0	0	6	0	6	0
Covellite	927	36089	1100	15499	433	53896
Crandellite	2242	2214	4047	4693	3337	4095
Dolomite	29	1	57	18	10	87
Domeykite	0	0	14	2	0	0
Fayalite	0	237	0	600	0	0
Fe_xO_y	171903	87628	227055	128857	227299	119486
Florencite	187	87	174	68	218	369
Fluorite	9118	40	14231	61	18710	455
Galena	24	1	33	25	46	5
Ilmenite	0	0	0	0	0	0

Ilmenorutile	0	0	3	1	0	0
Kaolinite	7	3	16	3	0	12
Löllingite	0	0	3	0	0	0
Molybdenite	139	39	45	12	64	458
Monazite	76	14	33	39	55	88
Native Cu	4370	123	1084	216	16	6
Orthoclase	1023	1326	3360	6961	574	944
Pyrite	128312	161441	72773	90162	61575	78831
Pyrrhotite	0	0	0	0	0	0
Quartz	25930	34496	29751	50680	31696	67610
Rutile	478	237	411	727	262	441
Safflorite	0	0	1	0	0	0
Schorl	62	93	232	86	14	44
Sellaite	0	0	0	0	0	0
Sericite	30676	21385	41358	38234	38769	41707
Siderite	8765	8	7370	24	6842	43
Siderite - Mn	2110	5	2702	9	1749	8
Slag glass	0	181	0	94	0	0
Sphalerite	528	467	137	760	137	3
Synchysite	71	0	146	0	64	0
Tellurobismuthite	2	7	1	1	3	0
Tennantite	1	20	11	0	0	37
Thorite	32	0	3	0	18	5
Topaz	7	14	68	132	104	381
Unknown	79	0	299	0	185	2
Uraninite	293	3	652	2	475	3
Uranothorite	0	0	0	0	0	0
Xenotime	40	24	35	94	26	15
Zircon	67	3	57	157	10	99

Table 11.4. Assay data for selected concentrate samples, +53 µm size fraction, in ppm. Solution ICP-MS data provided by BHP.

	0815_FC	0815_CLD	1216_FC	1216_CLD	1217_FC	1217_CLD
Ag	38	21	38	25	41	30
Al	8500	4300	12400	9100	10500	7500
As	125	133	128	125	231	211
Au	7	5	4	5	6	7
Ba	1100	1100	1300	1500	2000	2200
Bi	37	41	49	59	66	63
Ca	5300	200	7800	200	8900	400
Cd	0	0	3	3	0	0
Ce	900	400	1200	800	1500	1100
Co	735	886	676	660	515	686
CO_2	6600	2900	7000	2600	6300	4300
Cu	265000	301000	274000	319000	300000	350000
Fe	300000	269000	307000	260000	290000	247000
K	3300	2000	4900	4400	3600	3000
La	630	320	860	590	930	710
Mg	400	200	500	200	500	200

Mn	400	100	400	100	300	100
Mo	48	39	61	59	85	109
Na	300	300	700	700	100	100
P	1300	900	1500	1300	1000	700
Pb	122	107	165	147	196	140
S	261000	317000	220000	265000	217000	265000
Sb	5	6	4	11	9	9
Se	74	82	79	78	76	93
Si	23600	21600	29000	35600	28000	34400
Sr	152	107	255	230	222	221
Te	14	15	11	15	16	17
Th	16	4	25	9	22	11
Ti	300	200	400	400	400	400
U_3O_8	573	81	847	198	769	206
Zn	213	246	135	93	106	104
Zr	33	21	31	45	29	31

Table 11.5. Assay data for selected concentrate samples, head (unsized material), in ppm. Solution ICP-MS data provided by BHP.

	0815_FC	0815_CLD	1216_FC	1216_CLD	1217_FC	1217_CLD
Ag	60	74	84	104	78	95
Al	8900	6100	7400	5400	7700	5800
As	244	260	241	314	427	470
Au	9	10	8	8	10	11
Ba	1200	1400	700	1000	1500	1800
Bi	72	104	84	150	108	126
Ca	3400	800	3200	800	4000	500
Cd	0	0	0	0	0	0
Ce	900	600	900	800	1000	1000
Co	616	680	636	669	691	744
CO_2	5100	3700	3300	2600	3700	3300
Cu	354000	402000	381000	438000	385000	436000
F	3100	300	3010	320	3740	450
Fe	266000	218000	259000	190000	260000	187000
K	3500	2500	3000	2500	2800	2200
La	550	460	580	530	670	680
Mg	400	100	300	100	400	100
Mn	200	100	100	100	100	100
Mo	220	242	215	240	339	379
Na	400	200	300	200	400	200
Ni	30	33	29	32	29	32
P	2100	2300	100	100	500	500
Pb	353	397	392	414	319	337
S	253000	287000	251000	282000	244000	276000
Sb	8	15	10	17	15	15
Se	88	118	96	109	101	111

Si	20300	22600	15300	18700	16000	19700
Sr	145	156	172	190	173	197
Te	18	37	16	41	24	33
Th	22	6	22	8	24	11
Ti	300	200	300	300	300	300
U_3O_8	1130	120	1310	205	1180	223
Zn	134	141	89	68	100	82
Zr	27	24	10	21	27	26

ADDITIONAL MATERIAL B

Conference Abstract:

Identification and characterisation of extremely low-concentration non-target components in copper ores and concentrates

Rollog, M.[1,3], Cook, N.J.[1,2], Schmandt, D.S.[1], Clarke, M.[3,4], Ottaway, D.J.[3,4], Spooner, N.A.[3,4,5], Kalnins, C.A.G.[3,4], Ehrig, K.[6], Ciobanu, C.L.[1], Triffett, B.[7] and Grano, S.[2]

[1]*School of Chemical Engineering, University of Adelaide, Adelaide, Australia*

[2]*Institute of Minerals and Energy Research, University of Adelaide, Adelaide, Australia*

[3]*School of Physical Sciences, University of Adelaide, Adelaide, Australia*

[4]*Institute for Photonics and Advanced Sensing, University of Adelaide, Adelaide, Australia*

[5]*DST Group, PO Box 1500, Edinburgh, Australia*

[6]*BHP Billiton Olympic Dam, Adelaide, Australia*

[7]*OZ Minerals, 162 Greenhill Rd., Parkside, Australia*

Abstract (oral presentation given by Mark Rollog), Australian Earth Science Conference (AESC), Adelaide, Australia, 26-30 June, 2016

Identification and characterisation of extremely low-concentration non-target components in copper ores and concentrates

Rollog, Mark[1,3], Cook, Nigel[1,2], Schmandt, Danielle[1], Clarke, Michael[3,4], Ottaway, David[3,4], Spooner, Nigel[3,4,5], Kalnins, Chris[3,4], Ehrig, Kathy[6], Ciobanu, Cristiana[1], Triffett, Brett[7], and Grano, Stephen[2]

[1]*School of Chemical Engineering, University of Adelaide, Adelaide, Australia*
[2]*Institute of Minerals and Energy Research, University of Adelaide, Adelaide, Australia*
[3]*School of Physical Sciences, University of Adelaide, Adelaide, Australia*
[4]*Institute for Photonics and Advanced Sensing, University of Adelaide, Adelaide, Australia*
[5]*DST Group, PO Box 1500, Edinburgh, Australia*
[6]*BHP Billiton Olympic Dam, Adelaide, Australia*
[7]*OZ Minerals, 162 Greenhill Rd., Parkside, Australia*

Mesoproterozoic copper ores in South Australia contain low to moderate concentrations of uranium, representing either a potential economic by-product - or an unwanted contaminant - depending on concentration. The daughter products of uranium decay, including the short half-life α-emitters, ^{210}Po and ^{210}Pb (hereafter ^{210}RN), are present within the parent orebody at extremely low concentrations. Over geologic time, substantially different physical behaviours of U and its daughters may result in spatial and chemical decoupling as a result of fluid- and pore-driven migration. Remarkably little reliable information is currently available regarding mineralogical hosts for ^{210}RN in any solid media, thus making the search for ^{210}RN in complex, fine-grained ores or concentrates a major challenge. Identification and characterisation of mineral hosts for ^{210}RN are, however, essential to guide attempts to eliminate or reduce unwanted ^{210}RN in industrial copper concentrates. These are the overarching goals of the Australian Copper-Uranium Transformation Research Hub.

Concentrations of ^{210}RN are so low (< parts-per-trillion) that they cannot be measured directly by conventional microanalytical methods. Bulk measurements of mill feed and concentrates give quantitative abundances, but no information on specific mineral hosting (or lack of hosting, in the potential case of liberated nanoparticles) of ^{210}RN. High-resolution scanning electron microscopy (SEM) provides detailed mineralogy of concentrates down to ~1 micron, but fails to discern if our target radionuclides are in solid solution in a mineral or exist as discrete nanoparticles within grain boundaries.

Our solution is to use a multi-faceted approach, starting with new techniques designed to accurately track the location of α-emitters in-situ within a polished thin section. Once areas likely to contain ^{210}RN are located, ca. 10 x 30 μm-sized slices are extracted in-situ from the section using focussed-ion-beam SEM and prepared as thin foils for transmission electron microscopy (TEM), permitting visualization of, and compositional data on the smallest particles of interest.

Thus far we have identified several potential ^{210}RN hosts, including <5μm crystals of galena and its selenide and telluride analogues (clausthalite and altaite.) Subordinate hosts may include barite and other sulphates, iron oxides and hydroxides, and various rare earth element-bearing minerals known to contain uranium and lead.

ADDITIONAL MATERIAL C

Conference Poster:

Identifying and characterising non-target elements in South Australian iron oxide-copper-gold (IOCG) deposits

Rollog, M.[1,3], Cook, N.J.[1,2], Schmandt, D.S.[1], Clarke, M.[3,4], Ottaway, D.J.[3,4], Spooner, N.A.[3,4,5], Kalnins, C.A.G.[3,4], Ehrig, K.[6], Ciobanu, C.L.[1], Triffett, B.[7] and Grano, S.[2]

[1]*School of Chemical Engineering, University of Adelaide, Adelaide, Australia*

[2]*Institute of Minerals and Energy Research, University of Adelaide, Adelaide, Australia*

[3]*School of Physical Sciences, University of Adelaide, Adelaide, Australia*

[4]*Institute for Photonics and Advanced Sensing, University of Adelaide, Adelaide, Australia*

[5]*DST Group, PO Box 1500, Edinburgh, Australia*

[6]*BHP Billiton Olympic Dam, Adelaide, Australia*

[7]*OZ Minerals, 162 Greenhill Rd., Parkside, Australia*

Poster, Australian Earth Science Conference (AESC), Adelaide, Australia, 26-30 June, 2016

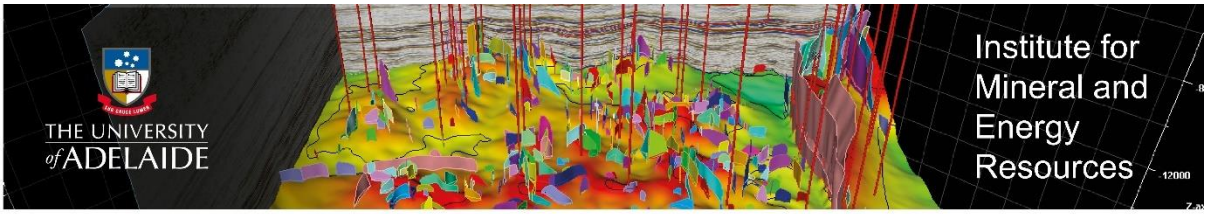

ARC Copper-Uranium Hub – The Minerals Group

Identifying and characterising non-target elements in South Australian Iron Oxide-Copper-Gold (IOCG) deposits

As one of three Nodes of the Hub, the Minerals Group has been tasked with the identification and characterisation of certain ultra-trace "penalty" components of copper ore, notably ^{210}Pb and ^{210}Po. We are employing a three-vectored approach to the problem, each complimenting the other two.

The Micro-Scale

Samples of ore concentrates from various stages in the industrial process are analysed down to the micron scale using techniques such as Scanning Electron Microscopy (SEM), Laser-Ablation Inductively-Coupled Plasma Mass Spectrometry, Mineral Liberation Analyses, and Electron Micro-Probe Analyses. Target minerals containing combinations of Pb-Ag-U-Bi-REY-S-Se-Te are identified, characterised, and marked for further analyses.

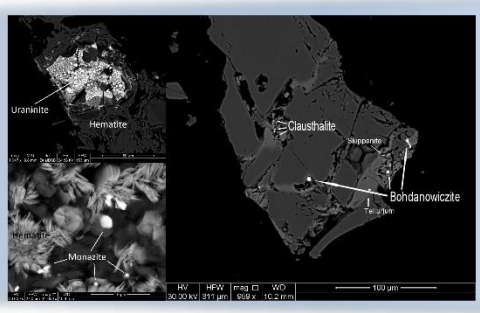

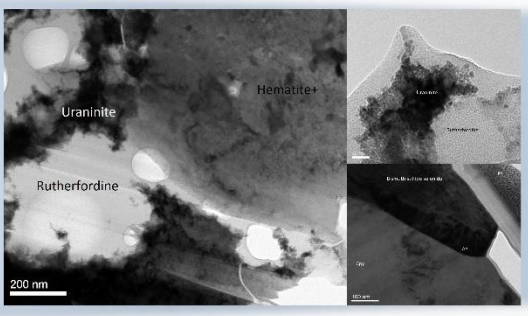

The Nano-Scale

Thin foils, 100nm thick, are cut from samples using a Focussed Ion Beam SEM. These foils are suitable for High Resolution Transmission Electron Microscopy (TEM), capable of imaging on the atomic level. Atom Probe Tomography, nanoSIMS (Secondary-Ion Mass Spectrometry), Sensitive High Resolution Ion Micro Probe (SHRIMP), and X-ray Absorption Near Edge Spectrum (XANES) may also be utilised for analyses.

Experimental Mineralogy

An effort will also be made to better understand the chemistry of polonium. Nano-scale plating experiments (tested first using Au, Pt, Ir, and Pd as proxies – at right) will be performed to image polonium and its compounds. Minerals spiked with polonium will be grown and analysed using techniques listed above. This should give us valuable insight into the chemistry of polonium, and the ability to model its behaviour in ore deposits.

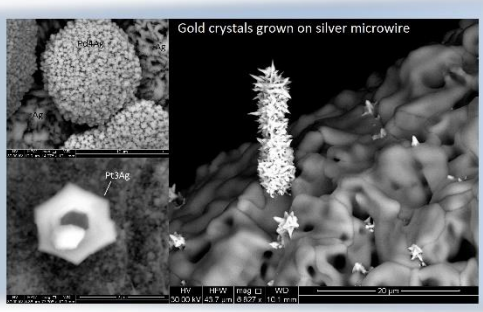

bhpbilliton

Government of South Australia
Department of State Development

Australian Government
Australian Research Council

IMER: Answering the challenge of sustainable and efficient use of global resources

For further Information Contact: **Mark Rollog** – mark.rollog@adelaide.edu.au **Dr. Chris Matthews**- chris.matthews@adelaide.edu.au
www.adelaide.edu.au/imer/ imer@adelaide.edu.au

ADDITIONAL MATERIAL D

Conference Abstract:

A pathway to improving methods for remediation of uranium and daughter products from South Australian iron oxide-copper-gold (IOCG) deposits

Rollog, M.[1], Cook, N.J.[1], Schmandt, D.S.[1], Clarke, M.[1], Ottaway, D.J.[1], Spooner, N.A.[1,2], Kalnins, C.A.G.[1], Ehrig, K.[3], Ciobanu, C.L.[1], Triffett, B.[4] and Grano, S.[1]

[1]*School of Chemical Engineering, University of Adelaide, Adelaide, Australia*

[2]*DST Group, PO Box 1500, Edinburgh, Australia*

[3]*BHP Billiton Olympic Dam, Adelaide, Australia*

[4]*OZ Minerals, 162 Greenhill Rd., Parkside, Australia*

Abstract (oral presentation given by Mark Rollog), Australasian Radiation Protection Society (ARPS) conference, Adelaide, Australia, 11-14 September, 2016

A Pathway to Improving Methods for Remediation of Uranium and Daughter Products from South Australian Iron Oxide-Copper-Gold (IOCG) deposits

Rollog, M.[1], Cook, N.J.[1], Schmandt, D.S.[1], Clarke, M.[1], Ottaway, D.J.[1], Spooner, N.A.[1,2], Kalnins, C.A.G.[1], Ehrig, K.[3], Ciobanu, C.L.[1], Triffett, B.[4] and Grano, S.[1]

[1]University of Adelaide, Adelaide, Australia
[2]DST Group, PO Box 1500, Edinburgh, Australia
[3]BHP Billiton Olympic Dam, Adelaide, Australia
[4]OZ Minerals, 162 Greenhill Rd., Parkside, Australia

Mesoproterozoic IOCG deposits in South Australia contain low to moderate (<1000ppm) concentrations of uranium, representing either a potential economic by-product – or unwanted contaminant – depending on concentration. Additionally, the ore contains trace amounts of daughter products from uranium decay. Over geologic time, these daughters become spatially and chemically decoupled from the uranium due to differences in physical characteristics from one element to the next in the decay series. Most of these are efficiently separated from the target metals (copper, gold, silver) during processing, but two radionuclides, ^{210}Po and ^{210}Pb (hereafter ^{210}RN) are found in elevated concentrations in copper concentrate. Smelting the concentrate on-site alleviates this, but is expensive. The Australian Copper-Uranium Transformation Research Hub was formed to find an economical alternative method for removing ^{210}RN from the valuable commodity.

Concentrations of ^{210}RN are so low (< parts per trillion) that conventional microanalytical techniques are inadequate. Alpha-counting of bulk samples can accurately determine activities of ^{210}RN at each stage of ore processing, but gives no information on specific mineral hosting (or lack of hosting, in the potential case of intra-grain nanoparticles.) Understanding the exact characteristics of both ^{210}Po and ^{210}Pb with regard to distribution, oxidation state, bonding energies, host minerals or co-precipitation elements, mobility, and concentration/coagulation pathways will be critical in developing an efficient method for their extraction.

Our solution is to use a multi-faceted approach, starting with micro-scale techniques and continuing into nano-scale methods. Scanning electron microscopy (SEM) will be used in concert with high resolution alpha-decay tracking to locate potential regions of ^{210}RN accumulation. Small, thin sample foils (10 x 20μm) will be cut using focussed-ion-beam SEM and analysed on a transmission electron microscope (TEM), capable of both imaging and compositional analysis on a sub-nanometre scale.

Thus far we have identified several potential ^{210}RN hosts, including numerous microcrystals of minerals belonging to the lead-silver-bismuth-sulphide-selenide-telluride family. Subordinate hosts may include barite and other sulphates, iron oxides and hydroxides, and various rare earth element-bearing minerals known to contain uranium and lead. Once identified, characterisation of the radionuclides and their environments is an important step in developing an economic solution for the mining industry.

ADDITIONAL MATERIAL E

Conference Abstract:

Hosts for non-target uranium and associated radionuclides in South Australian copper ores and concentrates

Rollog, M.[1], Cook, N.J.[1], Schmandt, D.S.[1], Ehrig, K.[2], Triffett, B.[3]

[1]*School of Chemical Engineering, University of Adelaide, Adelaide, Australia*

[2]*BHP Billiton Olympic Dam, Adelaide, Australia*

[3]*OZ Minerals, 162 Greenhill Rd., Parkside, Australia*

Abstract (oral presentation given by Mark Rollog), Chemeca Conference, Adelaide, Australia, 25-28 September, 2016

Hosts for non-target uranium and associated radionuclides in South Australian copper ores and concentrates

M. Rollog[1*], N.J. Cook[1], D.S. Schmandt[1], K. Ehrig[2], B. Triffett[3]

[1]School of Chemical Engineering, Univ. of Adelaide, Adelaide, SA 5005, Australia (*Correspondence: mark.rollog@adelaide.edu.au)

[2]BHP Billiton Olympic Dam, Adelaide, SA 5000, Australia

[3]OZ Minerals, 162 Greenhill Rd., Parkside SA 5063, Australia

South Australian copper ores contain low to moderate concentrations of uranium - treated as an economic by-product, contaminant, or both, dependent on concentration. Daughter products of ^{238}U decay are also present, including the α-emitters ^{210}Po and ^{210}Pb (^{210}RN). Each daughter radionuclide has distinct physical and chemical properties likely resulting in natural decoupling through different re-mobilization pathways of parents and daughter element isotopes. This decoupling could be further exacerbated during ore processing, potentially creating processing products enriched in ^{210}RN relative to ^{238}U.

There is currently limited data about mineralogical hosts for ^{210}RN, making prediction of location within complex, fine-grained ores or concentrates a significant challenge. Information on potential mineral hosts for ^{210}RN is essential to guide attempts to eliminate or reduce unwanted ^{210}RN in copper concentrates and tailings. Concentrations of ^{210}RN are so low (<1 part-per-trillion) that their presence in individual minerals cannot be measured directly by conventional microanalytical methods. In order to understand the ^{210}RN mineralogical deportment in mill feed and concentrates, we rely on indirect information drawn from assays and RN measurements on bulk material, micron-scale mineralogical characterization, and determination of concentrations of proxy elements and isotopes within the lattices of specific minerals. SEM analysis provides identification of potential sub-µm-sized ^{210}RN-bearing mineral grains, including nanoparticles within sulfides and gangue, and at mineral-mineral boundaries. These data and focused ion bean (FIB)-SEM and TEM investigations assist in building a robust qualitative model for ^{210}RN deportment and an understanding of the different pathways responsible for changes in that deportment.

Key words: radionuclides, uranium, copper mining, mineral processing, nanoparticles

ADDITIONAL MATERIAL F

Conference Abstract:

NanoSIMS mapping of ^{210}RN and ^{226}Ra in South Australian copper concentrates

Rollog, M.[1,2], Cook, N.J.[1,2], Guagliardo, P.[3], Kilburn, M.R.[3], Ehrig, K.[4], Ciobanu, C.L.[1]

[1]*School of Chemical Engineering, University of Adelaide, Adelaide, SA 5005, Australia*

[2]*The ARC Transformation Research Hub for Australian Copper-Uranium*

[3]*University of Western Australia, Perth, WA 6009, Australia*

[4]*BHP Billiton Olympic Dam, Adelaide, SA 5000, Australia*

Abstract (oral presentation given by Mark Rollog), Goldschmidt Conference, Paris, France, 13-18 August, 2017

NanoSIMS mapping of ^{210}RN and ^{226}Ra in South Australian copper concentrates

M. ROLLOG[1,2]*, N.J. COOK[1,2], P. GUAGLIARDO[3], M.R. KILBURN[3], K. EHRIG[4], C.L. CIOBANU[1]

[1]The University of Adelaide, Adelaide, SA 5005, Australia (*correspondence:mark.rollog@adelaide.edu.au), (nigel.cook@adelaide.edu.au; cristiana.ciobanu@adelaide.edu)

[2]The ARC Transformation Research Hub for Australian Copper-Uranium

[3]University of Western Australia, Perth, WA 6009, Australia (paul.guagliardo@uwa.edu.au, matt.kilburn@uwa.edu.au)

[4]BHP Billiton Olympic Dam, Adelaide, SA 5000, Australia (Kathy.J.Ehrig@bhpbilliton.com)

South Australian iron-oxide copper gold (IOCG) deposits contain uranium and its decay products. Efficient separation of radionuclides – specifically ^{210}Pb and ^{210}Po (hereafter ^{210}RN) from copper sulphide concentrates has proven to be difficult due to poor constraints on their mineralogical deportment and behaviour throughout the metallurgical extraction process. To date, efforts to determine host mineralogy of RNs have been hampered by concentrations far below minimum detection limits of most instrumentation – on the order of parts per trillion to quadrillion.

We present here the first direct evidence for the location of ^{210}RN and ^{226}Ra within specific mineral grains, as imaged by the Cameca nanoSIMS 50L at the University of Western Australia. Compositional maps confirm, for example, the presence of ^{210}RN in apatite (Fig. 1), brannerite, and uraninite, and of ^{226}Ra in barite.

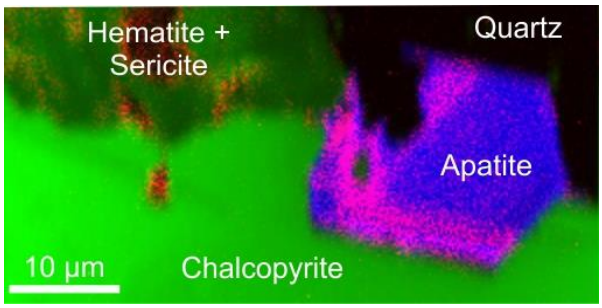

Figure 1: ^{210}RN in zoned apatite from Olympic Dam. Green = Fe, blue = Ca, red/pink = ^{210}RN.

Mapping individual grains via nanoSIMS unlocks the possibility of creating and validating a mineralogical budget for RNs in copper ores and their host minerals. This is a pre-requisite for develeping methods to eliminate or reduce their abundance in copper concentrates.

ADDITIONAL MATERIAL G

Conference Abstract:

Nanoscale spatial distribution maps of trace elements/isotopes in South Australian copper concentrates

Rollog, M.[1], Cook, N.J.[1], Guagliardo, P.[2], Kilburn, M.R.[2], Ehrig, K.[3], Ciobanu, C.L.[1]

[1]*School of Chemical Engineering, University of Adelaide, Adelaide, SA 5005, Australia*

[2]*University of Western Australia, Perth, WA 6009, Australia*

[3]*BHP Billiton Olympic Dam, Adelaide, SA 5000, Australia*

Abstract (oral presentation given by Mark Rollog), Goldschmidt Conference, Boston, MA, 12-17 August, 2018

Nanoscale spatial distribution maps of trace elements/isotopes in South Australian copper concentrates

M. ROLLOG[1]*, N.J. COOK[1], P. GUAGLIARDO[2], M.R. KILBURN[2], K. EHRIG[3], C.L. CIOBANU[1]

[1]The University of Adelaide, Adelaide, SA 5005, Australia (*correspondence:mark.rollog@adelaide.edu.au), (nigel.cook@adelaide.edu.au; cristiana.ciobanu@adelaide.edu)
[2]University of Western Australia, Perth, WA 6009, Australia (paul.guagliardo@uwa.edu.au, matt.kilburn@uwa.edu.au)
[3]BHP Billiton Olympic Dam, Adelaide, SA 5000, Australia (Kathy.J.Ehrig@bhpbilliton.com)

Copper, Uranium, gold and silver are the final products from mining and processing of the supergiant Olympic Dam deposit, South Australia. The presence of economic concentrations of U necessitates a thorough understanding of the deportment of U and its daughter isotopes, both in the deposit and during extraction, to ensure efficient removal of non-economic metals. The extremely fine-grained nature of the deposit has precluded many conventional microscale analytical techniques, so we have begun exploring the nanoscale.

The Cameca nanoSIMS 50L is capable of providing spatial distrubutions of trace elements in copper ore, including ^{230}Th, ^{226}Ra, and ^{210}RN, to a resolution of 40nm (Fig. 1). Although not yet a quantifiable method, this powerful imaging technique provides invaluable insight into the deportment, mobility, and potential hosts of trace elements in the orebody. NanoSIMs isotopic mapping has been instrumental in deciphering ore formation pathways at the nano scale.

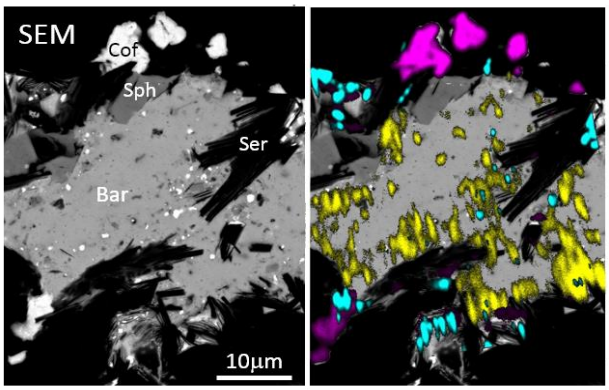

Figure 1. Barite, coffinite, sphalerite, and sericite from core 3554, Olympic Dam. Left pane shows SEM image, right pane shows nanoSIMS distribution overlays of ^{206}Pb (cyan), ^{226}Ra (yellow), and ^{238}U (magenta).

ADDITIONAL MATERIAL H

Conference Abstract:

Mobility of radionuclides in the Olympic Dam Cu-U-Au-Ag deposit, South Australia

Rollog, M.[1], Cook, N.J.[1], Guagliardo, P.[2], Ciobanu, C.L.[1], Ehrig, K.[3], Kilburn, M.R.[2]

[1]*School of Chemical Engineering, University of Adelaide, Australia*

[2]*Ucentre for Microscopy, Characterisation, and Analysis, University of Western Australia*

[3]*BHP Olympic Dam, Adelaide, Australia*

Abstract (oral presentation given by Mark Rollog), International Association on the Genesis of Ore Deposits (IAGOD) quadrennial symposium, Salta, Argentina, 28-31 August, 2018

MOBILITY OF RADIONUCLIDES IN THE OLYMPIC DAM Cu-U-Au-Ag DEPOSIT, SOUTH AUSTRALIA

Mark Rollog[1], Nigel J. Cook, Paul Guagliardo, Cristiana L. Ciobanu, Kathy Ehrig, Matt Kilburn

[1]*School of Chemical Engineering, University of Adelaide, Australia - Mark.rollog@adelaide.edu.au*

BACKGROUND

The Olympic Dam (OD) IOCG-U deposit, South Australia, has a complex history dating back to 1.6 Ga. Discovered under 350 m of sedimentary cover, the deposit contains a resource approximately 80 Mt Cu, 2.6 Mt U_3O_8, 334 Moz t. Ag, and 107 Moz t. Au (Ehrig, *et al.*, 2017). Based on uraninites, at least two stages of mineralization and multiple occurrences of dissolution, mobilization, and recrystallisation have been identified (MacMillan *et al.*, 2016). Coffinite ($USiO_4 \bullet nH_2O$) and brannerite ($(U^{4+}, REE,Th,Ca)(Ti,Fe^{3+},Nb)_2(O,OH)_6$ are cautiously considered late-stage minerals formed from dissolved uraninite, but may also be the result of U addition (MacMillan *et al.*, 2017).

Radionuclide (RN) daughters of U and Th decay have been dissociated and locally redistributed throughout the orebody

METHODS

Drill cores were sliced and polished as-is. Copper sulfide flotation concentrate (<53 µm) was suspended in 25 mm epoxy resin mounts and polished (~20,000 exposed grains per cm2). Mineral surveys were performed by scanning electron microscopy (SEM), and grains of interest recorded. Isotopic distributions of select grains/regions of interest (ROI) were mapped on a Cameca nanoSIMS 50L. Seven isotopes may be mapped at once, and the standard practice was to map $^{46 \text{ or } 47}Ti$, $^{54 \text{ or } 57}Fe$, ^{63}Cu, $^{86 \text{ or } 87}Sr$, ^{137}Ba, ^{206}Pb, and ^{238}U with a 50 pA beam current (effective spot size ~500 nm), then repeat the same area for $^{54 \text{ or } 57}Fe$, $^{142 \text{ or } 144}Nd$, ^{169}Tm, ^{210}RN (dominantly ^{210}Pb), ^{226}Ra, ^{230}Th, and ^{234}U using a 250 pA beam current (effective spot size ~700 nm). All maps are 50x50 Mm, 512x512 pixels. Results were processed by the OpenMIMS plugin (Poczatek *et al.*, 2009) in ImageJ (Fiji) (Schindelin *et al.*, 2012; Schindelin *et al.*, 2015).

Maps could be colorized and overlain on backscattered electron maps for comparison. Figure 1 shows the distribution of six detectable members of the 238U decay chain in an Olympic Dam core sample containing sericite, coffinite, and barite with small inclusions of galena. Variations in ionization potentials for elements in different matrices prevent accurate quantification, but spatial distributions within each map remain true.

RESULTS AND DISCUSSION

Analyses of over 200 grains of interest reveal patterns in radionuclide (RN) distribution. Uraninite tends to contain all members of the ^{238}U decay chain, indicating resistance to dissolution and redistribution – at least within the last few million years but the presence of high concentrations of (exclusively) ^{226}Ra and ^{210}Pb in barites suggests mineral-scale dissociation to some extent in the chain. ^{222}Rn, being a gas, is one speculative source of dissociation; however observed ^{226}Ra and ^{210}Pb distributions almost always correlate, signifying continuity for this section of the decay chain. Coffinite and particularly brannerite are chemically more resistant to dissolution, Ra and Pb are less structurally compatible, and less likely to retain radon within decay-induced transient porosity. The lack of ^{226}Ra and ^{210}Pb in some coffinite and brannerite may indicate either very recent formation or partial dissolution with preferential removal of sulfate-insoluble daughters – possibly through chloride leaching. Figure 1 clearly shows ^{226}Ra and ^{210}Pb preference for barite, while the U and Th species remain in coffinite. ^{206}Pb prefers neither coffinite nor barite but instead forms small inclusions of galena throughout the matrix, suggesting redistribution during an earlier event. These distributions may be the result of one complex dissolution event from one RN source (coffinite), or multiple events from multiple sources. The exceptionally high response on masses 226 and 210 suggest the latter.

Other patterns are present, including an abundance of ^{226}Ra and ^{210}Pb in molybdenite, covellite replacing bornite, and sericite/chlorite (when in proximity to a U-bearing mineral). This, in coordination with spots of RN activity on grain surfaces and at mineral boundaries, suggests that surface features also play an important role in sequestering RN. Basal cleavage planes or charge-imbalanced surfaces may act as filters for RN-bearing fluids or nanoparticles of RN sulfates.

CONCLUSIONS

NanoSIMS isotopic distribution maps show that radionuclides exhibit local scale mobility within the OD deposit. Some mineral groups such as sulfates and phosphates have the ability to scavenge RN – at least from ^{226}Ra down the chain – while many mineral groups remain barren (notably sulfides and most silicates). High surface area minerals and electron-imbalanced surfaces may also act as traps for RN-bearing fluids or nanoparticles.

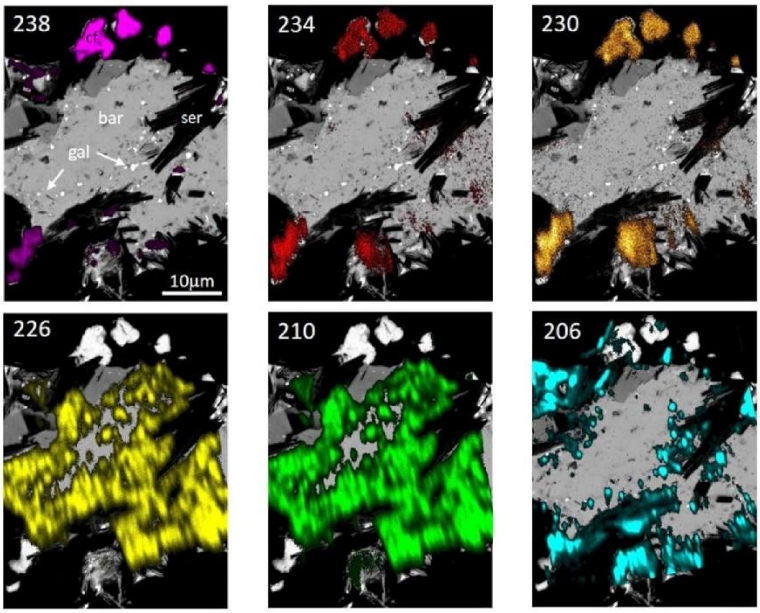

Figure 1. Barite (bar) - coffinite (cf) - sericite (ser) - galena (gal) assemblage from Olympic Dam. Members of the ^{238}U decay chain have dissociated in favor of more compatible mineral hosts.

REFERENCES

Ehrig, K., Kamenetsky, V. S., McPhie, J., Cook, N. J. and Ciobanu, C. L. 2017. Olympic Dam iron oxide Cu-U-Au-Ag deposit. In: Phillips, G.N., ed., Australian Ore Deposits, AusIMM, p: 601-610.

Macmillan, E., Ciobanu, C.L., Ehrig, K., Cook, N. J. and Pring, A., 2016. Chemical zoning and lattice distortion in uraninite from Olympic Dam, South Australia. American Mineralogist 101 (10): 2351-2354.

Macmillan, E., Cook, N. J., Ehrig, K., A., Pring, A., 2017. Chemical and textural interpretation of late-stage coffinite and brannerite from the Olympic Dam IOCG-Ag-U deposit. Mineralogical Magazine 81 (6): 1323-1366. https://doi.org/10.1180/minmag.2017.081.006.

Poczatek, C., Kauman, Z., and Lechene, C.P., 2009. OpenMIMS ImageJ plugin Guide. Harvard Medical School, Boston, Massachusetts, USA.

Schindelin, J., Rueden, C. T., Hiner, M. C. and Eliceiri, K. W., 2015. The ImageJ ecosystem: An open platform for biomedical image analysis. Molecular Reproduction and Development 82, p: 518-529. https://doi.org/10.1002/mrd.22489.

Schindelin,J., Arganda-Carreras, I., Frise, E., Kaynig, V., Longair, M., Pietzsch,T., Preibisch, S., Rueden, C., Saalfeld, S., Schmid, B., Tinevez, J-Y., White, D. J., Hartenstein, V., Eliceiri, K., Tomancak, P. and Cardona, A., 2012. Fiji: an open-source platform for biological-image analysis. Nature Methods volume 9, p: 676–682.

ADDITIONAL MATERIAL I

Conference Abstract:

In situ mapping of radionuclides in Olympic Dam copper concentrates by nanoSIMS

Rollog, M.[1], Cook, N.J.[1], Guagliardo, P.[2], Ciobanu, C.L.[1], Ehrig, K.[3], Kilburn, M.R.[2]

[1]*School of Chemical Engineering, University of Adelaide, Australia*

[2]*Ucentre for Microscopy, Characterisation, and Analysis, University of Western Australia*

[3]*BHP Olympic Dam, Adelaide, Australia*

Abstract (oral presentation given by Mark Rollog), AusIMM Uranium 2019 conference , Adelaide, Australia, 4-5 June, 2019

In situ mapping of radionuclides in Olympic Dam copper concentrates by nanoSIMS

Mark Rollog[1]*, Nigel J. Cook[1], Paul Guagliardo[2], Kathy Ehrig[3], Matt Kilburn[2]

[1] School of Chemical Engineering, University of Adelaide, Australia

[2] *Centre for Microscopy, Characterisation, and Analysis, University of Western Australia*

[3] BHP Olympic Dam, Adelaide, Australia

Mark.rollog@adelaide.edu.au

The Olympic Dam iron oxide-copper-gold-uranium deposit, South Australia, not only contains significant copper, gold and silver resources, but is also the world's largest uranium resource. Complex ore processing strategies endeavour to extract target metals and separate them efficiently from unwanted components. Of particular interest during copper concentrate production are the ^{238}U decay chain radionuclides (RNs) ^{226}Ra, ^{210}Pb, and ^{210}Po, which have maximum concentration requirements far below minimum detection limits for most *in situ* analytical techniques. Fine- to ultrafine-grained ore textures prohibit conventional mineral separation and bulk activity measurements, hindering identification and targeting of RN host minerals for removal.

The CAMECA nanoSIMS platform provides the capability to map RN distributions *in situ*, at sub-micron spatial resolution, within individual minerals. Sample grains collected from various stages of processing were embedded in epoxy resin, polished, and mapped for up to 21 isotopes. Evaluation of the 4000+ resulting isotope maps has provided a wealth of information regarding the deportment of radionuclides in the deposit and throughout the processing stream. Uranium-bearing phases (uraninite, coffinite, uraniferous thorianite, euxenite) tend to retain all daughter isotopes, albeit to varying degrees. Phosphates (xenotime, apatite, monazite) readily incorporate Th, and usually retain the rest of the decay chain. Sulphates (baryte, anglesite, aluminium-sulphate-phosphates) can uptake substantial amounts of ^{226}Ra and ^{210}Pb, especially during acid leaching. Other minerals, including hematite, fluorite, rutile, molybdenite and covellite have been identified as potentially

significant reservoirs of RNs at Olympic Dam. Recognition of the carrier phases for specific radionuclides facilitates their targeted removal.

ADDITIONAL MATERIAL J

^{210}Pb and ^{210}Po in Geological and Related Anthropogenic Materials: Implications for Their Mineralogical Distribution in Base Metal Ores

Cook, N.J.[1], Ehrig, K.[2], Rollog, M.[1], Ciobanu, C.L.[1], Lane, D.J.[1], Schmandt, D.S.[1], Owen, N.D.[1], Hamilton, T.[3], and Grano, S.R.[4]

[1]*School of Chemical Engineering, The University of Adelaide, Adelaide, SA 5005, Australia*

[2]*BHP Olympic Dam, Adelaide, SA 5000, Australia*

[3]*School of Chemical Engineering, The University of Queensland, Brisbane, QLD 4072, Australia*

[4]*Institute for Mineral and Energy Resources, The University of Adelaide, Adelaide, SA 5005, Australia*

Article published in *Minerals* 8(5), p. 211 (1-28).

minerals

MDPI

Review

^{210}Pb and ^{210}Po in Geological and Related Anthropogenic Materials: Implications for Their Mineralogical Distribution in Base Metal Ores

Nigel J. Cook [1,*], Kathy J. Ehrig [2], Mark Rollog [1], Cristiana L. Ciobanu [1], Daniel J. Lane [1], Danielle S. Schmandt [1], Nicholas D. Owen [1], Toby Hamilton [3] and Stephen R. Grano [4]

1 School of Chemical Engineering, The University of Adelaide, Adelaide, SA 5005, Australia; mark.rollog@adelaide.edu.au (M.R.); cristiana.ciobanu@adelaide.edu.au (C.L.C.); daniel.lane@adelaide.edu.au (D.J.L.), danielle.schmandt@adelaide.edu.au (D.S.S); nicholas.owen@adelaide.edu.au (N.D.O.)
2 BHP Olympic Dam, Adelaide, SA 5000, Australia; Kathy.J.Ehrig@bhpbilliton.com
3 School of Chemical Engineering, The University of Queensland, Brisbane, QLD 4072, Australia; t.hamilton1@uq.edu.au
4 Institute for Mineral and Energy Resources, The University of Adelaide, Adelaide, SA 5005, Australia; stephen.grano@adelaide.edu.au
* Correspondence: nigel.cook@adelaide.edu.au; Tel.: +61-8-8313-1096

Received: 19 April 2018; Accepted: 10 May 2018; Published: 13 May 2018

Abstract: The distributions of ^{210}Pb and ^{210}Po, short half-life products of ^{238}U decay, in geological and related anthropogenic materials are reviewed, with emphasis on their geochemical behaviours and likely mineral hosts. Concentrations of natural ^{210}Pb and ^{210}Po in igneous and related hydrothermal environments are governed by release from crustal reservoirs. ^{210}Po may undergo volatilisation, inducing disequilibrium in magmatic systems. In sedimentary environments (marine, lacustrine, deltaic and fluvial), as in soils, concentrations of ^{210}Pb and ^{210}Po are commonly derived from a combination of natural and anthropogenic sources. Enhanced concentrations of both radionuclides are reported in media from a variety of industrial operations, including uranium mill tailings, waste from phosphoric acid production, oil and gas exploitation and energy production from coals, as well as in residues from the mining and smelting of uranium-bearing copper ores. Although the mineral hosts of the two radionuclides in most solid media are readily defined as those containing parent ^{238}U and ^{226}Ra, their distributions in some hydrothermal U-bearing ores and the products of processing those ores are much less well constrained. Much of the present understanding of these radionuclides is based on indirect data rather than direct observation and potential hosts are likely to be diverse, with deportments depending on the local geochemical environment. Some predictions can nevertheless be made based on the geochemical properties of ^{210}Pb and ^{210}Po and those of the intermediate products of ^{238}U decay, including isotopes of Ra and Rn. Alongside all U-bearing minerals, the potential hosts of ^{210}Pb and ^{210}Po may include Pb-bearing chalcogenides such as galena, as well as a range of sulphates, carbonates, and Fe-oxides. ^{210}Pb and ^{210}Po are also likely to occur as nanoparticles adsorbed onto the surface of other minerals, such as clays, Fe-(hydr)oxides and possibly also carbonates. In rocks, unsupported ^{210}Pb- and/or ^{210}Po-bearing nanoparticles may also be present within micro-fractures in minerals and at the interfaces of mineral grains. Despite forming under very limited and special conditions, the local-scale isotopic disequilibrium they infer is highly relevant for understanding their distributions in mineralized rocks and processing products.

Keywords: ^{210}Pb; ^{210}Po; uranium decay chain; radionuclides; mineral deportment

ADDITIONAL MATERIAL K

Uptake of trace elements by baryte during copper ore processing: a case study from Olympic Dam, South Australia

Schmandt, D.S.[a], Cook, N.J.[a], Ehrig, K.[b], Gilbert, S.E.[c], Wade, B.P.[c], Rollog, M.[a], Ciobanu, C.L.[a], Kamenetsky, V.S.[d]

[a]*School of Chemical Engineering, The University of Adelaide, Adelaide, SA 5005, Australia*

[b]*BHP Olympic Dam, Adelaide, SA 5000, Australia*

[c]*Adelaide Microscopy, The University of Adelaide, Adelaide, SA 5005, Australia*

[d]*School of Physical Sciences, University of Tasmania, Hobart, TAS 7001, Australia*

Article published in *Minerals Engineering*, 135, pp. 83-94.

Minerals Engineering 135 (2019) 83–94

Contents lists available at ScienceDirect

Minerals Engineering

journal homepage: www.elsevier.com/locate/mineng

Uptake of trace elements by baryte during copper ore processing: A case study from Olympic Dam, South Australia

Danielle S. Schmandt[a,*], Nigel J. Cook[a], Kathy Ehrig[b], Sarah Gilbert[c], Benjamin P. Wade[c], Mark Rollog[a], Cristiana L. Ciobanu[a], Vadim S. Kamenetsky[d]

[a] School of Chemical Engineering, The University of Adelaide, Adelaide, SA 5005, Australia
[b] BHP Olympic Dam, Adelaide, SA 5000, Australia
[c] Adelaide Microscopy, The University of Adelaide, Adelaide, SA 5005, Australia
[d] School of Physical Sciences, University of Tasmania, Hobart, TAS 7001, Australia

ARTICLE INFO

Keywords:
Baryte
Mineral processing
LA-ICP-MS
Olympic Dam
Radionuclides

ABSTRACT

Baryte is a common gangue mineral in many ore systems. Here, we report on a study of baryte chemistry in samples of ore and processing materials (flotation feed, flotation concentrate, flotation tailings, concentrate leach discharge, and tailings leach discharge) from the Olympic Dam Cu-U-Au-Ag deposit, South Australia. Elements that commonly substitute for Ba in the baryte lattice, including Sr and Ca, are measured in variable concentrations reflecting grain-scale zonation and heterogeneity at the scale of the deposit but appear unaffected during processing. Variation in the concentration of some other elements, notably Cu, reflect both the heterogeneous nature of flotation feed and the intimately intergrown character of the sulfide-sulfate assemblage. Measured Pb concentrations in baryte progressively increase during processing from flotation feed to flotation concentrate, and particularly in concentrate leach discharge. Such data suggest that, during sulfuric acid leaching, baryte contained within the concentrate is able to incorporate quantities of Pb that have been mobilized during break-down of Pb-bearing minerals (notably U-minerals containing radiogenic lead). This takes place via surface adsorption followed by rapid coupled dissolution-replacement driven incorporation throughout the grain. Results suggest that baryte may scavenge non-target elements during processing and contribute to an understanding of mobility, mineralogical location, and evolution in the deportment of radionuclides through the processing cycle.

1. Introduction

Mineralogy, grain size, grain shape, and intergrowth relationships between minerals are the fundamental controllers of sulfide liberation and sulfide concentrate quality in processing plants. Although recovery is optimized for the economic metals, the presence and distribution of non-payable (often process deleterious) elements within an ore (e.g., Lane et al., 2016) needs to be taken into consideration. Identifying and quantifying the physical location and chemical speciation of non-target elements in an ore at the mineral grain scale can be challenging, especially when that ore is heterogeneous, fine-grained, texturally complex, and mineralogically diverse.

Models of element deportment and distributions can be calculated from a combination of assays and measurements of mineral abundances via automated mineralogical data collection. For this method to be entirely accurate, a comprehensive understanding of mineral chemistry is needed. Targeted detailed geochemical analysis of mineral grains, including quantification of the concentrations of trace elements in common minerals, can underpin the chemical budget for elements of interest and facilitate in-depth understanding of the relative contributions made by each mineral. A knowledge of mineral chemistry in ore or flotation feed is important, as is understanding how distributions of a given element or isotope might change during processing.

The processing facilities at Olympic Dam, South Australia (Ehrig et al., 2012), produces copper cathode, uranium oxide concentrate, and gold and silver bullion from a complex, fine-grained ore that contains anomalous concentrations of several non-target elements, including the products of natural U decay. In this study we targeted the mineral baryte because it is a relatively abundant gangue phase in the deposit and is known to incorporate non-target elements such as Pb (e.g., Takano and Watanuki, 1974) as well as actively scavenge elements, including radium (Ra), Pb, and other products of U decay (e.g., Courtin-

* Corresponding author.
E-mail address: danielle.schmandt@adelaide.edu.au (D.S. Schmandt).

https://doi.org/10.1016/j.mineng.2019.02.034
Received 21 August 2018; Received in revised form 10 December 2018; Accepted 18 February 2019
Available online 02 March 2019
0892-6875/

ADDITIONAL MATERIAL L

REE- Sr- Ca-aluminum-phosphate-sulfate minerals of the woodhouseite series and their role as hosts for radionuclides

Owen, N.D.[1,2*], Cook, N.J.[1], Rollog, M.[1], Ehrig, K.[3], Schmandt, D.S.[1], Ram, R.[2], Brugger, J.[2], Ciobanu, C.L.[1], Wade, B.P.[4], Guagliardo, P.[5]

[1]*School of Chemical Engineering, The University of Adelaide, Adelaide, SA 5005, Australia*

[2]*School of Earth and Environmental Sciences, Monash University, VIC 2800, Australia*

[3]*BHP Olympic Dam, Adelaide, SA 5000, Australia*

[4]*Adelaide Microscopy, The University of Adelaide, Adelaide, SA 5005, Australia*

[5]*Centre for Microscopy, Characterisation, and Analysis, University of Western Australia, 35 Stirling Highway, Crawley, WA 6009, Australia*

Article accepted by *American Mineralogist*, 16 July 2019.

REE-, Sr- Ca-aluminium-phosphate-sulfate minerals of the woodhouseite series and their role as hosts for radionuclides

Nicholas D. Owen[1,2,*], Nigel J. Cook[1], Mark Rollog[1], Kathy J. Ehrig[3], Danielle S. Schmandt[1], Rahul Ram[2], Joel Brugger[2], Cristiana L. Ciobanu[1], Benjamin Wade[4], Paul Guagliardo[5]

[1]*School of Chemical Engineering, The University of Adelaide, SA 5005, Australia*

[2]*School of Earth and Environmental Sciences, Monash University, VIC 2800, Australia*
[3]*BHP Olympic Dam, Adelaide, SA 5000, Australia*
[4]*Adelaide Microscopy, The University of Adelaide, SA 5005, Australia*
[5]*Centre for Microscopy, Characterisation, and Analysis, University of Western Australia, 35 Stirling Highway, Crawley, 6009 W.A., Australia*
**nicholas.owen@adelaide.edu.au*

Abstract

Aluminium-phosphate-sulfates (APS) of the Alunite Supergroup are minor components of uranium-bearing copper ores from the Olympic Dam deposit, South Australia. They typically represent a family of paragenetically-late replacement phases after pre-existing REE-phosphates. Characterization with respect to textures, composition, and relationships with other minerals allows two groups to be distinguished: Ca-Sr-dominant aluminium-phosphate-sulfates that fall within the woodhouseite and svanbergite compositional fields; and a second REE- and phosphate-dominant group closer to florencite in composition. All phases nevertheless display extensive solid solution among end-members in the broader APS clan and show extensive compositional zoning at the grain-scale. NanoSIMS isotope mapping provides evidence that the APS minerals scavenge and incorporate daughter radionuclides of the ^{238}U decay chain, notably ^{226}Ra and ^{210}Pb, both over geological time within the deposit and during flotation and subsequent acid leaching. These data highlight the role played by minor APS phases as hosts for non-target (deleterious?) components during processing, as well as offering potential pathways to their elimination and reduction.

Keywords: Alunite Supergroup; aluminium-phosphate-sulfates; ^{238}U decay series radionuclides; mineral processing.

Introduction

Minerals of the Alunite Supergroup (Jambor 1999; Bayliss et al. 2010), especially the beudantite and crandallite groups, have found extensive application in environmental remediation and storage of toxic metals as they undergo extensive solid solution with the exchange of bi- to hexavalent cations at multiple sites in their structures (Kolitsch and Pring 2001). Elements that can be incorporated include As, Pb, Bi, Hg, Tl, Sb, Cr, Se, and rare earth elements (REE), as well as radioisotopes generated by decay of radioactive K, Sr, Th and U. Most beudantite and crandallite group minerals are stable up to high temperatures (400-500 °C) and remain insoluble even over a wide range of pH and Eh conditions (Kolitsch and Pring 2001). These robust characteristics also make them potential hosts for daughter products of U decay (notably ^{210}Pb and ^{210}Po, hereafter ^{210}RN) in U-bearing ore deposits and in materials resulting from the processing of such ores.

ADDITIONAL MATERIAL M

A sponge for radionuclides: A study on the dynamic uptake of lead by synthetic aluminium phosphate-sulphates

Nicholas D. Owen[1,2,*], Nigel J. Cook[1], Rahul Ram[2], Barbara Etschmann[2], Kathy Ehrig[3], Danielle S. Schmandt[1], Mark Rollog[1], Paul Guagliardo[4], Joël Brugger[2]

[1]*School of Chemical Engineering and Advanced Materials, The University of Adelaide, SA 5005, Australia*

[2]*School of Earth, Atmosphere and Environment, 9 Rainforest Walk, Monash University, VIC 2800, Australia*

[3]*BHP Olympic Dam, Adelaide, SA 5000, Australia*

[4]*Centre for Microscopy, Characterisation, and Analysis, University of Western Australia, 35 Stirling Highway, Crawley, WA 6009, Australia*

[5]*Adelaide Microscopy, The University of Adelaide, SS 5005, Australia*

*Corresponding author email address: nicholas.owen@adelaide.edu.au

Article submitted to *Journal of Hazardous Materials*, 28 August 2019.

A sponge for radionuclides: a study on the dynamic uptake of lead by synthetic aluminium-phosphate-sulphates

Nicholas D. Owen[1,2,*], Rahul Ram[2], Barbara Etschmann[2], Kathy Ehrig[3], Danielle S. Schmandt[1], Mark Rollog[1], Paul Guagliardo[4], Joël Brugger[2], Nigel J. Cook[1]

[1]*School of Chemical Engineering and Advanced Materials, The University of Adelaide, SA 5005, Australia*

[2]*School of Earth, Atmosphere and Environment, 9 Rainforest Walk, Monash University, VIC 2800, Australia*

[3]*BHP Olympic Dam, Adelaide, SA 5000, Australia*

[4]*Centre for Microscopy, Characterisation, and Analysis, University of Western Australia, 35 Stirling Highway, Crawley, WA 6009, Australia*

[5]*Adelaide Microscopy, The University of Adelaide, SA 5005, Australia*

*Corresponding author email address: nicholas.owen@adelaide.edu.au

Abstract

The ability of aluminium-phosphate-sulphate (APS) phases to preferentially sorb radionuclides, particularly ^{210}Pb, from metallurgical processing streams make them ideal candidates as natural additives for the separation and removal of radionuclides from environments. In the present study, the nature and mechanism of their sorption capabilities were investigated in a range of Pb concentrations (10-1000 ppm) and pH (1.5-5.5), mimicking that of metallurgical processes and adverse environmental conditions, as is the case with acid mine drainage. Through a combination of surface characterization and bulk characterization techniques including solution-ICP-MS, EPMA, LA-ICP-MS and XAS analysis, we confirmed the successful incorporation of Pb by synthesized APS phases and provided a mechanistic pathway, with Pb sorption favoured at pH 3.5-5.5 via the direct replacement of lattice bound Ca by Pb within the APS crystal structure. Further, XANES and EXAFS analysis showed that while the formation of Pb-APS was favored at higher pH, the formation of a pyromorphite-

like structure with available PO_4^{3-} ligands following the dissolution of accessory augelite was favored at pH 1.5. The observed Pb-incorporation dynamics of APS Minerals, discussed in this comprehensive study, along with their insolubility and high thermodynamic stabilities, highlights the use of APS minerals as a novel future pathway for the uptake and isolation of Pb, radiogenic and non-radiogenic, from surface and groundwater environments. Further, their ability as an environmental remediation agent in a number of settings, from metallurgical processing to contaminated soil and groundwater remediation, to reduce the bioavailability of other toxic metals in soil horizons in a similar manner is yet to be fully realised.

Chapter 12

References

Aaseth, J., Skaug, M.A., Cao, Y., Andersen, O., 2015 Chelation in metal intoxication—principles and paradigms. Journal of Trace Elements in Medicine and Biology 31, 260-266.

Adams, F., Dams, R., 1970. Semiconductor gamma detectors. In: Belcher, R., Freiser, H., (Eds.), Applied Gamma-Ray Spectrometry: Volume 2 in International Series of Monagraphs on Analytical Chemistry 41, pp. 69-110.

Agarwal, S., Kim, H.I., Park, K.H., Lee, J.Y., 2017. Monazite Mineral Processing. In: Kumar, J.R., (Ed.). Mineral Processing: Methods, Applications and Technology. Nova Science, New York, NY, 39-56.

Allen, S.R., McPhie, J., Ferris, G., Simpson, C., 2008. Evolution and architecture of a large felsic igneous province in western Laurentia: The 1.6 Ga Gawler Range Volcanics, South Australia. Journal of Volcanology and Geothermal Research 172, 132-147.

Alonso, U., Missana, T., Patelli, A., Ceccato, D., Albarran, N., Garcia-Gutierrez, M., Lopez-Torrubia, T., Rigato, V., 2009. Quantification of Au nanoparticles retention on a heterogeneous rock surface. Colloids and Surfaces A: Physicochemical and Engineering Aspects 347, 230-238.

Åmli, R., 1975. Mineralogy and-Rare Earth Geochemistry of Apatite and Xenotime from the Gloserheia Granite Pegmatite, Froland, Southern Norway. American Mineralogist 60, 607–620.

Anderson, J.G., Larson, M.A., Doraiswamy, L.K., 1998. Microphase-assisted "autocatalysis" in a solid–liquid reaction with a precipitating product—II. Experimental. Chemical Engineering Science 53, 2459-2468.

Anvia, M., 2015. Radionuclide Deportment in Rare Earth Processing from Monazite and Bastnäsite using Conventional and Alternative Processing Routes. Unpublished Ph.D. thesis, The University of Syndey. http://hdl/handle.net/2123/13886.

Appleby, P.G., Nolan, P.J., Gifford, D.W., Godfrey, M.J., Oldfield, F.J.A.N., Anderson, N.J., Battarbee, R.W., 1986. 210 Pb dating by low background gamma counting. Hydrobiologia 143, 21-27.

Apukhtina, O.B., 2016. Distribution, petrology, geochemistry and geochronology of carbonate assemblages at the Olympic Dam deposit, University of Tasmania, Hobart, unpublished Ph.D. thesis. https://eprints.utas.edu.au/23013/.

Apukhtina, O.B., Kamenetsky, V.S., Ehrig, K., Kamenetsky, M.B., Maas, R., Thompson, J., McPhie, J., Ciobanu, C.L., Cook, N.J., 2017. Early, deep magnetite-fluorapatite mineralization at the Olympic Dam Cu-U-Au-Ag deposit, South Australia. Economic Geology 112, 1531-1542.

Arrowsmith, P., 1987. Laser ablation of solids for elemental analysis by inductively coupled plasma mass spectrometry. Analytical Chemistry 59, 1437-1444.

Atkinson, A., 1985. Grain boundary diffusion-structural effects and mechanisms. Le Journal de Physique Colloques 46(C4), 379-391.

Ault, T., Gosen, B.V., Krahn, S., Croff, A., 2016. Natural thorium resources and recovery: options and impacts. Nuclear Technology 194, 136-151.

Ayache, J., Beaunier, L., Boumendil, J., Ehret, G., Laub, D., 2010. Sample Preparation Handbook for Transmission Electron Microscopy: Techniques. Springer-Verlag, New York, NY. 338 pp.

Baba, A., 2002. Assessment of radioactive contaminants in by-products from Yatagan (Mugla, Turkey) coal-fired power plant. Environmental Geology 41, 916-921.

Bagnall, K.W., 1957. The chemistry of polonium. Quarterly Reviews, Chemical Society 11, 30-48.

Bagnall, K.W., 1973. The Chemistry of Sulphur, Selenium, Tellurium and Polonium. Pergamon Press, New York, NY. pp. 935-1008.

Bailey, D.J., Stennett, M.C., Hyatt, N.C., 2016. Synthesis and characterization of brannerite wasteforms for the immobilization of mixed oxide fuel residues. Procedia Chemistry 21, 371-377.

Barker, S.L.L., Hickey, K.A., Cline, J.S., Dipple, G.M., Kilburn, M., Vaughan, J.R., Longo, A.A., 2009. Uncloaking invisible gold: Use of nanoSIMS to evaluate gold, trace elements, and sulfur isotopes in pyrite from Carlin-type gold deposits. Economic Geology 104, 897–904.

Barton, M., 2014. Iron oxide (–Cu–Au–REE–P–Ag–U–Co) systems. In: Holland, H.D., Turekian, K.K., (Eds.), Treatise on Geochemistry 2nd ed., vol. 13, Elsevier, Amsterdam, pp. 515–541.

Baskaran, M., 2016. Radon: A Tracer for Geological, Geophysical and Geochemical Studies, Springer International. pp. 37-62.

Bebie, J., Schoonen, M.A., Fuhrmann, M., Strongin, D.R., 1998. Surface charge development on transition metal sulfides: an electrokinetic study. Geochimica et Cosmochimica Acta 62, 633-642.

Becker, J.S., 2005. Inductively coupled plasma mass spectrometry (ICP-MS) and laser ablation ICP-MS for isotope analysis of long-lived radionuclides. International Journal of Mass Spectrometry 242, 183-195.

Becquerel, A.H., 1896. Sur les radiations invisibles émises par les corps phosphorescents. Comptes Rendus de l'Academie des Science 122, 501.

Becquerel, H., 1901. The radio-activity of matter. Nature 63, 396-398.

Beklemishev, M.K., Elshani, S., Wai, C.M., 1994. Solvent extraction of radium with crown ether carboxylic acids. Analytical Chemistry 66, 3521-3524.

Bekri, S., Thovert, J.F., Adler, P.M., 1997. Dissolution and deposition in fractures. Engineering Geology 48, 283-308.

Bettencourt, A.O., Teixeira, M.M., Elias, M.D., Madruga, M.J., 1990. Environmental monitoring in uranium mining areas. In: The Environmental Behavior of Radium, IAEA Technical Reports Series 310, 2, pp. 281-294.

Bhargava, S.K., Ram, R., Pownceby, M., Grocott, S., Ring, B., Tardio, J., Jones, L., 2015. A review of acid leaching of uraninite. Hydrometallurgy 151, 10-24.

BHP Billiton, 2009. Olympic Dam Expansion Draft Environmental Impact Statement 2009. Appendix S. Uranium and Radiation. Available online: www.bhp.com. Accessed on 25.03.2019.

BHP Billiton, 2011. Olympic Dam Expansion Supplementary Environmental Impact Statement. Chapter 26, 689–758. Available online: www.bhp.com. Accessed on 25.03.2019.

BHP Annual Report 2018. Section 6, 2018, 259. Available online: www.bhp.com. Accessed on 25.03.2019.

Bister, S., Birkhan, J., Lüllau, T., Bunka, M., Solle, A., Stieghorst, C., Riebe, B., Michel, R., Walther, C., 2015. Impact of former uranium mining activities on the floodplains of the Mulde River, Saxony, Germany. Journal of Environmental Radioactivity 144, 21-31.

Blazek, M.C., 1979. Classification of Pseudomorphs. Rocks & Minerals 54, 194-197.

Bonczyk, M., 2013. A Determination of the Concentration Level of Lead ^{210} PB Isotope in Solid Samples for the Assessment of Radiation Risk Occurring in Coal Mines. Journal of Sustainable Mining 12, 1-7.

Borkowski, C.J., 1949. Instruments for measuring radioactivity. Analytical Chemistry 21, 348-352.

Boujrhal, F.Z., Sabbani, H., 2015. Radon diffusion in rocks and minerals. In: Merkel, B.J., Arab, A. (Eds.), Uranium-Past and Future Challenges, Proceedings, 7th International Conference on Uranium Mining and Hydrogeology. Springer International Publishing. pp. 545-552.

Boulyga, S.F., Desideri, D., Meli, M.A., Testa, C., Becker, J.S., 2003. Plutonium and americium determination in mosses by laser ablation ICP-MS combined with isotope dilution technique. International Journal of Mass Spectrometry 226, 329-339.

Boulyga, S.F., Tibi, M., Heumann, K.G., 2004. Application of isotope-dilution laser ablation ICP–MS for direct determination of Pu concentrations in soils at pg g^{-1} levels. Analytical and Bioanalytical Chemistry 378, 342-347.

Bowles, J.F., 1990. Age dating of individual grains of uraninite in rocks from electron microprobe analyses. Chemical Geology 83, 47-53.

Brady, J.B., 1995. Diffusion data for silicate minerals, glasses, and liquids. In: Ahrens, J., (Ed.), Mineral Physics and Crystallography: A Handbook of Physical Constants vol. 2. American Geophysical Union. pp. 269-290.

Brandt, F., Curti, E., Klinkenberg, M., Rozov, K., Bosbach, D., 2015. Replacement of barite by a (Ba,Ra)SO_4 solid solution at close-to-equilibrium conditions: A combined experimental and theoretical study. Geochimica et Cosmochimica Acta 155, 1-15.

Brandt, F., Klinkenberg, M., Poonoosamy, J., Weber, J., Bosbach, D., 2018. The Effect of Ionic Strength and Sr_{aq} upon the Uptake of Ra during the Recrystallization of Barite. Minerals 8, 502, 1-22. doi:10.3390/min8110502

Brown, P.L., Ekberg, C., Ramebäck, H., Hedström, H., Matyskin, A., 2015. Solubility of radium and strontium sulfate across the temperature range of 0 to 300 °C. In: Merkel, B.J., Arab, A., (Eds.), Uranium-Past and Future Challenges. Springer International Publishing. pp. 553-564.

Brown, R.J., Milton, M.J., 2005. Analytical techniques for trace element analysis: An overview. Trends in Analytical Chemistry 24, 266–274.

Byrne, K., Hawker, W., Vaughan, J., 2018. Deportment of radionuclides during copper concentrate metathesis reactions. Proceedings ALTA 2018, 19-26 May 2018, Perth, WA, 12 pp.

Cameca (2019). Introduction to APT. www.cameca.com/products/apt/technique. Accessed 13 August 2019.

Cantrell, K.J., Felmy, A.R., 2012. Plutonium and americium geochemistry at Hanford: a site-wide review. Pacific Northwest National Laboratory, Report PNNL-21651, 1-32.

Carvalho, F.P., Oliveira, J.M., Libânio, A., Lopes, I., Ferrador, G., Madruga, M.J., 2005. Radioactivity in public water supplies in the uranium mining regions of Portugal. In: Environmental contamination from uranium production facilities and their remediation. Proceedings of an International Workshop, Lisbon, Portugal, February 11-13, 2004. International Atomic Energy Agency. pp. 29-40.

Carvalho, F.P., Madruga, M.J., Reis, M.C., Alves, J.G., Oliveira, J.M., Gouveia, J., Silva, L., 2007. Radioactivity in the environment around past radium and uranium mining sites of Portugal. Journal of Environmental Radioactivity 96, 39-46.

Carvalho, F.P., Oliveira, J.M., Malta, M., 2014. Radioactivity in soils and vegetables from uranium mining regions. Procedia Earth and Planetary Science 8, 38-42.

Case, G.N., McDowell, W.J., 1982. An improved sensitive assay for polonium-210 by use of a background-rejecting extractive liquid-scintillation method. Talanta 29, 845-848.

Ceccarello, S., Black, S., Read, D., Hodson, M.E., 2004. Industrial radioactive barite scale: suppression of radium uptake by introduction of competing ions. Minerals Engineering 17, 323-330.

Chao, J.H., Chuang, C.Y., Yeh, S.A., Wu, J.M., 2009. Relationship between radioactivity of radium and concentrations of barium and lead in hokutolite. Applied Radiation and Isotopes 67, 650-653.

Charalambous, F.A., Ram, R., Pownceby, M.I., Tardio, J., Bhargava, S.K., 2012. Chemical and microstructural characterisation studies on natural and heat treated brannerite samples. Minerals Engineering 39, 276-288.

Cherry, A.R., Ehrig, K., Kamenetsky, V.S., McPhie, J., Crowley, J.L., Kamenetsky, M.B., 2018. Precise geochronological constraints on the origin, setting and incorporation of ca. 1.59 Ga surficial facies into the Olympic Dam Breccia Complex, South Australia. Precambrian Research 315, 162–178.

Cherry, A., Kamenetsky, V., McPhie, J., Kamenetsky, M., Ehrig, K., Keeling, J., 2017. Post-1590 Ma modification of the supergiant Olympic Dam deposit: links with regional tectonothermal events. Extended abstract, 14th SGA Biennial Meeting 3, 847-850.

Cherry, S.R., Sorenson, J.A., Phelps, M.E., 1995. Physics in Nuclear Medicine E-Book, 4th edition. Elsevier Health Sciences.

Christy, A.G., Putnis, A., 1993. The kinetics of barite dissolution and precipitation in water and sodium chloride brines at 44–85 C. Geochimica et Cosmochimica Acta 57, 2161-2168.

Ciobanu, C.L., Cook, N.J., Kelson, C.R., Guerin, R., Kalleske, N., Danyushevsky, L., 2013. Trace element heterogeneity in molybdenite fingerprints stages of mineralization. Chemical Geology 347, 175–189.

Ciobanu, C.L., Wade, B.P., Cook, N.J., Schmidt Mumm, A., Giles, D., 2013. Uranium-bearing hematite from the Olympic Dam Cu-U-Au deposit, South Australia: A geochemical tracer and reconnaissance Pb-Pb geochronometer. Precambrian Research 238, 129–147.

Ciobanu, C.L., Cook, N.J., Ehrig, K., 2017. Ore minerals down to the nanoscale: Cu-(Fe)-sulphides from the iron oxide copper gold deposit at Olympic Dam, South Australia. Ore Geology Reviews 81, 1218–1235.

Ciobanu, C.L., Kontonikas-Charos, A., Slattery, A., Cook, N.J., Ehrig. K., Wade, B.P., 2017. Short-range stacking disorder in mixed-layer compounds: A HAADF-STEM study of bastnäsite-parisite intergrowths. Minerals 7, 227. doi:10.3390/min7110227.

Ciobanu, C.L., Verdugo-Ihl, M.R., Slattery, A., Cook, N.J., Ehrig, K., Courtney-Davies, L., Wade, B.P., 2019. Silician magnetite: Si-Fe-nanoprecipitates and other mineral inclusions in magnetite from the Olympic Dam deposit, South Australia. Minerals 9, 311.

Clayton, R.F., Bradley, E.J., 1995. A cost effective method for the determination of 210 Po and 210 Pb in environmental materials. Science of the Total Environment 173, 23-28.

Collins, A.G., Davis, J.W., 1971. Solubility of barium and strontium sulfates in strong electrolyte solutions. Environmental Science & Technology 5, 1039-1043.

Cook, N.J., Ciobanu, C.L., Danyushevsky, L.V., Gilbert, S., 2011. Minor elements in bornite and associated Cu-(Fe)-sulfides: A LA-ICPMS study. Geochimica et Cosmochimica Acta 73, 4761–4791.

Cook, N.J., Ciobanu, C.L., George, L., Ehrig, K., 2016. Trace element analysis of minerals in magmatic-hydrothermal ores by laser ablation inductively-coupled plasma mass spectrometry: Approaches and opportunities. Minerals 6, 111.

Cook, N.J., Ciobanu, C.L., Ehrig, K., Slattery, A., Verdugo-Ihl, M.R., Courtney-Davies, L., Gao, W., 2017. Advances and opportunities in ore mineralogy. Minerals 7, 233. doi:10.3390/min7120233.

Cook, N.J., Ehrig, K.J., Rollog, M., Ciobanu, C.L., Lane, D.J., Schmandt, D.S., Owen, N.D., Hamilton, T., Grano, S., 2018. ^{210}Pb and ^{210}Po in geological and related anthropogenic materials: implications for their mineralogical distribution in base metal ores. Minerals 8, 211. doi:10.3390/min8050211.

Cotton, F.A., Wilkinson, G., Murillo, C.A., Bochmann, M., 1999. Advanced Inorganic Chemistry. John Wiley and Sons, Hoboken, NJ. 1376 pp.

Courtney-Davies, L., Zhu, Z., Ciobanu, C., Wade, B., Cook, N., Ehrig, K., Cabral, A., Kennedy, A., 2016. Matrix-matched iron-oxide laser ablation ICP-MS U–Pb geochronology using mixed solution standards. Minerals 6, 85.

Courtney-Davies, L., Tapster, S.R., Ciobanu, C.L., Cook, N.J., Verdugo-Ihl, M.R., Ehrig, K.J., Kennedy, A.K., Gilbert, S.E., Condon, D.J., Wade, B.P., 2019. A multi-technique evaluation of hydrothermal hematite U-Pb isotope systematics: Implications for ore deposit geochronology. Chemical Geology 513, 54–72.

Courtney-Davies, L., Ciobanu, C.L., Verdugo-Ihl, M.R., Slattery, A., Cook, N.J., Dmitrijeva, M., Keyser, W., Wade, B.P., Dominick, U.I., Ehrig, K., Xu, J., Kontonikas-Charos, A., 2019. Zircon at the nanoscale records metasomatic processes leading to large magmatic-hydrothermal ore systems. Minerals 2019, 9(6), 364; doi:10.3390/min9060364.

Cowart, J.B., Burnett, W.C., 1994. The distribution of uranium and thorium decay-series radionuclides in the environment—a review. Journal of Environmental Quality 23, 651-662.

Creaser, R.A., Cooper, J.A., 1993. U-Pb geochronology of middle Proterozoic felsic magmatism surrounding the Olympic Dam Cu-U-Au-Ag and Moonta Cu-Au-Ag deposits, South Australia. Economic Geology 88, 186-197.

Crockett, G.M., Smith, K.R., Oatway, W.B., Mobbs, S.F., 2003. Radiological Impact on the UK Population of Industries which Use or Produce Materials Containing Enhanced Levels of Naturally

Occurring Radionuclides: The Steel Production Industry. National Radiological Protection Board Report R-327. 87 pp.

Curie, P., Curie, M., Becquerel, H., 1898. Sur une substance nouvelle radio-active, contenue dans la pechblende. Comptes Rendus 127, 1215-1217.

Curti, E., Fujiwara, K., Iijima, K., Tits, J., Cuesta, C., Kitamura, A., Glaus, M.A., Müller, W., 2010. Radium uptake during barite recrystallization at 23±2° C as a function of solution composition: An experimental ^{133}Ba and ^{226}Ra tracer study. Geochimica et Cosmochimica Acta 74, 3553-3570.

Dai, Z., Kan, A.T., Shi, W., Yan, F., Zhang, F., Bhandari, N., Ruan, G., Zhang, Z., Liu, Y., Alsaiari, H.A., Lu, Y.T., 2017. Calcite and Barite Solubility Measurements in Mixed Electrolyte Solutions and Development of a Comprehensive Model for Water-Mineral-Gas Equilibrium of the Na-K-Mg-Ca-Ba-Sr-Cl-SO_4-CO_3-HCO_3-CO_2 (aq)-H_2O System up to 250° C and 1500 bar. Industrial & Engineering Chemistry Research 56, 6548-6561.

Davis, D.W., Krogh, T.E., Williams, I.S., 2003. Historical development of zircon geochronology. Reviews in Mineralogy and Geochemistry 53, 145-181.

DePaolo, D.J., Maher, K., Christensen, J.N., McManus, J., 2006. Sediment transport time measured with U-series isotopes: results from ODP North Atlantic drift site 984. Earth and Planetary Science Letters 248, 394-410.

Dickey, E.E., 1953. Separation of radium D, E, and F by paper chromatography. Journal of Chemical Education 30, 525-526.

Didier, A., Bosse, V., Bouloton, J., Mostefaoui, S., Viala, M., Paquette, J.L., Devidal, J.L., Duhamel, R., 2016. NanoSIMS mapping and LA-ICP-MS chemical and U-Th-Pb data in monazite from a xenolith enclosed in andesite (Central Slovakia Volcanic Field). Contributions to Mineralogy and Petrology 170, 45, 1-21, doi:10.1007/s00410-015-1200-1.

Dijk, P., Berkowitz, B., 1998. Precipitation and dissolution of reactive solutes in fractures. Water Resources Research 34, 457-470.

Dill, H.G., 2001. The geology of aluminum phosphates and sulfates of the alunite group minerals: A review. Earth-Science Reviews 53, 35–93.

Ditchburn, R.G., de Ronde, C.E.J., 2017. Evidence for Remobilization of Barite Affecting Radiometric Dating Using ^{228}Ra, ^{228}Th, and ^{226}Ra/Ba Values: Implications for the Evolution of Sea-Floor Volcanogenic Massive Sulfides. Economic Geology 112, 1231-1246.

Dmitrijeva, M., Ehrig, K.J., Ciobanu, C.L., Cook, N.J., Verdugo-Ihl, M.R., Metcalfe, A.V., 2019. Defining IOCG signatures through compositional data analysis: A case study of lithogeochemical zoning from the Olympic Dam deposit, South Australia. Ore Geology Reviews 105, 86–101.

Doerner, H.A., Hoskins, W.M., 1925. Co-Precipitation of Radium and Barium Sulphates. Journal of the American Chemical Society 47, 662-675.

Dosseto, A., Bourdon, B., Turner, S.P., 2008. Uranium-series isotopes in river materials: insights into the timescales of erosion and sediment transport. Earth and Planetary Science Letters 265, 1-17.

Dunn, G.M., Saich, S., Bartsch, P.J., 2017. Hydrometallurgical method for the removal of radionuclides from radioactive copper concentrates. United States Orway Mineral Consultants Pty. Ltd. Patent no. US9587290B2.

Dostal, J., Capedri, S., 1978. Uranium in metamorphic rocks. Contributions to Mineralogy and Petrology 66, 409-414.

Dyar, M.D., Gunter, M.E., Tasa, D., 2008. Mineralogy and Optical Mineralogy. Mineralogical Society of America, Chantilly, VA. 708 pp.

Ehrig, K., McPhie, J., Kamenetsky, V.S., 2012. Geology and mineralogical zonation of the Olympic Dam iron oxide Cu-U-Au-Ag deposit, South Australia. In: Hedenquist, J.W., Harris, M., Camus, F., (Eds.), Geology and Genesis of Major Copper Deposits and Districts of the World, a Tribute to Richard Sillitoe. Society of Economic Geologists Special Publication 16, Littleton, CO, pp. 237–267.

Ehrig, K., Kamenetsky, V.S., McPhie, J., Cook, N.J., Ciobanu, C.L., 2017. Olympic Dam iron oxide Cu-U-Au-Ag deposit. In: Phillips, G.M., (Ed.), Australian Ore Deposits. AusIMM, Melbourne. pp. 601-610.

Emrich Jr., W.J., 2016. Principles of Nuclear Rocket Propulsion. Butterworth-Heinemann. 344 pp.

Evans, N.J., Byrne, J.P., Keegan, J.T., Dotter, L.E., 2005. Determination of uranium and thorium in zircon, apatite, and fluorite: Application to laser (U-Th)/He thermochronology. Journal of Analytical Chemistry 60, 1159–1165.

Eyal, Y., Fleischer, R.L., 1985. Timescale of natural annealing in radioactive minerals affects retardation of radiation-damage-induced leaching. Nature 314, 518–520.

Fanning, C.M., Flint, R.B., Parker, A.J., Ludwig, K.R., Blissett, A.H., 1988. Refined Proterozoic evolution of the Gawler craton, South Australia, through U-Pb zircon geochronology. Precambrian Research 40, 363-386.

Fenter, P., Sturchio, N.C., 2004. Mineral–water interfacial structures revealed by synchrotron X-ray scattering. Progress in Surface Science 77(5-8), 171-258.

Fews, A.P., Henshaw, D.L., 1982. High resolution alpha particle spectroscopy using CR-39 plastic track detector. Nuclear Instruments and Methods in Physics Research 197, 517-529.

Figgins, P.E., 1961. The radiochemistry of polonium. Mound Lab, Miamisburg, OH. 74 pp.

Fleischer, R.L., 1980. Isotopic disequilibrium of uranium: alpha-recoil damage and preferential solution effects. Science 207(4434), 979-981.

Flint, R.B., 1993. Hiltaba suite. In: Drexel, J.F., Preiss, W.V., Parker, A.J., (Eds.), The Geology of South Australia 1, pp. 127-131.

Foden, J., Elburg, M.A., Dougherty-Page, J., Burtt, A., 2006. The timing and duration of the Delamerian Orogeny: correlation with the Ross Orogen and implications for Gondwana assembly. The Journal of Geology 114, 189-210.

Förster, H.J., 2006. Composition and origin of intermediate solid solutions in the system thorite–xenotime–zircon–coffinite. Lithos 88, 35-55.

Fougerouse, D., Micklethwaite, S., Halfpenny, A., Reddy, S.M., Cliff, J.B., Martin, L.A.J., Kilburn, M., Guagliardo, P., Ulrich, S., 2016. The golden ark: Arsenopyrite crystal plasticity and the retention of gold through high strain and metamorphism. Terra Nova 28, 181–187.

Fougerouse, D., Micklethwaite, S., Tomkins, A.G., Mei, Y., Kilburn, M., Guagliardo, P., Fisher, L.A., Halfpenny, A., Gee, M., Paterson, D., Howard, D.L., 2016. Gold remobilisation and formation of

high-grade ore shoots driven by dissolution-reprecipitation replacement and Ni substitution into auriferous arsenopyrite. Geochimica et Cosmochimica Acta 178, 143–159.

Fu, W., 2019. Node 3: Radionuclide Separation. Unpublished presentation, May 2019, 13 pp.

Fukuma, H.T., Fernandes, E.A.N., Quinelato, A.L., 2000. Distribution of natural radionuclides during the processing of phosphate rock from Itataia-Brazil for production of phosphoric acid and uranium concentrate. Radiochimica Acta 88, 809-814.

Ganeev, A.A., Gubal, A.R., Potapov, S.V.E., Agafonova, N.N., Nemets, V.M., 2016. Mass spectrometric methods for the direct elemental and isotopic analysis of solid material. Russian Chemical Reviews 85, 427-444.

Gao, D., Huang, X., Tao, Y., 2016. A critical review of NanoSIMS in analysis of microbial metabolic activities at single-cell level. Critical Reviews in Biotechnology 36, 884–890.

Gazineu, M.H.P., Hazin, C.A., 2008. Radium and potassium-40 in solid wastes from the oil industry. Applied Radiation and Isotopes 66, 90-94.

George, L.L., Cook, N.J., Crowe, B.B.P., Ciobanu, C.L., 2018. Trace elements in hydrothermal chalcopyrite. Mineralogical Magazine 82, 59-88.

Germann, F.E., 1921. Adsorption of radium by barium sulfate. Journal of the American Chemical Society 43, 1615-1621.

Gilligan, R., 2017. The extractive metallurgy of brannerite: Leaching kinetics, reaction mechanisms and mineralogical transformations. Unpublished Ph.D. dissertation, Murdoch University, Perth, Australia. 433 pp.

Gilligan, R., Nikoloski, A.N., 2015. The extraction of uranium from brannerite–A literature review. Minerals Engineering 71, 34-48.

Gleason, G., 1980. Improved ion exchange procedure for the separation of barium from radium. In: Lyons, W.S. (Ed.), Radioelement analysis: progress and problems. Ann Arbor Science Publishers, Inc. pp. 47-50.

Godbee, H.W., Fitzgerald, C.L., Blomeke, J.O., Blanco, R.E., 1969. Diffusion of radioisotopes through waste solids. Transactions of the American Nuclear Society 12, 450-451.

Gramaccioli, C.M., Segalstad, T.V., 1978. A uranium-and thorium-rich monazite from a south-alpine pegmatite at Piona, Italy. American Mineralogist 63, 757-761.

Grandstaff, D.E., 1976. A kinetic study of the dissolution of uraninite. Economic Geology 71, 1493-1506.

Halmshaw, R., 1996. Introduction to the non-destructive testing of welded joints. Woodhead Publishing, Cambridge, England. 124 pp.

Hamlat, M.S., Kadi, H., Fellag, H., 2003. Precipitate containing norm in the oil industry: modelling and laboratory experiments. Applied Radiation and Isotopes 59, 95-99.

Hansen, E., Peatross, J., Bergeson, S., Ware, M., 2014. Precision Measurements of Beta-Decay Rates (abstract). Bulletin of the American Physical Society, 59(11). BAPS.2014.4CF.K7.8.

Haring, M.M., Yalman, R.G., 1949. Solution chemistry of polonium. (Interim Report). No. MLM-211. Mound Laboratory, Miamisburg, Ohio. 12 pp.

Hashimoto, T., Aoyagi, Y., Kudo, H., Sotobayashi, T., 1985. Range calculation of alpha-recoil atoms in some minerals using LSS-theory. Journal of Radioanalytical and Nuclear Chemistry 90, 415-438.

Hauri, E.H., Papineau, D., Wang, J., Hillion, F., 2016. High-precision analysis of multiple sulfur isotopes using NanoSIMS. Chemical Geology 420, 148–161.

Haynes, W.M., 2014. CRC Handbook of Chemistry and Physics, CRC Press, Boca Raton, FL, 2643 pp.

Hedström, H., Ramebäck, H., Ekberg, C., 2013. A study of the Arrhenius behavior of the co-precipitation of radium, barium and strontium sulfate. Journal of Radioanalytical and Nuclear Chemistry 298, 847-852.

Henisch, H.K., 1996. Crystal growth in gels. Pennsylvania State University Press, University Park, PA, 107 pp.

Henriksen, G., Hoff, P., Larsen, R. H., 2002. Evaluation of potential chelating agents for radium. Applied Radiation and Isotopes 56, 667-671.

Herschel, J.F.W., 1843. Note on the Art of Photography, or the Application of the Chemical Rays of Light to the Purposes of Pictorial Representation. In: Abstracts of the Papers Printed in the Philosophical Transactions of the Royal Society of London 4, pp. 131-133.

Hetherington, C.J., Harlov, D.E., Budzyń, B., 2010. Experimental metasomatism of monazite and xenotime: mineral stability, REE mobility and fluid composition. Mineralogy and Petrology 99, 165-184.

Hillion, F., Daigne, B., Girard, F., Slodzian, G., Schuhmacher, M., 1993. A new high performance instrument: the CAMECA NanoSIMS 50. Secondary Ion Mass Spectrometry, SIMS IX, 254-57.

Hitzman, M.W., Oreskes, N., Einaudi, M.T., 1992. Geological characteristics and tectonic setting of Proterozoic iron oxide (Cu-U-Au-REE) deposits. Precambrian Research 58, 241-287.

Hitzman, M.W., Valenta, R.K., 2005. Uranium in iron oxide-copper-gold (IOCG) systems. Economic Geology 100, 1657-1661.

Holland, H.D., Gottfried, D., 1955. The effect of nuclear radiation on the structure of zircon. Acta Crystallographica 8, 291-300.

Hondros, J., 2014. Background Radiation Briefing presentation. Unpublished document. 69 pp.

Hoppe, P., 2006. NanoSIMS: A new tool in cosmochemistry. Applied Surface Science 252, 7102–7106.

Hu, Q.H., Weng, J.Q., Wang, J.S., 2010. Sources of anthropogenic radionuclides in the environment: a review. Journal of Environmental Radioactivity 101, 426-437.

Huang, Q., Kamenetsky, V.S., McPhie, J., Ehrig, K., Meffre, S., Maas, R., Thompson, J., Kamenetsky, M., Chambefort, I., Apukhtina, O., Hu, Y., 2015. Neoproterozoic (ca. 820–830 Ma) mafic dykes at Olympic Dam, South Australia: links with the Gairdner large igneous province. Precambrian Research 271, 160-172.

Hurley, P.M., Fairbairn, H.W., 1953. Radiation damage in zircon: a possible age method. Geological Society of America Bulletin 64, 659-673.

Institute of Experimental Mineralogy: Internet Database. http://database.iem.ac.ru/mincryst. Updated 01 March 2019, Accessed 21 March 2019.

International Atomic Energy Agency, 2004. Application of the Concepts of Exclusion, Exemption and Clearance. International Atomic Energy Agency, Vienna. IAEA Safety Standards Series: Safety Guide No. RS-G-1.7

International Atomic Energy Agency, 2019. Reference products for Environment and Trade. https://nucleus.iaea.org/rpst/ReferenceProducts. Accessed 16 August 2019.

Ito, M., Messenger, S., 2008. Isotopic imaging of refractory inclusions in meteorites with the NanoSIMS 50L. Applied Surface Science 255, 1446–1450.

Itzkovitch, I.J., Ritcey, G.M., 1979. Removal of Radionuclides from Process Streams—A Survey, CANMET Report 79-21, Energy, Mines, and Resources Canada, Ottawa, Canada. 171 pp.

Jackson, P.E., Carnevale, J., Fuping, H., Haddad, P.R., 1994. Determination of thorium and uranium in mineral sands by ion chromatography. Journal of Chromatography A 671, 181-191.

Janković, M.M., Todorović, D.J., Nikolić, J.D., 2011. Analysis of natural radionuclides in coal, slag and ash in coal-fired power plants in Serbia. Journal of Mining and Metallurgy B: Metallurgy 47, 149-155.

Jia, G., Torri, G., Ocone, R., 2007. Determination of radium isotopes in soil samples by alpha-spectrometry. Journal of Radioanalytical Nuclear Chemistry 273, 779-783.

Johnson, J.P., Cross, K.C., 1995. U-Pb geochronological constraints on the genesis of the Olympic Dam Cu-U-Au-Ag deposit, South Australia. Economic Geology 90, 1046–1063.

Kalmykov, S.N., Kriventsov, V.V., Teterin, Y.A., Novikov, A.P., 2007. Plutonium and neptunium speciation bound to hydrous ferric oxide colloids. Comptes Rendus Chimie 10, 1060-1066.

Kalnins, C.A., Spooner, N.A., Clarke, M.J., Ottaway, D., 2019. Alpha particle autoradiography for high spatial resolution mapping of radionuclides. Journal of Environmental Radioactivity 197, 9-15.

Kathren, R.L., 1998. NORM sources and their origins. Applied Radiation and Isotopes 49, 149-168.

Kendi, A.T., Moncayo, V.M., Nye, J.A., Galt, J.R., Halkar, R., Schuster, D.M., 2017. Radionuclide therapies in molecular imaging and precision medicine. PET Clinics 12, 93-103.

Kerisit, S., Liu, C., 2009. Molecular simulations of water and ion diffusion in nanosized mineral fractures. Environmental Science & Technology 43, 777-782.

Kersting, A.B., 2013. Plutonium transport in the environment. Inorganic Chemistry 52, 3533-3546.

Kersting, A.B., 2017. LLNL SFA OBER SBR FY17 Program Management and Performance Report: Subsurface Biogeochemistry of Actinides (No. LLNL-TR-733899). Lawrence Livermore National Lab (LLNL), Livermore, CA.

Kikuchi, S., 1928. Diffraction of cathode rays by mica. Proceedings of the Imperial Academy 4, 271-274.

Kilburn, M.R., Wacey, D., 2014. Nanoscale secondary ion mass spectrometry (NanoSIMS) as an analytical tool in the geosciences. In: Grice, K. (Ed.), Principles and Practice of Analytical Techniques in Geosciences. Royal Society of Chemistry, London, UK. pp. 1–34.

Kilburn, M.R., Clode, P.L., 2014. Elemental and isotopic imaging of biological samples using NanoSIMS. In: Kuo, J., (Ed.), Electron Microscopy – Methods and Protocols. Humana Press, Totowa, NJ. pp. 733–755.

Kirchenbauer, M., Maas, R., Ehrig, K., Kamenetsky, V.S., Strub, E., Ballhaus, C., Münker, C., 2016. Uranium and Sm isotope studies of the supergiant Olympic Dam Cu–Au–U–Ag deposit, South Australia. Geochimica et Cosmochimica Acta 180, 15-32.

Klinkenberg, M., Brandt, F., Breuer, U., Bosbach, D., 2014. Uptake of Ra during the recrystallization of barite: a microscopic and time of flight-secondary ion mass spectrometry study. Environmental Science & Technology 48, 6620-6627.

Klinkenberg, M., Weber, J., Barthel, J., Vinograd, V., Poonoosamy, J., Kruth, M., Bosbach, D. Brandt, F., 2018. The solid solution–aqueous solution system (Sr, Ba, Ra) SO_4 + H_2O: A combined experimental and theoretical study of phase equilibria at Sr-rich compositions. Chemical Geology 497, 1-17.

Kontonikas-Charos, A., Ciobanu, C.L., Cook, N.J., Ehrig, K., Krneta, S., Kamenetsky, V.S., 2017. Feldspar evolution in the Roxby Downs Granite, host to Fe-oxide Cu-Au-(U) mineralisation at Olympic Dam, South Australia. Ore Geology Reviews 80, 838–859.

Kontonikas-Charos, A., Ciobanu, C.L., Cook, N.J., Ehrig, K., Ismail, R., Krneta, S., Basak, A., 2018. Feldspar mineralogy and rare earth element (re)mobilization in iron-oxide copper gold systems from South Australia: A nanoscale study. Mineralogical Magazine 82, S173–S197.

Krneta, S., Ciobanu, C.L., Cook, N.J., Ehrig, K., Kontonikas-Charos, A., 2016. Apatite at Olympic Dam, South Australia: a petrogenetic tool. Lithos 262, 470-485.

Krneta, S., Ciobanu, C.L., Cook, N.J., Ehrig, K., Kontonikas-Charos, A., 2017. Rare Earth Element Behaviour in Apatite from the Olympic Dam Cu-U-Au-Ag Deposit, South Australia. Minerals 7, 135, 1-26.

Krumgalz, B.S., 2018. Temperature Dependence of Mineral Solubility in Water, Part 3: Alkaline and Alkaline Earth Sulfates. Journal of Physical and Chemical Reference Data 47(2), 023101, 1-30.

Krupp, K., Baskaran, M., Brownlee, S.J., 2017. Radon emanation coefficients of several minerals: How they vary with physical and mineralogical properties. American Mineralogist 102, 1375–1383.

Landa, E.R., Gray, J.R., 1995. US Geological Survey research on the environmental fate of uranium mining and milling wastes. Environmental Geology 26, 19-31.

Lane, D.J., Cook, N.J., Grano, S.R., Ehrig, K., 2016. Selective leaching of penalty elements from copper concentrates: A review. Minerals Engineering 98, 110–121.

Langmuir, D., Riese, A.C., 1985. The thermodynamic properties of radium. Geochimica et Cosmochimica Acta 49, 1593-1601.

L'Annunziata, M.F., 1987. Radionuclide Tracers. Academic Press, London, UK. 505 pp.

Law, J.D., Brewer, K.N., Herbst, R.S., Todd, T.A., Wood, D.J., 1999. Development and demonstration of solvent extraction processes for the separation of radionuclides from acidic radioactive waste. Waste Management 19, 27-37.

Lehman, T.A., Everett, W.W., 1982. Solubility of lead sulfate in water and in sodium sulfate solutions: An experiment in atomic absorption spectrophotometry. Journal of Chemical Education 59, 797.

Li, G., You, Z., Sun, H., Sun, R., Peng, Z., Zhang, Y., Jiang, T., 2016. Separation of rhenium from lead-rich molybdenite concentrate via hydrochloric acid leaching followed by oxidative roasting. Metals 6, 282, 1-12.

Liatsou, I., Pashalidis, I., 2016. Radium concentration in uranium-bearing rocks and minerals by radon emanation after acidic sample dissolution. Journal of Radioanalytical Nuclear Chemistry 309, 1327-1332.

Linke, W.F., Seidell, A., 1965. Solubilities, Inorganic and Metal-organic Compounds, K-Z: A Compilation of Solubility Data from the Periodical Literature. A Revision and Continuation of the

Compilation Originated by Atherton Seidell. American Chemical Society, Van Nostrand, NewYork, NY. 904 pp.

Longerich, H.P., Jackson, S.E., Günther, D., 1996. Inter-laboratory note. Laser ablation inductively coupled plasma mass spectrometric transient signal data acquisition and analyte concentration calculation. Journal of Analytical Atomic Spectrometry 11, 899-904.

Lucchesi, P.J., Whitney, E.D., 1962. Solubility of strontium sulphate in water and aqueous solutions of hydrogen chloride, sodium chloride, sulphuric acid and sodium sulphate by the radiotracer method. Journal of Applied Chemistry 12, 277-279.

Ludwig, K.R., 1977. Effect of initial radioactive-daughter disequilibrium on U-Pb isotope apparent ages of young minerals. Journal of Research of the US Geological Survey 5, 663-667.

Ludwig, K.R., 1978. Uranium-daughter migration and U/Pb isotope apparent ages of uranium ores, Shirley Basin, Wyoming. Economic Geology 73, 29-49.

Ludwig, R., 1998. Scanning electron microscopy. Springer, Berlin, Germany. 529 pp.

Lumpkin, G.R., Leung, S.H.F., Ferenczy, J., 2012. Chemistry, microstructure, and alpha decay damage of natural brannerite. Chemical Geology 291, 55-68.

Maas, R., Kamenetsky, V., Ehrig, K., Meffre, S., McPhie, J., Diemar, G., 2011. Olympic Dam U-Cu-Au deposit, Australia: New age constraints. Mineralogical Magazine 75, 1375.

Macmillan, E., Ciobanu, C.L., Ehrig, K., Cook, N.J., Pring, A., 2016. Chemical zoning and lattice distortion in uraninite from Olympic Dam, South Australia. American Mineralogist 101, 2351–2354.

Macmillan, E., Ciobanu, C.L., Ehrig, K., Cook, N.J., Pring, A., 2016. Replacement of uraninite by bornite via coupled dissolution-reprecipitation: Evidence from texture and microstructure. Canadian Mineralogist 54, 1369–1383.

Macmillan, E., Cook, N.J., Ehrig, K., Ciobanu, C.L., Pring, A., 2016. Uraninite from the Olympic Dam IOCG-U-Ag deposit: Linking textural and compositional variation to temporal evolution. American Mineralogist 101, 1295–1320.

Macmillan, E., Cook, N.J., Ehrig, K., Pring, A., 2017. Chemical and textural interpretation of late-stage coffinite and brannerite from the Olympic Dam IOCG-Ag-U deposit. Mineralogical Magazine 81, 1323–1366.

Maity, S., Mishra, S., Bhalke, S., Pandit, G., Puranik, V., Kushwaha, H., 2011. Estimation of distribution coefficient of polonium in geological matrices around uranium mining site. Journal of Radioanalytical and Nuclear Chemistry 290, 75-79.

Martin, P., 2000. Radiological impact assessment of uranium mining and milling. Unpublished Ph.D. thesis, Queensland University of Technology, Brisbane, QLD, Australia.

Martland, H.S., Conlon, P., Knef, J.P., 1925. Some unrecognized dangers in the use and handling of radioactive substances: with especial reference to the storage of insoluble products of radium and mesothorium in the reticulo-endothelial system. Journal of the American Medical Association 85, 1769-1776.

Martz, P., Mercadier, J., Perret, J., Villeneuve, J., Deloule, E., Cathelineau, M., Quirt, D., Doney, A., Ledru, P., 2019. Post-crystallization alteration of natural uraninites: implications for dating, tracing, and nuclear forensics. Geochimica et Cosmochimica Acta 249, 138-159.

Maruyama, I., Muto, S., 2016. Change in relative density of natural rock minerals due to electron irradiation. Journal of Advanced Concrete Technology 14, 706-716.

Matthews, K.M., Kim, C.K., Martin, P., 2007. Determination of 210-Po in environmental materials: a review of analytical methodology. Applied Radiation and Isotopes 65, 267-279.

Maxwell, C.R., 1946. Physical properties and crystal structure of polonium, Retrospective Theses and Dissertations, Iowa State University, Paper 13649. 71 pp.

McPhie, J., Kamenetsky, V., Allen, S., Ehrig, K., Agangi, A., Bath, A., 2011. The fluorine link between a supergiant ore deposit and a silicic large igneous province. Geology 39, 1003-1006.

McPhie, J., Orth, K., Kamenetsky, V., Kamenetsky, M., Ehrig, K., 2016. Characteristics, origin and significance of Mesoproterozoic bedded clastic facies at the Olympic Dam Cu–U–Au–Ag deposit, South Australia. Precambrian Research 276, 85-100.

Melekestseva, I.Y., Maslennikov, V.V., Maslennikova, S.P., Danyushevsky, L.V., Large, R., 2017. Covellite of the Semenov-2 hydrothermal field (13° 31.13′ N, Mid-Atlantic Ridge): Enrichment in trace elements according to LA ICP MS analysis. Doklady Earth Sciences 473, 291-295.

Michel, H., Champion, J., 2019. ^{210}Po sequential extraction applied to wetland soils at uranium mining sites. Journal of Environmental Radioactivity 199, 1-6.

Mikhlin, Y.L., Romanchenko, A.S., 2007. Gold deposition on pyrite and the common sulfide minerals: an STM/STS and SR-XPS study of surface reactions and Au nanoparticles. Geochimica et Cosmochimica Acta 71, 5985-6001.

Miller, M.K., 2012. Atom Probe Tomography: Analysis at the Atomic Level. Springer Science & Business Media, New York, NY. 239 pp.

Mironov, A.G., Karmanov, N.S., Mironov, A.A., Khodyreva, E.V., 2008. Gold-brannerite nuggets in placers of the Ozernoe ore cluster (Buryatia). Russian Geology and Geophysics 49, 743–748.

Moggi-Cecchi, V., Cipriani, C., Rossi, P., Ceccato, D., Rudello, V., Somacal, H., 2002. Trace element contents and distribution maps of chalcopyrite: a micro-PIXE study. Periodico di Mineralogia 71, 101-109.

Momoshima, N., Nita, J., Maeda, Y., Sugihara, S., Shinno, I., Matsuoka, N., Huang, C.W., 1997. Chemical composition and radioactivity in hokutolite (plumbian barite) collected at Peito hot spring, Taiwan. Journal of Environmental Radioactivity 37, 85-99.

Morawska, L., Jeffries, C., 1994. Distribution of radium in mineral sand grains and its potential effect on radon emanation. Radiation Protection Dosimetry 56, 199-200.

Moyer, H.V., 1956. Chemical Properties of Polonium. Mound Laboratory, Dayton, OH. 401 pp.

Murakami, T., Chakoumakos, B.C., Ewing, R.C., Lumpkin, G.R., Weber, W.J., 1991. Alpha-decay event damage in zircon. American Mineralogist 76, 1510-1532.

Natural Resources Canada, 2019. https://www.nrcan.gc.ca/our-natural-resources/minerals-and-mining/mining-resources/certified-reference-materials/ Updated 16 July 2019, Accessed 16 August 2019.

Nguyen, C.K., Clark, B.N., Stone, K.R., Edwards, M.A., 2011. Role of chloride, sulfate, and alkalinity on galvanic lead corrosion. Corrosion 67(6), 065005, 1-9.

Novikov, A.P., Kalmykov, S.N., Utsunomiya, S., Ewing, R.C., Horreard, F., Merkulov, A., Myasoedov, B.F., 2006. Colloid transport of plutonium in the far-field of the Mayak Production Association, Russia. Science 314(5799), 638-641.

Nowell, M.M., Witt, R.A., True, B.W., 2005. EBSD sample preparation: Techniques, tips, and tricks. Microscopy Today 13(4), 44-49.

Ojovan, M.I., Lee, W.E., Kalmykov, S.N., 2019. An Introduction to Nuclear Waste Immobilisation. Elsevier. 512 pp.

Oldfield, F., Appleby, P.G., 1984. Empirical testing of 210 Pb-dating models for lake sediments. In: Haworth, E., Lund, J.W.G., (Eds.), Lake sediments and environmental history. University of Minnesota Press, Minneapolis, MN. pp. 93-124.

Oliveira, J.M., Carvalho, F.P., 2006. Sequential extraction procedure for determination of uranium, thorium, radium, lead and polonium radionuclides by alpha spectrometry in environmental samples. Czechoslovak Journal of Physics 56, D545-D555.

Onetto Carvallo, C.A., 2018. Identity and physiology of glycogen accumulating organisms in activated sludge. Unpublished Ph.D. thesis, The University of Adelaide, Adelaide, Australia. 129 pp.

Osmanlioglu, A.E., Adiguzel, D., Tuylu, S., Bascetin, A., 2017. Acid mine drainage and environmental impacts of uranium deposits. International Multidisciplinary Scientific GeoConference: SGEM: Surveying Geology & Mining Ecology Management 17, 9-14.

Owen, N.D., Ciobanu, C.L., Cook, N.J., Slattery, A., Basak, A., 2018. Nanoscale study of clausthalite-bearing symplectites in Cu-Au-(U) ores: Implications for ore genesis. Minerals 8, 67. doi:10.3390/min8020067.

Owen, N.D., Cook, N.J., Ram, R., Etschmann, B., Ehrig, K., Schmandt, D.S., Rollog, M., Guagliardo, P., Brugger, J., 2019. A sponge for radionuclides: A study on the dynamic uptake of lead by synthetic aluminium-phosphate-sulphates. The Journal of Hazardous Materials. (submitted 28 August 2019).

Owen, N.D., Cook, N.J., Rollog, M., Ehrig, K.J., Schmandt, D.S., Ram, R., Brugger, J., Ciobanu, C.L., Wade, B., Guagliardo, P., 2019. REE-, Sr- Ca-aluminum-phosphate-sulfate minerals of the alunite supergroup and their role as hosts for radionuclides. American Mineralogist, (in press).

Palache, C., Berman, H., Frondel, C., Dana, E.S., 1951. The System of Mineralogy of James Dwight Dana and Edward Salisbury Dana, Yale University, 1837–1892: Halides, Nitrates, Borates, Carbonates, Sulfates, Phosphates, Arsenates, Tungstates, Molybdates, etc., John Wiley and Sons, Hoboken, NJ, 1124 pp.

Parker, C., Nilsson, S., Heinrich, D., Helle, S.I., O'Sullivan, J.M., Fosså, S.D., Chodacki, A., Wiechno, P., Logue, J., Seke, M.,Widmark, A. and 19 co-authors, 2013. Alpha emitter radium-223 and survival in metastatic prostate cancer. New England Journal of Medicine 369, 213-223.

Parman, S.W., 2015. Going small: Nanoscale geochronology using atom probe tomography. American Mineralogist 100, 1333-1334.

Patel, A.R., Bhat, H.L., 1984. Gel growth of lead sulphate single crystals. In: Chernov, A.A. (Ed.), Рост Кристаллоь/Rost Kristallov/Growth of Crystals. Springer, Boston, MA, 122-125.

Perks, H., Cook, N.J., Ciobanu, C.L., Ehrig, K., Basak, A., 2018. Orientation maps for copper cathodes with defect growth: and EBSD study. Goldschmidt 2018, August 12-17, Boston, MA. Goldschmidt Conference Abstracts, 2005.

Peteranderl, R., Lechene, C., 2004. Measure of carbon and nitrogen stable isotope ratios in cultured cells. Journal of the American Society of Mass Spectrometry 15, 478–485.

Peterman, E.M., Reddy, S.M., Saxey, D.W., Snoeyenbos, D.R., Rickard, W.D., Fougerouse, D., Kylander-Clark, A.R., 2016. Nanogeochronology of discordant zircon measured by atom probe microscopy of Pb-enriched dislocation loops. Science Advances 2(9), e1601318, 1-9.

Pheiffer Madsen, P., Sørensen, J., 1979. Validation of the lead-210 dating method. Journal of Radioanalytical and Nuclear Chemistry 54, 39-48.

Piazolo, S., Belousova, E., La Fontaine, A., Corcoran, C., Cairney, J.M., 2017. Trace element homogeneity from micron-to atomic scale: Implication for the suitability of the zircon GJ-1 as a trace element reference material. Chemical Geology 456, 10-18.

Pina, C.M., Putnis, A., 2002. The kinetics of nucleation of solid solutions from aqueous solutions: a new model for calculating non-equilibrium distribution coefficients. Geochimica et Cosmochimica Acta 66, 185-192.

Pina, C.M., Becker, U., Risthaus, P., Bosbach, D., Putnis, A., 1998. Molecular-scale mechanisms of crystal growth in barite. Nature 395, 483-486.

Pluta, I., 2001. Barium and radium discharged from coal mines in the Upper Silesia, Poland. Environmental Geology 40, 345-348.

Poczatek, C., Kaufman, Z., Lechene, C., 2009. OpenMIMS ImageJ Plugin Guide. Harvard Medical School, Boston, MA.

Poggi, C.M.B., de Farias, E.E.G., Silveira, P.B., Silva Filho, C.A., De França, E.J., Gazineu, M.H.P., Hazin, C.A., 2015. ^{226}Ra, ^{228}Ra and ^{40}K in scales from boilers of industrial installations. Journal of Radioanalytical and Nuclear Chemistry 306, 667-672.

Pracejus, B., 2015. The ore minerals under the microscope – an optical guide, 2nd Edition. Elsevier Publishing. 1118 pp.

Pratt, R.M., 1993. Review of radium hazards and regulation of radium in industry. Environment International 19, 475-489.

Prince, J.R., 1979. Comments on equilibrium, transient equilibrium, and secular equilibrium in serial radioactive decay. Journal of Nuclear Medicine 20, 162-164.

Prior, D.J., Mariani, E., Wheeler, J., 2009. EBSD in the earth sciences: applications, common practice, and challenges. In: Schwartz, A.J., Kumar, M., Adams, B.L., Field, D.P., (Eds.), Electron backscatter diffraction in materials science. Springer Science+Business Media, Boston, MA. pp. 345-360.

Puch, K.H., Bialucha, R., Keller, G., 2005. Naturally occurring radioactivity in industrial by-products from coal-fired power plants, from municipal waste incineration and from the iron-and steel-industry. Radioactivity in the Environment 7, 996-1008.

Putnis, A., 2002. Mineral replacement reactions: from macroscopic observations to microscopic mechanisms. Mineralogical Magazine 66, 689-708.

Putnis A., 2009. Mineral replacement reactions. Reviews in Mineralogy and Geochemistry 70, 87-124.

Putnis, A., 2014. Why mineral interfaces matter. Science 343(6178), 1441-1442.

Putnis, A., Fernandez-Diaz, L., Prieto, M., 1992. Experimentally produced oscillatory zoning in the (Ba, Sr)SO_4 solid solution. Nature 358(6389), 743-745.

Putnis, A., Mauthe, G., 2001. The effect of pore size on cementation in porous rocks. Geofluids 1, 37-41.

Putnis, C.V., Tsukamoto, K., Nishimura, Y., 2005. Direct observations of pseudomorphism: compositional and textural evolution at a fluid-solid interface. American Mineralogist 90, 1909-1912.

Quinto, F., Blechschmidt, I., Garcia Perez, C., Geckeis, H., Geyer, F., Golser, R., Huber, F., Lagos, M., Lanyon, B., Plaschke, M., Steier, P., 2017. Multiactinide Analysis with Accelerator Mass Spectrometry for Ultratrace Determination in Small Samples: Application to an *in situ* Radionuclide Tracer Test within the Colloid Formation and Migration Experiment at the Grimsel Test Site (Switzerland). Analytical Chemistry 89, 7182-7189.

Radhamani, R., Mahanta, P.L., Murugesan, P., Chakrapani, G., 2010. Novel fusion method for direct determination of uranium in ilmenite, rutile, columbite, tantalite, and xenotime minerals by laser induced fluorimetry. Journal of Radioanalytical and Nuclear Chemistry 285, 287-292.

Ragozzini, R.J., Sparrow, G.J., 1987. Selective dissolution of uranium from Olympic Dam copper concentrates. Hydrometallurgy 18, 367-382.

Raju, K., Atkinson, G., 1988. Thermodynamics of "scale" mineral solubilities. 1. Barium sulfate (s) in water and aqueous sodium chloride. Journal of Chemical and Engineering Data 33, 490-495.

Raju, K., Atkinson, G., 1989. Thermodynamics of "scale" mineral solubilities. 2. Strontium sulfate (s) in aqueous sodium chloride. Journal of Chemical and Engineering Data 34, 361-364.

Ram, R., Charalambous, F.A., McMaster, S., Pownceby, M.I., Tardio, J., Bhargava, S.K., 2013. An investigation on the dissolution of natural uraninite ores. Minerals Engineering 50, 83-92.

Ram, R., Vaughan, J., Etschmann, B., Brugger, J., 2019. The aqueous chemistry of Polonium (Po) in environmental and anthropogenic processes. Journal of Hazardous Materials 380, 120725, 1-17.

Reddy, S.M., van Riessen, A., Saxey, D.W., Johnson, T.E., Rickard, W.D., Fougerouse, D., Fischer, S., Prosa, T.J., Rice, K.P., Reinhard, D.A. Chen, Y., 2016. Mechanisms of deformation-induced trace element migration in zircon resolved by atom probe and correlative microscopy. Geochimica et Cosmochimica Acta 195, 158-170.

Reeve, J.S., Cross, K.C., Smith, R.N., Oreskes, N., 1990. Olympic Dam copper-uranium-gold-silver deposit. In: Hughes, F.E., (Ed.), Geology of the Mineral Deposits of Australia and Papua New Guinea. AusIMM, Melbourne, Australia. pp. 1009–1035.

Reid, A., 2019. The Olympic Cu-Au Province, Gawler Craton: A Review of the Lithospheric Architecture, Geodynamic Setting, Alteration Systems, Cover Successions and Prospectivity. Minerals 9(6), 371. doi:10.3390/min9060371.

Rigali, M.J., Brady, P.V., Moore, R.C., 2016. Radionuclide removal by apatite. American Mineralogist 101, 2611-2619.

Roberts, D.E., Hudson, G.R.T., 1983. The Olympic Dam copper-uranium-gold deposit, Roxby Downs, South Australia. Economic Geology 78, 799–822.

Roessler, C.E., 1990. Control of radium in phosphate mining, beneficiation and chemical processing. The environmental behaviour of radium vol. 2, Technical Report Series 310, International Atomic Energy Agency, pp. 270-279.

Rollog, M., Cook, N.J., Schmandt, D.S., Clarke, M., Ottaway, D.J., Spooner, N.A., Kalnins, C.A.G., Ehrig, K., Ciobanu, C.L., Triffett, B., Grano, S., 2016. Identification and characterisation of extremely low-concentration non-target components in copper ores and concentrates (abstract, oral presentation). Australian Earth Science Conference (AESC), Adelaide, Australia, 26-30 June 2016. p.386.

Rollog, M., Cook, N.J., Schmandt, D.S., Clarke, M., Ottaway, D.J., Spooner, N.A., Kalnins, C.A.G., Ehrig, K., Ciobanu, C.L., Triffett, B., Grano, S., 2016. Identifying and characterising non-target elements in South Australian iron oxide-copper-gold (IOCG) deposits (poster). Australian Earth Science Conference (AESC), Adelaide, Australia, 26-30 June 2016.

Rollog, M., Cook, N.J., Schmandt, D.S., Clarke, M., Ottaway, D.J., Spooner, N.A., Kalnins, C.A.G., Ehrig, K., Ciobanu, C.L., Triffett, B., Grano, S., 2016. A pathway to improving methods for remediation of uranium and daughter products from South Australian iron oxide-copper-gold (IOCG) deposits (abstract, oral presentation). Australasian Radiation Protection Society (ARPS) conference, Adelaide, Australia, 11-14 September 2016.

Rollog, M., Cook, N.J., Schmandt, D.S., Ehrig, K., Triffett, B., 2016. Hosts for non-target uranium and associated radionuclides in South Australian copper ores and concentrates (abstract). Chemeca Conference, Adelaide, Australia, 25-28 September 2016.

Rollog, M., Cook, N.J., Guagliardo, P., Kilburn, M.R., Ehrig, K., Ciobanu, C.L., 2017. NanoSIMS mapping of ^{210}Rn and ^{226}Ra in South Australian copper concentrates (abstract, oral presentation). Goldschmidt Conference, Paris, France, 13-18 August 2017. https://goldschmidtabstracts.info/2017/3392.pdf.

Rollog, M., Cook, N.J., Guagliardo, P., Kilburn, M.R., Ehrig, K., Ciobanu, C.L., 2018. Nanoscale spatial distribution maps of trace elements/isotopes in South Australian copper concentrates (abstract, oral presentation). Goldschmidt Conference, Boston, MA, 12-17 August 2018. https://goldschmidtabstracts.info/2018/2177.pdf.

Rollog, M., Cook, N.J., Guagliardo, P., Ciobanu, C.L., Ehrig, K., Kilburn, M.R., 2018. Mobility of radionuclides in the Olympic Dam Cu-U-Au-Ag deposit, South Australia (extended abstract). Proceedings, 15th Quadrennial International Association on the Genesis of Ore Deposits (IAGOD) symposium, Salta, Argentina, 28-31 August 2018. pp. 183-184.

Rollog, M., Cook, N.J., Ehrig, K.J., Gilbert, S.E., 2019. Rapid, competitive radium uptake in strontium, barium, and lead sulfates during sulfuric acid leaching. Applied Geochemistry (in review, submitted 18 July 2019).

Rollog, M., Cook, N.J., Guagliardo, P., Ciobanu, C.L., Ehrig, K., Kilburn, M.R., 2019. *In situ* mapping of radionuclides in Olympic Dam copper concentrates by nanoSIMS (abstract, oral presentation). AusIMM Uranium 2019 conference , Adelaide, Australia, 4-5 June 2019.

Rollog, M., Cook, N.J., Guagliardo, P., Ehrig, K.J., Ciobanu, C., Kilburn, M., 2019. Detection of trace elements/isotopes in Olympic Dam copper concentrates by nanoSIMS. Minerals 9, 336. doi:10.3390/min9060336.

Rollog, M., Cook, N.J., Guagliardo, P., Ehrig, K.J., Gilbert, S.E., Kilburn, M., 2019. Intermobility of barium, strontium, and lead in chloride and sulphate leach solution. Geochemical Transactions 20(4), 1-23.

Rollog, M., Cook, N.J., Guagliardo, P., Ehrig, K., Kilburn, M., 2019. *In situ* spatial distribution mapping of radionuclides in minerals by nanoSIMS. Geochemistry: Exploration, Environment, Analysis 19, 245-254. doi:10.1144/geochem2018-038.

Rollog, M., Cook, N.J., Guagliardo, P., Ehrig, K.J., Kilburn, M., 2019. Radionuclide-bearing minerals in Olympic Dam copper concentrates. Hydrometallurgy 190, 105153.

Rollog, M., Cook, N.J., Guagliardo, P., Ehrig, K.J., Kilburn, M., 2019. Radionuclide distributions in Olympic Dam copper concentrates: the importance of minor hosts, incorporation mechanisms, and mineral surfaces. Minerals Engineering (in review, submitted 19 June 2019).

Rosholt, J.N., 1983. Isotopic composition of uranium and thorium in crystalline rocks. Journal of Geophysical Research: Solid Earth 88(B9), 7315-7330.

Rumble, J., 2017. CRC Handbook of Chemistry and Physics. CRC press, Boca Raton, FL. 1532 pp.

Ruiz-Agudo, E., Putnis, C.V., Putnis, A., 2014. Coupled dissolution and precipitation at mineral–fluid interfaces. Chemical Geology 383, 132-146.

Russo, R.E., Mao, X., Gonzalez, J.J., Mao, S.S., 2002. Femtosecond laser ablation ICP-MS. Journal of Analytical Atomic Spectrometry 17, 1072-1075.

Sangwal, K., 1989. On the estimation of surface entropy factor, interfacial tension, dissolution enthalpy and metastable zone-width for substances crystallizing from solution. Journal of Crystal Growth 97, 393-405.

Sasaki, N., Minato, H., 1982. Relationship between lattice constants and strontium and calcium contents of hokutolite. Mineralogical Journal 11, 62-71.

Schäfer, T., Huber, F., Seher, H., Missana, T., Alonso, U., Kumke, M., Eidner, S., Claret, F., Enzmann, F., 2012. Nanoparticles and their influence on radionuclide mobility in deep geological formations. Applied Geochemistry 27, 390-403.

Schindelin, J., Arganda-Carreras, I., Frise, E., Kaynig, V., Longair, M., Pietzsch, T., Preibisch, S., Rueden, C, Saalfeld, S., Schmid, B., Tinevez, J.Y., 2012. Fiji: an open-source platform for biological-image analysis. Nature Methods 9, 676.

Schindelin, J., Rueden, C.T., Hiner, M.C., Eliceiri, K.W., 2015. The ImageJ ecosystem: An open platform for biomedical image analysis. Molecular Reproduction and Development 82, 518-529.

Schmandt, D.S., 2019. Mineralogical Distribution of Radionuclides in Copper-Uranium Ores, Olympic Dam, South Australia. Unpublished Ph.D. Thesis, The University of Adelaide, Adelaide, Australia, 371 pp.

Schmandt, D.S., Cook, N.J., Ciobanu, C.L., Ehrig, K., Wade, B.P., Gilbert, S., Kamenetsky, V.S., 2017. Rare Earth Element Fluorocarbonate Minerals from the Olympic Dam Cu-U-Au-Ag Deposit, South Australia. Minerals 7(10), 202, 1-24.

Schmandt, D.S., Cook, N.J., Ciobanu, C.L., Ehrig, K., Wade, B.P., Gilbert, S., Kametetsky, V.S., 2019. Rare earth element phosphate minerals from the Olympic Dam Cu-U-Au-Ag deposit, South Australia: Recognizing temporal-spatial controls on REE mineralogy in an evolved IOCG systems. Canadian Mineralogist 57, 3–24.

Schmandt, D.S., Cook, N.J., Ehrig, K., Gilbert, S., Wade, B.P., Rollog, M., Ciobanu, C.L., Kamenetsky, V.S., 2019. Uptake of trace elements by baryte during copper ore processing: A case study from Olympic Dam, South Australia. Minerals Engineering 135, 83–94.

Schuster, M., 2015. Entwicklung und Validierung einer kombinierten Schnellanalysenmethode zur Bestimmung der natürlichen Radionuklide ^{210}Pb, ^{210}Po, ^{226}Ra, ^{234}U, und ^{238}U in Trinkwasser. Unpublished Ph.D. thesis, Universität Regensburg, Germany. http://epub.uni-regensburg.de/32890/1/Diss_Schuster.pdf.

Schwartz, A.J., Kumar, M., Adams, B.L., Field, D.P., (Eds.), 2009. Electron backscatter diffraction in materials science. Springer Science+Business Media, Boston, MA. 403 pp.

Shannon, R.D., 1976. Revised effective ionic radii and systematic studies of interatomic distances in halides and chalcogenides. Acta Crystallographica section A: Crystal Physics, Diffraction, Theoretical and General Crystallography 32, 751-767.

Skirrow, R.G., Bastrakov, E., Davidson, G.J., Raymond, O.L., Heithersay, P., 2002. The Geological Framework, Distribution and Controls of Fe-oxide Cu-Au Mineralisation in the Gawler Craton, South Australia. Part II —Alteration and Mineralisation. In: Porter, T.M., (Ed.), Hydrothermal Iron Oxide Copper-Gold & Related Deposits: A Global Perspective. PGC Publishing, Adelaide, Australia. pp. 33–47.

Skirrow, R.G., Bastrakov, E.N., Baroncii, K., Fraser, G.L., Creaser, R.A., Fanning, C.M., Raymond, O.L., Davidson, G.J., 2007. Timing of iron oxide Cu-Au-(U) hydrothermal activity and Nd isotope constraints on metal sources in the Gawler craton, South Australia. Economic Geology 102, 1441–1470.

Skwarzec, B., 2009. Determination of Radionuclides in the Aquatic Environment. In: Namiesnik, J., Szefer, P., (Eds.), Analytical Measurements in Aquatic Environments, CRC Press, Boca Raton, FL. pp. 241-256.

Skwarzec, B., Boryło, A., Strumińska-Parulska, D., 2016. Alpha spectrometry in radiochemical analysis and its application in the study of the natural environment. Annales Universitatis Mariae Curie-Sklodowska, sectio AA–Chemia 71, 151-167. doi:10.17951/aa.2016.71.1.151.

Slodzian, G., Hillion, F., Stadermann, F.J., Horreard, F., Oxygen isotopic measurements on the CAMECA NanoSIMS 50. Applied Surface Science 203, 798–801.

Smith, A.L., 1987. Radioactive-scale formation. Journal of Petroleum Technology 39, 697–706.

Smith, D.K., 1984. Uranium mineralogy. In: de Vivo, B., (Ed.), Uranium geochemistry, mineralogy, geology, exploration and resources. Springer, Netherlands. pp. 43-88.

Söhnel, O., 1982. Electrolyte crystal-aqueous solution interfacial tensions from crystallization data. Journal of Crystal Growth 57, 101-108.

Solomon, A.K., Estes, H.D., 1948. The measurement of radioactivity in solution. Review of Scientific Instruments 19, 47-50.

Stadermann, F.J., Walker, R.M., Zinner, E., 1999. NanoSIMS: The next generation ion probe for the microanalysis of extra-terrestrial material. Meteoritics and Planetary Science Supplement 34, A111-A112.

www.statista.com/topics/1409/copper. Updated 23 November 2018, accessed 26 July 2019.

Steefel, C.I., Lichtner, P.C., 1998. Multicomponent reactive transport in discrete fractures: I. Controls on reaction front geometry. Journal of Hydrology 209, 186-199.

Steefel, C.I., Lichtner, P.C., 1998. Multicomponent reactive transport in discrete fractures: II: Infiltration of hyperalkaline groundwater at Maqarin, Jordan, a natural analogue site. Journal of Hydrology 209, 200-224.

Suman, G., Sreenath, R., Gopal, R., Yadagiri, R., Rama, R., 2017. Preliminary data of radiation levels near the proposed uranium mining site, Dasarlapally, Nalgonda, Telangana. In: Proceedings of the twentieth national conference on solid state nuclear track detectors and their applications: abstracts.

Mysuru, India, October 26-28, 2017. Vidya Vikas Institute of Engineering and Technology, Mysuru, India. p. 106.

Švedkauskaitė-LeGore, J., Rasmussen, G., Abousahl, S., Van Belle, P., 2008. Investigation of the sample characteristics needed for the determination of the origin of uranium-bearing materials. Journal of Radioanalytical Nuclear Chemistry 278, 201-209.

Swadźba-Kwaśny, M., 2015. Lead: Inorganic Chemistry. In: King, B. (Ed.), Encyclopedia of Inorganic and Bioinorganic Chemistry, John Wiley & Sons. pp. 1-24.

Szymanski, J.T., Scott, J.D., 1982. A crystal-structure refinement of synthetic brannerite, UTi_2O_6, and its bearing on rate of alkaline-carbonate leaching of brannerite in ore. The Canadian Mineralogist 20, 271-280.

Tartakovsky, A.M., Meakin, P., Scheibe, T.D., Wood, B.D., 2007. A smoothed particle hydrodynamics model for reactive transport and mineral precipitation in porous and fractured porous media. Water Resources Research 43(5), W05437, 1-18.

ThermoFisher Scientific, 2019. Helios nanoLab DualBeam. www.fei.com/products/dualbeam/helios-nanolab. Accessed 13 August 2019.

Vaasma, T., Bityukova, L., Kiisk, M., Özden, B., Tkaczyk, A.H., 2016. Behavior mechanisms and correlation between lead (Pb) and its isotope ^{210}Pb in industrial residue as an indicator for waste characterization. Environmental Technology 37, 3208-3218.

Valle, N., Drillet, J., Perlade, A., Migeon, H.N., Application of SIMS nano-analysis to the development of new metallurgical solutions. Applications of Surface Science 255, 1569–1571.

Vallini, D.A., Groves, D.I., McNaughton, N.J., Fletcher, I.R., 2007. Uraniferous diagenetic xenotime in northern Australia and its relationship to unconformity-associated uranium mineralisation. Mineralium Deposita 42, 51-64.

Vandenborre, J., Drot, R., Simoni, E., 2007. Interaction mechanisms between uranium (VI) and rutile titanium dioxide: From single crystal to powder. Inorganic Chemistry 46, 1291-1296.

Verdugo-Ihl, M.R., Ciobanu, C.L., Cook, N.J., Ehrig, K., Courtney-Davies, L., Gilbert, S., 2017. Textures and U-W-Sn-Mo signatures in hematite from the Cu-U-Au-Ag orebody at Olympic Dam, South Australia: Defining the archetype for IOCG deposits. Ore Geology Reviews 91, 173–195.

Verdugo-Ihl, M.R., Ciobanu, C.L., Cook, N.J., Ehrig, K.J., Courtney-Davies, L., 2019. Defining early stages of IOCG systems: evidence from iron-oxides in the outer shell of the Olympic Dam deposit, South Australia. Mineralium Deposita, 1-24, doi:10.1007/s00126-019-00896-2.

Verdugo-Ihl, M.R., Ciobanu, C.L., Slattery, A., Cook, N.J., Ehrig, K., Courtney-Davies, L., 2019. Copper-arsenic nanoparticles in hematite: fingerprinting fluid-mineral interaction. Minerals 9, 388. doi:10.3390/min9070388.

Vesterbacka, P., Ikäheimonen, T.K., 2005. Optimization of ^{210}Pb determination via spontaneous deposition of ^{210}Po on a silver disk. Analytica Chimica Acta 545, 252-261.

Vinograd, V.L., Kulik, D.A., Brandt, F., Klinkenberg, M., Weber, J., Winkler, B., Bosbach, D., 2018. Thermodynamics of the solid solution-aqueous solution system (Ba,Sr,Ra)SO_4 + H_2O: I. The effect of strontium content on radium uptake by barite. Applied Geochemistry 89, 59-74.

Vinograd, V.L., Kulik, D.A., Brandt, F., Klinkenberg, M., Weber, J., Winkler, B., Bosbach, D., 2018. Thermodynamics of the solid solution-Aqueous solution system (Ba,Sr,Ra)SO_4 + H_2O: II. Radium retention in barite-type minerals at elevated temperatures. Applied Geochemistry 93, 190-208.

von Gunten, H.R., Beneš, P., 1995. Speciation of radionuclides in the environment. Radiochimica Acta 69, 1-30.

Walder, A.J., Abell, I.D., Platzner, I., Freedman, P.A., 1993. Lead isotope ratio measurement of NIST 610 glass by laser ablation inductively coupled plasma mass spectrometry. Spectrochimica Acta Part B: Atomic Spectroscopy 48, 397-402.

Wasserstein, B., 1951. Precision lattice measurements of galena. American Mineralogist 36, 102–115.

Weber, J., Barthel, J., Brandt, F., Klinkenberg, M., Breuer, U., Kruth, M., Bosbach, D., 2016. Nano-structural features of barite crystals observed by electron microscopy and atom probe tomography. Chemical Geology 424, 51-59.

Weber, J., Barthel, J., Klinkenberg, M., Bosbach, D., Kruth, M., Brandt, F., 2017. Retention of ^{226}Ra by barite: The role of internal porosity. Chemical Geology 466, 722-732.

Weber, W.J., Roberts, F.P., 1983. A review of radiation effects in solid nuclear waste forms. Nuclear Technology 60, 178-198.

Weigel, F., 1959. Chemistry of Polonium. Angewandte Chemie 71, 289-299.

Wilkinson, A.J., Britton, T.B., 2012. Strains, planes, and EBSD in materials science. Materials Today 15, 366-376.

Wilson, R.G., Novak, S.W., 1991. Systematics of secondary-ion-mass spectrometry relative sensitivity factors versus electron affinity and ionization potential for a variety of matrices determined from implanted standards of more than 70 elements. Journal of Applied Physics 69, 466–474.

Wilson, R.G., Stevie, F.A., Magee, C.W., 1989. Secondary ion mass spectrometry: a practical handbook for depth profiling and bulk impurity analysis. Wiley-Interscience, New York, NY, 384 pp.

Winterholler, B., Hoppe, P., Foley, S., Andreae, M.O., 2008. Sulfur isotope ratio measurements of individual sulfate particles by NanoSIMS. International Journal of Mass Spectrometry 272, 63-77.

World Nuclear Association: Information Library. http://www.world-nuclear.org. Updated 2018, accessed 15 Feb 2019.

Wu, Y.F., Fougerouse, D., Evans, K., Reddy, S.M., Saxey, D.W., Guagliardo, P., Li, J.W., 2019. Gold, arsenic, and copper zoning in pyrite: A record of fluid chemistry and growth kinetics. Geology 47, 641-644.

Yang, W., Lin, Y.T., Zhang, J.C., Hao, J.L., Shen, W.J., Hu, S., 2012. Precise micrometre-sized Pb-Pb and U-Pb dating with NanoSIMS. Journal of Analytical Atomic Spectrometry 27, 479–487.

Yardley, S.S., Moore, K.L., Ni, N., Wei, J.F., Lyon, S., Preuss, M., Lozano-Perez, S., Grovenor, C.R., 2013. An investigation of the oxidation behavior of zirconium alloys using isotopic tracers and high resolution SIMS. Journal of Nuclear Materials 443, 436–443.

Zhang, J., Lin, Y., Yang, W., Shen, W., Hao, J., Hu, S., Cao, M., 2014. Improved precision and spatial resolution of sulfur isotope analysis using NanoSIMS. Journal of Analytical Atomic Spectrometry 29, 1934–1943.

Zhang, T., Gregory, K., Hammack, R.W., Vidic, R.D., 2014. Co-precipitation of radium with barium and strontium sulfate and its impact on the fate of radium during treatment of produced water from unconventional gas extraction. Environmental Science & Technology 48, 4596-4603.

Zhang, Y., Lumpkin, G.R., Li, H., Blackford, M.G., Colella, M., Carter, M.L., Vance, E.R., 2006. Recrystallisation of amorphous natural brannerite through annealing: The effect of radiation damage on the chemical durability of brannerite. Journal of Nuclear Materials 350, 293-300.

Zikovsky, L., 1998. Precipitation and solubility of some polonium compounds. Journal of Radioanalytical and Nuclear Chemistry 227, 171-172.